



energies

Heat Transfer and Heat Recovery Systems

Edited by
Jan Danielewicz and Krzysztof Rajski
Printed Edition of the Special Issue Published in *Energies*

Heat Transfer and Heat Recovery Systems

Heat Transfer and Heat Recovery Systems

Editors

Jan Danielewicz
Krzysztof Rajski

MDPI • Basel • Beijing • Wuhan • Barcelona • Belgrade • Manchester • Tokyo • Cluj • Tianjin



Editors

Jan Danielewicz
Department of
Air-Conditioning, Heating,
Gas Engineering and Air
Protection
Wroclaw University of
Science and Technology
Wroclaw
Poland

Krzysztof Rajski
Department of
Air-Conditioning, Heating,
Gas Engineering and Air
Protection
Wroclaw University of
Science and Technology
Wroclaw
Poland

Editorial Office

MDPI
St. Alban-Anlage 66
4052 Basel, Switzerland

This is a reprint of articles from the Special Issue published online in the open access journal *Energies* (ISSN 1996-1073) (available at: www.mdpi.com/journal/energies/special_issues/Heat_Transfer_and_Heat_Recovery_Systems).

For citation purposes, cite each article independently as indicated on the article page online and as indicated below:

LastName, A.A.; LastName, B.B.; LastName, C.C. Article Title. <i>Journal Name</i> Year , Volume Number, Page Range.
--

ISBN 978-3-0365-7369-4 (Hbk)

ISBN 978-3-0365-7368-7 (PDF)

© 2023 by the authors. Articles in this book are Open Access and distributed under the Creative Commons Attribution (CC BY) license, which allows users to download, copy and build upon published articles, as long as the author and publisher are properly credited, which ensures maximum dissemination and a wider impact of our publications.

The book as a whole is distributed by MDPI under the terms and conditions of the Creative Commons license CC BY-NC-ND.

Contents

Preface to “Heat Transfer and Heat Recovery Systems”	vii
Krzysztof Rajski and Jan Danielewicz Heat Transfer and Heat Recovery Systems Reprinted from: <i>Energies</i> 2023 , <i>16</i> , 3258, doi:10.3390/en16073258	1
Taha Baig, Zabdur Rehman, Hussain Ahmed Tariq, Shehryar Manzoor, Majid Ali and Abdul Wadood et al. Thermal Performance Investigation of Slotted Fin Minichannel Heat Sink for Microprocessor Cooling Reprinted from: <i>Energies</i> 2021 , <i>14</i> , 6347, doi:10.3390/en14196347	7
Zhen Zhao, Liang Xu, Jianmin Gao, Lei Xi, Qicheng Ruan and Yunlong Li Multi-Objective Optimization of Parameters of Channels with Staggered Frustum of a Cone Based on Response Surface Methodology Reprinted from: <i>Energies</i> 2022 , <i>15</i> , 1240, doi:10.3390/en15031240	23
Borys Basok, Vyacheslav Kremnev, Anatoliy Pavlenko and Andriy Timoshchenko Aerodynamics and Complicated Heat Transfer with the Mixed Motion of Air in the Flat Duct of a High-Temperature Heat Exchanger Reprinted from: <i>Energies</i> 2022 , <i>15</i> , 865, doi:10.3390/en15030865	43
Marcin Łecki, Dariusz Andrzejewski, Artur N. Gutkowski and Grzegorz Górecki Study of the Influence of the Lack of Contact in Plate and Fin and Tube Heat Exchanger on Heat Transfer Efficiency under Periodic Flow Conditions Reprinted from: <i>Energies</i> 2021 , <i>14</i> , 3779, doi:10.3390/en14133779	61
Anatoliy M. Pavlenko and Hanna Koshlak Application of Thermal and Cavitation Effects for Heat and Mass Transfer Process Intensification in Multicomponent Liquid Media Reprinted from: <i>Energies</i> 2021 , <i>14</i> , 7996, doi:10.3390/en14237996	87
Xander van Heule, Michel De Paepe and Steven Lecompte Two-Phase Volumetric Expanders: A Review of the State-of-the-Art Reprinted from: <i>Energies</i> 2022 , <i>15</i> , 4991, doi:10.3390/en15144991	107
Jie Liu, Sung-Chul Kim and Ki-Yeol Shin Feasibility Study and Economic Analysis of a Fuel-Cell-Based CHP System for a Comprehensive Sports Center with an Indoor Swimming Pool Reprinted from: <i>Energies</i> 2021 , <i>14</i> , 6625, doi:10.3390/en14206625	121
Ramin Manouchehri and Michael R. Collins Investigating the Impact of Plumbing Configuration on Energy Savings for Falling-Film Drain Water Heat Recovery Systems Reprinted from: <i>Energies</i> 2022 , <i>15</i> , 1141, doi:10.3390/en15031141	143
Leyla Amiri, Edris Madadian, Navid Bahrani and Seyed Ali Ghoreishi-Madiseh Techno-Economic Analysis of Waste Heat Utilization in Data Centers: Application of Absorption Chiller Systems Reprinted from: <i>Energies</i> 2021 , <i>14</i> , 2433, doi:10.3390/en14092433	157

Adnan Ayaz, Faraz Ahmad, Mohammad Abdul Aziz Irfan, Zabdur Rehman, Krzysztof Rajski and Jan Danielewicz Comparison of Ground-Based Global Horizontal Irradiance and Direct Normal Irradiance with Satellite-Based SUNY Model Reprinted from: <i>Energies</i> 2022 , <i>15</i> , 2528, doi:10.3390/en15072528	169
Hadeed Ashraf, Muhammad Sultan, Redmond R. Shamshiri, Farrukh Abbas, Muhammad Farooq and Uzair Sajjad et al. Dynamic Evaluation of Desiccant Dehumidification Evaporative Cooling Options for Greenhouse Air-Conditioning Application in Multan (Pakistan) Reprinted from: <i>Energies</i> 2021 , <i>14</i> , 1097, doi:10.3390/en14041097	183
Adriana Greco, Edison Gundabattini, Darius Gnanaraj Solomon, Raja Singh Rassiah and Claudia Masselli A Review on Geothermal Renewable Energy Systems for Eco-Friendly Air-Conditioning Reprinted from: <i>Energies</i> 2022 , <i>15</i> , 5519, doi:10.3390/en15155519	205
Piotr Michalak Impact of Air Density Variation on a Simulated Earth-to-Air Heat Exchanger's Performance Reprinted from: <i>Energies</i> 2022 , <i>15</i> , 3215, doi:10.3390/en15093215	223
Łukasz Amanowicz Peak Power of Heat Source for Domestic Hot Water Preparation (DHW) for Residential Estate in Poland as a Representative Case Study for the Climate of Central Europe Reprinted from: <i>Energies</i> 2021 , <i>14</i> , 8047, doi:10.3390/en14238047	247
Mirosław Zukowski and Walery Jezierski New Deterministic Mathematical Model for Estimating the Useful Energy Output of a Medium-Sized Solar Domestic Hot Water System Reprinted from: <i>Energies</i> 2021 , <i>14</i> , 2753, doi:10.3390/en14102753	263
Agnieszka Żelazna and Justyna Gołebiowska Designing for the Environment: An Example of Multi-Criteria Analysis Used for Solar Hot Water System Selection Reprinted from: <i>Energies</i> 2021 , <i>15</i> , 65, doi:10.3390/en15010065	281

Preface to “Heat Transfer and Heat Recovery Systems”

In the domain of modern engineering, heat transfer is universally present, playing a vital role in boosting the efficiency of energy conversion systems. The mechanisms of heat transfer are primarily responsible for determining the efficiency and overall performance of these energy conversion processes. Thus, a profound understanding of these mechanisms is crucial for cultivating sustainable and efficient energy management practices.

Moreover, the retrieval of waste heat is considered the leading approach to achieving sustainable energy management by reducing energy consumption. The capturing and recycling of waste heat from various sources is an increasingly popular strategy for enhancing energy efficiency. Waste heat recovery technologies are progressively adopted in numerous industrial processes, enabling the repurposing of heat that would have otherwise been lost. This approach holds significant potential in lowering energy consumption and greenhouse gas emissions, promoting sustainable energy management.

This reprint aims to highlight the latest advancements in heat transfer technology and heat recovery systems for sustainable development. Although heat recovery systems have received considerable attention, a persistent demand for innovative solutions to address challenges in this field remains. An extensive analysis of the chapters in this reprint reveals four primary categories that represent the majority of the content: heat transfer and heat exchangers, heat recovery, renewables, and domestic hot water preparation systems.

Jan Danielewicz and Krzysztof Rajski

Editors

Heat Transfer and Heat Recovery Systems

Krzysztof Rajski * and Jan Danielewicz

Faculty of Environmental Engineering, Wrocław University of Science and Technology, 50-377 Wrocław, Poland
* Correspondence: krzysztof.rajski@pwr.edu.pl

1. Introduction

Heat transfer is present in all modern engineering applications and plays a fundamental role in improving the efficiency of energy conversion systems. Within these systems, the efficiency and overall performance of various energy conversion processes are predominantly determined by the mechanisms of heat transfer. Hence, a comprehensive understanding of these mechanisms is essential for the development of sustainable and efficient energy management practices.

In addition, the mitigation of energy consumption via the retrieval of waste heat is deemed as the predominant course of action towards accomplishing sustainable energy management. One promising strategy to improve energy efficiency is to capture and recycle waste heat from different sources. Waste heat recovery technologies have been increasingly adopted in several industrial processes to retrieve and repurpose heat that would otherwise be lost to the surroundings. This approach holds immense potential in reducing energy consumption and greenhouse gas emissions, thereby promoting sustainable energy management.

The goal of this Special Issue is to showcase the latest developments in the field of heat transfer technology and heat recovery systems that promote sustainable development. While considerable attention has been paid to heat recovery systems, there remains a persistent demand for innovative solutions to address the vast array of challenges in this field. Therefore, this Special Issue endeavors to emphasize and provide novel solutions for these challenges.

2. A Review of the Contributions in This Issue

A word cloud has been created to offer a more comprehensive grasp of the content featured in the Special Issue, as depicted in Figure 1. This figure presents a visual representation of the frequently used words in the titles and abstracts of the published research papers, revealing insights into the key topics explored in this collection. Upon conducting a thorough examination of the articles featured in this Special Issue, four primary categories that encapsulate the majority of the content were identified. These categories consist of heat transfer and heat exchangers, heat recovery, renewables, and domestic hot water preparation systems.

2.1. Heat Transfer and Heat Exchangers

Baig et al. investigated a slotted fin minichannel heat sink (SFMCHS) to manage high heat flux generated in microprocessors [1]. The SFMCHS was developed by modifying a conventional straight integral fin minichannel heat sink (SIFMCHS). The study numerically compared SFMCHSs with fin spacings of 0.5 mm, 1 mm, and 1.5 mm with SIFMCHSs. Two slots per fin minichannel heat sink (SPFMCHS) reduced the base temperature by 9.20%, 8.74%, and 7.39% for 0.5 mm, 1 mm, and 1.5 mm fin spacings, respectively, compared to SIFMCHSs. The 0.5 mm-spaced SPFMCHS had better heat transfer performance compared to 1 mm and 1.5 mm fin spacings, with a uniform temperature distribution at the heat sink base observed in all cases.

Citation: Rajski, K.; Danielewicz, J. Heat Transfer and Heat Recovery Systems. *Energies* **2023**, *16*, 3258. <https://doi.org/10.3390/en16073258>

Received: 3 April 2023
Accepted: 4 April 2023
Published: 5 April 2023



Copyright: © 2023 by the authors. Licensee MDPI, Basel, Switzerland. This article is an open access article distributed under the terms and conditions of the Creative Commons Attribution (CC BY) license (<https://creativecommons.org/licenses/by/4.0/>).

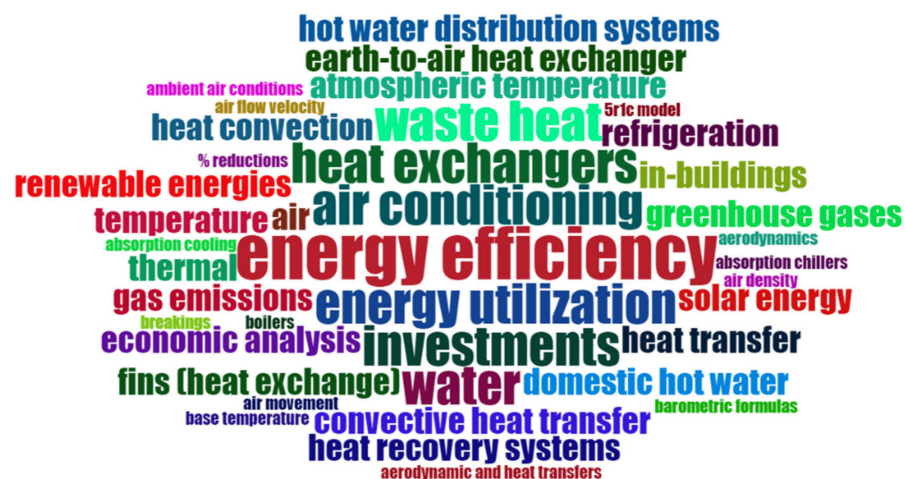


Figure 1. A word-cloud created from the articles published in the Special Issue.

Zhao et al. aimed to optimize the flow and heat transfer performance of channels with frustums of a cone by using Response Surface Methodology (RSM) and multi-objective genetic algorithm [2]. Central composite face-centered design (CCF) was used for the experimental design of channel parameters, and response surface models were constructed. The sensitivity of the channel parameters was analyzed using Sobol's method. Four optimized channels were selected from the Pareto solution set. The response surface models had high accuracy with an RSME of less than 0.25 and R^2 of greater than 0.93.

Basok et al. analyzed the heat transfer and aerodynamics in a high-temperature recuperation system's duct [3]. The research involved a flat duct with a thickness-to-height ratio of 1:10, length of 400a, and one-sided heat input, and mixed air movement. The objective was to determine the average temperatures, air temperature distribution, and heat flow densities along with the heat exchange coefficients and Nusselt numbers. The research method comprised mathematical numerical experimentation and physical modeling. The results showed a difference in the intensity of convective heat transfer between the hot and non-heated surfaces of the duct. The findings suggest that the resistance of the boundary layer in high-temperature heat exchangers and recuperation systems will not exceed 10% of the total pressure losses in the system.

Moreover, the use of plate fin-tube heat exchangers is prevalent in various industries, including air conditioning and refrigeration systems. However, during the manufacturing process, errors can lead to the formation of an air gap between the tube and fin. The effect of the air gap on heat transfer was studied by Łęcki et al. [4] using numerical simulations for a symmetric section of the heat exchanger under periodic flow conditions. The results showed that the fin discontinuity along the circumference reduces the heat transfer rate compared to the perfect fin-tube contact case. The location and size of the gap also affect heat transfer, with the rear gap position being the worst scenario. Reversing the flow direction can lead to up to a 15% increase in heat transfer, especially if the rear gaps are present.

Pavlenko and Koshlak discussed the dynamic interaction between boiling particles in an emulsion, which leads to droplet breakup [5]. They analyzed the forces that determine the breaking of non-boiling and boiling droplets and determine the displacement, deformation, and fragmentation of the dispersed phase. They also studied the dynamics of bubbles in a compressible liquid with consideration for interfacial heat and mass transfer and the effect of standard and system parameters on cavitation processes. The study proposed a new method to assess dynamic effects, which considers all determining factors and accurately represents thermophysical system parameters. The method was validated using superheated emulsion boiling with a sharp decrease in pressure. This study should be considered as the initial stage of rational designs and optimal operating modes of cavitating devices for solving various technological problems.

The process of two-phase expansion, where a fluid undergoes a pressure drop in the liquid-vapor dome, is gaining interest for various processes, especially in low-temperature two-phase heat-to-power cycles. However, modeling and understanding the phenomena in volumetric two-phase expanders are still limited. This topic was reviewed by van Heule et al. [6]. While screw expanders can be modeled using the homogeneous equilibrium model, reciprocating expanders require further investigation. The boiling delay model and homogeneous relaxation model are promising techniques, but more research is needed to apply them. More experimental data on different expander types is also required to understand the impact of design parameters. The review provided a comprehensive overview of available data and modeling techniques, but more research is necessary to achieve efficient volumetric expansion machines.

2.2. Heat Recovery

Liu et al. analyzed the potential of a combined heat and power (CHP) system for heating a building with an indoor swimming pool in Korea, which traditionally uses boilers and heat storage tanks that emit greenhouse gases [7]. The CHP system uses electricity and waste heat from a Phosphoric Acid Fuel Cell (PAFC) system and was analyzed for energy savings, CO₂ reduction, efficiency, and economic feasibility. A dynamic simulation model was developed, and results showed that the CHP system can save up to 15% of energy compared to the conventional heating system, and the FTO model presents the highest efficiency and CO₂ reduction. The FTO model also presents a better economic feasibility than the ELT model.

Manouchehri and Collins validated a model that can predict the performance of drain water heat recovery (DWHR) systems, which are used in residential buildings to recover energy from greywater [8]. The model was implemented into software to perform energy simulations and analyze the impact of different plumbing configurations on energy savings. The study found that the plumbing configuration significantly affects the energy savings expected from DWHR heat exchangers, with the greatest savings achieved in equal-flow configurations. However, the mains temperature could dictate which configuration provides higher energy savings, and designers should consider this when implementing a DWHR heat exchanger. Manufacturers are encouraged to adjust the coil diameter to improve heat transfer rates and increase energy savings when equal flow rates through the heat exchanger are not possible.

The low-grade waste heat generated by data centers is difficult to recover due to its decentralized and low-quality nature, making it a challenge to maximize energy efficiency and utilize heat recovery. However, absorption chiller systems are a promising solution for this issue. In the study by Amiri et al. [9], the feasibility of using an absorption chiller system for waste heat recovery from data centers was analyzed. The proposed system could save 4.3 GWh/year and 13.0 GWh/year of electricity, resulting in a reduction of 3068 and 9208 tons of CO₂ equivalent greenhouse gas emissions annually. The payback period for investors was estimated to be 2.76 and 2.56 years for a 4.5 MW and 13.5 MW data center, respectively. The study highlights the need to consider technical and economic aspects simultaneously. Future research could focus on employing higher-performance absorbers and generators to enhance the capacity of the absorption chiller system.

2.3. Renewables

The depletion of fossil reserves has led to a shift towards renewable energy sources, particularly solar power plants. However, the construction of these plants requires a feasibility study to estimate the solar potential in a particular region. Ayaz et al. [10] compared ground-based measurements of global horizontal irradiance (GHI) and direct normal irradiance (DNI) in Peshawar, Pakistan, with satellite-based model SUNY. The data revealed a significant difference between the two, with maximum differences of 42.90% for GHI and 55.86% for DNI. The study recommends establishing more ground measurement stations across the country to assess solar resources more accurately. It

also recommends future studies in different locations with longer time series data. The difference between satellite and ground-based measurements is considerable, and relying solely on satellite-modeled data is not recommended for establishing solar energy programs in Pakistan. Real-time ground measurements are necessary for accurate estimates of solar energy resources.

The feasibility of a desiccant dehumidification-based Maisotsenko cycle evaporative cooling (M-DAC) system for greenhouse air-conditioning in Multan, Pakistan was investigated by Ashraf et al. [11]. Traditional cooling methods were deemed unsuitable for greenhouse production due to their high energy costs and inability to provide an optimum microclimate. The M-DAC system was proposed as an alternative solution. The study aimed to evaluate the system's thermodynamic performance in relation to temperature gradient, relative humidity, vapor pressure deficit (VPD), and dehumidification gradient. Results showed that the M-DAC system achieved a maximum air temperature gradient of 21.9 °C at 39.2 °C ambient air conditions, which was considered optimal for most greenhouse crops. The system also created a dehumidification gradient of 16.8 g/kg at 24 g/kg ambient air conditions, which was within the optimum humidity range for greenhouse growing conditions.

Air conditioning is responsible for consuming around one-fifth of the total power used in buildings worldwide. To reduce energy consumption and its impact on the environment, Earth-to-Air Heat exChangers (EAHX) are being utilized. Greco et al. reviewed the different applications and peculiarities of EAHX and focused on the hybrid applications where EAHXs are coupled with advanced systems [12]. An IoT-based EAHX control system was proposed to optimize energy efficiency and thermal comfort under different operating conditions. EAHXs utilize geothermal energy, which is renewable and sustainable, and do not emit greenhouse gases. Different parameters such as pipe diameter, length of pipe, and number of pipes affect the performance of EAHX. EAHXs are effective in heating the air during winter and cooling it during summer. Hybrid EAHX systems based on Phase-Change Materials and an Air-Source Heat Pump, finned vertical solar chimney, and placed upstream of air conditioning systems' AHU can achieve improvements in terms of energy performance and reduce greenhouse gas emissions.

Michalak analyzed the impact of air density variation on the operation of earth-to-air heat exchangers (EAHE) coupled with the ventilation system of a residential building [13]. The analysis took into account air density variation with ambient air temperature as Polish hourly typical meteorological years do not contain atmospheric pressure. The energy use for space heating and cooling was computed using the 5R1C thermal network model of EN ISO 13790. Depending on the chosen method, a reduction in annual heating and cooling needs of 7.5% to 8.8% in heating and from 15.3% to 19% in cooling was obtained. The study shows the need to include atmospheric pressure in typical Polish meteorological years and indicates the need for future consideration about an assessment of air humidity impact on the simulated EAHE performance.

2.4. Domestic Hot Water Preparation Systems

A comparison of various methods for calculating the peak power required for domestic hot water (DHW) preparation in buildings was presented by Amanowicz [14]. The study highlighted that DHW has become an important component of energy consumption in buildings, and its peak power can be as high as that required for heating and ventilation. This makes it necessary to select the correct peak power of the heat source, particularly when using renewable energy sources, as it affects the size, investment cost, and economic efficiency of the system. The study showed that accumulative systems with hot water storage tanks are more suitable for modern buildings as they are less sensitive to design errors and result in acceptable peak power for DHW.

Żukowski and Jeziński used a mathematical approach to investigate the impact of various factors on the thermal performance of solar domestic hot water (SDHW) systems in different European climates [15]. They created three deterministic mathematical models

using data from computer simulations of SDHW systems in Madrid, Budapest, and Helsinki. The models consider the influence of five factors: volume of heat storage tanks, solar collector total area, maximum efficiency, heat loss coefficient of solar collector, and daily consumption of DHW on the annual useful energy output. The results of the optimization procedure indicate that the maximum annual useful energy output is 1303 kWh/m² for Madrid, 918.5 kWh/m² for Budapest, and 768 kWh/m² for Helsinki.

Żelazna and Gołębiowska proposed a multi-criteria analysis for selecting system parameters such as collector type and solar tank volume [16]. A model of the SHW system was used to calculate possible solutions, ensuring the same comfort of usage for several design options. Three indicators, Simple Payback Time (SPBT), Primary Energy consumption (PE), and IMPACT 2002+, were calculated for the analyzed model. The most favorable solution included a heat-pipe-evacuated tube collector, copper pipes, and a 200 dm³ water tank. The multi-criteria analysis can be used as a tool for the optimization of selection in the green designing process, significantly improving the environmental balance of analyzed technologies.

3. Conclusions

The heat transfer and heat exchangers category of the Special Issue discusses the development of new heat sink designs and the optimization of existing heat exchangers to improve the efficiency of heat transfer mechanisms in various industrial processes. The heat recovery category highlights the importance of capturing and recycling waste heat from different sources to reduce energy consumption and greenhouse gas emissions. The studies examine combined heat and power systems, acid fuel cells, and drain water heat recovery systems in residential and commercial buildings. The renewables category explores the use of renewable energy sources such as solar thermal energy, biomass, and geothermal energy to provide sustainable energy solutions. The domestic hot water preparation systems category focuses on developing efficient water heating systems for residential buildings. The studies emphasize the importance of reducing energy consumption in water heating processes and developing sustainable solutions.

The articles in this Special Issue provide innovative solutions to address the challenges in heat transfer technology and heat recovery systems, promoting sustainable development and energy efficiency. These solutions can be applied in various settings to improve energy management practices and reduce greenhouse gas emissions.

Author Contributions: Conceptualization, K.R.; writing—original draft preparation, K.R.; writing—review and editing, K.R. and J.D. All authors have read and agreed to the published version of the manuscript.

Data Availability Statement: Data are contained within the article.

Conflicts of Interest: The authors declare no conflict of interest.

References

1. Baig, T.; Rehman, Z.; Tariq, H.A.; Manzoor, S.; Ali, M.; Wadood, A.; Rajski, K.; Park, H. Thermal Performance Investigation of Slotted Fin Minichannel Heat Sink for Microprocessor Cooling. *Energies* **2021**, *14*, 6347. [CrossRef]
2. Zhao, Z.; Xu, L.; Gao, J.; Xi, L.; Ruan, Q.; Li, Y. Multi-Objective Optimization of Parameters of Channels with Staggered Frustum of a Cone Based on Response Surface Methodology. *Energies* **2022**, *15*, 1240. [CrossRef]
3. Basok, B.; Kremnev, V.; Pavlenko, A.; Timoshchenko, A. Aerodynamics and Complicated Heat Transfer with the Mixed Motion of Air in the Flat Duct of a High-Temperature Heat Exchanger. *Energies* **2022**, *15*, 865. [CrossRef]
4. Łęcki, M.; Andrzejewski, D.; Gutkowski, A.N.; Górecki, G. Study of the Influence of the Lack of Contact in Plate and Fin and Tube Heat Exchanger on Heat Transfer Efficiency under Periodic Flow Conditions. *Energies* **2021**, *14*, 3779. [CrossRef]
5. Pavlenko, A.M.; Koshlak, H. Application of Thermal and Cavitation Effects for Heat and Mass Transfer Process Intensification in Multicomponent Liquid Media. *Energies* **2021**, *14*, 7996. [CrossRef]
6. Van Heule, X.; de Paepe, M.; Lecompte, S. Two-Phase Volumetric Expanders: A Review of the State-of-the-Art. *Energies* **2022**, *15*, 4991. [CrossRef]
7. Liu, J.; Kim, S.-C.; Shin, K.-Y. Feasibility Study and Economic Analysis of a Fuel-Cell-Based CHP System for a Comprehensive Sports Center with an Indoor Swimming Pool. *Energies* **2021**, *14*, 6625. [CrossRef]

8. Manouchehri, R.; Collins, M.R. Investigating the Impact of Plumbing Configuration on Energy Savings for Falling-Film Drain Water Heat Recovery Systems. *Energies* **2022**, *15*, 1141. [CrossRef]
9. Amiri, L.; Madadian, E.; Bahrani, N.; Ghoreishi-Madiseh, S.A. Techno-Economic Analysis of Waste Heat Utilization in Data Centers: Application of Absorption Chiller Systems. *Energies* **2021**, *14*, 2433. [CrossRef]
10. Ayaz, A.; Ahmad, F.; Irfan, M.A.A.; Rehman, Z.; Rajska, K.; Danielewicz, J. Comparison of Ground-Based Global Horizontal Irradiance and Direct Normal Irradiance with Satellite-Based SUNY Model. *Energies* **2022**, *15*, 2528. [CrossRef]
11. Ashraf, H.; Sultan, M.; Shamshiri, R.R.; Abbas, F.; Farooq, M.; Sajjad, U.; Md-Tahir, H.; Mahmood, M.H.; Ahmad, F.; Taseer, Y.R.; et al. Dynamic Evaluation of Desiccant Dehumidification Evaporative Cooling Options for Greenhouse Air-Conditioning Application in Multan (Pakistan). *Energies* **2021**, *14*, 1097. [CrossRef]
12. Greco, A.; Gundabattini, E.; Solomon, D.G.; Singh Rassiah, R.; Masselli, C. A Review on Geothermal Renewable Energy Systems for Eco-Friendly Air-Conditioning. *Energies* **2022**, *15*, 5519. [CrossRef]
13. Michalak, P. Impact of Air Density Variation on a Simulated Earth-to-Air Heat Exchanger's Performance. *Energies* **2022**, *15*, 3215. [CrossRef]
14. Amanowicz, Ł. Peak Power of Heat Source for Domestic Hot Water Preparation (DHW) for Residential Estate in Poland as a Representative Case Study for the Climate of Central Europe. *Energies* **2021**, *14*, 8047. [CrossRef]
15. Zukowski, M.; Jezierski, W. New Deterministic Mathematical Model for Estimating the Useful Energy Output of a Medium-Sized Solar Domestic Hot Water System. *Energies* **2021**, *14*, 2753. [CrossRef]
16. Żelazna, A.; Gołębiowska, J. Designing for the Environment: An Example of Multi-Criteria Analysis Used for Solar Hot Water System Selection. *Energies* **2021**, *15*, 65. [CrossRef]

Disclaimer/Publisher's Note: The statements, opinions and data contained in all publications are solely those of the individual author(s) and contributor(s) and not of MDPI and/or the editor(s). MDPI and/or the editor(s) disclaim responsibility for any injury to people or property resulting from any ideas, methods, instructions or products referred to in the content.

Article

Thermal Performance Investigation of Slotted Fin Minichannel Heat Sink for Microprocessor Cooling

Taha Baig^{1,2}, Zabdur Rehman^{3,*}, Hussain Ahmed Tariq⁴, Shehryar Manzoor², Majid Ali¹, Abdul Wadood⁵, Krzysztof Rajski⁶ and Herie Park^{7,*}

- ¹ Department of Mechanical Engineering, Wah Engineering College, University of Wah, Wah Cantt 47040, Pakistan; taha.baig@wecuw.edu.pk (T.B.); majidmaju995@gmail.com (M.A.)
- ² Department of Mechanical Engineering, University of Engineering and Technology Taxila, Taxila 47080, Pakistan; m.shehryar@uettaxila.edu.pk
- ³ Department of Mechanical Engineering, Air University Islamabad, Aerospace and Aviation Campus, Kamra 43570, Pakistan
- ⁴ Department of Mechanical Engineering, Institute of Space Technology, Islamabad 44000, Pakistan; ahmedtariq90@gmail.com
- ⁵ Department of Electrical Engineering, Air University Islamabad, Aerospace and Aviation Campus, Kamra 43570, Pakistan; wadood@au.edu.pk
- ⁶ Faculty of Environmental Engineering, Wrocław University of Science and Technology, 50-370 Wrocław, Poland; krzysztof.rajski@pwr.edu.pl
- ⁷ Department of Electrical Engineering, Dong-A University, Busan 49315, Korea
- * Correspondence: zabd@aack.au.edu.pk (Z.R.); park.herie@gmail.com (H.P.)

Citation: Baig, T.; Rehman, Z.; Tariq, H.A.; Manzoor, S.; Ali, M.; Wadood, A.; Rajski, K.; Park, H. Thermal Performance Investigation of Slotted Fin Minichannel Heat Sink for Microprocessor Cooling. *Energies* **2021**, *14*, 6347. <https://doi.org/10.3390/en14196347>

Academic Editor: Marco Marengo

Received: 24 August 2021

Accepted: 29 September 2021

Published: 4 October 2021

Publisher's Note: MDPI stays neutral with regard to jurisdictional claims in published maps and institutional affiliations.

Abstract: Due to high heat flux generation inside microprocessors, water-cooled heat sinks have gained special attention. For the durability of the microprocessor, this generated flux should be effectively removed. The effective thermal management of high-processing devices is now becoming popular due to high heat flux generation. Heat removal plays a significant role in the longer operation and better performance of heat sinks. In this work, to tackle the heat generation issues, a slotted fin minichannel heat sink (SFMCHS) was investigated by modifying a conventional straight integral fin minichannel heat sink (SIFMCHS). SFMCHSs with fin spacings of 0.5 mm, 1 mm, and 1.5 mm were numerically studied. The numerical results were then compared with SIFMCHSs present in the literature. The base temperatures recorded for two slots per fin minichannel heat sink (SPFMCHS), with 0.5 mm, 1 mm, and 1.5 mm fin spacings, were 42.81 °C, 46.36 °C, and 48.86 °C, respectively, at 1 LPM. The reductions in base temperature achieved with two SPFMCHSs were 9.20%, 8.74%, and 7.39% for 0.5 mm, 1 mm, and 1.5 mm fin spacings, respectively, as compared to SIFMCHSs reported in the literature. The reductions in base temperature noted for three SPFMCHSs were 8.53%, 9.05%, and 5.95% for 0.5 mm, 1 mm, and 1.5 mm fin spacings, respectively, at 1 LPM, as compared to SIFMCHSs reported in the literature. In terms of heat transfer performance, the base temperature and thermal resistance of the 0.5 mm-spaced SPFMCHS is better compared to 1 mm and 1.5 mm fin spacings. The uniform temperature distribution at the base of the heat sink was observed in all cases solved in current work.

Keywords: slotted fin minichannel heat sink; base temperature; thermal management; numerical simulation



Copyright: © 2021 by the authors. Licensee MDPI, Basel, Switzerland. This article is an open access article distributed under the terms and conditions of the Creative Commons Attribution (CC BY) license (<https://creativecommons.org/licenses/by/4.0/>).

1. Introduction

With the rapid development in the information technology sector, the thermal management of electronic devices is becoming essential due to the high generation of heat flux. The world is advancing rapidly towards compact devices; however, this presents the challenging task of the effective and timely removal of unwanted heat. Therefore, this problem has attracted many researchers to create efficient cooling techniques while avoiding any losses in functioning of the devices. The heat transfer can be increased either by enhancing the thermal physical properties of ordinary fluid or by optimizing the heat

sink surface to volume ratio. Previously, air was used for the removal of heat from the electronic devices, but it is now unable to remove high heat fluxes. Therefore, attention is now being focused upon liquid cooling techniques, due to their higher efficiency when compared to air.

Saeed and Kim [1] numerically investigated the thermal performance of a water-cooled straight fin minichannel heat sink with varying fin spacings, fin thicknesses, and fin heights. In 1981, Tuckerman and Pease [2], for the first time, circulated water directly through a microchannel. Huang et al. [3] numerically investigated the thermal performance of parallel, staggered, and trapezoidal stagger slotted microchannel heat sinks. Knight et al. [4] proposed a scheme to optimize the geometry of microchannels in both turbulent and laminar regions. Gawali et al. [5] used a straight microchannel heat sink to absorb a large quantity of heat. Wang et al. [6] suggested a numerical model to examine the thermal performance of a microchannel heat sink. They optimized the channel number, channel aspect ratio under a fixed pressure drop, volume flow rate, and pumping power. Hung et al. [7] investigated the thermal performance of a porous microchannel heat sink with rectangular, block, trapezoidal, thin rectangular, and sandwich distributions. Gunnasegaran et al. [8] studied the different geometrical effect on microchannel heat sinks. They found a high heat transfer coefficient using a rectangular shape followed by a trapezoidal and a triangular shape. Qu et al. [9] performed an experimental study on heat transfer enhancement in a trapezoidal silicon microchannel. Kumar and Singh [10] investigated pressure drop and heat transfer in a microchannel heat sink with a trapezoidal shape.

Minichannel heat sinks are popular due to lower pressure drops in comparison to microchannel heat sinks. Xie et al. [11] performed a numerical study for heat sinks with normal, mini, and microchannels with bottom dimensions of 20 mm × 20 mm, by using water as a coolant. Dixit and Gosh [12] performed an experimental study on minichannel heat sinks to investigate the thermal performance of diamond, offset, and straight heat sinks. They observed that the pressure drop for an offset minichannel is lower than in a diamond minichannel. Saini and Webb [13] found that an impinging flow can dissipate 94.4 W as compared to duct flow, which can dissipate 84 W. Naphon and Wiriyaart [14] studied the liquid cooling of a minichannel rectangular heat sink with and without a thermoelectric effect. They found that thermoelectric material has a great impact on CPU temperature, as well as on energy consumption. Saeed and Kim [15] performed both numerical and experimental studies on minichannel heat sinks with fin spacings of 0.5 mm, 1 mm, and 1.5 mm using Al₂O₃-H₂O nanofluids. Al-Taey et al. [16] investigated whether the CPU temperature has a direct relationship with the cooling fluid (water). They also noticed a direct relation of mass flow rate with heat transfer rate and Nusselt number but an inverse relation with thermal resistance. Yu et al. [17] performed both numerical and experimental studies to compare a plate fin heat sink with a plate-pin fin heat sink using air as a cooling fluid. Tariq et al. performed experimental and numerical studies to investigate the thermal performance of cellular structures using air [18], water [19], and nanofluids [20]. Valueva and Purdin [21] numerically investigated the effect of aspect ratio of a rectangular channel on pulsating flow dynamics. Valueva and Purdin [22] developed a numerical model for the heat exchange between stationary and pulsating laminar flow inside a rectangular channel.

Many interrupted fin geometries have reported achieving high heat transfer as compared to integral fin geometries. Khoshvaght-Aliabadi et al. [23] calculated the hydrothermal performance of plate and plate-pins in triangular, trapezoidal, and sinusoidal configuration in a minichannel. Rezaee et al. [24], in their numerical and experimental studies, evaluated the effects of variable pin length and longitudinal pitch in a pin-fin heat sink. Khoshvaght-Aliabadi et al. [25] found that the hydrothermal performance of an interrupted fin is higher as compared to integral fin geometry. Ali et al. [26], in their experimental and numerical studies, investigated the thermal performance of integral-fin and pin-fin heat sinks.

Many studies addressing the thermal performance of minichannel heat sinks can be found in the literature. However, work on minichannel slotted fin heat sinks using a numerical study is rare. In this study, the thermal performance of heat sinks with varying fin spacings of 0.5 mm, 1 mm, and 1.5 mm was numerically investigated. These fin spacings were selected from the literature, and these geometries were optimized by creating slots inside the heat sinks. These were named slotted per fin minichannel heat sink SPFMCHSs. These selected SPFMCHSs were then compared to the straight integral fin minichannel heat sink (SIFMCHS) present in the literature [1] using the same heating power of 325 W. In this study, the conventional SIFMCHS was replaced by a novel SPFMCHS, which had varying fin spacings. To the best of the authors' knowledge, none of the previously mentioned studies have reported the effect of slots and slot thickness in a minichannel heat sink with integral fin spacings of 0.5 mm, 1 mm, and 1.5 mm. Numerical simulations were performed using ANSYS Fluent as a solver. The Reynolds number range for this study was 1900, 2900, and 3800, respectively. Uniform temperature distribution was observed at the base of the heat sink. The selection of both the slot thickness and the number of slots was also discussed in detail.

2. Numerical Model

The problem of the conjugate heat transfer was solved numerically using ANSYS Fluent. Assumptions made in this study were as follows: incompressible flow, turbulent model (k-epsilon), no viscous heating, no inside heat generation, and the same thermal properties during the flow. Absolute velocity formulation was used, along with a pressure-based solver. For this study, transport equation K- ϵ , with realizable and standard wall functions, was used. Velocity and pressure coupling was controlled by a Semi-Implicit Method for Pressure-Linked Equations (SIMPLE). For pressure, a second-order spatial discretization scheme was used, while for the turbulent dissipation rate, turbulent kinetic energy, and discretization of momentum, a second order upwind scheme was used. The outlet was at zero gauge pressure. For the conjugate problem inside the solid region, velocities were zero everywhere [11,27]. The selected base temperature was 46.424 °C, and the inlet temperature was 27 °C. The following governing equations were used for the conservation of energy, mass, and momentum [28]. For validation, conventional SIFMCHSs with 1 mm spacing were solved numerically by applying the same methodology, and the results were then compared with the literature [1], as shown in Figure 1.

$$\frac{\partial}{\partial x_i}(qu_i) = 0 \quad (1)$$

$$\frac{\partial}{\partial x_i}(qu_iu_j) = -\frac{\partial p}{\partial x_j} + \frac{\partial}{\partial x_i} \left[(\mu + \mu_t) \frac{\partial u_j}{\partial x_i} \right] + \frac{\partial}{\partial x_i} \left[(\mu + \mu_t) \frac{\partial u_i}{\partial x_j} \right], j = 1, 2, 3 \quad (2)$$

$$\frac{\partial}{\partial x_i}(qu_iT) = \frac{\partial}{\partial x_i} \left[\left(\frac{\lambda}{c_p} + \frac{\mu_t}{\sigma_t} \right) \frac{\partial T}{\partial x_i} \right] \quad (3)$$

$$\frac{\partial}{\partial x_i}(qku_i) = \frac{\partial}{\partial x_i} \left[\left(\mu + \frac{\mu_t}{\sigma_k} \right) \frac{\partial k}{\partial x_i} \right] + G_k - \rho\epsilon \quad (4)$$

$$\frac{\partial}{\partial x_i}(q\epsilon u_i) = \frac{\partial}{\partial x_i} \left[\left(\mu + \frac{\mu_t}{\sigma_\epsilon} \right) \frac{\partial \epsilon}{\partial x_i} \right] + \frac{\epsilon}{k} (c_1G_k - c_2\rho\epsilon) \quad (5)$$

where "k" is kinetic turbulence energy, " ϵ " is turbulence rate of dissipation and " G_k " is the generation of kinetic turbulence energy.

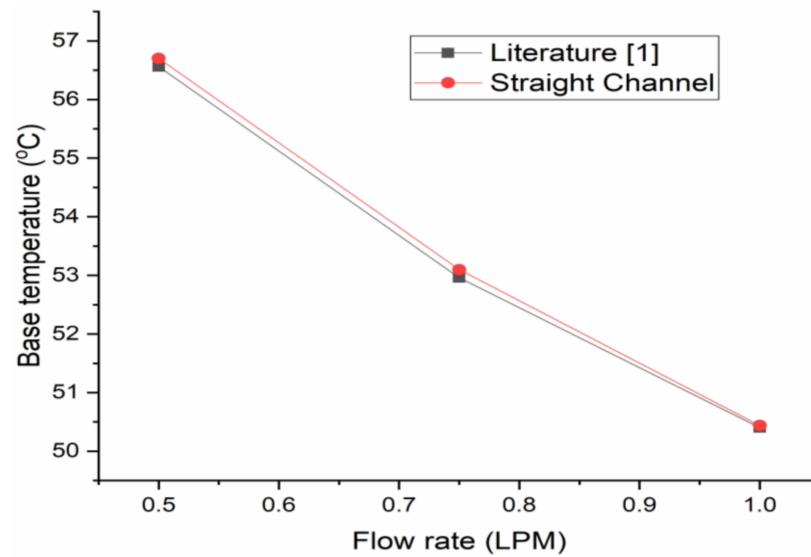


Figure 1. Validation of numerical model.

2.1. Boundary Condition

The following boundary conditions were used to solve the conjugate heat transfer problem:
No-slip conditions at the wall.

Uniform velocity was considered as the inlet of the heat sink

$$\text{At } y = h, u = 0, v = -U_{in}, w = 0 \quad (6)$$

Heat flux was provided at the bottom of the heat sink

$$\text{At } y = 0, -\lambda \frac{\partial T}{\partial y} = q \quad (7)$$

The right and left surface walls were considered as adiabatic.

$$\begin{aligned} \text{At } x = 0, \frac{\partial t}{\partial x} &= 0 \\ \text{At } x = w_s, \frac{\partial t}{\partial x} &= 0 \end{aligned} \quad (8)$$

The fluid inlet temperature was considered as constant

$$\text{At } y = h, T = T_i \quad (9)$$

2.2. Data Reduction

The following procedure was adopted for data evaluation. The removal of heat from the heat sink was calculated using Equation (6).

$$\dot{Q} = \dot{m}C_p(T_o - T_i) \quad (10)$$

The log of mean temperature difference can be calculated from Equation (7).

$$\text{LMTD} = \frac{(T_b - T_i) - (T_b - T_o)}{\ln\left(\frac{T_b - T_i}{T_b - T_o}\right)} \quad (11)$$

Thermal resistance of the heat sink was calculated using Equation (8).

$$R_{th} = \frac{\text{LMTD}}{\dot{Q}} \quad (12)$$

2.3. Independent Mesh Study

An intensive study was carried out to ensure that the solution is independent of the mesh. The mesh is considered independent when the temperature difference (between the maximum base temperature and the inlet temperature) shows less than 1% deviation as shown in Figure 2. Six cases with a different number of elements were examined, the number of elements being 2138709, 2358425, 2525411, 2700599, 2912432, and 3102635. The results obtained for case 5 and case 6 were very close to each other, showing a deviation of 0.3% in temperature difference. The number of elements for case 5 was used for the entire study to save computation time and memory.

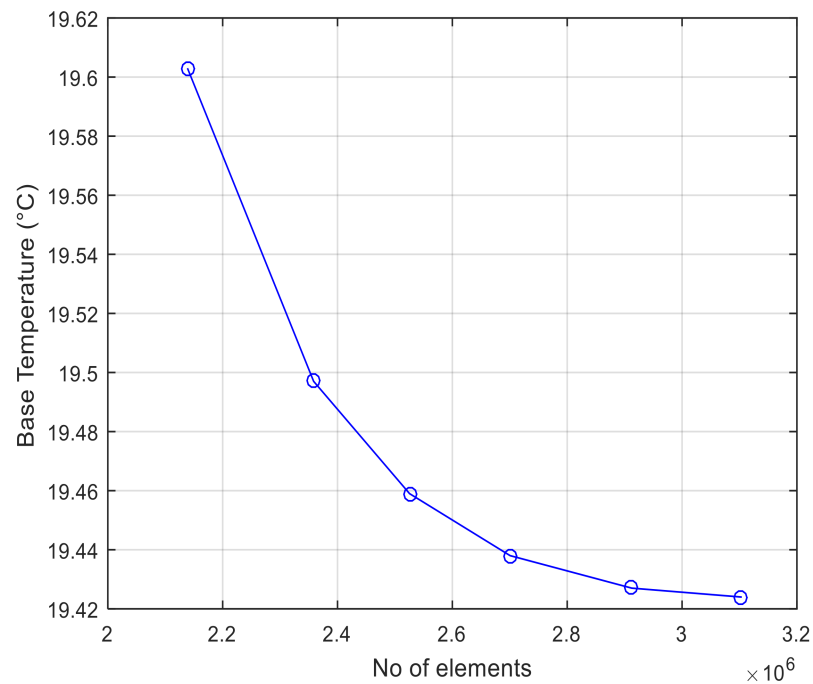


Figure 2. Temperature difference with number of elements.

2.4. Heat Sink

The heat sink was designed on an ANSYS Design Modeler. All of the heat sinks were modeled according to dimensions obtained in the literature [1]. A cubic chip was made at the bottom of the heat sink with dimensions of 28.7 mm \times 28.7 mm \times 0.5 mm in order to provide 325 W of heat. The dimensions of two SPFMCHSs with 1 mm fin spacing are shown in Figure 3. The details of all the cases solved in this numerical study are provided in Table 1. The isometric view of two SPFMCHSs, three SPFMCHSs, and SIFMCHSs, along with a co-ordinate axis, is shown in Figure 4. SIFMCHSs with varying fin spacings of 0.5 mm, 1 mm, and 1.5 mm are shown in Figure 5. The propagation of flow through two SPFMCHSs from the inlet to outlet is shown in Figure 6.

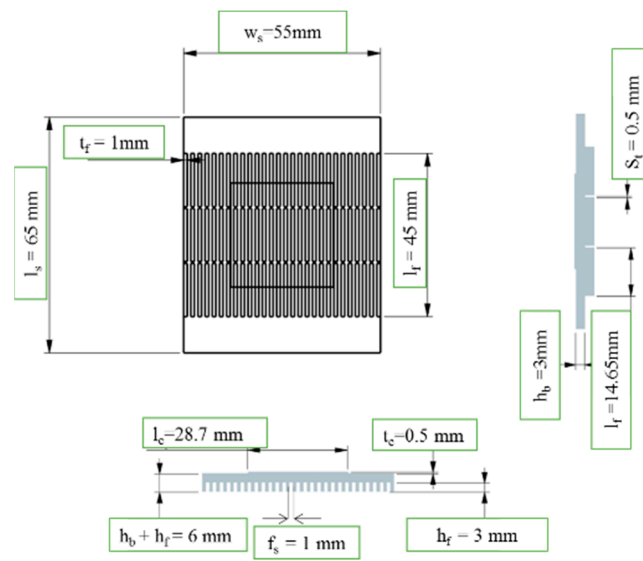


Figure 3. Dimensions of two SPFMCHSs with 1 mm fin spacing.

Table 1. Detail of cases solved with numerical simulations.

No. of Slots Per Fin	f_s (mm)	t_f (mm)	h_f (mm)	S_t (mm)
2	0.5	1	3	0.5
2	1	1	3	0.5
2	1.5	1	3	0.5
3	0.5	1	3	0.5
3	1	1	3	0.5
3	1.5	1	3	0.5

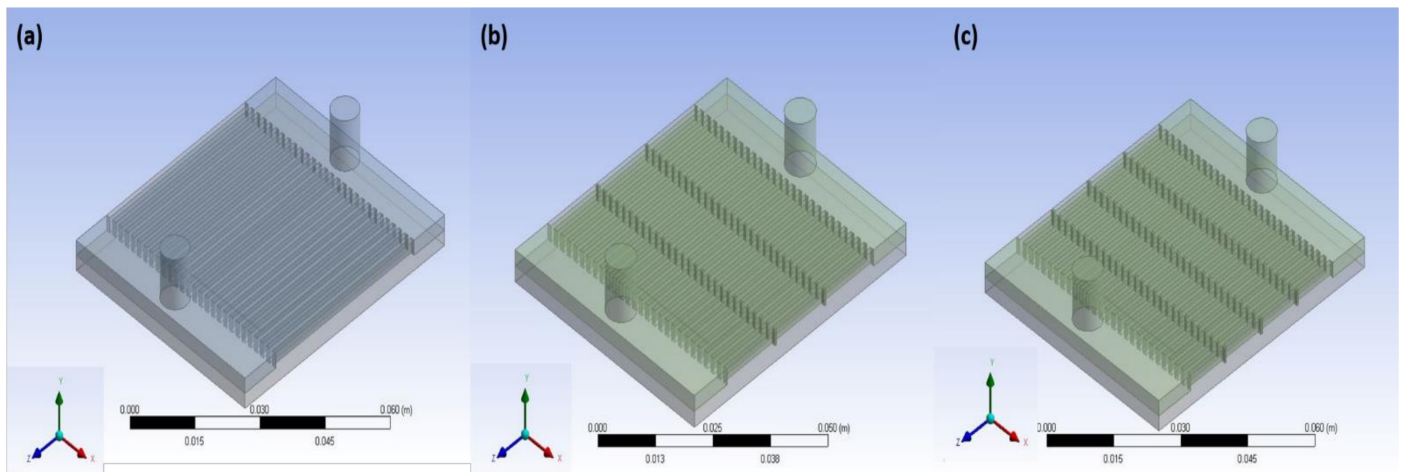


Figure 4. Isometric views for 0.5 mm fin spacing: (a) SIFMCHS [1], (b) two SPFMCHSs, and (c) three SPFMCHSs.

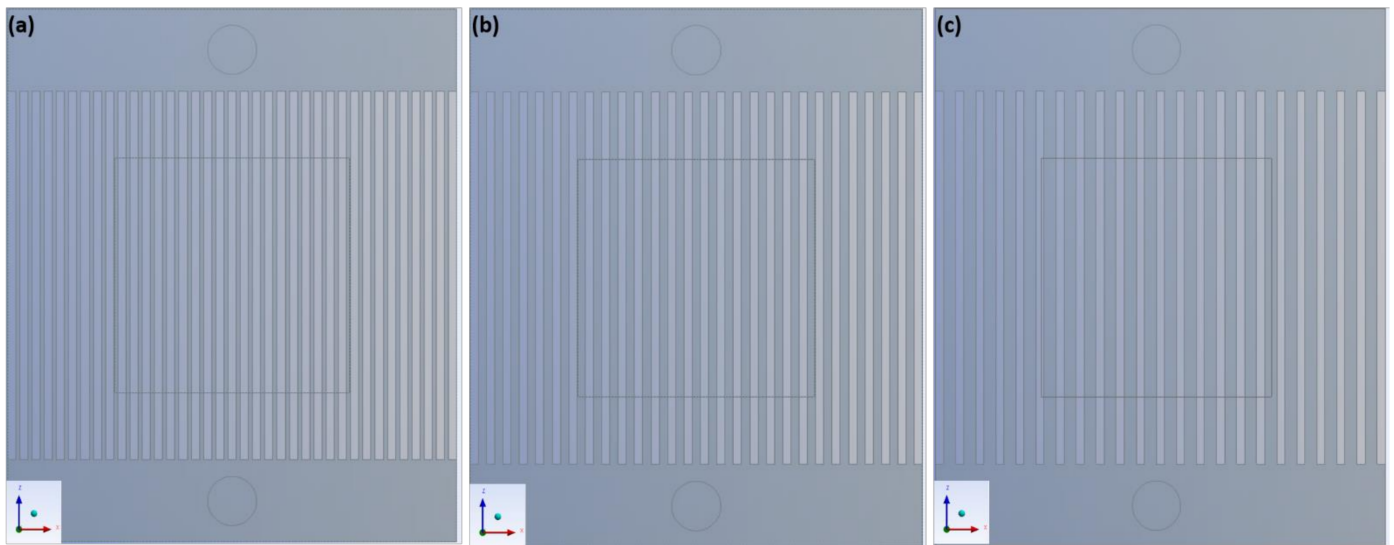


Figure 5. SIFMCHSs: (a) 0.5 mm, (b) 1 mm, and (c) 1.5 mm fin spacing.

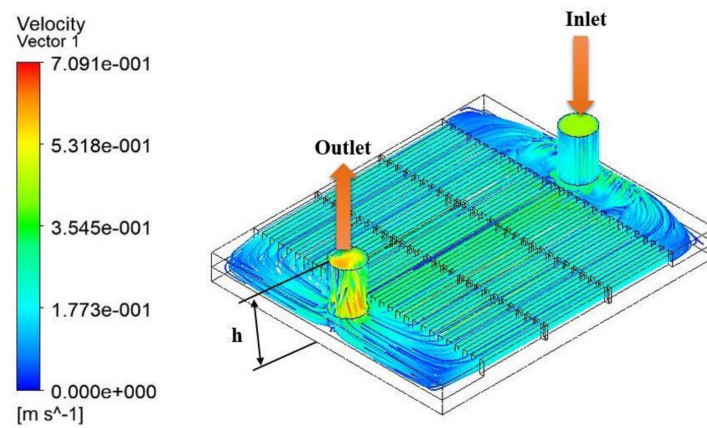


Figure 6. Propagation of flow through two SPFMCHSs.

2.5. Uniformity in Temperature Distribution

For the longer operation and durability of electronic devices, temperature uniformity was essential. All cases that were examined had a uniform temperature distribution inside the heat sink. The contours of the base temperature for two SPFMCHSs and three SPFMCHSs are shown in Figures 7 and 8.

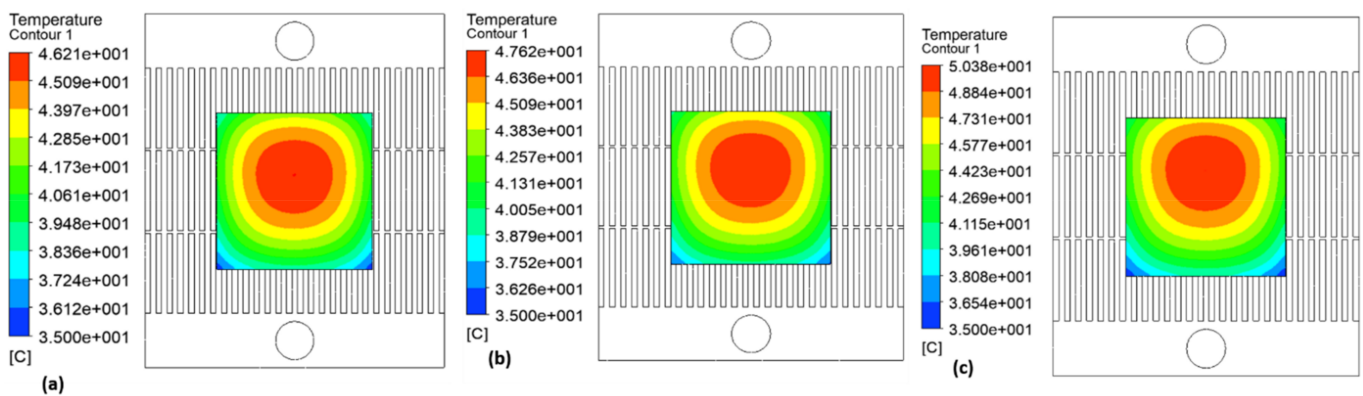


Figure 7. Base temperature distribution of two SPFMCHSs with 1 mm fin spacing: (a) 0.5 LPM, (b) 0.75 LPM, and (c) 1 LPM.

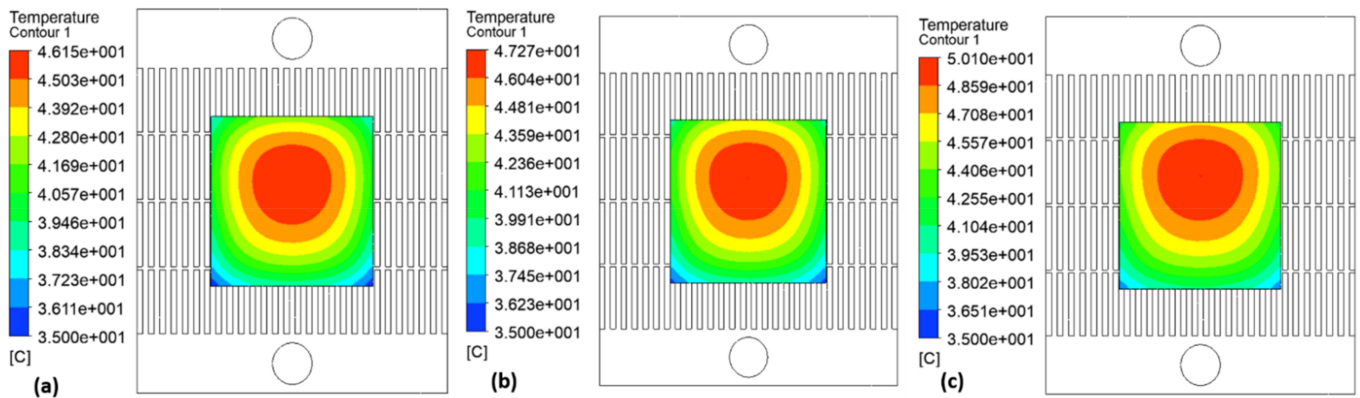


Figure 8. Base temperature distribution of three SPFMCHSs with 1 mm fin spacing: (a) 0.5 LPM, (b) 0.75 LPM, and (c) 1 LPM.

2.6. Selection of Slot Thickness

The flow becomes developed at one quarter of the distance from the entrance between the fins of heat sink. At this stage, the fluid velocity reaches the maximum at the center and the minimum at the boundaries of the flow. To reinitialize the velocity boundary layer, slots were added into the straight integral fins. This made a good contact between the flow and fins. The fully developed flow in between the fins in a 2D plane is shown in Figure 9. The slots were of varying thickness from 0.3 mm up to 1 mm, and the base temperature was recorded against each slot thickness. The thickness of the slot was selected finally as 0.5 mm for both the cases (two and three SPFMCHSs), as the minimum base temperature was recorded using 0.5 mm-thick slots. The formation of vortices took place inside the slots. This led to turbulence and enhanced heat transfer. There was a notable increment in the base temperature recorded for slot thicknesses of 0.5 mm to 0.6 mm. This is the point where the base temperature started to increase instead of decrease. The details are shown in Figure 10. The temperature distribution for two and three SPFMCHSs with 1 mm fin spacing is shown in Figures 7 and 8.

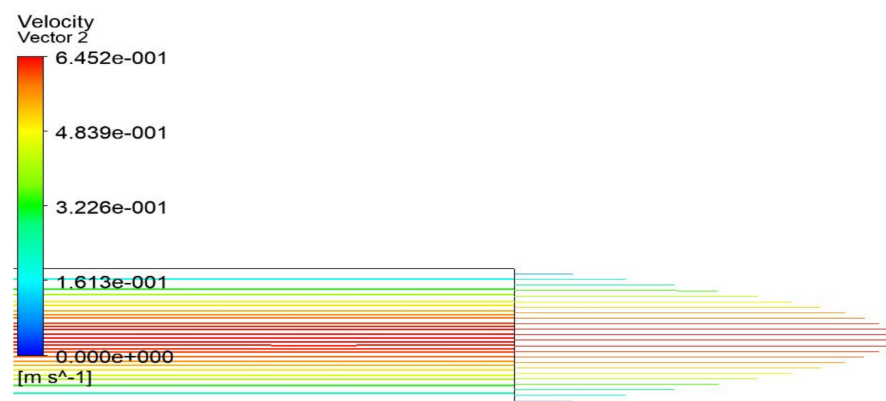


Figure 9. Two-dimensional pictorial view of the fully developed flow in between the fins.

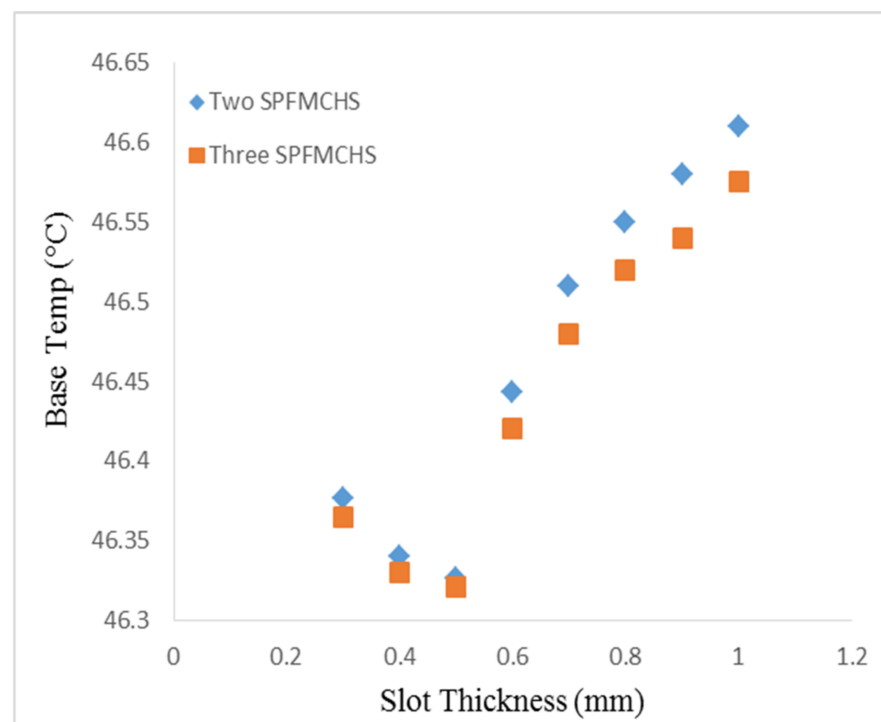


Figure 10. Base temp vs. slot thickness.

3. Results and Discussion

3.1. Heat Transfer

A direct relation was observed between the flow rate and the heat transfer, as shown in Figure 11. The graph shows that heat transfer is dependent on fin spacing and the number of slots. Increasing fin spacing resulted in a reduction in heat transfer. The maximum heat transfer observed in two SPFMCHSs, with 0.5 mm fin spacing, was 316 W at 1 LPM. The minimum heat transfer rate observed in three SPFMCHSs, with 1.5 mm fin spacing, was 280 W at 0.5 LPM. The heat sinks with two SPFMCHSs showed a higher heat transfer as compared to three SPFMCHSs with varying LPM and fin spacings. There was little difference in the heat transfer recorded for two and three SPFMCHSs with 1 mm fin spacing. When comparing two SPFMCHSs to three SPFMCHSs at 1 LPM, the percentage enhancement in heat transfer recorded for 0.5 mm, 1 mm, and 1.5 mm fin spacings was 0.95%, 0.32%, and 0.68%, respectively.

3.2. Base Temperature Drop

The base temperature drop for two and three SPFMCHSs was calculated by subtracting the base temperature of a conventional SIFMCHS [1] from two and three SPFMCHSs with varying fin spacings and LPM, as shown in Figure 12. The maximum temperature drop was recorded in two and three SPFMCHSs with 1 mm fin spacing. The maximum base temperature drop value was 6.31 °C for three SPFMCHSs with 1 mm fin spacing at 0.5 LPM. The minimum base temperature drop value was 3.14 °C for three SPFMCHSs with 1.5 mm fin spacing.

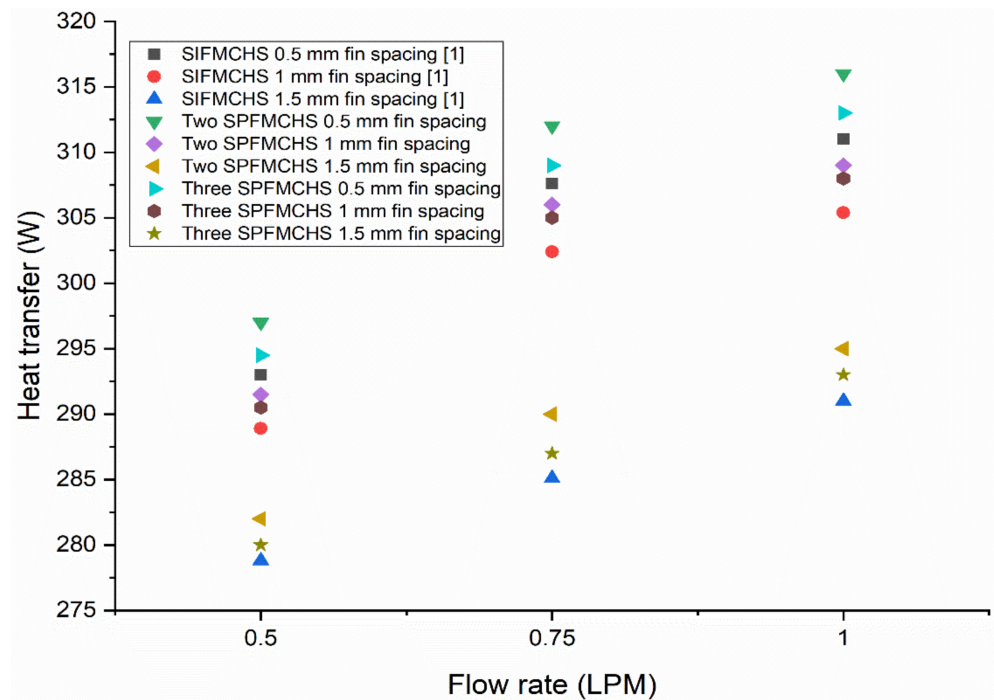


Figure 11. Heat transfer with volumetric flow rate.

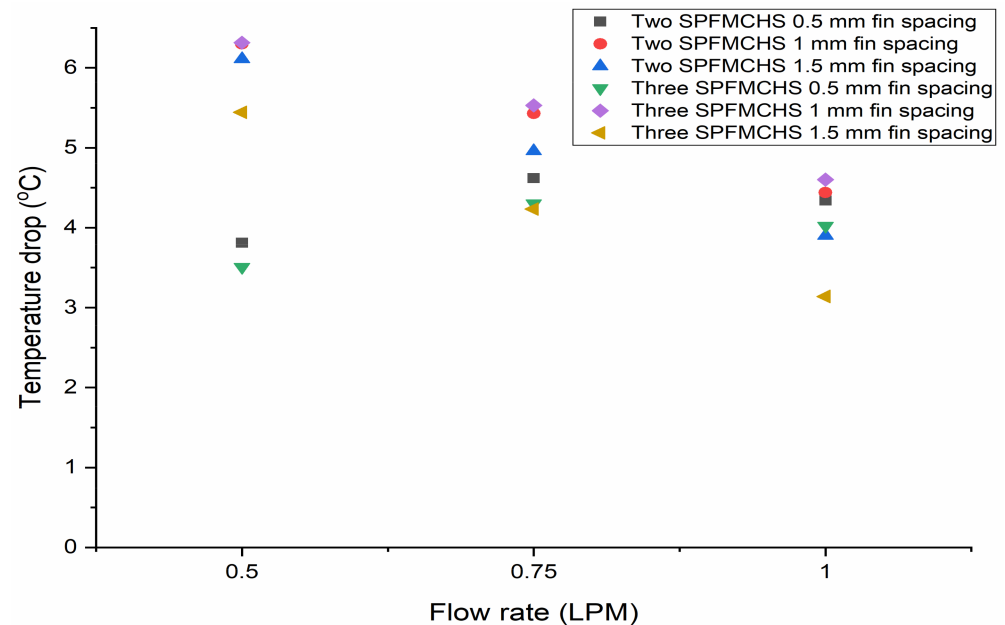


Figure 12. Temperature drop with volumetric flow rate.

3.3. Base Temperature

The base temperatures of SPFMCHSs at different volumetric flow rates are shown in Figure 13. The base temperature increases by increasing the fin spacing as the active area of the heat sink decreases. The minimum base temperature noted for two SPFMCHSs with 0.5 mm fin spacing was 42.81 °C at 1 LPM. The maximum base temperature, observed in two SPFMCHSs with 1.5mm fin spacing, was 53.51 °C at 0.5 LPM. An inverse relation was observed between the flow rate and the base temperature. The reduction in base temperature using SPFMCHSs was greater than that in SIFMCHSs [1]. This clearly highlights the importance of making slots in straight integral fins. The base temperature recorded for two SPFMCHSs with 0.5 mm and 1.5 m fin spacings was lower than for three SPFMCHSs

with the same fin spacing. For three SPFMCHSs, the percentage reduction in the base temperature was recorded as 8.53%, 9%, and 5.95% for 0.5 mm, 1 mm, and 1.5 mm fin spacings, respectively, compared to SIFMCHSs [1] at 1 LPM with the same fin spacing. The base temperature recorded in two SPFMCHSs with 0.5 mm, 1 mm, and 1.5 mm fin spacings at 1 LPM was 42.81 °C, 46.36 °C, and 48.87 °C, respectively, which is 9.20%, 8.74%, and 7.39% lower than the reported values in the literature [1] for SIFMCHSs. The base temperature distribution is shown in Figures 7 and 8 for two and three SPFMCHSs, respectively, with 1 mm fin spacing.

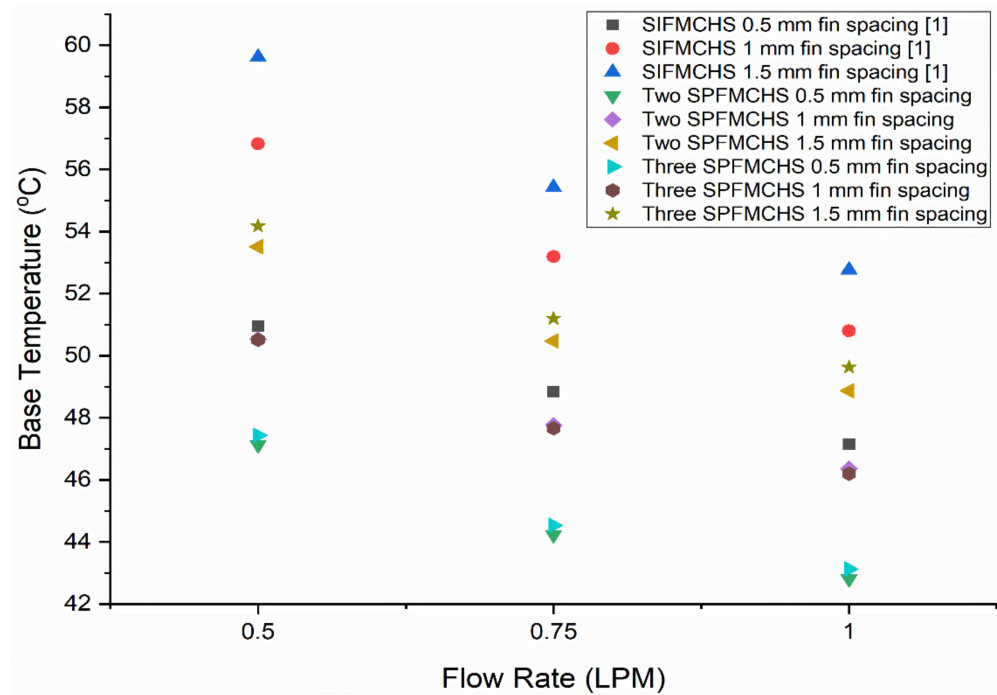


Figure 13. Base temperature with volumetric flow rate.

3.4. Pressure Drop

The pressure drops observed for SPFMCHSs across various volumetric flow rates are shown in Figure 14. By increasing the flow rate, the pressure drop increases. An inverse relationship was observed between the flow rate and the pressure drop. Increasing fin spacing results in a decreased pressure drop at varying LPM. The pressure drops recorded for two and three SPFMCHSs with varying fin spacings were found to be equal. The percentage reduction in the pressure drop observed at 0.5 mm, 1 mm, and 1.5 mm fin spacings for two SPFMCHSs was 0.64%, 20.68%, and 27.12% respectively, when compared to SIFMCHSs at 1 LPM. The percentage difference noted for three SPFMCHSs was 1.50%, 21.26%, and 27.93% at 0.5 mm, 1 mm, and 1.5 mm fin spacings, respectively, when compared to SIFMCHSs. The minimum pressure drops recorded for two SPFMCHSs and three SPFMCHSs with 1.5 mm fin spacing were 356.7 Pa and 352.68 Pa, respectively, at 0.5 LPM. The maximum pressure drops recorded for two and three SPFMCHSs with 0.5 mm fin spacing were 1127.65 Pa and 1117.96 Pa, respectively, at 1 LPM. The pumping power increases as the pressure drops to maintain the desired flow rate. The pressure drops recorded for two and three SPFMCHSs with 0.5 mm fin spacing at varying LPM were found to be equal to the reported value in [1] for SIFMCHSs.

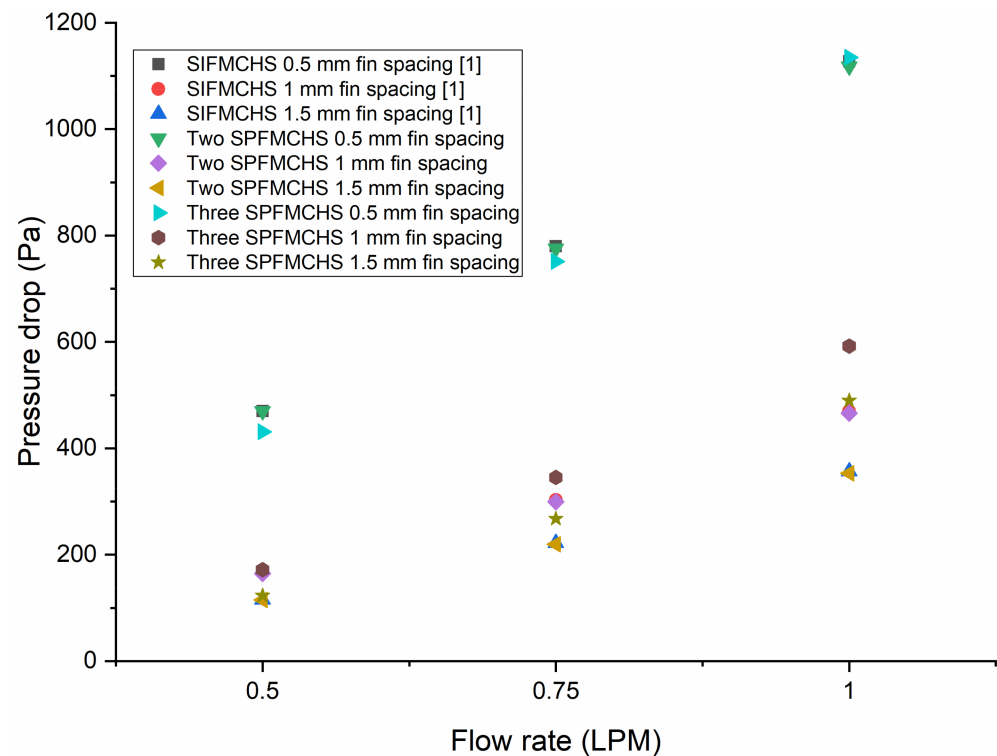


Figure 14. Pressure drop with volumetric flow rate.

3.5. Thermal Resistance

The effect of thermal resistance with volumetric flow rate for SPFMCHSs with two and three SPFMCHSs is shown in Figure 15. The thermal resistance decreases as the flow rate increases. By increasing the fin spacing, the thermal resistance also increases. The minimum thermal resistance recorded in two SPFMCHSs with 0.5 mm fin spacing was $0.036\text{ }^{\circ}\text{C}/\text{W}$ at 1 LPM. A similar level of thermal resistance was recorded in two and three SPFMCHSs with various fin spacings. The maximum thermal resistance was recorded in three SPFMCHSs with 1.5 mm fin spacing at 0.5 LPM. The reduction in thermal resistance was recorded as 11.24%, 4.48%, and 8.80% in two SPFMCHSs with 0.5 mm, 1 mm, and 1.5 mm fin spacings, respectively, as compared to the reported values for SIFMCHSs [1] at 1 LPM. The reduction in thermal resistance was observed as 6.31%, 4.83%, and 7.83% in three SPFMCHSs with 0.5 mm, 1 mm, and 1.5 mm fin spacings, respectively, as compared to the reported values for SIFMCHSs [1] at 1 LPM.

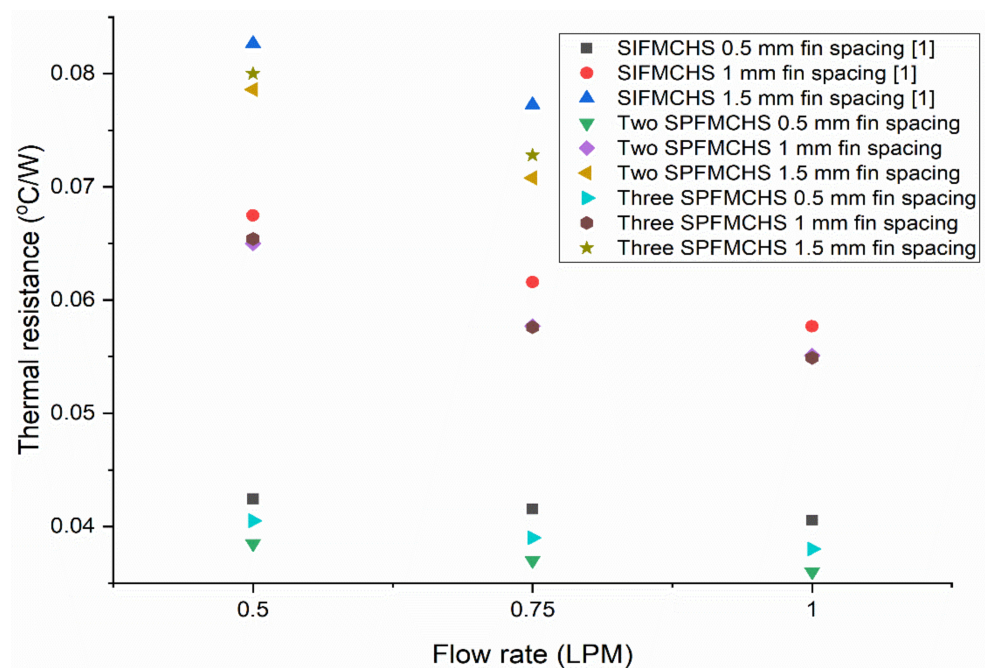


Figure 15. Thermal resistance with volumetric flow rate.

4. Conclusions

A thermal investigation of SPFMCHSs with fin spacings of 0.5 mm, 1 mm, and 1.5 mm was conducted numerically and compared to the SIFMCHS, using water as the cooling fluid, present in the literature. The findings of this detailed numerical study are:

- The base temperature recorded in two SPFMCHSs with 0.5 mm, 1 mm, and 1.5 mm fin spacings at 1 LPM was 42.81 °C, 46.36 °C, and 48.869 °C, respectively. This was 9.20%, 8.74%, and 7.39%, respectively, less than the SIFMCHSs. The minimum base temperature was recorded in two SPFMCHSs with 0.5 mm fin spacing, and the maximum base temperature was recorded in SIFMCHSs with a fin spacing of 1.5 mm at varying LPM. The reduction in the base temperature recorded for 0.5 mm, 1 mm, and 1.5 mm in two SPFMCHSs was 9.2%, 7.61%, and 7.39%, respectively, and in three SPFMCHSs was 8.23%, 7.22%, and 5.95%, respectively, from the reported value in the literature [1].
- The maximum heat transfer was recorded in two SPFMCHSs as compared to three SPFMCHSs with 0.5 mm fin spacing. The minimum heat transfer recorded was for 1.5 mm fin spacing in three SPMCHSs at 0.5 LPM. The percentage increase in the heat transfer recorded for 0.5 mm, 1 mm, and 1.5 mm in two SPFMCHSs was 1.6%, 1.16%, and 1.02%, respectively, and for three SPFMCHSs was 0.64%, 0.52%, and 0.44 %, respectively, from the reported value in the literature [1].
- The percentage reduction in the base temperature recorded in three SPFMCHSs with 0.5 mm, 1 mm, and 1.5 mm fin spacings at 1 LPM was 8.53%, 9%, and 5.95%, respectively, when compared to SIFMCHSs.
- The reduction in the thermal resistance was observed as 11.24%, 4.48%, and 8.80% in two SPFMCHSs with 0.5 mm, 1 mm, and 1.5 mm fin spacings, respectively, when compared to SIFMCHSs at 1 LPM. The minimum thermal resistance was recorded in two SPFMCHSs with 0.5 mm fin spacing, and the maximum thermal resistance was recorded in SIFMCHSs with 1.5 mm fin spacing.
- The reduction in the thermal resistance was observed to be 6.31%, 4.83%, and 7.83% in three SPFMCHSs with 0.5 mm, 1 mm, and 1.5 mm fin spacings when compared to SIFMCHSs at 1 LPM. The reduction in the thermal resistance recorded for 0.5 mm, 1 mm, and 1.5 mm fin spacings in two SPFMCHSs was 11.33%, 9.1%, and 8.83%, respectively, from the reported value in the literature [1]. In three SPFMCHSs, the

reduction in the thermal resistance for fin spacings of 0.5 mm, 1 mm, and 1.5 mm was 6.40%, 5.84%, and 4.85%, respectively, from the reported value in the literature.

- The percentage reduction in the pressure drop observed for 0.5 mm, 1 mm, and 1.5 mm fin spacings in two SPFMCHSs was 0.64%, 20.68%, and 27.12%, respectively, as compared to SIFMCHSs at 1 LPM. The percentage difference noted in three SPFMCHSs was 1.50%, 21.26%, and 27.93% at 0.5 mm, 1 mm, and 1.5 mm fin spacings, respectively, when compared to SIFMCHS.

Author Contributions: Conceptualization, Z.R. and H.A.T.; Data curation, T.B., M.A. and H.P.; Formal analysis, M.A.; Funding acquisition, K.R. and H.P.; Investigation, Z.R., H.A.T. and A.W.; Methodology, T.B. and Z.R.; Project administration, H.A.T., S.M. and A.W.; Resources, S.M. and K.R.; Supervision, Z.R.; Validation, Z.R.; Writing—original draft, T.B.; Writing—review and editing, Z.R. and H.P. All authors have read and agreed to the published version of the manuscript.

Funding: This research was funded by the Basic Science Research program through the National Research Foundation of Korea (NRF) funded by the ministry of Education, grant number 2020R1I1A1A01073797.

Conflicts of Interest: The authors declare no conflict of interest.

Nomenclature

C_p	= specific heat, kJ/kg °C
w_s	= width of heat sink, mm
l_s	= length of heat sink, mm
l_f	= length of fin, mm
t_f	= Thickness of fin, mm
S_t	= slot thickness, mm
h_b	= height of heat sink base plate, mm
h_f	= height of fin, mm
l_c	= length of chip, mm
t_c	= thickness of chip, mm
l_t	= total length, mm
f_s	= fin spacing, mm
LMTD	= log of mean temperature difference, °C
\dot{m}	= mass flow rate, kg/s
\dot{Q}	= heat transfer rate, W
R_{th}	= thermal resistance, °C/W
T_b	= base temperature, °C
T_i	= fluid inlet temperature, °C
T_o	= fluid outlet temperature, °C

Abbreviations

SFMCHS	= slotted fin minichannel heat sink
SIFMCHS	= straight integral fin minichannel heat sink
SPFMCHS	= slots per fin minichannel heat sink
LPM	= liters per minute

References

1. Saeed, M.; Kim, M.H. Numerical study on thermal hydraulic performance of water cooled mini-channel heat sinks. *Int. J. Refrig.* **2016**, *69*, 147–164. [CrossRef]
2. Tuckerman, D.B.; Pease, R.F. High-Performance Heat Sinking for VLSI. *IEEE Electron. Device Lett.* **1981**, *EDL-2*, 126–129. [CrossRef]
3. Huang, S.; Zaho, J.; Gong, L.; Duan, X. Thermal performance and structure optimization for slotted microchannel heat sink. *Appl. Therm. Eng.* **2016**, *115*, 1266–1276. [CrossRef]
4. Knight, R.W.; Hall, D.J.; Goodling, J.S.; Jaeger, R.C. Heat Sink Optimization with Application. *IEEE Trans. Compon. Hybrids Manuf. Technol.* **1992**, *5*, 832–842. [CrossRef]
5. Gawali, B.S.; Swami, V.B.; Thakre, S.D. Theoretical and Experimental Investigation of Heat Transfer Characteristics through a Rectangular Microchannel Heat Sink. *Int. J. Innov. Res. Sci. Eng. Technol.* **2014**, *3*, 8. [CrossRef]
6. Wang, X.D.; An, B.; Xu, J.L. Optimal geometric structure for nanofluid-cooled microchannel heat sink under various constraint conditions. *Energy Convers. Manag.* **2013**, *65*, 528–538. [CrossRef]

7. Hung, T.C.; Huang, Y.X.; Yan, W.M. Thermal performance analysis of porous-microchannel heat sinks with different configuration designs. *Int. J. Heat Mass Transf.* **2013**, *66*, 235–243. [CrossRef]
8. Gunnasegaran, P.; Mohammed, H.A.; Shuaib, N.H.; Saidur, R. The effect of geometrical parameters on heat transfer characteristics of microchannels heat sink with different shapes. *Int. Commun. Heat Mass Transf.* **2010**, *37*, 1078–1086. [CrossRef]
9. Qu, W.; Mala, G.m.; Li, D. Heat transfer for water flow in trapezoidal silicon microchannel. *Int. J. Heat Mass Transf.* **2000**, *43*, 3925–3936. [CrossRef]
10. Kumar, N.; Singh, N.K. Study and Analysis on Micro Channel Heat Sink in Trapezoidal Shape. *Int. J. Curr. Eng. Technol.* **2017**, *7*, 1115–1118.
11. Xie, X.L.; Tao, W.Q.; He, Y.L. Numerical study of turbulent heat transfer and pressure drop characteristics in water cooled mini channel heat sink. *J. Electron. Packag.* **2007**, *129*, 247–255. [CrossRef]
12. Dixit, T.; Ghosh, I. Low Reynolds number thermo-hydraulic characterization of offset. *Exp. Therm. Fluid Sci.* **2013**, *51*, 227–238. [CrossRef]
13. Saini, M.; Webb, R.L. Heat Rejection Limits of Air Cooled Plane Fin Heat. *IEEE Trans. Compon. Packag. Technol.* **2003**, *26*, 71–79. [CrossRef]
14. Naphon, P.; Wiriyaart, S. Liquid cooling in the mini-rectangular fin heat sink with and without thermoelectric for CPU. *Int. Commun. Heat Mass Transf.* **2009**, *36*, 166–171. [CrossRef]
15. Saeed, M.; Kim, M.H. Heat Transfer enhancement using Nano fluids ($\text{Al}_2\text{O}_3\text{-H}_2\text{O}$) in mini channel heat sink. *Int. J. Heat Mass Transfer* **2018**, *120*, 671–682. [CrossRef]
16. Al-Tae'y, K.A.; Ali, E.H.; Jebur, M.N. Experimental Investigation of Water Cooled Minichannel Heat Sink for Computer Processing Unit Cooling. *Int. J. Eng. Res. Appl.* **2017**, *7*, 38–49.
17. Yu, X.; Feng, J.; Feng, Q.; Wang, Q. Development of a plate-pin fin heat sink and its performance comparisons with a plate fin heat sink. *Appl. Therm. Eng.* **2005**, *25*, 173–182. [CrossRef]
18. Tariq, H.A.; Israr, A.; Khan, Y.I.; Anwar, M. Numerical and experimental study of cellular structures as a heat dissipation media. *Heat Mass Transf.* **2019**, *55*, 510–511. [CrossRef]
19. Tariq, H.A.; Shoukat, A.A.; Anwar, M.; Ali, H.M. Water Cooled Micro-hole Cellular Structure as a Heat Dissipation Media: An Experimental and Numerical Study. *Therm. Sci.* **2018**, *2018*, 184. [CrossRef]
20. Tariq, H.A.; Shoukat, A.A.; Hassan, M.; Anwar, M. Thermal management of microelectronic devices using micro-hole cellular structure and nanofluids. *J. Therm. Anal. Calorim.* **2019**, *136*, 2171–2182. [CrossRef]
21. Valueva, E.P.; Purdin, M.S. The pulsating laminar flow in a rectangular channel. *Thermophys. Aeromechanics* **2015**, *22*, 733–744. [CrossRef]
22. Valueva, E.P.; Purdin, M.S. Heat exchange at laminar flow in rectangular channels. *Thermophys. Aeromechanics* **2016**, *23*, 857–867. [CrossRef]
23. Khoshvaght-Aliabadi, M.; Hassani, S.M.; Mazloumi, S.H. Comparison of hydrothermal performance between plate fins and plate-pin fins subject to nanofluid-cooled corrugated miniature heat sinks. *Microelectron. Reliab.* **2017**, *70*, 84–96. [CrossRef]
24. Rezaee, M.; Khoshvaght-Aliabadi, M.; Arani, A.A.A.; Mazloumi, S.H. Heat transfer intensification in pin-fin heat sink by changing pin-length/longitudinal-pitch. *Chem. Eng. Process.-Process. Intensif.* **2019**, *141*, 107544. [CrossRef]
25. Khoshvaght-Aliabadi, M.; Hassani, S.M.; Mazloumi, S.H. Performance enhancement of straight and wavy miniature heat sinks using pin-fin interruptions and nanofluids. *Chem. Eng. Process.* **2017**, *122*, 90–108. [CrossRef]
26. Ali, M.; Shoukat, A.A.; Tariq, H.A.; Anwar, M.; Ali, H. Header Design Optimization of Mini-channel Heat Sinks Using $\text{CuO-H}_2\text{O}$ and $\text{Al}_2\text{O}_3\text{-H}_2\text{O}$ Nanofluids for Thermal Management. *Arab. J. Sci. Eng.* **2019**. [CrossRef]
27. Wang, W.; Li, Y.; Zhang, Y.; Li, B.; Sundén, B. Analysis of laminar flow and heat transfer in an interrupted microchannel heat sink with different shaped ribs. *J. Therm. Anal. Calorim.* **2020**, *140*, 1259–1266. [CrossRef]
28. Tran, N.G.R.; Chang, Y.; Teng, J. A study on five different channel shapes using a novel scheme for meshing and a structure of a multi-nozzle microchannel heat sink. *Int. J. Heat Mass Transf.* **2017**, *105*, 429–442. [CrossRef]

Article

Multi-Objective Optimization of Parameters of Channels with Staggered Frustum of a Cone Based on Response Surface Methodology

Zhen Zhao, Liang Xu ^{*}, Jianmin Gao, Lei Xi , Qicheng Ruan and Yunlong Li

State Key Laboratory for Manufacturing Systems Engineering, Mechanics Institute, Xi'an Jiaotong University, Xi'an 710049, China; zhaozhen.900803@stu.xjtu.edu.cn (Z.Z.); gjm@mail.xjtu.edu.cn (J.G.); xilei100@mail.xjtu.edu.cn (L.X.); ruanqicheng93@stu.xjtu.edu.cn (Q.R.); ylongli@mail.xjtu.edu.cn (Y.L.)

* Correspondence: xuliang@mail.xjtu.edu.cn; Tel.: +86-(18)-691861949

Abstract: In this study, Response Surface Methodology (RSM) and multi-objective genetic algorithm were used to obtain optimum parameters of the channels with frustum of a cone with better flow and heat transfer performance. Central composite face-centered design (CCF) was applied to the experimental design of the channel parameters, and on this basis, the response surface models were constructed. The sensitivity of the channel parameters was analyzed by Sobol's method. The multi-objective optimization of the channel parameters was carried out with the goal of achieving maximum Nusselt number ratio (Nu/Nu_0) and minimum friction coefficient ratio (f/f_0). The results show that the root mean square errors (RSME) of the fitted response surface models are less than 0.25 and the determination coefficients (R^2) are greater than 0.93; the models have high accuracy. Sobol's method can quantitatively analyze the influence of the channel parameters on flow and heat transfer performance of the channels. When the response is Nu/Nu_0 , from high to low, the total sensitivity indexes of the channel parameters are frustum of a cone angle (α), Reynolds number (Re), spanwise spacing ratio (Z_2/D), and streamwise spacing ratio (Z_1/D). When the response is f/f_0 , the total sensitivity indexes of the channel parameters from high to low are Re , Z_1/D , α and Z_2/D . Four optimization channels are selected from the Pareto solution set obtained by multi-objective optimization. Compared with the reference channel, the Nu/Nu_0 of the optimized channels is increased by 21.36% on average, and the f/f_0 is reduced by 9.16% on average.

Citation: Zhao, Z.; Xu, L.; Gao, J.; Xi, L.; Ruan, Q.; Li, Y. Multi-Objective Optimization of Parameters of Channels with Staggered Frustum of a Cone Based on Response Surface Methodology. *Energies* **2022**, *15*, 1240. <https://doi.org/10.3390/en15031240>

Academic Editors: Jan Danielewicz and Krzysztof Rajski

Received: 11 January 2022

Accepted: 3 February 2022

Published: 8 February 2022

Publisher's Note: MDPI stays neutral with regard to jurisdictional claims in published maps and institutional affiliations.



Copyright: © 2022 by the authors. Licensee MDPI, Basel, Switzerland. This article is an open access article distributed under the terms and conditions of the Creative Commons Attribution (CC BY) license (<https://creativecommons.org/licenses/by/4.0/>).

Keywords: channels with frustum of a cone; multi-objective optimization; Response Surface Methodology; Sobol's method; sensitivity analysis

1. Introduction

To cope with severe global climate change and reflect the responsibility assumed by a major country, "carbon peak and carbon neutrality" is an important national strategic goal. Therefore, it is urgent to develop more efficient thermal energy equipment to reduce carbon emissions and improve energy efficiency. Plate air heat exchangers are a compact and efficient piece of heat exchange equipment that is widely used in the chemical industry, electric power, metallurgy, and other industrial sectors.

Selecting appropriate channel parameters can effectively improve the flow and heat transfer performance of heat exchanger channels. Response Surface Methodology (RSM) can be used to obtain the combination of design variables under the optimal target response through the explicit functional relationship between design variables and response. Refs. [1,2] used the CCF method combined with response surface method to optimize the rib structure of a steam-cooled rectangular channel, and reported that the multi-objective optimization for lower pressure drop and higher heat transfer could be achieved at Re of 90,000, α of 41.515, e/D of 0.116 and P/D of 0.975. Izadi et al. [3] numerically analyzed the natural convection of a porous enclosure under a nonuniform magnetic field using

the Local Thermal Non-Equilibrium (*LTNE*) model. The results indicated that the Nusselt numbers of the two phases of porous material converged when increasing the power ratio of the two magnetic sources, and these two thermal indices varied when reducing the power ratio of the two magnetic sources. Jeong et al. [4] numerically analyzed the cooling performance of a cooling channel with a V-shaped rib structure, and then optimized the structural parameters of the V-shaped rib using *RSM*. Seo et al. [5] used the genetic algorithm and *RSM* to optimize a cooling channel with a boot-shaped rib. Mamuria et al. [6] used *RSM* to analyze the sensitivity of four variable parameters of a solar heat exchanger. Bu et al. [7] studied the structural parameters of typical matrix channels by *RSM*, and fitted the polynomial expressions of channel friction coefficient ratio and Nusselt number ratio with respect to rib angle and rib density. Shi et al. [8] used *RSM* to optimize the geometric parameters of microchannels with secondary flow, and selected five optimized structures from the optimized Pareto solution set. Wen Jian et al. [9] combined *RSM* and the multi-objective genetic algorithm to optimize the structure of a serrated fin, studying the effects of fin-height, fin-distance and fin-thickness on flow and heat transfer in the fin channel, finally obtaining three optimized structures. Zheng et al. [10] conducted numerical research on a channel with discrete inclined ribs, studying the effects of Reynolds number, rib-spacing and rib-height ratio on the flow and heat transfer performance of the channel, and analyzed the sensitivity of parameters based on *RSM*.

However, the research on turbulent channels in the above references focuses on the flow and heat transfer performance of the channels, and rarely considers the strength of the turbulent structure. With improvements in the performance of turbulent channels, the problem of fluid excitation can no longer be ignored [11]. High-strength plates can be obtained by the hot stamping forming process [12], and parallel high-strength plates can form a turbulent channel for flow and heat transfer. Considering the fluid excitation in the turbulent channels and the advantages of the hot stamping forming process, our research group proposed a new frustum of a cone structure that can be formed by hot stamping formation [13]. Nevertheless, Ref. [13] only studied a channel with frustum of a cone under a certain structure, and the results showed that the flow and heat transfer performance of the channel was poor. Hence, based on this research, in order to obtain the parameters for a channel with frustum of a cone with better flow and heat transfer performance, *RSM* and the multi-objective genetic algorithm were used to optimize the channel parameters. The experimental design of the channel parameters, including Reynolds number (Re), frustum of a cone angle (α), streamwise spacing ratio (Z_1/D), and spanwise spacing ratio (Z_2/D), was carried out by using central composite face-centered design (*CCF*). In addition, on this basis, the second-order polynomial was selected to construct the response surface model. With respect to global sensitivity analysis, Sobol's method was used to analyze the sensitivity of the channel parameters, with the responses being the Nusselt number ratio (Nu/Nu_0) and the friction coefficient ratio (f/f_0) of the channels. To maximize the Nu/Nu_0 and minimize the f/f_0 of the channels, the non-dominated sorting genetic algorithm with elite strategy (*NSGA-II*) was used. These research results can serve as a reference for the parametric multi-objective optimized design of channels with frustum of a cone.

2. Physical Model and Numerical Methods

2.1. Physical Model

The research object of the present study is the channel with staggered frustums of a cone proposed by our research group [13], and the purpose is to carry out multi-objective optimization of the channel parameters. Since the thickness of the channel metal plates is only 1 mm, ignoring the thermal conductivity of the plates, the fluid domain is taken out separately for research. After a certain number of frustum of a cone structures, the fluid will develop into a typical periodic convective heat transfer. For convenience, the minimum periodic model of the channel with frustum of a cone was taken out separately for research. Figure 1 shows the physical model of the periodic channel with staggered frustums of a cone, in which Figure 1a is the diagram of the heat exchanger, Figure 1b is the overall fluid

domain model, Figure 1c is the periodic model with central symmetry, and Figure 1d is the side view of the periodic model. As can be seen from Figure 1a, the frustums of a cone have the function of supporting the channel. It can also be seen from Figure 1 that the bottom diameter of each frustum of a cone is D , the height is H , the angle is α , the streamwise spacing and spanwise spacing are Z_1 and Z_2 respectively, and the channel height is $2H$.

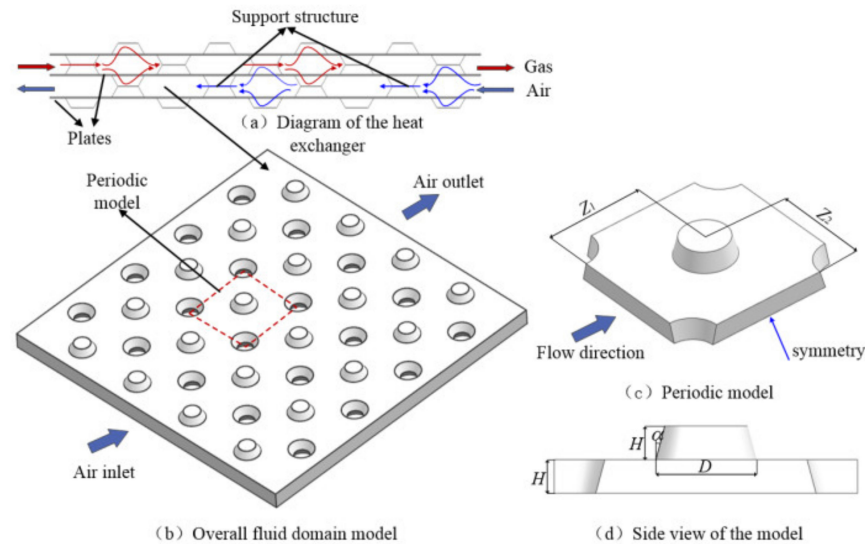


Figure 1. Physical model of the periodic channel with staggered frustums of a cone.

2.2. Numerical Methods

The three-dimensional incompressible Reynolds time-averaged Navier Stokes ($N-S$) equation is solved by FLUENT software. The expressions of continuity, momentum, and energy equations were introduced in detail in Ref. [14]. References [15,16] reported that the Renormalization Group RNG $k-\epsilon$ turbulence model can better simulate the flow and heat transfer performance of the turbulent channels. Therefore, the RNG $k-\epsilon$ turbulence model was selected to study the performance of the channels with frustum of a cone in this study. In the calculation, the Semi-Implicit Method for Pressure Linked Equation $SIMPLEC$ algorithm was used to solve the velocity and pressure coupling equation, and the discrete format of momentum and energy equation was set as the second-order upwind format. It is required that the energy residual converges to 10^{-8} , and the velocity, continuity, k parameter and ϵ parameter residuals converge to 10^{-6} . The continuity, momentum and energy Equations are as follows:

$$\frac{\partial}{\partial x_i}(\rho u_i) = 0 \quad (1)$$

$$\frac{\partial}{\partial x_i}(\rho u_i u_k) = \frac{\partial}{\partial x_i}(\eta \frac{\partial u_k}{\partial x_i}) - \frac{\partial p}{\partial x_k} \quad (2)$$

$$\frac{\partial}{\partial x_i}(\rho u_i T) = \frac{\partial}{\partial x_i}(\frac{\lambda}{c_p} \frac{\partial T}{\partial x_i}) \quad (3)$$

where ρ is the fluid density; u_i is the vector velocity; η is the viscosity, p is the pressure; T is the temperature; λ is the thermal conductivity of the fluid; c_p is the specific heat capacity at constant pressure; k is the turbulent kinetic energy equation; ∂ is the diffusion equation.

The RNG $k-\epsilon$ turbulence model is as follows:

$$\frac{\partial}{\partial t}(\rho k) + \frac{\partial}{\partial x_i}(\rho k u_i) = \frac{\partial}{\partial x_j} \left(\alpha_k \mu_{eff} \frac{\partial k}{\partial x_j} \right) + G_k - \rho \epsilon \quad (4)$$

$$\frac{\partial}{\partial t}(\rho\varepsilon) + \frac{\partial}{\partial x_i}(\rho\varepsilon u_i) = \frac{\partial}{\partial x_j} \left(\alpha_\varepsilon \mu_{eff} \frac{\partial \varepsilon}{\partial x_j} \right) + C_{1\varepsilon} \frac{\varepsilon}{k} (G_k + C_{3\varepsilon} G_b) - C_{2\varepsilon} \rho \frac{\varepsilon^2}{k} - R_\varepsilon \quad (5)$$

where α_k and α_ε are the inverse effective Prandtl numbers for k and ε , respectively, G_k is the generation of turbulence kinetic energy, and μ_{eff} is the effective viscosity coefficient.

Figure 2 shows the specific calculation model of the channel with frustums of a cone. Referring to the setting of periodic convective heat transfer boundary conditions in reference [17], the inlet and outlet of the channel were set as periodic boundary conditions, and the mass flow was given. The left and right sides of the channel were also set as periodic boundary conditions. Different from Ref. [17], for convenience, the center of the calculation model was set as a symmetric boundary condition in the present study. The lower wall surface of the channel, including the surface of the frustum of a cone, was the heat transfer wall, which was set to a uniform heat flux of $1000 \text{ W} \times \text{m}^{-2}$. In addition, the average inlet temperature of the air was set to 300 K.

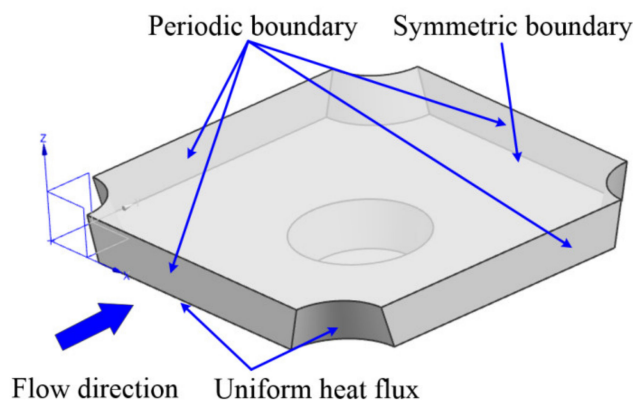


Figure 2. The calculation model of the channel.

Figure 3 shows the grid diagram of the calculation model. The model was divided into hexahedral structured meshes using ICEM software. The mesh near the wall was encrypted. The grid size of the first layer was 0.02 mm, the grid expansion ratio was 1.2, and the maximum grid size was 1 mm. The value of y^+ (symbol indicating the sparsity of near wall mesh division) near the wall was less than or equal to 1, and the enhanced wall function was used. Such an arrangement can better obtain the flow and heat transfer information near the wall.

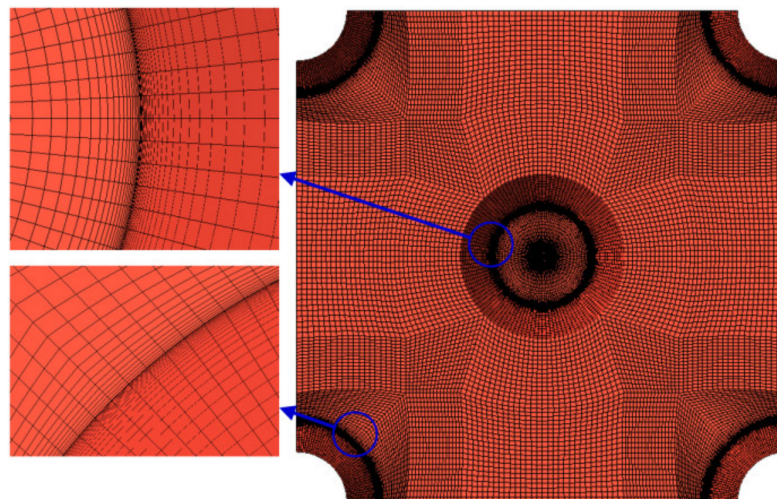


Figure 3. The grid diagram of the calculation model.

The numerical method in the present study was verified using the experimental data for the channel with frustum of a cone presented in Ref. [13]. Figure 4 shows the comparison of the experimental and numerical results of the Nusselt number ratio and friction coefficient ratio of the channel under different Reynolds numbers. It can be seen from Figure 4 that the distribution trends of the experimental and numerical results are basically consistent. Through calculation, the maximum deviation of the Nusselt number ratio is 5.1%, and the maximum deviation of the friction coefficient ratio is 4.3%. These demonstrate the accuracy and feasibility of the numerical method in the present study. Therefore, this numerical method was used in the subsequent numerical studies of the channels with different frustum of a cone structures. In addition, the grid independence of the calculation model was verified. Five sets of grids were divided for the calculation model; when meshing, set the grid size of the first layer to 0.02 mm, and change the number of grids by changing the grid growth ratio (1.5–1.1) and the maximum grid size (0.8 mm–0.4 mm). The total numbers of grids were 75,000, 150,000, 300,000, 600,000 and 1,200,000, respectively. When the number of the grid was 600,000, the deviations of the Nusselt number ratio and friction coefficient ratio of the channel were less than 2%, indicating that the grid met the requirement of independence. The mesh generation strategy mentioned above was adopted in the subsequent calculation models.

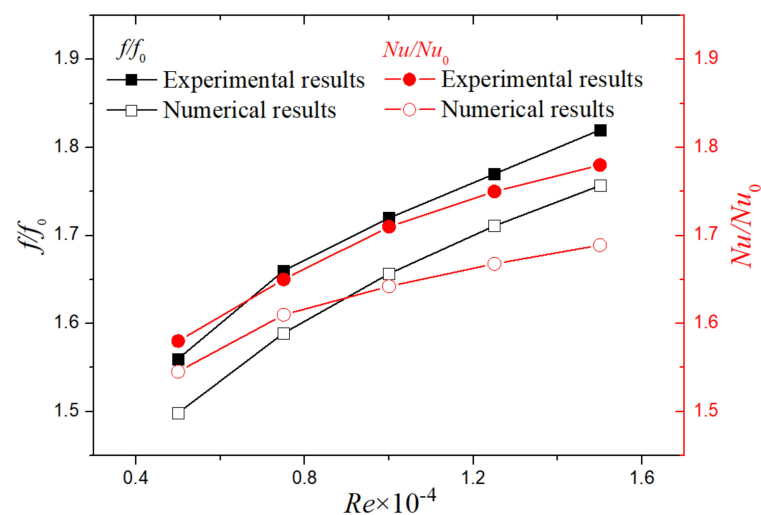


Figure 4. Verification of the numerical method.

2.3. Data Reduction

Reynolds number Re is defined as

$$Re = VP/\nu \quad (6)$$

where V is the average inlet velocity of airflow; P is the characteristic length, and the height of the channel is selected in the present study; ν is the kinematic viscosity of air.

The local Nusselt number Nu_x is defined as

$$Nu_x = q_x P / [\lambda(T_w - T_f)] \quad (7)$$

where q_x is the local heat flux; λ is the thermal conductivity of air flow; T_w is the local temperature of the wall; T_f is the reference temperature, and its value is the average temperature of inlet and outlet airflow.

The average Nusselt number Nu is defined as

$$Nu = \int Nu_x dA / A \quad (8)$$

where A is the area of the heat transfer wall.

The friction coefficient f is defined as

$$f = \Delta p P / (2\rho L V^2) \quad (9)$$

where L is the channel length, Δp is the pressure drop at the inlet and outlet of the channel; ρ is the air density.

Nu_0 and f_0 are the average Nusselt number and friction coefficient of smooth parallel plate channel, respectively [18], and the calculation formulas are as follows:

$$Nu_0 = \frac{(f_0/2)(Re - 500)Pr}{1 + 12.7(f_0/2)^{1/2}(Pr^{2/3} - 1)} \quad (10)$$

$$f_0 = (1.58 \ln Re - 2.185)^{-2} \quad (11)$$

3. Optimization Methods

3.1. Response Surface Methodology and Experimental Design

Response Surface Methodology (RSM) can be used to obtain explicit functional relationships between design variables and responses in the global scope by testing local design points. The optimal combination of design variables can be obtained through RSM to achieve the optimal target response. The relationship between system response and design variable is as follows:

$$Y = f(X) + \varepsilon = X\beta + \varepsilon \quad (12)$$

where Y is the response, X is the design variable, $f(X)$ is the approximate function of the target, β is the fitting coefficient, and ε is the prediction error.

The formula for the sum of squares of system residuals is as follows:

$$SS_E(\beta) = (X\beta - Y)^T (X\beta - Y) \quad (13)$$

Through the principle of the least square method, calculate the derivative of function $SS_E(\beta)$ with respect to vector β and set it to zero. We can draw:

$$\frac{\partial}{\partial \beta} SS_E(\beta) = 2X^T (X\beta - Y) = 0 \quad (14)$$

After finishing Equation (9), the coefficient β of the response surface with minimum sum of squares of residuals can be obtained:

$$\beta = (X^T X)^{-1} X^T Y \quad (15)$$

The commonly used second-order polynomial response surface model with high accuracy was selected as the approximate function $f(x)$, and the formula is as follows:

$$f(x) = \beta_0 + \sum_{i=1}^k \beta_i x_i + \sum_{i=1}^k \beta_{ii} x_i^2 + \sum_{i=1}^{k-1} \sum_{i < j}^k \beta_{ij} x_i x_j \quad (16)$$

where coefficient $\beta = [\beta_0, \dots, \beta_k, \beta_{11}, \dots, \beta_{kk}, \beta_{12}, \dots, \beta_{\times(k-1)k}]^T$; x_i and x_j are the design variables; k is the number of design variables.

To evaluate the fitting accuracy of the obtained response surface model to the test data, the root mean square error (RMSE) and determination coefficient (R^2) were selected to evaluate the response surface model. The specific expression of the evaluation index is shown in Ref. [19]. If RMSE is closer to 0, the error of the response surface model is smaller.

If R^2 is closer to 1, the accuracy of the response surface model is higher. $RMSE$ and R^2 are calculated as follows:

$$RMSE = \frac{1}{k\bar{y}} \sqrt{\sum_{i=1}^k (y_i - \tilde{y}_i)^2} \quad (17)$$

$$R^2 = 1 - \frac{\sum_{i=1}^k (y_i - \tilde{y}_i)^2}{\sum_{i=1}^k (y_i - \bar{y})^2} \quad (18)$$

where k is the number of sample points, y_i is the test result of the i th sample, \bar{y} is the average of the test results of all samples, and \tilde{y}_i is the calculated value of the response surface model of the i th sample.

The fitting accuracy of the response surface model also depends on the selection of design sample points, so it is necessary to carry out experimental design for design variables. The design variables in the present study are the channel parameters. For convenience of research, frustum of a cone structures with a constant height and bottom diameter were selected, in which the height H was 10 mm and the bottom diameter D was 30 mm. The optimal channel parameter configurations were obtained by changing Reynolds number Re , frustum of a cone angle α , streamwise spacing Z_1 and spanwise spacing Z_2 . During the study, the streamwise spacing Z_1 and spanwise spacing Z_2 were dimensionless variables treated as Z_1/D , and Z_2/D . The variation ranges of the design parameters are shown in Table 1.

Table 1. Variation range of channel parameters.

Channel Parameters	Variation Ranges
Reynolds number Re	5000 to 15,000
Frustum of a cone angle $\alpha/^\circ$	0 to 30
Streamwise spacing ratio Z_1/D	1 to 1.5
Spanwise spacing ratio Z_2/D	1 to 1.5

Central composite face-centered design (CCF) is one kind of central composite design (CCD) that can fit the complete quadratic model and obtain the response surface model with high precision through fewer test points. Therefore, CCF was selected for experimental design in the present study. Table 2 shows the central composite face-centered design table, mainly including order, design variables, and responses. Since there are four design variables, $2^4(16)$ cubic points, $2 \times 4(8)$ axial points and one center point can be obtained using CCF design, so there are 25 sample points in total.

3.2. Parameter Sensitivity Analysis Based on Sobol's method

Many factors affect the flow and heat transfer performance of channels with frustums of a cone, including Reynolds number, frustum of a cone angle, streamwise spacing, and spanwise spacing. Therefore, exploring the impact of the changes of these parameters on the channel performance is of great help to the subsequent parameter optimization. Compared with the local sensitivity analysis method for linear models, the global sensitivity analysis method is suitable for nonlinear complex models. Sobol's method based on variance is a global sensitivity analysis method proposed by the mathematician Sobol [20]. Compared with other global sensitivity analysis methods, Sobol's method can quantitatively analyze the impact of input variables on system output. Its outstanding advantage is that it has no special requirements for analysis function and has a wide range of applications [21].

Table 2. Central composite face-centered design table.

Order	Design Variables				Responses	
	<i>Re</i>	α	Z_1/D	Z_2/D	f/f_0	Nu/Nu_0
1	5000	0	1.50	1.50	1.38	1.39
2	10,000	15	1.25	1.25	1.91	1.65
3	5000	0	1.00	1.50	1.46	1.28
4	15,000	0	1.50	1.50	1.53	1.46
5	10,000	15	1.25	1.00	2.30	1.60
6	10,000	0	1.25	1.25	1.79	1.37
7	5000	0	1.50	1.00	2.10	1.40
8	15,000	15	1.25	1.25	2.09	1.71
9	15,000	30	1.00	1.00	4.96	2.45
10	10,000	15	1.00	1.25	2.65	1.85
11	10,000	15	1.25	1.50	1.64	1.64
12	15,000	0	1.00	1.00	3.26	1.15
13	15,000	0	1.50	1.00	2.38	1.41
14	5000	30	1.00	1.00	2.99	2.04
15	15,000	30	1.50	1.50	2.46	2.35
16	5000	30	1.00	1.50	1.91	1.90
17	15,000	30	1.50	1.00	2.51	1.99
18	15,000	0	1.00	1.50	2.88	1.80
19	5000	15	1.25	1.25	1.69	1.56
20	15,000	30	1.00	1.50	3.29	2.45
21	10,000	15	1.50	1.25	1.74	1.67
22	5000	30	1.50	1.00	2.17	1.93
23	10,000	30	1.25	1.25	3.04	2.37
24	5000	0	1.00	1.00	2.39	1.28
25	5000	30	1.50	1.50	1.49	1.82

The core idea of Sobol's method is to decompose the model into a single parameter and functions composed of parameters. The basic principle of Sobol's method can be seen in Ref. [22]. Assuming that $x = [x_1, \dots, x_m]$ is an independent input variable defined on I^m , then I^m can be expressed as:

$$I^m = (x | 0 \leq x_{i_t} \leq 1; i_t = 1, 2, \dots, m) \quad (19)$$

Assuming that the model $F(x)$ is a square-integrable function, it can be decomposed into the sum of 2^m sub-functions:

$$F(x) = F_0 + \sum_{t=1}^m \sum_{i_1 < \dots < i_t} F_{i_1 \dots i_t}(x_{i_1}, \dots, x_{i_t}) \quad (20)$$

where $1 = i_1 < \dots < i_t \dots < i_m = m$, m is the number of variables and F_0 is a constant.

If the conditions are met, it can be obtained:

$$\int_0^1 F_{i_1 \dots i_t}(x_{i_1}, \dots, x_{i_t}) dx_{i_n} = 0, 1 \leq n \leq t \quad (21)$$

The total variance M and partial square deviation $M_{i_1 \dots i_t}$ of the $F(x)$ can be obtained by integrating the squares of Equation (20):

$$M = \sum_{t=1}^m \sum_{i_1 < \dots < i_t} M_{i_1 \dots i_t} \quad (22)$$

$$M_{i_1 \dots i_t} = \int F_{i_1 \dots i_t}^2 dx_{i_1} \dots dx_{i_t} \quad (23)$$

According to the definition, the sensitivity index of the variable $S_{i_1 \dots i_t}$ is defined as:

$$S_{i_1 \dots i_t} = \frac{D_{i_1 \dots i_t}}{D} \quad (24)$$

Then, the sum of sensitivity indexes of all variables is 1. It can be expressed as follows:

$$\sum_{t=1}^m \sum_{i_1 < \dots < i_t} S_{i_1 \dots i_t} = 1 \quad (25)$$

Equation (25) can be rewritten as follows:

$$\sum_{t=1}^m S_{i_t} + \sum_{1 \leq q < t \leq m} S_{i_q i_t} + \dots + S_{i_1 \dots i_m} = 1 \quad (26)$$

According to the definition, the total sensitivity index of an input variable $S_{T_{i_t}}$ is:

$$S_{T_{i_t}} = S_{i_t} + \sum_{q \neq t}^m S_{i_q i_t} + \dots + S_{i_1 \dots i_m} \quad (27)$$

where S_{i_t} is the first-order sensitivity index, which represents the impact of input variable x_{i_t} on system output; the second-order sensitivity index $S_{i_q i_t}$ represents the influence of the interaction between input variable S_{i_q} and variable S_{i_t} on the system output. The total sensitivity index $S_{T_{i_t}}$ indicates the common influence of input variable S_{i_t} and its interaction with other input variables on system output. When the first-order sensitivity index of the input variable S_{i_t} is quite different from the total sensitivity index, it indicates that the interaction between the variable S_{i_t} and other input variables has a great influence on the system output.

3.3. Optimization Process of the Channel with Frustums of a Cone

Figure 5 shows the flow chart for the parameter optimization of the channel with frustums of a cone. As can be seen from Figure 5, the present study optimizes the four design parameters of the channel with frustums of a cone, including Reynolds number Re , frustum of a cone angle α , streamwise spacing ratio Z_1/D , and spanwise spacing ratio Z_2/D . CCF was used for the experimental design of design parameters, and 25 sample points were obtained. The reliability of the numerical method in the present study was verified by the experimental data. Then, 25 sample points were numerically simulated by CFD to obtain the responses (the Nu/Nu_0 and f/f_0 of the channels). On this basis, the response surface models were constructed by the second-order polynomial. Root mean square error (RMSE) and determination coefficient (R^2) were selected to evaluate the response surface models. If the models did not meet the requirements, the experimental design of the parameters was optimized, and the simulation was run again according to the above procedure. Then, based on the response surface model, Sobol's method was used to analyze the sensitivity of the parameters. Aiming at achieving minimum f/f_0 and maximum Nu/Nu_0 in the channels, NSGA-II was used to carry out the multi-objective optimization of the parameters. Finally, the optimized channels were selected from the Pareto solution set.

Genetic algorithm (GA) is a family of global optimization algorithms that simulate natural selection and the genetic mechanism based on biological evolution. Among them, the non-dominated sorting genetic algorithm with elite strategy (NSGA-II) was proposed by Deb based on the non-dominated sorting genetic algorithm (NSGA). It has the advantages of low computational complexity, fast running speed, and good convergence of solution set [23]. It is worth noting that the multi-objective optimization algorithm does not have a unique global optimal solution, but a set of optimal solutions, namely the Pareto solution set. In practical application, one or more solutions can be selected from the Pareto solution set as the final result.

4. Results Analysis and Discussion

4.1. Construction of Response Surface Model

The second-order polynomial response surface model was obtained based on CCF fitting. The specific test design table is shown in Table 2. The design parameters were Re , α , Z_1/D and Z_2/D , and the responses were Nu/Nu_0 and f/f_0 . The coefficients of the response surface model are given in Table 3.

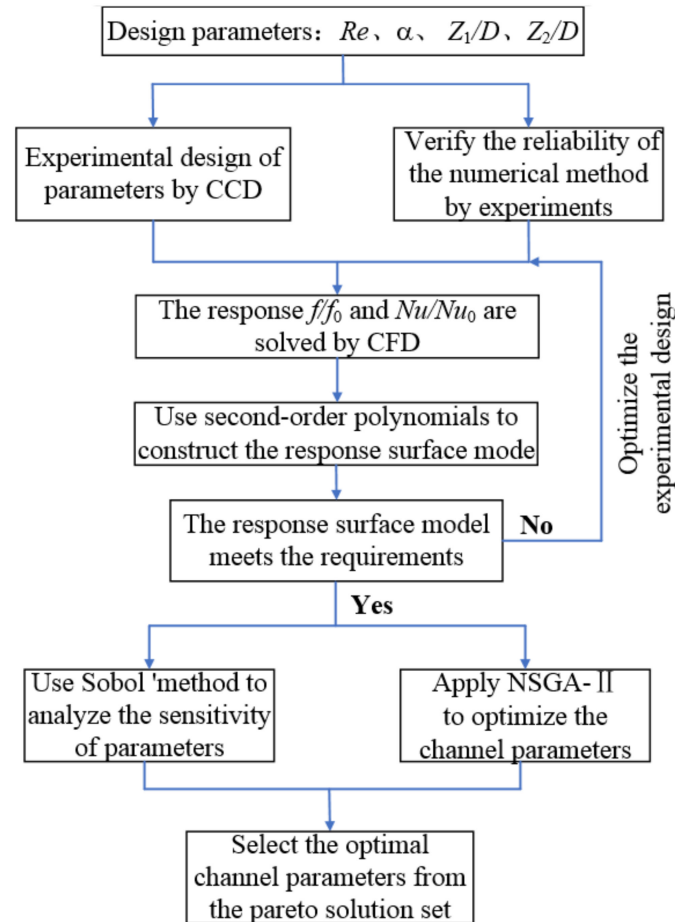


Figure 5. Flow chart of the optimization of the channel parameters.

Table 3. Coefficients of response surface model.

Coefficients	Nu/Nu_0	f/f_0
β_0	0.230	9.66
β_1	0.240×10^{-4}	0.355×10^{-3}
β_2	0.239×10^{-1}	0.800×10^{-3}
β_3	-1.78	-9.75
β_4	3.09	-3.04
β_{11}	0.000	0.000
β_{22}	0.758×10^{-3}	0.188×10^{-2}
β_{33}	0.980	3.28
β_{44}	-1.26	-0.320
β_{12}	0.100×10^{-5}	0.200×10^{-5}
β_{13}	-0.340×10^{-4}	-0.195×10^{-3}
β_{14}	0.650×10^{-4}	0.230×10^{-4}
β_{23}	-0.149×10^{-1}	-0.319×10^{-1}
β_{24}	-0.955×10^{-2}	-0.990×10^{-2}
β_{34}	-0.218	1.76

Figure 6 shows the comparison between the numerically calculated values of the sample points of the experimental design and the corresponding RSM predicted values. In the figure, the dotted line represents a deviation of $\pm 10\%$ from the numerical calculation values, the straight line represents the numerical calculation values, and the scattered points represent the RSM prediction values. Figure 6a,b presents a comparison of the values when the responses are Nu/Nu_0 and f/f_0 , respectively. It can be seen from Figure 6 that the RSM predicted values are distributed near the numerically calculated values, and the errors are basically less than 10%. After calculation, the root mean square error RMSE and determination coefficient R^2 of the response surface model can be obtained. The calculation results are shown in Table 4. When the responses are Nu/Nu_0 and f/f_0 , the RMSE of the models is less than 0.25 and R^2 is greater than 0.93, showing that the fitted response surface model has small error and high accuracy.

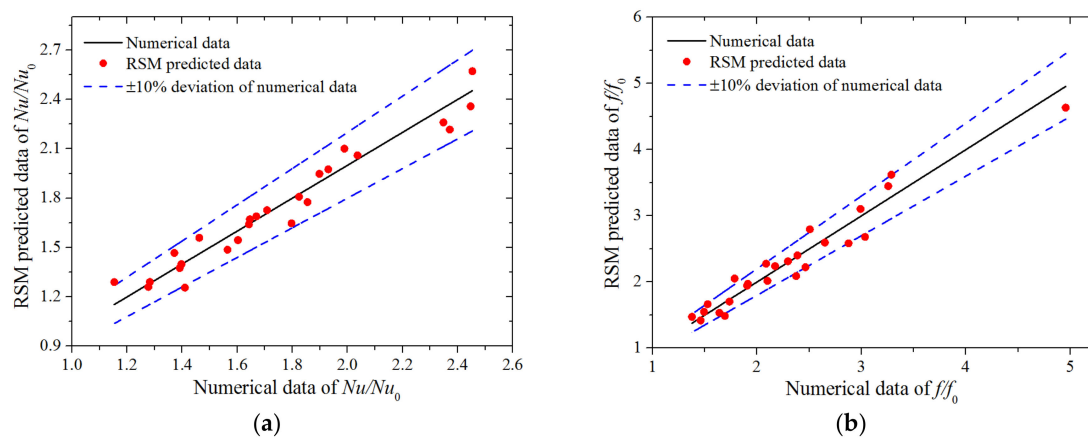


Figure 6. Comparison between numerical calculation and RSM prediction: (a) Nu/Nu_0 ; (b) f/f_0 .

Table 4. Fitting accuracy of response surface model.

Evaluation Index	Nu/Nu_0	f/f_0
RMSE	0.1048	0.2445
R^2	0.9491	0.9399

4.2. Effect of Channel Parameters on Flow and Heat Transfer

The three-dimensional surface and contour map of the Nu/Nu_0 and f/f_0 of the channels are shown in Figures 7 and 8, respectively, to reveal the influence of channel parameters on the heat transfer performance and flow performance of the channels with frustums of a cone. Figure 7a–f show the influence of the combined action of $Re-\alpha$, $Re-Z_1/D$, $Re-Z_2/D$, $\alpha-Z_1/D$, $\alpha-Z_2/D$ and $Z_1/D-Z_2/D$ on the response in turn.

As can be seen from Figure 7a, when Re is constant, increasing α increases the Nu/Nu_0 of the channel, while when α is constant, the increase of the Nu/Nu_0 of the channel along with the increase of Re is not very significant. When Re is 5000 and α is 0° , the Nu/Nu_0 of the channel reaches its minimum value, while when Re is 15,000 and α is 30° , the Nu/Nu_0 of the channel reaches its maximum value. As can be seen from Figure 7b, when Re is constant, increasing Z_1/D makes the Nu/Nu_0 of the channel first increase and then decrease. It can be seen from Figure 7c that the increase in Z_2/D under different values of Re and the increase in Re under different values of Z_2/D can improve the Nu/Nu_0 of the channel. As can be seen from Figure 7d,e, when α is constant, the Nu/Nu_0 of the channel remains basically unchanged with increasing Z_1/D and Z_2/D . When Z_1/D and Z_2/D remain unchanged, increasing α can significantly increase the Nu/Nu_0 of the channel. As can be seen from Figure 7f, when Z_1/D is constant and Z_2/D is increased, Nu/Nu_0 of the channel first decreases and then increases. When Z_2/D is constant, increasing Z_1/D causes the Nu/Nu_0 of the channel to first increase and then decrease.

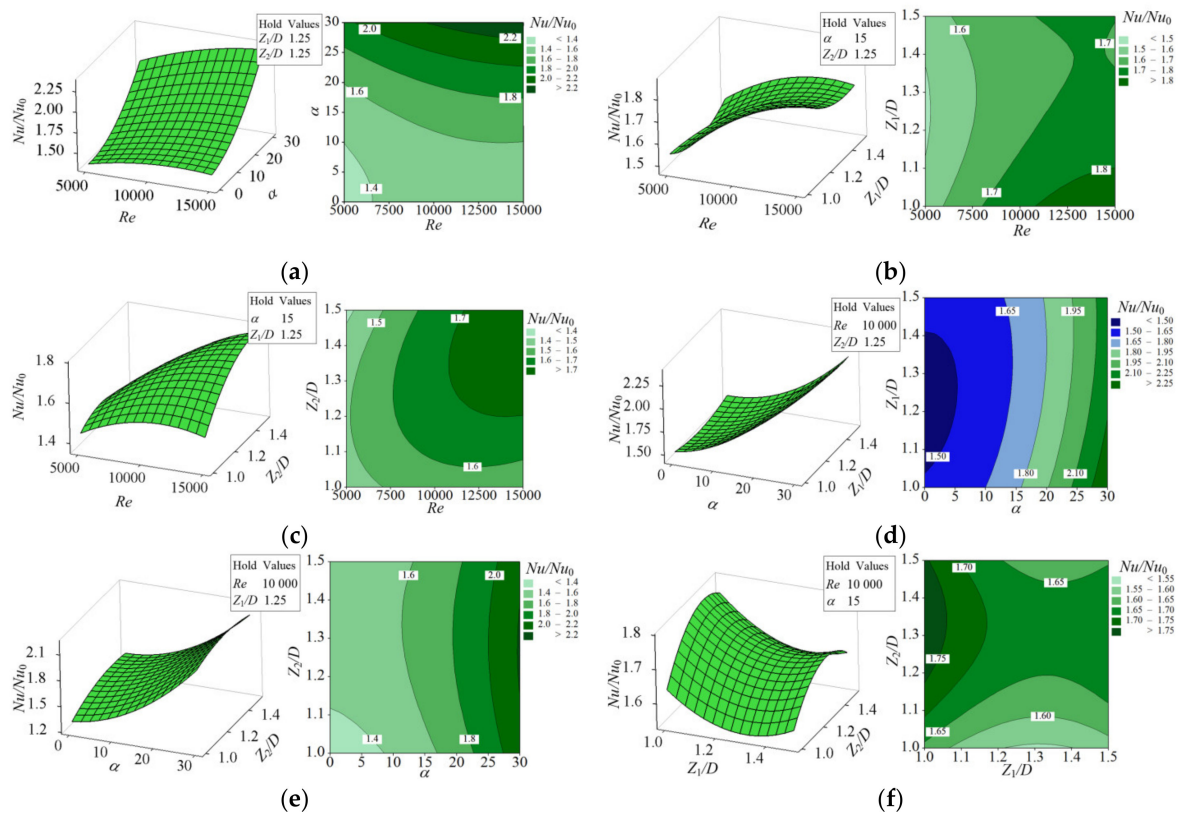


Figure 7. 3D surface and contour map of Nu/Nu_0 : (a) $Re-\alpha$; (b) $Re-Z_1/D$; (c) $Re-Z_2/D$; (d) $\alpha-Z_1/D$; (e) $\alpha-Z_2/D$; (f) $Z_1/D-Z_2/D$.

As can be seen from Figure 8a, at low Re , the ff_0 of the channel first decreases and then increases with increasing α , while at high Re , increasing α leads to an increase in the ff_0 of the channel. When α is constant, the ff_0 of the channel increases with increasing Re . It can be seen from Figure 8b,c that increasing Re and decreasing Z_1/D and Z_1/D result in an increase in the ff_0 of the channel. As can be seen from Figure 8d, when α is constant and Z_1/D is increased, and when Z_1/D is constant and α is increased, the ff_0 of the channel first decreases and then increases. According to Figure 8e, when α is constant, the ff_0 of the channel decreases with increasing Z_2/D . When Z_2/D remains unchanged, the ff_0 of the channel first decreases and then increases with increasing α . As can be seen from Figure 8f, increasing Z_2/D and Z_1/D reduces the ff_0 of the channel.

The above research shows that when analyzing the flow and heat transfer performance of channels with frustums of a cone, the information obtained limited to a fixed channel parameter is not sufficient to describe the performance of the channels. Building the function of channel performance related to channel parameters based on response surface method is of great significance to studying the influence of channel parameters on channel performance and guiding the parameter optimization and structural design of channels with frustums of a cone.

4.3. Sensitivity Analysis of the Channel Parameters

Figure 9 shows the first-order sensitivity index and total sensitivity index of channel parameters when the response is Nu/Nu_0 . The first-order parameter sensitivity index represents the influence of a single parameter on the Nu/Nu_0 of the channels. The total sensitivity index represents the combined influence of a single parameter and its interaction with other parameters on the Nu/Nu_0 of the channels. As can be seen from Figure 9a, when the response is Nu/Nu_0 , the first-order sensitivity indexes of the channel parameters from high to low are α , Re , Z_2/D and Z_1/D . Among them, the changes of α and Re have

an important influence on the Nu/Nu_0 of the channel. According to Figure 9b, the total parameter sensitivity indexes are α , Re , Z_2/D and Z_1/D from high to low, which is the same as the ranking of the first-order sensitivity indexes of the channel parameters. Through calculation, the difference between them is less than 0.02, indicating that the interaction between a single parameter and other parameters of the channels has no significant impact on the Nu/Nu_0 of the channels. In addition, the proportions of α and Re in the total sensitivity index are 50.6% and 47.9%, indicating that α and Re have a greater impact on the Nu/Nu_0 of the channels compared with Z_1/D and Z_2/D .

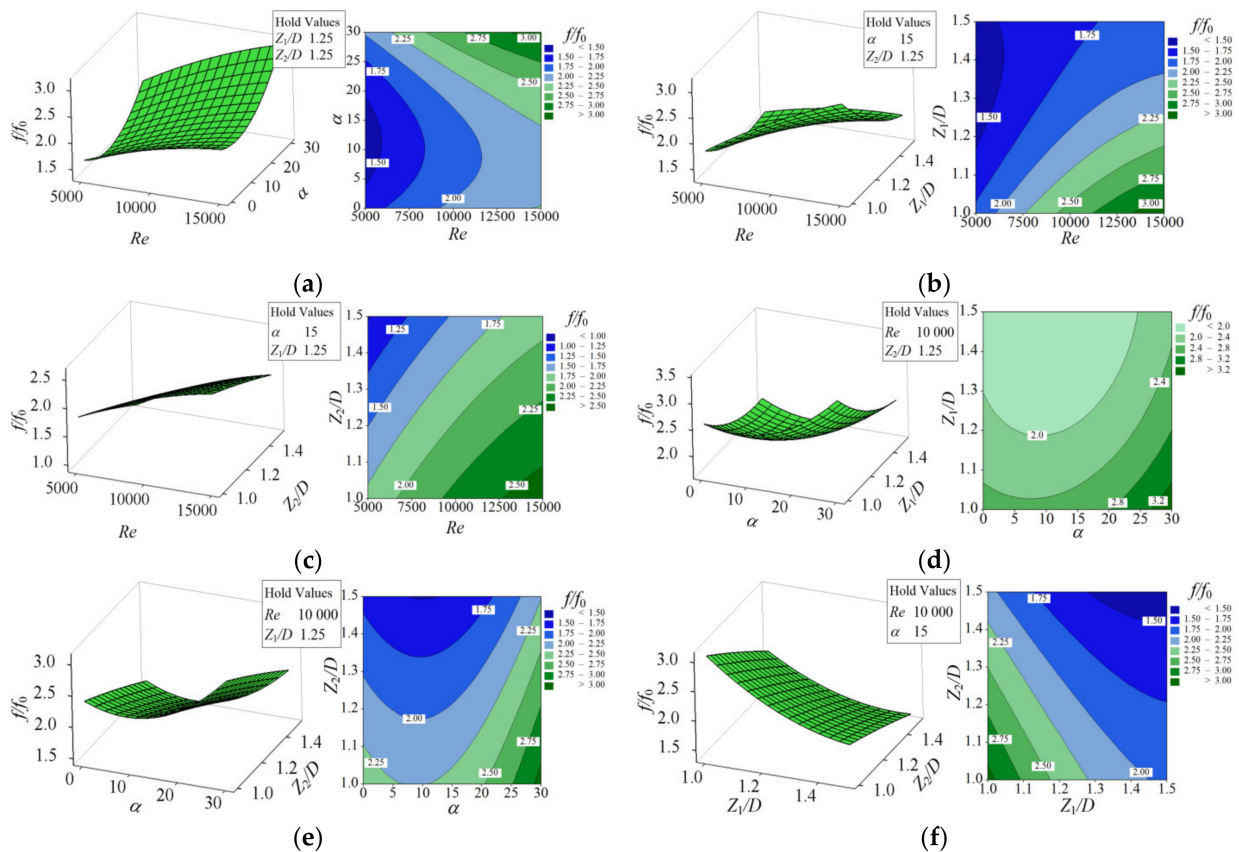


Figure 8. 3D surface and contour map of f/f_0 : (a) $Re-\alpha$; (b) $Re-Z_1/D$; (c) $Re-Z_2/D$; (d) $\alpha-Z_1/D$; (e) $\alpha-Z_2/D$; (f) $Z_1/D-Z_2/D$.

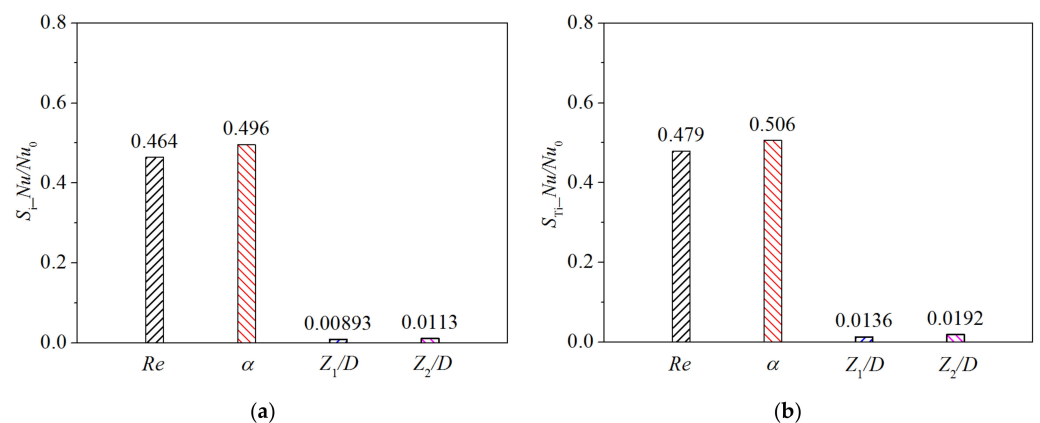


Figure 9. Sensitivity of the parameters when the response is Nu/Nu_0 : (a) first-order sensitivity index; (b) total sensitivity index.

Figure 10 shows the sensitivity index of the channel parameters when the response is f/f_0 , where Figures 10a and 10b are the first-order sensitivity index and total sensitivity index, respectively. It can be seen from Figure 10a that when the response is f/f_0 , the first-order sensitivity indexes of the channel parameters are Re , Z_1/D , α and Z_2/D from high to low. Among them, the first-order sensitivity index of Re is significantly higher than other channel parameters, and the first-order sensitivity indexes of α , Z_1/D and Z_2/D are basically the same, all distributed around 0.15. According to Figure 10b, the total sensitivity indexes of the parameters are Re , Z_1/D , α and Z_2/D from high to low, which is the same as the first-order sensitivity indexes. Through calculation, it can be seen that the difference between the two is less than 0.021, indicating that the interaction between a single parameter and other parameters of the channels has no significant impact on the f/f_0 of the channels. In addition, the proportion of Re in the total sensitivity index is 57.4%, while the proportions of the total sensitivity coefficient of the other three channel parameters are all about 15%, which indicates that Re has the greatest impact on the f/f_0 of the channels, while α , Z_1/D and Z_2/D have a fairly small impact.

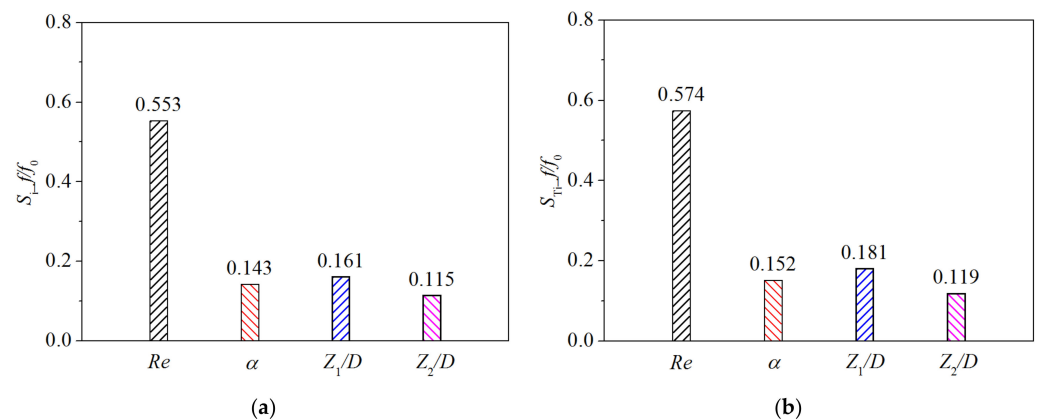


Figure 10. Sensitivity of the parameters when the response is f/f_0 : (a) first-order sensitivity index; (b) total sensitivity index.

4.4. Multi-Objective Optimization Results of the Parameters

With the aim of obtaining the maximum values of Nu/Nu_0 and the minimum values of f/f_0 for the channel, the NSGA-II was used to find the optimal combination of channel parameters in the global range. The population number of the genetic algorithm was 12, the genetic algebra was 40, the crossover probability was 0.9, the mutation probability was 0.1, the crossover distribution index was 10, and the mutation distribution index was 20. The specific settings can be found in Ref. [24]. After the operation, a total of 481 solutions were generated, of which the Pareto solution set, the set of optimal solutions, had a total of 130 solutions. Figure 11 shows the solution set of multi-objective optimization. In Figure 11, the blue dots represent all of the solution sets, and the red curve represents the Pareto front connected by the Pareto solution sets. According to Figure 11, when the f/f_0 of the channel is constant, the Nu/Nu_0 of the channel of the point on Pareto front must be at its maximum. Similarly, when the Nu/Nu_0 of the channel is constant, the f/f_0 of the channel of the point on the Pareto front must be at its minimum.

On the basis of the sensitivity analysis of the parameters, the parameter Re has the greatest impact in the performance of the channel in terms of the flow and heat transfer performance of the channel. Consequently, the K-means clustering algorithm was used to cluster the Pareto solution sets under different values of Re . Figure 12 illustrates the results of K-means clustering of the Pareto solution set. As can be seen from Figure 12, the Pareto solution sets can be divided into four categories—A, B, C and D—under different values of Re . Without considering the influence of α , Z_1/D and Z_2/D , when Re increases, the Nu/Nu_0 and f/f_0 of the channel under the Pareto solution set increase slightly.

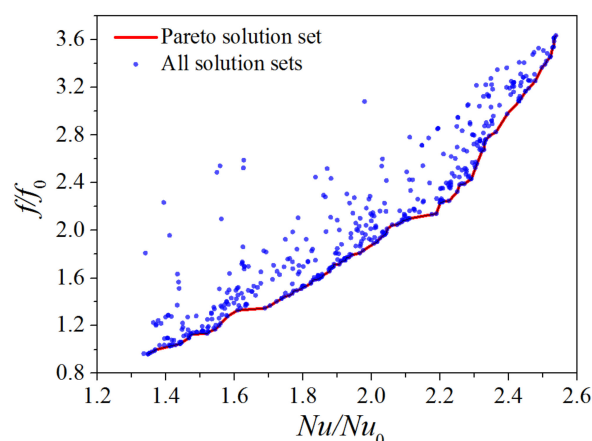


Figure 11. Solution set of multi-objective optimization.

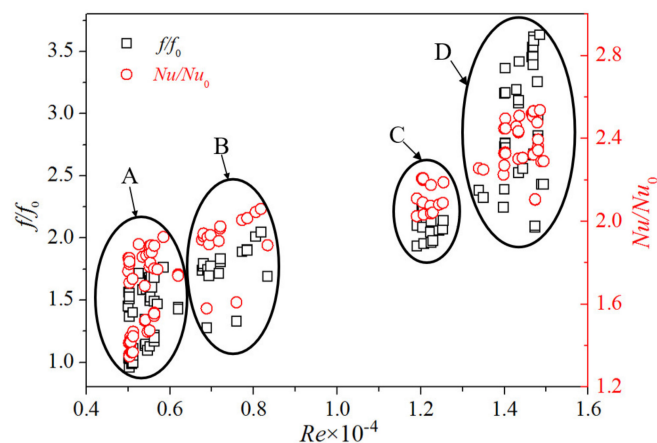


Figure 12. Result of K-means clustering of the Pareto solution set.

An optimal solution was selected from each of the four categories A, B, C and D in Figure 12 for comparative analysis. The specific optimal parameter combinations are provided in Table 5. According to Table 5, the Nu/Nu_0 of optimization points A, B, C and D increased by 9.70%, 21.82%, 26.06% and 27.88%, respectively, compared with the reference channel. In addition, the f/f_0 of the optimization points decreased by 19.89%, 1.05%, -7.85% and -9.42% , respectively, compared with the reference channel. Among them, the Nu/Nu_0 and f/f_0 of optimization points A and B were optimized, while the Nu/Nu_0 of optimization points C and D was considerably improved, but the f/f_0 had increased moderately. This is because the values of Re for optimization points C and D are large. When the Nu/Nu_0 increases, f/f_0 will also increase. Overall, compared with the reference channel, the Nu/Nu_0 of the optimized channels increased by 21.36% on average, and the f/f_0 decreased by 9.16% on average. This shows that the optimization results of the channel parameters in the present study are good, and can serve as a reference for the multi-objective optimization of channels with turbulent structures.

Table 5. Optimal channel parameters.

Type	Re	α	Z_1/D	Z_2/D	Nu/Nu_0	f/f_0
Reference channel	10,000	15	1.25	1.25	1.65	1.91
Optimization point A	5030	29.94	1.29	1.49	1.81	1.53
Optimization point B	7723	29.88	1.39	1.46	2.01	1.89
Optimization point C	12,433	26.62	1.42	1.44	2.08	2.06
Optimization point D	14,730	26.10	1.40	1.49	2.11	2.09

To further explore the influence of channel parameters on the flow and heat transfer performance of the channels, Figure 13 shows the comparison of surface streamline, temperature distribution, and Nu distribution of the heat transfer walls of the reference channel and optimization point C. Figure 13a,c shows the reference channel, and Figure 13b,d gives the optimization points C. It can be seen from Figure 13a,b that the high-temperature area of the heat transfer wall is mainly distributed upstream and downstream of the convex and upstream of the bottom of the concave. In comparison, the temperature of the high-temperature region of the optimized channel is lower and the area with high temperature is smaller. There are large vortices upstream of the bottom of the concave and upstream and downstream of the convex in the reference channel, while the vortices in the optimized channel are improved. The improvement of the vortices will reduce the frictional resistance of the channel and the accumulation of airflow, thus reducing the local temperature of the heat transfer wall and reducing the area with high temperature. According to Figure 13c,d, contrary to the temperature distribution of the heat transfer wall, the high-temperature area had a lower Nu and the low-temperature area had a higher Nu . In comparison, the Nu value of the high- Nu region of the optimized channel was higher and the area with high Nu was larger. The results show that the optimized channel improves the vortices at the bottom of the concave and upstream and downstream of the convex, so that the heat transfer wall of the channel has a lower temperature distribution and a higher Nu distribution.

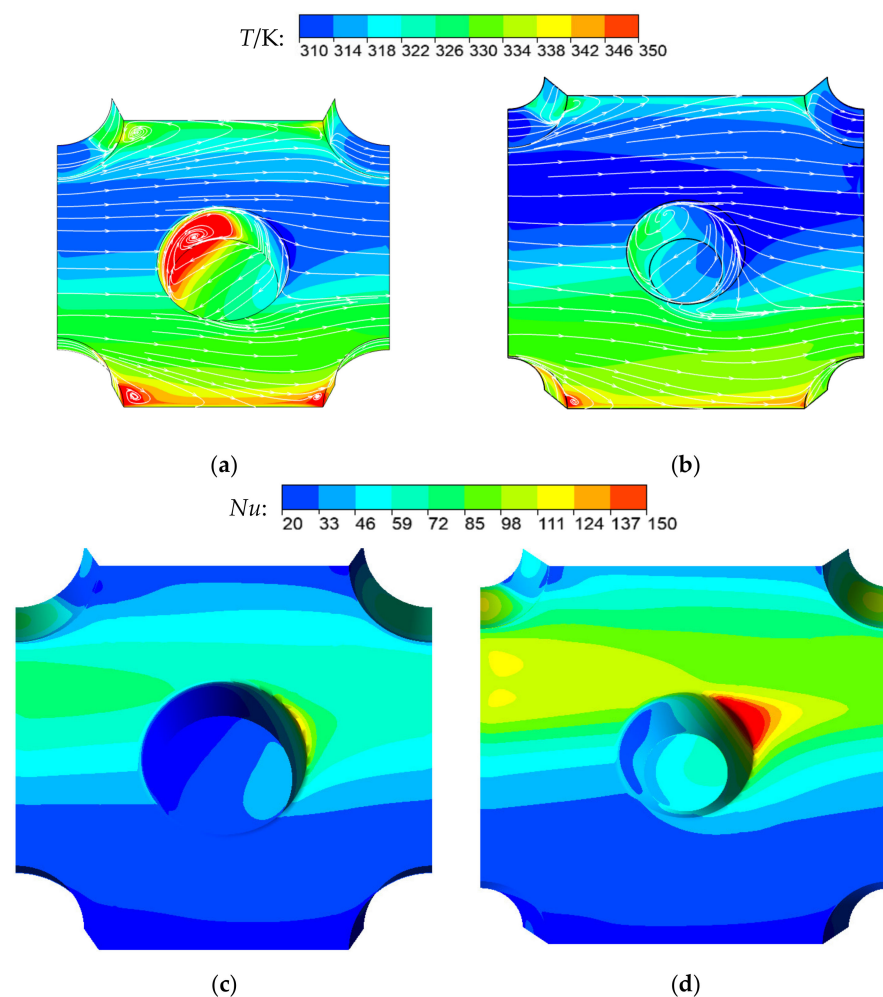


Figure 13. The Comparison of Reference Channel and Optimization Point C: (a) Surface Streamline and Temperature Distribution of the Reference Channel; (b) Surface Streamline and Temperature Distribution of the Optimized Channel; (c) Nu Distribution of the Reference Channel; (d) Nu Distribution of the Optimized Channel.

5. Conclusions

The multi-objective parameter optimization of channels with frustums of a cone was carried out. The design variables were Re , α , Z_1/D and Z_2/D . The optimization objective was to maximize the Nu/Nu_0 and minimize the f/f_0 . Firstly, the experimental design of the channel parameters was carried out, and the second-order response surface model was constructed. Then, the accuracy of the response surface model was tested. Once the response surface met the requirements, the sensitivity of the channel parameters was analyzed, and the Pareto solution set was obtained. The Pareto solution set was analyzed by K-means clustering, and finally, four optimization channels were selected. The main conclusions can be drawn as follows:

- (1) The second-order response surface models obtained by CCF have small errors and high accuracy. When the response is Nu/Nu_0 , the $RMSE$ of the model is 0.1048 and R^2 is 0.9491. When the response is f/f_0 , the $RMSE$ of the model is 0.2445 and R^2 is 0.9399.
- (2) Compared with Z_1/D and Z_2/D , α and Re have the greatest impact on the Nu/Nu_0 of the channels. Parameter Re has the greatest influence on the f/f_0 of the channels, while α , Z_1/D and Z_2/D have the same, small influence on the f/f_0 of the channels.
- (3) By comparing the reference channel with the optimized channel, the results show that the optimized channel improves the vortexes at the bottom of the concave and upstream and downstream of the convex, so that the heat transfer wall of the channel has lower temperature distribution and higher Nu distribution.
- (4) Compared with the reference channel, the Nu/Nu_0 of the four optimized channels are increased by 9.70%, 21.82%, 26.06% and 27.88%, respectively; the f/f_0 decreased by 19.89%, 1.05%, -7.85% and -9.42%, respectively. The Nu/Nu_0 of the channels increased by 21.36% on average and the f/f_0 declined by 9.16% on average, which demonstrates that the optimization method of the channel parameters in the present study has a good effect.

Author Contributions: Conceptualization, Z.Z. and L.X. (Lei Xi); methodology, Z.Z. and L.X. (Liang Xu); software, Z.Z.; validation, Z.Z., L.X. (Liang Xu) and Q.R.; formal analysis, Z.Z. and J.G.; investigation, Z.Z., Q.R. and Y.L.; resources, Z.Z., L.X. (Lei Xi) and J.G.; data curation, Z.Z. and Y.L.; writing—original draft preparation, Z.Z. and L.X. (Liang Xu); writing—review and editing, L.X. (Liang Xu), Z.Z. and L.X. (Lei Xi); visualization, L.X. (Lei Xi) and Z.Z.; supervision, L.X. (Liang Xu) and J.G.; project administration, J.G.; funding acquisition, L.X. (Liang Xu). All authors have read and agreed to the published version of the manuscript.

Funding: The authors would like to express their sincere gratitude to the National Key R&D Program of China (2018YFB1106400), the National Natural Science Foundation of China (Grant No.51876157), and Natural Science Foundation of Shanxi Province in China (2019JM-096) for providing financial support for this work.

Institutional Review Board Statement: Not applicable.

Informed Consent Statement: Informed consent was obtained from all subjects involved in the study.

Data Availability Statement: Not applicable.

Conflicts of Interest: The authors declare no conflict of interest.

Nomenclature

RSM	Response Surface Methodology
Nu/Nu_0	Nusselt number ratio
f/f_0	Friction coefficient ratio
$RMSE$	Root mean square errors
R^2	Determination coefficients
α	Frustum of a cone angle ($^\circ$)
Re	Reynolds number
Z_2/D	Spanwise spacing ratio

Z_1/D	Streamwise spacing ratio
NSGA-II	Non-dominated sorting genetic algorithm with elite strategy
CCF	Central composite face-centered design
D	Bottom diameter of the frustum of a cone (mm)
N-S	Navier Stokes
GA	Genetic Algorithm
k	Turbulent kinetic energy equation
ε	Diffusion equation
CCD	central composite design
RNG	Renormalization Group
SIMPLEC	Semi-Implicit Method for Pressure Linked Equation
Z_2	Spanwise spacing (mm)
H	Height of the frustum of a cone (mm)
Z_1	Streamwise spacing (mm)
V	Average inlet velocity of air flow (m/s)
P	Characteristic length (mm)
ν	Kinematic viscosity of air (m ² /s)
Nu_x	Local Nusselt number
q_x	Local heat flux (W/m ²)
T_w	Local temperature of the wall (K)
T_f	Reference temperature (K)
Nu	Average Nusselt number
A	Area of heat transfer wall (m ²)
f	Friction coefficient
L	channel length (mm)
Δp	Pressure drop (Pa)
ρ	Air density (kg/m ³)
λ	Thermal conductivity of air (W/m K)
Nu_0	Average Nusselt number of smooth parallel plate channel
f_0	Friction coefficient of smooth parallel plate channel
Y	Response
X	Design variable
$f(X)$	Approximate function of the target
β	Fitting coefficient
ε	Prediction error
$F(x)$	A square integrable function
M	Total variance of the $F(x)$
$M_{i_1 \dots i_t}$	Partial square deviation of the $F(x)$
$S_{i_1 \dots i_t}$	Sensitivity index of the variable
S_{i_t}	First order sensitivity index
$S_{i_t^2}$	Second-order sensitivity index
S_{Ti_t}	Total sensitivity index



References

- Zheng, N.; Liu, P.; Shan, F.; Liu, Z.; Liu, W. Sensitivity analysis and multi-objective optimization of a heat exchanger tube with conical strip vortex generators. *Appl. Therm. Eng.* **2017**, *122*, 642–652. [CrossRef]
- Xi, L.; Xu, L.; Gao, J.; Zhao, Z.; Li, Y. Numerical analysis and optimization on flow and heat transfer performance of a steam-cooled ribbed channel. *Case Stud. Therm. Eng.* **2021**, *28*, 101442. [CrossRef]
- Izadi, M.; Mohebbi, R.; Sajjadi, H.; Delouei, A.A. LTNE modeling of Magneto-Ferro natural convection inside a porous enclosure exposed to nonuniform magnetic field. *Phys. A Stat. Mech. Appl.* **2019**, *535*, 122394. [CrossRef]
- Jeong, H.-S.; Seo, J.-W.; Kim, K.-Y. Multi objective optimization of a slit rib in a rectangular cooling channel. *Heat Transf. Res.* **2018**, *49*, 395–412. [CrossRef]
- Seo, J.-W.; Afzal, A.; Kim, K.-Y. Efficient multi-objective optimization of a boot-shaped rib in a cooling channel. *Int. J. Therm. Sci.* **2016**, *106*, 122–133. [CrossRef]
- Mamourian, M.; Milani Shirvan, K.; Mirzakhani, S. Two phase simulation and sensitivity analysis of effective parameters on turbulent combined heat transfer and pressure drop in a solar heat exchanger filled with nanofluid by Response Surface Methodology. *Energy* **2016**, *109*, 49–61. [CrossRef]

7. Bu, S.; Yang, Z.; Zhang, W.; Liu, H.; Sun, H. Research on the thermal performance of matrix cooling channel with response surface methodology. *Appl. Therm. Eng.* **2016**, *109*, 75–86. [CrossRef]
8. Shi, X.; Li, S.; Mu, Y.; Yin, B. Geometry parameters optimization for a microchannel heat sink with secondary flow channel. *ICHMT* **2019**, *104*, 89–100. [CrossRef]
9. Wen, J.; Li, K.; Liu, Y.; Wu, M.; Wang, S. Multi-objective optimization of serrated fin in plate-fin heat exchanger by fluid structure interaction. *J. Xi'an Jiaotong Univ.* **2018**, *52*, 130–135. (In Chinese)
10. Zheng, N.; Liu, P.; Liu, Z.; Liu, W. Numerical simulation and sensitivity analysis of heat transfer enhancement in a flat heat exchanger tube with discrete inclined ribs. *Int. J. Heat Mass Transf.* **2017**, *112*, 509–520. [CrossRef]
11. Feng, G. Research progress in the flow induced vibration mechanism of tube bundles in heat exchangers and precautionary measures. *Chem. Ind. Eng. Prog.* **2012**, *31*, 508–512. (In Chinese)
12. Abdulhay, B.; Bourouga, B.; Dessain, C. Experimental and theoretical study of thermal aspects of the hot stamping process. *Appl. Therm. Eng.* **2011**, *31*, 674–685. (In Chinese) [CrossRef]
13. Zhao, Z.; Xu, L.; Gao, J.; Xi, L.; Li, Y. Study on the Flow and Heat Transfer Characteristics of the Heat Exchanger with Cone-Type Vortex Generators. *J. Xi'an Jiaotong Univ.* **2021**, *10*, 131–143. (In Chinese)
14. Luo, L.; Du, W.; Wang, S.; Wang, L.; Sundén, B.; Zhang, X. Multi-objective optimization of a solar receiver considering both the dimple/protrusion depth and delta-winglet vortex generators. *Energy* **2017**, *137*, 1–19. [CrossRef]
15. Zeng, M.; Zhang, G.; Li, Y.; Niu, Y.; Ma, Y.; Wang, Q. Geometrical Parametric Analysis of Flow and Heat Transfer in the Shell Side of a Spiral-Wound Heat Exchanger. *HTrEn* **2015**, *36*, 790–805. [CrossRef]
16. Liu, J.; Song, Y.; Xie, G.; Sunden, B. Numerical modeling flow and heat transfer in dimpled cooling channels with secondary hemispherical protrusions. *Energy* **2015**, *79*, 1–19. [CrossRef]
17. Kim, H.-M.; Moon, M.-A.; Kim, K.-Y. Multi-objective optimization of a cooling channel with staggered elliptic dimples. *Energy* **2011**, *36*, 3419–3428. [CrossRef]
18. Elyyan, M.A.; Rozati, A.; Tafti, D.K. Investigation of dimpled fins for heat transfer enhancement in compact heat exchangers. *Int. J. Heat Mass Transf.* **2008**, *51*, 2950–2966. [CrossRef]
19. Courand, A.; Metz, M.; Héran, D.; Feilhes, C.; Prezman, F.; Serrano, E.; Bendoula, R.; Ryckewaert, M. Evaluation of a robust regression method (RoBoost-PLSR) to predict biochemical variables for agronomic applications: Case study of grape berry maturity monitoring. *Chemom. Intell. Lab. Syst.* **2022**, *221*, 104485. [CrossRef]
20. Sobol', I.M. Global sensitivity indices for nonlinear mathematical models and their Monte Carlo estimates. *Math. Comput. Simul.* **2001**, *55*, 271–280. [CrossRef]
21. Song, Y.; Wang, Y.; Yang, S.; Wang, S.; Yang, M. Sensitivity analysis and parameter optimization of energy consumption for underwater gliders. *Energy* **2020**, *191*, 116506. [CrossRef]
22. Saltelli, A.; Annoni, P.; Azzini, I.; Campolongo, F.; Ratto, M.; Tarantola, S. Variance based sensitivity analysis of model output. Design and estimator for the total sensitivity index. *Comput. Phys. Commun.* **2010**, *181*, 259–270. [CrossRef]
23. Deb, K.; Pratap, A.; Agarwal, S.; Meyarivan, T. A fast and elitist multiobjective genetic algorithm: NSGA-II. *IEEE Trans. Evol. Comput.* **2002**, *6*, 182–197. [CrossRef]
24. Xu, L.; Ruan, Q.; Shen, Q.; Xi, L.; Gao, J.; Li, Y. Optimization Design of Lattice Structures in Internal Cooling Channel with Variable Aspect Ratio of Gas Turbine Blade. *Energies* **2021**, *14*, 3954. [CrossRef]

Article

Aerodynamics and Complicated Heat Transfer with the Mixed Motion of Air in the Flat Duct of a High-Temperature Heat Exchanger

Borys Basok ¹, Vyacheslav Kremnev ¹, Anatoliy Pavlenko ^{2,*}  and Andriy Timoshchenko ¹ 

¹ Institute of Engineering Thermophysics, National Academy of Sciences of Ukraine, 03057 Kiev, Ukraine; basok@itf.kiev.ua (B.B.); kremnev@ukr.net (V.K.); a_timoshchenko@ukr.net (A.T.)

² Department of Building Physics and Renewable Energy, Kielce University of Technology, al. Tysiąclecia Państwa Polskiego 7, 25-314 Kielce, Poland

* Correspondence: apavlenko@tu.kielce.pl; Tel.: +48-883-741-291

Abstract: The purpose of the research is to study the aerodynamics and heat transfer in the duct of a high-temperature recuperation system. The object of the research is a flat duct with a thickness-to-height ratio $a:b = 1:10$, length $c = 400 \cdot a$ with one-sided heat input to the duct surface, complicated heat transfer and mixed air movement in the duct. The objectives of the research are to determine: (a) average temperatures on the duct surfaces; (b) air temperature distribution along the length of the duct; (c) local and average integral temperature values along the length of the duct; (d) local and average integral heat flow densities on the duct surfaces; (e) local and average integral heat exchange coefficients and Nusselt numbers on the duct surfaces; and (f) pressure distribution along the length and total pressure drop in the duct. The research method is based on conducting a mathematical numerical experiment in a stationary three-dimensional Cartesian formulation and physical modeling of processes on a prototype. It is established that the dominant heat transfer between the duct walls and the air is a complicated convective heat transfer, in which forced convection is affected by free convection. There is a 1.5–2.0-fold difference in the values of the heat flow density on the hot and non-heated surfaces of the duct. Generalizing dependences of Nusselt numbers, temperature pressures and friction resistance coefficients as functions of a dimensionless coordinate are obtained.

Keywords: radiation-convective heat transfer; high-temperature recuperation system

Citation: Basok, B.; Kremnev, V.; Pavlenko, A.; Timoshchenko, A. Aerodynamics and Complicated Heat Transfer with the Mixed Motion of Air in the Flat Duct of a High-Temperature Heat Exchanger. *Energies* **2022**, *15*, 865. <https://doi.org/10.3390/en15030865>

Academic Editor: Jan Danielewicz

Received: 27 December 2021

Accepted: 23 January 2022

Published: 25 January 2022

Publisher's Note: MDPI stays neutral with regard to jurisdictional claims in published maps and institutional affiliations.



Copyright: © 2022 by the authors. Licensee MDPI, Basel, Switzerland. This article is an open access article distributed under the terms and conditions of the Creative Commons Attribution (CC BY) license (<https://creativecommons.org/licenses/by/4.0/>).

1. Introduction

Issues of high-temperature recuperation have an attitude to the processes of transferring of substance and energy, which are complicated by the simultaneous action of various factors. These are and different kinds and regimes of substance motion, and different mechanisms of transferring heat in the objects that are investigated. Many works are devoted to studying complicated heat transfers in compact high-temperature heat exchangers of various types [1–4]. The dominant mechanisms of transferring in them are convective and radiative heat transfer [5–10]. The feature of the work consists of the applied nature of the research aimed at studying the conditions of flow and heat transfer in an air-cooled duct, which is the basis of heat recuperation devices for high-temperature industrial plants. The formulation of the research tasks most fully describes the conditions-temperature, magnitude and direction of the heat flow density, the type of coolant and its mass flow, the geometry of the duct and the main physical and mechanical characteristics of its surfaces observed in modern high-temperature processes for the production of glass and stone fibers. The research and processing of the results were carried out using classical methods [11,12]. At the same time, for each of the duct surfaces involved in heat transfer and differing in the magnitude and direction of the supplied heat flow, Nusselt numbers and temperature pressures are determined. The results of the research were

compared with the case of convective heat transfer in pipes and ducts with symmetrical heat supply to the duct surfaces, which allowed us to establish the nature and magnitude of the influence of complicated heat transfer on the characteristics of the process, in order to obtain their qualitative and quantitative indicators. The generalized dependences obtained make it possible to calculate the aerodynamic drag, temperature and energy parameters of the process, with complicated heat transfer and mixed motion necessary for the design of high-temperature heat recuperation systems in order to increase the energy efficiency of production processes. Utilization and reduction of heat losses in high-temperature industrial plants in order to increase their energy efficiency is implemented on the basis of the use of innovative heat exchange devices or heat recuperation systems. Heat transfer processes in them are carried out at high temperature heads, one-sided heat input, complicated radiation-conductive-convective heat transfer and mixed motion of air as a heat carrier.

Problem definition.

The simplified scheme of heat flow densities for a fragment of the lining is shown, which is typical for high-temperature heat recuperation systems with an air heat curtain, Figure 1.

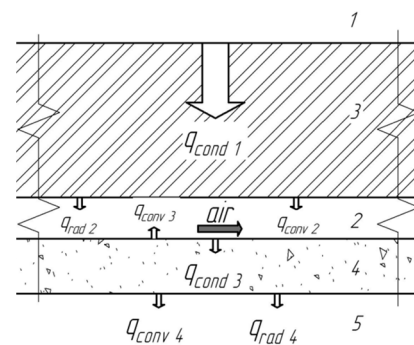


Figure 1. Scheme of heat transfer: 1—internal space of the technological equipment; 2—air duct for recuperation of the heat loss, type the heat curtain; 3—lining; 4—thermal insulation of the lining to reduce dissipative heat loss; 5—environment; $q_{cond 1}$, $q_{cond 3}$ —conductive heat flow; $q_{conv 2}$, $q_{conv 3}$, $q_{conv 4}$ —convective heat flow; $q_{rad 2}$, $q_{rad 4}$ —radiation heat flow.

In the summary conductive heat flow through the lining $q_{cond 1}$, one consists of losses with convective $q_{conv 2}$ and radiation $q_{rad 2}$ heat flows from the internal surface of the air duct $q_{cond 1} = q_{conv 2} + q_{rad 2}$; the radiation heat flow $q_{rad 2}$ makes up for convective heat transfer from the surface of the duct $q_{conv 3}$ and heat loss by conductive $q_{cond 3}$ through thermal insulation $q_{rad 2} = q_{conv 3} + q_{cond 3}$. The heat losses through thermal insulation $q_{cond 3}$ consists from convective $q_{conv 4}$ and radiation $q_{rad 4}$ heat flows from external surface of the equipment to environment. As can be seen, the heat losses to the environment comprise complicated radiation-convective heat transfer. For an integral description of all heat flows, the classical expressions presented in [13–16] are used to calculate the value of the convective and radiation heat exchange coefficients. It is assumed that each of the heat transfer mechanisms is independent, and there is no interaction between them.

2. Methodology of the Research

The complicated heat transfer in the air duct is determined by the action radiation and convective mechanisms of the transfer. Cases of such heat transfer do not have universal generalizing correlations, so they should be studied individually for each variant of technological equipment [13,17,18]. In particular, for our problem, the conditions that determine the features of complicated heat transfer in the duct are as follows:

- the Boltzmann criterion is much larger than 1, $Bo \in (10^2; 3 \cdot 10^3)$, so the
- mechanism of heat transfer between the duct surfaces and the air flow is
- convection;
- the high temperature of the hot surface of duct-up to 700 °C;

- presence of a temperature difference between the duct surfaces;
- radiation transfer of heat from the hot wall of the duct to the cold one;
- turbulent flow regime, $Re \in (4 \cdot 10^3; 10^4)$;
- the combined influence of free and forced convection on heat transfer in the
- duct, $Ra \in (10^5; 6 \cdot 10^6)$.

Research objective. The research objective is to determine: (a) average temperatures on the duct surfaces; (b) distribution of air temperature along the duct length; (c) local and average integral temperature heads along the duct length; (d) local and average integral heat flow density on the duct surfaces; (e) local and average integral heat exchange coefficients and Nusselt numbers on the duct surfaces; and (f) pressure distribution along the length and total pressure drop in the duct.

The object of the research is a flat duct with the ratio of sides of thickness to height $a:b = 1:10$, length $c = 400 \cdot a$ with one-sided heat input (boundary conditions of the 2nd kind) and complicated heat transfer with mixed air motion, Figure 2.

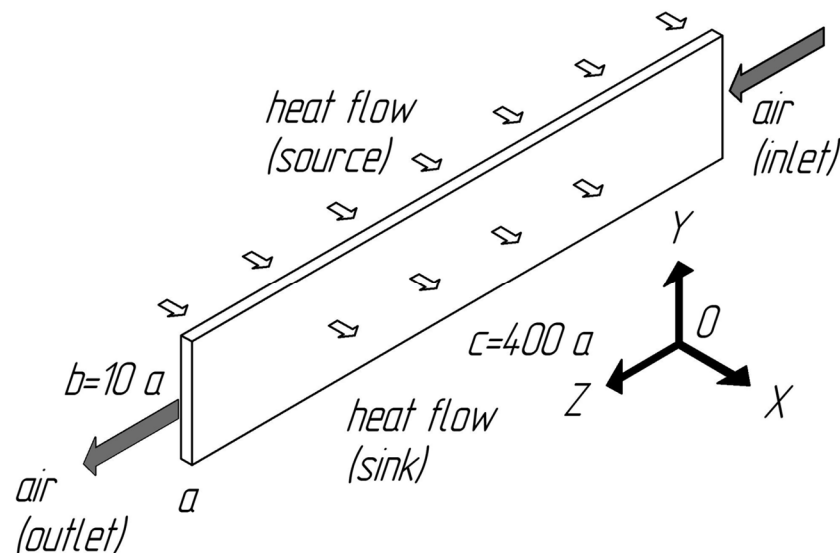


Figure 2. Scheme of the modelling area.

The subject of the research is the aerodynamics of air flow and heat transfer in the duct. The research is based on mathematical and physical modeling of processes. The mathematical numerical experiment is performed on a stationary three-dimensional Cartesian model. Physical modeling of the operation of the air-cooling system is carried out during pilot tests.

3. Physical Model of Complicated Heat Transfer and Mixed Air Motion in the Flat Duct

Features of the problem are: (a) one-sided heat input, as a result of which traditional convective heat transfer in the duct is complicated by radiation heat transfer between the hot surface (source) and other surfaces of the duct that are not heated; (b) air is considered as a diathermal medium; and (c) multidirectional action of vectors of volume forces and pressure forces. The research is conducted using a CFD package for turbulent flow. In particular, to describe radiation heat transfer in the duct, the surface-to-surface (S2S) model of radiation heat transfer in space bounded by gray diffuse surfaces is used. The main assumption in the S2S model-absorption, radiation or scattering by a gas medium is ignored, and only surface radiation is considered in the analysis. A non-isothermal flow is modeled, turbulent flow regime is considered, the air flow is taken as a Newtonian liquid and the dependence of the thermophysical properties of air on temperature is considered.

Mathematical model of flow and complicated heat transfer in the duct with mixed motion of air. In a general view, the expressions for the S2S model are written as follows [15,16]
 energy flow transmitted by other surfaces— $A_k \cdot q_{in,k} = \sum_{j=1}^N A_j \cdot q_{out,j} \cdot F_{jk}$;
 mathematical formulation of the principle of reciprocity— $A_j \cdot F_{jk} = A_k \cdot F_{kj}$;
 heat flow that is gotten on the surface k from surfaces $N - q_{in,k} = \sum_{j=1}^N q_{out,j} \cdot F_{jk}$;
 factor of mutual influence F_{ij} between the two surfaces with final sizes i and j —

$$F_{ij} = \frac{1}{A_i} \int_{A_i} \int_{A_j} \frac{\cos \theta_i \cdot \cos \theta_j}{\pi \cdot r^2} \delta_{ij} dA_i dA_j;$$

radiation energy flow that transfers from surface k

$$q_{out,k} = \varepsilon_k \cdot \sigma \cdot T_k^4 + \rho_k \cdot \sum_{j=1}^N q_{out,j} \cdot F_{jk},$$

where A_k —area of the surface k ; F_{jk} —factor which consider geometrical features position of the surfaces k and j and influence on the part of the energy that transmitted from surface j to surface k ; $q_{in,k}$ —heat flow that get in the surface k from environmental; δ_{ij} —defines the visibility dA_j to dA_i ($\delta_{ij} = 1$ if dA_j is visible from dA_i or 0 otherwise); ε_k —radiant emittance of the surface k ; ρ_k —radiant reflectance of the surface k ; σ —Stefan-Boltzmann constant. Indexes: *in*, *out*—indexes refer to data that get in or get out, correspondingly; i , j , k , N to refer to the surfaces i , j , k , N , correspondingly.

In convective heat transfer, the equations of continuity, momentum transfer, energy, kinetic energy dissipation and kinetic energy dissipation rate were used.

The following boundary conditions were set

$$\begin{aligned} x = -\frac{a}{2}; y \in \left[-\frac{b}{2}; \frac{b}{2}\right]; z \in [0; c], \quad q_0 = -\lambda_{air} \left(\frac{\partial T}{\partial x}\right)_{x=-\frac{a}{2}} + q_{rad, -\frac{a}{2}}; \\ x = \frac{a}{2}; y \in \left[-\frac{b}{2}; \frac{b}{2}\right]; z \in [0; c], \quad 0 = -\lambda_{air} \left(\frac{\partial T}{\partial x}\right)_{x=\frac{a}{2}} - q_{rad, \frac{a}{2}}; \\ x \in \left[-\frac{a}{2}; \frac{a}{2}\right]; y = \frac{b}{2}; z \in [0; c] \quad 0 = -\lambda_{air} \left(\frac{\partial T}{\partial y}\right)_{y=\frac{b}{2}} - q_{rad, \frac{b}{2}}; \\ x \in \left[-\frac{a}{2}; \frac{a}{2}\right]; y = -\frac{b}{2}; z \in [0; c] \quad 0 = -\lambda_{air} \left(\frac{\partial T}{\partial y}\right)_{y=-\frac{b}{2}} - q_{rad, -\frac{b}{2}}; \\ x \in \left[-\frac{a}{2}; \frac{a}{2}\right]; y \in \left[-\frac{b}{2}; \frac{b}{2}\right]; z = 0; \quad G_{inlet} = G_0; T = T_{inlet}; u = v = 0; \\ x \in \left[-\frac{a}{2}; \frac{a}{2}\right]; y \in \left[-\frac{b}{2}; \frac{b}{2}\right]; z = c; \quad p = 0; G_{outlet} = G_{inlet}; u = v = 0; \left(\frac{\partial T}{\partial z}\right)_{z=c} = 0, \end{aligned}$$

where $q_0 \in [5000; 6000]$ W/m², $G_{inlet} \in [100; 200]$ kg/h, $t_{inlet} = 30$ °C, $c = 13.0$ m—the parameters of the pilot plant; radiant emittance of duct surfaces $\varepsilon = 0.93$.

4. Data Processing and Displaying Technique

Results of the research are viewed as integral characteristics, namely: average heat exchange coefficient from the duct surface in the i section $\alpha = \frac{\bar{q}_w}{(t_w - t_a)}$; average heat flow density at the wall of the duct $\bar{q}_w = \frac{1}{b} \int_{-\frac{b}{2}}^{\frac{b}{2}} q_w(y) dy$; average temperature of the wall of the duct $\bar{t}_w = \frac{1}{b} \int_{-\frac{b}{2}}^{\frac{b}{2}} t_w(y) dy$; average mass air temperature $\bar{t}_{air} = \frac{\int_f \rho w t_a df}{\int_f \rho w df}$; average mass air flow rate $\bar{w} = \frac{\int_f \rho w df}{\int_f \rho df}$; average integral heat exchange coefficient over the length of the duct $\bar{\alpha} = \frac{1}{c} \int_0^c \alpha(z) dz$; average integral temperature head $\bar{\Delta t} = \frac{1}{c} \int_0^c (\bar{t}_w(z) - \bar{t}_a(z)) dz$;

average integral temperature of air $\overline{t_{air}} = \frac{1}{c} \int_0^c \overline{t_a(z)} dz$; dimensionless average integral temperature head $\overline{\Theta} = \frac{\Delta t}{\overline{t_{air}}} = \frac{\int_0^c (\overline{t_w(z)} - \overline{t_a(z)}) dz}{\int_0^c \overline{t_a(z)} dz}$; Nusselt average number $\overline{Nu} = \overline{\alpha} \cdot \frac{X}{\lambda}$; pressure losses in the duct caused by friction, Darcy-Weisbach formula, $\Delta p = \overline{\xi} \cdot \frac{c}{X} \cdot \frac{\rho \cdot \overline{w}^2}{2}$; average coefficient of friction resistance $\overline{\xi} = \frac{8 \cdot \overline{\tau_w}}{\rho \cdot \overline{w}^2}$ and Nusselt local number $Nu = \alpha \cdot \frac{X}{\lambda}$, where a, b, c —linear dimensions of the duct, respectively: width, height and length; $q_w(y)$ —local heat flow density on the wall in the i section, is determined by the numerical experiment; t_a —temperature of air, is determined by the numerical experiment; $t_w(y)$ —local temperature of the wall in the i section, is determined by the numerical experiment; w —air velocity, is determined by the numerical experiment; x, y, z —coordinates along the axes, respectively, OX, OY, OZ; X —characteristic linear duct size; $\alpha(z)$ —average heat exchange coefficient from the duct surface; λ, ρ —the coefficient of thermal conductivity and density, respectively, depend on the air temperature; $\overline{\tau_w}$ —average tangential stress on the duct wall is determined by the experiment for the hot surface and the unheated surface. Indexes: *air*—value is determined for the air flow; and *w*—value is determined for the duct wall.

For the analysis of the obtained results of a numerical experiment and the convenience of comparing them with the known results of convective heat exchange in pipes under turbulent flow [19–22], the data are presented in a criterion form. The thermophysical properties that are part of dimensionless complexes are determined for the average mass temperature of the flow in this section. The hydraulic diameter is used as the characteristic linear size of the duct cross-section. The effect of free and forced convection on the heat transfer intensity is determined from the Rayleigh (Ra) and Peckle (Pe) complexes, respectively. The intensity of heat transfer in the dimensionless view is presented by Nusselt number.

Generalization of the results of the numerical research was carried out by: dimensionless local coordinate— $Z = Re \cdot Pr \cdot \frac{X}{z}$; average dimensionless coordinate $\overline{Z} = \overline{Re} \cdot \overline{Pr} \cdot \frac{X}{c}$; average Reynolds integral number along the length of the calculated region $\overline{Re} = \frac{1}{c} \int_0^c Re(z) dz$; reduced heat transfer intensity from the hot surface ($\overline{Nu}_1 / \overline{Nu}$); dimensionless temperature head from the hot surface $\overline{\Theta}_1$; dimensionless temperature head from the unheated surface $\overline{\Theta}_2$; average coefficient of friction resistance, where is: $Re(z)$ —local Reynolds number based on the results of a numerical experiment; \overline{Pr} —the average Prandtl integral number along the length of the calculated region, determined by analogy with the number \overline{Re} . Indexes: 1, 2—the value refers to the hot surface and the non-heated surface, respectively.

Verification of the adequacy of the mathematical model is carried out according to the test research, in which the intensity of convective heat transfer is determined for the described duct geometry under turbulent flow, double-sided heat input and boundary conditions of the 2nd kind. Radiation heat transfer in the duct is not considered. Other characteristics of the test research model correspond to the values taken for the main research. The heat flux density for double-sided heat input is chosen by the condition— $q_1 = 0.5q_0$, where q_0 is the heat flux density for double-sided heat input (main research).

The results of the test research are presented in a generalized form in the $\overline{Z} - \overline{Nu}$ coordinate system and compared with the existing results of the research of convective heat transfer in pipes with turbulent flow at small heat flow densities, when there is still no effect on heat transfer of non-isothermicity through natural convection and there is no change in the thermophysical properties of the heat carrying agent [22]

$$\overline{Nu} = \frac{(\overline{\xi}/8) \overline{Re} \cdot \overline{Pr}}{K_1 + K_2 \sqrt{\frac{\overline{\xi}}{8} \left(\overline{Pr}^2 - 1 \right)}}, \quad (1)$$

where is $K_1 = 1 + \frac{900}{\overline{Re}}$, $K_2 = 12.7$.

The coefficient of hydraulic friction resistance is calculated as follows:

$$\overline{\xi} = (1.82 \lg(\overline{Re}) - 1.64)^{-2}.$$

Limits of application of expression (1): $\overline{Re} = 4 \cdot 10^3 \div 5 \cdot 10^6$; $\overline{Pr} = 0.5 \div 5.0$ [22]. The discrepancy between the experimental data and the results of calculations using expression (1) does not exceed 8%.

5. Results of Research Aerodynamics and Heat Transfer for One-Sided Heat Input

The initial data and algorithm for performing a numerical experiment are selected from real experiments of testing a pilot plant, and are shown in Table 1.

Table 1. Plan for performing the numerical experiment with one-sided heat input.

Heat Flow Density, W/m ²	Mass Flow Rate of Air, kg/h			Notes
	100	150	200	
5000	5000_100_1	5000_150_1	5000_200_1	Hot surface
5000	5000_100_2	5000_150_2	5000_200_2	Non-heated surface
5500	5500_100_1	5500_150_1	5500_200_1	Hot surface
5500	5500_100_2	5500_150_2	5500_200_2	Non-heated surface
6000	6000_100_1	6000_150_1	6000_200_1	Hot surface
6000	6000_100_2	6000_150_2	6000_200_2	Non-heated surface

The designations of experiments are given in Table 1, and are used as captions in the figures (Figures 3–18). Figures 3–6 show the velocity and temperature distributions in the air flow, in the vertical ZOY and horizontal ZOY central-section of the duct. The profiles are constructed for cross-sections located at a distance of 10, 100 and 200 calibers from the entry plane. As the caliber, the value of the hydraulic diameter of the duct X is taken.

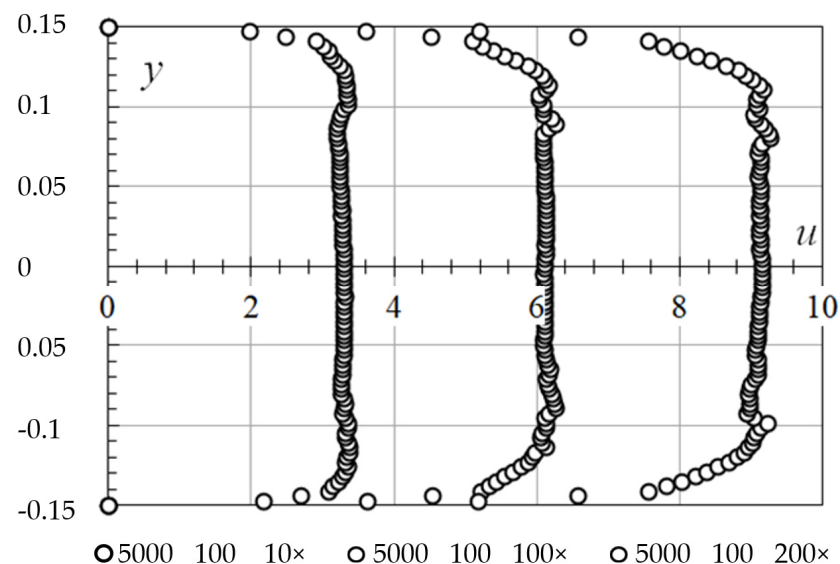


Figure 3. Air velocity profiles in the vertical central-section ZOY at 100 kg/h (y [m], u [m/s]), curves from left to right, respectively: 10 \times ; 100 \times ; 200 \times .

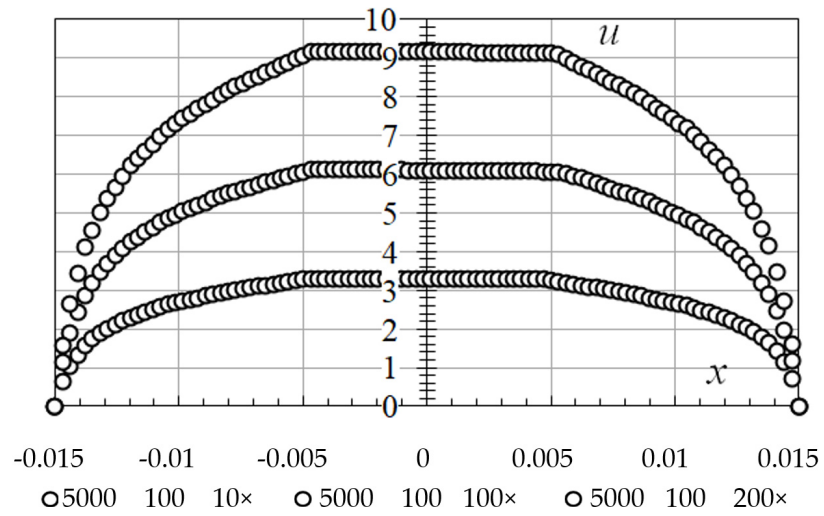


Figure 4. Air velocity profiles in the horizontal central-section of ZOX at 100 kg/h (x [m], u [m/s]), bottom-up curves, respectively: 10 \times ; 100 \times ; 200 \times .

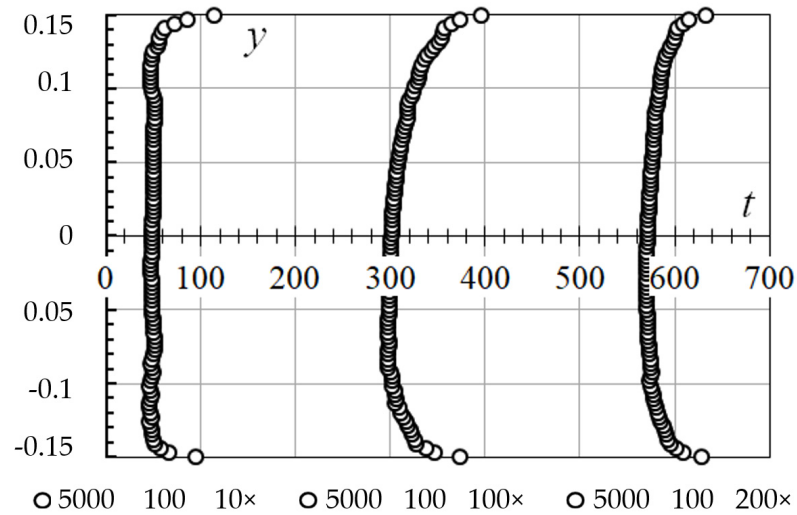


Figure 5. Air temperature profiles in the vertical central-section ZOY, 100 kg/h (t [°C], y [m]), curves from left to right, respectively: 10 \times ; 100 \times ; 200 \times .

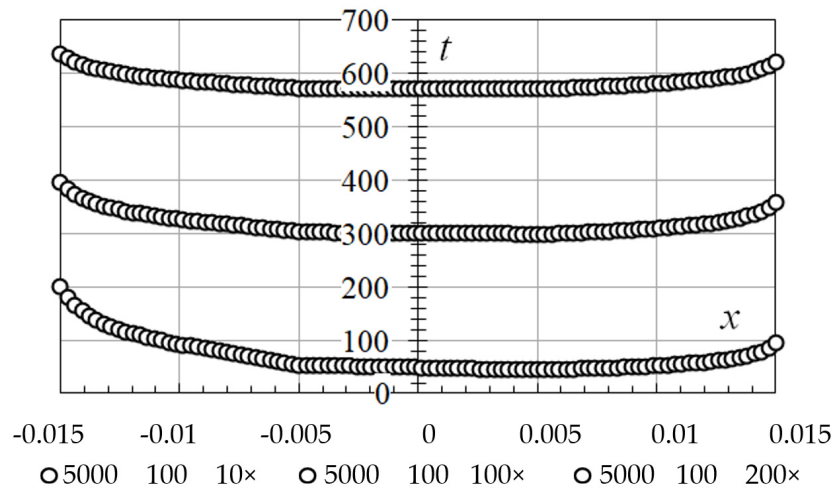


Figure 6. Air temperature profiles in the horizontal central-section ZOX, 100 kg/h (x [m], t [°C]): bottom-up curves, respectively: 10 \times ; 100 \times ; 200 \times .

For the results obtained for the mass flow rates of air of 100, 150 and 200 kg/h, an asymmetry of the temperature profiles relative to the central axes (cross-sections) of the duct symmetry is observed. The influence of free convection in the central part of the duct on vertical temperature profiles (Figure 5) is observed—the profiles are more filled than in the lower part, below the plane of symmetry. It is observed a higher temperature at the end of duct with a lower air flow rate, than with a higher air flow rate. It is observed decreasing the temperature difference between the duct surfaces as the air temperature increases. The surface temperature of the source (with one-sided heat input) is higher than the temperature of the non-heated surface along the entire length of the duct (Figure 6). Along the perimeter of the duct cross-section, its surface temperature does not have the same value, just as local heat exchange coefficients differ along the duct perimeter. Processing of the results of the research consisted in determining local, average heat exchange coefficients over the duct cross-section. At the same time, considered that the average duct surface temperatures have different values, the heat exchange coefficients are determined separately for the hot surface and the non-heated surface. In Figure 7 shows graphs of changes in the average temperatures (main axis on the left) of the hot surface and the non-heated surface and air along the length of the duct. In addition, this figure shows the temperature heads (auxiliary axis on the right) to the hot surface and the non-heated surface along the length of the duct.

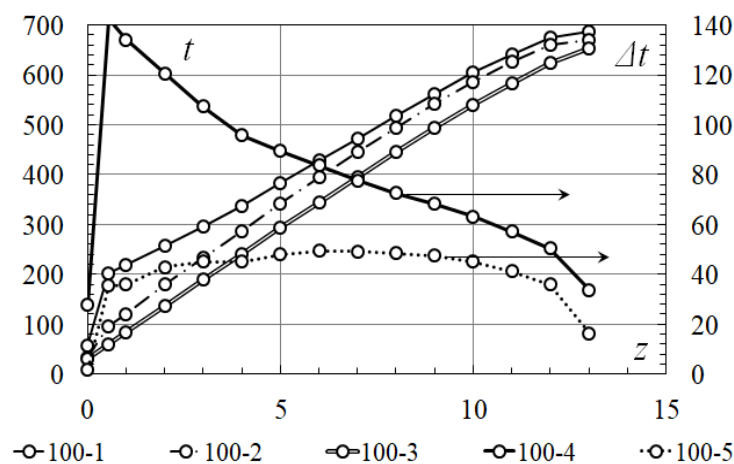


Figure 7. Change of the temperature t [°C] and the temperature head Δt [°C] by the length of the duct z [m] ($G = 100$ kg/h, $q_0 = 5000$ W/m²): 100-1—the average temperature of the hot surface; 100-2—the average temperature of the non-heated surface; 100-3—the average temperature of air; 100-4—the temperature head to the hot surface; and 100-5—the temperature head to the non-heated surface.

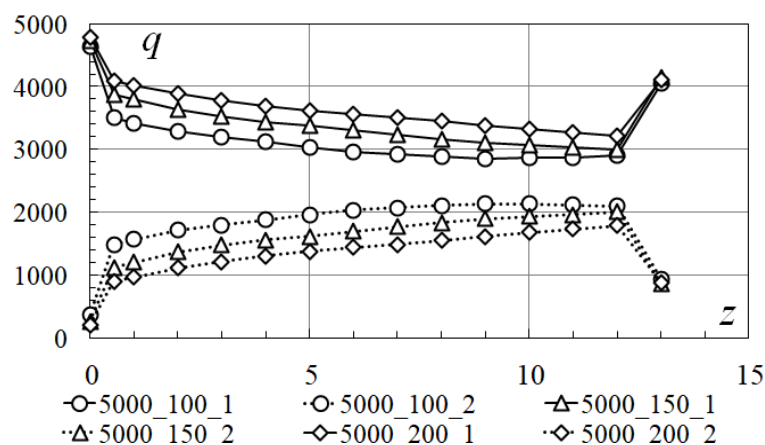


Figure 8. Distribution of the heat flow density q [W/m²] by the length of the duct z [m]: $q_0 - Const$; $G - Varia$.

The qualitative valuation, which is obtained for one-sided heat input at $q_0 = 5000 \text{ W/m}^2$, is also observed for cases of heat transfer at $q_0 = 5500$ and 6000 W/m^2 .

It is the lower the mass flow rate of air, than is the higher the overall temperature level of the process: (a) higher temperatures of the surfaces of the duct; (b) higher air temperature at the outlet of the duct; (c) smaller temperature difference between the hot surface and the non-heated surface at the outlet of the duct; and (d) smaller difference in temperature heads on the hot surface and on the non-heated surface. It should be expected that at the lower mass flow rate of air, at the end of the duct, the heat transfer rate on the hot surface of the duct and on the non-heated surface will approach a certain equal value. The different pattern of change in the value of the temperature head along the length of the duct on its hot surface and the non-heated surface indicates a qualitative difference in the heat transfer processes on these surfaces. It should also expect different patterns of changes in local heat exchange coefficients on these surfaces along the length of the duct. The distribution of the heat flow density along the length of the duct on the hot surface and the non-heated surface for different conditions of the experiment is shown in Figure 8. The results obtained have well-defined sections with a non-monotonous change in the value of the heat flow density—sections at the inlet/outlet of the duct. The non-monotonicity of the q value at the beginning of the duct- $\frac{z}{X} \leq 10$ -is due to the influence of the initial hydrodynamic and thermal regions, as well as the conditions for formulating a numerical experiment. The non-monotonicity of q at the end of the duct- $218 \leq \frac{z}{X} < 236$ -is due only to the conditions of the numerical experiment. When processing the results of the research, empirical correlations are approximated by power dependences of the species- $q(z) = Az^B$ (approximation reliability $R^2 > 0.96$). When constructing approximation dependencies, the plots $\frac{z}{X} \leq 10$ and $218 \leq \frac{z}{X} < 236$ are excluded from consideration. Further processing of the research results is carried out using approximation dependencies.

In Figure 9 shows the results of calculating local heat exchange coefficients (α) along the duct length (z), on the hot surface of the duct and on the non-heated surface of the duct. The present results demonstrate that: (a) the behavior of changes in heat exchange coefficients is different, if for the hot surface it qualitatively approaches the process of forced convection, then for the non-heated surface, such an analogy is not observed; (b) the heat exchange coefficients on the non-heated surface are greater than the heat exchange coefficients on the hot surface; and (c) as the air heats up, the difference between the heat exchange coefficients on opposite duct surfaces decreases.

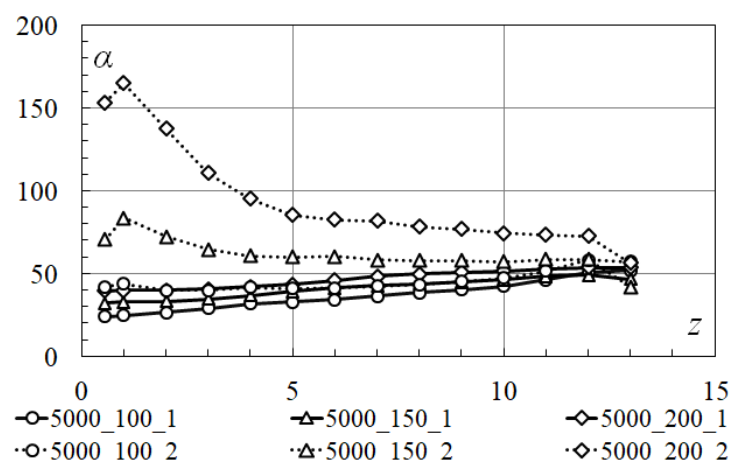


Figure 9. Changing the local heat exchange coefficients α [$\text{W}/(\text{m}^2 \cdot ^\circ\text{C})$] along the length of the duct z [m] $q_0 = 5000 \text{ B}/\text{m}^2$, $G = \text{Varia}$.

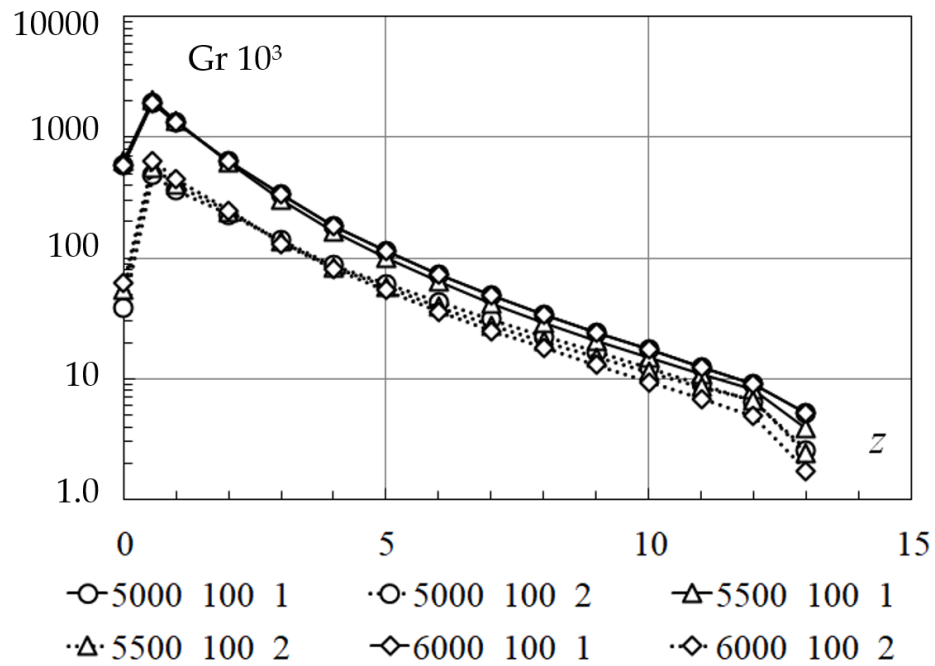


Figure 10. Changing the Grashof numbers along the length of the duct z [m] $q_0 - \text{Varia}; G - \text{Const.}$

Further generalization of the research results is carried out in the form of dimensionless complexes. Evaluation of the influence of gravitational and inertial forces on the intensity of heat transfer in the duct begins with determining the value of the Grashof Gr and Reynolds Re numbers along the length of the duct. As noted above, the thermophysical properties that make up dimensionless complexes are determined for the average mass temperature of the flow. The behavior of the Grashof numbers along the length of the duct, on the hot surface of the duct and on the non-heated surface for different regimes of the experiment is shown in Figure 10. The behavior of the Grashof numbers remains the same for all cases provided for in the experiment plan (Table 1). By analogy with the Grashof number, dependencies are also obtained for Reynolds number. The Reynolds numbers dynamics is shown in Figure 11, and is similar for all experiments performed.

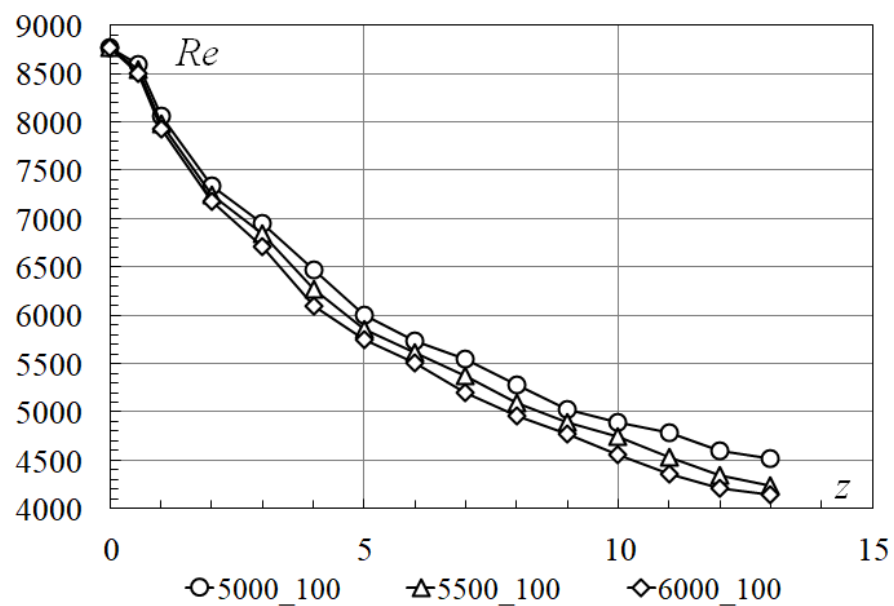


Figure 11. Changing the Reynolds numbers along the length of the duct z [m] $q_0 - \text{Varia}; G - \text{Const.}$

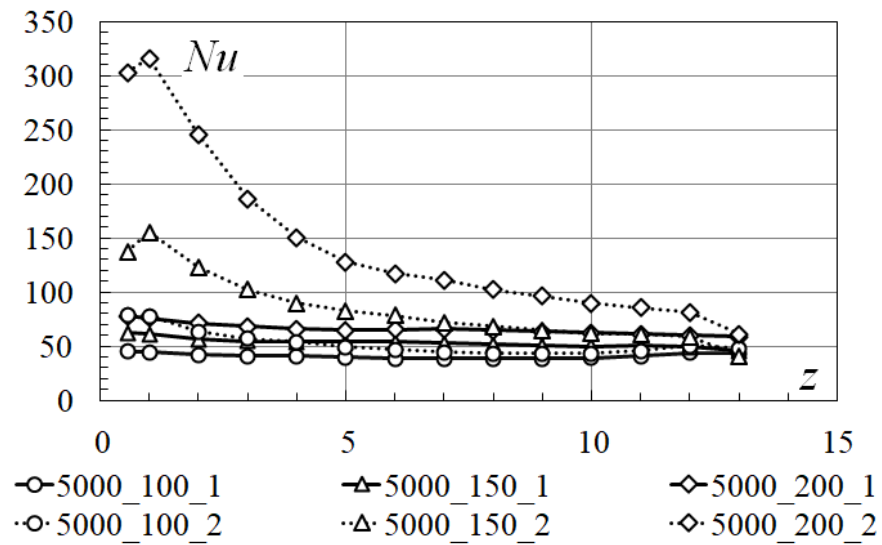


Figure 12. Changing the Nusselt numbers along the length of the duct z [m] $q_0 - Const; G - Varia$.

The greatest influence of gravitational forces on the heat transfer intensity is observed in one-third of the duct ($10 \leq \frac{z}{X} < 100$). At the hot surface, the effect of gravitational forces is 1.5–4.0 times higher than at the non-heated surface. The absolute values of the Grashof numbers allow us to assume about the undisputed effect of free convection on the intensity of convective heat transfer in the duct and about the expected differences in the values of heat exchange coefficients for mixed convection from their values for purely forced convection. Absolute values and the behavior of changes in Reynolds numbers indicate a developed turbulent flow regime along the entire length of the duct. The Reynolds number weakly depends on the value of the heat flux density on the hot surface. The difference in local values of the Reynolds numbers increases along the length of the duct, but does not exceed 8% of the initial value.

The dependence of the local Nusselt numbers along the length of the duct on the hot surface and on the non-heated surface is shown in Figure 12. The summary graph of the results of the research of complicated heat transfer in one-sided heat input and mixed motion of air is presented in Figure 13. The results are presented as the dependence of the local Nusselt numbers on the value of the dimensionless coordinate Z , which is determined by the expression $Z = Re \cdot Pr \cdot \frac{X}{z}$.

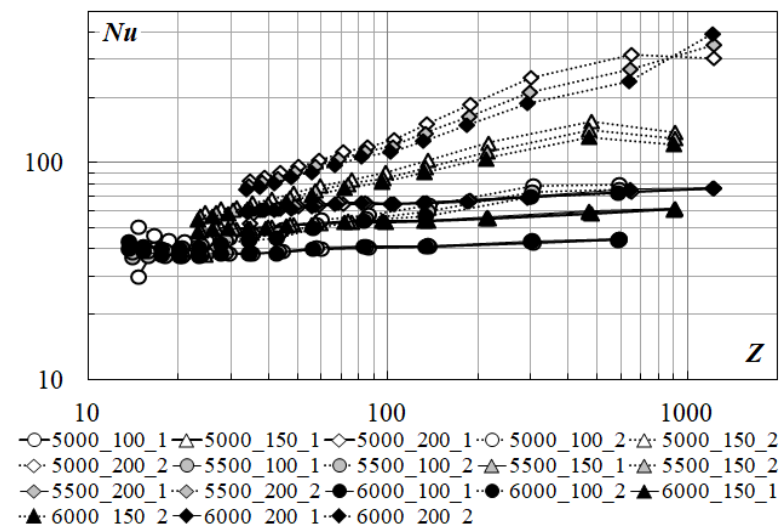


Figure 13. Dependence of the local Nusselt numbers on the dimensionless coordinate.

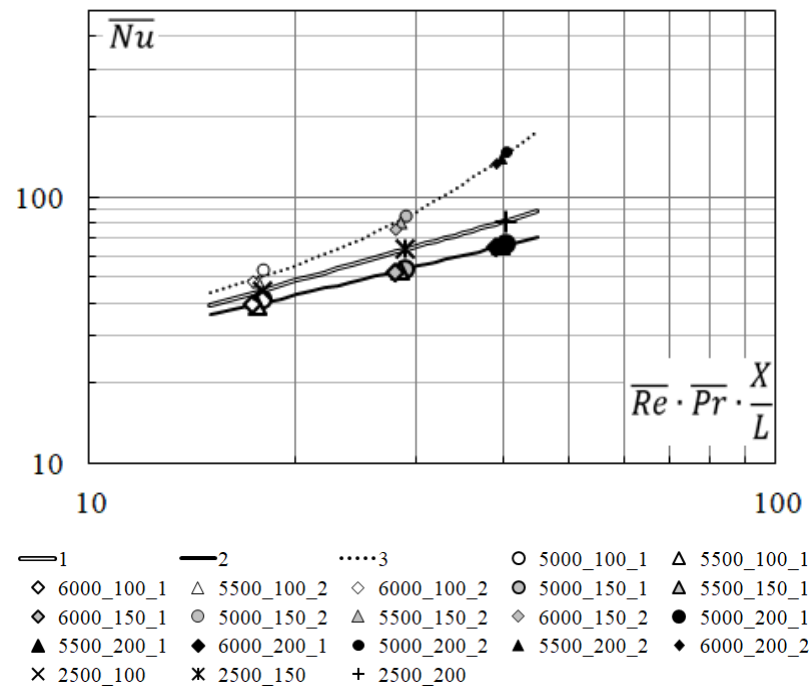


Figure 14. Generalizing dependences of average Nusselt numbers on the dimensionless coordinate. Curve 1—symmetrical two-sided heat input, curve 2—one-sided heat input, the hot surface; curve 3—one-sided heat input, the non-heated surface.

The intensity of convective heat transfer on the hot surface is less than the intensity of ones on the non-heated surface. The intensity of convective heat transfer on the hot surface is more affected by the mass flow rate of air in the duct than by the value of the heat flow density on the surface. On the summary graph Figure 13, it can be seen that the local Nusselt numbers on the hot surface for different values of the q_0 value almost coincide. With sufficient accuracy for technical calculations, it can be argued that in the range of values $q_0 \in [5000; 6000] \text{ W/m}^2$, the intensities of convective heat transfer are the same. For the non-heated surface, the local Nusselt numbers depend on both the mass flow rate of air in the duct and the value of the heat flow density. In this case, the dependence from the heat flow density q_0 is more significant than for the hot surface. As the q_0 value increases, the local Nusselt number curves on the non-heated surface approach similar curves on a hot surface. As the Z coordinate decreases, the difference in the values of local Nusselt numbers decreases for different heat flow densities q_0 and different air mass flows in duct G .

Before plotting generalizing dependences of the average Nusselt numbers (\overline{Nu}) as functions on the dimensionless coordinate ($\overline{Re} \cdot \overline{Pr} \cdot \frac{X}{L}$), it is verified the mathematical model and calculation methods used on the traditional problem of convective heat transfer in the duct with symmetric two-sided heat input.

The research of aerodynamics and heat transfer in symmetric two-sided heat input and turbulent flow regime in the duct (Table 2) has the following goals:

- verification of the mathematical model and computational methods;
- comparison of the results of the research with existing solutions for convective heat transfer in pipes and ducts;
- comparison and generalization of the results of the research of flow and heat transfer in the duct under turbulent flow regime and symmetric two-sided heat input with the results of the research of one-sided heat input, complicated heat transfer and mixed motion.

The following boundary conditions were set

$$\begin{aligned}
 x = -\frac{a}{2}; y \in \left[-\frac{b}{2}; \frac{b}{2}\right]; z \in [0; c] \quad & 0 = -\lambda_{air} \left(\frac{\partial T}{\partial x}\right)_{x=-\frac{a}{2}} - q_{x=-\frac{a}{2}}; q_{x=-\frac{a}{2}} = q_0/2; \\
 x = \frac{a}{2}; y \in \left[-\frac{b}{2}; \frac{b}{2}\right]; z \in [0; c] \quad & 0 = -\lambda_{air} \left(\frac{\partial T}{\partial x}\right)_{x=\frac{a}{2}} - q_{x=\frac{a}{2}}; q_{x=\frac{a}{2}} = q_0/2; \\
 x \in \left[-\frac{a}{2}; \frac{a}{2}\right]; y = \frac{b}{2}; z \in [0; c] \quad & 0 = -\lambda_{air} \left(\frac{\partial T}{\partial y}\right)_{y=\frac{b}{2}} - q_{y=\frac{b}{2}}; q_{y=\frac{b}{2}} = 0; \\
 x \in \left[-\frac{a}{2}; \frac{a}{2}\right]; y = -\frac{b}{2}; z \in [0; c] \quad & 0 = -\lambda_{air} \left(\frac{\partial T}{\partial y}\right)_{y=-\frac{b}{2}} - q_{y=-\frac{b}{2}}; q_{y=-\frac{b}{2}} = 0; \\
 x \in \left[-\frac{a}{2}; \frac{a}{2}\right]; y \in \left[-\frac{b}{2}; \frac{b}{2}\right]; z = 0; \quad & G_{inlet} = G_0; T = T_{inlet}; u = v = 0; \\
 x \in \left[-\frac{a}{2}; \frac{a}{2}\right]; y \in \left[-\frac{b}{2}; \frac{b}{2}\right]; z = c; \quad & p = 0; G_{outlet} = G_{inlet} = G_0; u = v = 0; \\
 \left(\frac{\partial T}{\partial z}\right)_{z=c} = 0.
 \end{aligned}$$

where is $q_0 = 5000 \text{ W/m}^2$; $G_{inlet} \in [100; 200] \text{ kg/h}$; $t_{inlet} = 30 \text{ }^\circ\text{C}$; $c = 13.0 \text{ m}$.

Table 2. Plan for performing the numerical experiment with two-sided heat input.

Heat Flow Density, W/m^2	Mass Flow Rate of Air, kg/h			Notes
	100	150	200	
Two-Sided Heat Input				
2500	2500_100	2500_150	2500_200	Symmetrical heating

The results of the test computational experiment are presented in a dimensionless form. They are compared with the results of the computational experiment on the complicated heat transfer and mixed motion of air (Figures 14–16). Figure 14 shows local Nusselt numbers on the hot surface, the non-heated surface and surfaces with symmetric two-sided heat input, respectively. Figure 15 shows the reduced Nusselt numbers on the hot surface and the non-heated surface, respectively. Figure 16 shows dimensionless average integral temperature heads for the three cases described above. Figures 14 and 16 obtained the qualitatively identical situation—the objective function under symmetric two-sided heat input occupies the intermediate position between the values of the corresponding objective functions on the hot surface and the surface that is non-heated.

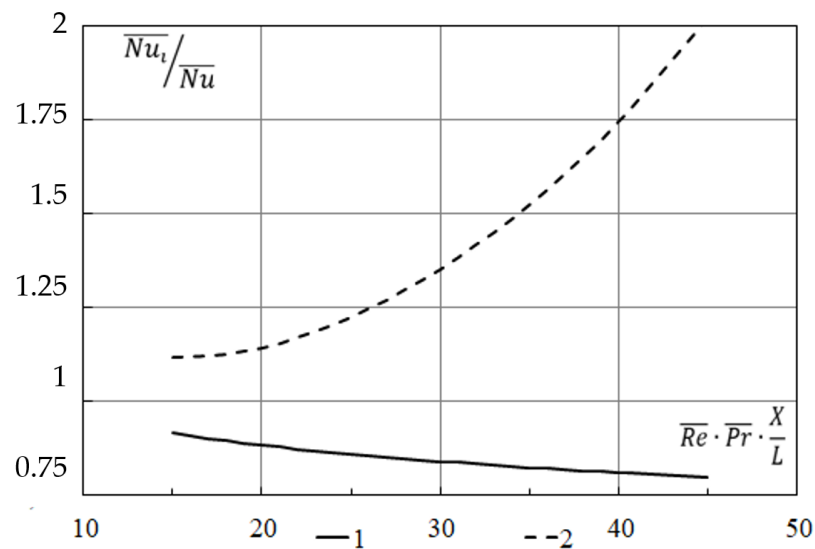


Figure 15. Dependence of relative Nusselt numbers on the dimensionless coordinate. Curve 1—one-sided heat input, hot surface; curve 2—one-sided heat input, non-heated surface.

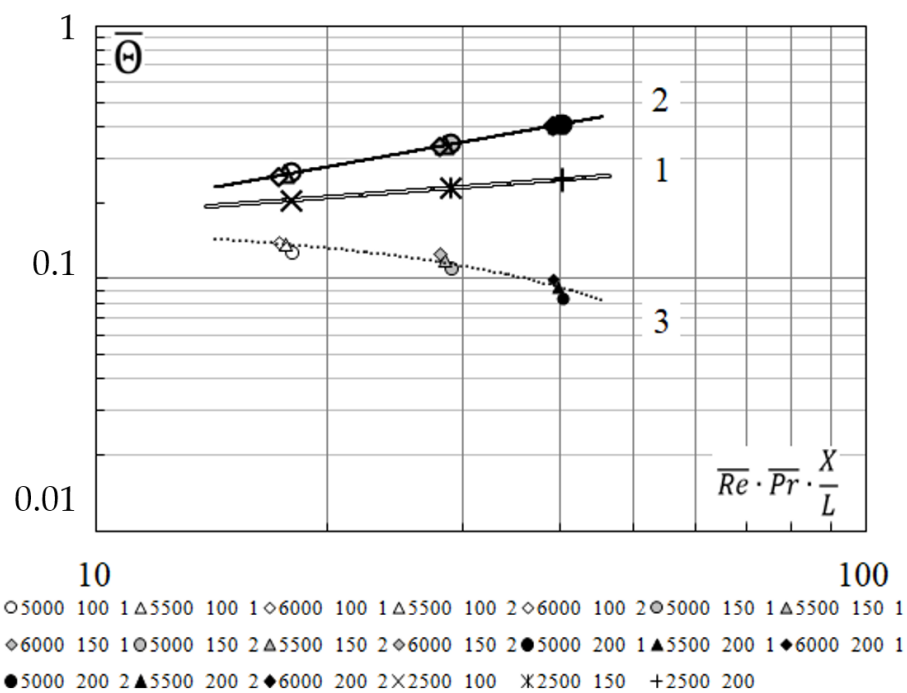


Figure 16. Generalizing dependence of dimensionless average integral temperature heads on the dimensionless coordinate. The designation of curves is similar to Figure 15.

Further final processing of the research results consisted in plotting the generalizing dependence of the average Nusselt numbers (\overline{Nu}) on the value of the dimensionless coordinate ($\overline{Re} \cdot \overline{Pr} \cdot \frac{X}{L}$). On the graph, Figure 14 presents the results of researches of complicated heat transfer with the mixed motion of air on the hot surface (curve 2) and the non-heated surface (curve 3); the results of the test research and the results of convective heat transfer in pipes and ducts under turbulent flow regime, published in [22] (curve 1).

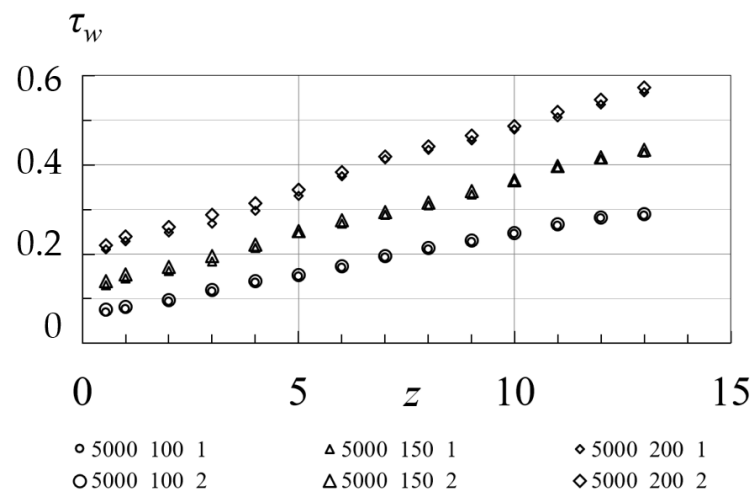


Figure 17. Distribution of tangential stresses τ_w [Pa] on the duct walls along its length z [m] ($q_0 - Const$; $G - Varia$).

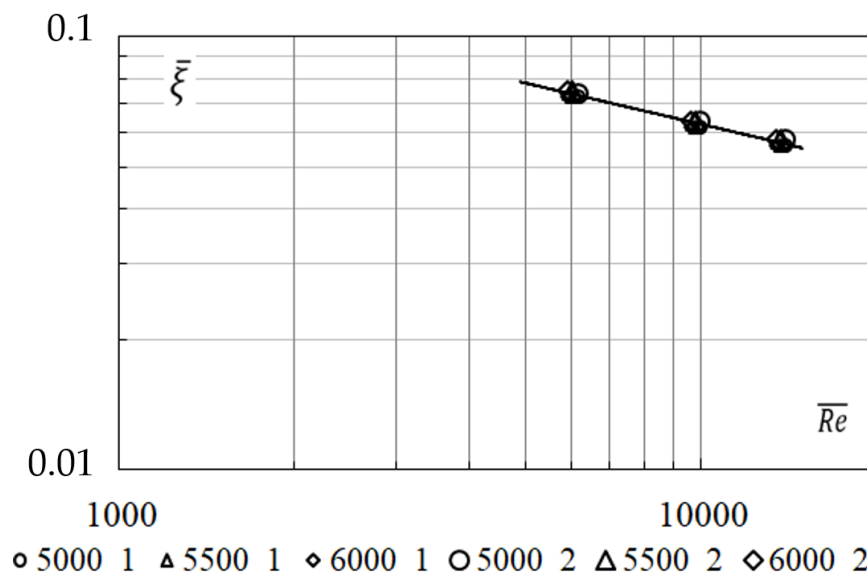


Figure 18. Generalized dependence of average coefficient of resistance of friction $\bar{\xi}$ on the dimensionless coordinate \bar{Re} .

The average Nusselt numbers (\overline{Nu}_1) and (\overline{Nu}_2) are calculated using the known dependence for the average Nusselt number (\overline{Nu}), which describes convective heat transfer in pipes and ducts under turbulent flow regime, but using correction factors

$$\left(\frac{\overline{Nu}_1}{\overline{Nu}}\right) = \frac{5}{3.9} \cdot \left(\overline{Re} \cdot \overline{Pr} \cdot \frac{X}{L}\right)^{-\frac{1}{8}}, \tag{2}$$

$$\left(\frac{\overline{Nu}_2}{\overline{Nu}}\right) = 0.99 \cdot e^{[4.26 \cdot 10^{-4} \cdot (\overline{Re} \cdot \overline{Pr} \cdot \frac{X}{L})^{1.95}]}, \tag{3}$$

where is \overline{Nu}_1 —average Nusselt number on the hot surface, curve 2; \overline{Nu}_2 —average Nusselt number on the non-heated surface, curve 3; \overline{Nu} —average Nusselt number on the symmetrical two-sided heat input, curve 1, Formula (1). The accuracy approximation is ($R^2 \geq 0.98$).

The change in the dimensionless average integral temperature head along the length of the dimensionless coordinate for the hot surface (curve 2) and the non-heated surface (curve 3) is shown in Figure 16. For comparison, the same graph shows the dependence of

the average integral temperature head for the case of symmetric two-sided heated input (curve 1).

$$\Theta_1 = \frac{1}{19} \cdot \left(\overline{Re} \cdot \overline{Pr} \cdot \frac{X}{L} \right)^{\frac{1}{18}}, \quad (4)$$

the accuracy approximation is ($R^2 > 0.99$).

$$\Theta_2 = \frac{1}{5.28} \cdot e^{[-\frac{1}{55.87} \cdot (\overline{Re} \cdot \overline{Pr} \cdot \frac{X}{L})]}, \quad (5)$$

the accuracy approximation is ($R^2 = 0.90$).

The distribution of tangential stresses on the walls along length of the duct, for different experimental conditions ($q_0 = 5000 \text{ W/m}^2$, $G = 100; 150; 200 \text{ kg/h}$), is shown in Figure 17.

The distribution plotting of the value τ_w obtained for the value of the heat flux density $q_0 = 5000 \text{ W/m}^2$ remains relevant for another values q_0 . It can be seen that there is the minimal difference in the values of τ_w obtained for different duct surfaces. The observed difference may not be considered, and the values of tangential stresses on the walls may be considered the same.

The results of the research are presented in the form of the generalizing dependence of the average coefficient of friction resistance on the value of the dimensionless coordinate (Figure 18). The generalizing graphical dependence is satisfactorily approximated by the power dependence (6), the accuracy approximation is ($R^2 > 0.99$).

$$\bar{\xi} = \left(\frac{3.633}{\overline{Re}^{3.14}} \right)^{0.1}. \quad (6)$$

6. Conclusions

It is established that in the considered range of values of heat flow density and mass flow rate of air, the dominant heat transfer between the walls and air is complicated convective heat transfer, in which forced convection ($Re > 4000$) is affected by free convection ($10^3 < Gr < 10^7$).

There is the difference in the intensity of convective heat transfer on the hot surface and on the non-heated surface. The difference in the density of heat flux transmitted by convection to air on the hot surface, and the non-heated surface is proportional to the expression $((\overline{Nu}_1 \cdot \overline{\Theta}_1) / (\overline{Nu}_2 \cdot \overline{\Theta}_2))$ and is 1.5–2.0.

Generalizing dependences are obtained that allow calculating the average Nusselt numbers and average temperature heads on the duct surfaces. Limits for applying dependencies (2)–(5): $Re = 4 \cdot 10^3 \div 10^4$; $Pr = 0.68 \div 0.70$; $10^3 < Gr < 10^7$.

The generalizing dependence of the value of the coefficient of friction resistance as a function of the value of the dimensionless coordinate (6) is obtained. The obtained values of the resistance value allow us to assume that in the hardware design of high-temperature heat exchangers and heat recuperation systems, the value of pressure losses to overcome the resistance of the boundary layer will not exceed 10% of the total pressure losses in the system.

The research results became the basis for the creation of the engineering methodology for calculating the heat engineering indicators of high-temperature heat exchangers and heat recuperation systems, which are widely used in the production of basalt and glass fibers at the enterprises “Chernivtsi plant of thermal insulation materials” (Chernivtsi, Ukraine) and “Innovation Basalt Technology Sp. z.o.o.” (Gdansk, Poland). Their use in heat technologies allows you to return part of the heat with heated air to the technological cycle, provide controlled cooling of the equipment lining and obtain secondary energy resources in a form that is convenient for further use for one’s own technological needs or sanitary needs of production.

Author Contributions: Conceptualization, B.B. and A.P.; methodology, V.K.; software, A.T.; validation, B.B., V.K. and A.P.; formal analysis, B.B.; data curation, A.P.; writing—original draft preparation, B.B.; writing—review and editing, A.P.; visualization, A.T.; supervision, A.T.; project administration B.B.; funding acquisition, A.P. All authors have read and agreed to the published version of the manuscript.

Funding: This research received no external funding.

Data Availability Statement: Not applicable.

Conflicts of Interest: The authors declare no conflict of interest. The funders had no role in the design of the study; in the collection, analyses or interpretation of data; in the writing of the manuscript or in the decision to publish the results.

References

- Govern, J.C.; Herman, C.V.; Nagle, D.C. High Temperature Heat Exchangers (HTHX) for Nuclear Applications. In Proceedings of the ASME 2006 International Mechanical Engineering Congress and Exposition, Chicago, IL, USA, 5–10 November 2006; Volume 1, pp. 713–718.
- Alkasassbeh, M.; Omar, Z.; Mebarek-Oudina, F.; Raza, J.; Chamkha, A. Heat transfer study of convective fin with temperature-dependent internal heat generation by hybrid block method. *Heat Transfer-Asian Res.* **2019**, *48*, 1225–1244. [CrossRef]
- Shah, P.K. *Heat Exchangers for Fuel Cell Systems, in Compact Heat Exchangers and Enhancement Technology for the Process Industries*; Begell House: New York, NY, USA, 2003; pp. 205–215.
- Marzougui, S.; Mebarek-Oudina, F.; Magherbi, M.; Mchirgui, A. Entropy generation and heat transport of Cu–water nanoliquid in porous lid-driven cavity through magnetic field. *Int. J. Numer. Methods Heat Fluid Flow* **2021**. ahead-of-print. [CrossRef]
- Djebali, R.; Mebarek-Oudina, F.; Rajashekhar, C. Similarity solution analysis of dynamic and thermal boundary layers: Further formulation along a vertical flat plate. *Phys. Scr.* **2021**, *96*, 085206. [CrossRef]
- Kumada, M. A Study on the High Performance Ceramic Heat Exchanger for Ultra High Temperatures. *Heat Transfer Enhanc. Heat Exch.* **1999**, *IV*, 301–324. [CrossRef]
- McDonald, C.F. Recuperator considerations for future higher efficiency microturbines. *Appl. Therm. Eng.* **2003**, *23*, 1463–1487. [CrossRef]
- Rafidi, N.; Blasiak, W. Thermal performance analysis on a two composite material honeycomb heat regenerators used for HiTAC burners. *Appl. Therm. Eng.* **2005**, *25*, 2966–2982. [CrossRef]
- Tsuji, H.; Gupta, A.; Hasegawa, T.; Katsuki, M.; Kishimoto, K.; Morita, M. *High Temperature Air Combustion; from Energy Conservation to Pollution Reduction*; CRC Press LLC: New York, NY, USA, 2003. [CrossRef]
- Dadheech, P.K.; Agrawal, P.; Mebarek-Oudina, F.; Abu-Hamdeh, N.H.; Sharma, A. Comparative Heat Transfer Analysis of MoS₂/C₂H₆O₂ and SiO₂-MoS₂/C₂H₆O₂ Nanofluids with Natural Convection and Inclined Magnetic Field. *J. Nanofluids* **2020**, *9*, 161–167. [CrossRef]
- C Ranganayakulu, K.N.S. *Compact Heat Exchangers: Analysis, Design and Optimization Using FEM and CFD Approach*; ASME Press: New York, NY, USA, 2018; 546p, ISBN 9781119424185. [CrossRef]
- Wong, H. *Basic Formulas and Data on Heat Transfer for Engineers*; Addison-Wesley Longman Ltd.: New York, NY, USA, 1977; 236p, ISBN-10:0582460506.
- Kakaç, S.; Liu, H.; Pramuanjaroenkij, A. *Heat Exchangers: Selection, Rating, and Thermal Design*, 2nd ed.; CRC Press: Boca Raton, FL, USA, 2002. [CrossRef]
- Minkowycz, W.J.; Sparrow, E.M.; Abraham, J.P.; Gorman, J.M. (Eds.) *Advances in Numerical Heat Transfer: Numerical Simulation of Heat Exchangers*, 1st ed.; CRC Press: Boca Raton, FL, USA, 2016. [CrossRef]
- Howell, J.R.; Mengüç, M.P.; Daun, K.; Siegel, R. *Thermal Radiation Heat Transfer*, 7th ed.; CRC Press: Boca Raton, FL, USA, 2020. [CrossRef]
- Basok, B.; Davydenko, B.; Pavlenko, A. Numerical Network Modeling of Heat and Moisture Transfer through Capillary-Porous Building Materials. *Materials* **2021**, *14*, 1819. [CrossRef] [PubMed]
- Asli, K.H.; Aliyev, S.A.O. *Applied Research in Hydraulics and Heat Flow*, 1st ed.; Apple Academic Press: New York, NY, USA, 2014. [CrossRef]
- Pavlenko, A.M.; Koshlak, H. Application of Thermal and Cavitation Effects for Heat and Mass Transfer Process Intensification in Multicomponent Liquid Media. *Energies* **2021**, *14*, 7996. [CrossRef]
- Kremnev, V.; Basok, B.; Timoshchenko, A.; Tymchyshyn, S. Energy Saving in Construction by Wide Application of High-Quality Insulation Based on Basalt Fibers. *J. Mod. Phys.* **2018**, *09*, 1724–1734. [CrossRef]
- Kremnev, V.; Basok, B.; Davydenko, B.; Timoshchenko, A.; Timoshchenko, A. Flow and Heat Transfer of Basalt Melt in the Feeder of the Smelter Furnace. *J. Appl. Math. Phys.* **2019**, *07*, 2555–2563. [CrossRef]
- Oleinik, O.A.; Samokhin, V.N. *Mathematical Models in Boundary Layer Theory*, 1st ed.; Chapman & Hall/CRC: London, UK, 1999. [CrossRef]
- Merkin, J.H. Mixed convection in a Falkner–Skan system. *J. Eng. Math.* **2016**, *100*, 167–185. [CrossRef]

Article

Study of the Influence of the Lack of Contact in Plate and Fin and Tube Heat Exchanger on Heat Transfer Efficiency under Periodic Flow Conditions

Marcin Łęcki *, Dariusz Andrzejewski, Artur N. Gutkowski  and Grzegorz Górecki

Faculty of Mechanical Engineering, Institute of Turbomachinery, Lodz University of Technology, 219/223 Wolczanska Street, 90-924 Lodz, Poland; dariusz.andrzejewski@p.lodz.pl (D.A.); artur.gutkowski@p.lodz.pl (A.N.G.); grzegorz.gorecki@p.lodz.pl (G.G.)

* Correspondence: marcin.lecki@p.lodz.pl; Tel.: +48-42631-23-20

Abstract: Plate fin-tube heat exchangers are widely used in air conditioning and refrigeration systems and other industry fields. Various errors made in the manufacturing process can result in the formation of an air gap between the tube and fin. Several numerical simulations were carried out for a symmetric section of plate fin-tube heat exchanger to study the influence of air gap on heat transfer under periodic flow conditions. Different locations and sizes of an air gap spanning 1/2 circumference of the tube were considered for the range of airflow velocities. Velocity and temperature fields for cases with air gap were compared with ideal thermal contact cases. Blocking of heat flow by the gap leads to the reduction of heat transfer rate. Fin discontinuity in the front of the tube causes the smallest reduction of the heat transfer rate in comparison to the ideal tube-fin contact, especially for thin slits. The rear gap position is the worst in the smallest gap range. Therefore, reversing the flow direction can lead to up to a 15% heat transfer increase, if mainly the rear gaps are present. The introduction of a thin slit in the front of the tube leads to convective heat transfer enhancement, which should be further investigated.

Keywords: heat exchanger; plate-fin tube; tube-fin contact; CFD

Citation: Łęcki, M.; Andrzejewski, D.; Gutkowski, A.N.; Górecki, G. Study of the Influence of the Lack of Contact in Plate and Fin and Tube Heat Exchanger on Heat Transfer Efficiency under Periodic Flow Conditions. *Energies* **2021**, *14*, 3779. <https://doi.org/10.3390/en14133779>

Academic Editor: Angelo Zarrella

Received: 17 May 2021

Accepted: 17 June 2021

Published: 23 June 2021

Publisher's Note: MDPI stays neutral with regard to jurisdictional claims in published maps and institutional affiliations.



Copyright: © 2021 by the authors. Licensee MDPI, Basel, Switzerland. This article is an open access article distributed under the terms and conditions of the Creative Commons Attribution (CC BY) license (<https://creativecommons.org/licenses/by/4.0/>).

1. Introduction

Plate-fin and tube heat exchangers are most widely used as evaporators and condensers in refrigeration systems (commercial refrigeration) and in other applications where heat transfer between liquid or evaporating/condensing fluid and gaseous working fluid is required. Proven technology, reliability, and relatively low cost of manufacture make plate-fin and tube heat exchangers very popular, not only as components of refrigeration units but also as gas coolers/heaters, recuperative heaters, dryers or heat pipe, thermosyphon radiators [1–3]. Nowadays, when detailed numerical simulations of fluid flow with heat transfer are within reach, many of the researchers carry out Computational Fluid Dynamics (CFD) studies to optimize the geometry of plate-fin and tube heat exchangers [4,5]. The majority of these works assume an ideal tube fin contact that in practice has to be created during the manufacturing process. The contact is usually achieved by a tube expansion (plastic deformation of the tube by moving the expansion die or by applying pressure at its inner surface). These mechanical methods of expansion cause additional thermal resistance at the tube–fin interface, due to the gaps between the contact surfaces of the fin collars and tubes [4]. Formation of the gap can be also a result of the nonideal joint formation process or assembly requirements. For the egg-crate-type heat exchangers, which are used as evaporators in domestic refrigerators, slits between the tubes are introduced to allow one to pull the whole tube coil through the plate-fin packet [6]. In this case, the lack of contact is always present at approximately 1/2 perimeter of the tube, and it is a feature essential for the assembly of the heat exchanger.

The gaps can be also created because of the wear of the heat exchanger, e.g., as the result of corrosion by exposure to difficult weather conditions or by strong chemical interactions. In Figure 1, one can see a picture (courtesy of Blygold company [7]) of a corroded heat exchanger surface with gaps on the circumference of the tube. In this case, fin discontinuities are just one of the factors affecting heat transfer; there are also white corrosion products around the tubes that impede heat transfer (AlOH thermal conductivity is smaller than for Al).

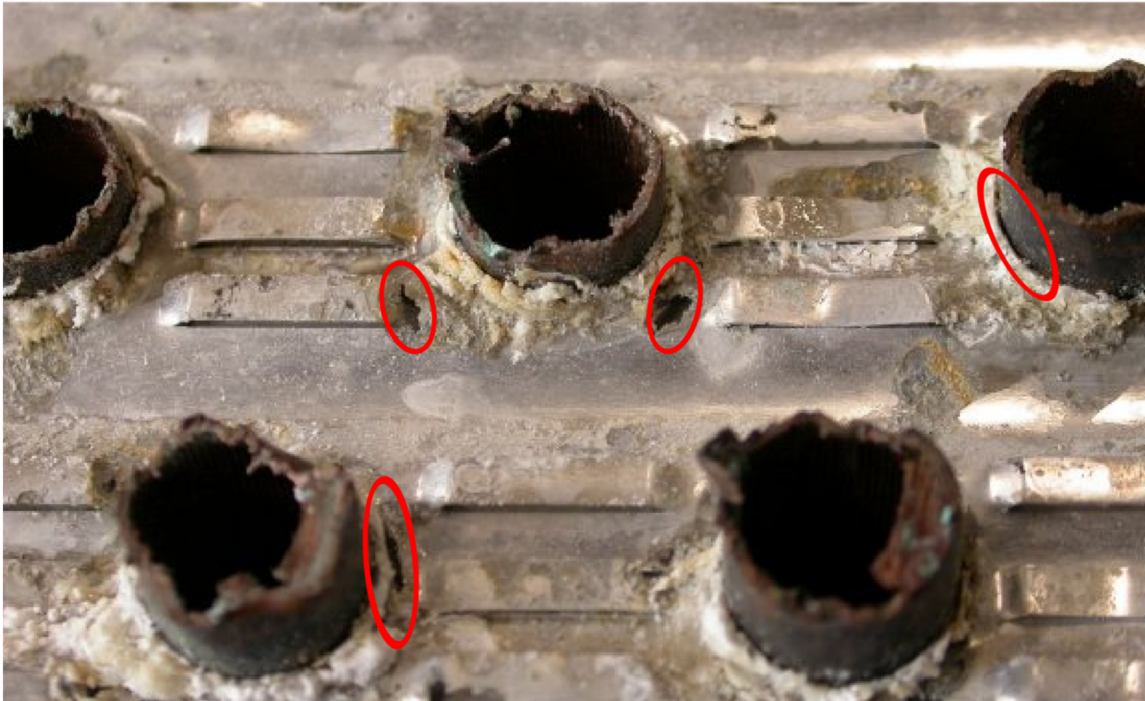


Figure 1. Gaps in the fin on the circumference of the tube created by a corrosion process, marked areas in the Figure (photo provided by courtesy of Blygold company [7]).

The quality of the joint can be improved by brazing the tube to the fin (the soldering process and its impact on heat transfer are discussed in detail in [8–10]). Because of the additional amount of energy needed for the soldering process and some technical difficulties (ensuring high purity of soldered surfaces), mechanical methods of expansion are most frequently chosen. Non-ideal tube fin connection can cause significant thermal contact resistance which deteriorates heat transfer. Therefore, some of the researchers have undertaken studies taking into account the realistic fin-tube thermal contact and its impact on the thermal efficiency of heat exchangers. Aside from the experimental research aimed at estimating the thermal contact resistance [11,12], its value is also obtained through semiempirical methods, partly based on numerical analysis. Taler and Oclon [13] and Taler and Cebula [14] changed iteratively the value of contact resistance in their CFD model in such a way that the thermal and flow quantities obtained from the numerical solution agreed with the measured ones. Less attention has been paid to cases where there is a lack of contact with the plate-fin along a part of the tube perimeter (no contact between the fin collar and tube). Recently, the topic was addressed by Singh et al. [15] who proposed a CFD model of a finned heat exchanger with a variable contact surface area between the tube and the fin. They considered several cases of gaps of different sizes. They found that the presence of gaps influenced heat transfer and flow (pressure drop) in a significant way. In contrast to [15], where several triangular gaps are distributed evenly along the joint circumference, our work presents a CFD analysis of plate-fin and tube heat exchanger, where there is a lack of contact between the tube and the fin at the half of the tube's circumference. The present study aims to numerically investigate the effect of the

lack of contact on the energy efficiency of the heat exchanger for variable parameters, such as different air velocities and various positions of the gap relative to the flow direction. The CFD model is developed with the assumption of periodic flow boundary conditions. The novelty of the present work lies mostly in the consideration of the different locations and sizes of the gaps between the tube and fin relative to the flow direction. Because of the nonuniform heat transfer coefficients on the fin and tube surfaces, the expected degree of heat transfer deterioration is a function of the position of the cavity. Only in [15] was a similar CFD analysis done, but evenly distributed triangular voids excluded the possibility of dependency on the flow direction; additionally, the authors of [15] considered a slightly different geometry of the plate-fin tube heat exchanger than the typical one (with slitted fins). The present work assumes more realistic positions of gaps resulting from wear (corrosion) or erroneous tube expansion in the classic type of plate-fin tube heat exchanger. It contributes to the current area of research by expanding knowledge about the magnitude of heat transfer deterioration (fin efficiency) caused by the lack of contact between fin and tube depending on flow conditions. It can help to understand and predict the thermal effects of wear and manufacture errors on the functioning of compact heat exchangers.

2. Numerical Model of a Heat Exchanger

The heat exchanger under consideration works as a condenser in a refrigeration system. It is a plate-fin and tube heat exchanger, in which tubes are arranged in-line. It was recognized that the location of the gap relative to the flow direction is an important parameter because of the variation in the local heat transfer coefficients on the surface of the fin and the locally variable velocity field [16]. The gap location along tube-fin joint circumference should therefore have a significant impact on heat exchange and flow patterns. Figure 2 shows the analyzed configurations.

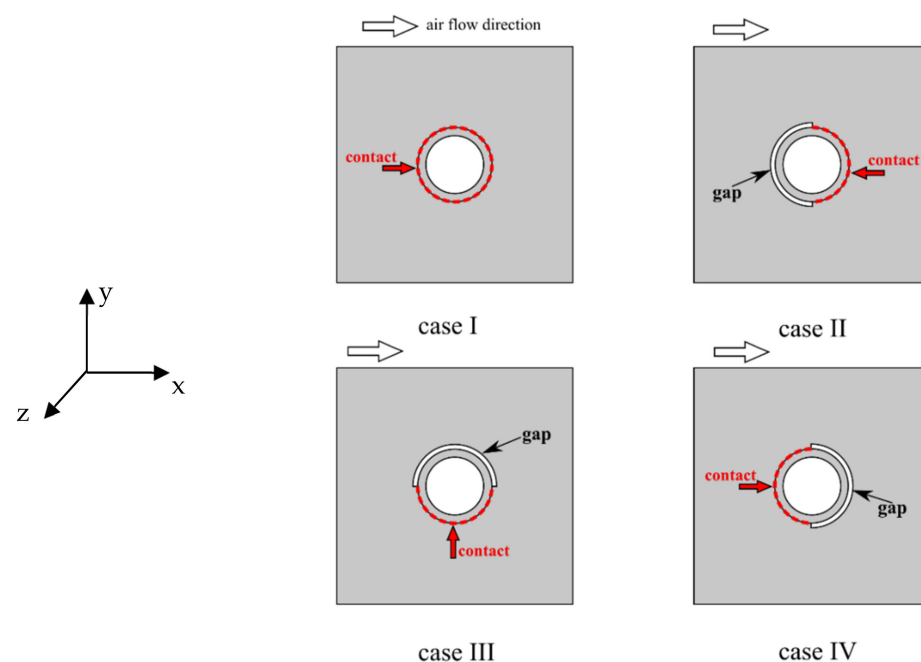


Figure 2. Different positions of the gap with respect to airflow: Case I—without gap; Case II—the gap in the front of the tube; Case III—the gap in the top position; Case IV—gap in the back of the tube.

Case I (without a gap—thickness of discontinuity $\delta = 0$ mm) is treated as a reference. The slit position is nondimensionalized as $\theta/180^\circ$, where θ is an angular position. In the second case, the gap spans the front side of the circumference ($\theta = 0^\circ$). In Case III, it is placed on the upper half perimeter ($\theta = 90^\circ$), in the last IV variant—in the back of the tube ($\theta = 180^\circ$). The angles indicate the centers of the gaps, taking into account the slit circumference span the corresponding angle ranges are front gap ($90^\circ \leq \theta \leq 270^\circ$), top gap ($0^\circ \leq \theta \leq 180^\circ$),

and back gap ($-90^\circ \leq \theta \leq 90^\circ$). Four gap thicknesses were taken into account: 0.25, 0.5, 1.0, and 2 mm, corresponding to the following dimensionless values (relative to tube diameter): 0.03125, 0.0625, 0.125, and 0.25. Numerical simulations were carried out for airflow through the heat exchanger equal to 1, 2, 3, 4, and 5 m/s average velocities at the flow area directly upstream of the entrance to the device under consideration.

2.1. Geometry of the Computational Domain

The computational domain is a repeatable slice of the heat exchanger geometry, which is shown in Figure 3. The length and width of the domain are equal to the distance between axes of the tubes L_f . The thickness of the fin in the computational domain is half of the actual fin thickness δ_f , as the temperature field is symmetric at the opposite half of the fin (see the symmetry plane in Figure 3). Tube length in the domain equals $\frac{1}{2}$ of the distance between fins. Taking the half of inter-fin spacing is a consequence of the flow symmetry assumption. The actual domain boundary is marked in Figure 3 by a dashed line and spans up to the symmetry plane. The specific dimensions of the domain are given in Table 1.

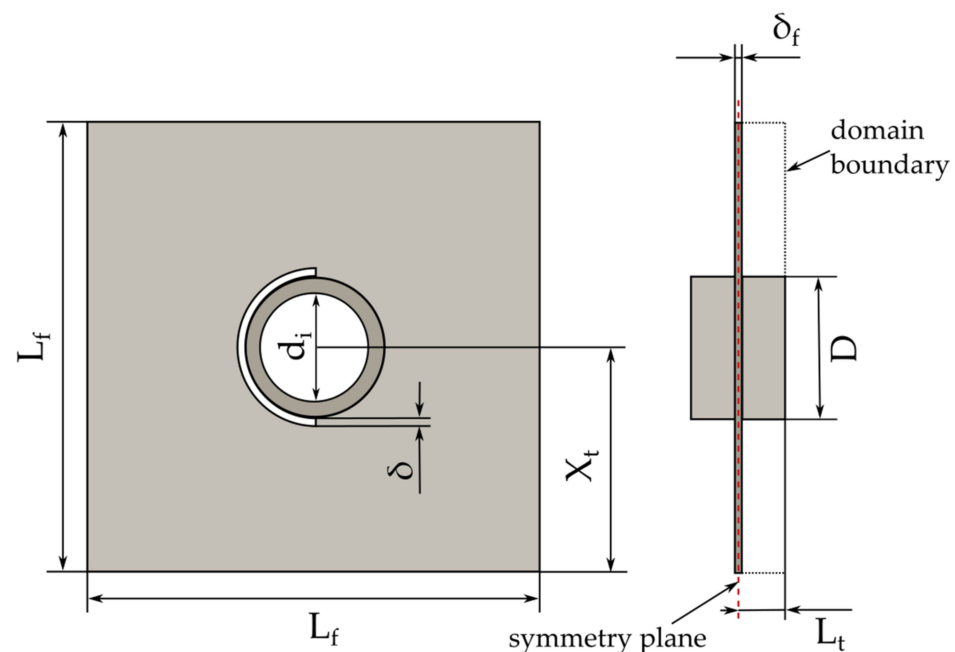


Figure 3. The geometry the simulated slice of the heat exchanger.

Table 1. The dimensions of the domain for the analyzed cases.

Description	Symbol	Value [mm]
Length and width of the fin	L_f	25
Tube length	L_t	2.5
Outside diameter of the tube	D	8
Internal diameter of the tube	d_i	6.2
Fin thickness	δ_f	0.05
Gap thickness	δ	0.25–2.0
Tube spacing	X_t	12.5

2.2. Boundary Conditions and Governing Equations

The shear stress transport (SST) turbulence model was chosen to solve Reynolds (time) averaged Navier-Stokes equations (RANS). SST combines the best features of $k-\epsilon$

and $k-\omega$ models. In the near-wall region, approximately up to half of the boundary layer $k-\omega$ formulation is used, which does not require any damping functions, while for the outer zone of the boundary layer $k-\varepsilon$ is the governing turbulence model—it eliminates the problem of $k-\omega$ sensitivity to values of ω in the freestream (outside the boundary layer). The other advantage of SST is the accurate prediction of the boundary layer separation by application of the turbulence production limiter in stagnation regions [17]. The SST model is also characterized by very good accuracy of the numerical solutions for wall-bounded, complicated geometry flows, obtained with relatively low computational power. Recently, Lindqvist et al. have performed an extensive analysis of RANS turbulence models in the application to numerical simulation of airflow and heat transfer in plate-fin and tube heat exchangers [18]. The $k-\omega$ SST was chosen as optimal and used for further validation against experimental data. It was utilized in many works where CFD analysis of the heat transfer for finned and enhanced surfaces was carried out [4,13,19–21].

The following simplifying assumptions were made in the present work:

- Steady-state fluid flow and heat transfer;
- Fluid flow and heat transfer are periodic (fully-developed), meaning that pattern of flow/thermal solution has a periodically repeating nature (this condition is generally fulfilled for tube rows greater than the fourth row);
- Thermophysical properties of air are temperature-dependent (ideal gas);
- Natural convection was not considered as the highest Richardson number calculated for simulation conditions is $Ri = (g \cdot \beta \cdot \Delta T \cdot L) / u^2 = 0.025$ (for $Ri < 0.1$ mechanism of natural convection can be typically considered negligible).

Numerical calculations were carried out using the commercial ANSYS CFX code capable of solving the Navier-Stokes equations [22]:

$$\frac{\partial u_i}{\partial x_i} = 0, \quad (1)$$

$$\rho \frac{\partial}{\partial x_j} (u_i u_j) = - \frac{\partial p}{\partial x_i} + \frac{\partial}{\partial x_j} (\tau_{ij} - \rho \overline{u_i u_j}) \quad (2)$$

where τ is a stress tensor in the fluid, and $\rho \overline{u_i u_j}$ are Reynolds stresses (turbulent), which depend on average velocity gradients (Boussinesq hypothesis):

$$- \rho \overline{u_i u_j} = \mu_t \left(\frac{\partial u_i}{\partial x_j} + \frac{\partial u_j}{\partial x_i} \right) - \frac{2}{3} \left(\rho k + \mu_t \frac{\partial u_k}{\partial x_k} \right) \delta_{ij} \quad (3)$$

where k —turbulence kinetic energy and μ_t —turbulent viscosity.

The SST turbulence model allows for obtaining turbulent viscosity by using two transport equations of kinetic turbulence energy k and specific dissipation rate ω . Due to the extensive definition of the model, it will not be presented here; its formulation can be found in [17]. The turbulent viscosity is calculated using the equation:

$$\mu_t = \rho \frac{k}{\omega} \quad (4)$$

The energy equation for fluid is given by:

$$\frac{\partial}{\partial x_i} [u_i (\rho \cdot e + p)] = \frac{\partial}{\partial x_j} \left[\left(\lambda + \frac{c_p \mu_t}{Pr_t} \right) \frac{\partial T}{\partial x_j} \right] \quad (5)$$

where e —total fluid energy, T —temperature, λ —thermal conductivity, c_p —specific heat at constant pressure, and Pr_t —turbulent Prandtl number for energy (assumed value: 0.9). In the solid body (fin and tube domain), the heat is exchanged by means of steady conduction:

$$\frac{\partial}{\partial x_j} \left(\lambda \frac{\partial T}{\partial x_j} \right) = 0 \quad (6)$$

The computational domain is divided into three parts: air (fluid), fin, and tube (solids). It was assumed that the thermal conductivity of the solid (aluminum) is constant in the tested temperature range, which is $\lambda = 202.4 \text{ W/m}\cdot\text{K}$. A periodic flow was solved with the following boundary conditions and parameters:

- Average air temperature at the inlet: $T_{ave} = 22 \text{ }^\circ\text{C}$,
- $u = 0 \text{ m/s}$ on the fin and tube surfaces (no-slip condition),
- Uniform temperature at the inner surface of the tube wall: $T_w = 40 \text{ }^\circ\text{C}$ —which corresponds to the condensation conditions of the working fluid flowing inside the tube.

On the other surfaces of the computational domain, a symmetry boundary condition was assigned, which can be expressed mathematically as:

$$-\bar{n} \cdot \dot{q} = 0, \quad u \cdot \bar{n} = 0, \quad \nabla k \cdot \bar{n} = 0, \quad \nabla \omega \cdot \bar{n} = 0 \quad (7)$$

where \bar{n} is a normal vector to the surface on which the boundary condition was set. Additionally, on the solid–fluid contact surfaces, a coupled boundary condition was present, ensuring the energy balance is satisfied between domains.

The periodic condition of the velocity in the x-direction can be written as:

$$u_1(\bar{r}) = u_1(\bar{r} + \bar{L}) = u_1(\bar{r} + 2\bar{L}) = \dots \quad (8)$$

where \bar{r} —position vector and \bar{L} —the periodic length vector (equations in the rest of the Cartesian directions are analogous).

For viscous flows, the pressure field is considered periodic if the following condition is met:

$$\Delta p = p(\bar{r}) - p(\bar{r} + \bar{L}) = p(\bar{r} + \bar{L}) - p(\bar{r} + 2\bar{L}) = \dots \quad (9)$$

The pressure gradient is divided into two parts: a periodic gradient and a linear gradient:

$$\nabla p(\bar{r}) = \beta \frac{\bar{L}}{|\bar{L}|} + \nabla \tilde{p}(\bar{r}) \quad (10)$$

where $\tilde{p}(\bar{r})$ is so-called periodic pressure and $\beta \frac{\bar{L}}{|\bar{L}|}$ —linearly variable pressure component. Periodic pressure is the remainder after subtracting the linear pressure. On the other hand, the linearly variable component results in a force acting on the fluid in the momentum equations. During the solution process, the value of the coefficient β is iteratively changed until the desired convergence between the set and the calculated mass flow is obtained.

The temperature field is analogously divided into two components for periodic simulation:

$$T(\bar{r}) = \sigma |\bar{r}| + \tilde{T}(\bar{r}) \quad (11)$$

where:

$$\sigma = \frac{\dot{Q}}{\dot{m} \cdot c_p \cdot L} \quad (12)$$

and \dot{Q} —net heat transfer rate in a periodic domain.

At the inlet and outlet, the periodic boundary condition has the form:

$$T(\bar{r}) = \tilde{T}(\bar{r} + \bar{L}), \quad p(\bar{r}) = p(\bar{r} + \bar{L}), \quad u_1(\bar{r}) = u_1(\bar{r} + \bar{L}) \quad (13)$$

The above-mentioned conditions for the periodicity of the airflow are practically implemented in the Ansys-CFX CFD software. The boundaries named in Figure 4 as periodic inlet and periodic outlet are coupled as two flow interfaces; the target mass flow can be specified, which is obtained by iteratively changing the pressure gradient β . Negative heat flux has to be fixed at the periodic outlet boundary to balance the heat transfer rate gained by air flowing through the domain, as the outflowing fluid is “returned” to the inlet (Figure 4). If a heat sink is not introduced, the air temperature rises infinitely during the solution process of the numerical simulation, causing the solver to crash after reaching some maximum temperature level. In the case of numerical simulations carried out within this research, the domain was properly thermally balanced to keep the inlet temperature at an approximately constant level of 22 °C. The symmetry boundary condition is applied at domain boundaries that were not marked in Figure 4 (for both solid and fluid surfaces).

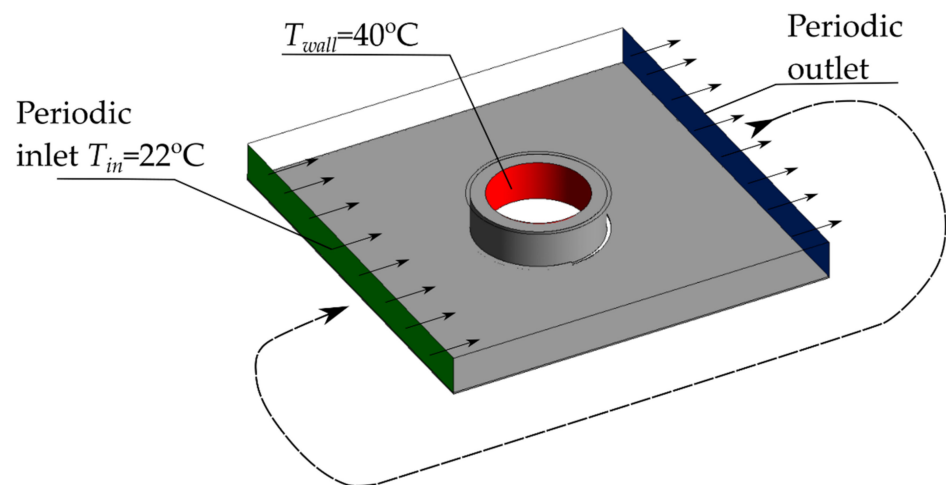


Figure 4. Boundary conditions for the computational domain.

2.3. Computational Grid

Numerical simulations of the fluid flow with coupled heat exchange process were carried out using ANSYS CFX CFD software. The computational grid for the case I is shown in Figure 5. It was created for the repetitive slice of heat exchanger with the use of ANSYS-Meshing application.

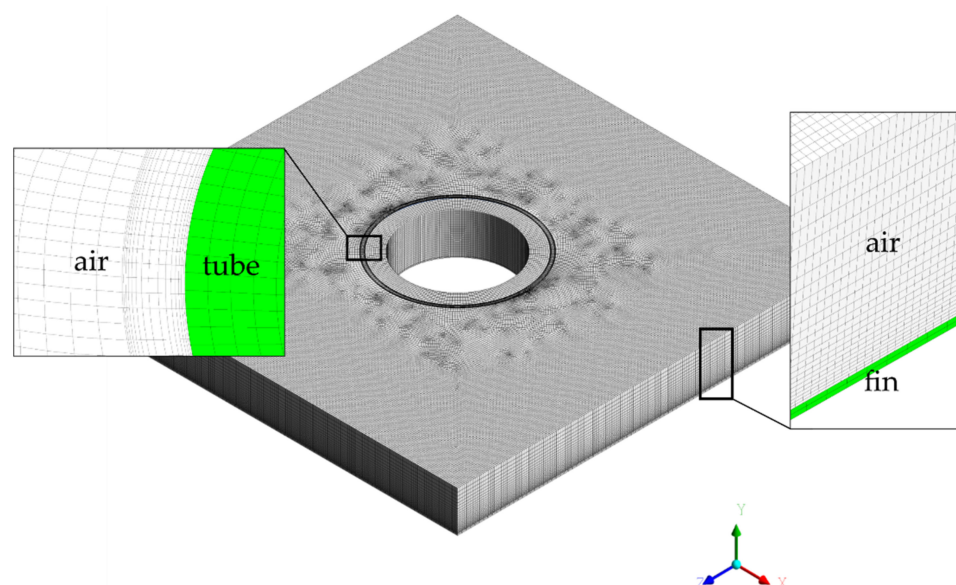


Figure 5. View of the computational mesh.

The grid independence study was performed using a methodology similar to used in works [23,24]. The five grids were tested, namely, coarse, average, fine, very fine, and the finest corresponding to mesh sizes: 0.2×10^6 , 1.8×10^6 , 2.14×10^6 , 2.48×10^6 , and 2.80×10^6 nodes. For all of the five meshes, the prism layer elements number at the wall was gradually increased, starting from 10 for the coarse grid by 25, 30, 35, up to 40 for the finest one. The Y^+ parameter and percent change of mean heat transfer coefficient $h_{\%}$ were presented in Figure 6. The $h_{\%}$ is the relative difference between the obtained average heat transfer coefficient for the i th mesh refinement level and $i - 1$ refinement (the one-step coarser mesh). The change does not exceed 0.5%; therefore, the average mesh (1.8×10^6 nodes) was chosen as optimal because it also satisfies the maximum $Y^+ < 1$ condition (maximum $Y^+ = 0.44$, average $Y^+ = 0.24$).

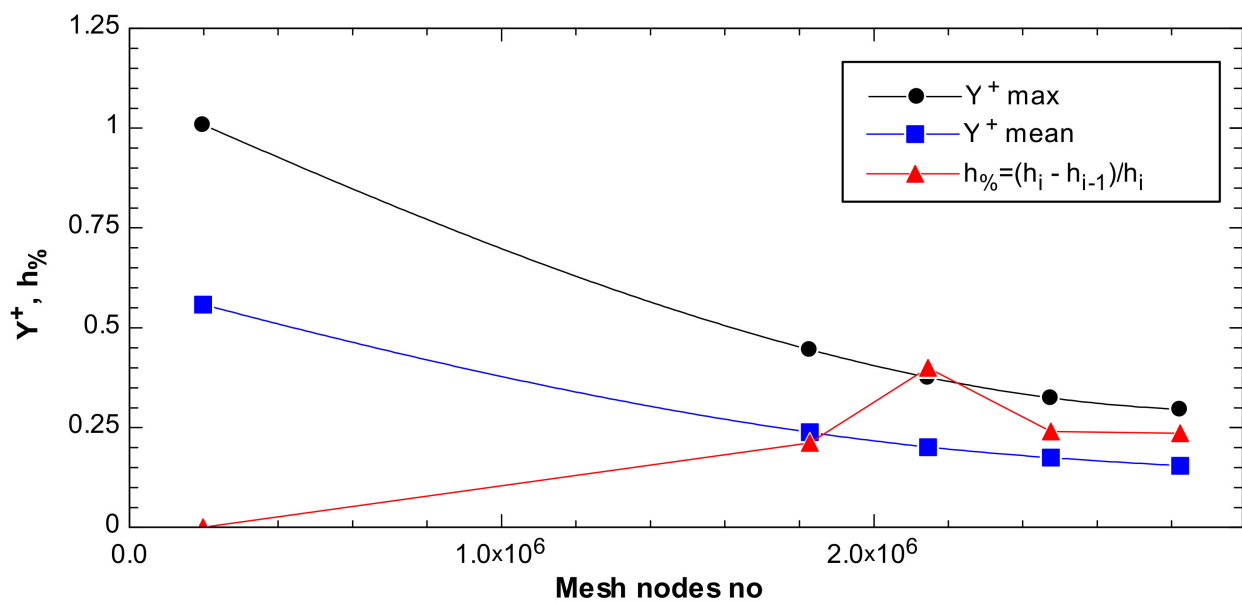


Figure 6. Dependence of an average and maximum Y^+ in the computational domain, and percent change of mean heat transfer coefficient $h_{\%}$ versus the number of mesh nodes.

2.4. Validation of the Numerical Model

The computational model was validated against data published in the work of Saboya and Sparrow [16] as their paper is widely acknowledged as the standard for validation of the studies of heat transfer from finned surfaces. They used the naphthalene sublimation technique [25] to obtain local mass transfer coefficients (Sherwood numbers Sh) on the fin surface of the one-row plate-fin tube heat exchanger. The Sherwood number distribution can be converted to heat transfer coefficients by utilization of the heat-mass transfer analogy:

$$h_{mass} = Sh \cdot \left(\frac{Pr}{Sc} \right)^n \cdot \left(\frac{\lambda}{d_h} \right) \quad (14)$$

where Sc —Schmidt number, d_h —hydraulic diameter according to Kays and London [26], and n —heat-mass transfer analogy exponent. Rosman et al. [27] have chosen the value of the $n = 0.4$ based on his experiment and measurements available in the literature. However, the latest careful measurements have reaffirmed that the most suitable value of the exponent for both laminar and turbulent boundary layers is approximately $n = 0.33$ [23]. Prandtl number and thermal conductivity are assumed as for pure air ($Pr = 0.7$, $\lambda = 0.026$ W/m/K)—the concentration of naphthalene is too low to significantly influence the thermophysical properties of the fluid. Saboya and Sparrow [16] assumed $Sc = 2.5$, yet it is an outdated value, and for room temperature the $Sc = 2.28$ is now recommended [25]. Local Sherwood numbers [16] were converted to heat transfer coefficients according to (14) and prepared to

validate the CFD simulation. On the left side of Figure 7, the distribution of heat transfer coefficients on the fin surface is shown obtained from [16] for $Re = 214$. The distribution of local h is only known along the horizontal black lines where the mass transfer coefficients are measured—a 2D contour map is a result of an inverse distance interpolation made in Tecplot 360 EX software [28]. On the right side, there are results from numerical simulation for analogous flow and thermal conditions as in the experimental work. This setup allows a direct comparison between two contour maps. As can be seen, the ranges of heat transfer coefficient values are nearly the same. Near the front edge of the fin, the convective heat transfer seems to be more intensive in the case of the numerical results, but the lower h are a consequence of the interpolation of the Saboya and Sparrow's [16] data from the location significantly upstream of the edge of the fin.

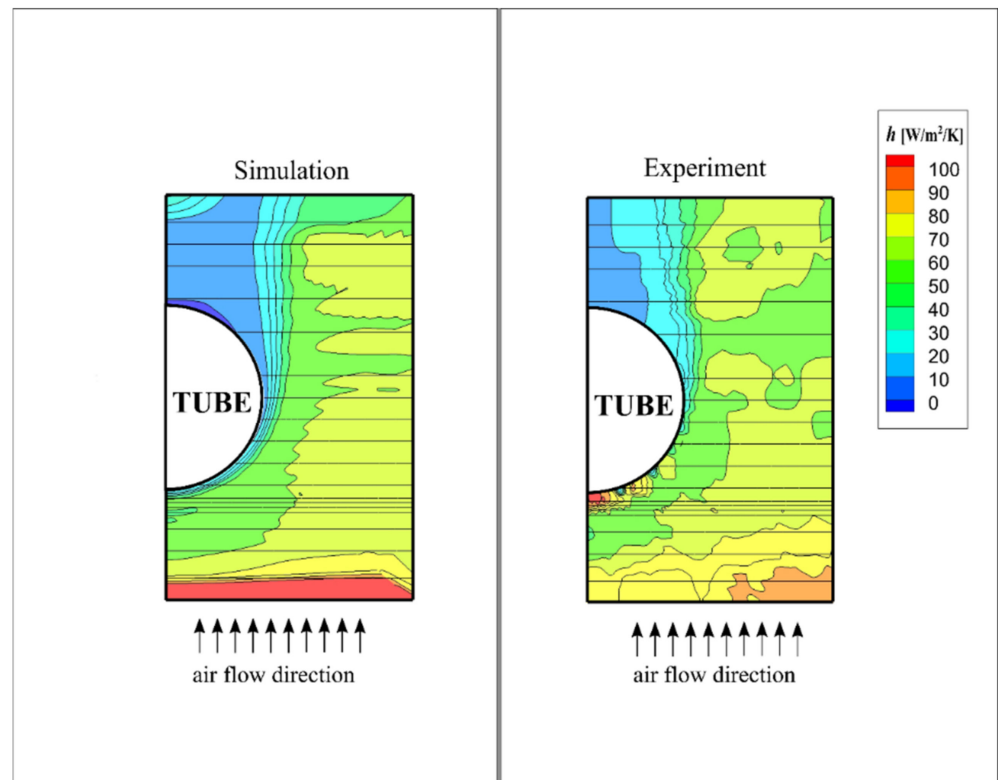


Figure 7. Comparison of local h on the surface of the fin between numerical simulation and experiment [16] for $Re = 214$.

The accordance of the simulation's local h with the experiment is shown in Figure 8. Four lines were chosen, where the measurements were taken exactly—at the front (line 1), back (line 4), and middle segments (lines 2, 3) of the fin. Most of the experimental data is in very good agreement with the CFD solution (maximally $\pm 20\%$ and better). The greatest discrepancies are noted in the near tube region, but they can be caused by the fact that in the experiment [16] the tube surface was adiabatic. The uncertainty of the experimental h was also plotted in the form of error bars. It was based on the estimation of the uncertainty of Sherwood number measurements done in [29] (uncertainty within 7.3%).

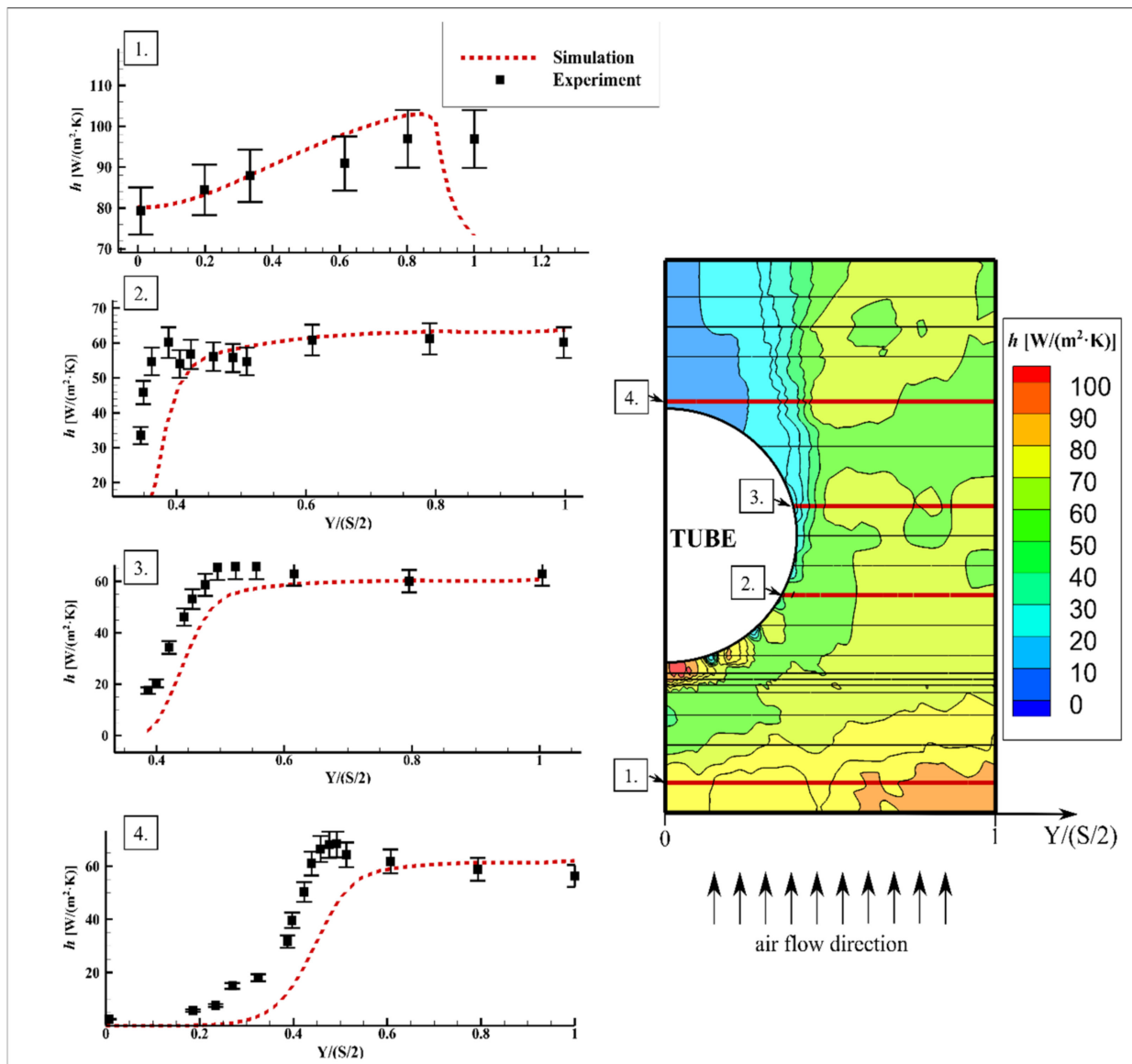


Figure 8. Local heat transfer coefficients from experiment versus CFD simulation at four lines transverse to the airflow at the front (line 1), back (line 4), and middle segments (lines 2, 3) of the fin for $Re = 214$.

The validation presented above was made to test the ability of the model to predict local coupled heat and fluid flow phenomena. Because the experimental flow arrangement (one-row tube-fin) is not adequate to the simulation settings (periodical flow—more than four-row inline tube-fin geometry), additional validation was performed. Mean heat transfer obtained from the simulation was compared against VDI correlation [30], which is true for three rows inline heat exchangers:

$$Nu_D = 0.20Re_D^{0.6} \left(\frac{A}{A_{t0}} \right)^{-0.15} Pr^{1/3} \quad (15)$$

A comparison between simulation heat transfer coefficients and VDI correlation is presented in Figure 9. The two data sets' values are very close. The relative difference varies from 4.9% for the lowest Re to 1.8% for the biggest airflow.

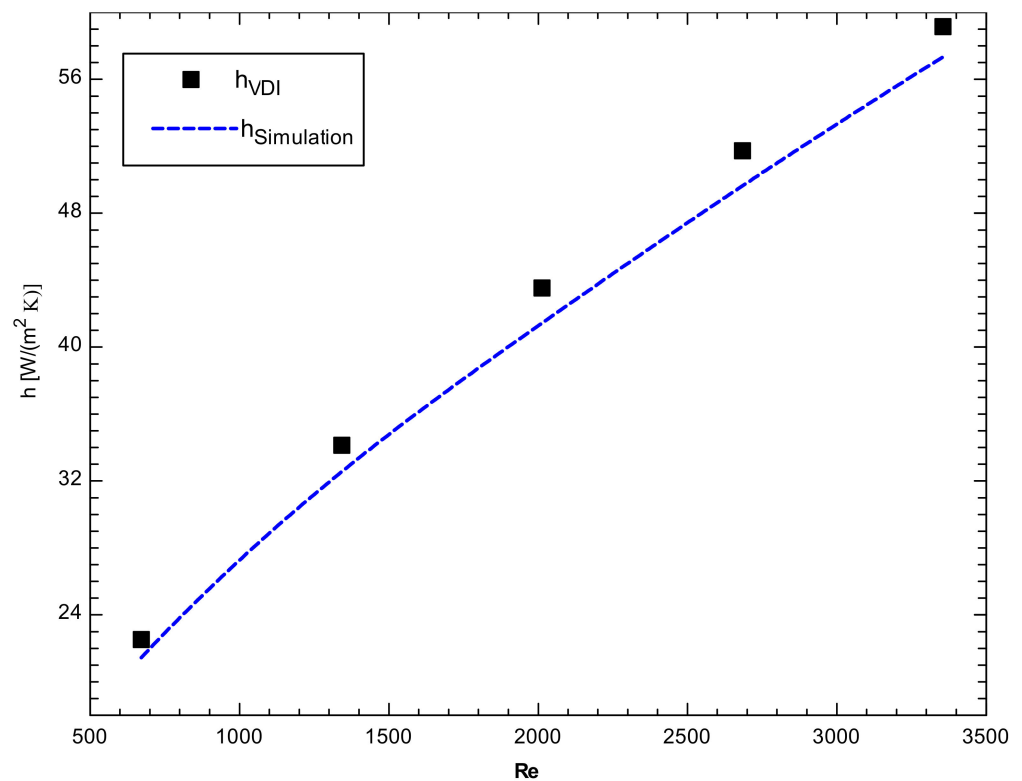


Figure 9. Comparison between heat transfer coefficients obtained from numerical simulation to the ones calculated with VDI correlation valid for three-row inline heat exchangers.

3. Results and Discussion

The results of the numerical simulations were put together in a form of a series of graphs, allowing for the evaluation of the thermal efficiency of the cases with the presence of the gap to perfect fin-tube contact example. In Figure 10, the ratios of heat transfer rates (discontinuity to no-slit heat transfer rate) are presented in the function of the dimensionless gap thickness (gap thickness to diameter). For each Reynolds number, a curve approximating the numerical data is presented. For the gap in the back and front, the minimal ratio of heat transfer rate is approx. 0.75 for the considered airflow span, whereas the side gap attains a slightly lower minimum of 0.72. For the front and side gap localization, there is a bigger spacing between the curves (stronger influence of the airflow velocity) than for the rear position. This effect is the strongest for smaller gaps. For $\delta/D > 0.1$, there is no significant difference between curves spacing for all examined cases. The shapes of the curves are similar for all the arrangements, although for the fin discontinuity in the rear of the tube the heat transfer ratio drop from unity ($\delta/D = 0$) is much steeper than for the other locations. Heat transfer rate ratios are significantly lower for back orientation, especially for small gap thickness and small Re . Usually the higher the Reynolds number the lower value of \dot{Q}/\dot{Q}_0 , although there is an exception for the lowest considered Reynolds number curve for nearly all gaps, excluding the biggest fin discontinuity.

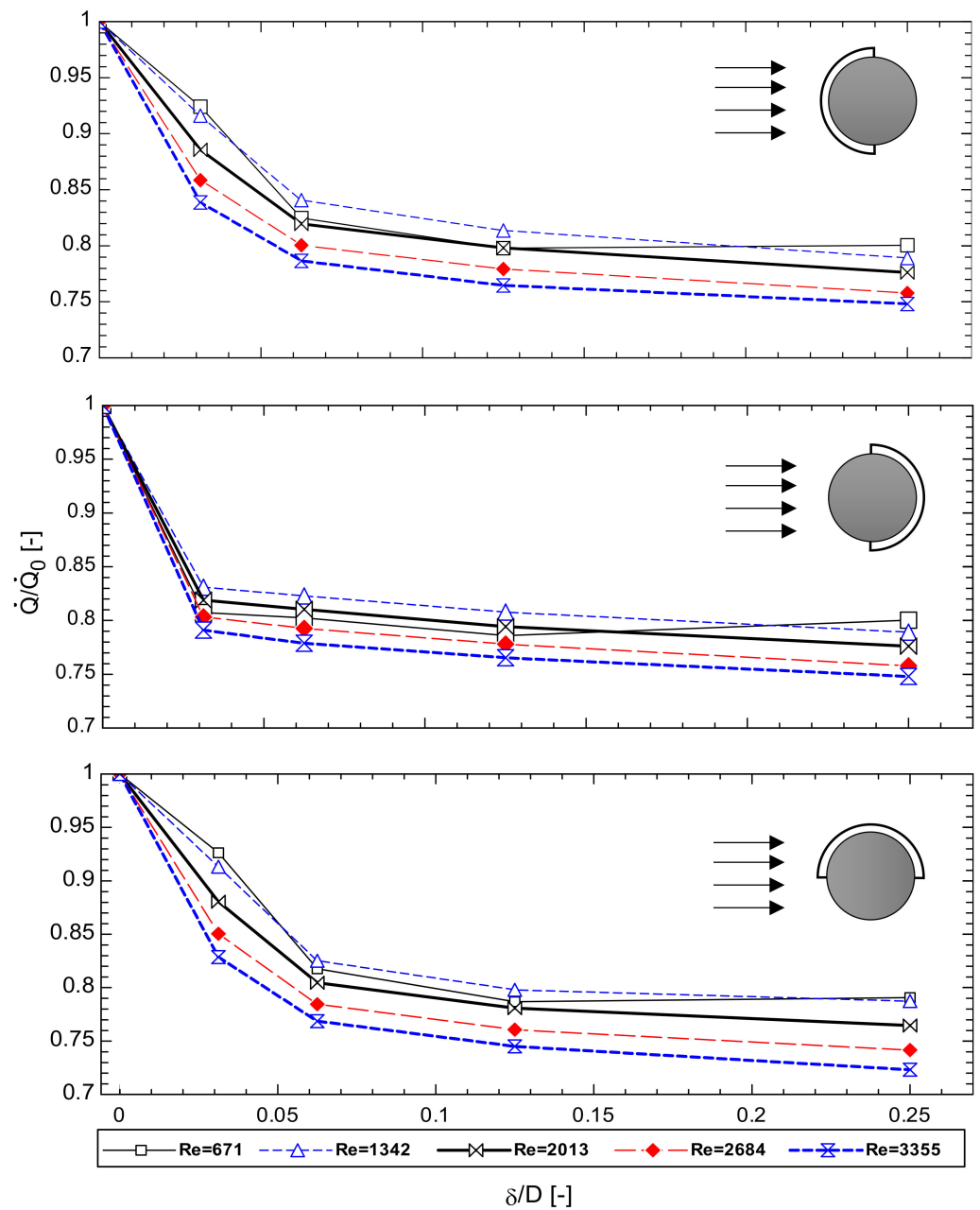


Figure 10. Heat transfer rate ratio in the function of dimensionless gap thickness.

For the rear-positioned slit at $Re = 671$ \dot{Q}/\dot{Q}_0 values are below these for $Re = 2013$. One can see a nearly monotonic decrease of the heat transfer rate ratio with increasing gap thickness, being the sharpest in the lower δ/D range and reaching practically a plateau for $\delta/D > 0.1$. The data points are connected by a piecewise linear function, instead of polynomial fit, because higher-order curve fitting produced slight inflection in the plateau range, which was a misleading artifact of the method.

A clearer picture of how the flow velocity influences heat transfer emerges from Figure 11. A decreasing trend of \dot{Q}/\dot{Q}_0 is seen with increasing Reynolds number, excluding the smallest Re departing from this pattern. In the range of $Re > 1342$, there is a nearly linear negative slope. However, in the span of $Re = 671-1342$, the decrease of heat transfer rate ratio is smaller or even there is a reverse trend (increase), indicating there can be a change of the flow regime. The curve for the smallest gap is placed remarkably higher than the other ones for the side and front location. Other δ/D cases, for all slit positions, exhibit

similar trends, with the $\delta/D = 0.125$ curve approaching or even crossing $\delta/D = 0.25$ with decreasing Re .

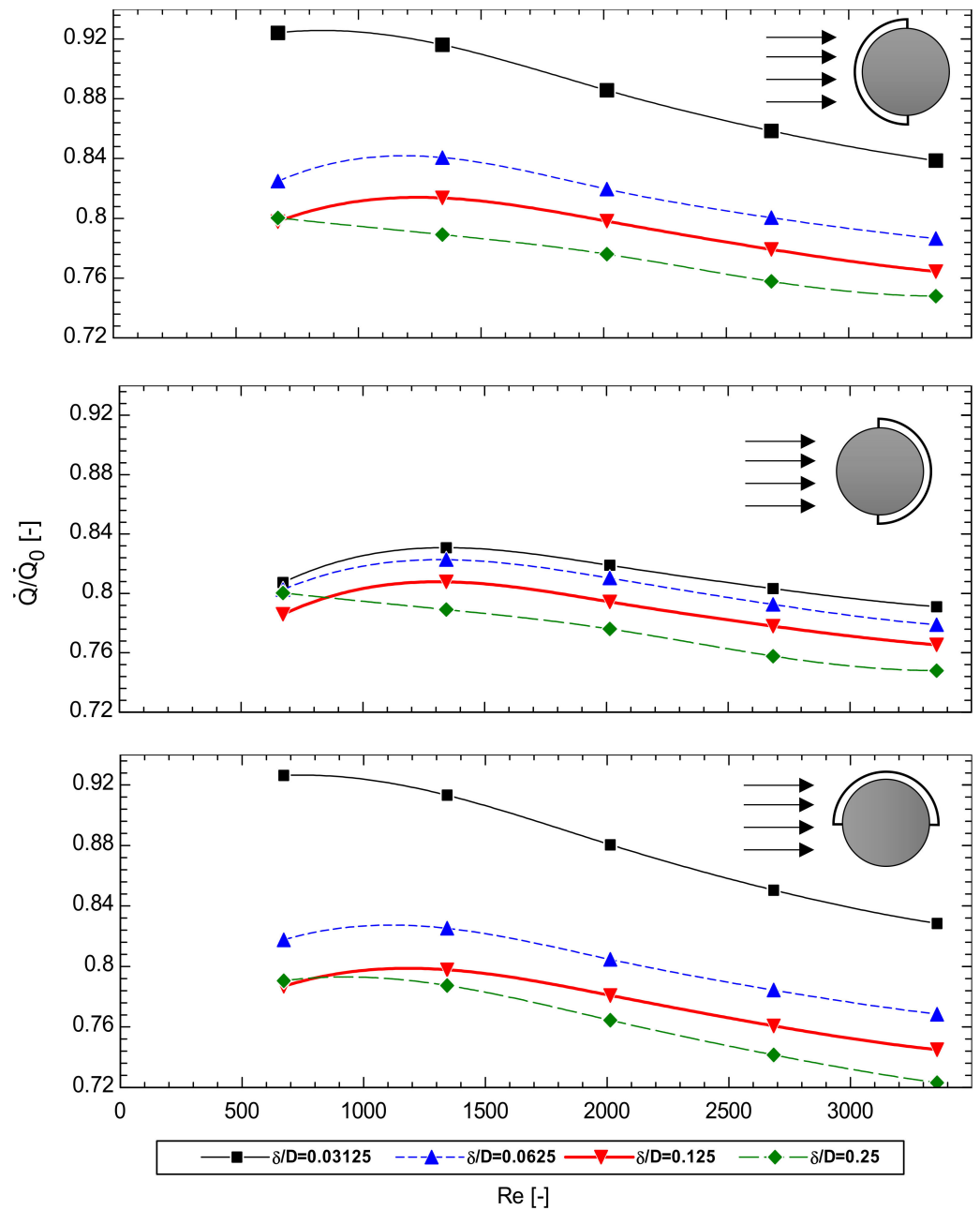


Figure 11. Heat transfer rate ratio in the function of Reynolds number.

The influence of the dimensionless gap position $\theta/180^\circ$ on the \dot{Q}/\dot{Q}_0 is addressed in Figure 12. In the case of the smallest gap, the front and side locations exchange nearly equal heat transfer rates, with a significant decrease that can be seen for slit in the back ($\theta/180^\circ = 1$). For the rest of the considered gap thicknesses, there are very small differences between the tube circumference and gap locations. The weak dependence in the range of $\delta/D = 0.0625-0.25$ is the most evident for the highest $Re = 3355$. The back and front slit cases indicate moderately higher, nearly equal thermal throughputs relatively similar to the side example.

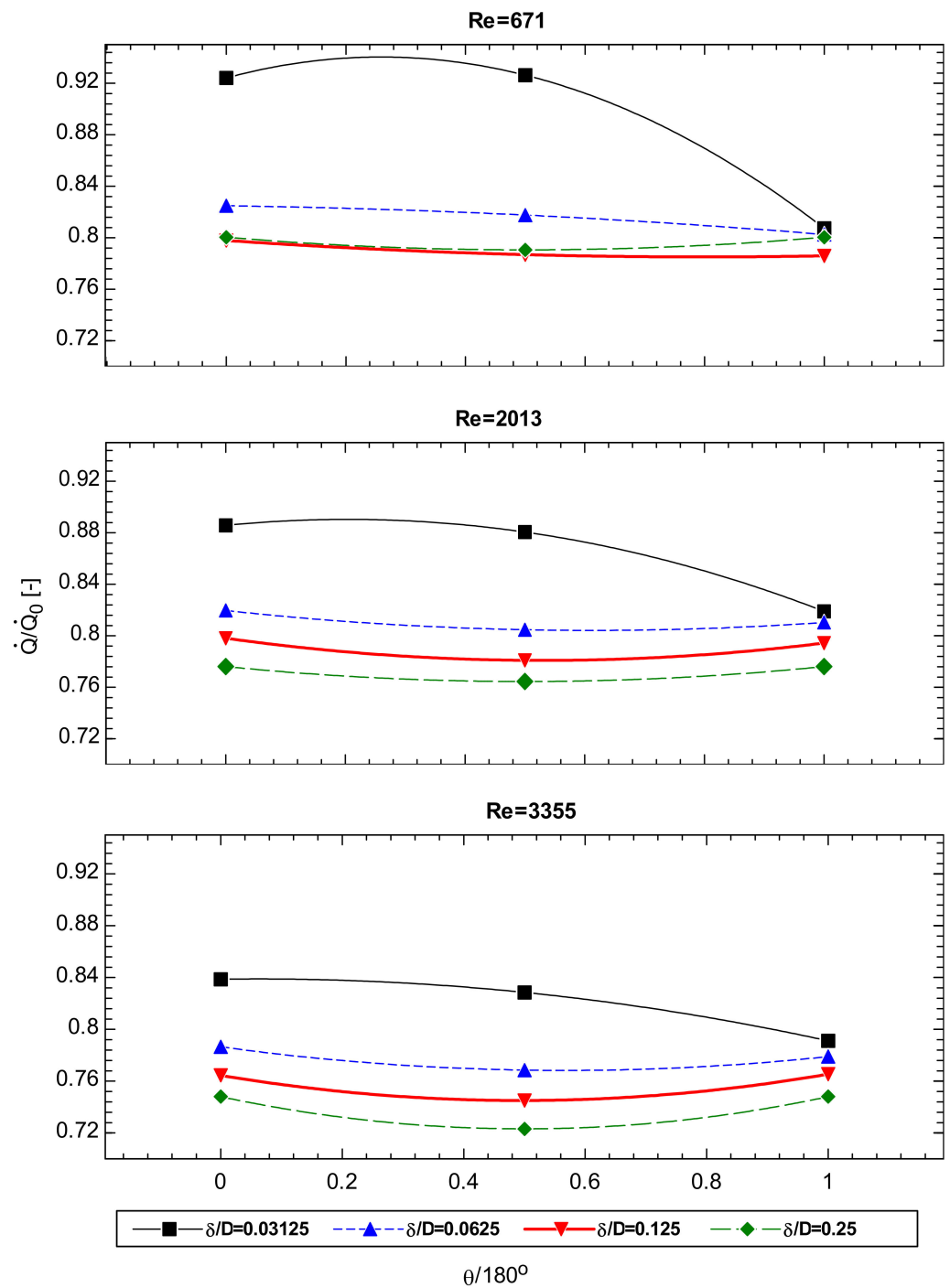


Figure 12. Heat transfer rate ratio in the function of gap position.

In Figure 13, the ratio of mean heat transfer coefficient with the gap presence to heat transfer ratio without any fin discontinuity is presented in the δ/D function. The front and side location results in enhancement of the mean convective heat transfer for the smallest discontinuity. This effect is not present in the rear location. For the remaining δ/D values, h/h_0 is below 1.0 (decrease of h). Besides, the local maximum at $\delta/D = 0.03125$ heat transfer coefficients ratio decreases nonlinearly with the increasing gap thickness, except for $\delta/D = 0.25$ where a slight increase can be observed. For the rear slit location, there is no local maximum and h/h_0 is at an approximately constant level of 0.9.

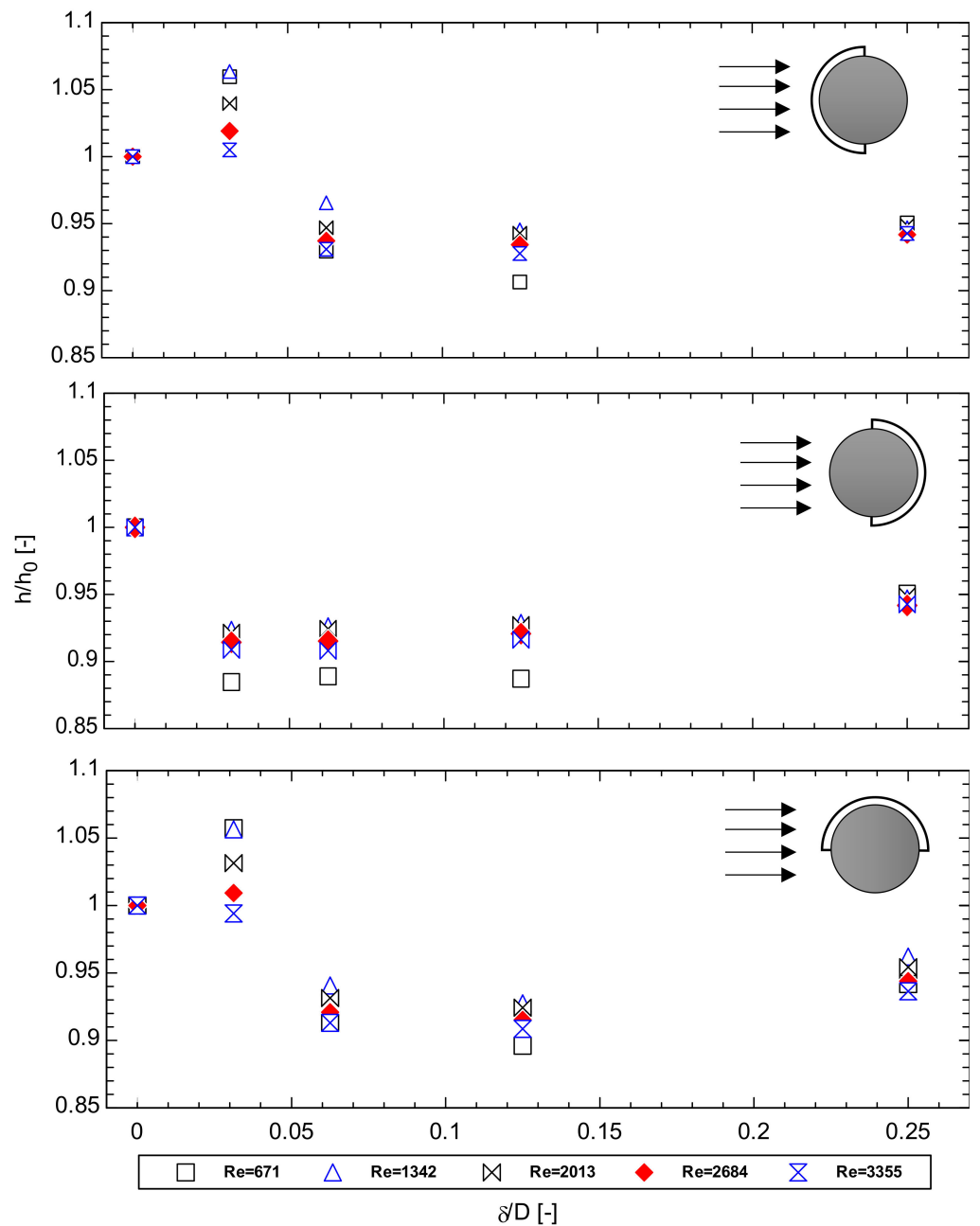


Figure 13. Heat transfer coefficient ratio in the function of dimensionless gap thickness.

In Figure 14, the h/h_0 dependence on the Reynolds number is shown. For the side and front cases at $\delta/D = 0.03125$, the convective heat transfer enhancement is existing at the whole range of Re numbers. For all slit thicknesses, there is a weak decrease of h/h_0 with the increase of the flow velocity. The smallest discontinuity heat transfer coefficients diverge from the wider gap cases, being at least 4% higher, whereas for the rest of the example values are adjacent to each other. There is not any enhancement for the rear position; the highest h/h_0 are noted for $\delta/D = 0.25$ at a nearly constant value of $h/h_0 = 0.95$ for the whole range of Reynolds numbers, diverging from the rest of the considered cases. At the lowest Re , for the remainder examples, the h/h_0 reaches a minimum of approx. 0.88, with a local maximum at $Re = 1342$, and for the rest of the volumetric flow range there is a decrease with the increase of Re .

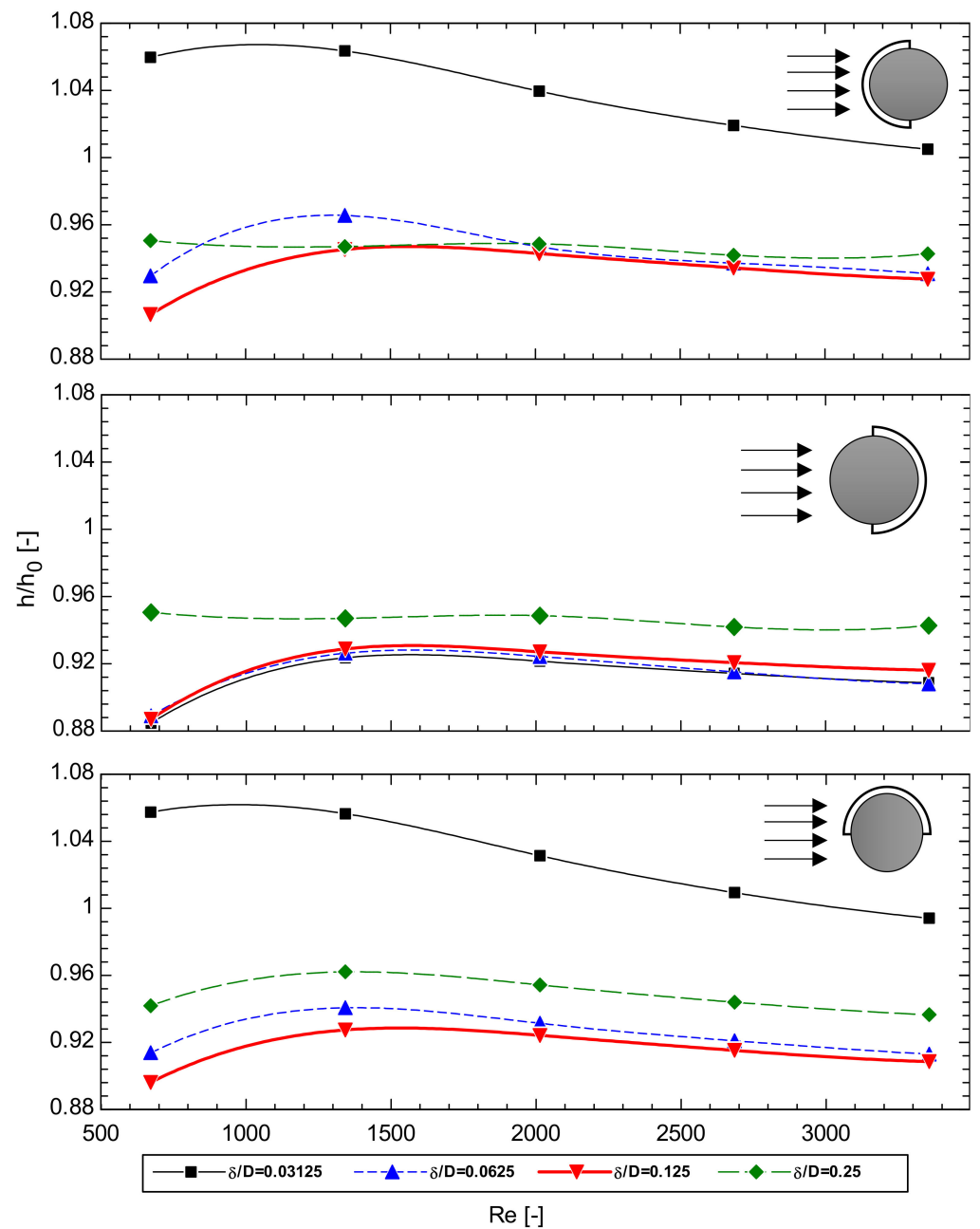


Figure 14. Heat transfer coefficient ratio in the function of Reynolds number.

The dependence on the gap position is shown in Figure 15. At $\delta/D = 0.03125$, there is the highest difference between the front, side, and back locations. The remaining slit thicknesses exhibit a very weak dependence on $\theta/180^\circ$, typically slightly reducing, with a maximum for the front and minimum for the back case.

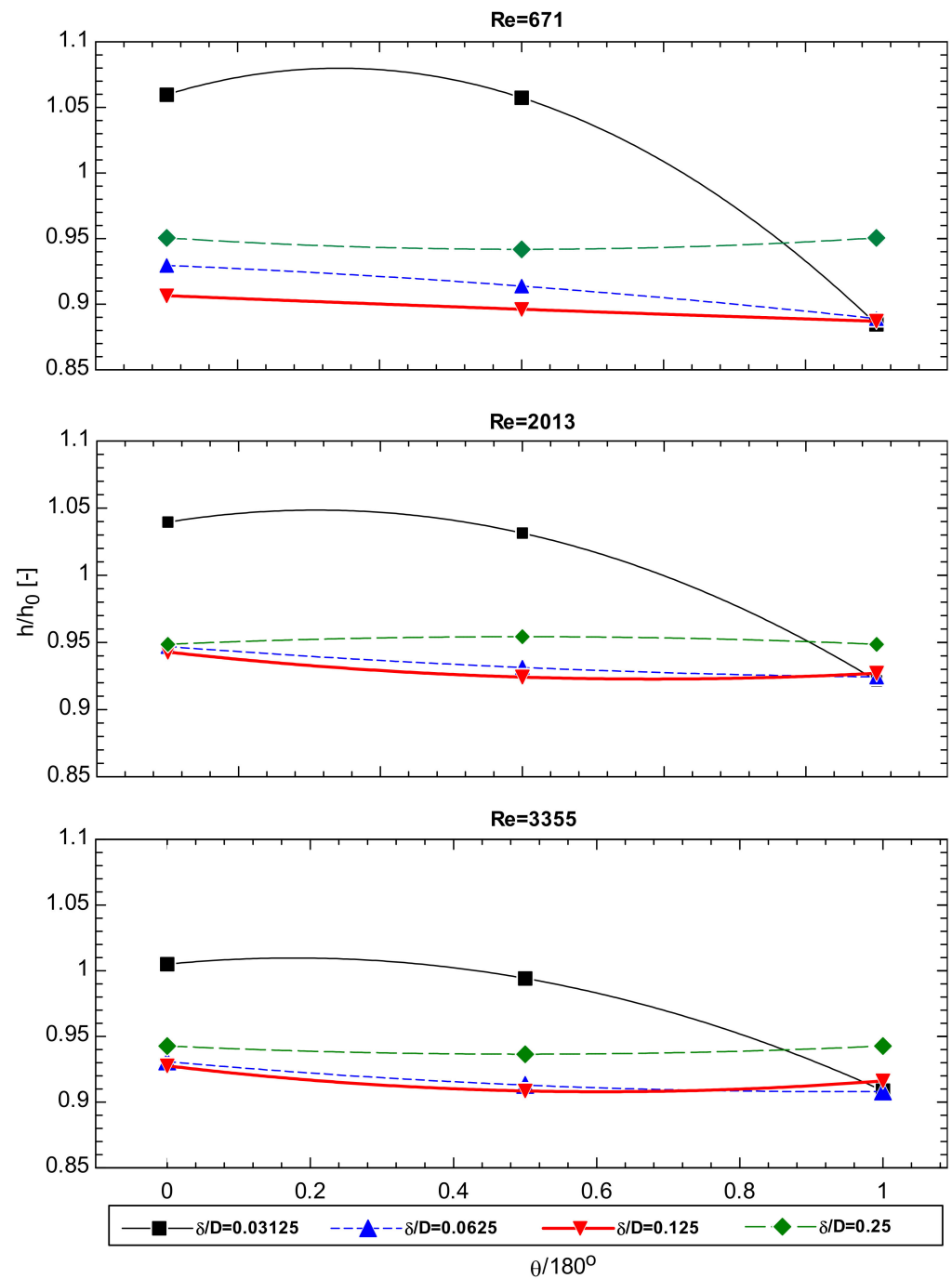


Figure 15. Heat transfer coefficient ratio in the function of the gap position.

In Figure 16, the contour map of a local heat transfer coefficient, which is defined as:

$$h_x = \frac{\dot{q}}{T_f - T_{in}}, \quad (16)$$

where T_{in} is periodic inlet air temperature, is presented for different gap sizes at the lowest Reynolds number ($Re = 671$) for front fin discontinuity location. Figure 16 was arranged to investigate the convective heat transfer enhancement relatively to no gap case. Intensification is present for the thinnest slit ($\delta/D = 0.03125$)—for bigger gaps, this effect diminishes (Figure 10). The contours are similar for all cases shown; therefore, the analysis starts with a description of common map characteristics. There is a high h_x zone

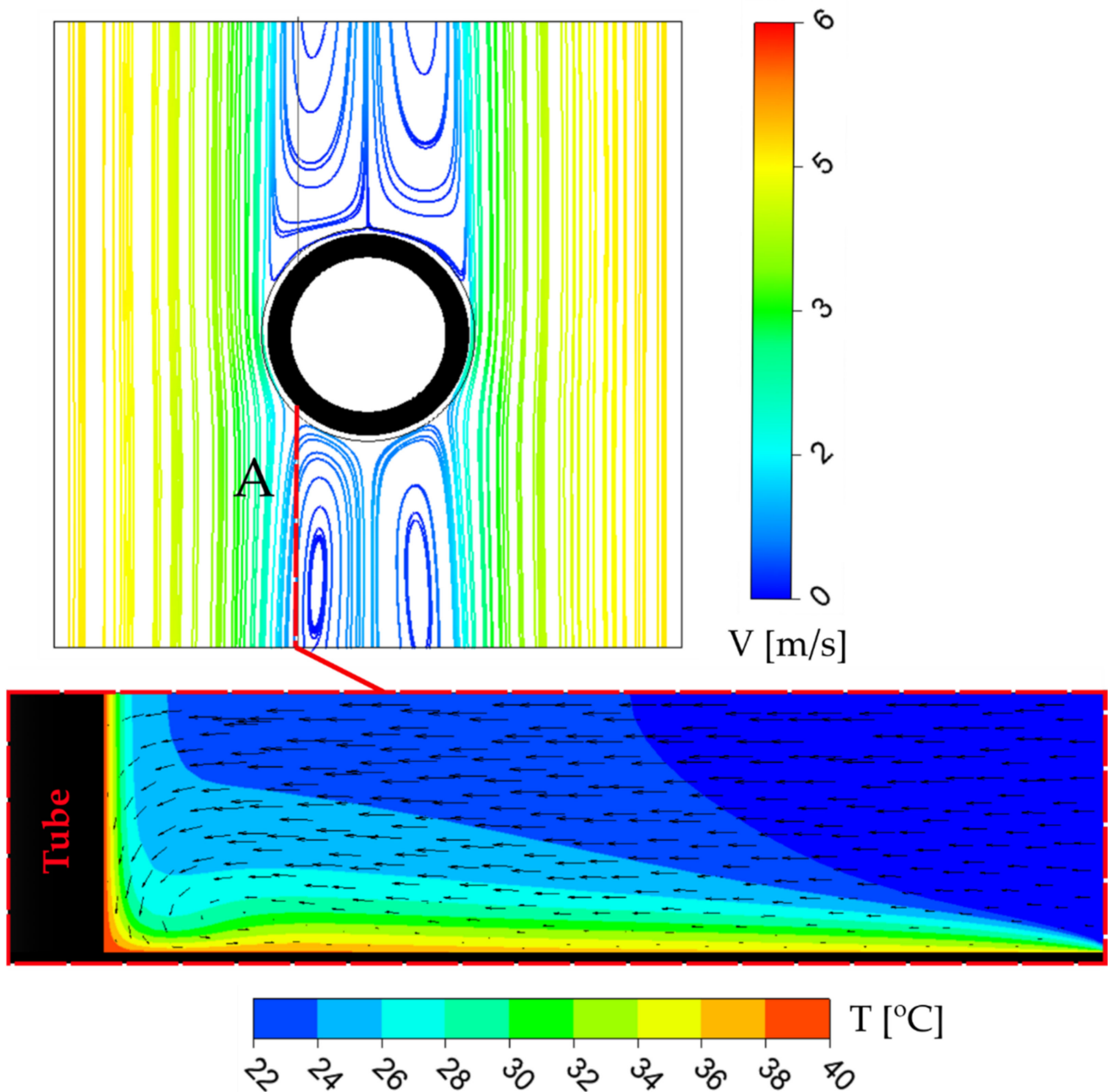


Figure 17. The top view of streamlines with the vector field showed on the face A upstream of the tube, at $Re = 2013$, for the ideal tube-fin contact case.

At the fin surface zone near the front part of the tube circumference, there are two bands of intensified heat transfer (placed symmetrically on the sides). This local enhancement is caused by a horseshoe vortex, which is visible in Figure 17, where the velocity vector field is visualized at plane A. The swirl of the fluid can be observed at the base of the tube. For the one-row or staggered arrangement plate-fin tube heat exchangers, the horseshoe vortex spans the whole half of the tube's circumference. In the present analysis, periodic flow simulations are equivalent to the inline arrangement. Therefore, the wake behind the preceding tube divides the horseshoe vortex in two (Figure 16— $\delta/D = 0$). There is also a thin region of enhanced heat transfer coefficient at the trailing edge, widening at the middle of the fin. This is the effect of the implementation of periodic heat transfer conditions in the simulations. Because the negative heat flux is set on the outlet, the small backflow of colder fluid causes this “artificial” heat transfer intensification. This effect

is practically of the same magnitude for all cases—it cancels in the comparative analysis. Even the h_x contour maps share the same characteristics; for $\delta/D = 0$, the strength of the heat transfer enhancement caused by the horseshoe vortex is the greatest. With the increase of the gap thickness, the horseshoe intensification becomes weaker. The thinnest slit covers partially the area of vortex action, whereas in the $\delta/D = 0.125$ case the vortex is present completely over the gap, which results in only moderately increased local h on the edges of the fin discontinuity. The introduction of the gap improves the heat transfer on the leading edge of the fin and changes somewhat the flow and heat transfer characteristics in the region downstream of the tube.

For $\delta/D = 0.03125$ and $\delta/D = 0.0625$, this alteration is not significant, yet for $\delta/D = 0.125$ there is a dramatic change—low heat transfer coefficient region (contour 3 in Figure 16) doubles its size and merges with the smaller one at the upstream part of the tube. The combined effect of the enhancement on the leading edge with still strong horseshoe vortex intensification can explain the observed augmentation of mean HTC for the thinnest slit relatively to no-gap example (Figure 13). The mean of heat transfer enhancement with thin slits cut in the front of the tube (for low airflow velocities) should be further studied. It could be a promising method of heat transfer intensification in compact heat exchangers.

The enhancement of h_x , by the presence of the slit, relative to ideal fin-tube contact example is not enough to cancel the negative effects of the fin discontinuity at its base (tube-fin junction)—in Figure 11 one can observe at least 6% lower heat transfer rate in the respect to $\delta/D = 0$. In Figure 18, the most obvious consequence of the introduction of the gap can be seen—the blockage of heat flow in the fin area adjacent to the discontinuity. This effect is visualized by dimensionless temperature excess Θ contour map, where:

$$\Theta = \frac{T_f - T_{in}}{T_w - T_{in}} \quad (17)$$

The fin is the most isothermal for the no-gap example, and the contour map is the most symmetrical. In Figure 18, the heat flux blockage is evident for the cases with the gap— Θ is significantly lower for nearly half of the fin on the side of the slit. For the gap in the front, the reduction of temperature is the smallest, while for the side location it is the highest (lowest fin efficiency). The mean h on the sides of the fin is the highest, and that is the reason for the severe temperature decrease. The Θ is the biggest on the average for the front case because the heat flux is directed backward (low h_x region) and the enhancing effect of the horseshoe vortex in the front of the tube is partially blocked. Analyzing the back gap position, the Θ is significantly lower on average. Heat flux is directed towards the front where the heat transfer intensification regions cause effective cooling of the fin. The result is substantially lower fin temperature in the back. In a conclusion, the gap placement in the front blocks the heat flow in the direction of the enhanced convective heat transfer area, which is not beneficial, although it results in higher fin efficiency than for the gap in the back. This can explain why there is a sudden heat transfer rate ratio drop for the rear slit position. The effect of low fin efficiency seems to combine with poorer convective heat transfer relatively similar to other discontinuity placement cases (Figure 10). The side gap position is the worst of the considered positions in terms of the fin temperature contour. The colder fin area is slightly bigger than the gap in the back. As the heat flux is directed to the side where high-velocity flow increases the intensity of heat transfer, the fin is efficiently cooled there. As the mean heat transfer coefficient is nearly as high as for the gap in the front, \dot{Q}/\dot{Q}_0 is slightly lower than the front gap for thin slits. The enhanced convective heat transfer compensates for the low fin efficiency. Figure 19 shows the influence of the flow Reynolds number on the h_x . The h_x contour maps are presented at four Reynolds numbers for a 1 mm thick gap in the back. The heat transfer intensification caused by the presence of the horseshoe vortex is less significant for the lowest Re , and it gets increasingly distinctive as the airflow velocity increases. The thermal boundary layer becomes thinner at the leading edge of the fin with the raising Re , which is visible as the wider high h_x area. As the Re increases, the h_x contours change their values proportionally, but the overall

topology (shape of the contours) is analogous for all airflow velocities. In Figure 14, one can see that for $Re = 671 h/h_0$ is the lowest—this is mainly caused by the low activity of the horseshoe vortex (Figure 19).

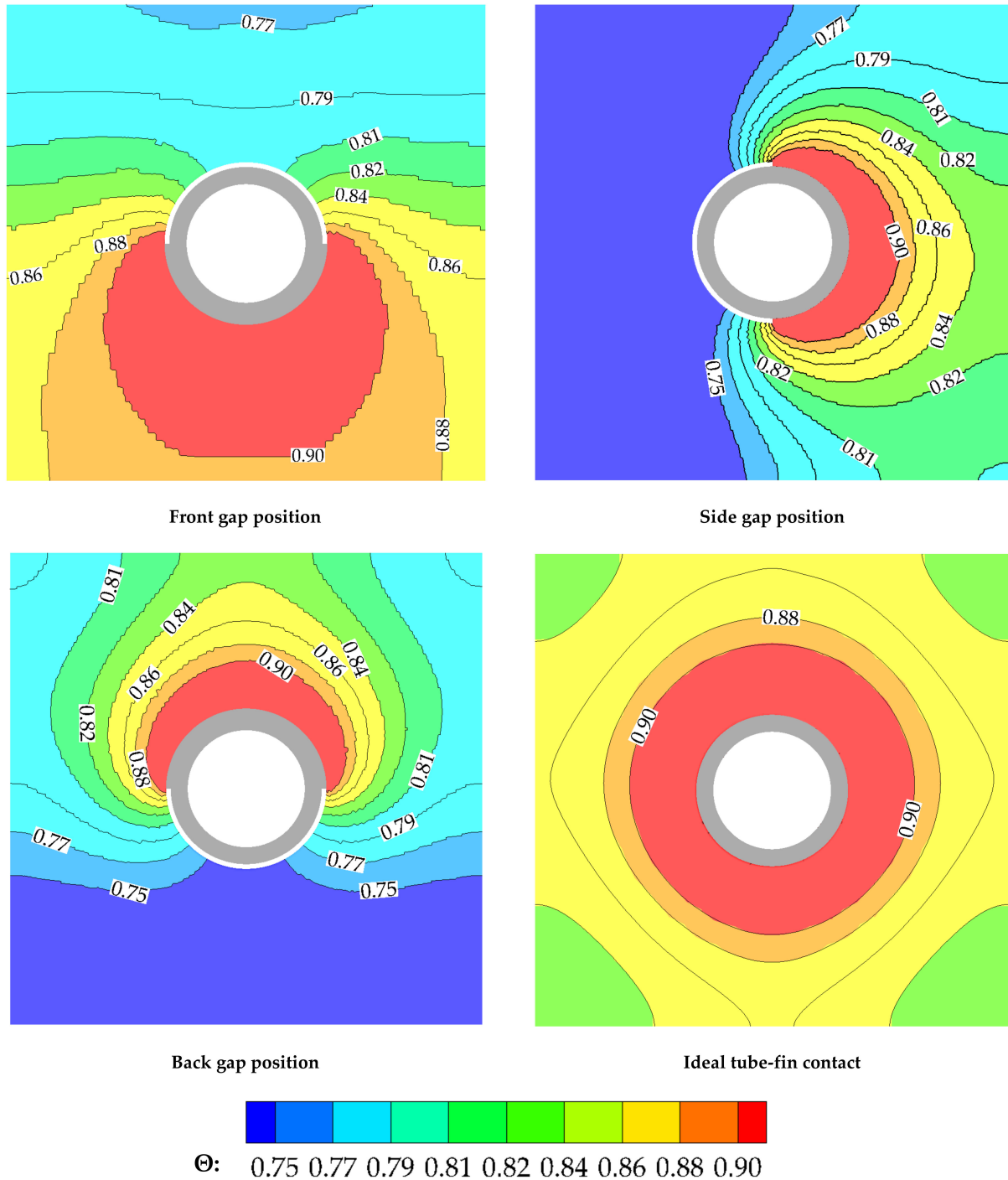


Figure 18. Dimensionless temperature excess Θ contour at $Re = 2013$ and $\delta/D = 0.03125$ for different gap positions.

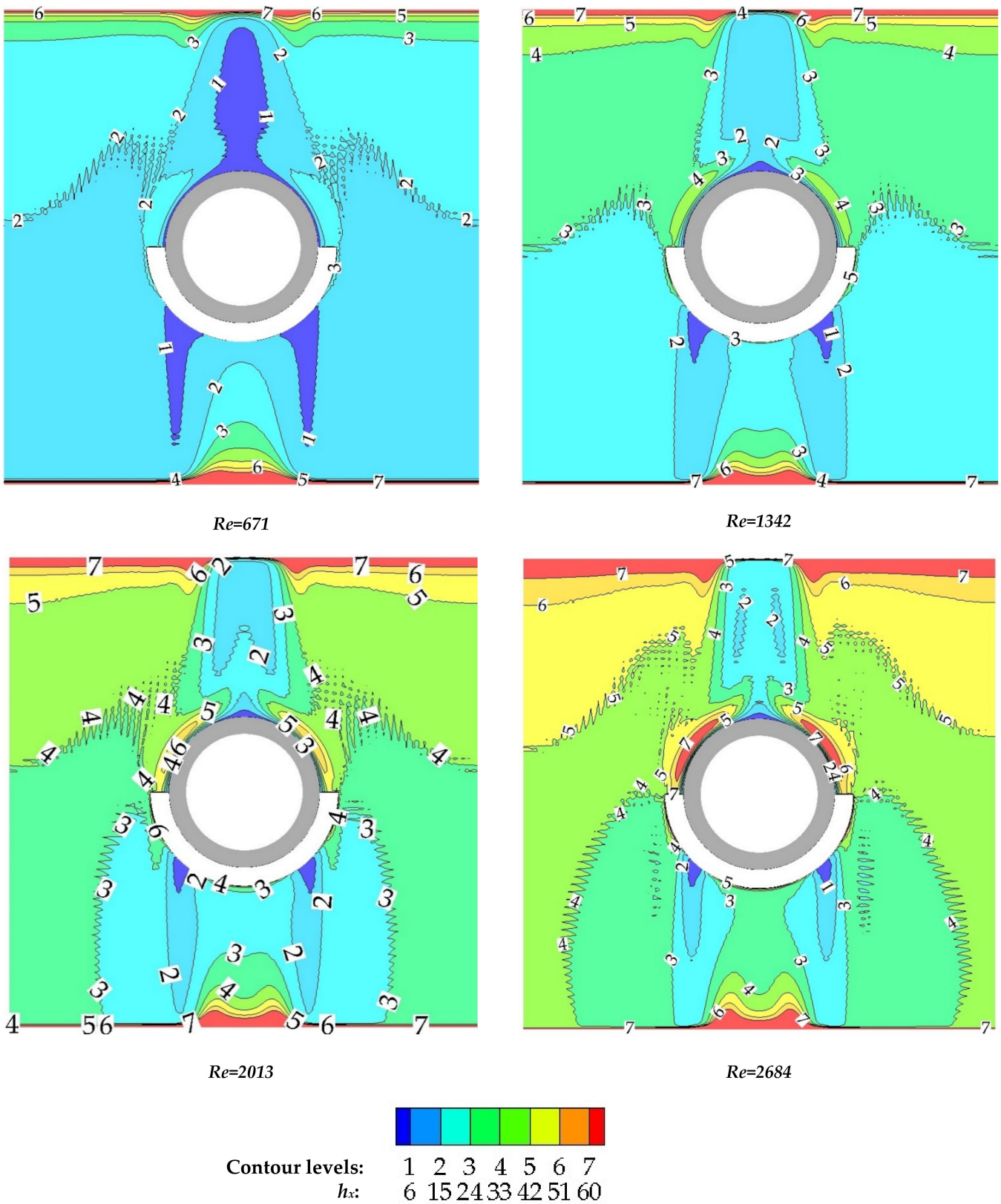


Figure 19. h_x map on the surface of the fin for various Reynolds numbers, with the gap size: $\delta/D = 0.125$ and back gap position.

4. Conclusions

To sum up the key findings from the numerical simulation, the fin discontinuity along the circumference reduces the heat transfer rate relatively to the perfect fin-tube contact case. The placement of the gap reduces the skin friction locally to zero, which can promote beneficial flow structures, which causes enhancement concerning the no-gap case, especially for small slit sizes. However, the convective heat transfer enhancement is overpowered by the heat flux blockage effect which leads to $\dot{Q}/\dot{Q}_0 < 1$ for all the cases. Fin discontinuity in front of the tube causes the smallest reduction of the heat transfer rate in comparison to the ideal tube-fin contact, especially for thin slits. Even the heat transfer rate ratio minimum is obtained for the gap at the side position (approx. 0.72), it performs slightly worse for the small gap range than the front location. The rear gap is characterized by the mean $\dot{Q}/\dot{Q}_0 = 0.8$ for all the gap sizes and therefore is considered the worst scenario, without the advantage of the smallest gap range. For gaps wider than $\delta/D > 0.1$, the heat transfer rate reduction becomes nearly constant for a specified Reynolds number. Generally, the higher the airflow, the \dot{Q}/\dot{Q}_0 becomes lower. For multirow plate-fin tube heat exchangers with small fin discontinuities, reversing the flow direction can result in an even 15% heat transfer increase if most of the gaps are in the rear of the tube (low airflow velocity). Realistically, obtaining this maximum is not very probable, although the present study shows that reversing the flow can have a positive effect on the plate-fin tube heat exchanger performance, and its longevity depends on the nature of the origin of the discontinuities (are they, and how fast they enlarge). The convective heat transfer enhancement for thin slits in the front should be further investigated to test the possibility of the introduction of fin cut-outs as heat transfer intensification structures in compact heat exchangers.

Author Contributions: Conceptualization, A.N.G. and M.L.; methodology, A.N.G. and M.L.; software, G.G.; validation, M.L., A.N.G. and D.A.; writing—original draft preparation, M.L. and D.A.; writing—review and editing, G.G.; visualization, D.A.; supervision, A.N.G. All authors have read and agreed to the published version of the manuscript.

Funding: This research received no external funding.

Data Availability Statement: Not applicable.

Conflicts of Interest: The authors declare no conflict of interest.

Nomenclature

A	finned side heat transfer surface, m^2
A_{t0}	bare outside tube surface, m^2
CFD	computational fluid dynamics
c_p	specific heat at constant pressure, $J/kg/K$
d	diameter, m
d_h	$(4 \cdot (L_f - D) \cdot L_t \cdot L_f) / (2 [L_f^2 - (\pi \cdot D^2 / 4)] + \pi \cdot D \cdot L_t)$ —hydraulic diameter, m
D	outer diameter of the tube
e	total fluid energy, J/kg
g	gravitational acceleration, m/s^2
h	heat transfer coefficient, $W/m^2/K$
h_x	local heat transfer coefficient
$h\%$	$(h_i - h_{i-1})/h_i$, relative change of heat transfer coefficient, %
k	$0.5 \cdot u_i' \cdot u_i'$ —kinetic energy of turbulence m^2/s^2
L	length, m
\vec{L}	periodic length vector, m
\dot{m}	mass flow, kg/s
n	heat-mass transfer analogy exponent
\vec{n}	vector normal to a surface
Nu	Nusselt number

p	pressure, Pa
\tilde{p}	periodic pressure, Pa
Pr	Prandtl number
Pr_t	turbulent Prandtl number
\dot{q}	heat flux (vector), W/m ²
\dot{Q}	heat transfer rate, W
\bar{r}	position vector, m
Re	$V \cdot d_h / \nu$ —Reynolds number
Ri	$(g \cdot \beta \cdot \Delta T \cdot L) / V^2$ —Richardson number
Sc	Schmidt number
Sh	Sherwood number
SST	shear stress transport
T	temperature, K
\tilde{T}	periodic temperature, K
V	average velocity (scalar), m/s
u	velocity vector, m/s
\bar{u}	time-averaged velocity vector, m/s
x	cartesian coordinates vector, m
X_t	tube spacing, m
Y^+	non-dimensional distance between the first mesh node and the wall

Greek symbols

β	volumetric expansion coefficient, 1/K
δ	gape thickness, thickness, spacing, m
δ_{ij}	Kronecker delta
Δ	difference of a quantity
θ	the gap placement angle
Θ	temperature excess
λ	thermal conductivity, W/m/K
μ	dynamic viscosity, kg·m/s
ν	kinematic viscosity, m ² /s
ρ	density, kg/m ³
$\rho \overline{u_i u_j}$	Reynolds stresses, Pa
σ	linear temperature gradient, K/m
τ_{ij}	stress tensor, Pa/m
ω	specific dissipation rate, 1/s

Subscripts

0	zero gap thickness
ave	average
d	based on the tube outside diameter
f	fin
g	gap
i	inside, inner, for i-th mesh refinement
i, j, k	indices (1, 2, 3)
in	inlet
o	outlet, outer
t	tube, turbulent
w	wall

References

1. Gorecki, G. Investigation of two-phase thermosyphon performance filled with modern HFC refrigerants. *Heat Mass Transf.* **2018**, *54*, 2131–2143. [CrossRef]
2. Chai, L.; Tassou, S. A Review of Airside Heat Transfer Augmentation with Vortex Generators on Heat Transfer Surface. *Energies* **2018**, *11*, 2737. [CrossRef]
3. Taler, D.; Taler, J.; Trojan, M. Experimental Verification of an Analytical Mathematical Model of a Round or Oval Tube Two-Row Car Radiator. *Energies* **2020**, *13*, 3399. [CrossRef]
4. Lotfi, B.; Sundén, B.; Wang, Q. An investigation of the thermo-hydraulic performance of the smooth wavy fin-and-elliptical tube heat exchangers utilizing new type vortex generators. *Appl. Energy* **2016**, *162*, 1282–1302. [CrossRef]

5. Välikangas, T.; Karvinen, R. Conjugated Heat Transfer Simulation of a Fin-and-Tube Heat Exchanger. *Heat Transf. Eng.* **2018**, *39*, 1192–1200. [CrossRef]
6. Bansal, P.; Wich, T.; Browne, M. Optimisation of egg-crate type evaporators in domestic refrigerators. *Appl. Therm. Eng.* **2001**, *21*, 751–770. [CrossRef]
7. Blygold Blygold—Example of Galvanic Corrosion Damage. Available online: <https://www.blygold.com/services/coil-coating/> (accessed on 15 May 2021).
8. Critoph, R.; Holland, M.; Turner, L. Contact resistance in air-cooled plate fin-tube air-conditioning condensers. *Int. J. Refrig.* **1996**, *19*, 400–406. [CrossRef]
9. Jannick, P.; Meurer, C.; Swidersky, H. Potential of Brazed Finned Tube Heat Exchangers in Comparison to Mechanical Produced Finned Tube Heat Exchangers. In Proceedings of the International Refrigeration and Air Conditioning Conference, West Lafayette, IN, USA, 16–19 July 2002.
10. Zhao, H.; Salazar, A.J.; Sekulic, D.P. Analysis of Fin-Tube Joints in a Compact Heat Exchanger. *Heat Transf. Eng.* **2009**, *30*, 931–940. [CrossRef]
11. Jeong, J.; Nyung Kim, C.; Youn, B.; Saeng Kim, Y. A study on the correlation between the thermal contact conductance and effective factors in fin-tube heat exchangers with 9.52 mm tube. *Int. J. Heat Fluid Flow* **2004**, *25*, 1006–1014. [CrossRef]
12. Cheng, W.; Madhusudana, C. Effect of electroplating on the thermal conductance of fin-tube interface. *Appl. Therm. Eng.* **2006**, *26*, 2119–2131. [CrossRef]
13. Taler, D.; Ocloń, P. Thermal contact resistance in plate fin-and-tube heat exchangers, determined by experimental data and CFD simulations. *Int. J. Therm. Sci.* **2014**, *84*, 309–322. [CrossRef]
14. Taler, D.; Cebula, A. A new method for determination of thermal contact resistance of a fin-to-tube attachment in plate fin-and-tube heat exchangers. *Chem. Process Eng.* **2010**, *31*, 839–855.
15. Singh, S.; Sørensen, K.; Condra, T.J. Influence of the degree of thermal contact in fin and tube heat exchanger: A numerical analysis. *Appl. Therm. Eng.* **2016**, *107*, 612–624. [CrossRef]
16. Saboya, F.E.M.; Sparrow, E.M. Local and Average Transfer Coefficients for One-Row Plate Fin and Tube Heat Exchanger Configurations. *J. Heat Transf.* **1974**, *96*, 265. [CrossRef]
17. Menter, R.F. Zonal Two Equation Kappa-Omega Turbulence Models for Aerodynamic Flows. In Proceedings of the 23rd Fluid Dynamics, Plasmadynamics, and Lasers Conference, Orlando, FL, USA, 6–9 July 1993.
18. Lindqvist, K.; Skaugen, G.; Meyer, O.H.H. Plate fin-and-tube heat exchanger computational fluid dynamics model. *Appl. Therm. Eng.* **2021**, *189*, 116669. [CrossRef]
19. Taler, D.; Ocloń, P. Determination of heat transfer formulas for gas flow in fin-and-tube heat exchanger with oval tubes using CFD simulations. *Chem. Eng. Process. Process Intensif.* **2014**, *83*, 1–11. [CrossRef]
20. Jasiński, P.B. Numerical study of the thermo-hydraulic characteristics in a circular tube with ball turbulators. Part 2: Heat transfer. *Int. J. Heat Mass Transf.* **2014**, *74*, 473–483. [CrossRef]
21. Ocloń, P.; Łopata, S. Study of the Effect of Fin-and-Tube Heat Exchanger Fouling on its Structural Performance. *Heat Transf. Eng.* **2018**, *39*, 1139–1155. [CrossRef]
22. Ansys Inc. *ANSYS CFX Theory Guide*; Ansys Inc.: Canonsburg, PA, USA, 2013.
23. Shevchuk, I.V.; Jenkins, S.C.; Weigand, B.; Von Wolfersdorf, J.; Neumann, S.O.; Schnieder, M. Validation and analysis of numerical results for a varying aspect ratio two-pass internal cooling channel. *J. Heat Transf.* **2011**, *133*. [CrossRef]
24. Siddique, W.; El-Gabry, L.; Shevchuk, I.V.; Fransson, T.H. Validation and Analysis of Numerical Results for a Two-Pass Trapezoidal Channel With Different Cooling Configurations of Trailing Edge. *J. Turbomach.* **2012**, *135*. [CrossRef]
25. Goldstein, R.J.; Cho, H.H. A review of mass (heat) transfer measurements using naphthalene sublimation. *Exp. Heat Transf. Fluid Mech. Thermodyn.* **1993**, *10*, 21–40. [CrossRef]
26. Kays, W.M.; William, M.; London, A.L.; Alexander, L. *Compact Heat Exchangers*; Krieger Pub. Co.: Malabar, FL, USA, 1998; ISBN 1575240602.
27. Rosman, E.C.; Carajilescov, P.; Saboya, F.E.M. Performance of One- and Two-Row Tube and Plate Fin Heat Exchangers. *J. Heat Transf.* **1984**, *106*, 627. [CrossRef]
28. Tecplot Inc. *Tecplot.360 EX User's Manual*; Tecplot Inc.: Bellevue, WA, USA, 2018.
29. Saboya, S.M.; Saboya, F.E.M. Transfer coefficients for plate fin and elliptical tube heat exchangers. In Proceedings of the 6th Brazilian Congress of Mechanical Engineering, Rio de Janeiro, Brazil, 15–18 December 1981.
30. Stephan, P. B1 Fundamentals of Heat Transfer. In *VDI Heat Atlas*; Springer: Berlin/Heidelberg, Germany, 2010; pp. 15–30.

Article

Application of Thermal and Cavitation Effects for Heat and Mass Transfer Process Intensification in Multicomponent Liquid Media

Anatoliy M. Pavlenko *  and Hanna Koshlak 

Department of Building Physics and Renewable Energy, Kielce University of Technology, 25-314 Kielce, Poland; hkoshlak@tu.kielce.pl

* Correspondence: apavlenko@tu.kielce.pl; Tel.: +48-883-741-291

Abstract: In this paper, the authors consider the processes of dynamic interaction between the boiling particles of the dispersed phase of the emulsion leading to the large droplet breakup. Differences in the consideration of forces that determine the breaking of non-boiling and boiling droplets have been indicated in the study. They have been determined by the possibility of using the model to define the processes of displacement, deformation, or fragmentation of the inclusion of the dispersed phase under the influence of a set of neighboring particles. The dynamics of bubbles in a compressible liquid with consideration for interfacial heat and mass transfer has also been analyzed in the paper. The effect of standard and system parameters on the intensity of cavitation processes is considered. Physical transformations during the cavitation treatment of liquid are caused not only by shock waves and radiated pressure pulses but also by extreme thermal effects. At the stage of ultimate bubble compression, vapor inside the bubble and the liquid in its vicinity transform into the supercritical fluid state. The model analyzes microflow features in the inter-bubble space and quantitatively calculates local values of the velocity and pressure fields, as well as dynamic effects.

Keywords: breaking; desorption; force; speed; acceleration; pressure; dispersed phase

Citation: Pavlenko, A.M.; Koshlak, H. Application of Thermal and Cavitation Effects for Heat and Mass Transfer Process Intensification in Multicomponent Liquid Media. *Energies* **2021**, *14*, 7996. <https://doi.org/10.3390/en14237996>

Academic Editors: Jan Danielewicz and Krzysztof Rajski

Received: 8 November 2021

Accepted: 24 November 2021

Published: 30 November 2021

Publisher's Note: MDPI stays neutral with regard to jurisdictional claims in published maps and institutional affiliations.



Copyright: © 2021 by the authors. Licensee MDPI, Basel, Switzerland. This article is an open access article distributed under the terms and conditions of the Creative Commons Attribution (CC BY) license (<https://creativecommons.org/licenses/by/4.0/>).

1. Introduction

Cavitation phenomena have been studied by many authors [1–6] and can be used to intensify heat and mass transfer processes [7–9]. In order to develop an effective method of a controlled cavitation effect on technological processes, one should have a clear understanding of the physical nature of cavitation mechanisms and their relevant description in spatial and temporal scales.

For years, cavitation has been considered one of the areas of hydrodynamics associated with the elucidation and elimination of negative causes of erosion destruction of the surfaces of propellers, hydraulic turbine blades, and hydraulic devices [10–12]. It was determined that surfaces are eroded under the action of shock waves and cumulative jets formed by the micro-explosions of bubbles, considered as hollow caverns in hydrodynamics [13–15]. Within these mechanisms alone it is difficult to explain the destruction of molecular and colloidal structures and other cavitation effects at the microlevel in the liquid itself. When cavitation is analyzed within hydrodynamics, the impact of thermal factors on the development and specific manifestation of cavitation effects is excluded. To a certain extent, such an approach has been valid to date, although it has been determined that at the maximum compression stage, the vapor–gas medium temperature inside the cavitation bubble exceeds 5000 K, and the pressure increases up to 1000 MPa [16–18]. It is assumed that the thermal energy released in the bubble volume is sufficient for the excitation, ionization, and dissociation of water vapor molecules and gases present in the bubble, the formation of free radicals, acceleration by 5–6 orders of magnitude of the rates of gas-phase chemical reactions [19–21], and even initiation of nuclear fusion reactions in

cavitation bubbles [22,23]. That is, under certain conditions, various physical or chemical processes can be initiated in local zones of the liquid while concentrating energy to abnormally high values. The following problem is still to be solved: What conditions are required for the appearance of such effects? At the same time, high-temperature processes in the gas phase (in the cavitation region) do not explain the cavitation effect on disperse inclusions present in the liquid phase (droplets of another liquid in emulsions, particles in suspensions, etc.), assuming the existence of alternative mechanisms.

Reliable theoretical analysis of cavitation mechanisms is hindered, in the authors' opinion, by the lack of generalizing mathematical models with maximum consideration of the main physical factors. Modeling is usually performed with respect to the analysis of a specific experiment without considering the interfacial heat exchange and kinetics of phase transitions; the bubble compression process is assumed to be adiabatic [2,24,25]. The principles of a mathematical model for the dynamics of bubble formation and development in emulsions based on the laws of cavitation described above, with the effect of thermodynamic processes in the cavitation region, are considered in [26,27]. The model validation in the analysis of experimental results defines this approach as having potential.

The purpose of this study is to investigate the mechanisms of the cavitation effect on water emulsions (Figure 1) containing micro-dispersions, molecular and colloidal structures relevant to improving the design of cavitating devices, and substantiating their optimal operating modes.

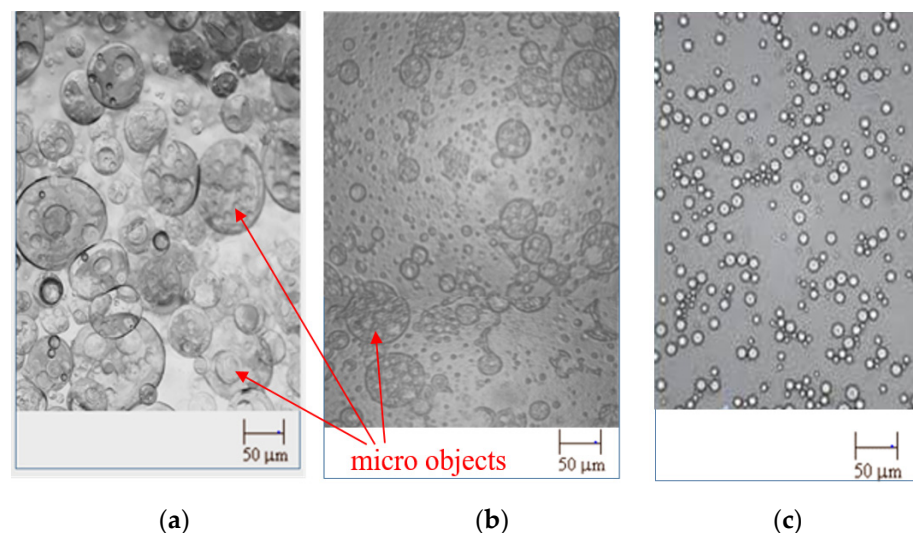


Figure 1. Photos of emulsion: (a) fuel emulsion “water–fuel oil” before thermal cavitation treatment, (b) after hydrodynamic cavitation, and (c) after thermal cavitation treatment.

Figure 1 shows one example of how thermal cavitation treatment can be applied to homogenization technologies for liquid fuels.

The tasks aimed at the efficiency increase of heat and mass transfer processes are very important for almost all heat technologies. One of the most efficient methods used to increase the intensification of heat and mass transfer processes is the use of emulsions as operating media [28–32], containing various mutually insoluble liquids with certain thermophysical characteristics. An increase in the emulsion temperature is accompanied by their structure change, the breakage of dispersed fluid droplets, or their merging. When thermolabile liquid boils, heat and mass transfer processes are intensified in the emulsion due to the abnormally rapid change in the vapor phase volume and turbulence transition of the medium flow; it undoubtedly increases the efficiency of these processes. The phenomena similar to those described above (cavitation) occur in the vapor layer of the boiling thermolabile part. They have been studied by many researchers [33–35], but these phenomena require further consideration in terms of heat and mass transfer efficiency. Moreover, the processes which induce abnormal values of pressures and temperatures in

the case of thermodynamic cavitation and their application represent a separate important problem. One of the possible issues to be solved using such thermal cavitation initiation is homogenization technology.

It is worth mentioning that there is no general approach to the management of cavitation processes to obtain the expected disperse structure. Our proposed thermal cavitation method may be used to evaluate such effects. Its main ideas are described below.

2. Assessment of Dynamic and Thermal Cavitation Effects

Despite different and often contradictory definitions of cavitation, we will adhere to the following general formulation. Cavitation is a set of phenomena in a liquid when the pressure p_e drops below the saturation pressure at temperature $p_s(T)$, and then it rises sharply above this level. If $p_e < p_s(T)$, it is possible to observe the formation and growth of vapor bubbles both during hydrodynamic cavitation and thermal cavitation, when the pressure in a liquid, preliminarily superheated under excess pressure, is sharply reduced. Then, vapor bubbles appear at the interface of the dispersed inclusions of the emulsion. At $p_e > p_s(T)$ they get compressed and subsequently destroyed (explosion). In both cases, a nonequilibrium process of the bubble system proceeds to the state of thermodynamic equilibrium, making it possible to describe bubble boiling and cavitation within the framework of one model, using the same Equations but under different initial conditions.

This concept forms the basis of the mathematical model of bubble dynamics, presented in [26,27].

The entire period of the cavitation effect development is accompanied by the growth and subsequent destruction of bubbles. A pulsating cavitation cluster inevitably appears in hydraulic turbines, pumps, and in various devices where the above conditions of pressure drop are realized [36].

Let us consider the process of vapor bubble compression in water under condition $p_e > p_s(T)$. At the beginning of compression, the vapor pressure inside the bubble is $p_{int} \approx p_s(T)$ and the pressure in a liquid at the bubble wall is $p_i = p_{int} - 2\sigma(T)/R - \mu(T) \cdot v/R$, where R is the bubble radius, v is the liquid radial rate at the bubble interface, and $\sigma(T)$ and $\mu(T)$ are surface tension and viscosity coefficients. As a result of the pressure difference $p_e - p_i$, the liquid moves rapidly towards the bubble center, resulting in a sharp increase in vapor pressure and temperature in the collapsing bubble. The compression rate is regulated by interfacial heat transfer and vapor condensation on the “cold” bubble wall with condensation heat release. When vapor pressure p_{int} , compressed in the bubble, exceeds external pressure p_e , the liquid begins to decelerate, and its kinetic energy is converted into the potential energy of the compressed vapor and into the potential energy of the compressed liquid around the bubble. When kinetic energy is completely transformed, the bubble compression stops while pressure in the liquid at its boundary reaches its maximum value. The hydraulic hammer effect is realized, a compression wave propagates from the bubble into the liquid volume at the velocity of sound and its amplitude decreases with distance. Normally, when cavitation processes are modeled, the liquid is considered incompressible, while the hydraulic hammer phenomenon is not considered. To analyze the degree of the hydraulic hammer effect, the model [27] was modified taking into account liquid compressibility. The liquid compressibility coefficient $k_\beta = f(T, p)$ and the temperature coefficient of adiabatic compression $\alpha(T, p) = \partial T / \partial p$ are introduced into the model as new parameters. Taking into account the compressibility, the motion Equation, included in the model’s basic system of Equations, is presented in the following form:

$$\frac{dv}{d\tau} = \frac{p_{int} - p_{ext} + 1.5(p_{int} - p_{ext})^2 k_\beta - 1.5\rho v^2}{\rho R} \quad (1)$$

where $\rho(T)$ is the liquid density. The derived Equation (1) differs from the classical Rayleigh–Plesset Equation usually used to describe cavitation processes in an incompressible liquid,

by the term $1.5(p_{int} - p_e)^2 k_\beta$ in the numerator, considering the potential energy contribution of a compressed liquid, which is then realized in a force impulse form.

After the transition of the vapor parameters in the compressed bubble to the supercritical region, ($T_{steam} > T_{critical}$ and $p_{steam} > p_{critical}$), the liquid–vapor interface disappears ($\sigma(T_{critical}) = 0$) and a quasi-spherical local zone is formed in place of a bubble with R_{min} radius within which water passes from a supercritical state to a condensed one. Similar effects are observed when the above is exposed to high pressures, even if the water temperature is below critical [37]. We can assert that the thermal cavitation effect is not limited by the volume of a bubble with R_{min} radius where, as it is believed, only the ionization of vapor and gas molecules takes place, though covering a wider area.

When cavitation conditions are realized in a liquid, numerous vapor–gas bubbles forming a cavitation cluster grow and then simultaneously explode. The cavitation action effect is determined by the combined influence of all the cluster bubbles.

The superposition of shock waves from each individual bubble forms a single destructive shock wave. However, this concept fails to explain the destruction of micro objects (micro objects in Figure 1) within the cluster itself. When cavitation cluster features are modeled and analytical calculation methods for cavitation reactors are developed, the temperature is often not even included in the model parameters [14,15]. In [27], regarding the analysis of boiling processes, a model of the bubble ensemble dynamics is considered based on a model of the single bubble dynamics. Considering the liquid compressibility, we propose for it to be included in Equation (1), as this model makes it possible to predict the evolution of a cavitation cluster at all stages of its development and to describe the nature of microflows in the interbubble space of the cluster associated with bubble expansion or contraction. Nevertheless, in this work, a uniform distribution of gas bubbles in a liquid is assumed, which is practically unrealizable in real processes. Moreover, if we consider the problem with the temperature effect, then cluster sizes should be different, as shown in Figure 1 since the clusters have a more complex structure.

Figure 2 shows the distribution of microflow velocity vectors at local points around vapor bubbles, modeled using the technique proposed in [27] (gas bubble radii $R = 10\text{--}100\ \mu\text{m}$ (in the diagram, the size of each bubble increases by $10\ \mu\text{m}$)), with the maximum liquid rate at the interface with bubbles being $v_i = 220\ \text{m/s}$ (superheating temperature is $110\ ^\circ\text{C}$).

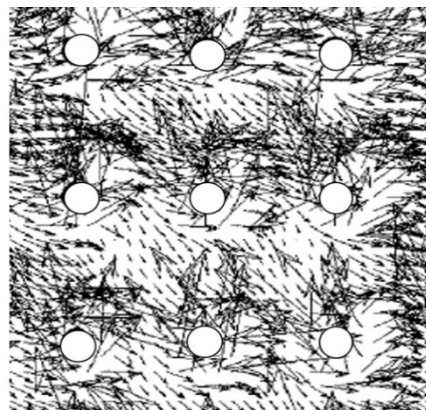


Figure 2. Distribution of velocity vectors inside the cavitation cluster.

Due to the superposition of radial flows of all the bubbles in the cluster, the pattern is quite complex. However, in real emulsions (Figure 1), with distance from the bubble, the rate should change sharply in magnitude and direction, since the dynamics of bubble development depend on its size and distance to the neighboring bubbles, as well as their sizes.

Calculations show that shear rates in the interbubble space at local points at the boundaries of the interaction between flows can reach $10^4\ \text{s}^{-1}$, thus corresponding to a shear stress of about $0.8\ \text{kPa}$ if the dispersion phase is water (in these calculations, a

water emulsion in fuel oil was used). However, if we use a procedure that focuses on a uniform distribution of low-boiling liquid droplets, as shown in Figure 2, we will not get the resultant flux. The dynamic effects are identical around each droplet and they will be mutually compensated. It does not correspond to the effects in real emulsions, where under similar conditions a circulating flow in the emulsion volume would occur. It is thought that the values of local velocities and accelerations will be different as they should also affect adjacent droplets. Since they have different sizes and are arranged in a chaotic manner, these effects will differ in level and direction. The resulting effect can be much more significant when the dynamic effects are directed towards the opposite droplets. It is also important to bear in mind that depending on the size of the droplets, dynamic effects can occur at different times. For example, if a small droplet evaporates very quickly, resulting in a strong dynamic effect, it may already be realized before the effect of a relatively larger droplet occurs; the resulting effect can be turbulization of the fluid volume, an increase in heat flow, or emulsion homogenization.

It is essential that even at the stage of monotonic cluster expansion when the bubble growth rate does not exceed 2 m/s, the shear rates in liquid local zones are quite high—in the order of $7 \times 10^3 \text{ s}^{-1}$, comparable to the shear rates achieved in homogenizers. Thus, if a high level of thermal action is realized only at the stage of maximum cluster bubble compression, at a time interval of tens of nanoseconds, then the effective influence of shear stresses manifests itself during the entire cluster lifetime. We can consider the additional effect of liquid temperature on the above processes in terms of, for example, homogenization technologies. We assume that the creation of cavitation effects through increasing the superheated pressure with a subsequent sharp decrease will create anomalous dynamic effects at the boundaries of growing vapor bubbles (at the moment of their explosion), which make it possible to crush all the dispersed inclusions in a liquid. We refer to this method as the thermal cavitation homogenization; Figure 1 shows the effect of such an initiation (Figure 1c), as a result of which a homogeneous emulsion is obtained.

However, the method described in [27], used for the assessment of microflow intensity and resulting dynamic effects, does not ensure a result ready for practical use but only reflects some of the physical processes inherent in the model. To assess the real practical effects, it is necessary to modify the model, as proposed in [27], taking into account the real structure of the liquid.

Thus, cavitation effects can also be used for breaking secondary phases in liquids. To do this, it is necessary to develop a quantitative assessment for these phenomena, which would also be suitable for their management.

3. Determination of a Sufficient Level of Supplied Energy to Intensify Heat and Mass Transfer Processes

There is a fundamental difference in the application of methods to affect a dispersed system to crush the dispersed phase and intensify transfer processes. Dispersion breaking is a one-stage action that can either take place instantly, if the intensification level is high enough, or it will not proceed at all, even with an infinitely long energy impact, if the intensification level is below a critical value. Heat and matter transfer in the system, on the contrary, proceed even at the lowest levels of intensification, and any increase in external action only proportionally increases the speed of these processes. However, transfer processes at a certain energy level can also intensify a mass transfer (breaking processes subject to the conversion of thermal energy into kinetic energy).

If, for example, the problem is solved using a certain mixing device to create an emulsion with a given particle size of the dispersed substance in a small container, then you can stir the liquid mixture as long as you like and spend a huge amount of energy, but the required result cannot be achieved if the speed of the mixer (introduced power W_0) is not high enough. At $\Delta\tau \rightarrow \infty$ energy, consumption is $E = W \times \Delta\tau \rightarrow \infty$. It is enough to slightly increase the number of revolutions to achieve the required power level W_{eff} and under specified conditions, an emulsion with a given particle distribution will be obtained in a very short time $\Delta\tau_{min}$ with low energy consumption $E = W_{eff} \times \Delta\tau_{min}$.

In this example, the result is achieved with the mandatory exceeding of a certain power level W_{eff} in the working volume of the apparatus, whilst W_{eff} and $\Delta\tau_{min}$ are mutually independent parameters.

Thus, with the intensification of mass transfer processes, a maximum power value is also obtained. Therefore, when intensification methods are used to break up dispersions, the specific power level must exceed a certain value \tilde{W}_{eff} to ensure a positive effect of the operation. To obtain the required effect with minimal energy consumption, it is necessary to provide a specified power level ($W \geq \tilde{W}_{eff}$) for a short time ($\Delta\tau \rightarrow \Delta\tau_{min}$) or, in other words, convert the input energy into short but powerful impulses.

In this work, within the framework of the model of cavitation bubble growth, the authors studied velocity fields and pressures in the liquid phase (in emulsion) at the final stage of destruction (explosion) of the cavitation cluster, i.e., at the moment of transformation of the liquid thermal energy into the kinetic energy of motion at the vapor cluster boundary. These processes take place in zones of low surface tension—at the interface between emulsion phases (Figure 3). When the vapor cavity expands, the pressure decreases and, accordingly, the vapor temperature. Compression is accompanied by an increase in temperature and pressure as well as the corresponding phase transitions. These processes are considered by the authors to be an “internal” task, well addressed in previously published works (e.g., [26,27]). An abrupt expansion of the vapor region boundary causes a dynamic effect on the neighboring droplets and, as a result, they can split into smaller (thermodynamically stable) clusters if the condition $W \geq \tilde{W}_{eff}$ is met. The combined effect of these phenomena and the external effects, described in Sections 1 and 2, provide a significant dynamic effect that can be used practically in homogenization technologies.

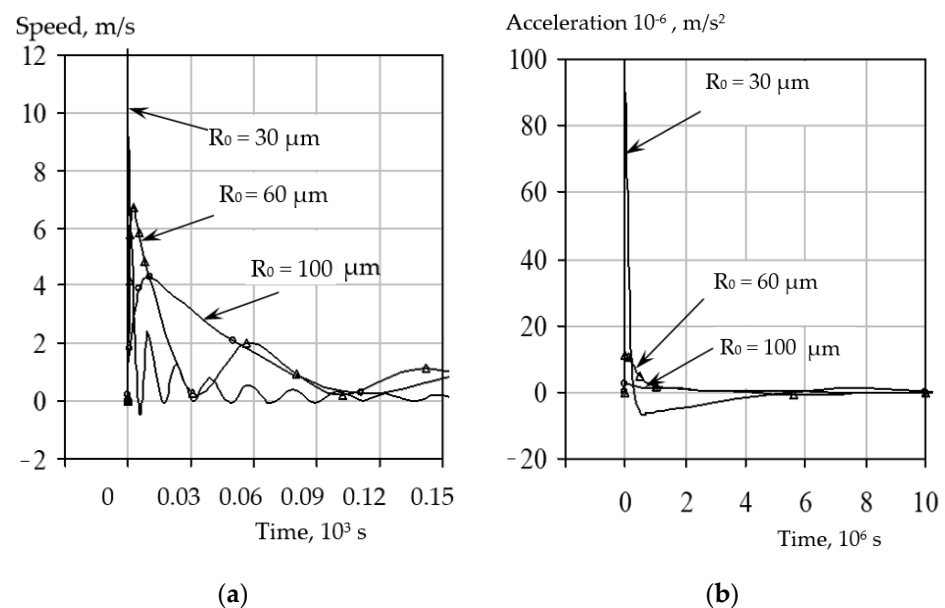


Figure 3. The rate (a) and acceleration (b) changes of the liquid–vapor interface for different initial droplet radii.

The mathematical models, presented in the works cited above, enable qualitative assessment of the described phenomena; however, they cannot be used to determine the effective power in homogenization technologies and to predict the effect when such a power is introduced into the emulsion.

4. An Estimation Procedure for Dynamic Effects in a Cluster during the Liquid Boiling Estimation of the Energy Input Level

We first demonstrate how to estimate the effects that can be achieved when energy is input into the emulsion volume, e.g., by preheating and rapid pressure release, for a single low-boiling liquid droplet.

Calculations have been shown in Figure 3, using the mathematical model given in [27], taking into account the modified Equation (1) to determine the acceleration of the vapor–liquid interface and the conditions below. The superheating temperature of the primary emulsion (Figure 1) is 180 °C, for droplet sizes of the dispersed phase shown in Figure 2.

The resulting acceleration, taking into account (1), is calculated as follows:

$$g(x, \tau) = \frac{dv}{d\tau}; \quad (2)$$

$$g(x, \tau) = \sum_{i=0}^n \left[p_{int} - p_{ext} + 1.5(p_{int} - p_{ext})^2 k_{\beta} - 1.5\rho v^2 \right] \frac{(x_i - x)R_i}{\rho \times d^3} \quad (3)$$

where x_i are the initial coordinates of droplet centers; $d_i = |x_i - x|$ is the radius vector; x is a coordinate of the acceleration calculation point; v is the oil–vapor interface motion rate for the i -th droplet; and R_i is the radius of the oil–vapor interface of the i -th droplet. The higher the acceleration of the phase interface, the higher the force that occurs when water starts boiling.

The graphs show that the smaller the initial droplet radius is, the more intensively the vapor phase grows, i.e., the interface rate and acceleration are higher. Therefore, in real emulsions where dispersed particles of different diameters are present, remote from each other at different distances, the dynamic effects during boiling of the thermolabile emulsion part (water in our example) will have different dynamics of cavitation effects. In this case, the idealized picture of dynamic effects shown in Figure 2 and, accordingly, their assessment methods, cannot be applied. At different droplet radii, both joint maximums (minimums) of the rate (acceleration) and significant differences in these rates (accelerations) can be observed. Considering that rates (accelerations) for different initial radii have different amplitudes and frequencies of variation in time, it can be assumed that at some point in time Kelvin–Helmholtz instability is possible, and, for acceleration, Rayleigh–Taylor instability.

Let us analyze the conditions that can result in a certain instability. By joint analysis of the Bond and Weber criterion [27], as well as their critical values, with the Rayleigh–Plesset Equation, it follows that critical forces, resulting in Rayleigh–Taylor or Kelvin–Helmholtz instability, respectively, are as follows:

$$F_{Bo}^{cr} = 40\pi\sigma R_i \quad (4)$$

$$F_{We}^{cr} = 30\pi\sigma R_i. \quad (5)$$

Comparison of (4) and (5) shows that $F_{Bo}^{cr} = 1.33F_{We}^{cr}$, but these forces are caused by various factors, and they cannot be identified.

Deformation and breaking of both the vapor layer and water droplets in water–oil emulsions can be caused by different directions of both the acceleration vector and velocity vector. Let us assume that deformation, breaking, or displacement will occur only if the acceleration vector has a positive direction and, regardless of it, the rate vector is also positive. If we consider the mutual influence of droplets No. 1 and No. 2 (Figure 4) located

at a distance l , i.e., $x_1 = 0, x_2 = l$, then the acceleration tending to destruct the interface of droplet No. 1 is

$$g(x, \tau)_{p1} = \begin{cases} \sum_{i=1}^2 g(x, \tau)_i; k_1 \geq 0; k_2 \geq 0; \\ -\sum_{i=1}^2 g(x, \tau)_i; k_1 \leq 0; k_2 \leq 0; \\ g(x, \tau)_2; k_1 < 0; k_2 > 0; \\ -g(x, \tau)_2; k_1 > 0; k_2 < 0. \end{cases} \quad (6)$$

where g_i is determined by Equation (7);

$$k_i = [p_{int} - p_{ext} + 1.5(p_{int} - p_{ext})^2 k_\beta - 1.5\rho v^2]; \quad d_i = |x_i - R_i|. \quad (7)$$

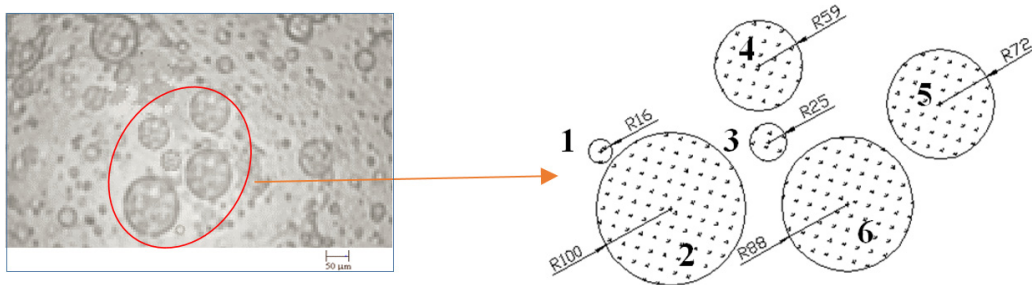


Figure 4. To the calculated model of droplet breakup of the emulsion dispersed phase (characteristic dimensions in microns).

Then, the force caused by the flow acceleration or deceleration is

$$F_{Bo1} = 4\pi\rho_1 g_1 R_1^3 \quad (8)$$

Similarly, it can be written for the rate

$$v_{p1} = \begin{cases} \sum_{i=1}^2 v_{ri}; v_1 \geq 0; v_2 \geq 0; \\ -\sum_{i=1}^2 v_{ri}; v_1 \leq 0, v_2 \leq 0; \\ v_{r2}; v_1 < 0, v_2 > 0; \\ -v_{r2}; v_1 > 0, v_2 < 0. \end{cases} \quad (9)$$

where $v_{ri} = v_i R_i^2 \frac{(x_i - R_i)}{d_i^2}$.

Then the dynamic head force is

$$F_{We1} = 6\pi\rho_1 R_1^2 |v_{p1}| v_{p1} \quad (10)$$

As is known, the capillary force F_σ , regardless of a deformed droplet shape, is always directed so as to restore the spherical shape, i.e., in order for Gibbs free energy to be minimal. Therefore, if a deformed droplet takes the shape of an oblate ellipsoid, the capillary force opposes the external force. If it is deformed into an oblong ellipsoid, then the capillary force coincides in direction with the external force and the droplet will be unstable, while the shape of an oblate ellipsoid can be quasi-stable.

The minimum of a given capillary force is possible. We will assume that this minimum is determined by the Laplace force:

$$F_{\sigma 1} = 8\pi\sigma R_1 \quad (11)$$

Thus, if the dynamic action from the neighboring droplet exceeds the force F_σ , the droplet will be deformed or broken; if the forces are equal, equilibrium will occur; and if $F_\sigma > F_{Bo,We}$, repulsion without deformation will take place.

Differences between $F_{Bo,We}$ and F_σ are equal:

$$\Delta F_{Bo} = F_{Bo} - F_\sigma; \Delta F_{We} = F_{We} - F_\sigma \tag{12}$$

Following the example of the force, resulting from flow acceleration or deceleration, the following conditions can be written: $\Delta F_{Bo} \geq F_{Bo}^{cr}$ —breaking; $\Delta F_{Bo} \geq 0$ —deformation; $\Delta F_{Bo} = 0$ —equilibrium; and $\Delta F_{Bo} < 0$ —displacement.

The system of Equations (7)–(11) for particle No. 2, located at a distance of l from the first particle, will take the following form:

$$g(x, \tau)_{p2} = \begin{cases} -\sum_{i=1}^2 g(x, \tau)_i; k_1 \geq 0; k_2 \geq 0; \\ \sum_{i=1}^2 g(x, \tau)_i; k_1 \leq 0; k_2 \leq 0; \\ g(x, \tau); k_1 < 0; k_2 > 0; \\ -g(x, \tau)_1; k_1 > 0; k_2 < 0; \end{cases} \quad v_{p2} = \begin{cases} -\sum_{i=1}^2 v_{ri}; v_1 \geq 0; v_2 \geq 0; \\ \sum_{i=1}^2 v_{ri}; v_1 \leq 0; v_2 \leq 0; \\ v_{r1}; v_1 < 0; v_2 > 0; \\ -v_{r1}; v_1 > 0; v_2 < 0; \end{cases} \tag{13}$$

where $g(x, \tau)_i = k_i \frac{R_i(x_i-j)}{\rho d_i^3}$; $v_{ri} = v_i R_i^2 \frac{(x_i-j)}{d_i^3}$; and $d_i = |x_i - j|$; $j = l - R_2$.

$$F_{Bo2} = 4\pi\rho_2 g_2 R_2^3 \tag{14}$$

$$F_{We2} = 6\pi\rho_2 R_2^2 |v_{p2}| v_{p2} \tag{15}$$

$$F_{\sigma 2} = 8\pi\sigma R_2 \tag{16}$$

Thus, dynamic effects from neighboring droplets of low-boiling liquid can make them move or break if critical values of the ΔF_{Bo} criterion are reached. If opposing forces are approximately equal, abnormal pressure can be observed, as pointed out by the authors of [16–18]. However, each liquid droplet forms its own local dynamic effect during boiling and therefore the effect of all cluster particles shall be considered.

5. Condition for the Formation of a Superposition of Dynamic Effects and the Resulting Effect

The above considerations are valid for the determination of the resulting force sufficient to break the droplet. However, different situations of cluster development are possible. For instance, if equal forces act on the droplet (No. 3, Figure 4) from all sides, or their resultant does not exceed F_{Bo}^{eff} , in this local vapor volume, it is possible to achieve the anomalous pressure and temperature values mentioned at the beginning of this paper. It is also important to evaluate the influence of the dynamic effect angle of action on the droplet surface.

In this part, breaking processes of dispersed phase droplets, surrounded by other droplets during their boiling up, will be analyzed. We take the emulsion shown in Figures 1, 4 and 5 as a study object. This figure shows that there are “small” droplets between “large” droplets: the former serve as sources of increased dynamic forces at boiling up, thus initiating breaking processes of larger droplets due to significant differences in accelerations and growth rates between them.

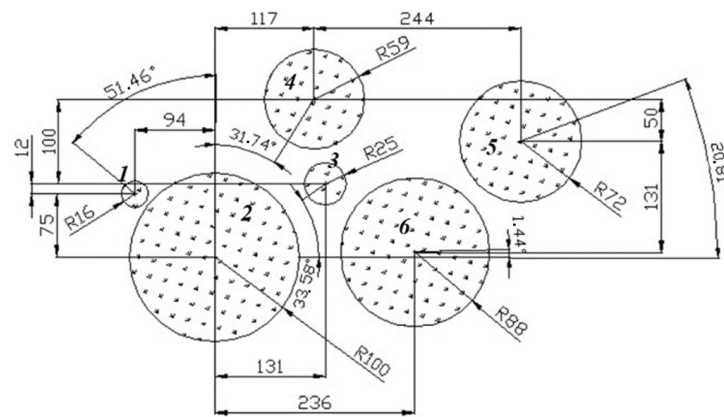


Figure 5. To the calculated model of droplet breakup of the emulsion dispersed phase (characteristic dimensions in microns).

The main types of instability emulsion structure will be considered: Kelvin–Helmholtz instability caused by the difference in rates and Rayleigh–Taylor instability, resulting from the difference in accelerations [27].

When analyzing the possibility of dynamic effects, one can assume that the main role will be played by the forces acting along a normal component to the droplet surface, i.e., forces directed either towards the droplet center or away from it. Thus, the acceleration and rate, acting on the particle surface and directed towards its center (from the center) can be determined from the following Equations:

$$g_{nr}(x_0, y_0) = g(x_0, y_0)k_{nr} \tag{17}$$

$$v_{nr}(x_0, y_0) = v(x_0, y_0)k_{nr} \tag{18}$$

where x_0, y_0 are coordinates of the droplet surface point and k_{nr} is a correction for the normal component.

Correction k_{nr} can be determined by Figure 6:

$$k_{nr} = \cos\gamma = \frac{(x_i - x_0)\sin\beta + (y_i - y_0)\cos\beta}{d_i(x_0, y_0)}. \tag{19}$$

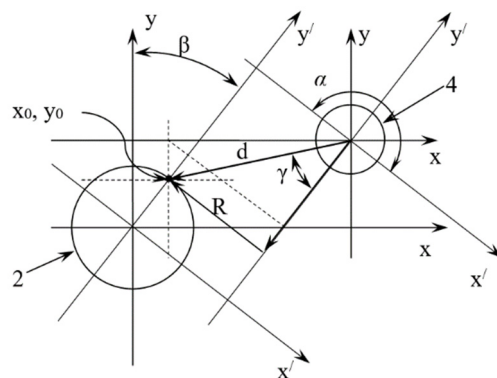


Figure 6. Determination of correction for the normal component and angle α .

The authors assume that acceleration and its resulting force are positive if they are directed towards the center and negative if they are directed away from the center. The rate (acceleration) vector of the liquid–vapor interface of the considered boiling up particle is considered positive if it is directed from the droplet center and negative if it is directed to the center.

The acceleration and velocity of the phase interface movement are determined by the following expressions:

$$g_{nr}(x_0, y_0) = \sum_{i=1}^{N-1} g_i(x_0, y_0)k_{nr_i}; \tag{20}$$

$$v_{nr}(x_0, y_0) = \sum_{i=1}^{N-1} v_i(x_0, y_0)k_{nr_i}, \tag{21}$$

where N is the total number of boiling up dispersed phase droplets.

Taking angle β as a variable (Figure 6), the coordinates of the required opposite points of the particle surface may be represented, where dynamic effects are directed to

$$\begin{aligned} x_{s1} &= x + \Delta x; y_{s1} = y + \Delta y; \\ x_{s2} &= x - \Delta x; y_{s2} = y - \Delta y; \\ \Delta x &= R\sin\beta; \Delta y = R\cos\beta; 0 \leq \beta \leq 180^\circ \end{aligned} \tag{22}$$

where x, y are the particle coordinates; x_{s1}, y_{s1} are coordinates of the droplet side surface ($0 \leq \alpha \leq 180$) from Figure 6; and x_{s2}, y_{s2} are the opposite side coordinates ($180 \leq \alpha \leq 360$).

Then, correction k_{nr} will be determined by the following expressions:

$$k_{nr1} = \frac{(x_i - x_{s1})\sin\beta + (y_i - y_{s1})\cos\beta}{d_i(x_{s1}, y_{s1})}; 0 \leq \beta < 180^\circ; \tag{23}$$

$$k_{nr2} = \frac{(x_i - x_{s2})\sin\beta + (y_i - y_{s2})\cos\beta}{d_i(x_{s2}, y_{s2})}; 180 \leq \beta < 360^\circ. \tag{24}$$

In Equation (24), x_{s2}, y_{s2} are calculated, taking into account $0 \leq \alpha \leq 180$ and k_{nr} at $\beta = \beta + 180$.

Let us consider how the magnitude and direction of the force acting on the surface of the analyzed droplets (Figures 4 and 5) changes. Its value is determined by the acceleration of the vapor cavity boundary when the pressure of the emulsion preheated to $t_0 \approx 105^\circ\text{C}$ decreases, to an atmospheric pressure equal to 10^5 Pa. For all droplets, a vapor layer equal to $1\ \mu\text{m}$ at the initial moment of time is assumed. The acceleration change pattern on the surface of the analyzed droplets shows in which direction and how the resulting force will change. Calculation results for water–oil emulsion according to Equations (20)–(24) are shown in Figures 7 and 8.

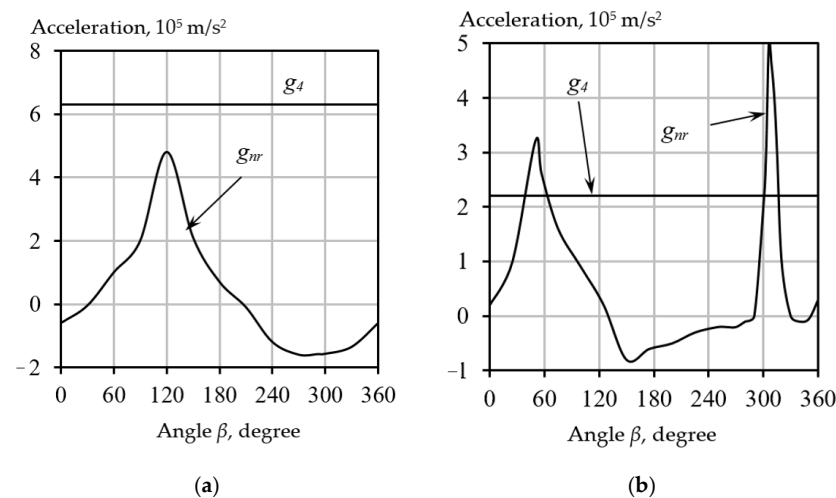


Figure 7. The pattern of acceleration, acting on the surfaces of droplet No. 1 (a) and droplet No. 2 (b) (Figure 4) and the resulting acceleration flow from neighboring boiling up particles (g_{nr}), acceleration of the oil–vapor interface of the particle itself (g_4) at initial pressure relief from 0.125 MPa down to 0.1 MPa.

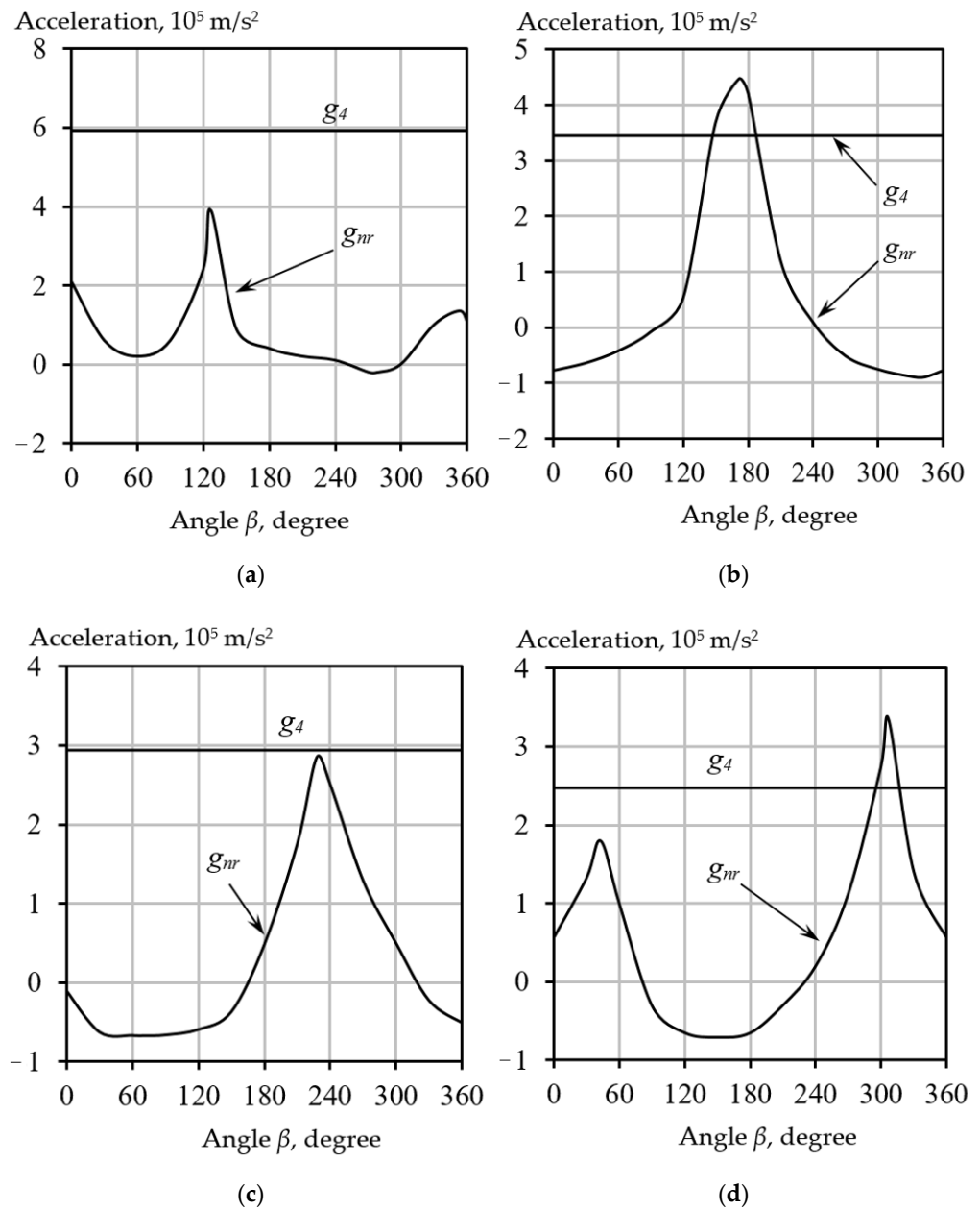


Figure 8. The pattern of acceleration of the interface near the droplet No. 3 (a), No. 4 (b), No. 5 (c), and No. 6 (d) with a decrease in pressure.

The graphs clearly show the relationship between the angles of the droplets and the acceleration values of the interface. Thus, for example, for droplet No. 2 (Figure 4) there are two acceleration maximums at once: angle $\beta \approx 55^\circ$ and $\beta \approx 315^\circ$, corresponding to angles of the nearest neighboring droplet No. 1 and No. 3 arrangement, respectively. As the Figures show, there are always several acceleration (force) maximums.

Let us analyze a boiling emulsion droplet (Figure 9) affected by external forces.

If the maximum of two forces acting on opposite sides is $F' = F'_{s1} + F'_{s2}$ and is at an angle of β_1 to axis y , the maximum force acting on one side is F_{s1} and at an angle of β_2 from axis y ($F' > F$, where $F = F_{s1} + F_{s2}$). The force acting from the droplet side is F , with $F > F'_{s1}$, $F > F'_{s2}$, $F > F_{s2}$, $F < F_{s1}$. Then, the opposing force will be able to mitigate all forces, except F_{s1} . Therefore, only one difference will determine the resulting force, which can cause either deformation or breaking. This force is equal to $\Delta F = F_{s1} - F$.

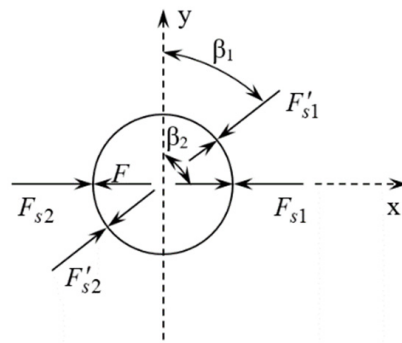


Figure 9. Forces acting on the emulsion droplet (designations are given in the text).

Thus, it is obvious that though the maximum of two opposing forces is at angle β_1 to axis y , the determining maximum is the one caused by force F_{s1} (angle β_2).

This is the distinguishing feature of our method used for the assessment of dynamic effects from those cited in Sections 1 and 2. They basically do not consider the dynamic effects from all cluster droplets and the superposition principle implies the coincidence of the force vector direction, as shown in Figure 2. However, a (secondary) liquid droplet can be deformed or even destroyed when tangential stresses arise inside the cluster. Therefore, the issue of what initiation level should be used to destruct the clusters and what sizes of secondary liquid droplets in the emulsion will be formed under such an action is still to be solved.

For a non-boiling droplet, the force acting on its surface, considering the assumed conditions, is determined by the following acceleration:

$$\Delta g = \begin{cases} g_{s1} + g_{s2}; z > 0; \\ g_{s1}; z < 0; |g_{s1}| > |g_{s2}|; \\ g_{s2}; z < 0; |g_{s2}| > |g_{s1}|, \end{cases} \quad (25)$$

where $z = \frac{g_{s1}}{g_{s2}}$ is a coefficient, considering the direction of the acceleration action; g_{s1} is acceleration, acting on the inclusion surface at $0 \leq \alpha < 180^\circ$; and g_{s2} is acceleration, acting on the inclusion surface at $0 \leq \alpha < 360^\circ$.

The force that can result in breaking of a non-boiling inclusion of a dispersed phase is determined by the maximum acceleration:

$$g_d = \max\{|\Delta g|\}, \quad 0 \leq \alpha < 180^\circ \quad (26)$$

For a boiling up particle, two force maximums are determined due to accelerations, acting on one side of the inclusion:

$$g_{d1} = \max\{|g_{si}|\}, \quad g_{si} = \begin{cases} g_{s1}; |g_{s1}| > |g_{s2}|; \\ g_{s2}; |g_{s1}| < |g_{s2}|; 0 \leq \beta < 180^\circ; \end{cases} \quad (27)$$

and on opposing sides of the inclusion:

$$g_{s1,s2} = \begin{cases} g_{s1} + g_{s2}; z > 0; \\ g_{s1}; z < 0; |g_{s1}| > |g_{s2}|; \\ g_{s2}; z < 0; |g_{s2}| > |g_{s1}|; \end{cases} \quad g_{d2} = \max\{|g_{s1,s2}|\}, \quad 0 \leq \beta < 180^\circ \quad (28)$$

The acceleration maximums g_{d1} and g_{d2} correspond to accelerations g_{s1} and g_{s2} , respectively.

Considering that the droplet dynamic effect cannot destruct the droplet itself, it is possible to write Equations to calculate the acceleration and rates of flow in the cluster

resulting in its destruction. If the resulting acceleration or rate is positive, then they cause instability, and if they are negative, then there is no destabilizing effect. One may write

$$g_{p1} = \begin{cases} g_{s1} - g_4; g_4 \geq 0; g_{s1} \geq 0; \\ -g_{s1}; g_4 > 0; g_{s1} < 0; \\ g_{s1}; g_4 < 0; g_{s1} > 0; \\ g_4 - g_{s1}; g_4 \leq 0; g_{s1} \leq 0, \end{cases} \quad (29)$$

where g_{p1} is the resulting acceleration, acting on one side of the inclusion and g_4 is the acceleration of the oil-vapor inclusion interface.

For the opposite side, one can write an Equation similar to (29) but inserting g_{p2} and g_{s2} instead of g_{p1} and g_{s1} , respectively.

Then, the resulting acceleration will be determined by the following Equation:

$$\Delta g_d = g_{p1} + g_{p2} \quad (30)$$

with the following required conditions:

$$g_{p1} = \begin{cases} 0; z < 0; |g_{s1}| - |g_{s2}| < 0; \\ 0; z > 0 : \begin{cases} g_4 > 0; g_{s1} > 0; g_{s2} > 0; g_{s1} - g_4 < 0; g_{s2} - g_4 > 0; \\ g_4 < 0; g_{s1} < 0; g_{s2} < 0; g_{s1} - g_4 > 0; g_{s2} - g_4 < 0; \end{cases} \end{cases} \quad (31)$$

$$g_{p2} = \begin{cases} 0; z < 0; |g_{s1}| - |g_{s2}| > 0; \\ 0; z > 0 : \begin{cases} g_4 > 0; g_{s1} > 0; g_{s2} > 0; g_{s1} - g_4 > 0; g_{s2} - g_4 < 0; \\ g_4 < 0; g_{s1} < 0; g_{s2} < 0; g_{s1} - g_4 < 0; g_{s2} - g_4 > 0. \end{cases} \end{cases}$$

If the force maximums (accelerations, rates) do not coincide, acting on the opposite sides of the inclusion and on the one side, we consider that the total force that is of greater importance is determined by

$$g_d = \begin{cases} \Delta g_{d1}; \Delta g_{d1} > \Delta g_{d2}; \\ \Delta g_{d2}; \Delta g_{d1} < \Delta g_{d2}, \end{cases} \quad (32)$$

where $g_{d1}, \Delta g_{d2}$ is the resulting acceleration.

Similarly, we can get an Equation for the rate. At the same time,

$$\Delta v = k \sqrt{|v_p|} \quad (33)$$

where $k = \begin{cases} 1, v_p \geq 0; \\ -1, v_p < 0; v_p = v_{p1}|v_{p1}| + v_{p2}|v_{p2}|. \end{cases}$

It is generally accepted that the structural stability of the emulsion is determined by the instability according to the Bond criterion [27]. The force, acting at $0 \leq \alpha < 180^\circ$, is equal to

$$F_{g1} = 4\pi R_4^3 \rho g_{s1} \quad (34)$$

For $180^\circ \leq \alpha < 360^\circ$,

$$F_{g2} = 4\pi R_4^3 \rho g_{s2} \quad (35)$$

The opposing force from the oil-vapor interface of the droplet itself is

$$F_g = 4\pi R_4^3 \rho g_4 \quad (36)$$

The resulting force acting on the droplet is

$$F_{Bo} = 4\pi R_4^3 \rho g_d \quad (37)$$

The critical force, resulting in Bond instability, is

$$F_{Bo}^{eff} = 40\pi\sigma R_4. \tag{38}$$

The force determining a droplet deformation or displacement is

$$\Delta F_{Bo} = F_{Bo} - 8\pi\sigma R_4 \tag{39}$$

For each of the analysed droplets, the calculation is performed either until the condition

$$F_{Bo} \geq F_{Bo}^{eff} \tag{40}$$

is met, or until the mutual meeting of droplets, determined by condition

$$\Delta R_{i,j} \leq 0, \tag{41}$$

where $\Delta R_{i,j} = d_{i,j} - (R_{4i} + R_{4j})$, $d_{i,j} = \sqrt{(x_i - x_j)^2 + (y_i - y_j)^2}$; $i = 1, 2, \dots, N$; $j = i + 1, i + 2, \dots, N$; and i, j are droplet numbers with corresponding coordinates $x_i, y_i; x_j, y_j$.

6. Results and Discussion

The calculation results are presented in Figures 10–12. The performed calculations ($t_0 = 110\text{ }^\circ\text{C}$) showed that only droplets No. 2 and No. 6 will be destroyed at the initial moment of pressure release. This means that the level of the supplied effective power by emulsion superheating to the specified temperature is sufficient to break all emulsion droplets larger than droplet No. 6. To break smaller droplets, the superheat temperature must be increased.

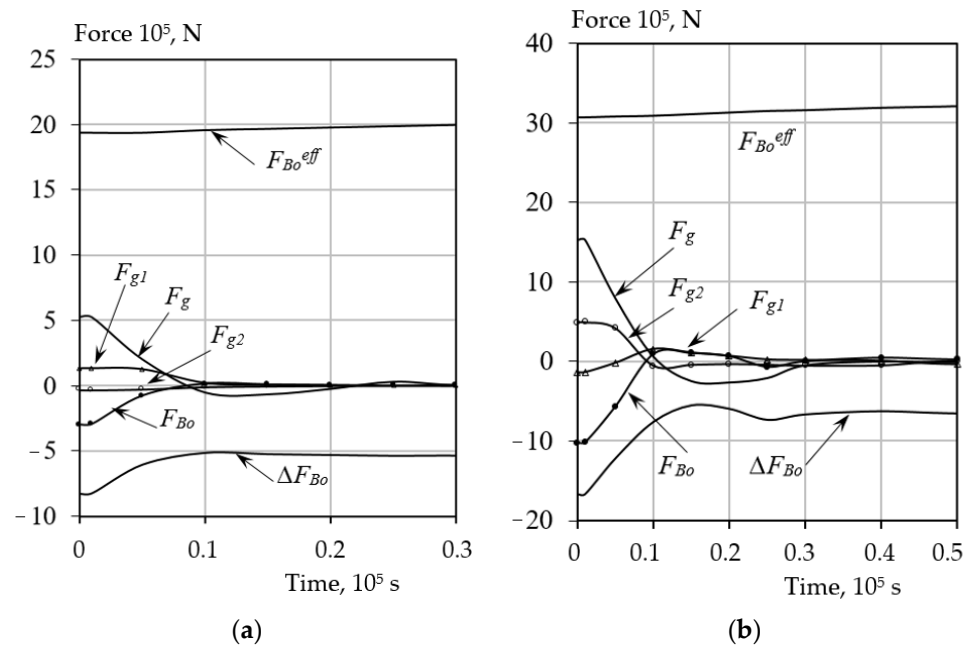


Figure 10. Changes in the forces acting on the surfaces of droplets No. 1 (a) and No. 3 (b) (Figure 4) in time.

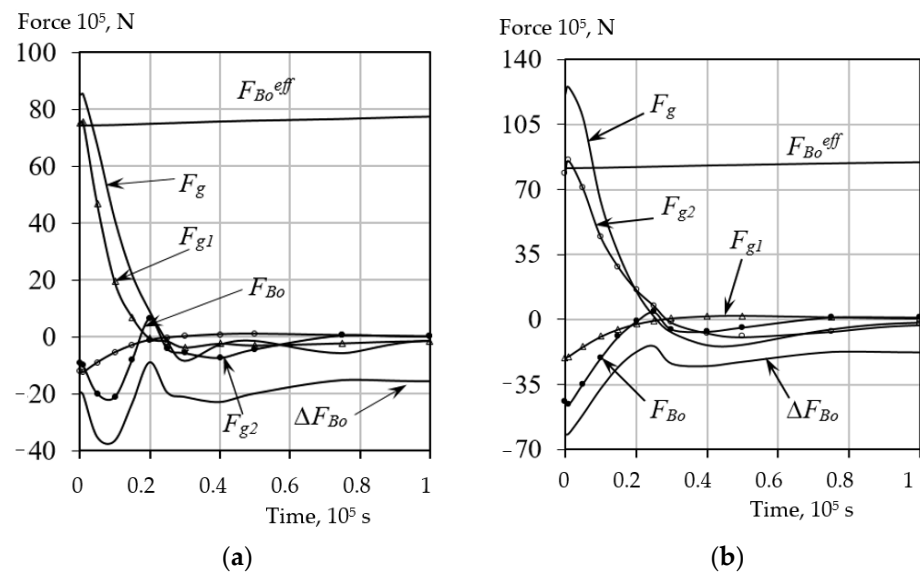


Figure 11. Changes in the forces acting on the surfaces of droplets No. 4 (a) and No. 5 (b) (Figure 4) in time.

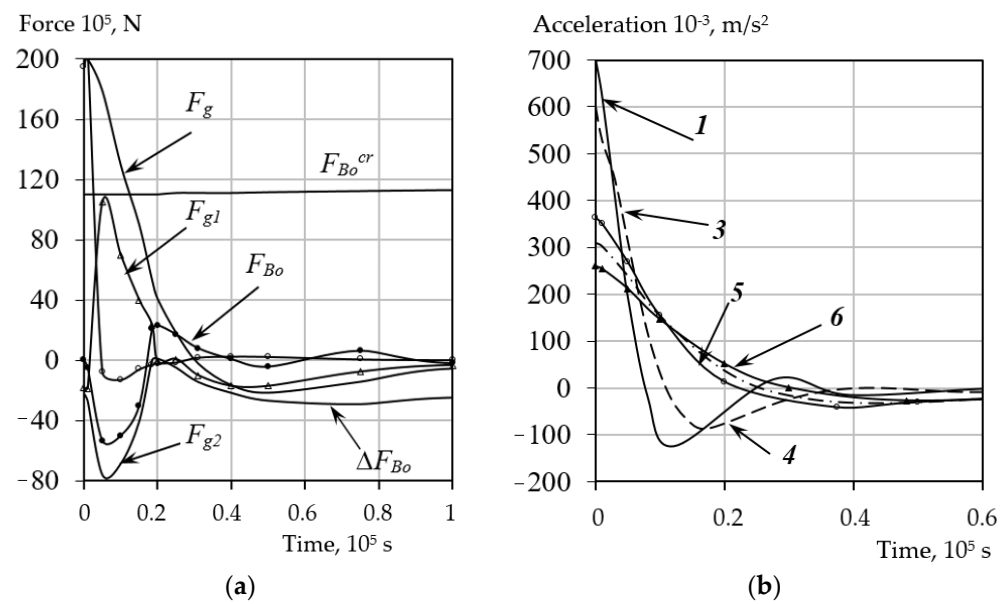


Figure 12. Change in the forces acting on the surface of droplet No. 6 (a) and change of oil–vapor interface acceleration (b) of analysed droplets (Figure 4) in time.

The joint consideration of all the dynamic effects in a cluster makes it possible to determine the force F_{Bo} that can correspond to the level of effective impact on the cluster, being the cause of the dispersed phase breaking. The figures show that for droplets No. 1, 3, 4, and 5 with a positive value of force F_{Bo} , only their mutual displacement is possible, as indicated by a negative sign (at $\tau \approx 2 \cdot 10^{-6}$ s).

To destroy these droplets, it is necessary to increase the supplied energy to the effective one. It can be achieved by raising superheating temperature and pressure (thermal cavitation initiation). The same effect can be obtained by using mixing devices, where local cavitation zones can appear on the blades at certain flow rates.

The calculations performed for overheating temperatures $t_o = 130$ °C and $t_o = 170$ °C demonstrated that, at the moment of instantaneous pressure release, almost all large droplets will be broken, while at $t_o = 110$ °C only two droplets will be broken due to boiling small neighboring particles.

As for the intensification of heat transfer processes, attention should be paid to the effect of heat accumulation by the high-boiling liquid. With a sudden drop in pressure of the superheated emulsion, the low-boiling liquid, e.g., water, evaporates partially or completely, depending on superheating level. The vapor temperature decreases during expansion. At the same time, a high-boiling fraction of the emulsion transfers the stored energy to vapor and water. Thus, we get an additional impulse of energy from the high-boiling phase. Temperature T can be determined if we know the total liquid volume, the proportion of emulsion phases, and the size and number of the low-boiling fraction droplets. For example, if emulsion volume V is known to contain 30% water and 70% fuel oil, the number of water particles is

$$N = \frac{0.75V}{\pi R^3} \quad (42)$$

where R is the water droplet radius.

Then variation of fuel oil temperature in time is

$$\frac{dE}{d\tau} = 4\pi R^2 N \frac{Q}{cm} \quad (43)$$

where m , c are fuel oil mass and heat capacity and Q is the fuel oil heat flow to be determined by the methods proposed in [38].

For example, for an emulsion volume $V = 0.3 \times 10^{-3} \text{ m}^3$ with 30% water and an average droplet size of $R = 100 \text{ }\mu\text{m}$, the number of these droplets is approximately $N = 1.8 \times 10^7$. The calculation results are shown in Figure 13.

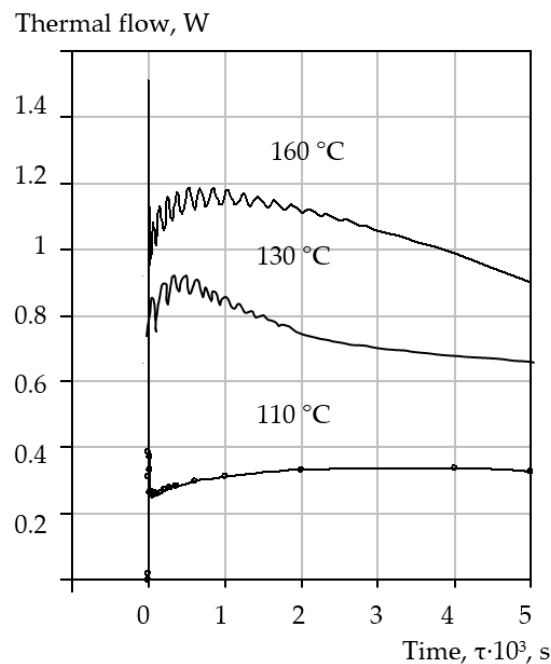


Figure 13. Local effect of the change in heat flow from high-boiling emulsion fraction in time.

Figure 13 shows that heat flow for the considered example is approximately 1 W per particle. As the number of particles is $N = 1.8 \times 10^7$, we can conclude that the heat exchange process is high-intensive, which would allow more heat to be removed or supplied in standard heat exchangers. Clearly, such effects can only be achieved with certain structural parameters of the emulsion, which can easily be determined using this method.

7. Conclusions

The study of hydrodynamic cavitation phenomena in relation to their targeted and effective use for technological process stimulation and intensification requires a unified approach that equally considers the hydrodynamic and heat and mass transfer aspects of these phenomena. Within the framework of this concept, we proposed a new method to assess dynamic effects. This method is based on an advanced model, considering all determining factors and an accurate representation of thermophysical system parameters, which relevantly describes the behavior of bubbles and bubble ensembles in the boiling and cavitation processes. The study results show that the cavitation effect analysis will involve liquid transition around the bubble, as well as the vapor–gas mixture in the bubble itself, into the supercritical fluid state. To assess the spatial and time boundaries of the supercritical region and to analyze the effects of a spherical hydraulic hammer in local zones of the cavitation cloud, the liquid compressibility will be considered in modeling.

The method for assessment of thermal cavitation effects was validated using superheated emulsion boiling with a sharp decrease in pressure. At the interface of the liquid phases (in the region of low surface tension, water in our example), vapor fluids are formed with rapidly increasing volumes. Thus, conditions for dynamic effects on the emulsion structure are provided. This method of local supply of energy W_{eff} makes it possible to implement the task of heat and mass transfer or homogenization process intensification. Moreover, the effect level is easy to regulate using the temperature and pressure of the emulsion preheating. The same phenomena can be used in jet devices.

This study should be considered as the initial stage of substantiation of rational designs and optimal operating modes of cavitating devices as a solution for solving various technological problems.

Author Contributions: Conceptualization, A.M.P. and H.K.; methodology, A.M.P.; validation, A.M.P. and H.K.; data curation, A.M.P.; writing—original draft preparation, A.M.P.; writing—review and editing, A.M.P.; visualization, A.M.P. All authors have read and agreed to the published version of the manuscript.

Funding: This research received no external funding.

Institutional Review Board Statement: Not applicable.

Informed Consent Statement: Not applicable.

Data Availability Statement: Not applicable.

Conflicts of Interest: The authors declare no conflict of interest.

References

1. Fuster, D.; Dopazo, C.; Hauke, G. Liquid compressibility effects during the collapse of a single cavitating bubble. *J. Acoust. Soc. Am.* **2011**, *129*, 122–131. [CrossRef] [PubMed]
2. Albanese, L.; Ciriminna, R.; Meneguzzo, F.; Pagliaro, M. Energy efficient inactivation of *Saccharomyces cerevisiae* via controlled hydrodynamic cavitation. *Energy Sci. Eng.* **2015**, *3*, 221–238. [CrossRef]
3. Zevnik, J.; Dular, M. Cavitation bubble interaction with a rigid spherical particle on a microscale. *Ultrason. Sonochem.* **2020**, *69*, 105252. [CrossRef]
4. Gogate, P.R.; Pandit, A.B. Engineering design methods for cavitation reactors II: Hydrodynamic cavitation. *AIChE J.* **2000**, *46*, 1641–1649. [CrossRef]
5. Kanthale, P.M.; Gogate, P.R.; Pandit, A.B. Dynamics of gravitational bubbles and design of a hydrodynamic cavitation reactor. *Ultrason. Sonochem.* **2005**, *12*, 441–452. [CrossRef] [PubMed]
6. Li, J.; Cheng, P. Bubble cavitation in a microchannel. *Int. J. Heat Mass Transf.* **2004**, *47*, 2689–2698. [CrossRef]
7. Melikhov, V.; Yakush, S.; Le, T. Evaluation of energy and impulse generated by superheated steam bubble collapse in subcooled water. *Nucl. Eng. Des.* **2020**, *366*, 110753. [CrossRef]
8. Roesle, M.; Kulacki, F. An experimental study of boiling in dilute emulsions, part A: Heat transfer. *Int. J. Heat Mass Transf.* **2012**, *55*, 2160–2165. [CrossRef]
9. Podnar, A.; Dular, M.; Sirok, B.; Hocevar, M. Experimental Analysis of Cavitation Phenomena on Kaplan Turbine Blades Using Flow Visualization. *J. Fluids Eng.* **2019**, *141*, 071101. [CrossRef]

10. Chernin, L.; Val, D.V. Probabilistic prediction of cavitation on rotor blades of tidal stream turbines. *Renew. Energy* **2017**, *113*, 688–696. [CrossRef]
11. Pham-Thanh, N.; Van Tho, H.; Yum, Y.J. Evaluation of cavitation erosion of a propeller blade surface made of composite materials. *J. Mech. Sci. Technol.* **2015**, *29*, 1629–1636. [CrossRef]
12. Dietzel, D.; Hitz, T.; Munz, C.-D.; Kronenburg, A. Expansion Rates of Bubble Clusters in Superheated Liquids. In Proceedings of the Germany ILASS–Europe 2017, 28th Conference on Liquid Atomization and Spray Systems, Valencia, Spain, 6–8 September 2017. [CrossRef]
13. Warjito, W.; Budiarto, B.; Syahputra, M.F.; Nasution, S.B. The Effect of Blades Gap on Propeller Openflume Picohydro Turbine Performance. *Int. J. Fluid Mach. Syst.* **2021**, *14*, 122–131. [CrossRef]
14. Tran, B.N.; Jeong, H.; Kim, J.-H.; Park, J.-S.; Yang, C. Effects of Tip Clearance Size on Energy Performance and Pressure Fluctuation of a Tidal Propeller Turbine. *Energies* **2020**, *13*, 4055. [CrossRef]
15. Adhikari, R.C.; Vaz, J.; Wood, D. Cavitation Inception in Crossflow Hydro Turbines. *Energies* **2016**, *9*, 237. [CrossRef]
16. Janssen, D.; Kulacki, F. Flow boiling of dilute emulsions. *Int. J. Heat Mass Transf.* **2017**, *115*, 1000–1007. [CrossRef]
17. Ganesan, B.; Martini, S.; Solorio, J.; Walsh, M.K. Determining the Effects of High Intensity Ultrasound on the Reduction of Microbes in Milk and Orange Juice Using Response Surface Methodology. *Int. J. Food Sci.* **2015**, *2015*, 1–7. [CrossRef]
18. Chandrapala, J.; Oliver, C.; Kentish, S.; Ashokkumar, M. Ultrasonics in food processing – Food quality assurance and food safety. *Trends Food Sci. Technol.* **2012**, *26*, 88–98. [CrossRef]
19. Sun, X.; Chen, S.; Liu, J.; Zhao, S.; Yoon, J.Y. Hydrodynamic Cavitation: A Promising Technology for Industrial-Scale Synthesis of Nanomaterials. *Front. Chem.* **2020**, *8*, 259. [CrossRef]
20. Prajapat, A.L.; Gogate, P.R. Depolymerization of carboxymethyl cellulose using hydrodynamic cavitation combined with ultraviolet irradiation and potassium persulfate. *Ultrason. Sonochem.* **2019**, *51*, 258–263. [CrossRef] [PubMed]
21. Merzkirch, W.; Rockwell, D.; Tropea, C. *Orifice Plates and Venturi Tubes*; Springer International Publishing: Cham, Switzerland; Heidelberg, Germany; New York, NY, USA; Dordrecht, The Netherlands; London, UK, 2015. Available online: <https://link.springer.com/content/pdf/bfm%3A978-3-319-16880-7%2F1.pdf> (accessed on 17 July 2015).
22. Nigmatulin, R.I.; Taleyarkhan, R.P.; Lahey, R.T. Evidence for nuclear emissions during acoustic cavitation revisited. *Proc. Inst. Mech. Eng. Part A J. Power Energy* **2004**, *218*, 345–364. [CrossRef]
23. Sun, X.; Wang, Z.; Xuan, X.; Ji, L.; Li, X.; Tao, Y.; Boczkaj, G.; Zhao, S.; Yoon, J.Y.; Chen, S. Disinfection characteristics of an advanced rotational hydrodynamic cavitation reactor in pilot scale. *Ultrason. Sonochem.* **2021**, *73*, 105543. [CrossRef] [PubMed]
24. Albanese, L.; Baronti, S.; Liguori, F.; Meneguzzo, F.; Barbaro, P.; Vaccari, F.P. Hydrodynamic cavitation as an energy efficient process to increase biochar surface area and porosity: A case study. *J. Clean. Prod.* **2019**, *210*, 159–169. [CrossRef]
25. Badve, M.; Alpar, T.; Pandit, A.B.; Gogate, P.R.; Csoka, L. Modeling the shear rate and pressure drop in a hydrodynamic cavitation reactor with experimental validation based on KI decomposition studies. *Ultrason. Sonochem.* **2015**, *22*, 272–277. [CrossRef]
26. Pavlenko, A. Dispersed phase breakup in boiling of emulsion. *Heat Transf. Res.* **2018**, *49*, 633–641. [CrossRef]
27. Pavlenko, A. Energy conversion in heat and mass transfer processes in boiling emulsions. *Therm. Sci. Eng. Prog.* **2019**, *15*, 1–8. [CrossRef]
28. Gasanov, B.M.; Bulanov, N.V. Effect of the droplet size of an emulsion dispersion phase in nucleate boiling and emulsion boiling crisis. *Int. J. Heat Mass Transf.* **2015**, *88*, 256–260. [CrossRef]
29. Roesle, M.L.; Lunde, D.L.; Kulacki, F.A. Boiling Heat Transfer to Dilute Emulsions from a Vertical Heated Strip. *J. Heat Transf.* **2015**, *137*, 8. [CrossRef]
30. Rozentsvaig, A.K.; Strashinskii, C.S. The Growth of Vapor Bubbles in the Volume of Superheated Drops, Dispersed in High-Boiling Liquid. *Appl. Math. Sci.* **2014**, *8*, 7519–7528. [CrossRef]
31. Rozentsvaig, A.K.; Strashinskii, C.S. Regimes of Heat Transfer during Boiling Emulsions with Low-Temperature Dispersed Phase. *Appl. Math. Sci.* **2015**, *9*, 5593–5601. [CrossRef]
32. Califano, V.; Calabria, R.; Massoli, P. Experimental evaluation of the effect of emulsion stability on micro-explosion phenomena for water-in-oil emulsions. *Fuel* **2015**, *117*, 87–94. [CrossRef]
33. Mura, E.; Massoli, P.; Josset, C.; Loubar, K.; Bellettre, J. Study of the micro-explosion temperature of water in oil emulsion droplets during the Leidenfrost effect. *Exp. Therm. Fluid Sci.* **2012**, *43*, 63–70. [CrossRef]
34. Aktershev, S.P.; Ovchinnikov, V.V. Modelling of boiling up of a metastable liquid with appearance of the evaporation fronts. *Mod. Sci. Res. Ideas Results Technol.* **2013**, *1*, 77–82.
35. Shinjo, J.; Xia, J.; Megaritis, A.; Ganippa, L.C.; Cracknell, R.F. Modeling temperature distribution inside an emulsion fuel droplet under convective heating: A key to predicting microexplosion and puffing. *At. Sprays* **2016**, *26*, 551–583. [CrossRef]
36. García, M.C.; Gucker, S.N.; Foster, J.E. Understanding the plasma and power characteristics of a self-generated steam bubble discharge. *J. Phys. D Appl. Phys.* **2015**, *48*, 355203. [CrossRef]
37. Feng, J.; Muradoglu, M.; Kim, H.; Ault, J.T.; Stone, H.A. Dynamics of a bubble bouncing at a liquid/liquid/gas interface. *J. Fluid Mech.* **2016**, *807*, 324–352. [CrossRef]
38. Pavlenko, A.M. Change of emulsion structure during heating and boiling. *Int. J. Energy Clean Environ.* **2019**, *20*, 291–302. [CrossRef]

Review

Two-Phase Volumetric Expanders: A Review of the State-of-the-Art

Xander van Heule ¹, Michel De Paepe ^{1,2,*} and Steven Lecompte ^{1,2}

¹ Department of Electromechanical, Systems and Metal Engineering, Ghent University, Sint-Pietersnieuwstraat 41, 9000 Ghent, Belgium; xander.vanheule@ugent.be (X.v.H.); steven.lecompte@ugent.be (S.L.)

² FlandersMake, Gaston Geenslaan 8, 3001 Leuven, Belgium

* Correspondence: michel.depaepe@ugent.be

Abstract: Two-phase expansion is the process where a fluid undergoes a pressure drop through or in the liquid–vapor dome. This operation was historically avoided. However, currently it is studied for a multitude of processes. Due to the volume increase in volumetric expanders, a pressure drop occurs in the fluid resulting in flashing phenomena occurring. These phenomena have been studied before in other processes such as two-phase flows or static flash. However, this has not been extensively studied in volumetric expanders and is mostly neglected. Even if data has shown this is not always neglectable depending on the expander type. The thermal non-equilibrium occurring can be modeled on different principles of flashing flows, such as the mixture model, boiling delay model, and homogeneous relaxation model. The main application area in current literature for volumetric two-phase expansion machines, is in low-temperature two-phase heat-to-power cycles. These cycles have shown benefit over classic options if expanders are available with efficiencies in the range of at least 75%. Experimental investigation of expanders in two-phase operation, though lacking in quantity, has shown that this is an achievable goal. However, the know-how to accomplish this requires more studies, both experimentally and in modeling techniques for the different phenomena occurring within these expanders. The present work provides a brief but comprehensive overview of the available experimental data, applicable flashing modeling techniques, and available models of volumetric two-phase expanders.

Keywords: two-phase; volumetric expander; review

Citation: van Heule, X.; De Paepe, M.; Lecompte, S. Two-Phase Volumetric Expanders: A Review of the State-of-the-Art. *Energies* **2022**, *15*, 4991. <https://doi.org/10.3390/en15144991>

Academic Editors: Jan Danielewicz and Krzysztof Rajski

Received: 31 May 2022

Accepted: 30 June 2022

Published: 8 July 2022

Publisher's Note: MDPI stays neutral with regard to jurisdictional claims in published maps and institutional affiliations.



Copyright: © 2022 by the authors. Licensee MDPI, Basel, Switzerland. This article is an open access article distributed under the terms and conditions of the Creative Commons Attribution (CC BY) license (<https://creativecommons.org/licenses/by/4.0/>).

1. Introduction

Expansion processes generating work from two-phase liquid–vapor flows are typically avoided. Common issues ranged from condensation in steam engines [1] to liquid impact erosion in turbomachinery [2]. Yet, this review handles exactly the particular topic of utilizing two-phase fluid expansion, its possibilities, and the current status of experimental knowledge.

1.1. Two-Phase Expander Applications

Applications for two-phase expanders are where a single working fluid two-phase liquid–vapor mixture undergoes a pressure drop. Such as in liquid injection cycles [3] or instead of a throttling valve in a heat pump cycle [4–6]. This throttling valve could also be substituted by a two-phase ejector, which will not be included within this review as it was elaborately discussed by [7,8].

Another important application of two-phase expanders is found in the scope of low-grade heat-to-power conversion. These low-grade heat sources range from geothermal or solar heat to the residual heat of industrial processes. The recuperation of low-grade heat-to-power is commercially available technology through the use of the Organic Rankine Cycle (ORC). The ORC can be a basic Rankine cycle or one of the many variations with,

for example, multiple pressure levels, the addition of a recuperator or, among others, can include two-phase expansion. Ref. [9] recommends the investigation of two-phase expanders to increase the performance of heat-to-power cycles. However, this technology is not commercially available. Based on the modeling work of [10,11] the authors concluded that optimized two-phase operation of expanders can improve the system power by nearly 50% in specific operating conditions.

An ORC with two-phase expansion occurs when saturated liquid enters the expander of the ORC architecture, the cycle is called a trilateral cycle (TLC) or a trilateral flash cycle (TFC). The inlet state of the expander can also be in the two-phase region. If this is the case, then the cycle is referred to as a partial evaporation organic Rankine cycle (PEORC) or a wet organic Rankine cycle (WORC). A schematic diagram and a temperature-entropy diagram of the TLC are represented in Figure 1. It consists of four parts: a condenser, an evaporator, a pump, and an expander. The difference with a basic ORC is that the evaporator no longer evaporates the working fluid in the TLC. Instead, the fluid entering the expander is in a saturated liquid state and during the expansion process, the fluid is in the two-phase region as can be seen by point 3 on the T-s diagram in Figure 1b. There is thus a need for an efficient expander capable of two-phase expansion. The heat exchanger that adds heat to the working fluid no longer evaporates the fluid, yet it is still referred to as the evaporator in literature.

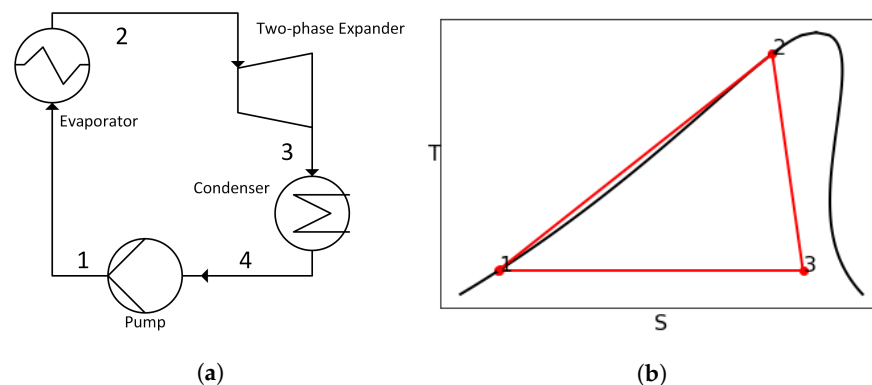


Figure 1. Trilateral Cycle (TLC) [12]. (a) Schematic diagram (b) T-s diagram.

It was concluded by [13] that two-phase expansion devices should have an isentropic efficiency of at least 75% to be interesting for power generation applications, which is a realistic design goal. The main difficulty is the lack of practical and efficient two-phase expanders capable of receiving a liquid or a single working fluid two-phase liquid–vapor mixture and the absence of the methods to design these.

Ref. [12] showed that the TLC obtains a larger net power output, thermal efficiency, and exergy efficiency compared to the basic ORC with an increase of 37%. Yet, for evaporation temperatures greater than 135 °C the TLC does perform worse from a financial aspect due to the extra requirements of the heat exchangers, although it does perform better thermodynamically. Ref. [14] also compared the exergy efficiency of power production of the TLC with the ORC. This was defined by the authors as the ratio of the produced power to the incoming exergy flow of the heat carrier which is also referred to as the second law efficiency. They conclude that the exergy efficiency of power production for the TLC is between 14% to 29% higher than the ORC. Yet, because the authors used water as the working fluid, the volume flow rate of the TLC was higher compared to the ORC by a factor of 2.8 or more. This is expected to drop when the working fluid is changed to current refrigerants. The TLC has been practically tested with a small-scale power plant [15] which resulted in 20–40% more power production compared to a conventional ORC. This power plant applied the VPT turbine mentioned before.

As mentioned earlier, another option is to partially evaporate the working fluid up to an optimal vapor quality. This was investigated by [16] where the PEORC was compared to the TLC. The authors also compared the PEORC to the subcritical ORC and

the transcritical ORC [17]. The authors show that the PEORC can improve the net power output in comparison to the TLC and that it has a greater second law efficiency than both the subcritical and transcritical ORCs.

1.2. Principles of Flashing

During expansion of a two-phase fluid, flashing will occur. Flashing [18,19] is a physical phenomenon in liquids. It represents a change from liquid to vapor as a result of a sudden decrease in the pressure below the saturation pressure. The heat cannot be contained in the liquid as sensible heat and a metastable superheated liquid occurs [20]. A rapid transfer of heat and mass occurs while the fluid returns to a stable thermodynamic state [21]. This metastable liquid also has a maximum value. This limit is known as the spinodal curve which separates the metastable region from the unstable region in equations of state (EOS) [22,23]. The process of flashing is found and studied in many places such as static flash, boiling liquid expanding vapor explosions (BLEVE) and safety valves, flashing jets, pressurized water reactors, and many more [24–26]. However, the phenomena known through these areas of study have not been directly applied to the case of volumetric two-phase expanders. That is where this review will focus hereafter.

1.3. Expander Types

When considering what type of expander is best suited for an application in single-phase operation, the similarity parameters, specific speed, and specific diameter are often used as defined, respectively, in Equations (1) and (2).

$$N_s = N \cdot \sqrt{\frac{\dot{V}}{(\Delta h)^{3/2}}} \quad (1)$$

$$D_s = \frac{D \cdot (\Delta h)^{1/4}}{\sqrt{\dot{V}}} \quad (2)$$

where N is the rotational speed of the expansion machine, \dot{V} is the volumetric flow rate, D is the characteristic diameter and Δh is the enthalpy difference across the machine. These two numbers can be calculated readily from the design requirements and, by presenting the different types of expansion machines on the same diagram, the most feasible turbine type can be chosen [27]. Balje diagrams can be created for every expander type [28,29] and later employed in design.

Yet, in the event where two-phase fluid is expected, it is not as straightforward to choose turbomachine expanders because the blades could be at risk of impact erosion. However, a plethora of applications where two-phase expansion can be used is suited well to volumetric machines.

1.4. Volumetric Expander Types for Two-Phase Expansion

Volumetric expanders are preferred for the low-temperature heat-to-power application as they have low rotational speeds with low flow rates. This matches well with the current requirements of ORCs. Furthermore, they can cope with relatively high-pressure ratios compared to single-stage turbo expanders and can also inherently handle liquid–vapor mixtures. Both of these traits are beneficial to the TLC and PEORC.

Each type of volumetric expander has some benefits and drawbacks, these are discussed by [30,31]. Currently, only two types are primarily considered for the use of two-phase expanders. These are the screw or Lysholm expander and the piston or reciprocating expander. The most promising type for two-phase expansion is the Lysholm expander. The main benefit of this type is that both phases can be considered to be mixed well. Giving acceptable results when thermodynamic equilibrium is assumed [32–34]. This implies that a simple homogeneous mixture model in thermodynamic equilibrium could be considered. The different modeling approaches for the fluid state are further discussed in Section 2.

Other types of screw expanders, such as the single screw, were deemed too mechanically complex [35]. However, even these are appearing as a possible alternative [36,37].

The reciprocating expander is interesting for applications with higher pressure ratios and lower velocities. The main benefit of this expander type is the built-in volume ratio (BVR). The reciprocating expander is the type that has the largest BVR of all volumetric expander types. This trait is in accordance with the requirements for two-phase expanders which require large volume ratios to accompany the flashing process. A drawback of using this type of expander is the modeling of the expansion process. Assuming thermodynamic equilibrium does not give acceptable results with actual experimental results [38] as it did for Lysholm expanders. It requires a better understanding of the flashing process taking place during expansion.

In volumetric expanders, this sudden depressurization is a result of the increasing working volume. Due to the shape of a reciprocating expander, the flashing process could be compared to static flash experiments [19]. Static flash stands for the case where the fluid remains static in the horizontal direction during the flashing process [39]. These processes have been researched before. For example, as occurring in the desalination process [40] of drinking water production from seawater or as a process taking place in safety valves [41]. The phenomena and data found in literature about static flashing could [20] prove to also be useful in describing the phenomena taking place in volumetric expanders, and most notably reciprocating expanders. To the author's knowledge, other volumetric expander types, such as scroll and vane expanders, have not been found in two-phase expansion research.

1.5. Positioning of This Review

Implementing two-phase expansion technology requires methods to accurately predict the expansion process in various thermodynamic cycles and expander types. Only with this fundamental data, efficient two-phase expanders can be designed. In the following, the review will first shortly describe the possible techniques to model the working fluids' thermodynamic state during the expansion process. Afterward, a summary of the available experimental data is given. Lastly, the specific models applicable to a volumetric expander are also detailed. The gaps in current literature are highlighted and recommendations for future work are given.

2. Methods for Modeling Two-Phase Expansion

There is a multitude of modeling techniques and codes developed for the simulation of flashing. They are often subdivided based on the made assumptions. The assumptions that can be made are that the phases are in thermal equilibrium and/or that they are in mechanical equilibrium. In the context of volumetric expanders, the mechanical equilibrium is assumed as both phases occupy the same expansion chamber or chambers. If thermal equilibrium is assumed as well, then the homogeneous equilibrium model (HEM) can be applied, in the other case, the homogeneous relaxation model (HRM), boiling delay model, or mixture model is used. These techniques will be elaborated upon in the following sections. For other modeling techniques where mechanical equilibrium is not assumed (i.e., in continuous flows), the authors refer to [26] for a review on flashing flow modeling.

2.1. Homogeneous Equilibrium Model

As stated previously, in the homogeneous equilibrium model it is assumed that there is thermal equilibrium between the phases. This implies that both phases share the same saturation temperature:

$$T_g = T_l \quad (3)$$

In which the subscript g stands for the vapor or gas phase and the subscript l for the liquid phase. From this, it follows that the two-phase mixture behaves such as a pseudo single-phase in which the thermodynamic properties can be expressed commonly as in Equation (4). In which x is the mass based vapor quality and y can be any fluid property [26].

$$y = x \cdot y_g + (1 - x) \cdot y_l \quad (4)$$

The HEM consists of three equations: the mass, momentum, and energy conservation equations [42] where the fluid is modeled as a homogeneous mixture of gas and liquid.

Due to its simplicity, it was often used in the past and chosen as the basis for many system codes. However, this approach induces large errors when the equilibrium assumptions do not apply, such as processes in very small time intervals. This is, for example, the case for the reciprocating expander. Even though the expansion process in screw expanders has a similar time constant compared to reciprocating expanders, the HEM can still be used to describe this type of volumetric expander as was shown by [43]. It is speculated that this approach is valid due to the better mixing of the phases within the chambers of a screw expander in comparison to reciprocating ones. Ref. [34] modeled a screw expander with liquid injection as well. The authors also found that assuming thermal equilibrium gives good results compared to the experiments. Ref. [44] used the HEM assumptions within a commercial software environment to model the screw expander within a TLC cycle. This model was studied by [45], in which the authors concluded that the intake phenomena have a large impact on the overall performance of the machine. The constructed model showed that isentropic efficiencies can go up to 83.1%, depending on the operation conditions.

Lastly, comprehensive research on screw expander TLC is found in the works of [33,46]. Due to developments in screw expander technology, they conclusively showed that with the right choice of working fluid a two-phase screw expander can be constructed for use in a TFC. However, water is not found a suitable working fluid within this type of cycle. The net output from the cycle is 10 to 80% greater when compared to a basic ORC. The machines retain a similar size as well.

2.2. Mixture Model

This methodology solves the continuity equations for both the phases and the mixture. The vapor generation rate is postulated to arise from interphase heat transfer. One equation that is often applied to calculate the vapor generation rate is the interfacial exchange model. Given in Equation (5).

$$\mathcal{T} = A_i \cdot \frac{\dot{q}}{h_{gl}} \quad (5)$$

wherein \mathcal{T} is the vapor generation rate, A_i the interfacial area, \dot{q} the total heat flux, from both phases, transferring to the phase interface and h_{gl} is the latent heat of vaporization.

This model is accurate but, depending on the complexity, requires several closure equations. Constitutive equations for the determination of friction force and nucleation rate can be implemented. This model was applied by [38,47], which was evaluated with their previously mentioned experiments [48,49]. The authors considered that the vaporization was mainly driven due to the heat transfer from the liquid to the phase change interface. The model is capable of predicting their data, both the pressure drop and adiabatic efficiency are within an accuracy window of about 5% and this considering both with and without charge and discharge processes. The adiabatic efficiencies are predicted to reach 84%.

2.3. Boiling Delay Model

The boiling delay model states that the boiling only happens when a certain degree of superheat in the liquid is reached. Then the nucleation of bubbles starts to take place. This liquid superheat implies that there is no thermal equilibrium assumption. The bubble nucleation and growth also limits the eventual vapor generation rate. There is a need for two-phase mixture conservation equations beyond the flashing inception, including property calculations for the metastable liquid thermodynamic properties. This modeling technique could be used in the future for very detailed reciprocating expander models. However, due to the need for sufficiently accurate analytical expressions for bubble nucleation and growth rate, there are currently no examples of its use in volumetric expanders. However, Ref. [50] did apply droplet modeling in the stator nozzles of the wet-to-dry cycle,

taking into account both thermal and mechanical non-equilibrium. As explained before, this cycle avoids erosion on the blades by only having liquid in the nozzles and superheated vapor in the rotor. This can be easily modeled in equilibrium but [50] showed that this is also feasible when taking non-equilibrium into account.

2.4. Homogeneous Relaxation Model

The homogeneous relaxation model (HRM) is similar to the HEM in the sense that it makes use of the same three continuity equations. However, there is no thermal equilibrium assumption. Instead, the following equation is added [42] which is the vapor mass balance equation.

$$\frac{\partial x}{\partial t} + w \frac{\partial w}{\partial z} = \frac{\mathcal{T}}{\rho} \quad (6)$$

Herein, \mathcal{T} represents the vapor generation rate and x is the actual vapor quality. An implication of not assuming thermal equilibrium is that the liquid and vapor phase temperatures are different, this implies that the total state cannot be represented by Equation (4) as the liquid is in a superheated state. The thermodynamic properties are instead defined as in Equation (7) [42].

$$y = x \cdot y_{s,g} + (1 - x) \cdot y_{m,l} \quad (7)$$

In which the subscripts s and g stand for saturated vapor which is only dependent on the saturation pressure, the subscripts m and l stand for metastable liquid which is dependent on both the pressure and the liquid temperature. From the previous, it thus follows that the fluid is assumed to be a mixture of saturated vapor and superheated liquid, both on the same pressure. Ref. [42] adopted the relaxation equation to the simplest linear approximation, as was successfully performed in the past by other researchers. This results in the following equation.

$$\frac{Dx}{Dt} = \frac{\mathcal{T}}{\rho} = -\frac{x - \bar{x}}{\theta} \quad (8)$$

Herein, x is the actual vapor quality and \bar{x} is the unconstrained equilibrium value of the vapor quality. θ is the local relaxation time and represents the time needed for the fluid to reach equilibrium, for which a relation is constructed. Lastly, Ref. [42] also presented correlations for θ but they were only verified for water with the Moby-Dick experiments. The first correlation gives comparatively good results for small pressures, up to 10 bar.

$$\theta = \theta_0 \cdot \epsilon^{-0.257} \cdot \psi^{-2.24} \quad (9)$$

$$\epsilon = \frac{x \cdot \mu_{s,g}}{\mu} \quad (10)$$

$$\psi = \frac{P_s(T_{in}) - P}{P_s(T_{in})} \quad (11)$$

where θ_0 is equal to 6.51×10^{-4} s. For higher pressures, greater than 10 bar, Equation (9) is substituted for Equation (12).

$$\theta = \theta_0 \cdot \epsilon^{-0.54} \cdot \phi^{-1.76} \quad (12)$$

$$\phi = \frac{P_s(T_{in}) - P}{P_c - P_s(T_{in})} \quad (13)$$

In Equation (12), θ_0 is equal to 3.84×10^{-7} s. P_c is the pressure at the critical point. These equations were tested by [51] and they concluded that this rather simple equation, which only describes one possible mechanism for mass exchange between the phases, can still represent complicated processes. The authors do note that the flashing rate is very sensitive to the value of θ .

Ref. [52] also defined an expression for the relaxation time. Instead of using dimensional analysis and construction of a correlation out of experimental data, the authors evaluated the relaxation time theoretically based on the heat flux around vapor bubbles

in the superheated liquid. The authors notice that an increase in the initial void fraction corresponds to a decrease in the relaxation time θ and that the relaxation time decreases for higher values of liquid superheat.

As mentioned before, the HRM model was found to be suited for reciprocating expanders while the HEM can be used for describing the expansion process in screw expanders. This observation is also made in the work of [53]. The authors evaluated the thermodynamic disequilibrium loss, of which the effects increase when the rotation speed increases or if the injection temperature decreases. In these scenarios, with high expander speeds and low heat source temperatures, the authors consider the screw expander to be more suitable. In [54], the authors develop a model for estimating these losses. This model is based on the intake ratio, as the temperature difference between the liquid and vapor phases mainly appears at the initial stage of the two-phase expansion process.

The HRM model has also not yet been fully implemented in an expander model, but [55] has started with the design of a reciprocating expander test-rig. The goal hereby is to gain a better understanding of the flashing principles during variable volume flashing. The model which is being created is based on the HRM model. Initially [56] the model did not yet include an equation for the relaxation variable, instead it was assumed that the evaporation happens instantly. In subsequent work, Ref. [57] the HRM model was included in the reciprocating expander model, but without fitting of the experimental parameters as there is no data available.

A similar method is known as the Delayed Equilibrium Model (DEM) [58] which works on the same principles but uses a three-phase mixture instead of a two-phase mixture. The three phases are saturated vapor, saturated liquid, and superheated liquid states.

2.5. Conclusions and Comparison

Many models have been constructed and used in literature to describe two-phase phenomena. These are mostly applied to flows and other continuous processes and can be subdivided based on taken assumptions. For the specific use of describing the flashing process in a volumetric expander, the possibilities are limited. Because, up until now, the working fluid is assumed to be in mechanical equilibrium, imposing an equilibrium pressure in the two phases, similar to the flashing process where thermal non-equilibrium is used to characterize the system. The most used technique assumes complete equilibrium due to its simplicity and ease of implementation in software. It was shown that this methodology suffices to describe the Lysholm expander, this is speculated to be due to the good mixing within this type of expander. When thermal non-equilibrium is assumed, three methodologies are possible. The mixture model, which solves a given set of continuity equations, was applied by [47] after the authors measured a superheated liquid. The authors were able to predict their experiments by the implementation of the interfacial heat and mass transfer model. Secondly, the boiling delay model would also be applicable, but this has up until now never been tried in literature. This is likely due to the importance of accurate bubble formation and growth equations, which are also impacted by short term mechanical non-equilibrium [26]. Lastly, the homogeneous relaxation model is a rather straightforward extension of the complete equilibrium assumption. It has been successfully used to describe complex systems. Recently, it has been implemented to describe the flashing process in a reciprocating expander [57]. However, experimental validation has to be conducted.

3. Experimental Available Data

The experimental data that have been published on two-phase expansion is hereafter summarized in this section. Firstly, the Lysholm expander will be elaborated on, as this type of expander has received the most attention in literature. Afterward, a brief look will be taken at static flash, as this type of flashing is closely related to what is happening in a reciprocating expander. Lastly, the available experiments on reciprocating expanders will be reviewed last.

3.1. Lysholm Expander

Table 1 shows the available experimental data on two-phase Lysholm expander. The used working fluid, power range, vapor quality range, and measured efficiencies. In the following, they will be compared to one another.

Table 1. Available literature about experimental Lysholm two-phase expanders.

	Working Fluid	Efficiency	Power	Vapor Quality
[59] (1975)	Water	49–55%	16–30 kW	0.12–0.34
[60] (1982)	Water	15–53%	1–60 kW	0.08–0.27
[61] (1982)	Brine	45%	1 MW	0–0.99
[46] (1993)	R113	over 70%	40 kW	-
[32] (1988)	R12	30–60%	10 kW	-
[43] (2013)	R134a	73–92%	50 kW	0.7–1

The screw (or Lysholm) expander is the most prevalent expander that has been studied experimentally in two-phase conditions. Ref. [59] was one of the earliest that published a dataset in 1975, several powers were tested ranging from 16 kW up to 30 kW. The efficiencies that were found for this engine do not come near the theoretical required value of 75% found by [13]. However, Lysholm machine technology has much improved over the years, primarily due to its compressor applications. The authors did not mention whether the vapor quality has an impact on the efficiency within the tested range of 0.12 to 0.34. Ref. [60] tested lower vapor qualities and only mentions an influence of the rotational speed of the screws and the back pressure on the measured efficiencies. Ref. [61] did field tests on a 1 MW screw installation over a range of vapor qualities from 0 to 1. The resulting efficiencies are on average around 45%, which are similar results as [59,60]. All previous experiments mentioned were performed with water as the working fluid. In the following, the reported data comes from the use of refrigerants. Ref. [32] used R12 while [62] executed their experiments with R113. They found efficiencies ranging from 40 to 70%. They concluded that the thermodynamic modeling techniques that are used for single-phase expanders could also be used for two-phase Lysholm expanders with some modifications. They also showed that similar efficiencies can be reached for single-phase and two-phase Lysholm machines. When comparing their efficiencies with single-phase experiments the same conclusions were made by [63]. Lastly, Ref. [43] performed tests with R134a as working fluid. The authors proposed a method to determine the adiabatic efficiency of two-phase operation based solely on single-phase experimental data. This in function of the adiabatic efficiency with saturated vapor and the peak adiabatic efficiency together with the inlet vapor quality. The authors tested their theory on the data of [60–62]. They concluded that for these cases their theory was correct, but that the amount of data is not sufficient to make any firm claims.

3.2. Static Flash

Before going to the specific experiments with reciprocating expanders or piston expanders, static flashing will be introduced. These are similar to reciprocating expander experiments which will be discussed later. This means that the only difference between the reciprocating experiments and the static flash experiments is the load profile which dictates the pressure drop over time. Table 2 shows the experimental static flash data which will be discussed later in this section. Ref. [18] used R12 as the working fluid. The authors installed seven capacitance measurement units over the height of the flashing chamber to measure the void fraction profiles in the cylinder as a function of time when sudden depressurization occurs. It was concluded that the void fraction only linearly increases with respect to the height of the cylinder after around 1.5 s have passed, by which time most thermodynamic disequilibrium has been reduced. Ref. [20] performed experiments on flashing water with a

constant initial liquid level of 15 mm and was able to construct a relation of proportionality between the final amount of flashed mass and the initial superheat of the liquid. This parameter is also found as an important quantity in the modeling techniques mentioned earlier. The authors also show that this proportionality can be derived from the heat balance within the flashing chamber. Their results are in good agreement with the results of [64] which performed similar experiments but with a higher initial liquid level. Later [21] also modeled the static flash phenomena and compared it with experiments on a wide variety of conditions in a rectangular enclosure. The authors concluded that the initial pressure has little effect on the flashed mass itself, it only affected the onset of flash evaporation, which is in accordance with previous research. Ref. [65] studied the amount of exergy that is lost due to flash evaporation, the authors concluded that most exergy loss can be avoided if the flashing process takes longer and has a lower superheat temperature of the flashing liquid, this result is beneficial for reciprocating expanders as the pressure drop takes place over a longer time period compared to static flash.

Table 2. Available literature about experimental static flashing.

	Working Fluid	Starting Pressure	Initial Liquid Level
[18] (1984)	R12	10.7 bar	600 mm
[20] (2002)	Water	0.05–0.2 bar	15 mm
[64] (1973)	Water	0.07–0.47 bar	196–225 mm
[21] (2019)	Water	0.05–0.3 bar	0.23–2.3 mm
[65] (2015)	Water	0.08–0.36 bar	100–300 mm

3.3. Reciprocating Expander

Only [38] have performed two-phase expansion experiments with a reciprocating engine. The working fluid used by the authors was water and later ethanol. These experiments are also very similar to static flash experiments with a slower pressure decrease. In the static flash experiments, the piston was suddenly connected to another larger vessel under vacuum conditions, resulting in larger depressurization rates compared to the experiments for reciprocating expanders. Here, the cylinder was loaded with liquid before the piston was set in motion using a linear actuator. The adiabatic efficiencies reached are in the range of 80–95% [38,48]. To compare with [43], the authors theoretically imposed mechanical and electrical losses, achieving a maximum adiabatic efficiency of around 80% which is similar as the Lysholm expander [49]. The authors also conclude that a two-phase reciprocating expander achieves similar efficiencies as a single-phase reciprocating expander.

3.4. Conclusions of Two-Phase Experimental Data

In general, the amount of experimental data on two-phase expanders is quite low considering the theoretically proven potential of some of its applications. Most of this available data was performed on the lysholm (screw) expander. These expanders are based on compressor design methods without a lot of adaptations. This is one area where more research has to be performed, the difference in the design of compressor and expander machines. The available data shows that the equilibrium assumption is sufficient to describe the process in these machines while this is not the case for the reciprocating type. Why this is the case is also only speculated and not yet conclusively shown. To study the flashing expansion phenomena itself, more research is required on other machine types where the liquid superheat is measurable.

4. Modeling of Two-Phase Volumetric Expanders

In the following section, an overview of models of two-phase volumetric expanders in open literature is summarized but first, the inlet and outlet flow valves are considered here shortly. These are often not taken into account or with a straightforward, often equilibrium,

process. However, it is possible to also apply the non-equilibrium models here. For example, Ref. [66] used the HRM for this modeling of expander valves, where the authors were able to accurately predict the operation of the inlet and outlet valves independent of the vapor fraction and oil content.

4.1. Lysholm Expander

One of the first analytical models for the two-phase Lysholm expanders is described by [32]. The authors mostly assume thermodynamic equilibrium and thus apply the HEM. The authors compared their analytical model with their performed experiments. Both methods showed an increase in internal efficiency with the rotor speed. Importantly, the authors also looked into a flashing delay. Included by adding a certain time delay between the start of the intake stroke and instantaneous flashing to equilibrium. The authors conclude that this can be omitted as the results for no delay time correspond just as well to their experiments. A similar methodology to [32] was applied by [33]. However, compared to a broader experimental dataset. The authors showed that the working fluid choice and correct rotor profiles are important in the design of TLC with a twin screw expander. Ref. [45] created a chamber model for a twin-screw expander within commercial software with the capability of integration in an entire TLC cycle. This methodology is specific to the machine as it requires geometrical data regarding cell volume evolution, suction and discharge ports as well as the multiple leakage paths in Lysholm expanders [44]. This model also uses thermodynamic equilibrium properties, and thus applies the HEM. The authors found a significant impact of the intake manifold expansion on the overall machine performance. Therefore, the authors designed a Lysholm expander with a variable built-in volume ratio [67]. The simulations show higher total power outputs for smaller BVR due to the higher mass flow rates, while the specific power decreases. Lower BVR also results in higher volumetric efficiencies but lower isentropic efficiencies due to under-expansion. In general, the simulation is capable to optimize the total power output in different operation conditions by varying the BVR. Lastly, Ref. [34] also assumed thermodynamic equilibrium in their initial simulation procedure. Additionally, they also assume that the work is performed by the vapor phase. Later, Ref. [68] modeled the chambers with flash vaporization based on an equation found by experimental spray flash evaporation. This model assumes a minimum superheat of 1 K before evaporation occurs. The amount of evaporation is a fraction of the evaporation needed to achieve equilibrium which was experimentally determined. Thus a boiling delay model was used. The model with thermal disequilibrium predicted slightly lower internal power and isentropic efficiency, but only in the order of 3%. This is in line with the general finding that the equilibrium assumption can be used for Lysholm expanders.

4.2. Reciprocating Expander

After experimental determination of a temperature difference between the liquid and vapor phase, Ref. [47] constructed a five equation flashing model consisting of three energy continuity equations (of the liquid, vapor, and housing) combined with the mass continuity and the interfacial exchange model Equation (5) to predict the experimental data. Ref. [21] compared the model proposed by [47] with the HEM for different expander frequencies and initial superheats. The authors find discrepancies of up to 8% in the isentropic efficiency and expansion work between the two models. These are attributed to the disequilibrium losses by the authors. Ref. [69] proposed a design for a two-phase reciprocating expander consisting of a cyclone separator and the piston itself. The applied modeling for this design was also based on equilibrium assumptions. The authors found isentropic efficiencies in the range of 65 to 85% depending on the working fluid and operational regime. They also noted lower efficiencies for higher engine speeds. Ref. [54] used this design with the model of [47] to estimate the intake losses. For this design, the authors found a linear relation between the intake losses and the intake ratio, defined as the intake time to the expansion time. Ref. [19] also modeled a two-phase expander with a cyclone separator. The authors

applied an evaporation model based on static flash pool evaporation and separated the phases in the cyclone and piston parts. Due to the better predicted performance at higher evaporation rates, the authors consider rotary expanders a better match for the two-phase expansion process.

4.3. Conclusions of Two-Phase Expander Modeling

Screw expanders have seen the most modeling of their use with two-phase expansion. Most of these assumed thermal equilibrium throughout expansion as these conform well with the available experimental data. The impact of the inlet port was found to have a non-negligible impact on the operation of the machine. More research about the design of the inlet manifold for two-phase expanders would thus be advised instead of basing the design on the machines compressor operation. When flash evaporation within the chamber was assumed, a discrepancy of only 3% was found with the equilibrium model. Reciprocating expanders on the other hand do require some modeling technique that takes into account the metastable conditions. Only one model of this type was available which takes the metastable condition in the working chamber into account via the mixture model. Other models split up the working volume in the expansion chamber and a phase separator cyclone. This process will have to be studied further, and described with more methods, to better understand the phenomena. These insights could make it possible to better design two-phase volumetric expanders.

5. Conclusions

The current review shows the possibilities and state-of-the-art of two-phase volumetric expansion machines. Research is scarce but promising results are presented. The most notable application for volumetric two-phase expanders is in low-temperature heat-to-power cycles. These cycles have around 20% higher exergy efficiency for power production compared to the basic organic Rankine cycle if efficient volumetric expansion machines are available. The required efficiencies of 75% are achievable, as was experimentally shown. However, consistent design and simulation models are still unavailable. This requires more research and a better understanding of the process and the occurring phenomena. The modeling of these types of machines is complex. For screw expanders, it was experimentally shown that it can be assumed that the phases are in thermal equilibrium, which implies that the vapor and liquid have the same temperature. Researchers simulate this type of two-phase expander with the use of the homogeneous equilibrium model. The available experimental data is predicted well by these models. On the other hand, it was shown that the thermal equilibrium cannot be assumed for reciprocating expanders. Experimental data and models are very limited for this type of expander. The only available data for reciprocating expanders was described with the use of the mixture model. Another rather simple technique to describe the metastable condition is the homogeneous relaxation model which has been shown to give promising results in other processes, including over inlet and outlet valves. Lastly, the boiling delayed model could also be applied, but presently this was not implemented due to the complexity of the technique and required understanding of the phenomena occurring.

In the near future more research and progress are expected in this area. This increase in interest is likely due to its main predicted application and its need in current times. More work in understanding the principles of flashing in the specific case of volumetric expanders should be performed. Initially, this can be inspired by methods of other flashing phenomenon. Primarily, those where mechanical equilibrium is assumed. For example, the boiling delay model has never been applied to any volumetric expander. Not only does the theoretical understanding need more research, experimental research requires more work as well. Currently, it mostly occurs on lysholm expanders and the experiments are few and far between. More experimental data is required and on a multitude of different expander types. The impact of design parameters on these experiments has to be studied as well.

Funding: This research was funded by FWO-Flanders grant number 1SD9721N.

Acknowledgments: I would like to thank the Research Foundation-Flanders for their financial support through FWO-Flanders grants (1SD9721N).

Conflicts of Interest: The authors declare no conflict of interest.

Abbreviations

The following abbreviations are used in this manuscript:

BLEVE	Boiling Liquid Expanding Vapor Explosion
EOS	Equation of State
LNG	Liquefied Natural Gas
VPT	Variable Phase Turbine
ORC	Organic Rankine Cycle
TLC	Trilateral Cycle
PEORC	Partial Evaporation Organic Rankine Cycle
BVR	Built in Volume Ratio
HEM	Homogeneous Equilibrium Model
HRM	Homogeneous Relaxation Model
WORC	Wet Organic Rankine Cycle

References

1. Cylinder Condensation. *J. Am. Soc. Nav. Eng.* **1909**, *21*, 294–297. Available online: <https://onlinelibrary.wiley.com/doi/abs/10.1111/j.1559-3584.1909.tb04491.x> (accessed on 30 May 2022). [CrossRef]
2. Di, J.; Wang, S.S.; Yan, X.J.; Cai, L.X.; Xie, Y.H. Experimental investigation on effect of surface strengthening process and roughness on water droplet erosion behavior in turbomachinery. *Tribol. Int.* **2020**, *153*, 106647. [CrossRef]
3. Eyerer, S.; Dawo, F.; Rieger, F.; Schuster, A.; Aumann, R.; Wieland, C.; Spliethoff, H. Experimental and numerical investigation of direct liquid injection into an ORC twin-screw expander. *Energy* **2019**, *178*, 867–878. [CrossRef]
4. Galoppi, G.; Secchi, R.; Ferrari, L.; Ferrara, G.; Karellas, S.; Fiaschi, D. Radial piston expander as a throttling valve in a heat pump: Focus on the 2-phase expansion. *Int. J. Refrig.* **2017**, *82*, 273–282. [CrossRef]
5. Mahmoud, A.M.; Sherif, S.A.; Lear, W.E. Frictional and internal leakage losses in rotary-vane two-phase refrigerating expanders. *J. Energy Resour. Technol. Trans. ASME* **2010**, *132*, 0210071. [CrossRef]
6. Xia, C.; Zhang, W.; Bu, G.; Wang, Z.; Shu, P. Experimental study on a sliding vane expander in the HFC410A refrigeration system for energy recovery. *Appl. Therm. Eng.* **2013**, *59*, 559–567. [CrossRef]
7. Sumeru, K.; Nasution, H.; Ani, F.N. A review on two-phase ejector as an expansion device in vapor compression refrigeration cycle. *Renew. Sustain. Energy Rev.* **2012**, *16*, 4927–4937. [CrossRef]
8. Ringstad, K.E.; Allouche, Y.; Gullo, P.; Ervik, Å.; Banasiak, K.; Hafner, A. A detailed review on CO₂ two-phase ejector flow modeling. *Therm. Sci. Eng. Prog.* **2020**, *20*, 100647. [CrossRef]
9. Panesar, A.S.; Bernagozzi, M. Two-phase expander approach for next generation of heat recovery systems. *Int. J. Renew. Energy Dev.* **2019**, *8*, 203–213. [CrossRef]
10. Lemort, V.; Quoilin, S.; Cuevas, C.; Lebrun, J. Testing and modeling a scroll expander integrated into an Organic Rankine Cycle. *Appl. Therm. Eng.* **2009**, *29*, 3094–3102. [CrossRef]
11. Giuffrida, A. Improving the semi-empirical modelling of a single-screw expander for small organic Rankine cycles. *Appl. Energy* **2017**, *193*, 356–368. [CrossRef]
12. Li, Z.; Lu, Y.; Huang, Y.; Qian, G.; Chen, F.; Yu, X.; Roskilly, A. Comparison study of Trilateral Rankine Cycle, Organic Flash Cycle and basic Organic Rankine Cycle for low grade heat recovery. *Energy Procedia* **2017**, *142*, 1441–1447. [CrossRef]
13. DiPippo, R. Ideal thermal efficiency for geothermal binary plants. *Geothermics* **2007**, *36*, 276–285. [CrossRef]
14. Fischer, J. Comparison of trilateral cycles and organic Rankine cycles. *Energy* **2011**, *36*, 6208–6219. [CrossRef]
15. Hays, L. Demonstration of a Variable Phase Turbine Power System for Low Temperature Geothermal Resources. *Energent Corp.* **2010**, 1–57. [CrossRef]
16. Lecompte, S.; van den Broek, M.; De Paepe, M. Thermodynamic analysis of the partially evaporating trilateral cycle. In Proceedings of the 2nd International Seminar on ORC Power Systems, Proceedings, Rotterdam, The Netherlands, 7–8 October 2013; p. 4.
17. Lecompte, S.; Huisseune, H.; van den Broek, M.; De Paepe, M. Methodical thermodynamic analysis and regression models of organic Rankine cycle architectures for waste heat recovery. *Energy* **2015**, *87*, 60–76. [CrossRef]
18. Friedel, L.; Purpst, S. Phase distribution in vessels during depressurisation. *Int. J. Heat Fluid Flow* **1984**, *5*, 229–234. [CrossRef]
19. Wu, W.; Wang, Q.; Zhang, Z.; Wu, Z.; Yang, X.; Xu, L. Influence of evaporating rate on two-phase expansion in the piston expander with cyclone separator. *Therm. Sci.* **2020**, *24*, 2077–2088. [CrossRef]

20. Saury, D.; Harmand, S.; Siroux, M. Experimental study of flash evaporation of a water film. *Int. J. Heat Mass Transf.* **2022**, *45*, 3447–3457. [CrossRef]
21. Wang, C.; Xu, R.; Chen, X.; Jiang, P.; Liu, B. Study on water flash evaporation under reduced pressure. *Int. J. Heat Mass Transf.* **2019**, *131*, 31–40. [CrossRef]
22. Lorenzo, M.D.; Modelling, M.D.L.; Lorenzo, M.D.; Lafon, P. *Modelling and Numerical Simulation of Metastable Two-Phase Flows*; To Cite This Version: HAL Id: Tel-01889103 Modélisation et Simulation Numérique des Ecoulements Diphasiques Métastables; HAL Open Science: Lyon, France, 2018.
23. Debenedetti, P.G. *Metastable Liquids: Concepts and Principles*; Princeton University Press: Princeton, NJ, USA, 1997; Volume 1, pp. 1–400.
24. Polanco, G.; Holdø, A.E.; Munday, G. General review of flashing jet studies. *J. Hazard. Mater.* **2010**, *173*, 2–18. [CrossRef][PubMed]
25. Pinhasi, G.; Ullmann, A.; Dayan, A.; Israel, T.A. Modeling of Flashing Two-Phase Flow Gad A. Pinhasi Department of Chemical Engineering and Biotechnology. *Rev. Chem. Eng.* **2005**, *21*, 133–264. [CrossRef]
26. Liao, Y.; Lucas, D. Computational modelling of flash boiling flows: A literature survey. *Int. J. Heat Mass Transf.* **2017**, *111*, 246–265. [CrossRef]
27. Balje', O.E. A Study on Design Criteria and Matching of Turbomachines: Part A—Similarity Relations and Design Criteria of Turbines. *J. Eng. Power* **1962**, *84*, 83–102. [CrossRef]
28. Francesconi, M.; Dori, E.; Antonelli, M. Analysis of Balje diagrams for a Wankel expander prototype. *Appl. Energy* **2019**, *238*, 775–785. [CrossRef]
29. Narasimhan, A.K.; Wickramaratne, C.; Kamal, R.; Goswami, D.Y.; Singh, P. Mapping scroll expander performance for organic working fluids using dimensionless parameters in Ns-Ds diagram. *Energy* **2019**, *182*, 739–752. [CrossRef]
30. Dumont, O.; Dickes, R.; Lemort, V. Experimental investigation of four volumetric expanders. *Energy Procedia* **2017**, *129*, 859–866. [CrossRef]
31. Imran, M.; Usman, M.; Park, B.S.; Lee, D.H. Volumetric expanders for low grade heat and waste heat recovery applications. *Renew. Sustain. Energy Rev.* **2016**, *57*, 1090–1109. [CrossRef]
32. Taniguchi, H.; Kudo, K.; Giedt, W.H.; Park, I.; Kumazawa, S. Analytical and Experimental Investigation of Two-Phase Flow Screw Expanders for Power Generation. *J. Eng. Gas Turbines Power* **1988**, *110*, 628–635. [CrossRef]
33. Smith, I.K.; Stošić, N.; Aldis, C.A. Development of the trilateral flash cycle system. Part 3: The design of high-efficiency two-phase screw expanders. *Proc. Inst. Mech. Eng. Part A J. Power Energy* **1996**, *210*, 75–92. [CrossRef]
34. Vasuthevan, H.; Brümmer, A. Thermodynamic Modeling of Screw Expander in a Trilateral Flash Cycle. In Proceedings of the International Compressor Engineering, Refrigeration and Air Conditioning, and High Performance Buildings Conferences, Virtual Conference, 23–28 May 2016; pp. 1–10.
35. Ohman, H.; Lundqvist, P. Screw expanders in ORC applications, review and a new perspective. In Proceedings of the 3rd International Seminar on ORC Power Systems, Brussels, Belgium, 12–14 October 2015.
36. Xia, G.D.; Zhang, Y.Q.; Wu, Y.T.; Ma, C.F.; Ji, W.N.; Liu, S.W.; Guo, H. Experimental study on the performance of single-screw expander with different inlet vapor dryness. *Appl. Therm. Eng.* **2015**, *87*, 34–40. [CrossRef]
37. Liu, X.; Zhang, H.; Wang, F.; Xia, G.; Li, Z.; Zhu, C.; Zhang, H. Numerical investigation of flow behavior and film thickness in the single screw expander. *Int. J. Mech. Sci.* **2021**, *190*, 106047. [CrossRef]
38. Kanno, H.; Shikazono, N. Experimental and modeling study on adiabatic two-phase expansion in a cylinder. *Int. J. Heat Mass Transf.* **2015**, *86*, 755–763. [CrossRef]
39. Zhang, D.; Chong, D.; Yan, J.; Zhang, Y. Study on steam-carrying effect in static flash evaporation. *Int. J. Heat Mass Transf.* **2012**, *55*, 4487–4497. [CrossRef]
40. Spiegler, K.; El-Sayed, Y. The energetics of desalination processes. *Desalination* **2001**, *134*, 109–128. [CrossRef]
41. Mayinger, F. Two-Phase Flow Phenomena with Depressurization-Consequences for the Design and Layout of Safety and Pressure Relief Valves Phnomena zweiphasiger Strömung bei Druckentlastung-Folgerungen fiir Konstruktion und Auslegung von Sicherheits-und Druckentlast. *Chem. Eng. Process. Process. Intensif.* **1988**, *23*, 1–11. [CrossRef]
42. Downar-Zapolski, P.; Bilickp, Z.; Bolle, L.; Franco, J. The Non-equilibrium relaxation model for one-dimensional flashing liquid flow. *Int. J. Multiph. Flow* **1996**, *22*, 473–483. [CrossRef]
43. Öhman, H.; Lundqvist, P. Experimental investigation of a Lysholm Turbine operating with superheated, saturated and 2-phase inlet conditions. *Appl. Therm. Eng.* **2013**, *50*, 1211–1218. [CrossRef]
44. Bianchi, G.; Kennedy, S.; Zaher, O.; Tassou, S.A.; Miller, J.; Jouhara, H. Two-phase chamber modeling of a twin-screw expander for Trilateral Flash Cycle applications. *Energy Procedia* **2017**, *129*, 347–354. [CrossRef]
45. Bianchi, G.; Kennedy, S.; Zaher, O.; Tassou, S.A.; Miller, J.; Jouhara, H. Numerical modeling of a two-phase twin-screw expander for Trilateral Flash Cycle applications. *Int. J. Refrig.* **2018**, *88*, 248–259. [CrossRef]
46. Smith, I.K. Development of the trilateral flash cycle system: Part 1: Fundamental considerations. *Proc. Inst. Mech. Eng. Part A J. Power Energy* **1993**, *207*, 179–194. [CrossRef]
47. Kanno, H.; Shikazono, N. Modeling study on two-phase adiabatic expansion in a reciprocating expander. *Int. J. Heat Mass Transf.* **2017**, *104*, 142–148. [CrossRef]
48. Kanno, H.; Shikazono, N. Experimental study on two-phase adiabatic expansion in a reciprocating expander with intake and exhaust processes. *Int. J. Heat Mass Transf.* **2016**, *102*, 1004–1011. [CrossRef]

49. Kanno, H.; Hasegawa, Y.; Hayase, I.; Shikazono, N. Experimental Study on Adiabatic Two-Phase Expansion in A Cylinder for trilateral cycle. In Proceedings of the 3rd International Seminar on ORC Power Systems, Brussels, Belgium, 12–14 October 2015.
50. White, M.T. Investigating the wet-to-dry expansion of organic fluids for power generation. *Int. J. Heat Mass Transf.* **2022**, *192*, 122921. [CrossRef]
51. Banaszekiewicz, M.; Kardaś, D. Numerical calculations of the Moby Dick experiment by means of unsteady relaxation model. *J. Theor. Appl. Mech.* **1997**, *35*, 211–232.
52. Bilicki, Z.; Kwidzilqski, R.; Ali Mohammade, S. Evaluation of the relaxation time of heat and mass exchange in the liquid-vapour bubble flow. *Int. J. Heat Mass Transf.* **1996**, *39*, 753–759. [CrossRef]
53. Wang, Q.; Huang, H.; Xu, L.; Yang, X.; He, Z.; Wu, W. Analysis of the thermodynamic disequilibrium loss of the two-phase expansion process and its influence on the performance of a reciprocating expander. In Proceedings of the IOP Conference Series: Materials Science and Engineering, London, UK, 9–11 September 2019; Institute of Physics Publishing: London, UK, 2019; Volume 604. [CrossRef]
54. Wang, Q.; Wu, W.; He, Z.; Ziviani, D. Analysis of the intake process and its influence on the performance of a two-phase reciprocating expander. *Appl. Therm. Eng.* **2019**, *160*, 113943. [CrossRef]
55. Lecompte, S.; Van Den Broek, M.; De Paepe, M. Design of an Optical-access Expansion Chamber for Two-phase Expansion. *Int. J. Heat Mass Transf.* **2012**, *86*, 755–763.
56. Lecompte, S.; Van Den Broek, M.; De Paepe, M. Initial Design of an Optical-Access Piston Expansion Chamber for Wet-Expansion. *Energy Procedia* **2017**, *129*, 307–314. [CrossRef]
57. van Heule, X.; Skiadopoulos, A.; Manolagos, D.; De Paepe, M.; Lecompte, S. Modelling and design of a two-phase reciprocating expander for integration in a trilateral flash cycle. In Proceedings of the 6th International Seminar on ORC Power Systems, Virtual Conference, 11–13 October 2021; Technical University of Munich: Munich, Germany, 2021.
58. Delayed Equilibrium Model (DEM) of Flashing Choked Flows Relevant to LOCA and Implementation in System Codes, Thermal Hydraulics. *Int. Conf. Nucl. Eng.* **2014**, *2B*, V02BT09A040. Available online: https://www.researchgate.net/publication/263652479_Delayed_Equilibrium_Model_DEM_of_Flashing_Choked_Flows_Relevant_to_LOCA_and_Implementation_in_System_Codes (accessed on 30 May 2022). [CrossRef]
59. Weiss, H.; Steidel, R.; Lundberg, A. Performance Test of a Lysholm Engine. Report. 3 July 1975. Available online: <https://digital.library.unt.edu/ark:/67531/metadc1061143/> (accessed on 30 May 2022).
60. Steidel, R.F., Jr.; Weiss, H.; Flower, J.E. Performance Characteristics of the Lysholm Engine as Tested for Geothermal Power Applications in the Imperial Valley. *J. Eng. Power* **1982**, *104*, 231–240. [CrossRef]
61. McKay, R. *Helical Screw Expander Evaluation Project; Final Report*; Jet Propulsion Laboratory, US Department of Energy: La Cañada Flintridge, CA, USA, 1982.
62. Smith, I.K.; Stosic, N.; Aldis, C.A. Lysholm machines as two-phase expanders. In Proceedings of the International Compressor Engineering Conference, West Lafayette, IN, USA, 19–22 July 1994; Purdue University: West Lafayette, IN, USA, 1994.
63. Merigoux, J.M.; Pocard, P. *Solar Power Units with Screw Expanders*; Pergamon Press Inc.: Oxford, UK, 1980; Volume 3, pp. 1293–1317.
64. Miyatake, O.; Murakami, K.; Kawata, Y.; Fujii, T. Fundamental experiments with flash evaporation. *Heat Transf.-Jpn. Res* **1973**, *2*, 89–100.
65. Zhang, D.; Yan, J.; Liu, Y.; Zhao, B. Preliminary exergy analysis of static flash of pure water. *Int. J. Heat Mass Transf.* **2015**, *86*, 377–387. [CrossRef]
66. Schweizer, F.; Fürst, M.; Wachtmeister, G. Modeling and Validation of a Two-Phase Flow Valve for Expanders in Waste Heat Recovery. *J. Therm. Sci. Eng. Appl.* **2021**, *13*, 031026. [CrossRef]
67. Bianchi, G.; Marchionni, M.; Miller, J.; Tassou, S.A. Modelling and off-design performance optimisation of a trilateral flash cycle system using two-phase twin-screw expanders with variable built-in volume ratio. *Appl. Therm. Eng.* **2020**, *179*, 115671. [CrossRef]
68. Vasuthevan, H.; Brümmer, A. Theoretical investigation of flash vaporisation in a screw expander You may also like Theoretical investigation of flash vaporisation in a screw expander. *IOP Conf. Ser. Mater. Sci. Eng.* **2017**, *232*, 012077. [CrossRef]
69. Steffen, M.; Löffler, M.; Schaber, K. Efficiency of a new Triangle Cycle with flash evaporation in a piston engine. *Energy* **2013**, *57*, 295–307. [CrossRef]

Article

Feasibility Study and Economic Analysis of a Fuel-Cell-Based CHP System for a Comprehensive Sports Center with an Indoor Swimming Pool

Jie Liu , Sung-Chul Kim and Ki-Yeol Shin * 

School of Mechanical Engineering, Yeungnam University, 280 Daehak-ro, Gyeongsan-si 712-749, Korea; lauj@ynu.ac.kr (J.L.); sungkim@ynu.ac.kr (S.-C.K.)

* Correspondence: shinky@ynu.ac.kr; Tel.: +82-53-810-3060

Abstract: Unlike a general commercial building, heating for a building with an indoor swimming pool is highly energy-intensive due to the high energy demand for swimming water heating. In Korea, the conventional heating method for this kind of building is to use boilers and heat storage tanks that have high fuel costs and greenhouse gas emissions. In this study, a combined heat and power (CHP) system for such a building using the electricity and waste heat from a Phosphoric Acid Fuel Cell (PAFC) system was designed and analyzed in terms of its primary energy saving, CO₂ reduction, fuel cell and CHP efficiency, and economic feasibility. The mathematical model of the thermal load evaluation was used with the 3D multi-zone building model in TRNSYS 18 software (Thermal Energy System Specialists, LLC, Madison, WI, USA) to determine the space heating demand and swimming pool heat losses. The energy efficiency of the fuel cell unit was evaluated as a function of the part-load ratio from the operating data. The fundamental components, such as the auxiliary boiler, thermal storage tank, and heat exchanger are also integrated for the simulation of the system's operation. The result shows that the system has a high potential to improve the utilization efficiency of fuel cell energy production. Referring to the local condition of the energy market in Korea, an economic analysis was also carried out by using a specific FC-CHP capacity at 440 kW. The economic benefit is significant in comparison with a conventional heating system, especially for the full-time operating (FTO) mode. The net profit made by comparison with the conventional energy supply system is about 178,352 to 273,879 USD per year, and the payback period is expected to be 6.9 to 10.7 years under different market conditions.

Citation: Liu, J.; Kim, S.-C.; Shin, K.-Y. Feasibility Study and Economic Analysis of a Fuel-Cell-Based CHP System for a Comprehensive Sports Center with an Indoor Swimming Pool. *Energies* **2021**, *14*, 6625. <https://doi.org/10.3390/en14206625>

Academic Editors: Jan Danielewicz and Krzysztof Rajski

Received: 31 August 2021

Accepted: 10 October 2021

Published: 14 October 2021

Publisher's Note: MDPI stays neutral with regard to jurisdictional claims in published maps and institutional affiliations.



Copyright: © 2021 by the authors. Licensee MDPI, Basel, Switzerland. This article is an open access article distributed under the terms and conditions of the Creative Commons Attribution (CC BY) license (<https://creativecommons.org/licenses/by/4.0/>).

Keywords: fuel cell (FC); phosphoric acid fuel cell (PAFC); combined heat and power (CHP); wasted heat recovery system (WHRS); strategic energy management planning; economic analysis

1. Introduction

The main motivations to seek more clean and efficient methods of energy production are the increasing cost of fuel and the need for the reduction of CO₂ and harmful emissions [1]. A combined heat and power (CHP) system has many benefits when it is used to provide electrical and thermal energy for commercial buildings, such as increasing power reliability; the reduction of primary energy consumption, greenhouse gas emissions and costs; and the improvement of power quality [2]. Furthermore, the owner of the CHP system can benefit from the higher efficiency of the fuel energy conversion, the lower cost of fuel per unit of energy, high-quality power, and the rapid variation of the distribution between electrical and thermal loads [3]. For the application of commercial buildings, CHP is decentralized electrical power generation coupled with thermally activated components [4]. In the CHP part, the interest in the improvements of the primary generator over a typical thermal engine to new is growing more, especially in Japan, and more recently in Europe [5]. Comparing with those other CHP technologies, such as Stirling engines or gas turbines, fuel cells—as an electrochemical generator—can achieve substantially higher

efficiencies and potentially compete even the most energy-efficient large-scale power plants in terms of electric efficiencies [6,7], due to their wide range of capacities which can be well matched with the energy demand, thereby increasing the energy utilization.

According to the electrolyte and operating temperature, fuel cells can be categorized into the following five major types: alkaline fuel cells (AFC), proton exchange membrane fuel cells (PEMFC), solid oxide fuel cells (SOFC), phosphoric acid fuel cells (PAFC), and molten carbonate fuel cells (MCFC). A comparison of the characteristics of different types of fuel cells is listed in Table 1 [8]. Referring to the features of different types of fuel cells, several studies about fuel-cell-based CHP systems were carried out. In Ivan Verhaert et al.'s study, an AFC based micro-CHP system was compared with other micro-CHP technologies, and it was shown that for buildings with a decreasing heating demand and increasing electricity demand, a fuel-cell-based micro-CHP has a better result, especially, in terms of thermal performance [9]. PEMFC has a major application in transportation due to its potential impact on the environment, such as the control of greenhouse gases emissions [10]. However, due to its high efficiency and low pollution in comparison with conventional combustion-based power generation technologies, PEMFC is also considered to be a prospective alternative power source for distributed energy or CHP applications [11]. A thermodynamic analysis for a combined cooling, heating, and power (CCHP) system based on PEMFC as a prime mover has been performed, and the results indicated that the energy and exergy efficiencies of the CCHP system are 81.55% and 54.5% [12]. SOFC has several advantages, such as high electrical efficiency, high-quality heat supply, small installation footprints, the flexibility of its fuel use, and the use of economical materials [13]; it has successfully been verified in long-term stationary power generation up to the Megawatt-scale, generally for the use of commercial CHP systems. A 175 kW SOFC-CHP system was analyzed, and it successfully decreased annual utility costs by up to 14.5% over a baseline HVAC system [14]. Techno-economic analyses of a PEMFC- and SOFC-based micro-CHP system for a residential application with [15] and without a heat pump [16] were carried out by Marta Gandiglio et al., and the results indicate that a SOFC-CHP system has a better total energy efficiency (up to 81%), and the PEMFC-CHP system presents a total efficiency of 75% and a 3-year payback period. PAFC has a relatively low operating temperature, low-electrolyte cost, and high durability in comparison with the other types of fuel cell technologies. Therefore, the PAFC is believed to be one of the most complete fuel cell technologies, and is easy to commercialize [17,18]. As early as 10 years ago, it was demonstrated that the PAFC has high reliability, efficiency, and flexibility for a variety of applications, especially for distributed power generation [19]. Compared with SOFC, the PAFC cannot be effectively used to drive a heat engine due to its relatively low working temperature. However, the operating temperature of PAFC is higher than PEMFC, and the waste heat recovered from PAFC includes a considerable amount of available energy [20]. The economic and environmental potential of a CHP system based on a 400 kW scale PAFC was introduced by a simulation-based analysis under two different operation strategies, and the results indicated that the electrical load following (ELF) model would be the advisable operation mode for this CHP system in the residential sector [21]. Salvador Acha et al. investigated the feasibility of a 460 kW PAFC-based CHP system in the application of a commercial building. The results indicated that the FC-CHP system is financially competitive against the internal combustion engine [22].

Table 1. Comparison of fuel cell technologies.

	AFC	MCFC	PEMFC	PAFC	SOFC
Operating temperature	60–90 °C	600–700 °C	<120 °C	150–200 °C	500–1000 °C
Electrical efficiency	45–60%	45–60%	45–60%	40%	60%
Typical capacity	<100 kW	300 kW–3 MW	<1–100 kW	5–440 kW	1 kW–2 MW
Applications	Military; Backup power;	Electric utility; Distributed generation;	Distributed generation; Transportation; Specialty vehicles;	Distributed generation; CHP;	Electric utility; Distributed generation;

From the above literature, for the analysis of the operating and economic performance of a fuel-cell-based CHP system, relatively accurate load data plays a vital role, as the CHP performance is highly dependent on the load matching condition. The analysis without complete annual load data [12,13] can just present the performance of the CHP system under specific operating conditions, but is limited to reflect the fluctuation of the load, which has the biggest impact on the performance of the CHP system. Some of the studies used measured data or standard profiles of electricity and thermal loads [5,15,16,21]. It is effective for the analysis of existing building or if the building has a relatively standard load profile according to their functions, such as a school, office, commercial buildings, etc. However, for buildings that are under construction and have a special load profile, such as a commercial building with an indoor swimming pool, the better way is to obtain the load through numerical simulation. The commercial software eQUEST [14] and EnergyPlus [23] were found to be used for the thermal load evaluation for the analysis of a fuel-cell-based CHP system. However, the effective verification of the simulation results of the load was not found. Therefore, in order to overcome the aforementioned limitations, a weather-data-based dynamic computation model for the fuel-cell-based CHP system, which includes the thermal load evaluation of a comprehensive sports center with an indoor swimming pool is developed in this study, and the obtained thermal load is validated by the measured data from a reference building.

The comprehensive sports center with an indoor swimming pool is planned and under construction in Donghae City, Gangwon Province, South Korea. Unlike general commercial buildings, a building with an indoor swimming pool is highly intensive in the use of thermal energy, due to the high heat loss from the pool water. The conventional strategy of energy supply for this kind of building is to provide electrical energy from the main grid and thermal energy from a combustion boiler. Normally, for a general commercial building in Korea, the thermal–electrical load ratio is around 0.5 [24]. However, for a building with an indoor swimming pool, it could be larger than 0.7. This characteristic will improve the utilization rate of waste heat from the fuel cell. The thermal–electrical ratio of the PAFC output is from 0.7 to 1.2 under different part-load conditions which are closer to the aimed-for building than the SOFC (0.5). Moreover, by considering its lower temperature of operating and waste heat, the PAFC is the better choice for the design building than SOFC, although the SOFC has a higher electrical efficiency. In this study, two operating strategies of the FC-CHP system are introduced and analyzed from the following aspects: primary energy consumption, fuel cell and CHP efficiency, and economic feasibility. In the aspect of the energy load, the measured data of the electricity load from a similar building is modified and used. The thermal energy demand, including the heating load, swimming pool heat loss, and domestic hot water demand, is evaluated by the commercial software TRNSYS, which is also used for the dynamic simulation of the system's operation. Figure 1 depicts the main configuration of the designed FC-CHP system for the building. In the PAFC system, the fuel cell stack produces both electrical and thermal energy from the hydrogen produced through the reforming of natural gas. The main electrical and thermal load are provided by fuel cell production. Simultaneously, the electricity from the main power grid and the heat from an auxiliary boiler are also required as a supplement. The performance of a CHP system is highly dependent on the operating strategies due to the unstable characteristics of the load over time. From the perspective of exergy efficiency, there are two representative regimes of operating strategies: electrical load tracking (ELT) and thermal load tracking (TLT) [23,25]. However, from the economic point of view, more electricity production means more revenue, especially in a country with an open electricity market, because the excess electricity production could be sold onto the grid. The TLT model presents a significant shortage in the total amount of power generation in the summer season. Therefore, the TLC model is not considered to be an operating strategy. Additionally, the operating strategy of so-called full time operating (FTO) is carried out in this study. This operating model is always applied in a large scale fuel cell plant [26,27], but is not common in CHP applications. The performance and economic feasibility should

be analyzed and compared with the ELT model and traditional energy supply method. In these regards, the main objectives of this study are as follows:

- The evaluation of the thermal loads—which includes the space heating load, swimming pool loss, and hot water demand—by developing a weather-data-based dynamic simulation model, and validation using reference data.
- The evaluation of the performance of the 440 kW PAFC-based CHP system in terms of primary energy saving, system efficiency, and CO₂ reduction with ELT and FTO models.
- The economic feasibility of the 440 kW PAFC-based CHP system in the aspects of net profit (NP) and payback period (PP) under different market conditions.

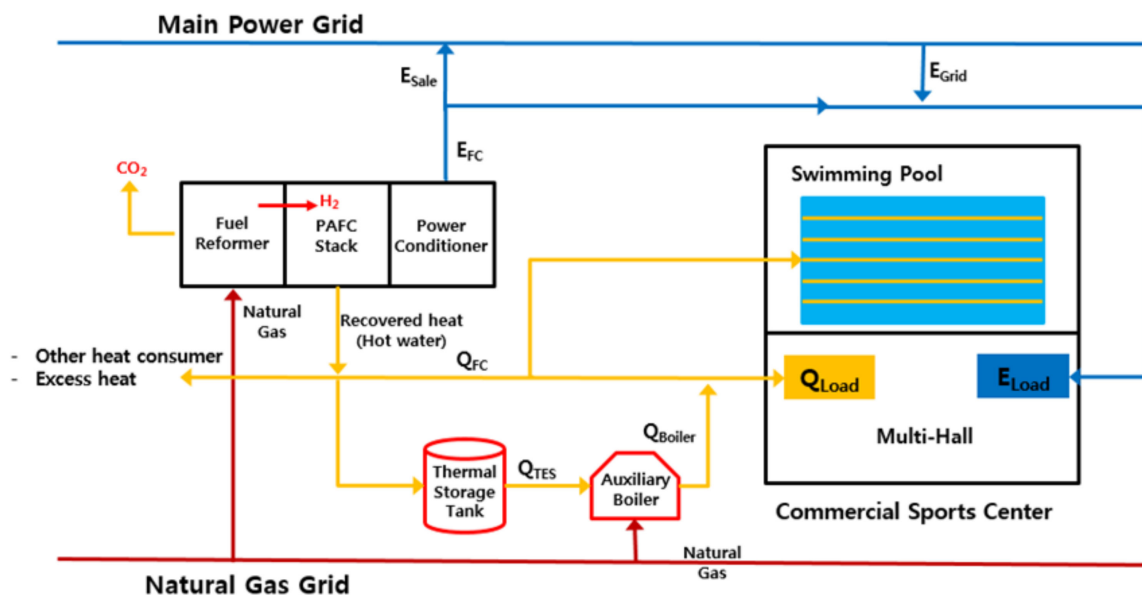


Figure 1. Configuration of the designed FC-CHP system.

2. Model Approach

Figure 2 describes the operating strategies of the designed FC-CHP system. For the ELT model, the fuel cell will operate following the building electricity demand. The power from the main city grid will be a supplement when the building electricity load is less than the minimum capacity (100 kW) or larger than the maximum capacity of the fuel cell (440 kW). In the meantime, the fuel cell's waste heat will be recovered and supply the building thermal energy demand directly, or will be re-stored in a thermal storage tank. When the fuel cell waste heat supply is insufficient, the heat in the heat storage tank will be released to meet the heating demand. When the system is operating under the FLO model, both the power and heat are the maximum generated. Unlike the ELT model, much more excess power is generated and could be sold onto the main power grid. An auxiliary boiler is used for some extreme conditions under both of the two operating models. The dynamic simulation results of the above two operating strategies of the FC-CHP system will be compared with the conventional energy supply strategy.

The dynamic simulation of the FC-CHP system based on the measured electricity load, evaluated thermal load, and fuel cell performance data was also produced in the TRNSYS software. Figure 3 presents the configuration of the model in the TRNSYS simulation studio. The components are modeled by parameters, inputs, and outputs, and are linked with each other by following the operating strategy. The parameters of the main components in the system are introduced in Table 2.

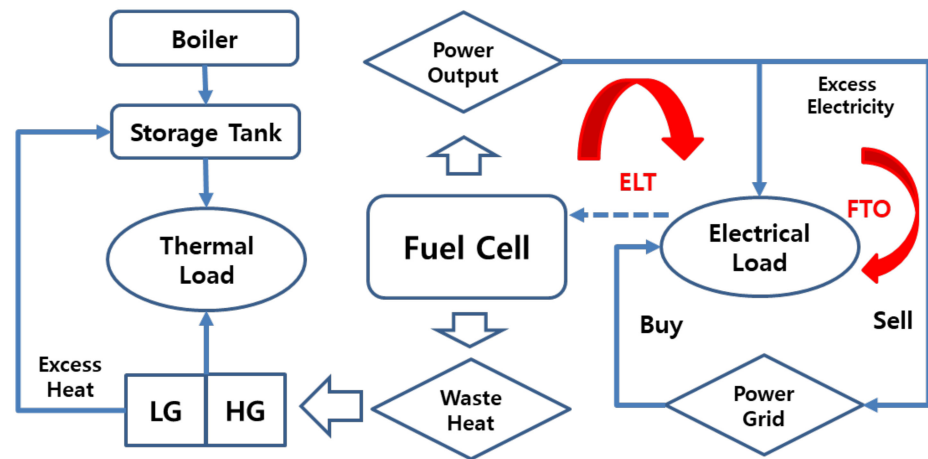


Figure 2. Operating strategy of FC-CHP system.

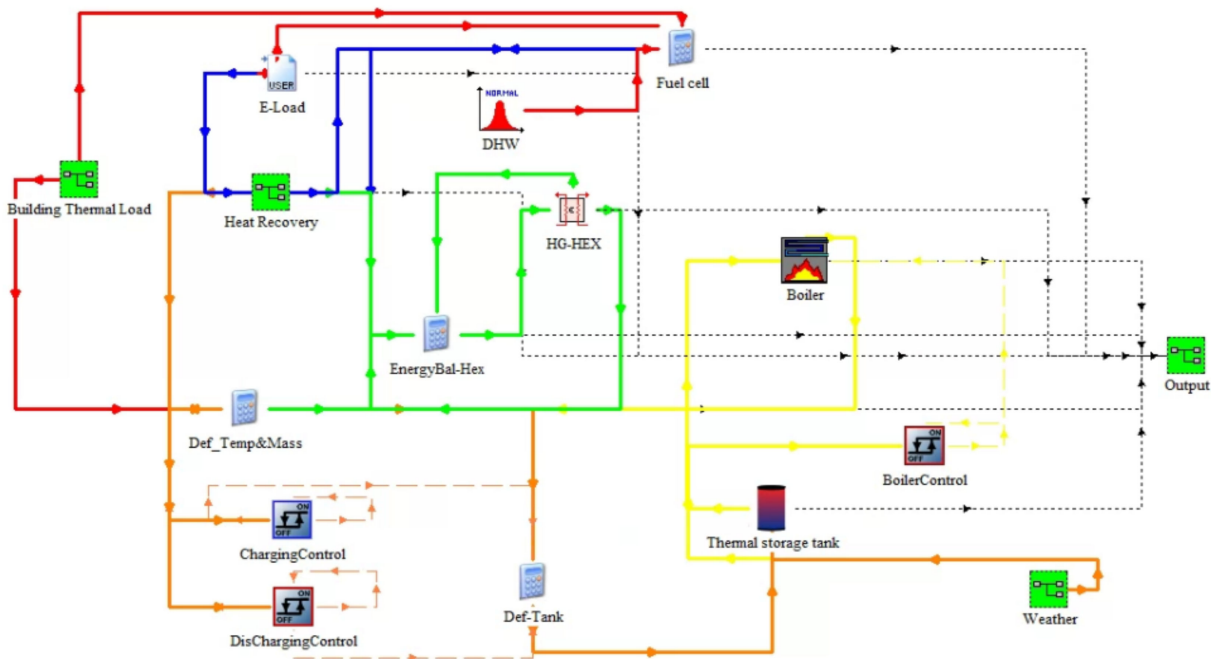


Figure 3. Interface of the fuel-cell-based CHP system simulation in the TRNSYS software.

Table 2. Parameters of the main components used in the system simulation.

Components	Parameters	Values
Fuel cell	Rated electrical capacity, kW	440
	Electrical efficiency, 100%	0.24–0.45
	Thermal efficiency, 100%	0.27–0.49
	Wasted water temperature, °C	60, 121
Heat exchanger	Efficiency, 100%	0.85
Thermal storage tank	Size, m ³	50
Auxiliary boiler	Rated capacity, kW	100

2.1. Performance Data of the PAFC

The performance data of the PAFC—which can present the correlations between the fuel cell’s operating part load and the power output, waste heat recovery, and the fuel energy consumption—was obtained from the fuel cell manufacturer [28], and is described in Figure 4. The PAFC can provide the maximum power of 440 kW, and was suggested

to operate with a turndown ratio of 0.227, which means the PAFC will not operate at less than 22.7% (about 100 kW) of its rated power. The recovered waste heat can be supplied to the thermal load of the building at two levels of water temperature: high-grade (HG, about 120 °C), and low-grade (LG, about 60 °C). Among them, the LG heat can be recovered over all of the operating time, and the HG heat can be recovered only when the part-load is larger than 51.1%. The electrical power efficiency and thermal efficiency of the fuel cell system are defined as:

$$\eta_{E-FC} = E_{FC} / F_{FC} \quad (1)$$

$$\eta_{Q-FC} = Q_{FC} / F_{FC} \quad (2)$$

where E_{FC} is the electric power produced by the fuel cell unit, Q_{FC} is the total recovered thermal energy, and F_{FC} is the fuel (natural gas) energy consumption of the fuel cell. Thus, the overall efficiency of the fuel cell system is given as:

$$\eta_{FC} = \eta_{E-FC} + \eta_{Q-FC} \quad (3)$$

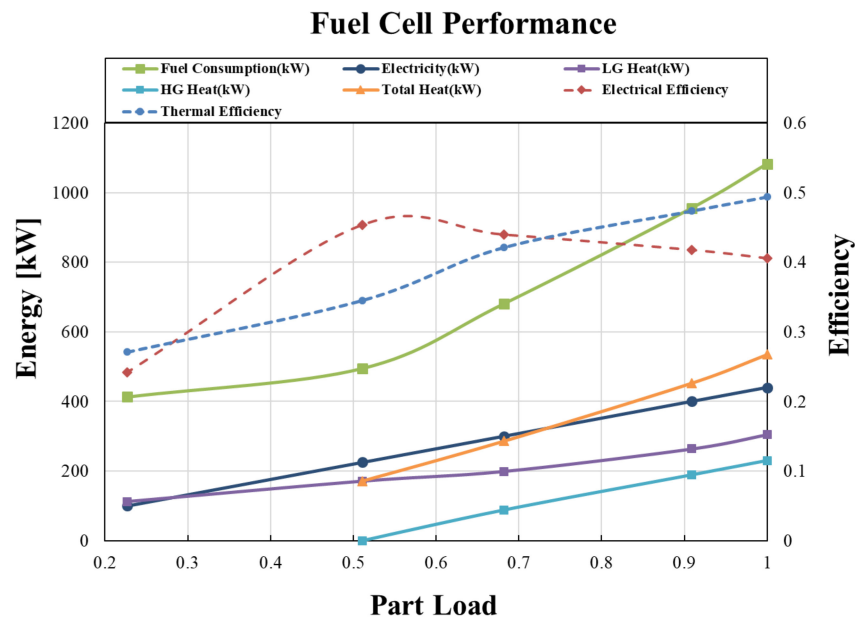


Figure 4. Correlation performance data for a 440 kW PAFC.

For the FTO model, it is suggested that the fuel cell is operated with the maximum power output all the time, even when the electrical power efficiency is not the highest. As shown in Figure 4, the η_{E-FC} , η_{Q-FC} and η_{FC} of the suggested PAFC with the maximum electrical power output reach 40.6%, 49.4%, and 90%, respectively. For the approached ELT model, the fuel cell energy production and efficiency will be calculated with the correlations by responding to the building energy load.

2.2. Electricity Load

In this study, a comprehensive sports center with an indoor swimming pool, which is under construction in Donghae City, Korea, is planned to use a 440 kW PAFC-based CHP system for its electrical and thermal energy supply. We first investigated the measured hourly electricity load of a referenced commercial building which has a similar location, construction, floor area, building function, and activity schedule for one year as the input data for the dynamic simulation. As shown in Figure 5a, high electricity demand is present in the summer season due to the large cooling energy which is consumed by the electric air conditioner, and after sorting the hourly load in descending order, it can be seen that there are about 2400 h of electricity demand in a year, which is higher than the maximum capacity of the fuel cell (440 kW), and thus requires auxiliary supply from the main power

grid if the fuel cell is operating with the FTO model. If the fuel cell is working with the ELT model, there is still about 3800 h of electricity demand that requires assistance from the main power grid, when the electricity load is lower than the minimum capacity of the fuel cell (100 kW). From a general calculation, about 4.18% and 13.28% electricity demand is required from the main power grid when the fuel cell is working with the FTO and ELT model respectively. The detailed electricity load distribution for the first week in January shown in Figure 5b presents a significant load profile of a commercial building. The measured data reflects the seasonal and daily characteristics of the electrical load well, and will be used as the input data for the dynamic system simulation.

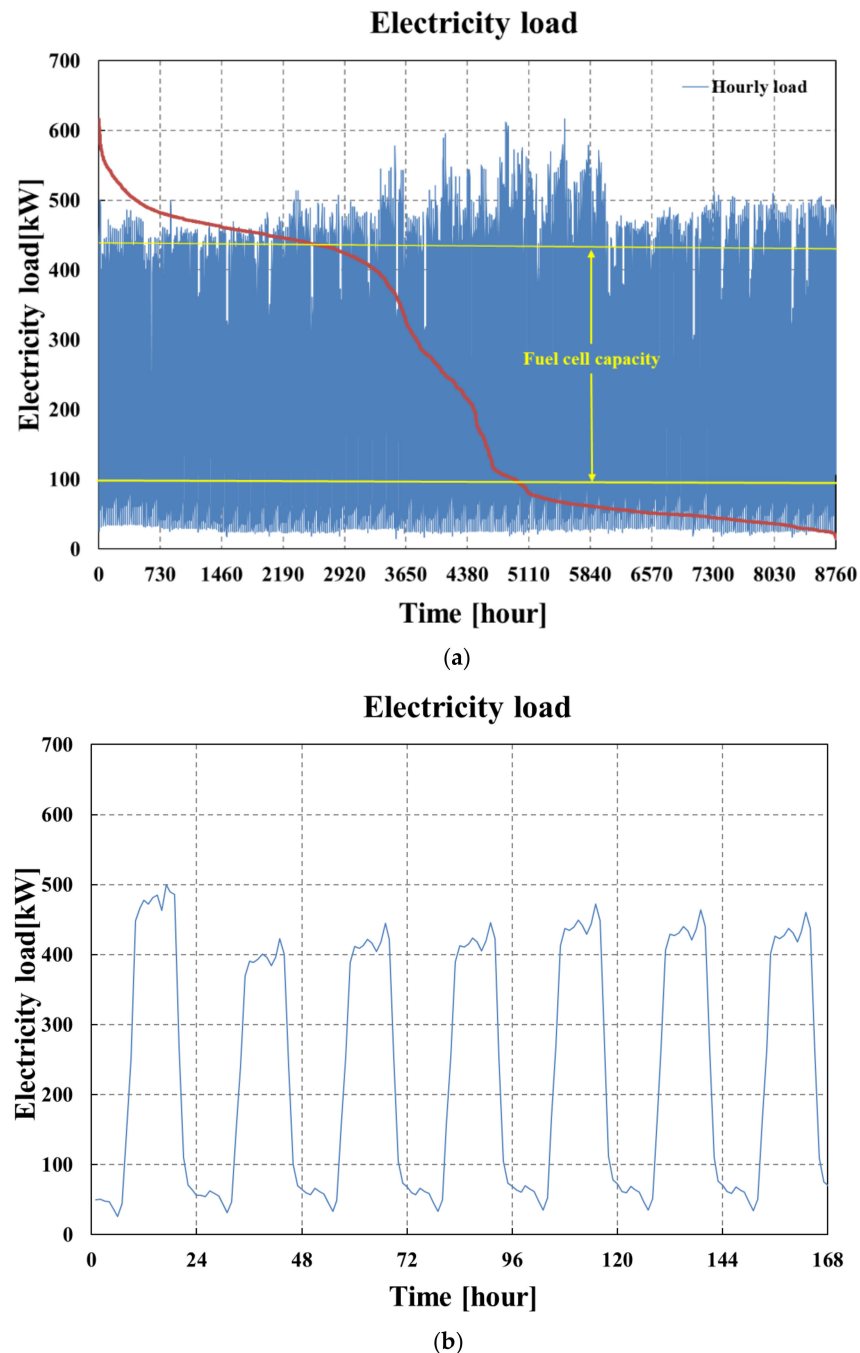
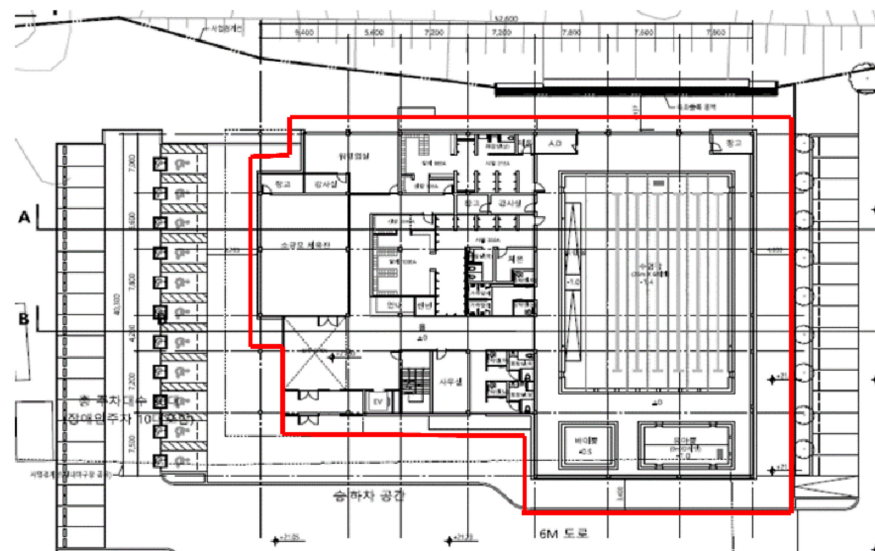


Figure 5. Measured electricity load ((a) annual; (b) weekly).

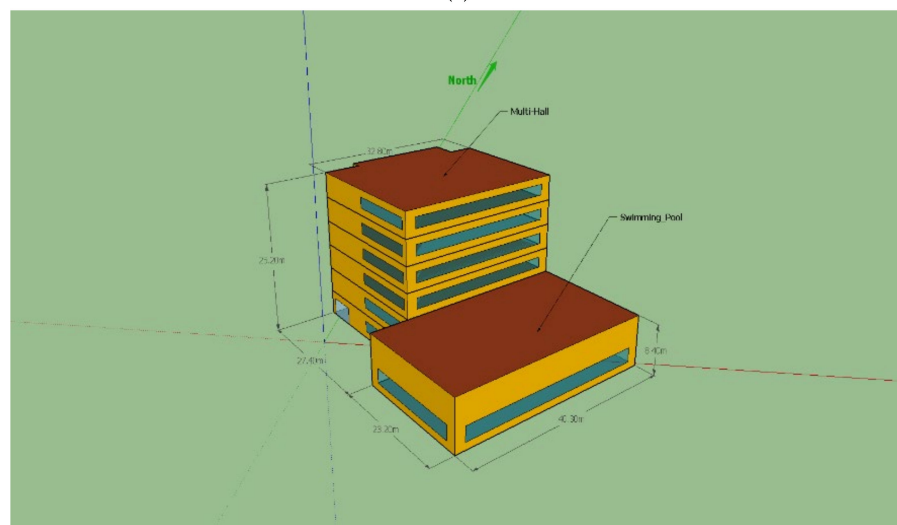
2.3. Thermal Load Evaluation

The thermal energy demand of the building is composed of three parts: space heating, swimming pool heat loss, and domestic hot water. A general method to investigate the thermal energy load is to account for the fuel consumption. However, in this study, it is difficult to obtain completed data on fuel consumption, especially in hours. Therefore, in this study, the commercial software TRNSYS—which has been approved by several researchers—is used to evaluate the thermal energy demand.

The 3D building model in TRNSYS is used for the space heating thermal load evaluation. The building geometry was first modelled using Google SketchUp, see Figure 6, then the material properties of the envelope were incorporated in TRNBuild, a 3D building-modelling program integrated into TRNSYS. After that, the weather data (ambient temperature, solar radiation, wind speed, soil temperature, etc.) were input to the TRNBuild component, and the hourly space heating load was calculated in TRNSYS Simulation Studio. The detailed configuration of thermal load macro that was integrated in the CHP system model is shown in Figure 7.



(a)



(b)

Figure 6. An architectural plan of the comprehensive sports center with an indoor swimming pool (a) and the 3D modeling (b).

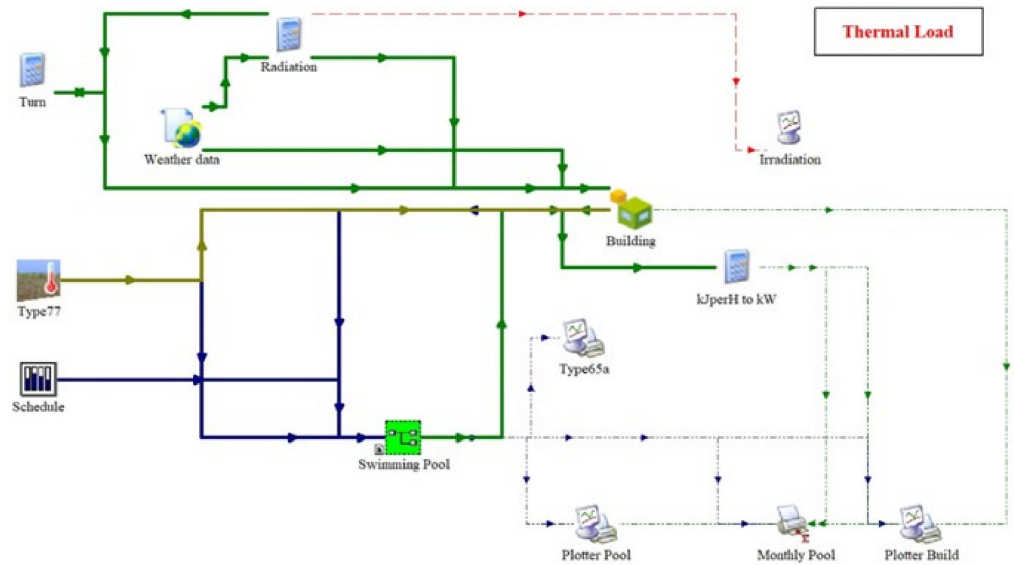


Figure 7. Interface of the building thermal load simulation macro in the TRNSYS software.

The evaluation of the heat loss of the indoor swimming pool is generally based on Thomas Auer’s model [29] and is integrated into the TRNSYS thermal load model. The heat loss of the swimming pool Q_{loss} includes four parts:

$$Q_{loss} = Q_{evp} + Q_{conv} + Q_{cond} + Q_{rad} \quad (4)$$

where Q_{evp} is the heat loss by evaporation from the swimming pool surface, which can be calculated by:

$$Q_{evp} = m_{evp}h_{evp} \quad (5)$$

where h_{evp} is the evaporation heat of the water at setting temperature (kJ/kg, 2439.3 kJ/kg for 26 °C water), and m_{evp} is the amount of evaporation water (kg/m²h), which can be calculated by [30]:

$$m_{evp} = A_s(4.08 + 4.28v)(x_{sa,m} - x_a) \quad (6)$$

where $x_{sa,m}$ and x_a are the maximum humidity ratio of saturated air at the same temperature as the water surface (kg/kg, 26 °C is 0.0212858 kg/kg) and the humidity ratio of ambient air (kg/kg, setting in TRNSYS). A_s is the surface area of the swimming pool.

The convection heat loss of swimming pool water Q_{conv} can be calculated on the basis of Newton’s formula:

$$Q_{conv} = hA_s(T_{sw} - T_{air}) \quad (7)$$

where T_{sw} and T_{air} are the temperatures of the swimming pool water and the indoor air, respectively. The convective heat transfer coefficient (W/m² °C) can be expressed as a linear function of the indoor air speed v , as follows [31]:

$$h = 2.8 + 3.0v \quad (8)$$

Due to the poor heat conductance of soil, the conductive heat loss through the side walls and bottom of the swimming pool is relatively small, and can be calculated by:

$$Q_{cond} = UA_{pw}(T_{sw} - T_{pw}) \quad (9)$$

where the A_{pw} is the wall and bottom area of the swimming pool. U is the conductive heat transfer coefficient (W/m² °C).

The heat transfer by long-wave radiation with the wall surfaces of the hall can be calculated on the basis of the Stefan–Boltzmann law (Equation (10)). For an indoor swimming pool, the pool area can be assumed to be completely enclosed.

$$Q_{rad} = \sigma \varepsilon A_s (T_{sw}^4 - T_{cel}^4) \quad (10)$$

where σ is the Stefan–Boltzmann constant ($5.67 \times 10^{-8} \text{ W/m}^2 \text{ }^\circ\text{C}^4$), and ε is the emissivity of the swimming pool water surface (0.9 in this study).

The domestic hot water is mainly consumed by the showering of the customers, and is given as normally distributed random values with a mean value of 25 kW in the simulation; the parameters for the TRNSYS simulation are listed in Table 3.

Table 3. Building and swimming pool parameters.

Components	Parameter with Units	Values
Building	Total floor area, m ²	7418.96
	Wall u-value, W/m ² K	0.651
	Window u-value, W/m ² K	1.1
	Window g-value, 100%	0.62
	Ground u-value, W/m ² K	0.295
	Indoor setting temperature, °C	25
	Indoor humidity ratio, 100%	0.5–0.7
Swimming pool	Surface area, m ²	25 × 15
	Depth, m	1.5
	Wall heat transfer coefficient, W/m ² K	0.25

3. Simulation Results

Thermal load validation is always required to validate a simulation result against measured data. In our case, due to the objective building being under plan, we collected the thermal energy consumption of the building which used to provide the electricity load. It is necessary to mention that unlike the electricity load, it is very difficult to obtain a complete fuel consumption, especially in hours. The daily fuel consumption data for the referenced commercial building is only available for the month of January 2020. The heat supply to the building is from a gas boiler with an average efficiency of 0.85 [32]. The loss from the delivery system is assumed to be 10%. The error indicators used in this study are the MBE (Mean Bias Error) and CV-RMSE (Coefficient of Variance of the Root Mean Square Error), defined as [33]:

$$\text{MBE} = \frac{\sum (\text{Measured}_{\text{day}} - \text{TRNSYS}_{\text{day}})}{\sum (\text{Measured}_{\text{day}})} \times 100\% \quad (11)$$

$$\text{CV-RMSE} = \frac{\text{RMSE}_{\text{day}}}{\text{Mean}(\text{Measured}_{\text{day}})} \times 100\% \quad (12)$$

$$\text{RMSE} = \sqrt{\frac{\sum (\text{Measured}_{\text{day}} - \text{TRNSYS}_{\text{day}})^2}{(\text{Numberofday}) - 1}} \quad (13)$$

Figure 8 compares the daily heating load predicted by TRNSYS with the measured data. Due to the missing measured data for the 1st, 23th, and 24th, the simulation result for these 3 days was also removed for the validation. After the processing, the MBE was within the acceptable range (less than 5%), but the CV-RMSE was above the criteria for a calibrated model (less than 15%). In consideration that the measured data was only evaluated from the normal record of boiler fuel consumption, not a strict experiment, we can say this is an acceptable error, and the thermal load evaluated by TRNSYS can be used in the dynamic simulation of the FC-CHP system. Figure 9 presents the results of the evaluation of the

space heating load and swimming pool heat loss based on the weather data of Donghae city. The peak load values are about 330 kW and 120 kW for space heating and swimming pool heat loss. For the swimming pool, high heat loss is also presented even in summer, due to the evaporation heat loss accounting for the largest proportion of the total heat loss.

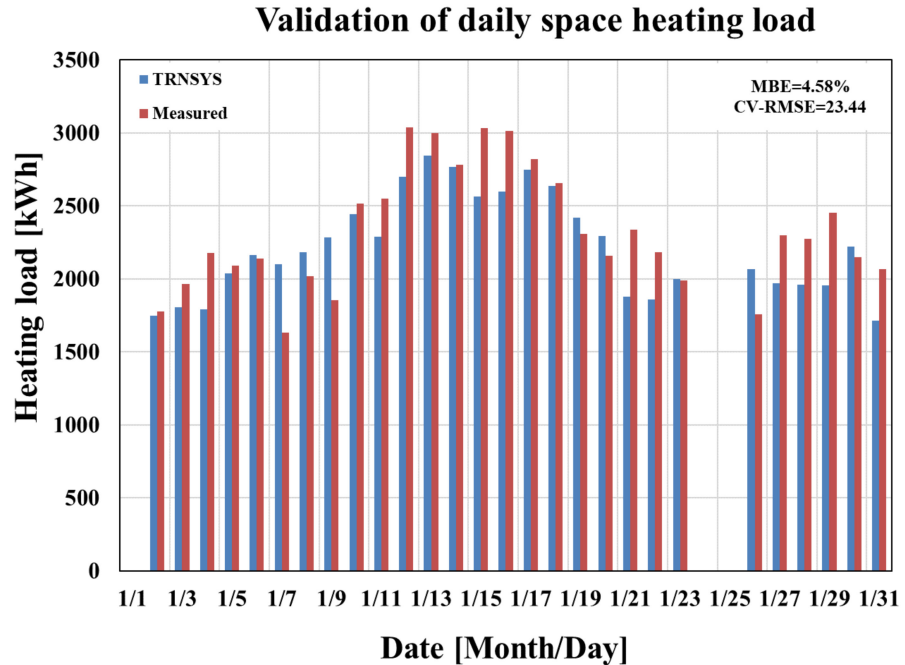


Figure 8. Validation of the daily heating energy consumption between the simulation data and measured data.

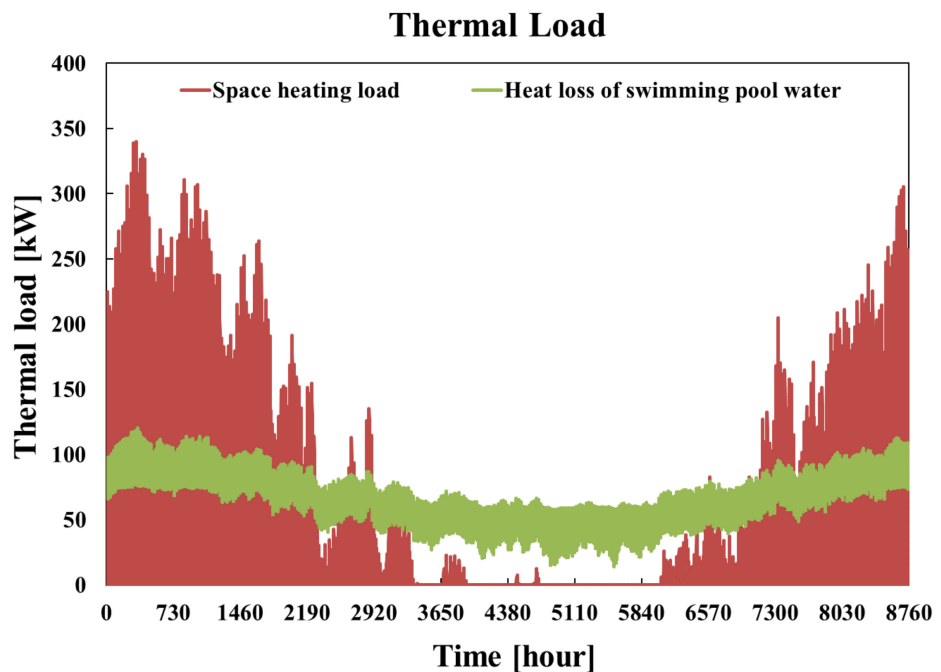
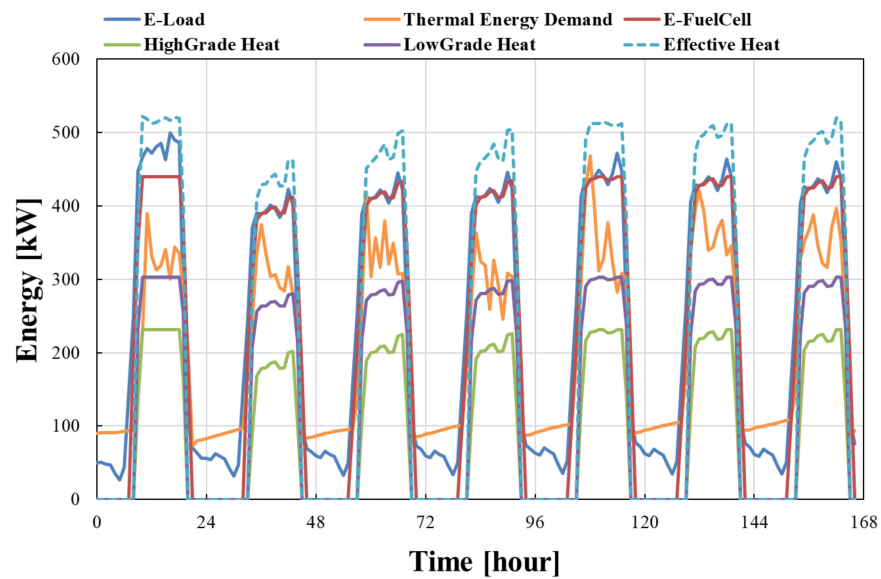


Figure 9. Building space heating load and swimming pool heat loss evaluated by the TRNSYS simulation.

Figure 10 presents the simulation results of the energy demand and supply of the FC-CHP system with the ELT (a) and FTO (b) FC operating strategy, including the building electricity load, thermal load, fuel cell electric power generation, heat generation (high grade and low grade), and effective heat. For the ELT model, the fuel cell will not work during the night time due to the electricity load being less than 100 kW, which is the

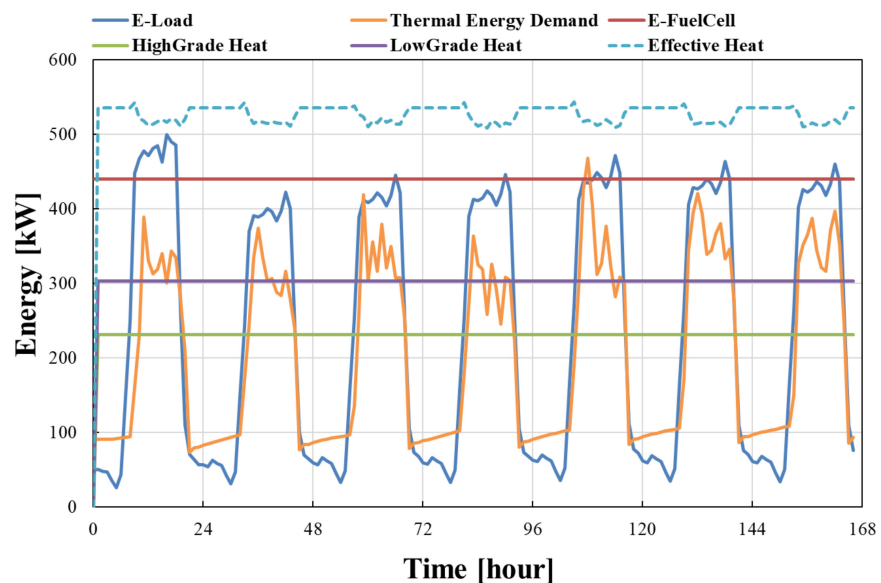
minimum electric power capacity of the fuel cell. For the FTO model, the fuel cell is working at the maximum capacity all of the time, so that both the electric power and thermal heat generation are presented as the constant maximum value. Here, it has to be mentioned that, for the thermal heat supply for a commercial building, the high-grade waste heat from a fuel cell that has a temperature of about 120 °C cannot be supplied to the building directly. A heat exchanger is recommended to transform the high-grade heat temperature to a low grade. Therefore, considering the heat exchanger efficiency, the effective heat is necessary to evaluate and be used for the analysis of the primary energy saving and economic feasibility.

Energy supply and demand (ELT)



(a)

Energy supply and demand (FTO)



(b)

Figure 10. Energy demand and supply of FC-CHP systems for the first week of January ((a) ELT model; (b) FTO model).

The primary energy consumption for both the ELT and FTO models are evaluated from the annual system simulation. The results are compared with a reference case with a conventional power and heat supply method. The primary energy consumption can be evaluated as:

$$PEC = F_{FC} + F_b + F_{GE} \quad (14)$$

where F_{FC} , F_b , and F_{GE} are the fuel energy consumption of the fuel cell, boiler, and electric power supplied from the main power grid. For the FC-CHP system, the fuel cell and boiler fuel energy consumption can be evaluated from the simulation directly. In the case of the conventional energy supply method, the efficiency of the gas boiler and grid power are assumed to be 0.85 [32] and 0.35 [34,35], respectively.

Figure 11 presents the monthly primary energy consumption in the case of the ELT and FTO models in the FC-CHP system, and the conventional energy supply. The ELT model has lower primary energy consumption than the other two cases, and compared with the reference case, it can save about 10% to 15% fuel energy in the winter season. During the summer, even the large heat loss of the swimming pool can be covered by the fuel cell waste heat; the energy saving is not obvious due to the fact that the fuel cell is always operated with a relatively low efficiency under the ELT model. The FTO model consumes much more fuel energy than the two other cases due to its longer working time and high electrical output capacity. However, from a macro point of view, the FTO model still has its own advantages, such as high electrical efficiency and high waste heat generation.

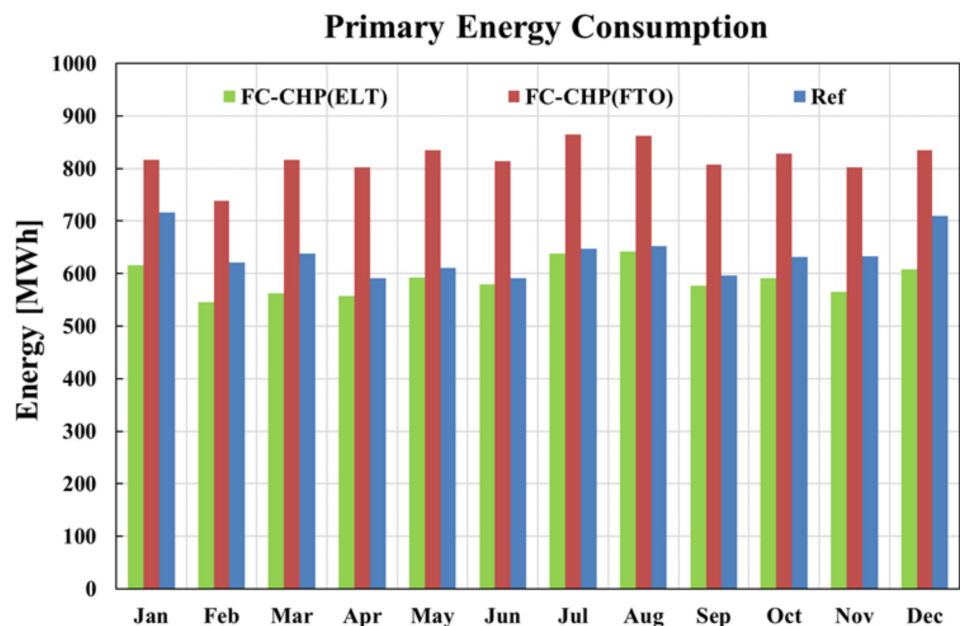


Figure 11. Primary energy consumption for the three case studies (ELT and FTO models in FC-CHP systems and the conventional energy supply model).

The CHP system can play an important role in both the primary energy saving and the reduction of CO₂ emissions. The evaluation of CO₂ emissions is complex due to its being highly dependent on the type of primary energy source. For the fuel cell system used in this study, from the manufacturer's report, the CO₂ emission factor is 0.453 tCO₂/MWh [28]. The CO₂ emission factors of coal and natural gas are assumed to be 0.9 and 0.4 tCO₂/MWh, respectively [36]. For the natural gas boiler, the emission factor is set to be 0.2 tCO₂/MWh. Therefore, by considering the fraction of electricity generation by the source types, the CO₂ emissions can be evaluated. As can be seen from Figure 12, whether the CHP system is operating in the ELT model or FTO model, the CO₂ emissions of the system are significantly lower than the traditional energy supply mode. Even the FTO model has a large primary energy consumption; the CO₂ emissions are still much lower than the conventional energy system due to the high fuel cell efficiency.

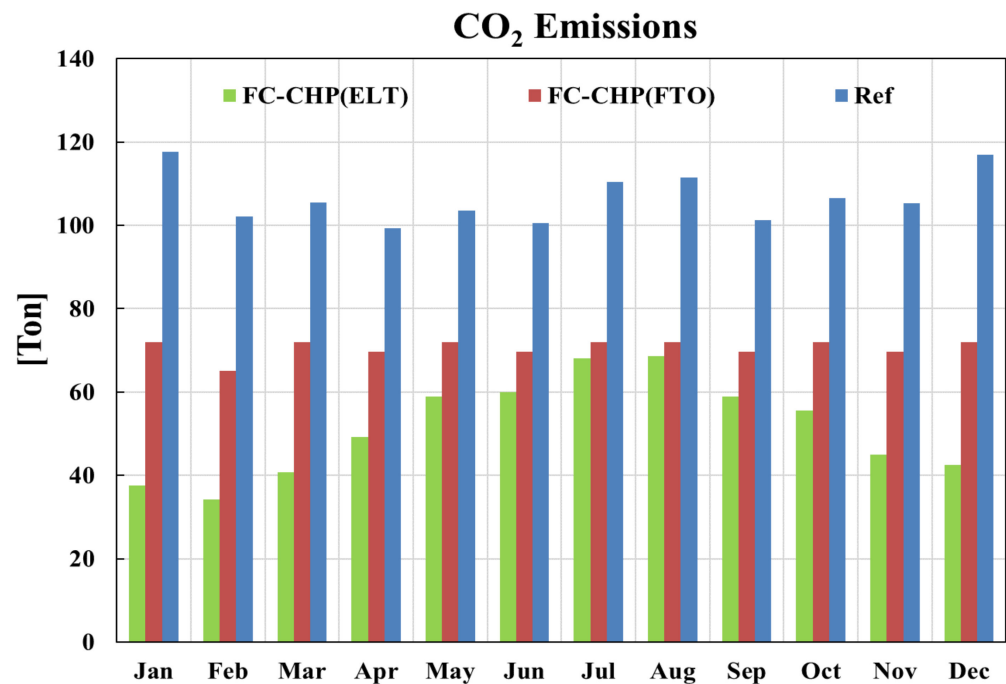


Figure 12. CO₂ emissions for the three case studies (ELT and FTO models in FC-CHP systems and the conventional energy supply model).

The fuel cell efficiency was defined in Equations (1)–(3). The fuel cell is supported to operate with a maximum capacity for all of the time under the FTO operating model so that it can give a significantly high efficiency than the ELT model which is operating by following the electricity load. Here, it has to be mentioned that, for the investigation of the fuel cell efficiency, only the total generation of power and heat are considered. Figure 13 shows the total efficiency of the fuel cell under both operating models. By considering the utilization of energy, the efficiency of the FC-CHP system can be evaluated as follows:

$$\eta_{FC-CHP} = (E_{FC} + Q_{FC-B}) / F_{FC} \quad (15)$$

where the E_{FC} is the electrical power generation from the fuel cell, Q_{FC-B} is the recovered heat from the fuel cell and supply to the building, and F_{FC} is the fuel (natural gas) energy consumption of the fuel cell. Here, the electric power generation for the FTO model includes both amounts which will be supplied to the building and sold to the grid. From Figure 14, we can see that for both the FTO and ELT models, the FC-CHP system presents higher efficiency in winter (about 55% to 60%) than in summer (40% to 50%), because of the high heating demand in winter. From the point of view of the overall efficiency of the fuel cell system, the FTO model has a large advantage over the ELT model. However, at the same time, a large amount of heat generated under the FTO operating model cannot be supplied to the building, but is released to the ambient environment. This is why, when it comes to the system's efficiency, there is not much difference between the two models.

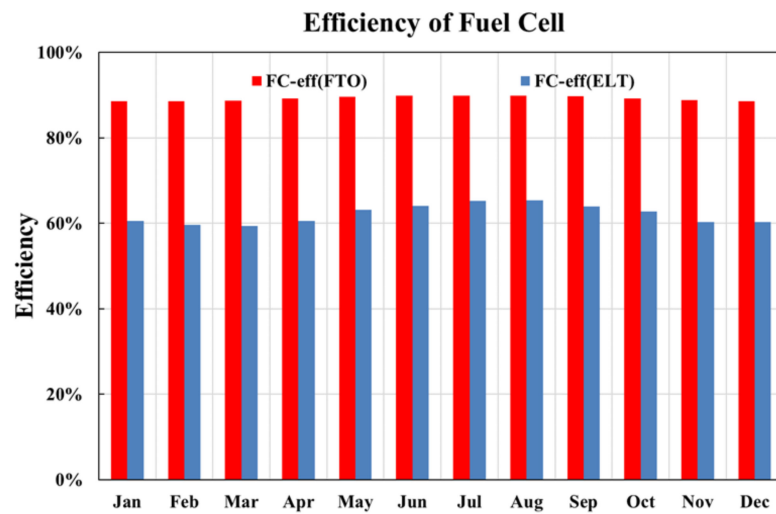


Figure 13. Total efficiency of the fuel cell under the FTO and ELT operating models.

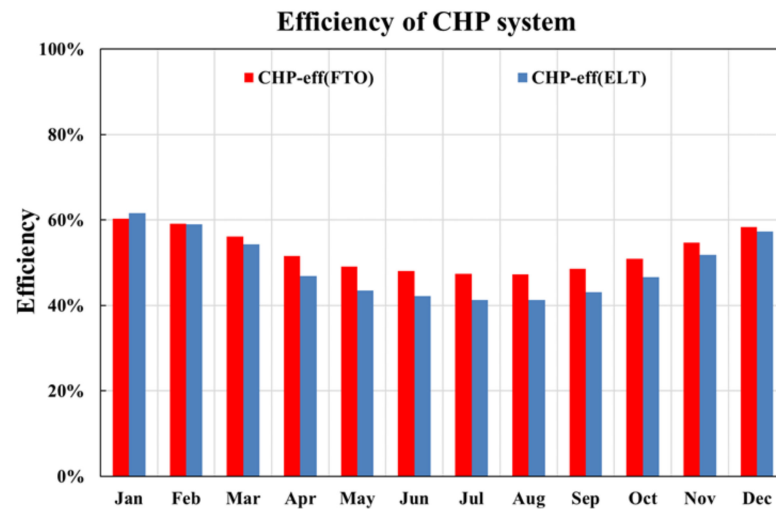


Figure 14. Efficiency of the FC-CHP system under the FTO and ELT operating models.

4. Economic Feasibility

From a general point of view, the fuel cell system is far from being economically feasible due to its high capital and operating cost [37]. However, a great potential has been presented for improving the utilization of energy productions, especially of thermal energy, due to the high heat demand of the commercial building in this study. The operating cost of the power and heat supply for the objective commercial building with an indoor swimming pool can be evaluated as:

$$C = C_f + C_{GE} - S_{EG} \quad (16)$$

where C_f is the cost of the fuel consumption of the fuel cell and boiler for both FC-CHP and conventional energy supply system. C_{GE} is the electric power cost from the main power grid, and S_{EG} is the income created by selling the excess electric power to the main power grid. The price of liquid natural gas (LNG) for industry and fuel cell applications is given as 44.98 and 44.13 USD/MWh (VAT included), respectively [38]. Unlike the price of natural gas, the selling price of fuel cell electricity to the grid is relatively unstable, and should be evaluated as:

$$p_{sell} = SMP + c_{FC}REC \quad (17)$$

In Korea, when selling electricity produced by fuel cell, the price is determined by the System Marginal Price (SMP) [39] and the unit price of Renewable Energy Certificates

(REC). REC certifies that power generators produced and supplied electricity by using new and renewable energy facilities, and the weighting factor of fuel cell (c_{FC}) application in Korea is given to be two [40]. Due to the fact that the SMP and the price of REC may fluctuate in real-time, which will have big impacts on the selling price of the electricity, a sensitivity analysis for the effect of the SMP and REC price was carried out by setting the selling price to low, medium and high levels. In Table 4, the monthly average value of the SMP and REC from January 2019 to present are evaluated and set to be the medium level of the price. The low and high level of the price are evaluated by raising and lowering the medium level price by 15%, respectively.

Table 4. SMP and REC prices.

	SMP (USD/MWh)	REC (USD/MWh)
Low (L)	60.24797	36.17903
Medium (M)	70.87996	42.56356
High (H)	81.51196	48.94809

Finally, the net profit (NP) for the FC-CHP system compared with the conventional energy supply system is evaluated as:

$$NP = C_{FC-CHP} - C_{REF} \quad (18)$$

The payback period (PP) is another important indicator for the evaluation of economic feasibility. Unlike a general economic model, the main benefit of applying the FC-CHP system is to obtain energy and cost saving by methods other than the traditional energy supply mode. Therefore, the payback period of the FC-CHP system could be simply evaluated by

$$PP = C_0 / (NP - C_{MD}) \quad (19)$$

Here, C_0 and C_{MD} are the initial cost of the fuel cell system installation, and the maintenance and depreciation cost, respectively. The investment costs, including the fuel cell cost, installation cost, maintenance and depreciation costs are listed in Table 5. Here, it has to be mentioned that for both of the CHP and traditional system, the boiler and storage tank are needed. In this study, the cost saving by the reduction of the storage tank and boiler capacities are ignored.

Table 5. Investigation of the investment and incentive.

Total cost for fuel cell CHP system	\$1,800,000
Installation cost	\$600,000
Maintenance and depreciation costs	\$50,000/year
Incentive from local government	\$500,000
Total initial cost (with incentive)	\$1,900,000
Total initial cost (without incentive)	\$2,400,000

Table 6 summarizes the monthly operating cost and the net profit of the FC-CHP system under the ELT by comparing it with the conventional system. For the ELT model, the economic benefits are not significant. Even in March, April, May, September, and October, there is not only the profit but also the amount of loss presented. In the case of the FTO model, a sensitivity analysis for the economic feasibility is needed due to the large fluctuation of the SMP and REC prices. As shown in Table 4, the SMP and REC price are evaluated into low (L), medium (M) and high (H) levels. Thus, a total of nine market conditions of the electricity selling price are defined by the combination of the SMP and REC prices in different levels. For example, the condition of “LM” indicates that the

electricity selling price will be calculated with the low level of the SMP and the medium level of the REC price. Table 7 presents the monthly and annual operating costs of the FC-CHP system under the FTO model and the net profit (NP) by comparing them with the conventional energy supply system in MM condition. A significant net profit is obtained due to that the fuel cell operating for the full time within its rated capacity. A large amount of excess electricity could be sold to the grid. The annual net profit is about 226,097 USD in the MM condition.

Table 6. Operating cost of the FC-CHP model under the ELT operating model and the net profit (NP), in comparison with the conventional energy supply system.

Comparison Data Sets of Operating Cost (\$: USD)							
Month	New System with FC-CHP (ELT)			Reference Data from Conventional System			NP
	Fuel Cost	e-Cost	Total	Fuel Cost	e-Cost	Total	
Jan	23,835	2861	26,696	9446	25,103	34,549	7853
Feb	21,217	2572	23,789	8049	22,489	30,538	6748
Mar	22,363	1930	24,293	7504	17,832	25,337	1043
Apr	21,782	2212	23,994	5174	17,993	23,168	−827
May	22,888	2458	25,347	4156	18,886	23,042	−2305
Jun	22,280	3605	25,885	3544	26,995	30,540	4655
Jul	23,710	3449	4655	3344	28,338	31,682	27,026
Aug	23,695	4830	28,525	3295	28,419	31,714	3188
Sep	22,247	2434	24,680	3780	18,642	22,422	−2259
Oct	22,896	2401	25,297	5033	19,252	24,285	−1012
Nov	21,905	3006	24,911	6604	24,344	30,948	6037
Dec	23,214	3394	26,608	8548	25,641	34,189	7581
Sum	272,032	35,152	284,680	68,478	273,934	342,412	57,728

Table 7. Operating cost of the FC-CHP model under the FTO operating model and net profit (NP), in comparison with the conventional energy supply system.

Comparison Data Sets of Operating Cost (\$: USD)								
Month	New System with FC-CHP (FTO)				Reference Data from Conventional System			NP
	Fuel Cost	e-Cost	e-Sale	Total	Fuel Cost	e-Cost	Total	
Jan	35,432	843	26,948	9327	9446	25,103	34,549	25,222
Feb	32,004	849	25,275	7578	8049	22,489	30,538	22,960
Mar	35,432	810	29,030	7212	7504	17,832	25,337	18,125
Apr	34,289	1104	27,468	7925	5174	17,993	23,168	15,242
May	35,432	1268	27,105	9596	4156	18,886	23,042	13,447
Jun	34,289	1857	25,853	10,294	3544	26,995	30,540	20,246
Jul	35,432	2881	25,409	12,904	3344	28,338	31,682	18,777
Aug	35,432	2780	25,074	13,139	3295	28,419	31,714	18,575
Sep	34,289	1250	25,538	10,001	3780	18,642	22,422	12,421
Oct	35,432	1122	26,630	9925	5033	19,252	24,285	14,359
Nov	34,289	1291	26,899	8682	6604	24,344	30,948	22,267
Dec	35,432	1514	27,214	9733	8548	25,641	34,189	24,456
Sum	417,189	17,569	318,442	116,315	68,478	273,934	342,412	226,097

Figure 15 presents the net profits and payback period in nine price conditions when the system is operating with the FTO model. The net profit made in comparison with the conventional energy supply system is about 178,352 to 273,879 USD per year. As we investigated, the initial costs for a 440 kW PAFC base CHP system with and without incentives are around 1,900,000 and 2,400,000 USD, respectively. If the system is operating with the FTO model, the payback periods with and without incentives from the local government are 6.9 to 10.7 years and 8.8 to 13.5 years, respectively.

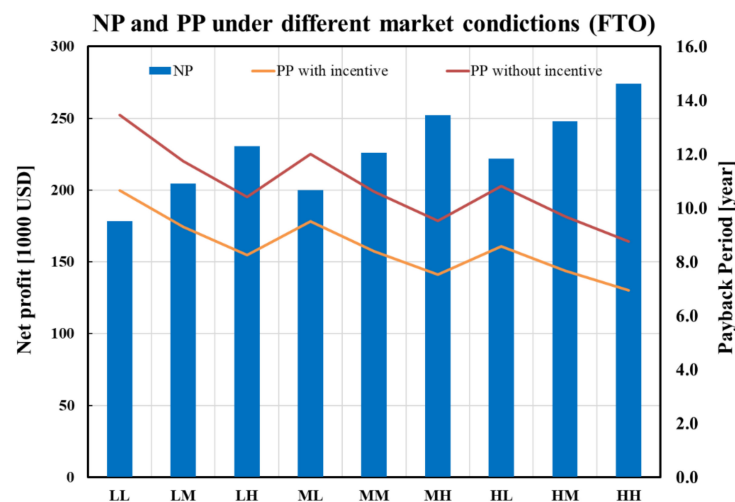


Figure 15. Net profit and payback period under the FTO model with different electricity market conditions.

5. Conclusions

In this study, a comprehensive sports center with an indoor swimming pool which is under construction in Donghae City, Korea is supported by a 440 kW PAFC-based CHP system for its electrical and thermal energy supply. The dynamic simulation of the energy supply system based on the investigated fuel cell performance data, the electrical load of a reference commercial building, and the evaluated thermal load was carried out for the cases with the ELT and FTO operating model. From the results, several key conclusions can be derived as follows:

1. A weather-data-based dynamic simulation model of the FC-CHP system including the components of the 3D-building load, fuel cell system, back-up boiler, heat exchanger, and storage tank was developed. The thermal load was obtained from the dynamic simulation, and was well-validated by the measured data. It can provide a reliable basis for the system simulation, thereby enhancing the credibility of the simulation results.
2. The FTO model was applied as one of the strategies for the fuel cell operating in a CHP system, and was simulated by the dynamic model and compared with the ELT model—which has been widely used in the CHP systems—and the conventional energy supply system in the aspects of primary energy consumption, fuel cell and system efficiency, and CO₂ emissions. From the simulation results, the FTO model presents the highest primary energy consumption and fuel cell efficiency, due to its long operating time and high capacity. The ELT model presents the lowest primary energy consumption, and can save 10% to 15% of the energy compared to the conventional energy system. However, the ELT model has a relatively low fuel cell efficiency compared to the FTO model. For both of FTO and ELT models, the FC-CHP system presents higher efficiency and CO₂ reduction.
3. In the analysis of the economic feasibility, the FTO model presents much better potential than the ELT model. The net profit made in comparison with the conventional energy supply system is about 178,352 to 273,879 USD per year, and the payback period is expected to be 6.9 to 10.7 years under different market conditions.
4. Based on the analyses of the performance and economic feasibility of the system, the FTO model is suggested to be the operating strategy for the design of the fuel cell CHP system. However, more case studies with novel design parameters and operating strategies should be tested in future work.
5. As the objective building in this study is in construction now, the results obtained in this study should be validated by the real measured data after the system's completion.

More verification and testing will be helpful to improve the computational model, and thus make it more widely utilized.

Author Contributions: J.L., performed the system modeling and numerical analyses, and drafted the manuscript. S.-C.K., discussed the results. K.-Y.S., collected the measured data, organized the overall evaluation, and reviewed the manuscript. All authors have read and agreed to the published version of the manuscript.

Funding: This research received no external funding.

Institutional Review Board Statement: Not applicable.

Informed Consent Statement: Not applicable.

Data Availability Statement: Not applicable.

Acknowledgments: This work was funded by Donghae City, Gangwon Province, and supported by Donghae Coal-Fired Power Plant in Korea East-West Power Company and A1 Engineering, as a project partner. The authors really appreciate their support during this project.

Conflicts of Interest: The authors declare no conflict of interest.

Nomenclature

A	Area (mm^2)
AFC	Alkaline fuel cell
c	Impact factor of renewable energy
C	Cost (\$USD)
CHP	Combined heat and power
CV-RMSE	Coefficient of variance of the root mean square error
E	Electric power, energy (kW, kWh)
F	Fuel energy consumption
FC-CHP	Fuel-cell-based combined heat and power
h	Convective heat transfer coefficient (W/mK);
h_{evp}	Evaporation heat (kJ/kg)
m_{evp}	Mass of evaporation water ($\text{kg}/\text{m}^2\text{h}$)
MBE	Mean bias error
MCFC	Molten carbonate fuel cell
NP	Net profit (USD/year)
p	Price (USD/kWh)
PAFC	Phosphoric acid fuel cell
PEMFC	Proton exchange membrane fuel cell
PP	Payback period (year)
Q	Heat (kW)
REC	Renewable energy certificates
S	Economic income
SMP	System marginal price (USD/MWh)
SOFC	Solid oxide fuel cell
T	Temperature ($^{\circ}\text{C}$)
U	Conductive heat transfer coefficient (W/mK)
v	Indoor air speed (m/s)
x	Humidity ratio (kg/kg)
Greek symbols	
ε	Emissivity
σ	Stefan–Boltzmann constant ($\text{W}/\text{m}^2\text{K}^4$)

Subscripts

0	Initial
<i>a</i>	Air
<i>b</i>	Boiler
<i>cel</i>	Celling
<i>cond</i>	Conduction
<i>conv</i>	Convection
<i>evp</i>	Evaporation
EG	Electric power sold to the main power grid
<i>f</i>	Fuel
FC	Fuel cell
FC-B	Fuel cell to building
FC-CHP	Fuel-cell-based CHP system
GE	Electric power supplied from the main power grid
<i>pw</i>	Wall surfaces of the swimming pool
<i>rad</i>	Radiation
REF	Reference
S	Surface of the swimming pool
<i>sw</i>	Swimming pool water

References

- Arsalis, A. A comprehensive review of fuel cell-based micro-combined-heat-and-power systems. *Renew. Sustain. Energy Rev.* **2019**, *105*, 391–414. [CrossRef]
- Mago, P.J.; Smith, A.D. Evaluation of the potential emissions reductions from the use of CHP systems in different commercial buildings. *Build. Environ.* **2012**, *53*, 74–82. [CrossRef]
- Ahmed, S.; Papadimas, D.D.; Ahluwalia, R.K. Configuring a fuel cell based residential combined heat and power system. *J. Power Sources* **2013**, *242*, 884–894.
- Chamra, L.M.; Mago, P.J. Micro-CHP power generation for residential and small commercial buildings (Ch. 2). In *Electric Power Research Trends*; Schmidt, M.C., Ed.; Nova Science Publisher, Inc.: New York, NY, USA, 2007.
- Gandiglio, M.; Lanzini, A.; Santarelli, M.; Leone, P. Design and optimization of a proton exchange membrane fuel cell CHP system for residential use. *Energy Build.* **2014**, *69*, 381–393.
- Löbberding, L.; Madlener, R. Techno-economic analysis of micro fuel cell cogeneration and storage in Germany. *Appl. Energy* **2019**, *235*, 1603–1613. [CrossRef]
- Staffell, I.; Ingram, A. Life cycle assessment of an alkaline fuel cell CHP system. *Int. J. Hydrogen Energy* **2010**, *35*, 2491–2505. [CrossRef]
- U.S. Department of Energy. Available online: https://www.energy.gov/sites/prod/files/2016/06/f32/fcto_fuel_cells_comparison_chart_apr2016.pdf (accessed on 15 March 2021).
- Verhaert, I.; Mulder, G.; De Paepe, M. Evaluation of an alkaline fuel cell system as a micro-CHP. *Energy Conv. Manag.* **2016**, *126*, 424–445.
- Wang, Y.; Chen, K.S.; Mishler, J.; Cho, S.C.; Adroher, X.C. A review of polymer electrolyte membrane fuel cells: Technology, applications, and needs on fundamental research. *Appl. Energy* **2011**, *88*, 981–1007. [CrossRef]
- Kang, K.; Yoo, H.; Han, D.; Jo, A.; Lee, J.; Ju, H. Modeling and simulations of fuel cell systems for combined heat and power generation. *Int. J. Hydrogen Energy* **2016**, *41*, 8286–8295.
- Chahartaghi, M.; Kharkeshi, B.A. Performance analysis of a combined cooling, heating and power system with PEM fuel cell as a prime mover. *Appl. Therm. Eng.* **2018**, *128*, 805–817.
- Park, Y.J.; Min, G.; Hong, J. Comparative study of solid oxide fuel cell-combined heat and power system designs for optimal thermal integration. *Energy Conv. Manag.* **2019**, *182*, 351–368. [CrossRef]
- Naimaster IV, E.J.; Sleiti, A.K. Potential of SOFC CHP systems for energy-efficient commercial buildings. *Energy Build.* **2013**, *61*, 153–160.
- Sorace, M.; Gandiglio, M.; Santarelli, M. Modeling and techno-economic analysis of the integration of a FC based micro-CHP system for residential application with a heat pump. *Energy* **2017**, *120*, 262–275.
- Napoli, R.; Gandiglio, M.; Lanzini, A.; Santarelli, M. Techno-economic analysis of PEMFC and SOFC micro-CHP fuel cell systems for the residential sector. *Energy Build.* **2015**, *103*, 131–146.
- Zhang, H.; Lin, G.; Chen, J. Multi-objective optimisation analysis and load matching of a phosphoric acid fuel cell system. *Int. J. Hydrogen Energy* **2012**, *37*, 3438–3446. [CrossRef]
- Wu, M.; Zhang, H.; Zhao, J.; Wang, F.; Yuan, J. Performance analyzes of an integrated phosphoric acid fuel cell and thermoelectric device system for power and cooling cogeneration. *Int. J. Refrig.* **2018**, *89*, 61–69. [CrossRef]
- Sammes, N.; Bove, R.; Stahl, K. Phosphoric acid fuel cells: Fundamentals and applications. *Curr. Opin. Solid State Mat. Sci.* **2004**, *8*, 372–378. [CrossRef]

20. Chen, X.; Wang, Y.; Cai, L.; Zhou, Y. Maximum power output and load matching of a phosphoric acid fuel cell-thermoelectric generator hybrid system. *J. Power Sources* **2015**, *294*, 430–436.
21. Ito, H. Economic and environmental assessment of phosphoric acid fuel cell-based combined heat and power system for an apartment complex. *Int. J. Hydrogen Energy* **2017**, *42*, 15449–15463. [CrossRef]
22. Acha, S.; Le Brun, N.; Damaskou, M.; Fubara, T.C.; Mulgundmath, V.; Markides, C.N.; Shah, N. Fuel cells as combined heat and power systems in commercial buildings: A case study in the food-retail sector. *Energy* **2020**, *206*, 118046. [CrossRef]
23. Mago, P.J.; Fumo, N.; Chamra, L.M. Performance analysis of CCHP and CHP systems operating following the thermal and electric load. *Int. J. Energy Res.* **2009**, *33*, 852–864. [CrossRef]
24. Im, Y.H.; Liu, J. Feasibility study on the low temperature district heating and cooling system with bi-lateral heat trades model. *Energy* **2018**, *153*, 988–999. [CrossRef]
25. Hawkes, A.D.; Leach, M.A. Cost-effective operating strategy for residential micro-combined heat and power. *Energy* **2007**, *32*, 711–723. [CrossRef]
26. Yan, H.L.; Wang, G.P.; Lu, Z.W.; Tan, P.; Kwan, T.H.; Xu, H.R.; Chen, B.; Ni, M.; Wu, Z. Techno-economic evaluation and technology roadmap of the MWe-scale SOFC-PEMFC hybrid fuel cell system for clean power generation. *J. Clean Prod.* **2020**, *255*, 120225. [CrossRef]
27. Al-Khori, K.; Bicer, Y.; Aslam, M.I.; Koç, M. Flare emission reduction utilizing solid oxide fuel cells at a natural gas processing plant. *Energy Rep.* **2021**, 5627–5638. [CrossRef]
28. Doosan Fuel Cell. Available online: <https://www.doosanfuelcell.com/en> (accessed on 21 May 2021).
29. Thomas Auer, Assessment of an Indoor or Outdoor Swimming Pool, TRNSYS-TYPE 144. Available online: <https://sel.me.wisc.edu/trnsys/components/type144-manual.pdf> (accessed on 20 March 2021).
30. Smith, C.C.; Lof, G.O.G.; Jones, R.W. Rates of evaporation from swimming pools in active use. *ASHRAE Trans* **1998**, *104*, 14–23.
31. Lam, J.C.; Chan, W.W. Life cycle energy cost analysis of heat pump application for hotel swimming pools. *Energy Conv. Manag.* **2001**, *42*, 1299–1306. [CrossRef]
32. Liu, J.; Chunga, D.H.; Chung, M.; Im, Y.H. Development of load models and operation simulator for a building complex with mixtures of multi-type engines and renewable devices. *Energy Build.* **2018**, *158*, 831–847. [CrossRef]
33. Djunaedy, E.; Van Den Wymelenberg, K. Targeted Calibration of Energy Models for Existing Building. In Proceedings of the ASHRAE 2014 Conference, Seattle, WA, USA, 28 June–2 July 2014.
34. IEA (2021). Available online: <https://www.iea.org/countries/korea> (accessed on 30 May 2021).
35. Hong, J.H.; Kim, J.; Son, W.; Shin, H.; Kim, N.; Lee, W.K.; Kim, J. Long-term energy strategy scenarios for South Korea: Transition to a sustainable energy system. *Energy Policy* **2019**, *127*, 425–473. [CrossRef]
36. Nam, H.; Nam, H.; Lee, D. Potential of hydrogen replacement in natural-gas-powered fuel cells in Busan, South Korea based on the 2050 clean energy Master Plan of Busan Metropolitan City. *Energy* **2021**, *221*, 119783. [CrossRef]
37. Sevenscan, S.; Lindbergh, G.; Lagergren, C.; Alvfors, P. Economic feasibility study of a fuel cell-based combined cooling, heating and power system for a data center. *Energy Build.* **2016**, *111*, 218–223. [CrossRef]
38. Korea City Gas Association. Available online: <http://www.citygas.or.kr/index.jsp> (accessed on 25 June 2021).
39. Ministry of Trade, Industry and Energy. Available online: <http://english.motie.go.kr/www/main.do> (accessed on 30 September 2021).
40. Korea Energy Agency. Available online: https://dco.energy.or.kr/renew_eng/main/main.aspx (accessed on 30 September 2021).

Article

Investigating the Impact of Plumbing Configuration on Energy Savings for Falling-Film Drain Water Heat Recovery Systems

Ramin Manouchehri * and Michael R. Collins

Solar Thermal Research Laboratory, Department of Mechanical and Mechatronics Engineering,
University of Waterloo, Waterloo, ON N2L 3G1, Canada; mike.collins@uwaterloo.ca

* Correspondence: ramin.manouchehri@uwaterloo.ca

Abstract: Falling-film drain water heat recovery (DWHR) systems are heat exchangers utilized in residential buildings for recovering energy from greywater. A recent publication by the authors contained a validated model that can be used to predict the performance of DWHR heat exchangers under variable flowrates and temperatures, and this work shows the implementation of the model into Transient System Simulation Tool (TRNSYS) software to perform energy simulations. This work aims to show the different plumbing configurations in which DWHR heat exchangers could be installed, and to simulate their performance under various conditions. The results show that plumbing configuration has a significant impact on energy savings expected from DWHR heat exchangers, and maximum savings are achieved in equal-flow configuration. However, other plumbing configurations provide significant savings, and the mains temperature could dictate which configuration provides higher energy savings.

Keywords: falling-film drain water heat recovery; heat exchanger; TRNSYS; energy simulations; variable plumbing configuration

Citation: Manouchehri, R.; Collins, M.R. Investigating the Impact of Plumbing Configuration on Energy Savings for Falling-Film Drain Water Heat Recovery Systems. *Energies* **2022**, *15*, 1141. <https://doi.org/10.3390/en15031141>

Academic Editor: Jan Danielewicz

Received: 31 December 2021

Accepted: 31 January 2022

Published: 3 February 2022

Publisher's Note: MDPI stays neutral with regard to jurisdictional claims in published maps and institutional affiliations.



Copyright: © 2022 by the authors. Licensee MDPI, Basel, Switzerland. This article is an open access article distributed under the terms and conditions of the Creative Commons Attribution (CC BY) license (<https://creativecommons.org/licenses/by/4.0/>).

1. Introduction

Since 2000, water heating has consistently been the second largest contributor to the total energy consumption in residential buildings in Canada. In the year 2018, 281.3PJ of energy consumed in the Canadian residential sector was attributed to water heating; this represents 17.4% of the total energy consumption and 19.2% of greenhouse gas emissions [1]. Similarly, domestic water heating accounted for 14.8% of the total energy consumption in the residential sector in Europe [2]. Evidently, hot water usage is a significant part of modern housing, and seeking to reduce its impact on the environment is worth investigating.

According to a recent study by Chen et al., an estimated 34.8% of total hot water used in residential buildings within the United States is attributed to showers [3]. Furthermore, on average, drain water holds 80–90% of its thermal energy relative to the mains water supply temperature [4]. Clearly, a significant amount of energy that is consumed towards domestic water heating is not fully utilized during showers, which presents an opportunity to use heat exchangers to recover thermal energy from greywater in residential buildings. This work focuses on the most common type of heat exchanger used for this purpose, namely Falling-Film Drain Water Heat Recovery (DWHR) units.

DWHR heat exchangers consist of a large diameter drainpipe which is wrapped tightly with a coil of smaller tubes. The drainpipe and the tubes are both made of copper. Figure 1 presents a selection of commercially available DWHR heat exchangers, highlighting variations in length, diameter, and coil design for different units. During operation, greywater goes down the drainpipe portion of the heat exchanger, which has a diameter matching the size of the drain stack it replaces. Concurrently, mains water is circulated within the coiled tubes wrapped around the drainpipe which recovers heat from greywater. These heat exchangers are designed to be installed vertically, which implies that greywater forms

a falling-film as it traverses down the drainpipe [5]. This falling-film of water ensures that the entire inner surface area of the drainpipe is covered in water, thus providing the heat transfer area for heat recovery to occur. It is worth noting that horizontal designs for such heat exchangers do not rely on a falling-film, and according to a study by Ravichandran et. al., horizontally installed heat exchangers have lower efficiencies than the ones installed vertically [6]. This study only considers heat exchangers that are designed and rated for vertical installation.

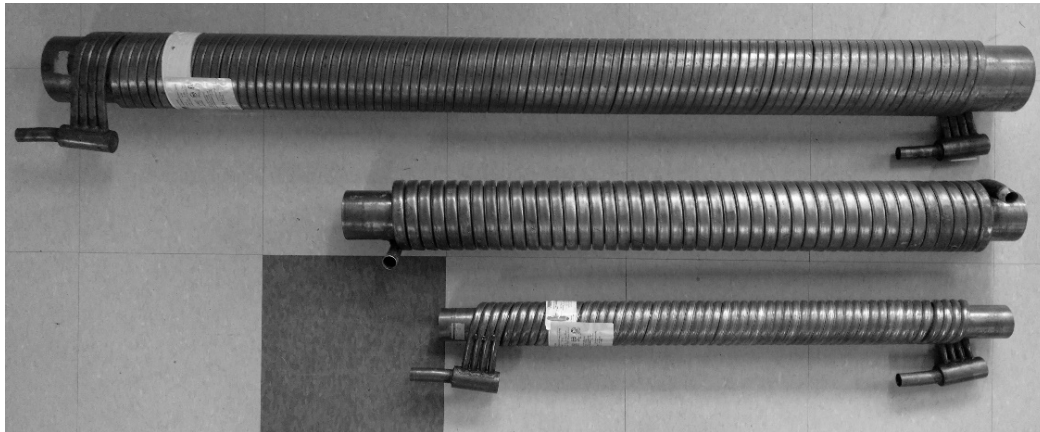


Figure 1. Common designs for falling-film drain water heat recovery (DWHR) heat exchangers.

DWHR systems can be installed in different configurations. Figure 2 shows three variations (A, B and C) which are simplified to only contain a DWHR heat exchanger in addition to a showerhead for water-draw purposes, and each showerhead is equipped with a thermostatic mixing valve. Figure 2A depicts a system where all preheated water from the DWHR system goes to the water heater, Figure 2B depicts a system where all preheated water goes to the mixing valve at the showerhead, and Figure 2C shows a combination of the two previous cases. Lastly, Figure 2D is provided to show the same plumbing system without a DWHR heat exchanger installed.

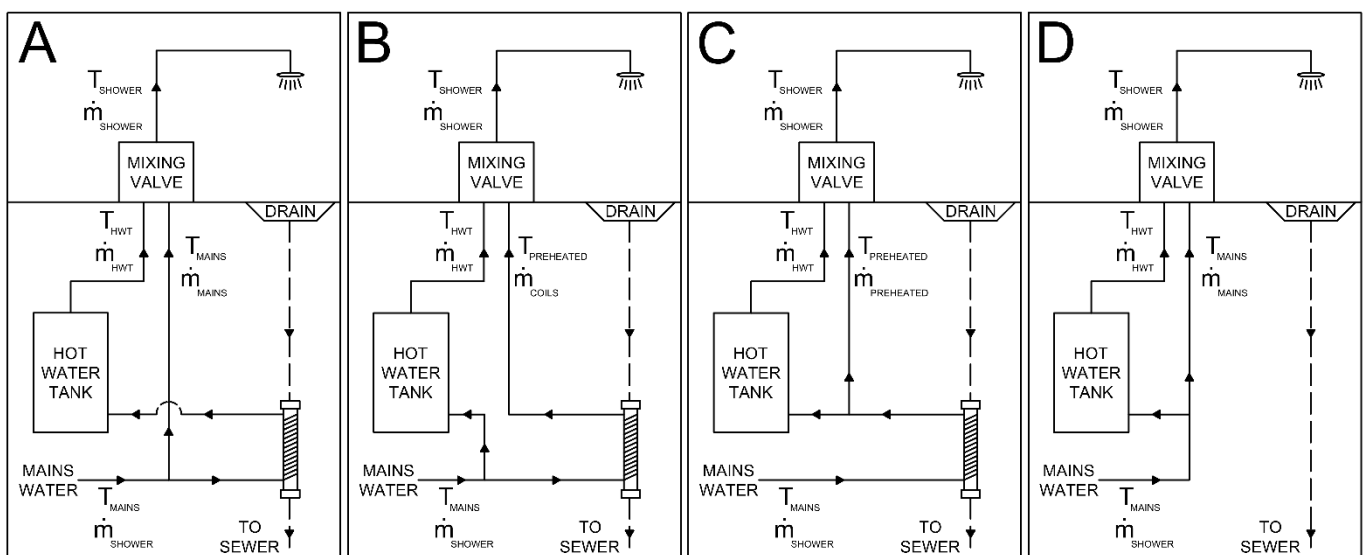


Figure 2. Possible plumbing configurations for DWHR systems in a residential building: (A) depicts a system where all preheated water from the DWHR heat exchanger is fed to the water heater; (B) depicts a system where all preheated water is fed to the mixing valve at the showerhead; (C) is a combination of (A) and (B); and (D) shows the same plumbing system without a DWHR heat exchanger installed.

Configuration C depicts equal flowrates of water through both sides of the heat exchanger, whereas configurations A and B depict unequal-flow conditions. The performance of DWHR systems is a strong function of flowrates [7] and based on the configurations shown, the flowrate of water through the heat exchanger coils is expected to vary based on plumbing configuration to provide the same temperature at the showerhead.

Researchers have been focused on simulating the performance of DWHR heat exchangers under equal-flow arrangements (i.e., config C). This is because the data available on the performance of DWHR heat exchangers is limited to the effectiveness data gathered during the CSA rating process [8]. The rating system is meant to provide a means for comparing different DWHR heat exchangers on an equal basis; it does not and cannot provide any accurate estimates for different configurations in which a heat exchanger could be installed. A study by Slys and Kordana discusses the process for estimating the energy savings associated with different plumbing configurations and highlights the numerous assumptions that need to be made for such calculations [9]. In their work, the authors did not have access to a system model that accounted for varying heat exchanger effectiveness. Without having a model that accounts for the changing effectiveness for the system, there is no way to compare the results numerically or experimentally. This highlights the need for further studies with models that do not rely on assumptions such as a constant effectiveness for the heat exchanger.

It is worth noting that despite being the only configuration covered in standards, configuration C is not always an option, especially in retrofit settings where the plumbing has already been installed and additional modifications are costly. Furthermore, local building codes can impose limitations on which configurations are allowed. For example, configurations B and C are not permitted in Québec, Canada [10]. This restriction is due to the possibility of bacteria growth, such as *Legionella*, in preheated water that bypasses the water heater. In other words, only plumbing setups in which all preheated water is directed to the water heater are allowed, and that limits the allowable configurations to what was shown in Figure 2A. Clearly, assuming that DWHR heat exchangers are always installed and operated under equal-flow conditions is incorrect, and potentially against local codes. Thus, building simulation models must be created to predict performance of such heat exchangers under unequal-flow conditions.

1.1. Model

A series of studies were undertaken at the University of Waterloo to address the limitations in modelling of DWHR systems. Most notably, the impact of varying inlet temperatures [11] and inlet flow rates [12] were empirically characterized, and the combination of all studies were compiled into a model that can predict the performance of a DWHR heat exchanger under steady-state conditions. A recent publication covers the development and validation of the model in detail [13]. The model is validated experimentally and the mean absolute error between model predictions and experimental results is less than 3% for a total of 135 different validation cases performed in the study. The validation temperatures range from 4 to 50 °C, and the volumetric flow rates range from 4 to 20 L/min.

A detailed description of the model and the principles on which those models are based are not repeated here; instead, this study aims to use the aforementioned model to perform energy simulations for DWHR systems installed in configurations depicted in Figure 2. To this end, the model is implemented into Transient System Simulation Tool (TRNSYS) software as a component and used in simulations described in the following sections.

1.2. TRNSYS

TRNSYS was selected as suitable software for simulations because it allows the performance of simulations while accounting for transient behaviour in components such as water heaters. Transient behaviour of DWHR systems is currently being studied and will be added to model in the future.

A TRNSYS simulation works by allowing interaction between different ‘components’ on a timestep-by-timestep basis, and this time step is selected by the user at the beginning of each simulation. Each component consists of ‘parameters’ and ‘inputs’ which are used to generate ‘outputs’ for the components for each time step.

Parameters are relevant values that are used by TRNSYS to simulate a component throughout the simulation period. Parameters are independent of time and remain the same throughout the modelling process. In the context of the DWHR component in TRNSYS, the size of the heat exchanger is a parameter in the simulations. On the other hand, inputs to the simulation are variables that can change as a function of time. The inputs to the DWHR component include the inlet water temperatures and flowrates to the heat exchanger. The simulation then uses the inputs and parameters to generate outputs for the component for each time step. The outputs for the DWHR component include the heat recovery rate, heat exchanger effectiveness, and the outlet temperatures for both streams. A summary of the parameters, inputs, and outputs for the DWHR component are shown in Table 1.

Table 1. Parameters, inputs, and outputs associated with the DWHR component created in Transient System Simulation Tool (TRNSYS) software.

Type	Variable Name	Unit	Notes
Parameter	a	min/L	Regression coefficients taken from the characteristic effectiveness curve for the DWHR unit being simulated.
	b	Dimensionless	
Input	$T_{c,i}$	°C	Inlet water temperature to the coils
	$T_{h,i}$	°C	Inlet water temperature to the drainpipe
	\dot{m}_{coils}	kg/s	Mass flowrate of water through the coils
	\dot{m}_{drain}	kg/s	Mass flowrate of water through the drainpipe
Output	$T_{c,o}$	°C	Outlet water temperature from the coils
	$T_{h,o}$	°C	Outlet water temperature from the drainpipe
	q	kW	Heat recovery rate
	ε	Dimensionless	Heat exchanger effectiveness

Parameters a and b are regression coefficients that are taken from the characteristic effectiveness vs. flowrate curve that is generated during the rating process under the CSA B55.15 standard [8]. Figure 3 shows an example of this characteristic curve, where parameters a and b are determined to be 0.0685 min/L and 1.2796, respectively, and \dot{V} denotes the volumetric flow rate in L/min. The TRNSYS component uses these parameters and the inputs assigned by the user to calculate outputs for each time step.

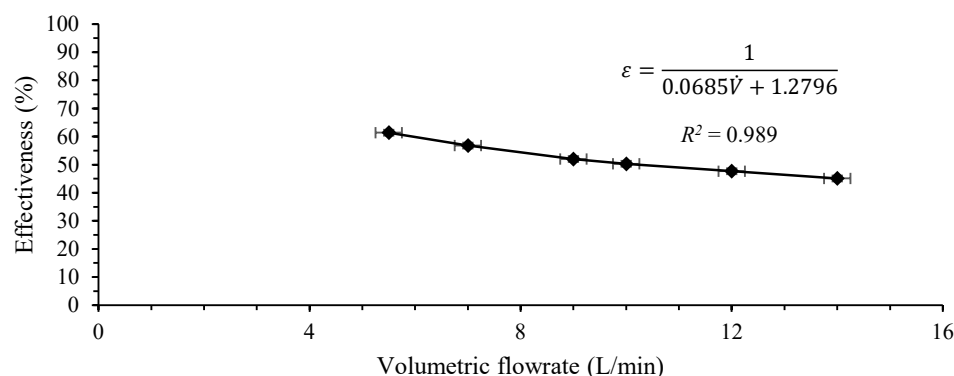


Figure 3. Equal-flow effectiveness vs. volumetric flowrate for a 7.6 cm diameter, 153 cm long DWHR heat exchanger.

2. Materials and Methods

The energy savings associated with a DWHR heat exchanger is highly impacted by the way it is installed in a particular home, and the conditions it is subjected to within the dwelling. The plumbing system within a house is impacted by local codes, the mains temperature depends on the location, and the duration for shower events is decided by the occupants. There are many possibilities for the conditions that a DWHR heat exchanger could be subjected to, and to allow comparison for energy savings under different conditions, a baseline must be established to provide consistency. This baseline is created based on Figure 2 for different plumbing configurations, but prior to running simulations, important simulation constraints, such as the shower condition, the water heater, and the water-draw schedule, must be selected. These key constraints will be discussed.

2.1. Shower Condition

A shower temperature of 38 °C was selected for all shower events. This temperature is based on the temperature used for rating all DWHR systems according to the CSA standard [8].

The flowrate of water through the showerhead is expected to have a significant impact on simulation results, as it would affect both the energy consumption by the water heater, and the energy recovery by the heat exchanger. It is difficult to select one showerhead flowrate to represent all households, as there are many fixtures available on the market, each having its own rated flowrate. In a typical dwelling, this flowrate is also affected by the available water pressure in the plumbing system. Hence, to simplify the matter, three flowrates were selected based on the range of flowrates prescribed by the CSA standard to represent showerheads having low, typical, and high flowrates. These flowrates are 5.5, 9.5 and 14 L/min.

The water draw schedule was chosen for a family of three, with three shower events per day, as noted in Table 2. Shower durations are highly subjective, and the chosen durations were meant to cover both reasonably short and long showers. As these simulations are focused only on savings associated with shower events, no other water draws were added to the daily water-draw schedule. To accommodate the water draws from Table 2, a typical 182 Litre (40-gallon) electric water heater was selected for simulations. The tank volume was found to be sufficient to accommodate all shower durations at all flowrates without depleting the tank. In other words, the shower temperatures do not drop below 38 °C during shower events.

Table 2. Start times and durations for shower events used in the simulations.

Shower Event #	Start Time	Duration
1	6:00 AM	6 min
2	7:00 AM	15 min
3	8:00 PM	9 min

2.2. Electric Water Heater

There are multiple water heaters available for simulation in TRNSYS, and it was crucial to select one that has been validated experimentally. An in-depth study by Allard et al. focused on validating different electric water heaters used in TRNSYS, and the results showed that TRNSYS 'Type 534' accurately depicts the variables of interest, namely the energy consumption and supply temperature during simulations [14]. Type 534 simulates the tank using a nodal approach while accounting for stratification effects. Hence, Type 534 was selected for simulation purposes. This tank was divided into 50 nodes for the simulations, which exceeds the minimum number of nodes recommended by Kleinbach et al. per Equation (1) [15]. Here, N_{FIXED} denotes the minimum number of nodes in the tank, and $Tank_{Turnover}$ is the ratio of daily water draw and total tank volume. $Tank_{Turnover}$ varies

based on the showerhead flowrate used in the simulation; hence, N_{FIXED} was calculated for all flowrates. As a result, the tank was divided into 50 nodes, as this number of nodes satisfies the minimum number of nodes required for all flowrates and having a consistent number of nodes in the tank for all simulations allows fair comparison of the results. Table 3 provides a summary of relevant parameters for the water heater used in all simulations in this study.

$$N_{FIXED} = 45.8 \times (Tank_{Turnover})^{-1.218} \quad (1)$$

Table 3. Parameters used to characterize TYPE 534 hot water tank in this study.

Parameter	Value Used in Simulations	Unit
Number of Nodes	50	Dimensionless
Tank Volume	182 (40)	Liters (Gallons)
Tank Height	105 (41.4)	Centimeters (Inches)
Tank Loss Coefficient	3.5	kJ/(hr·m ² ·K)
Environment Temperature	20 (68)	°C (°F)
Upper Element	3000	W
Lower Element	3000	W

2.3. Mains Temperature

The energy consumption associated with domestic water heating is directly tied to the mains temperature at the location where the water heater is located. To provide a fair assessment of the impact of mains temperature on the energy savings associated with DWHR heat exchangers, a large range of temperatures were required for simulations. The mains temperatures selected for the simulations were 2, 5, 10, 15, 20, and 25 °C.

The energy savings associated with DWHR systems can be looked at from different perspectives, and it is crucial to clarify how savings are presented in this study. It is insufficient to simply compare the magnitude of energy that was recovered by the DWHR system in each simulation, as there are other components present in domestic water heating. Most importantly, there are heat losses associated with the hot water tank, and the rate of heat recovery is expected to impact the losses, as well as how often the heating elements within the water heater must activate to provide auxiliary heat. Thus, it would be more appropriate to compare the total energy consumed by the water heater instead. For this purpose, the total energy consumed by the water heater in configurations A, B and C are compared to the energy consumption in configuration D (see Figure 2) under identical simulation parameters. This allows presentation of the savings in terms of percentages relative to configuration D.

Equation (2) is used to calculate the energy savings as a percentage of total energy consumed in the reference case (configuration D). E_D denotes the total auxiliary energy consumed by the water heater in configuration D, and E_{Sim} represents the total auxiliary energy consumed by the water heater in configurations A, B or C.

$$Energy\ Savings = \frac{E_D - E_{Sim}}{E_D} \times 100 \quad (2)$$

2.4. Heat Exchangers

Four heat exchangers were selected for this study. This selection spans different heat exchanger lengths and diameters. The corresponding characteristic effectiveness vs. flowrate equation obtained using the CSA standard procedure is also provided for each heat exchanger. See Table 4.

Table 4. Characteristics of the DWHR heat exchangers used in simulations.

	Diameter (cm)	Length (cm)	Curve-Fit Generated Using CSA Flow Rates
Heat Exchanger 1	5.1	91	$\varepsilon = \frac{1}{0.1548\dot{V}+1.7513}$
Heat Exchanger 2	7.6	122	$\varepsilon = \frac{1}{0.0918\dot{V}+1.3109}$
Heat Exchanger 3	7.6	152	$\varepsilon = \frac{1}{0.0681\dot{V}+1.2315}$
Heat Exchanger 4	10.2	152	$\varepsilon = \frac{1}{0.0529\dot{V}+1.2544}$

2.5. Simulation Time Step

Next, appropriate time step was to be determined. Selecting appropriate time steps is crucial for accurate simulations. Smaller time steps often provide higher accuracy at the expense of CPU-time. However, the time domain must be discretized such that all shower events can be appropriately captured by the chosen time step size. To investigate discretization errors, simulations were run for several time step sizes, and for all cases, the energy consumption by the water heater was calculated for a period of a month. A time step of 1 s was used as the reference, and the results from other time steps were compared to the reference case to estimate the discretization error. The results showed that a time step size of 5 min has a discretization error of approximately 17%, which was reduced to below 1% when a 1-min time step was used. Therefore, a time step of 1 min was found to be suitable for simulation purposes.

TRNSYS simulations were set up to perform a month (30 days) of simulation. The results are to be compared using the energy savings metric from Equation (2) for each heat exchanger.

3. Results and Discussion

The results showed that configuration C outperforms the other configurations for all simulations, regardless of flowrate or mains temperature. This is in-line with the expected performance of DWHR heat exchangers, as configuration C has the highest flow rate of water through the heat exchanger's coils during shower events. On the other hand, the mains temperature could dictate which unequal-flow configuration could lead to higher savings. At high mains temperatures, the savings associated with configuration B outpaced those of A, regardless of the heat exchanger being simulated or the showerhead flowrate. Figures 4–6 contain the results for simulations with showerhead flowrates of 5.5, 9.5 and 14 L/min respectively. Each figure contains four plots, which show the energy savings as a function of mains temperature for the three configurations. Note that each point on the plot represents a month of simulation.

It is important to note that significant energy savings can be achieved by installing a DWHR heat exchanger in plumbing systems regardless of the configuration. In situations where the equal-flow configuration is not possible, homeowners should not be discouraged from relying on configurations A or B. Unequal-flow configurations can be thought-of as having a slightly smaller heat exchanger installed relative to the equal-flow configuration, and selecting a larger heat exchanger has a more pronounced impact on energy savings compared to changing the plumbing configuration.

The energy-savings trend for configurations A and B can be explained through closer inspection of the mains side flowrate through the heat exchanger coils for different simulation scenarios. This is best done using the concept of heat capacity ratio, C_r , which is the ratio of heat capacity rates for the heat exchanger, as shown in Equation (3).

$$C_r = \frac{C_{min}}{C_{max}} = \frac{(\dot{m}C_p)_{min}}{(\dot{m}C_p)_{max}} \quad (3)$$

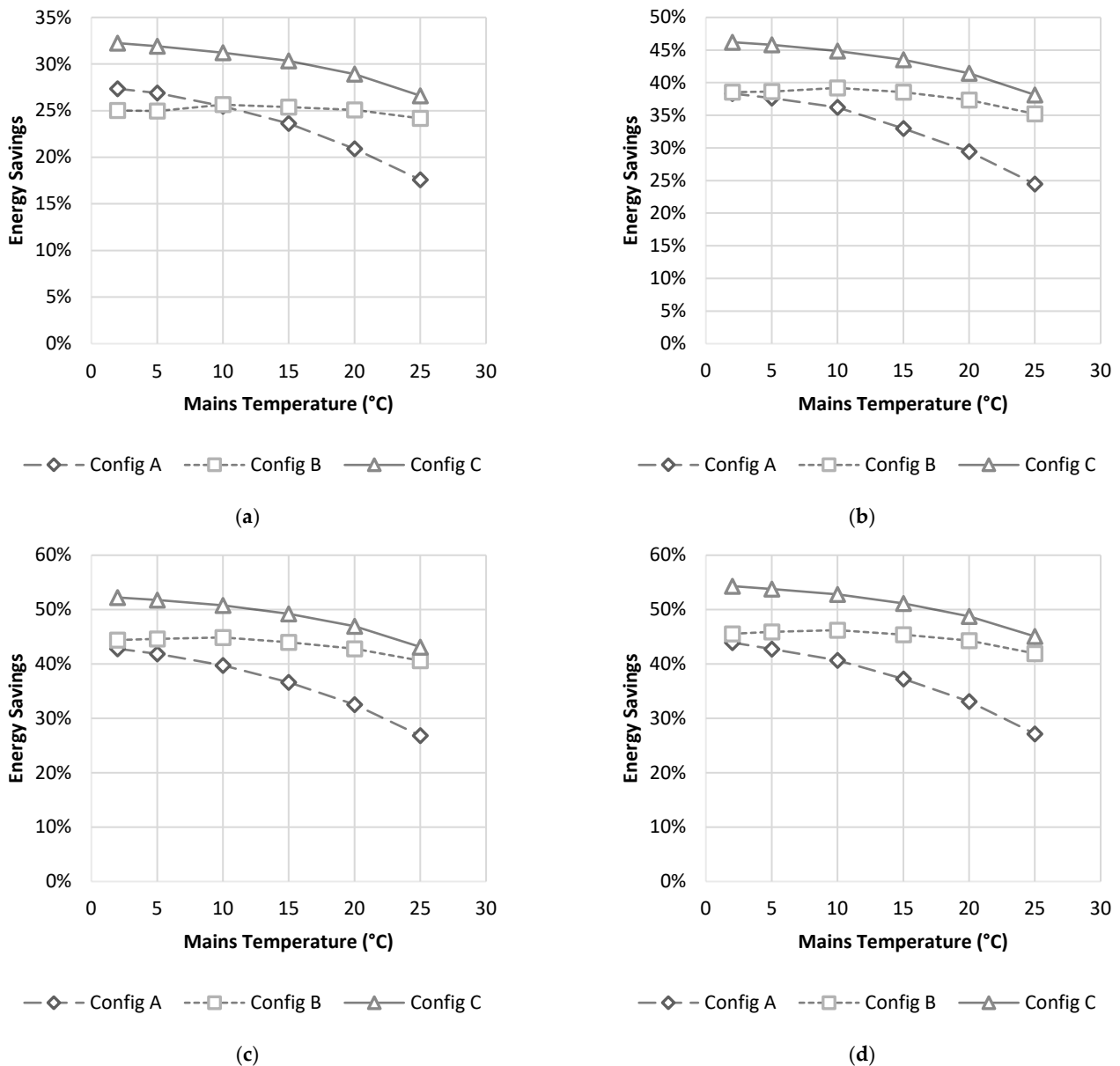


Figure 4. Energy savings as a function of mains temperature for a showerhead flowrate of 5.5 L/min for configurations A, B and C, as labelled. The plots correspond to heat exchanger 1 (a), heat exchanger 2 (b), heat exchanger 3 (c), and heat exchanger 4 (d).

In this equation, C represents the heat capacity rate ($\text{kW}/^\circ\text{C}$), \dot{m} is the mass flow rate (kg/s), and C_p is the specific heat ($\text{kJ}/\text{kg}^\circ\text{C}$). Equation (3) is often used in the ε -NTU method for heat exchanger analysis. For this study, constant properties were used, so Equation (3) can be reduced to a ratio of mass flowrates. Note that the maximum flowrate in this study always corresponds to the flowrate of water at the showerhead fixture, which is equal to the flowrate through the drain side of the heat exchanger. The minimum flowrate corresponds to the lower of \dot{m}_{coils} and \dot{m}_{drain} . The heat capacity ratio, C_r , is nondimensionalized, and is bound between 0 and 1. When the flowrates through the coils and drain are equal (i.e., Config C), C_r will be equal to 1; however, for the other two configurations, \dot{m}_{coils} will always be lower than \dot{m}_{drain} . Thus, C_r can be calculated using Equation (4):

$$C_r = \frac{\dot{m}_{\min}}{\dot{m}_{\max}} = \frac{\dot{m}_{\text{coils}}}{\dot{m}_{\text{shower}}} = \frac{\dot{m}_{\text{coils}}}{\dot{m}_{\text{drain}}} \quad (4)$$

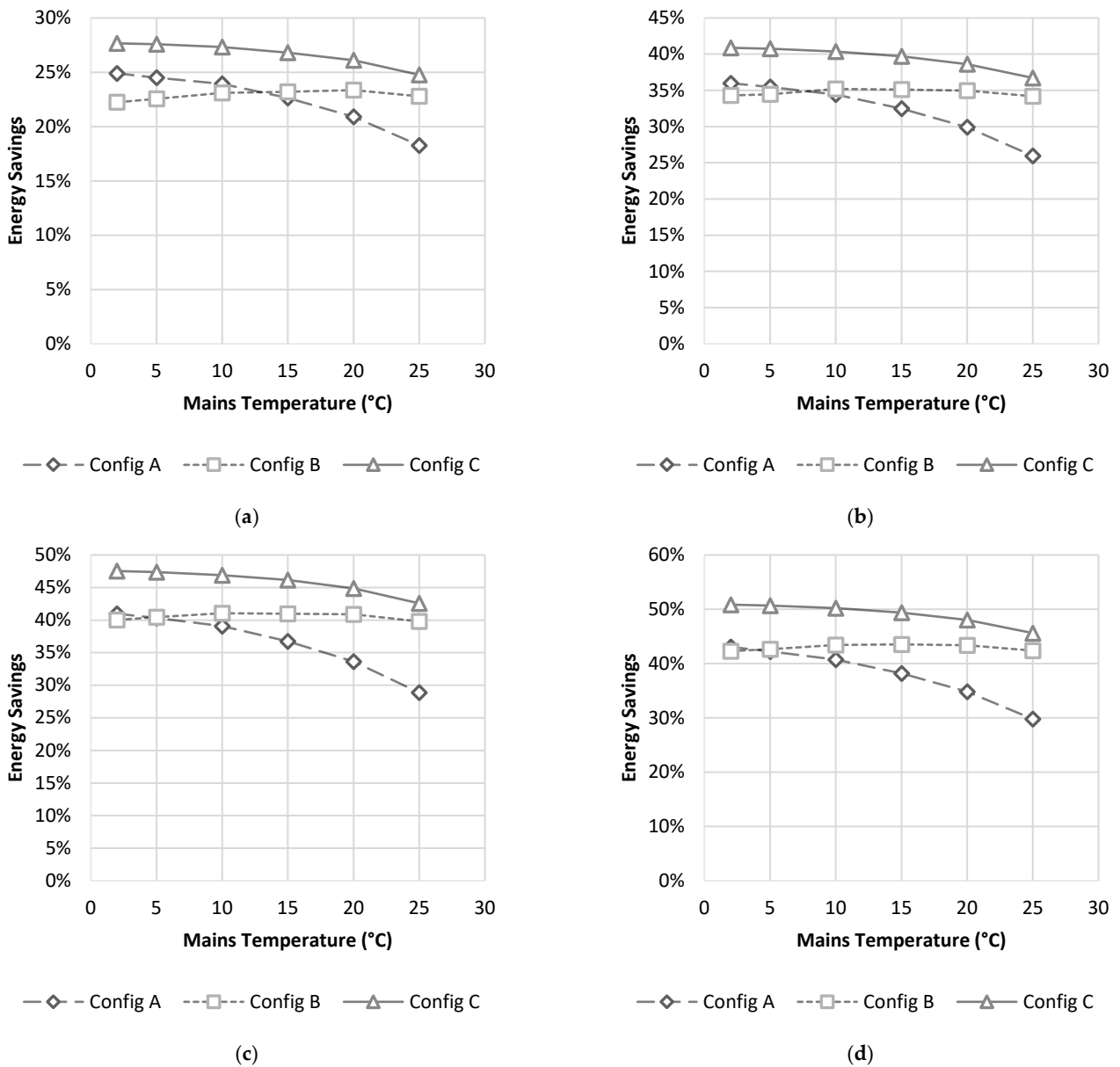


Figure 5. Energy savings as a function of mains temperature for a showerhead flowrate of 9.5 L/min for configurations A, B and C, as labelled. The plots correspond to heat exchanger 1 (a), heat exchanger 2 (b), heat exchanger 3 (c), and heat exchanger 4 (d).

For this analysis, the heat capacity ratio was calculated for all time steps in the monthly simulation when shower events occurred, and the results for heat exchanger 1 are shown in Figure 7. In this figure, the x-axis contains six sets labelled as 5.5A, 5.5B, 9.5A, 9.5B, 14A and 14B, where 5.5A implies the set of results are associated with configuration A for a showerhead flowrate of 5.5 L/min, and 5.5B implies the set of results are associated with configuration B for a showerhead flowrate of 5.5 L/min, and so on. Each set of results contains six bars, each of which corresponds to a mains temperature (T_m) between 2 and 25 °C, as labelled in the legend. Note that the heat capacity ratios for configuration C are not plotted here, as they are always equal to 1.

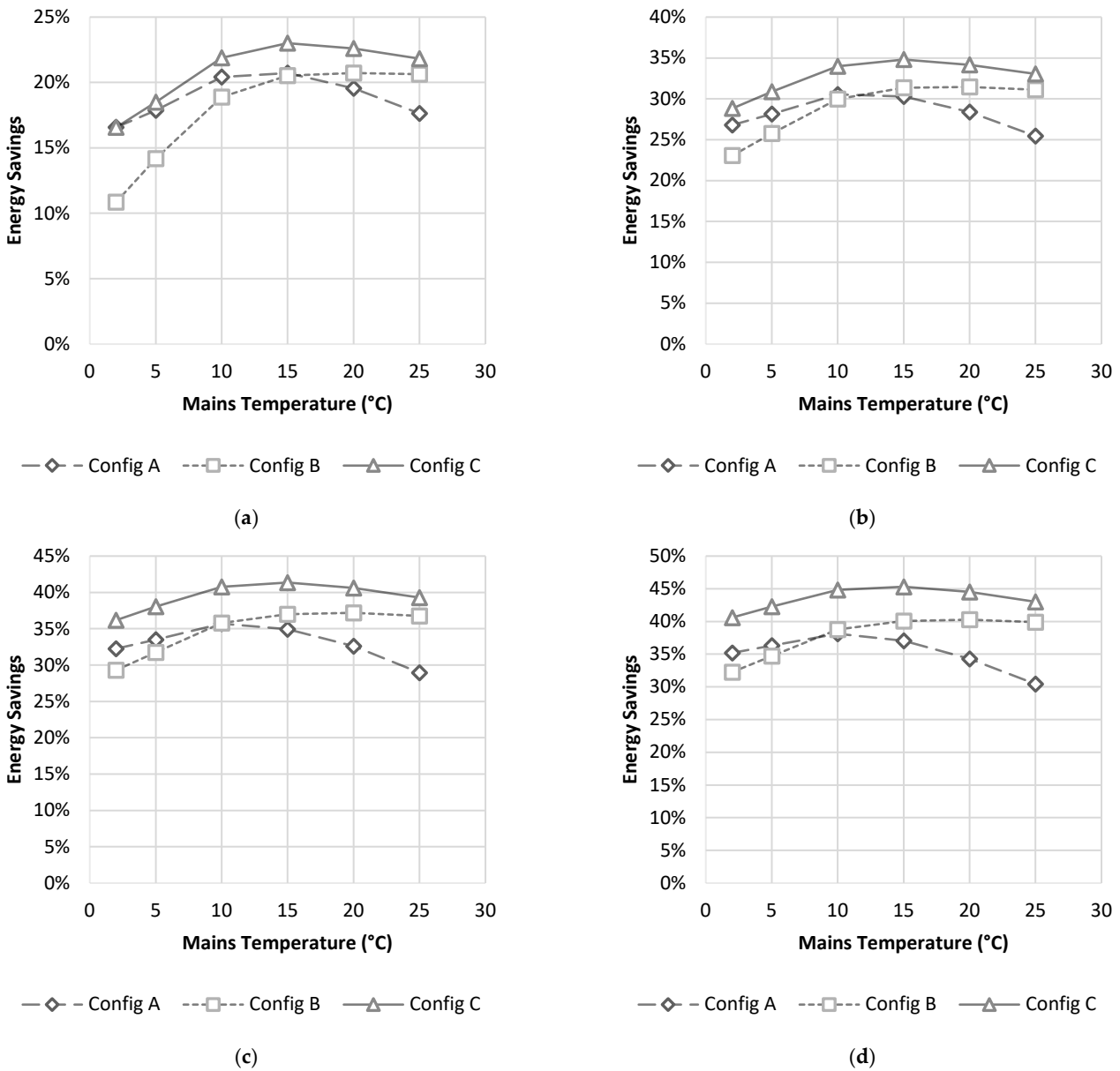


Figure 6. Energy savings as a function of mains temperature for a showerhead flowrate of 14 L/min for configurations A, B and C, as labelled. The plots correspond to heat exchanger 1 (a), heat exchanger 2 (b), heat exchanger 3 (c), and heat exchanger 4 (d).

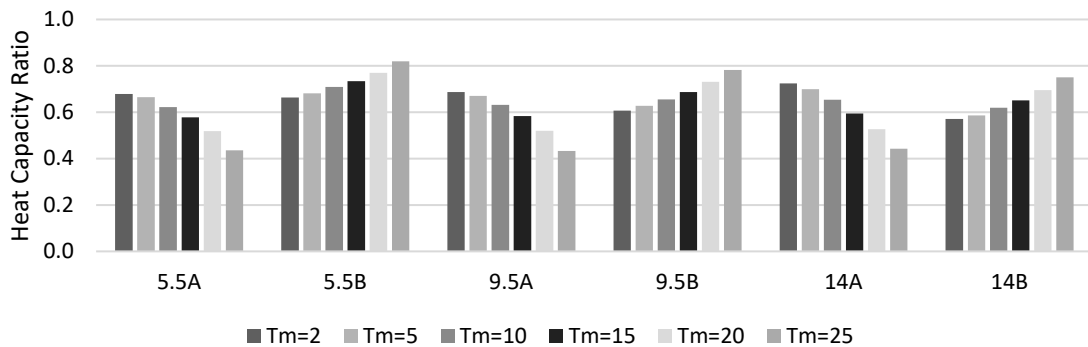


Figure 7. Heat capacity ratios for all simulated cases for heat exchanger 1.

Figure 7 shows that, for configuration A, as the mains temperature was increased in the simulations, the flowrate through the coils was decreased, thereby decreasing C_r . Conversely, configuration B resulted in higher flowrates through the coils as the mains temperature was increased. Figures 8–10 contain the results for heat exchangers 2, 3, and 4, respectively, all of which showed the same trends as Figure 7. Clearly, the mains temperature has a significant impact on \dot{m}_{coils} , which is directly tied to how much energy can be recovered by the heat exchangers. Lastly, the results corroborate what was shown previously in Figures 4–6, where the energy savings for the water heater was shown for different configurations.

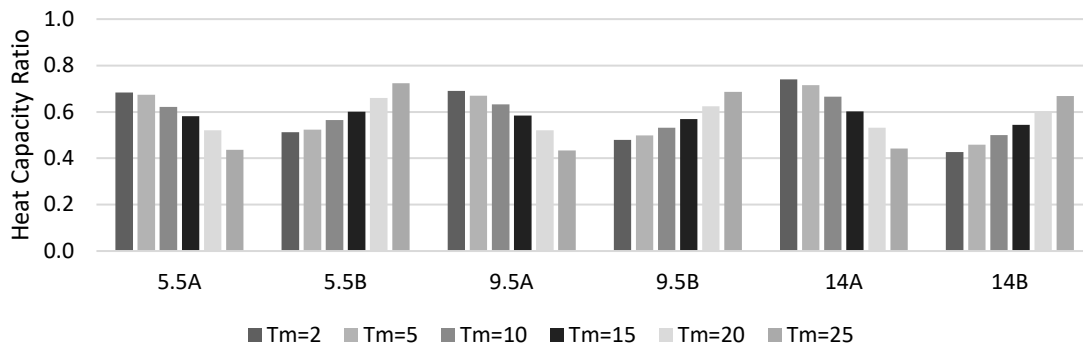


Figure 8. Heat capacity ratios for all simulated cases for heat exchanger 2.

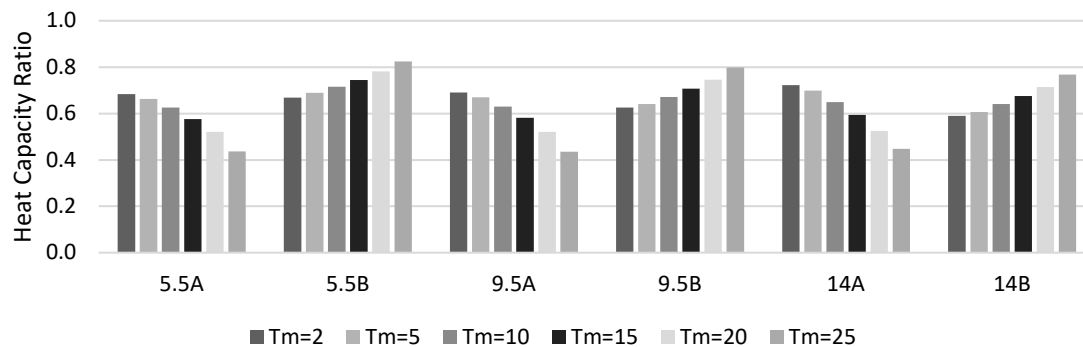


Figure 9. Heat capacity ratios for all simulated cases for heat exchanger 3.

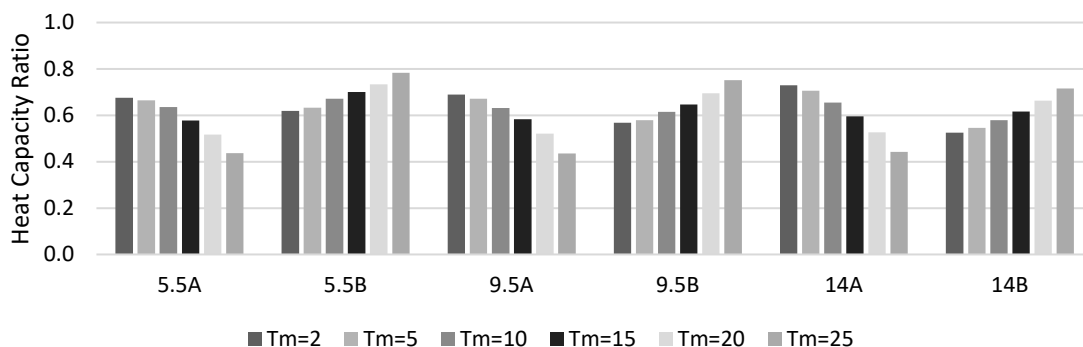


Figure 10. Heat capacity ratios for all simulated cases for heat exchanger 4.

To explain this behaviour, a closer inspection of the plumbing schematic shown in Figure 2 is required. For configuration A, \dot{m}_{coils} is equal to \dot{m}_{HWT} , and as the mains temperature is increased, a higher flow rate of water at T_{mains} would flow directly to the mixing valve; thereby decreasing \dot{m}_{coils} . In other words, the heat exchangers are less utilized in configuration A as the mains temperature is increased and is closer to the prescribed

showerhead temperature. On the other hand, in configuration B, \dot{m}_{coils} is not constrained by \dot{m}_{HWT} , and as the mains temperature is increased, higher flowrates of water would flow through the heat exchanger coils to be preheated. As a result, the heat exchanger is better utilized as the mains temperature is increased in configuration B.

The simulation results highlighted that the mains temperature could dictate the flowrate of water that gets preheated by the heat exchanger in unequal-flow configurations, thereby affecting the energy savings. The mains temperature is based on the location where the plumbing system is located and is expected to vary throughout the year. Designers should be mindful of these facts when implementing a DWHR heat exchanger into a residential plumbing system. The results can also be used by manufacturers as guidelines to improve the design of heat exchangers. Currently, DWHR heat exchangers are rated and sold based on data gathered from equal-flow conditions; hence, they are designed to work optimally in such conditions to be competitive on the market. However, the simulation results showed that if the heat exchangers are installed in unequal-flow configurations, the mass flowrate through the coils could be much lower than the rated conditions. Therefore, the manufacturers are encouraged to adjust the coil diameter to improve heat transfer rates, which increases energy savings when having equal flow rates through the heat exchanger is not an option.

The results from this work showed that plumbing configuration has a pronounced impact on energy savings expected from DWHR heat exchangers. This held true regardless of the heat exchanger size or the prescribed temperature and flowrate at the showerhead. It is noted that reporting simulation results without clarifying the plumbing configuration fails to account for variations in flowrate through the heat exchanger coils and is therefore not an advisable approach. It is the authors' hope that future publications in this field will follow suit and include sufficient information regarding the plumbing setup, such that simulations can be replicated.

Author Contributions: Conceptualization, R.M. and M.R.C.; methodology, R.M.; software, R.M.; validation, R.M.; formal analysis, R.M.; investigation, R.M.; resources, R.M. and M.R.C.; data curation, R.M.; writing—original draft preparation, R.M.; writing—review and editing, R.M. and M.R.C.; visualization, R.M.; supervision, M.R.C.; project administration, M.R.C.; funding acquisition, R.M. and M.R.C. All authors have read and agreed to the published version of the manuscript.

Funding: This research was funded by the Natural Sciences and Engineering Research Council of Canada (NSERC), and the Ontario Graduate Scholarship (OGS) program.

Data Availability Statement: Not applicable.

Conflicts of Interest: The authors declare no conflict of interest. The funders had no role in the design of the study; in the collection, analyses, or interpretation of data; in the writing of the manuscript, or in the decision to publish the results.

References

1. Natural Resources Canada, Comprehensive Energy Use Database, Residential Sector, Canada, Table 2: Secondary Energy Use and GHG Emissions by End-Use. 2020. Available online: <https://oee.nrcan.gc.ca/corporate/statistics/neud/dpa/showTable.cfm?type=CP§or=res&juris=ca&rn=2&page=0> (accessed on 1 October 2021).
2. Eurostat, Energy Consumption in Households. June 2021. Available online: https://ec.europa.eu/eurostat/statistics-explained/index.php?title=Energy_consumption_in_households#Energy_consumption_in_households_by_type_of_end-use (accessed on 2 October 2021).
3. Chen, Y.; Fuchs, H.; Schein, J.; Franco, V.; Stratton, H.; Dunham, C. *Calculating Average Hot Water Mixes of Residential Plumbing Fittings*; Energy Analysis And Environmental Impacts Division Lawrence Berkeley National Laboratory: Berkeley, CA, USA, 2020.
4. Cooperman, A.; Brodrick, J. Drain Water Heat Recovery. *ASHRAE J.* **2011**, *53*, 58–62.
5. Beentjes, I.; Manouchehri, R.; Collins, M.R. An investigation of drain-side wetting on the performance of falling film drain water heat recovery systems, Energy and Buildings. *Energy Build.* **2014**, *82*, 660–667. [CrossRef]
6. Ravichandran, A.; Diaz-Elsayed, N.; Thomas, S.; Zhang, Q. An assessment of the influence of local conditions on the economic and environmental sustainability of drain water heat recovery systems. *J. Clean. Prod.* **2021**, *279*, 123589. [CrossRef]
7. Collins, M.R.; van decker, G.W.E.; Murray, J. Characteristic effectiveness curves for falling-film drain water heat recovery systems. *HVACR Res.* **2013**, *19*, 649–662.

8. CSA. *B55.1-15 Test Method for Measuring Efficiency and Pressure Loss of Drain Water Heat Recovery Units*; Canadian Standards Association: Mississauga, ON, Canada, 2015.
9. Sty' s, D.; Kordana, S. Financial analysis of the implementation of a Drain Water Heat Recovery unit in residential housing. *Energy Build.* **2014**, *71*, 1–11. [CrossRef]
10. Régie du Bâtiment du Québec, Branchement des Systèmes de Récupération de Chaleur des Eaux de Drainage: Attention aux Légionelles. March 2013. Available online: <https://www.rbq.gouv.qc.ca/domaines-dintervention/plomberie/interpretations-et-directives-techniques/branchement-des-systemes-de-recuperation-de-chaleur-des-eaux-de-drainage-attention-aux-legionelles.html> (accessed on 6 June 2021).
11. Manouchehri, R.; Collins, M.R. An experimental analysis of the impact of temperature on falling film drain water heat recovery system effectiveness. *Energy Build.* **2016**, *130*, 1–7. [CrossRef]
12. Manouchehri, R.; Collins, M.R. An experimental analysis of the impact of unequal flow on falling film drain water heat recovery system performance. *Energy Build.* **2018**, *165*, 150–159. [CrossRef]
13. Manouchehri, R.; Collins, M.R. Modelling the Steady-State Performance of Coiled Falling-Film Drain Water Heat Recovery Systems Using Rated Data. *Resources* **2020**, *9*, 69. [CrossRef]
14. Allard, Y.; Kummert, M.; Bernier, M.; Moreau, A. Intermodel comparison and experimental validation of electrical water heater models in TRNSYS. In Proceedings of the 12th Conference of International Building Performance Simulation Association, Sydney, Australia, 14–16 November 2011.
15. Kleinbach, E.; Beckman, W.; Klein, S. Performance study of one-dimensional models for stratified thermal storage tanks. *Sol. Energy* **1993**, *50*, 155–166. [CrossRef]

Article

Techno-Economic Analysis of Waste Heat Utilization in Data Centers: Application of Absorption Chiller Systems

Leyla Amiri ^{1,*}, Edris Madadian ², Navid Bahrani ¹ and Seyed Ali Ghoreishi-Madiseh ³

¹ Department of Civil and Resource Engineering, Dalhousie University, Sexton Campus, Halifax, NS B3H 4R2, Canada; navid.bahrani@dal.ca

² Department of Chemical Engineering, University of Waterloo, Waterloo, ON N2L 3G1, Canada; Edris.madadian@uwaterloo.ca

³ Norman B. Keevil Institute of Mining Engineering, University of British Columbia, Vancouver, BC V6T 1Z4, Canada; ali.madiseh@ubc.ca

* Correspondence: leyla.amiri@dal.ca

Abstract: Modern data centers are playing a pivotal role in the global economic situation. Unlike high-quality source of waste heat, it is challenging to recover the decentralized and low-quality waste heat sourced from data centers due to numerous technological and economic hurdles. As such, it is of the utmost importance to explore possible pathways to maximize the energy efficiency of the data centers and to utilize their heat recovery. Absorption chiller systems are a promising technology for the recovery of waste heat at ultra-low temperatures. In fact, the low temperature heat discharged from data centers cannot be retrieved with conventional heat recovery systems. Therefore, the present study investigated feasibility of waste heat recovery from data centers using an absorption chiller system, with the ultimate goal of electrical energy production. To fulfill this objective, a techno-economic assessment of heat recovery using absorption chiller (AC) technique for the data centers with power consumption range of 4.5 to 13.5 MW is performed. The proposed AC system enables saving electricity for the value of 4,340,000 kWh/year and 13,025,000 kWh/year leading to an annual reduction of 3068 and 9208 tons CO₂ equivalent of greenhouse gas (GHG) emissions, respectively. The results of this study suggest an optimum change in the design of the data center while reducing the payback period for the investors.

Keywords: waste heat recovery; absorption chiller; data center; sustainability; thermal pollution

Citation: Amiri, L.; Madadian, E.; Bahrani, N.; Ghoreishi-Madiseh, S.A. Techno-Economic Analysis of Waste Heat Utilization in Data Centers: Application of Absorption Chiller Systems. *Energies* **2021**, *14*, 2433. <https://doi.org/10.3390/en14092433>

Academic Editors: Jan Danielewicz and Krzysztof Rajski

Received: 8 March 2021

Accepted: 22 April 2021

Published: 24 April 2021

Publisher's Note: MDPI stays neutral with regard to jurisdictional claims in published maps and institutional affiliations.



Copyright: © 2021 by the authors. Licensee MDPI, Basel, Switzerland. This article is an open access article distributed under the terms and conditions of the Creative Commons Attribution (CC BY) license (<https://creativecommons.org/licenses/by/4.0/>).

1. Introduction

The incessant growth in the use of conventional fuels and their enormous greenhouse gas emissions necessitate more attention to be brought to environmental awareness. Consequently, many scholars around the world have been encouraged to spend significant amount of work on innovative technologies to supply heating and cooling demands of urban areas via renewable sources of energy. Global technological advancements and development of internet of things (IoT) technologies, big data, and cloud computing have resulted in rapid growth in the number of data centers around the world [1,2]. Owing to the enormous energy consumption resulted from rapidly growing data centers, much attention has been devoted to the possibility of energy recovery from such centers by their authorities as well as energy organizations. The worldwide electricity consumption of data centers is presented in four main categories: (i) Infrastructure uses 44.4% of electricity consumption (mainly ventilation and cooling sectors). (ii) Servers use 38.9% of energy supply, followed by 9.3% and 7.4% of the electricity used by (iii) Communication and (iv) Storage sectors, respectively [3–5].

Over 416 billion kWh of electricity was reportedly consumed by virtue of data processing in around 8 million data centers around the globe in 2019 [6]. A typical data center produces heat values in the range of 3.2 to 6.4 MW comprising 250 sets of cabinets with

42 to 64 server racks [7]. The new generations of data centers follow a growing trend of heat production with recent ones producing 10–250 kW [8]. In the light of the typical design temperature of 25 °C for a data room, this makes data centers as a year-around stable source of heat, and there exists huge potential for waste heat recovery from data centers.

Waste heat recovery and utilization from data centers has been the subject of many research studies within the past decade leading to the introduction of several practices to recover low-grade waste heat. According to the literature, the waste heat can be categorized to four types based on temperature levels: high-grade, medium-grade, low-grade and ultra-low-grade waste heat in the temperature range of >600 °C, 200–600 °C, 80–200 °C, and 45–80 °C, respectively [9,10].

The most common practices include absorption cooling, district heating, and direct and/or indirect power generation [7,11,12]. Although several factors can affect selection of the best method, an overview of available techniques presents district heating as the most viable approach for waste heat recovery in data center. For example, ref. [13] investigated a hot water (60 °C) supercomputer prototype showing energetic and exergetic efficiencies of 80% and 34%, respectively. Huang et al. [6] studied a 1 MW data center showing over 97% of heat recovery, which is equivalent to the heat required of a 30,000 m² commercial property. Another study investigated possible strategies for cooling and waste heat recovery of information technology (IT) servers in UK which produced over 2 million tons of CO₂ [14]. They projected that the recovered heat would be sufficient to supply heat demands for some neighborhoods in London. A 4000 ton CO₂ equivalent emission reduction along with \$170,000 saving from waste heat recovery of a 3.5 MW data center was estimated. A universal design approach was proposed by Fang et al. [15] for district heating based on the industrial waste heat recovery. They estimated that 122 MW would suffice district heating of a city with a population of 4.6 million in Northern China resulting in reduction of 168,000 tons of CO₂ equivalent. A steady-state model was developed in [16] which utilized the recovered heat from a thermosyphon-assisted air conditioner.

A variety of studies have been published exploring cooling technologies for thermal management in data centers [17–19]. A common practice to form hot and cold aisles in data centers is to place server racks back to back and front to front in an open-aisle (OA) air-cooled configuration [20]. This technique, however, affects the electricity consumption dedicated to air conditioning due to temperature nonuniformity sourced from air circulation between the cold and hot aisle [21]. Similar results was presented in [22], indicating potential weakness of OA systems associated with airflow direction. Alternatively, enclosed aisle (EA) approach was considered by numerous studies to reduce the inhomogeneity of airflow [23,24]. Nevertheless, EA strategy may also raise a new issue with finding the right place to discharge the trapped hot air. Consequently, other promising cooling systems such as free cooling, liquid cooling, two-phase technologies, and building envelope have been subject of many studies up until now. For instance, the authors of [25] modeled the dynamic air conditioning load of a large data center in China to obtain cooling and index. Using simulation of building load characteristics, it appeared that the values of annual cumulative heat load was much higher than its cooling one. A novel heat recovery system composed of data room, refrigeration unit, cooling tower, double conditions heat pump unit, auxiliary boiler, water pump, and pipeline valve refrigeration was proposed.

The low temperature of the waste heat sourced from data centers hinders producing a high-quality energy which requires a reliable technology to make up for this weakness. Among the waste heat recovery technologies reported in the literature, absorption chiller (AC) and Organic Rankine Cycle (ORC) were identified as the most promising technologies for processing waste heat from data centers. Both technologies have shown reliable performance in recovering low-grade source of heats.

The ORC technology has been considered as a valid solution for ultra-low-grade data center waste heat recovery. For instance, the authors of [26] investigated the techno-economic performance of ORC as the means of waste heat recovery from data centers. Using a developed steady-state thermodynamic model, they examined the effect of different

types of working fluid (i.e., dry, wet, and isentropic) and the evaporator temperature on the competence of the system. It was concluded that ORC would show the greatest performance in extremely low temperature applications. It was shown that the addition of superheaters in the server cooling cycle demands extra power for the operation which ultimately caused a performance drop, albeit at the higher temperature, the performance of ORC in waste heat recovery improves. A payback period of 4–8 years was estimated for the use of ORC in the data center. In a similar study, the authors of [27] built a 20 kW ORC prototype receiving the waste heat from two common rack servers operating at full capacity and with temperature ranging from 60 °C to 85 °C. The results of the experimental rig demonstrated thermal efficiency of 3.33% which was in a good agreement with the range of efficiency (i.e., 2% to 8%) resulted from the thermodynamic model in the same study. The benefits of the ORC system were not limited to absorbing waste heat from the data center as it sent back the generated electricity to the data center. A recent study [28] investigated heat waste recovery from a simulated condition for a typical data center server rack using a lab-scale ORC. It was demonstrated that for the range of ultra-low waste heat (i.e., 45 °C to 80 °C), thermal efficiencies vary between 1.9% and 4.6%. It was shown that significant fluid temperature differences in the heat exchanger, caused exergy deterioration to the ORC system.

AC systems, on the other hand, are not only able to handle low temperature source of heats, but also adopt waste heats from liquid-cooled and two-phase cooled data centers which further enhance their applicability in the field. The other advantages of AC systems are their low electricity cost, while their requirement for larger cooling tower is considered as their main drawbacks. AC systems mainly address some serious energy and environment issues with the conventional compression chiller (CC) systems. Despite recent achievements in recovering waste heat from data centers, yet underlying concept needs to be further explored broadly. Therefore, the present research investigates feasibility of energy recovery from the heat dissipated by a number of servers to support an AC unit which can further supply cooling requirements for other centers.

2. Methodology

With the purpose of perform the techno-economic study, an inventory of information from a variety of AC manufacturers in the North America were established allowing to analyze utilization and performance of various types of AC systems which are now ready for use for many purposes. Trane and Yazaki [29,30] were selected as AC manufacturing pioneers in the North America. The main reason for the selection of the two manufacturers is their diversity in ultimate application of heat recovered from data centers. Trane develops AC systems working under the low-grade hot water in a range of 70 °C and 110 °C which makes them promising options to recover waste heat in in data centers [29]. Yazaki operates AC units using water–lithium–bromide as the refrigerant which is capable to operate with low quality waste heat (temperature: ~70–95 °C) [30]. The Yazaki AC units will shut down if the inlet hot water temperature exceeds 95 °C. The outlet hot water temperature is ~55 °C. It should be mentioned that the low-grade heat generated through industrial processes can be used by AC systems and generates cooling energy. Otherwise, this low-grade heat will be wasted and discarded through the environment. The other important point about the AC systems is their sensitivity to the temperature of the inlet hot water as an energy source. If the temperature of the inlet hot water is less than the desired temperature, the efficiency and the cooling capacity of the system is reduced as well.

This work provides a substantive methodological guide for district heating using the recovered heat from data centers. Thus, the main idea of this study is to employ an AC unit which is energized by the low-grade heated air in the data centers (Figure 1). When the enough heat load is supplied to AC system, the heat load on the CC unit is reduced. In the other words, a portion of the heated air in the data center will be removed by the AC, which reduces the total workload on the CC. Here, the heated air in the data center has a lower-grade heat compared to the higher-grade heat of the computing elements inside

the racks. This low-grade heat air can be effectively cooled down by the AC. Finally, any remaining heat can be removed by the CC.

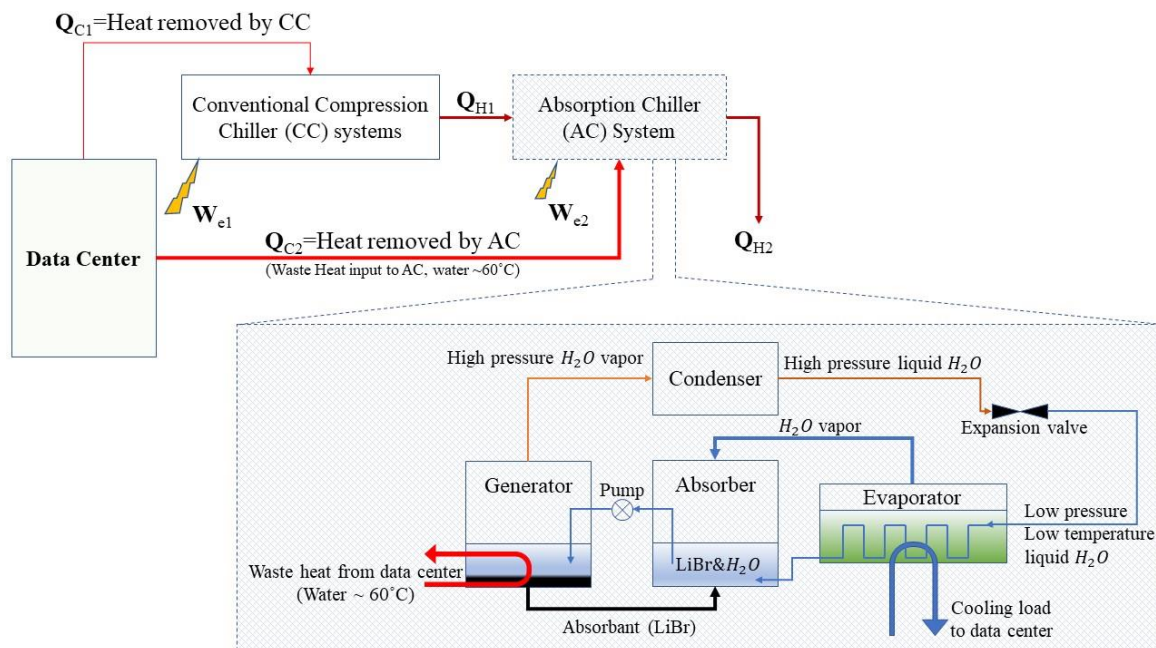


Figure 1. Heat flow of the proposed data center coupled with an absorption chiller system.

Analytical Model

The first step in developing the thermodynamic model for the proposed system is to apply governing equations predominantly conservation of mass and energy. The analytical model is implemented considering CC system as the point of comparison with the proposed AC system. Figure 1 presents the cycle under investigation for the heat flow of the proposed data center. Note that Q_{H1} is the heat rejected from the cycle through the condenser in the CC and can be proportionally considered as a heat source for the AC system. In addition, wet or dry cooling towers should be designed to transfer Q_{H2} (i.e., the heat rejected of the chiller coolant water by absorber and condenser) to the ambient.

According to Figure 1, the total cooling supplied by the hybrid CC system and AC system ($Q_{C-total}$) can be written as (Equation (1))

$$Q_{C-total} = Q_{C1} + Q_{C2} \tag{1}$$

where Q_{C1} and Q_{C2} are the provided cooling by the CC system and AC system, respectively.

Similarly, total electricity consumption by the proposed hybrid CC-AC system (W_{CC-AC}) can be written as follows (Equation (2)):

$$W_{CC-AC} = W_{e1} + \underbrace{W_{e2}}_{\approx zero} \tag{2}$$

where W_{e1} and W_{e2} are the electricity requirement for operating the CC system and AC system, respectively. Note that the energy consumption of the AC system in this integrated proposed system is negligible.

The provided cooling by the CC system (Q_{C1}) is a function of the Coefficient of Performance (COP) of the system as well as the dissipated heat (Q_{H1}) from the system and can be written as follows (Equations (3) and (4)):

$$Q_{C1} = COP_{CC} \times W_{e1} \tag{3}$$

$$Q_{C1} = \frac{COP_{CC}}{1 + COP_{CC}} \times Q_{H1} \tag{4}$$

According to the first and second law of thermodynamics, the dissipated heat and cooling by the CC system can be expressed as (Equations (5) and (6)):

$$Q_{H1} = Q_{C1} + W_{e1} = (1 + COP_{CC}) \times W_{e1} \tag{5}$$

$$Q_{C2} = COP_{AC} \times Q_{H1} = COP_{AC} \times (1 + COP_{CC}) \times W_{e1} \tag{6}$$

Combining Equations (3) and (5), the total cooling provided for the data center and the total electricity consumption by the proposed hybrid system can be rewritten as (Equation (7))

$$Q_{C-total} = Q_{C1} + Q_{C2} = COP_{CC} \times W_{e1} + COP_{AC} \times (1 + COP_{CC}) \times W_{e1} \tag{7}$$

The total electricity consumption by the proposed hybrid CC-AC system can be calculated using Equation (8):

$$W_{CC-AC} = \frac{Q_{C-total}}{COP_{CC} + COP_{AC} \times (1 + COP_{CC})} \tag{8}$$

The total electricity saving of using the proposed system can be calculated using Equations (9) and (10):

$$W_{saving} = W_{CC} - W_{CC-AC} \tag{9}$$

$$\text{Electricity saving (\%)} = \frac{W_{CC} - W_{CC-AC}}{W_{CC}} = 1 - \frac{COP_{CC}}{COP_{CC} + COP_{AC} \times (1 + COP_{CC})} \times 100 \tag{10}$$

A detailed economic analysis including both efficiency and performance for AC systems is carried out for a data center with a power consumption range of 4.5 to 13.5 MW.

In designing cooling system for modern data centers, the waste heat dissipated per rack could be assumed between 10 and 15 kW. Note that if the rack is occupied with supercomputers, the heat generation can be up to 60 kW from each rack [31]. Accordingly, in the calculations, it is assumed that maximum 15 kW of waste heat is dissipated by each server rack (Figure 2). Additionally, water is used as cooling agent with the flowrate of 0.3 to 0.6 l/s. The design temperature of outgoing water is assumed 70 °C which is somewhat lower than the typical temperature of 85 °C. This is ascribed to the heat loss of the intermediate heat exchanger.

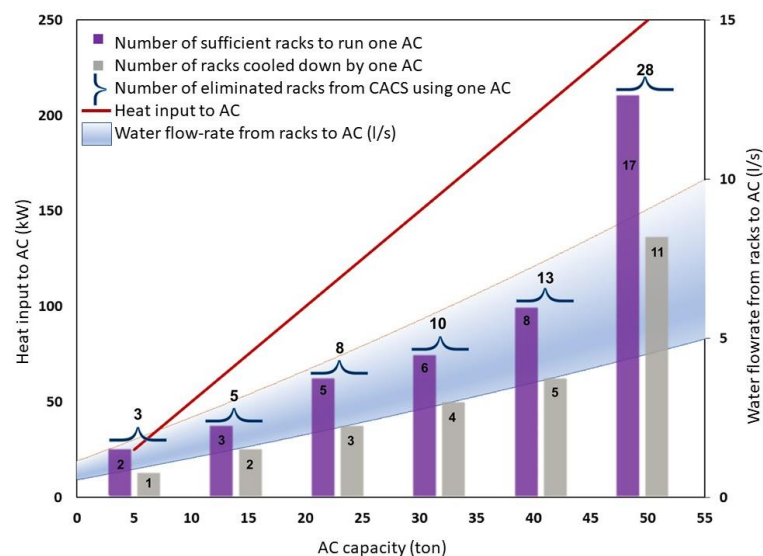


Figure 2. Heat dissipation by server racks and cooling process by AC chillers.

3. Results and Discussion

3.1. Energy Performance

An energy analysis is imperative to make a decision for the selection of the best design. Therefore, Tables 1 and 2 present a detailed energy performance for both 4.5 and 13.5 MW power consumed data centers, respectively. The cooling capacity and the performance of the AC systems depend on many parameters such as the heat source temperature, the flow rate, and the cooling water temperature. For example, for a 10 ton WFC-S10 Yazaki LiBr AC unit, the heat input and the pump power input are 15.2 kW_{th} and 0.18 kW_e, respectively [30,32]. Moreover, the cooling capacity is 9.8 kW_{th} [30,32]. It should be mentioned that kW_e represents the kilowatt electrical while kW_{th} is a representative of kilowatt thermal. Accordingly, COP_{CC} of 4 and COP_{AC} of 0.63 for the CC system and AC system, respectively are assumed when the inlet hot water temperature from data center to AC is 70 °C. We also assume the total of 8760 h data center operates in one year. As a rule of thumb, for a conventional data center energy consumption of cooling system is equivalent to energy consumption of server racks. Electricity consumption for the CC system is equal to the number of racks multiply by power of each rack and total working hours in a year. Accordingly, electricity consumption by the proposed integrated system can be calculated through Equations (9) and (10). Table 1 presents electricity consumption for a 4.5 MW and 13.5 MW data center comprising 300 and 900 server racks, respectively.

Table 1. Energy analysis for cooling a 4.5 MW and 13.5 MW data center comprising 300 and 900 racks with chillers of 575 ton and 1600 ton capacity.

Power Consumption	Conventional Compression Chiller (CC)	Proposed Waste Heat Recovery System	Energy Saving (kWh/Year)
4.5 MW	Cooling Electricity consumption (kWh/year)		4,340,000
	$W_{\text{electricity-conventional}} = 9,855,000$	$W_{\text{electricity-hybrid}} = 5,515,000$	
13.5 MW	Cooling Electricity consumption (kWh/year)		13,025,000
	$W_{\text{electricity-conventional}} = 29,565,000$	$W_{\text{electricity-hybrid}} = 16,540,000$	

For the 4.5 MW data center, it is estimated that 13 racks can be covered with AC systems of 25 ton capacity. The direct dissipation occurs by means of the AC system generator for eight of the racks, while the remaining five use the evaporator of the AC system. As a consequence, total of 299 server racks can be eliminated from a cold-aisle containment system (CACS) load (13 managed by each chiller) using 23 chillers of 25 ton capacity. The application of CACS is to confine the cold aisle allowing the rest of the data room to become a large hot-air return plenum. As a result, a drastic reduction is observed in the number of server racks cooled by CACS. This change results in a significant reduction in the CACS load. An alternative design for data centers can be considered as number of racks in multiples of 13 without any further need to CACS for cooling purposes. Note that each 25-ton AC unit is capable of saving footprint area of 2 racks.

For the 13.5 MW data center, the results indicate that a 50-ton AC chiller is sufficient to cover 28 racks in the data room. Approximately 60% of the racks (i.e., 17 out of 28) directly disperse the heat into the generator of the AC system. While the remaining 40% use evaporator of the AC system for the heat removal. Thus, it is estimated that 32 chillers of 50 ton capacity enables removal of 896 server racks from the CACS load (i.e., 28 managed by each chiller). Similarly, a significant reduction of 900 to 4 in the number of racks cooled by CACS unit is observed. Similarly, it is possible to design an alternate configuration of racks in multiples of 28 which ultimately drops the any need to cooling by CACS. However, a detailed calculation can be performed based on specific operational needs of the data center. Each 50 ton AC unit is capable of saving footprint area of 3 racks.

Table 2. Economic analysis for a 4.5 and 13.5 MW data center comprising 300 and 900 server racks with chillers of 575 ton and 1600 ton capacity.

Power Consumption	Conventional Compression Chiller (CC)	Proposed Waste Heat Recovery System
4.5 MW	Electricity cost (\$/year)	
	9,855,000 kWh × 0.12 (\$/kWh) = \$1,182,600	9,855,000 kWh × 0.12 (\$/kWh) = \$1,182,600
	Cooling cost (\$/year)	
	\$1,182,600 (typical value for energy usage of a data center which is proportional to the ones from server racks)	\$1,182,600 × (Equation (10)) = \$661,800
	Total annual cost (\$/year)	
\$2,365,200	\$1,844,400	
The prices of the chillers and cooling tower		575 * × \$2500 = \$1,437,500
13.5 MW	Electricity cost (\$/year)	
	29,565,000 kWh × 0.12 (\$/kWh) = \$3,547,800	29,565,000 kWh × 0.12(\$/kWh) = \$3,547,800
	Cooling cost (\$/year)	
	\$3,547,800 (typical value for energy usage of a data center which is proportional to the ones from server racks)	\$3,547,800 × (Equation (10)) = \$1,984,800
	Total annual cost (\$/year)	
\$7,095,600	\$5,532,600	
The prices of the chillers and cooling tower		1600 * × \$2500 = \$4,000,000

* Capacity of chillers and cooling towers.

3.2. Economic Performance

An economic analysis is imperative to make a decision for the selection of the best design. Therefore, Table 2 presents a detailed economic analysis for both 4.5 and 13.5 MW power consumed data centers, respectively. The total annual electricity cost for each scenario comprises (1) electricity cost to run the servers and (2) energy cost to operate the cooling infrastructure. Electricity consumption of the data center is calculated based on the average power per racks by the number of servers in each rack. Therefore, the electricity consumption and its associated costs for running the servers in each rack is equal for both scenarios. On the other hand, the electricity associated with the infrastructure equipment (i.e., cooling systems) is calculated for two different scenarios (i.e., the conventional system and the proposed hybrid system).

A rough payback period is calculated based on the given assumptions in Table 2. The rough payback analysis provides how long the obtained savings from the use of the new system will take to pay back for the initial capital cost of the introduced system. As the operating expense and maintenance cost of the AC system is not included in the calculations, it is not possible to have a precise number for the payback period. The simple payback period for the proposed CC-AC system is calculated through Equation (11).

$$\text{Payback period (year)} = \frac{\text{Saving Cooling Cost (\$/year)}}{\text{Total costs of the AC and cooling tower}} \quad (11)$$

Thus, the simple payback estimation of the employment of AC in a 4.5 MW data center is estimated 2.76 years. The payback period for the 13.5 MW data center is, however, calculated between 2.56 years indicating scaling up the data center can enhance the profitability of the low-grade waste heat recovery system.

The results indicate that an AC system with a range of 5 to 50 ton capacity can afford adequate coolth energy to keep one more rack in the safe temperature level by waste heat dissipation from 2 to 17 racks. It is also evident that the AC system provides a faster payback period for a larger scale data center.

3.3. Environmental Performance

As stated earlier, there is growing demand for computing capacity resulting in development of data centers with significant power loads and densities around the globe [33]. Furthermore, the new generation of Central Processing Units (CPUs) can dissipate a remarkable amount of power in excess of 400 watts across the surface area of a credit card [34]. Safe operation of data centers, including numerous pieces of electronic equipment, requires proper temperature management based on the thermal envelopes provided by standardization entities. Full thermo- hygrometric state of the data centers environment must be actively inspected to lessen the potential risk of waste heat discharge to the environment or condensate the moist air when humidity raises. Therefore, management of thermal pollution in data centers is of significant importance.

The principle objective of controlling environment in data centers is to meet the time-varying cooling demand. According to the American Society of Heating, Refrigerating and Air-Conditioning Engineers (ASHRAE) [35], economic considerations have been changing the controlled environmental conditions of the data centers. Cooling data centers can cost up to a quarter of total energy expenses. In its first thermal guidelines for data centers, ASHRAE recommended air temperature envelope for data centers was 20–25 °C based on both reliability and uptime (primary concerns) and energy costs secondary (concerns). As a result, four classes of data center equipment; A1, A2, A3 and A4 (Table 3).

Table 3. Four classes of data centers according to ASHRAE.

Class	Temperature Range (°C)	Humidity Range (%)
A1	15–32	20–80
A2	10–35	20–80
A3	5–40	8–85
A4	5–45	8–90

The majority of today's data centers falls into class A1 and A2, nonetheless, many of modern manufacturers have been commercializing equipment compatible with class A3 and A4 operation.

As shown in Table 1, the amount of energy saving from the proposed systems of 4.5 MW and 13.5 MW power consumed data centers are 4,340,000 kWh/year and 13,025,000 kWh/year, respectively. Considering every kWh emits averagely 7.07×10^{-4} metric tons CO₂ [36], the proposed AC system is estimated to save 3068 t CO₂/year and 9208 t CO₂/year. These amounts of CO₂ are approximately equal to 9066 and 27,190 barrels of crude oil. Furthermore, it is estimate that this GHG emission reduction is equivalent to 358 ha and 1074 ha of additional forest to adsorb this CO₂ from the atmosphere.

4. Conclusions

In the existing energy conversion systems for decentralized source of heat, the majority of primary energy is lost as waste heat. This could be an enormous source of energy particularly in high energy consumption enterprises such as data centers. The highest portion of the energy lost in the data centers are classified as a low-grade waste heat and basically is the most challenging part to be recovered, especially when the temperature of waste heat is below 100 °C. Absorption chiller systems are known as a well-established technology to recover the low-grade waste heat. The advancement of IoT technologies and its interaction with big data and could computing are extensively increasing leading to significant development of data centers. Thus, this research investigated feasibility of

heat recovery options and analyzed the techno-economic aspect of an absorption chiller system for the low-grade waste heat recovery from a data center. The results of this study necessitate consideration of both technical and economic aspects at the same time. The proposed hybrid system enables saving electricity for the value of 4.3 GWh/year and 13.0 GWh/year leading to an annual reduction of 3068 and 9208 tons CO₂ equivalent of greenhouse gas (GHG) emissions, respectively. Furthermore, the simple payback of 2.76 and 2.56 years, respectively, for the employment of proposed system in a 4.5 MW and 13.5 MW data center is estimated. Moreover, the environmental analysis also shows that AC system is a promising option for waste heat recovery and save notable equivalent carbon emissions to the environment. It is concluded that enhancing the capacity of the AC system enables waste heat dissipation of higher number of racks while shorten the payback period. Future work could focus on the employment of higher-performance absorbers and generators for designing new absorption cycles.

Author Contributions: L.A.: Conceptualization, investigation, methodology, software, validation, writing—original draft, writing—review and editing. E.M.: conceptualization, validation, writing—review and editing. N.B.: conceptualization, validation, writing—review & editing. S.A.G.-M.: supervision, writing—review and editing. All authors have read and agreed to the published version of the manuscript.

Funding: This research received no external funding.

Institutional Review Board Statement: Not applicable.

Informed Consent Statement: Not applicable.

Data Availability Statement: The data presented in this study are openly available at <https://doi.org/10.3390/xxxxx>.

Acknowledgments: The first author acknowledge the financial support provided by the Killam Trusts fund scholarships and Dalhousie University.

Conflicts of Interest: The authors declare no conflict of interest.

Abbreviations

CC	Conventional Compression Chiller
AC	Absorption Chiller
CACS	Cold-Aisle Containment System
IoT	Internet of Things
IT	Information Technology
ORC	Organic Rankine Cycle
EA	Enclosed Aisle
OA	Open Aisle
GHG	Greenhouse Gas

References

- Huang, P.; Copertaro, B.; Zhang, X.; Shen, J.; Löfgren, I.; Rönnelid, M.; Fahlen, J.; Andersson, D.; Svanfeldt, M. A review of data centers as prosumers in district energy systems: Renewable energy integration and waste heat reuse for district heating. *Appl. Energy* **2020**, *258*, 114109. [CrossRef]
- Koomey, J. *Growth in Data Center Electricity Use 2005 to 2010*; Anal. Press: City, Country, 2011; pp. 1–24. Available online: https://alejandrobarrros.com/wp-content/uploads/old/Growth_in_Data_Center_Electricity_use_2005_to_2010.pdf (accessed on 1 January 2020).
- Dandres, T.; Moghaddam, R.F.; Nguyen, K.K.; Lemieux, Y.; Samson, R.; Cheriet, M. Consideration of marginal electricity in real-time minimization of distributed data centre emissions. *J. Clean. Prod.* **2017**, *143*, 116–124. [CrossRef]
- Rong, H.; Zhang, H.; Xiao, S.; Li, C.; Hu, C. Optimizing energy consumption for data centers. *Renew. Sustain. Energy Rev.* **2016**, *58*, 674–691. [CrossRef]
- Van Heddeghem, W.; Lambert, S.; Lannoo, B.; Colle, D.; Pickavet, M.; Demeester, P. Trends in worldwide ICT electricity consumption from 2007 to 2012. *Comput. Commun.* **2014**, *50*, 64–76. [CrossRef]
- Huang, Q.; Shao, S.; Zhang, H.; Tian, C. Development and composition of a data center heat recovery system and evaluation of annual operation performance. *Energy* **2019**, *189*, 116200. [CrossRef]

7. Ebrahimi, K.; Jones, G.F.; Fleischer, A.S. A review of data center cooling technology, operating conditions and the corresponding low-grade waste heat recovery opportunities. *Renew. Sustain. Energy Rev.* **2014**, *31*, 622–638. [CrossRef]
8. Samadiani, E.; Joshi, Y. Energy efficient thermal management of data centers via open multi-scale design: A review of research questions and approaches. *J. Enhanc. Heat Transf.* **2011**, *18*, 15–30. [CrossRef]
9. van de Bor, D.; Ferreira, C.I.; Kiss, A.A. Low grade waste heat recovery using heat pumps and power cycles. *Energy* **2015**, *89*, 864–873. [CrossRef]
10. Yang, S.; Wang, Y.; Gao, J.; Zhang, Z.; Liu, Z.; Olabi, A.G. Performance Analysis of a Novel Cascade Absorption Refrigeration for Low-Grade Waste Heat Recovery. *ACS Sustain. Chem. Eng.* **2018**, *6*, 8350–8363. [CrossRef]
11. Amiri, L.; Madadian, E.; Hassani, F.P. Ergo- and exergo-technical assessment of ground-source heat pump systems for geothermal energy production from underground mines. *Environ. Technol.* **2018**, *40*, 3534–3546. [CrossRef]
12. Amiri, L.; De Brito, M.A.R.; Baidya, D.; Kuyuk, A.F.; Ghoreishi-Madiseh, S.A.; Sasmito, A.P.; Hassani, F.P. Numerical investigation of rock-pile based waste heat storage for remote communities in cold climates. *Appl. Energy* **2019**, *252*, 113475. [CrossRef]
13. Zimmermann, S.; Meijer, I.; Tiwari, M.K.; Paredes, S.; Michel, B.; Poulikakos, D. Aquasar: A hot water cooled data center with direct energy reuse. *Energy* **2012**, *43*, 237–245. [CrossRef]
14. Davies, G.; Maidment, G.; Tozer, R. Using data centres for combined heating and cooling: An investigation for London. *Appl. Therm. Eng.* **2016**, *94*, 296–304. [CrossRef]
15. Fang, H.; Xia, J.; Zhu, K.; Su, Y.; Jiang, Y. Industrial waste heat utilization for low temperature district heating. *Energy Policy* **2013**, *62*, 236–246. [CrossRef]
16. Wang, Z.; Ren, T.; Ma, L.; Zhang, J. Investigations of Ventilation Airflow Characteristics on a Longwall Face—A Computational Approach. *Energies* **2018**, *11*, 1564. [CrossRef]
17. Xie, M.; Wang, J.; Liu, J. Evaluation metrics of thermal management in data centers based on exergy analysis. *Appl. Therm. Eng.* **2019**, *147*, 1083–1095. [CrossRef]
18. Wang, Y.; Sun, X.; Dai, Y.; Wu, G.; Cao, Y.; Huang, D. Numerical investigation of drag reduction by heat-enhanced cavitation. *Appl. Therm. Eng.* **2015**, *75*, 193–202. [CrossRef]
19. Gupta, R.; Moazamigoodarzi, H.; MirhoseiniNejad, S.; Down, D.G.; Puri, I.K. Workload management for air-cooled data centers: An energy and exergy based approach. *Energy* **2020**, *209*, 118485. [CrossRef]
20. Ahmadi, V.E.; Erden, H.S. A parametric CFD study of computer room air handling bypass in air-cooled data centers. *Appl. Therm. Eng.* **2020**, *166*, 114685. [CrossRef]
21. Nadjahi, C.; Louahlia, H.; Lemasson, S. A review of thermal management and innovative cooling strategies for data center. *Sustain. Comput. Inform. Syst.* **2018**, *19*, 14–28. [CrossRef]
22. Schmidt, R.; Cruz, E. Cluster of High-Powered Racks Within a Raised-Floor Computer Data Center: Effect of Perforated Tile Flow Distribution on Rack Inlet Air Temperatures. *J. Electron. Packag.* **2004**, *126*, 510–518. [CrossRef]
23. Erden, H.S.; Koz, M.; Yildirim, M.T.; Khalifa, H.E. Experimental Demonstration and Flow Network Model Verification of Induced CRAH Bypass for Cooling Optimization of Enclosed-Aisle Data Centers. *IEEE Trans. Compon. Packag. Manuf. Technol.* **2017**, *7*, 1795–1803. [CrossRef]
24. Demetriou, D.W.; Khalifa, H.E. Optimization of Enclosed Aisle Data Centers Using Bypass Recirculation. *J. Electron. Packag.* **2012**, *134*, 020904. [CrossRef]
25. Yu, J.; Jiang, Y.; Yan, Y. A simulation study on heat recovery of data center: A case study in Harbin, China. *Renew. Energy* **2019**, *130*, 154–173. [CrossRef]
26. Ebrahimi, K.; Jones, G.F.; Fleischer, A.S. The viability of ultra low temperature waste heat recovery using organic Rankine cycle in dual loop data center applications. *Appl. Therm. Eng.* **2017**, *126*, 393–406. [CrossRef]
27. Araya, S.; Jones, G.F.; Fleischer, A.S. Organic Rankine Cycle as a Waste Heat Recovery System for Data Centers: Design and Construction of a Prototype. In Proceedings of the 2018 17th IEEE Intersociety Conference on Thermal and Thermomechanical Phenomena in Electronic Systems (ITherm); Institute of Electrical and Electronics Engineers (IEEE), San Diego, CA, USA, 29 May–1 June 2018; pp. 850–858.
28. Araya, S.; Wemhoff, A.P.; Jones, G.F.; Fleischer, A.S. Study of a Lab-Scale Organic Rankine Cycle for the Ultra-Low-Temperature Waste Heat Recovery Associated WITH Data Centers. *J. Electron. Packag.* **2020**, *143*. [CrossRef]
29. Thermax. Hot Water Driven Vapor Absorption Machine. Instrumentation. Available online: https://www.trane.com/content/dam/Trane/Commercial/global/products-systems/equipment/chillers/absorption-liquid/hotwater_drivenabsorptionchillers.pdf (accessed on 1 January 2020).
30. VAMTEC | YAZAKI Hot Water Absorption Chiller. Available online: <https://www.vamtec.com/absorption-chiller/> (accessed on 1 January 2020).
31. Marcinichen, J.B.; Olivier, J.A.; Thome, J.R. On-chip two-phase cooling of datacenters: Cooling system and energy recovery evaluation. *Appl. Therm. Eng.* **2012**, *41*, 36–51. [CrossRef]
32. Haywood, A.; Sherbeck, J.; Phelan, P.; Varsamopoulos, G.; Gupta, S.K. Thermodynamic feasibility of harvesting data center waste heat to drive an absorption chiller. *Energy Convers. Manag.* **2012**, *58*, 26–34. [CrossRef]
33. Dreibholz, T.; Becke, M.; Adhari, H. Report to Congress on Server and Data Center Energy Efficiency Public Law 109–431; Tdr.Wiwi.Uni-Due.De 109; 2007; p. 431. Available online: <https://www.osti.gov/biblio/929723> (accessed on 1 January 2020).
34. Corporation, I. *Product Specifications, Processors*; 2019.

35. ASHRAE. *Data Center Power Equipment Thermal Guidelines and Best Practices; Standard*, 2016; pp. 1–60.
36. EPA. *AVERT, U.S. National Weighted Average CO₂ Marginal Emission Rate, Year 2017 Data*; U.S. Environmental Protection Agency, 2018.

Article

Comparison of Ground-Based Global Horizontal Irradiance and Direct Normal Irradiance with Satellite-Based SUNY Model

Adnan Ayaz¹, Faraz Ahmad^{2,*} , Mohammad Abdul Aziz Irfan¹ , Zabdur Rehman^{2,*}, Krzysztof Rajski³ 
and Jan Danielewicz^{3,*}

¹ Mechanical Engineering Department, University of Engineering and Technology Peshawar, Peshawar 25120, Pakistan; adnanayaz@uetpeshawar.edu.pk (A.A.); mairfan@uetpeshawar.edu.pk (M.A.A.I.)

² Department of Mechanical Engineering, Aerospace and Aviation Campus Kamra, Air University Islamabad, Kamra 43570, Pakistan

³ Faculty of Environmental Engineering, Wrocław University of Science and Technology, PL50377 Wrocław, Poland; krzysztof.rajski@pwr.edu.pl

* Correspondence: faraz.ahmad0460@gmail.com (F.A.); zabd@aack.au.edu.pk (Z.R.); jan.danielewicz@pwr.edu.pl (J.D.)

Abstract: Since the fossil reserves are depleting day by day, the trend of modern energy sector is going towards renewable energy. The demand of solar power plants is therefore at the peak nowadays across the globe. However, the construction of these plants is extremely dependent on feasibility study to estimate the real solar potential before installing it in any region. To evaluate the solar energy potential of Peshawar region in Pakistan, Ground-based global horizontal irradiance (GHI) and direct normal irradiance (DNI) were compared with satellite-based model SUNY. Ground measurements were done at the University of Engineering and Technology Peshawar (UET Peshawar) with the help of pyranometer and shadowband irradiator. Comparison of the data showed that there was a maximum difference of 42.90% in ground and satellite-based GHI in the month of December. Minimum difference in GHI was found for the month of March that was -3.83% . Moreover, ground-based GHI was overestimated in the month of February, March, and April, while in rest of the months, satellite values of GHI exceeded the ground measurements. Similarly, maximum difference of 55.86% was found in the month of November between ground and satellite-based DNI while minimum difference of -3.34% was seen in DNI in the month of March between the two data. Furthermore, satellite-based DNI was underestimated in the months of February, March, and April while in rest of the months it was overestimated compared to ground measurements. In addition to this, correlation of ground and satellite-based GHI and DNI showed R^2 value of 0.8852 and 0.4139, respectively. The results of this study revealed that the difference between ground measurements and satellite values was considerable and hence real time measurements are necessary to properly estimate solar energy resource in the country.

Keywords: global horizontal irradiance; direct normal irradiance; satellite based SUNY model; combined uncertainty

Citation: Ayaz, A.; Ahmad, F.; Irfan, M.A.A.; Rehman, Z.; Rajski, K.; Danielewicz, J. Comparison of Ground-Based Global Horizontal Irradiance and Direct Normal Irradiance with Satellite-Based SUNY Model. *Energies* **2022**, *15*, 2528. <https://doi.org/10.3390/en15072528>

Academic Editor:

Juan Luis Bosch Saldaña

Received: 24 February 2022

Accepted: 28 March 2022

Published: 30 March 2022

Publisher's Note: MDPI stays neutral with regard to jurisdictional claims in published maps and institutional affiliations.



Copyright: © 2022 by the authors. Licensee MDPI, Basel, Switzerland. This article is an open access article distributed under the terms and conditions of the Creative Commons Attribution (CC BY) license (<https://creativecommons.org/licenses/by/4.0/>).

1. Introduction

Utilization of energy has become a vital part of our life and its demand is increasing day by day [1]. Like most of the countries across the globe, Pakistan is also facing a serious issue of energy crisis for past few decades and the problem is getting severe with the passage of time [2]. At the moment, most of the energy demands are met by utilizing fossil fuels like coal, oil, and gas. However, these fossil fuels are rapidly depleting and they will disappear completely in the coming years. Moreover, consumption of fossil fuels strongly affects natural environment by releasing greenhouse gases into the atmosphere. There is a dire need to shift from conventional energy resources to renewable resources of energy. Solar energy is considered to be one of the vital resources of renewable energy [3].

In the past few decades, numerous studies have been conducted to assess the solar energy resource potential and increasing its efficiency using different techniques [4]. For example, Gueymard et al. [5] conducted a study to assess solar energy resource in United States of America with respect to spatial and temporal variation. Data were taken mostly from SUNY model of National Solar Radiation Database (NSRDB) for a time span between 1998 and 2005. A similar kind of research was conducted by Zell et al. [6] in Saudi Arabia in which a solar energy monitoring program was devised by King Abdullah City for Atomic and Renewable Energy (KACARE). The annual average GHI varied from 5700 Wh/m² to 6700 Wh/m². Same study mentioned that performance of PV might be degraded because of higher temperature which is almost 30 °C on average at various locations of Saudi Arabia. Similarly, a study was carried out by Al Yahya and Irfan [7] which presented discussion on the new solar atlas of Saudi Arabia. This solar atlas consisted of 41 stations which were capable of delivering solar data across the various regions of the country. This study was part of the Renewable Resource Monitoring and Mapping (RRMM) program. Through RRMM, they found that direct normal irradiance (DNI) of the country ranged from 5000 Wh/m²/day which was recorded in winter to 9000 Wh/m²/day in summer.

Moreover, Alnaser et al. [8] presented a study in which they presented the data of Solar Radiation Atlas for the Arab World. For a period of 10 years in Arab world, the highest annual mean global solar irradiance was calculated to be 6.7 kWh/m²/day Nouakchott, Mauritania and 6.6 kWh/m²/day in Tamenraset, Algeria. However, the minimum mean global irradiance was calculated in Mosul, Iraq which was 4.1 kWh/m²/day. Similarly, Bachour and Perez [9] analyzed ground-based GHI at Doha International Airport in the time span between 2008 and 2012 which revealed that average daily GHI was 5.61 kWh/m²/day which in other words becomes 2048 kWh/m²/year. In addition to this, a maximum monthly average was calculated to be 6.97 kWh/m²/day for the month of June.

Satellite-based DNI is affected by several parameters out of which the most critical and important factor is aerosol optical depth (AOD) [10]. Aerosols are very crucial for calculation of solar energy resource and play a critical role to estimate surface irradiance from the available satellite-based solar irradiance. A study in Thailand revealed that in majority of the cases, 10 to 15% of total depletion of solar energy by all atmospheric particles occurred due to aerosols [10]. Moreover, it has been found that 5% of the total depletion of solar energy from aerosols occurs due to scattering of solar energy from continental aerosols. Similarly, a research in India was done to incorporate aerosols dataset to get an accurate satellite model for computing DNI [11]. It was noted that the fine aerosol particles could be removed from atmosphere in monsoon season. It was also noticed that due to wind, aerosols also moved from one location to another, hence creating uncertainty in the estimation of DNI. In addition to this, a study compared eight clear sky broadband models [12]. This study concluded that turbidity plays a very important and crucial role to estimate the irradiance received. This study also stated that the important factors that are considered for clearest atmospheric conditions are aerosol loads, water vapor component, and least turbidity. To account for such issues in analyzing the solar irradiance, Mueller et al. [13] devised a satellite-based model called The SOLIS clear-sky module. While making this model, ozone, water vapors, and aerosols were taken into the account. Results obtained from this model were compared with ground-based measurements.

Satellite-based data are acquired on the basis of forecasting techniques. Some satellite-based forecasting techniques use position of clouds to estimate solar energy over a particular location. A study showed that motion vectors were used to predict the upcoming position of the clouds over particular location of the ground and it was noted that they provided fine forecasting accuracy of almost 6 h. Predictions from cloud pose several problems to properly forecast solar irradiance [14]. Therefore, comparison of satellite-based solar data and ground-based measured solar data has been of much importance to many researchers across the globe. Vignola et al. [15] conducted a study at Kimberly, Idaho in which satellite-based solar data and ground-based solar data were analyzed to validate the satellite-based solar model. It was found that mean bias error for satellite-based global irradiance was 5%

and it was 2% for beam irradiance. Similarly, Blanksby et al. [16] conducted a research in Australia to check the accuracy of satellite-based solar model. It was noted that for lesser values of GHI, satellite-based data were overestimated compared to the ground-based data. However, for greater values of GHI, satellite-based data were either overestimated or underestimated compared to the ground-based data.

A study in Brazil compared satellite-based solar irradiance with ground-based measurements [17]. Irradiance was analyzed on the basis of monthly average daily mean values. Comparison of this satellite-based data and ground measurements showed a global root mean square error of 13% for all data points. To estimate the satellite-based direct normal irradiance in the tropical environment of Thailand, a method was devised by Janjai [18] where the satellite selected for this study was MTSAT-1R. First, data of this satellite were used to estimate the global horizontal irradiance and then satellite-based diffused fraction model was devised to estimate the diffuse solar irradiance. Based on global horizontal irradiance and diffuse irradiance, direct normal irradiance was estimated. A similar kind of research was conducted to verify the values of direct normal irradiance of SUNY which is a satellite-based model with the ground-based values in various locations of California [19]. The study focused on finding variation in both the data and also to find accuracy in SUNY model. Mean bias error was noted in the range of -6.39% to 14.21% and correlation coefficient was 0.90 to 0.95 for direct normal irradiance.

Perez et al. [20] compared the satellite-based data taken from GOES 8 with the data which was interpolated and extrapolated with respect to 12 ground-based measurement stations located in New York and Massachusetts in America. A satellite-based model was devised by Janjai et al. [21] to calculate global solar irradiance in tropical areas of Thailand. This study shows that tropical areas in Thailand have high aerosols load. Ambient temperature and relative humidity were used to predict absorption of solar rays due to water vapors in atmosphere. This model also explained how to relate visibility with depletion due to aerosols load. Monthly average hourly global irradiance calculated from both the satellite-based model and ground-based measurements was quite matching with each other by having a root mean square difference of 10% only. An experiment was conducted in the summer months of the year 1977 in United States to check whether ground-based solar irradiance could be obtained through estimation from geostationary satellites [22]. When satellite-based daily insolation was compared to ground-based pyranometers data, the standard error was calculated to be 10% of the mean data. Furthermore, three pyranometers stations were installed at three different locations of Canada which were Ottawa, Toronto, and Montreal [23]. Measurements done at these stations in the summer and spring duration of the year 1978 concluded that on the average, there measurements had 9% variation compared with satellite-based model for daily insolation data in cloudy conditions.

A lot of studies were conducted on ground-based data and satellite-based data [24–29]. Some of studies done in the past showed that there were various errors associated with satellite-based models and that is why there was a difference between solar data obtained from satellite models and ground measurements [30–32]. One such study in Northeastern US showed that there was relative root mean square error of 23% between satellite model (based on data of GOES-8) and 8 years on site measured hourly irradiance [30]. Pixel-to-irradiance conversion error in satellite model was calculated to be 12–13%. Another analysis was done to find long run variation in broadband solar irradiance at surface [31]. Data analyzed were based on three-hourly duration for a time of 18 years. Satellite data of this research were taken from ISCCP (International Satellite Cloud Climatology Project). The data taken were validated with the data based on two years, obtained from Meteosat. Validation of the data showed that when volcanic aerosols were not and were included, annual average of DNI was reduced by 16% while annual average of GHI was reduced by less than 2.2%. Cebecauer and Suri [32] developed a new model based on the data obtained from Meteosat MSG (Meteosat Second Generation). This improved model had the capability to better predict variation and improve accuracy in GHI and DNI, when there were high vapor contents and aerosols load.

Keeping in view the depletion of fossil fuels, the establishment of solar power plants is need of the hour for any country across the globe. However, their construction must be emphasized in order to overcome energy crises in the country. Feasibility study is one of the important phases in establishment of solar power plants. There is a need to estimate the solar energy potential at a particular site in order to have a clear overview to identify if the site is a good choice for the installation of any solar power plant. To identify the best site for the installation of solar power plants, solar energy resource assessment plays a vital role which can be done using various equipment like pyranometer and pyrheliometer. These equipment are used to measure ground-based solar energy resource at any location where establishment of solar power plant is desired. Therefore, ground stations are very important to measure the actual solar energy received with the help of these equipment. Besides ground measurements, there are various satellite models in use these days which show an estimation of solar energy potential and they can be widely used to guess the solar energy resource [33]. Problem associated with satellite models is that they are not accurate and there is significant variation between ground measurements and satellite modeled data. Therefore, satellite-based solar data are often compared to ground-based measurements to find the amount of variation between the two [33]. Comparison of ground measurements and satellite modeled solar data provides a clear insight to decide whether or not solar power plants can be established on the basis of satellite modeled data.

Keeping in view of the previous studies, it was clear that in some cases ground-based GHI and DNI were more accurate than satellite data. To accurately study the difference in results, an experimental study was performed in the current research, which will enable researchers to accurately use solar data in the applications of solar energy. In the present study, ground-based global horizontal irradiance (GHI), and direct normal irradiance (DNI) were measured and compared with satellite modeled data. Ground-based measurements were done at UET Peshawar by using its weather station. Weather station at UET Peshawar consists of various devices among which pyranometer and shadowband irradiometer are used to measure solar irradiance. Satellite-based solar energy was taken from a model called SUNY.

2. Materials and Methods

2.1. Equipment

Various equipment used in this study are part of the established weather station at University of Engineering and Technology (UET) Peshawar. Weather station at UET Peshawar was installed by World Bank under its program called Energy Sector Management Assistance Program (ESMAP). This project of World Bank aimed to map renewable energy resources in Pakistan. Several other weather stations were also established at different locations of Pakistan. Currently, weather station is maintained by UET Peshawar. Figure 1 shows weather station located at UET Peshawar.



Figure 1. Weather Station established at UET Peshawar.

This weather station consists of various equipment which were used in this study. Some of the equipment used in this study are discussed as follows.

2.1.1. Pyranometer

Pyranometer is used to measure solar irradiance received at a surface and there are various types of pyranometers available in the market with different technologies and specifications. However, pyranometers used in this study came from well-known manufacturer called Kipp and Zonen (Delft, The Netherlands) whose model is Kipp & Zonen CMP10. This pyranometer was used to collect global horizontal irradiance (GHI) received at UET Peshawar. Figure 2 shows pyranometer installed at UET Peshawar and its specifications are given in Table 1.



Figure 2. Kipp & Zonen CMP10 pyranometer installed at UET Peshawar.

Table 1. Specifications of Kipp & Zonen CMP10 pyranometer.

Properties	Values
Spectral range (50% Points)	285 to 2800 nm
Sensitivity	7 to 14 $\mu\text{V}/\text{W}/\text{m}^2$
Response Time	<5 s
Zero offset A	<7 W/m^2
Zero offset B	<2 W/m^2
Directional response (up to 80° with 1000 W/m^2 beam)	<10 W/m^2
Temperature dependence of sensitivity (−10 °C to +40 °C)	<1%
Operational temperature range	−40 °C to +80 °C
Maximum solar irradiance	4000 W/m^2

2.1.2. Rotating Shadowband Irradiometer (RSI)

Rotating shadowband irradiometer (RSI) is used to measure global horizontal irradiance (GHI), direct normal irradiance (DNI), and diffuse horizontal irradiance (DHI). RSI installed at UET Peshawar came from Concentrating Solar Power Services (CSPS) which is called CSPS Twin-RSI. It has two radiation detectors made from silicon located in the middle of a spherical shaped shadowband. The two radiations sensors called LI-200 came from LI-COR Inc. (Lincoln, NE, USA). When shadowband is below the sensor in rest position, the sensor measures GHI. Shadowband moves after some time and it comes in the path to block DNI. When DNI is blocked, the sensor measures DHI. When GHI and DHI both are known, DNI can easily be calculated. Figure 3 shows RSI installed at UET Peshawar. Specifications of CSPS Twin-RSI are given in Table 2.



Figure 3. CSPC Twin-RSI installed at UET Peshawar.

Table 2. Specifications of Twin-RSI.

Temperature range	−30 to +65 °C
Humidity	0 to 100% Rh
Dimensions	500 × 100 × 200 mm
Weight	2.1 kg
Power demand	<1 W at average
Output signal	≈90 μA per 1000 W/m ²
Response time	10 μs

2.1.3. Data Logger

Data logger is used for data acquisition which come from various components of weather station like pyranometer and RSI. Data which are collected by various components of weather station are stored in data logger and then extracted by connecting it with a computer. Data can also be transferred remotely. The data obtained from data logger contained missing and redundant values. Therefore, two types of quality controlled (QC) tests were performed to make the data ready to use. First, automatic QC tests were performed to identify the missing values, time shift, consistency of data by comparing the redundant values, and the data were compared with maximum and minimum irradiance values. Then, the visual QC tests were performed for flagging the data. A more detailed description of these tests can be found in [34,35].

Data logger used in UET Peshawar’s weather station is a product of Campbell Scientific Inc. and its model is CR1000. This data logger is very good for extreme conditions and remote environments. Figure 4 shows the data logger which is part of the weather station located at UET Peshawar.

2.2. Location of UET Peshawar

University of Engineering and Technology is located at Peshawar region of Pakistan having latitude of 34.0017° N and longitude of 71.4854° E. Data used in this study were taken from Weather station established at UET Peshawar. Then, these data were filtered through QC tests discussed in the data logger section.



Figure 4. CR1000 data logger installed at UET Peshawar’s weather station.

2.3. Methodology Adopted

In this part of the study, satellite-based GHI and DNI are compared with ground measurements for year 2017. As mentioned earlier, ground-based data were taken from weather station established at UET Peshawar.

Ground-based GHI and DNI were measured by pyranometer and Twin-RSI which both are already explained previously. These DNI and GHI were collected from data logger and were further analyzed. Data were available for the whole year 2017 except for the first 16 days of January and the last 19 days of December. Data were received at weather station after each 10 min duration. Available DNI and GHI for each month were processed on the basis of daily total monthly mean. When all the data were processed on the basis of daily total monthly mean, one data point was obtained for each month. In this way, 12 data points were available for the 12 months of 2017.

Satellite model chosen for analysis was SUNY (<https://nsrdb.nrel.gov/international-datasets>, accessed on 10 February 2021). National Renewable Energy Laboratory (NREL) made National Solar Radiation Database (NSRDB) which developed a model called SUNY. SUNY provides satellite-based data for South Asian countries mostly. SUNY has temporal and spatial resolution of 1 h and 10×10 km respectively. DNI and GHI from SUNY model are available after one hour duration. These satellite-based DNI and GHI available from SUNY were analyzed on the basis of daily total monthly mean averaged over 15 years i.e., from 2000 to 2014. Hourly data were summed up to measure the daily total for all 15 years. Then, daily total was further processed to measure daily total averaged over these 15 years and then finally monthly mean of daily total averaged over 15 years was measured. In this way, daily total monthly mean averaged over 15 years for DNI and GHI was calculated on the basis of SUNY satellite model data. For each month, one data point was obtained.

3. Results and Discussions

Satellite-modeled GHI and DNI were compared with ground measurements. Results were plotted and are discussed below.

Table 3 and Figure 5 show the comparison of satellite and ground-based GHI. Ground measurements showed that highest ground-based GHI was 6415 Wh/m^2 and lowest ground-based GHI was 1605 Wh/m^2 . Similarly, highest and lowest GHI measured by satellite model were for the months of June and December, respectively. Moreover, GHI showed by satellite model for the month of June was 7177 Wh/m^2 and for the month of December was 2811 Wh/m^2 . Comparison of both the data showed a clear trend and the highest difference of 42.90% in GHI was found for the month of December. In other words, satellite-based GHI was overestimated by a value of 1206 Wh/m^2 . Similarly, the lowest

difference in GHI was noted in the month of March, which was -3.83% . Satellite-based GHI in the month of March was underestimated by a value of -181 Wh/m^2 . The average difference in GHI was noted to be 556 Wh/m^2 which means that on average, satellite-based GHI was overestimated by a value of 556 Wh/m^2 for each month. Satellite-based GHI was greater for all the months except February, March, and April where ground measurements exceeded satellite values.

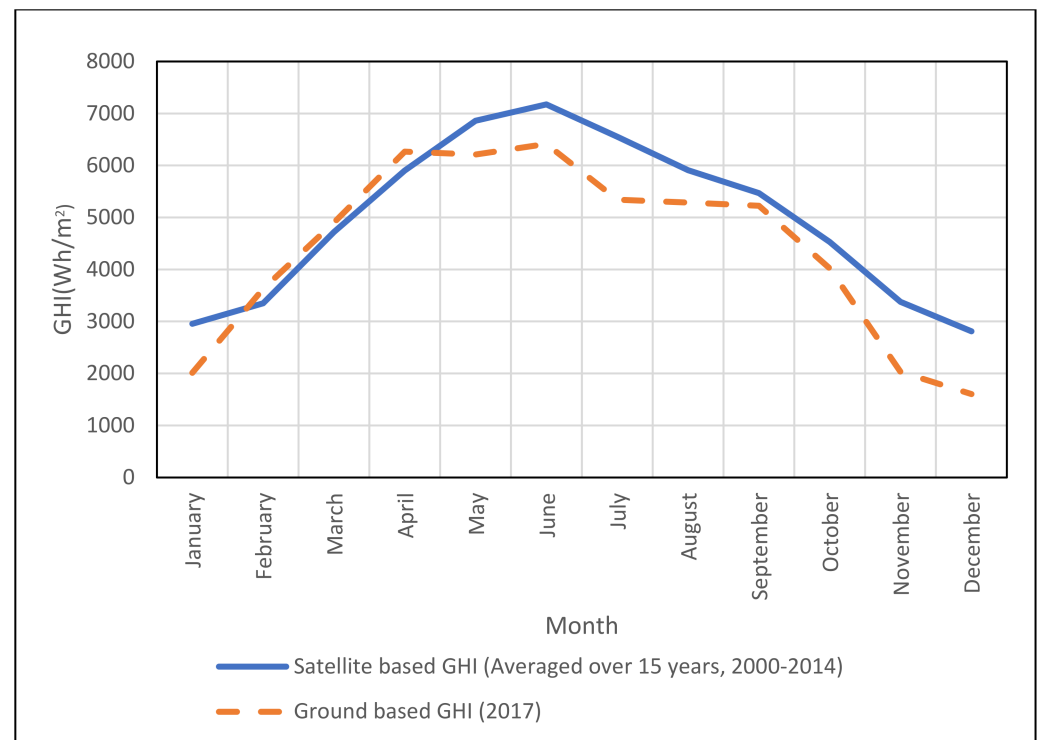


Figure 5. Comparison of ground-based GHI with satellite-based GHI.

Table 3. Comparison of ground-based GHI with satellite-based GHI.

Month	Satellite Value (Wh/m ²)	Ground Value (Wh/m ²)	Difference (Satellite-Ground) (Wh/m ²)	Percent Difference $\{(Sat-Ground)/Sat\} \times 100$
January	2955	2013	942	31.87%
February	3350	3627	-277	-8.26%
March	4721	4902	-181	-3.83%
April	5901	6267	-366	-6.20%
May	6861	6210	651	9.48%
June	7177	6415	762	10.61%
July	6553	5341	1212	18.49%
August	5909	5286	623	10.54%
September	5468	5226	242	4.42%
October	4530	4020	510	11.25%
November	3378	2032	1346	39.84%
December	2811	1605	1206	42.90%

The correlation of satellite-based GHI with ground-based GHI has been developed and shown in Figure 6 where each data point represents a month. There is a substantial positive correlation between satellite and ground-based GHI. The value of R^2 for the correlation is 0.8852 which shows that there is high correlation between these two.

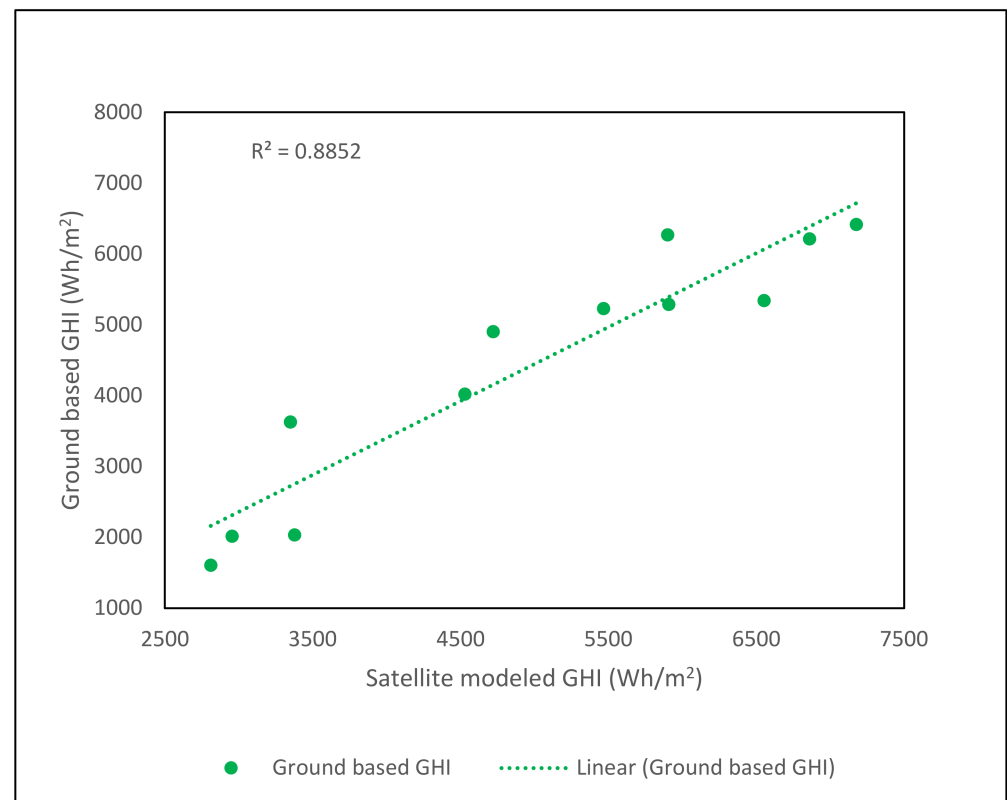


Figure 6. Correlation of satellite modeled GHI with ground-based GHI.

The comparison of ground-based monthly DNI with satellite-based DNI is given in Table 4 and Figure 7 which show that highest and lowest ground DNI were recorded in the months of April and January, respectively. It has been found that ground-based DNI in April was 5884 Wh/m^2 and it was 1718 Wh/m^2 in January. On the other hand, highest and lowest satellite-based DNI were seen in the months of May and February respectively. Satellite-based DNI in May was 6095 Wh/m^2 and it was 3240 Wh/m^2 in February. When satellite modeled and ground measured DNI were compared, satellite-based DNI overestimated ground measurements for all the months except February, March, and April. Maximum difference in DNI was found in the month of November which was 55.86%. Satellite-based DNI in November was overestimated by a value of 2348 Wh/m^2 . On the other hand, minimum difference was noted in the month of March which was -3.34% . In March, satellite-based DNI was underestimated by a value of -140 Wh/m^2 . Average difference in DNI between both data was 983 Wh/m^2 which means that on the average, for each month, satellite modeled DNI overestimated ground measurements by a value of 983 Wh/m^2 . Ground measurements showed lower values of DNI in comparison with satellite modeled value for all months except February, March and April where ground measurements exceeded satellite-based values of DNI.

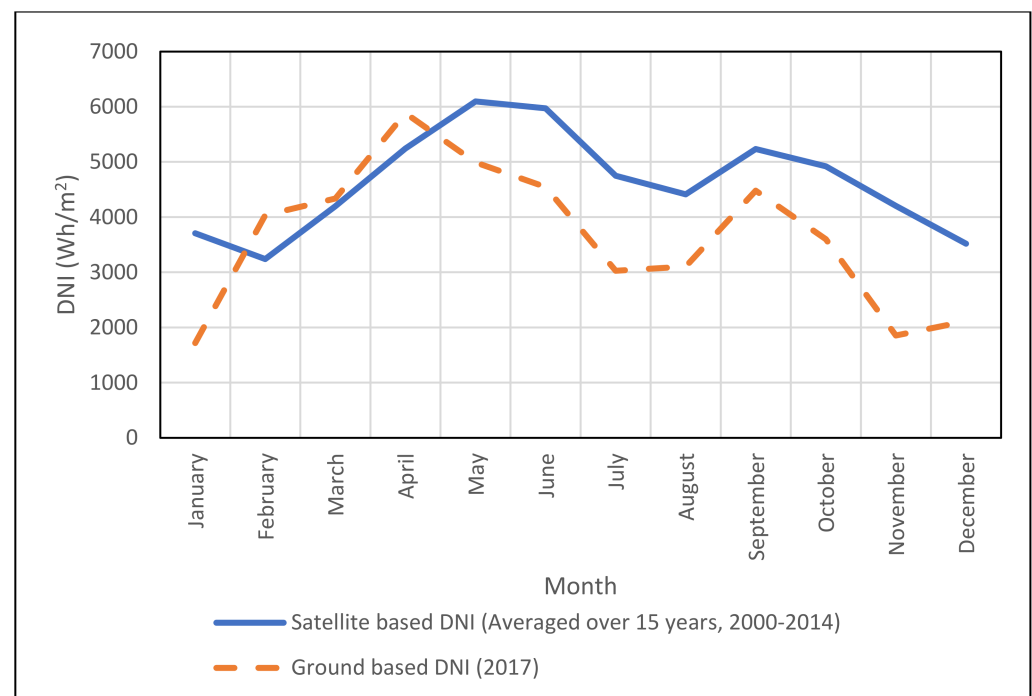


Figure 7. Comparison of ground-based monthly DNI with satellite-based DNI.

Table 4. Comparison of ground-based monthly DNI with satellite-based DNI.

Month	Satellite Value (Wh/m ²)	Ground Value (Wh/m ²)	Difference (Satellite-Ground) (Wh/m ²)	Percent Difference $\{(Sat-Ground)/Sat\} \times 100$
January	3706	1718	1988	53.64%
February	3240	4034	-794	-24.50%
March	4196	4336	-140	-3.34%
April	5243	5884	-641	-12.22%
May	6095	4989	1106	18.15%
June	5969	4545	1424	23.86%
July	4747	3027	1720	36.23%
August	4412	3103	1309	29.67%
September	5233	4478	755	14.43%
October	4920	3599	1321	26.85%
November	4203	1855	2348	55.86%
December	3517	2112	1405	39.95%

The correlation between satellite-modeled DNI and ground-based DNI has been developed which is shown in Figure 8 where each data point represents a month. There exists a moderate positive correlation between satellite and ground-based DNI having R^2 of 0.4139. Moreover, Table 5 shows uncertainties in ground measurements as well as satellite modeled GHI and DNI. Uncertainties in equipment were taken from CMP6/CMP10/CMP11/CMP21-Campbell Scientific (Logan, UT, USA) and Rotating Shadowband Irradiometer CSPS Twin-RSI of CSP Services Inc. (Cologne, Germany). Hourly uncertainties of SUNY model were 9.6% for GHI and 15.9% for DNI which were taken from (A Review of Measured/Modeled Solar Resource Uncertainty). Uncertainties in GHI and DNI of Shadowband irradiometer are <2% for annual sum. Daily uncertainties in GHI and DNI of Kipp and Zonen CMP10 pyranometer are <2%. On the basis of these values, in our study, we have assumed that our calculations have 2% uncertainty. Combined uncertainty of both the ground measurements and satellite model is 11.6% for GHI while maximum difference in GHI was found to be 42.90%. Difference in satellite and ground-based GHI exceeded from combined uncertainty which means the difference was significant and it needed to be taken into the account for calculations of solar

data in Peshawar. Moreover, combined uncertainty in DNI of satellite model and ground measurements is 17.9% whereas maximum difference in both the data of DNI is 55.86%. Maximum difference in DNI exceeds the combined uncertainty which means that the difference is significant and both the data have considerable variation.

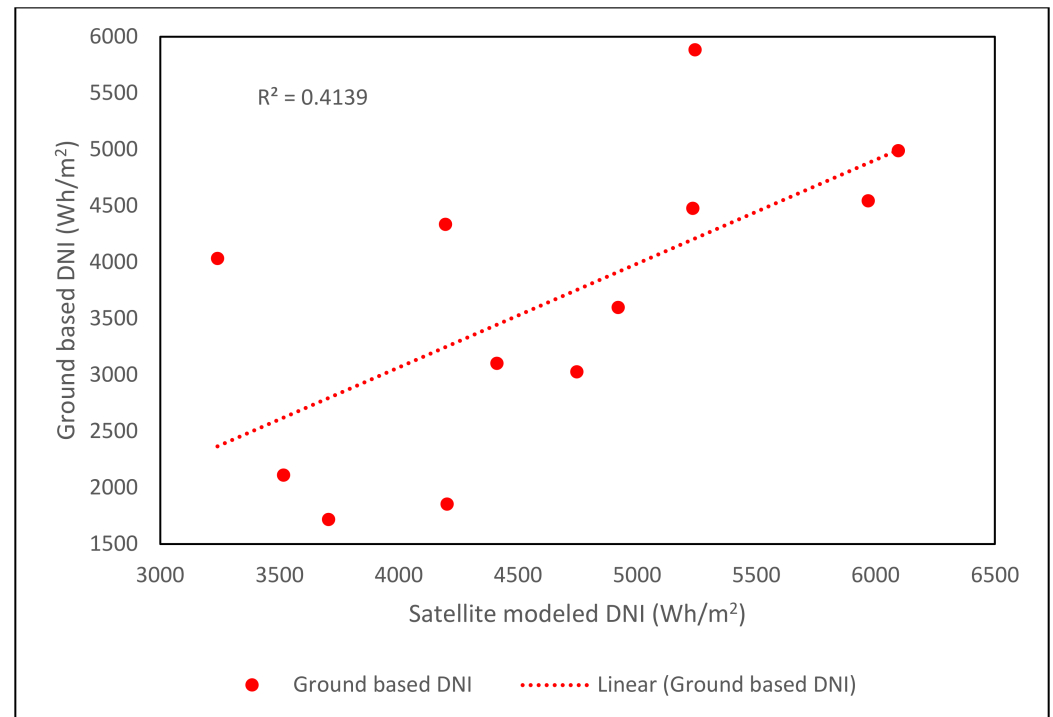


Figure 8. Correlation of satellite-modeled DNI with ground-based DNI.

Table 5. Comparison of uncertainties and maximum differences in GHI and DNI.

Property	Equipment Uncertainty (%)	SUNY Uncertainty (%)	Combined Uncertainty (%)	Maximum Difference (%)
GHI	2	9.6	11.6	42.9
DNI	2	15.9	17.9	55.86

From Table 5, it is evident that maximum difference in GHI and DNI is way greater than combined uncertainty, so there is significant difference which is worth considering in analysis.

Some of the reasons for variation between satellite and ground-based GHI and DNI in literature are [5,8,9]:

- Presence of aerosols in atmosphere;
- Presence of various gases in atmosphere;
- Presence of water vapors in air;
- Poor estimation of satellite model;
- Presence of mountains in vicinity;
- Shading of trees in the surrounding;
- Satellite confuses between clouds and snow.

4. Conclusions

The assessment of solar energy potential in a certain region is a basic step in establishing solar plants in that region. There is solar data available from satellite-based models. However, it is affected by some factors and should be validated using ground-based data. Therefore, there is a need of solar energy measurements based on ground-based data which can be obtained using different equipment like pyranometer and rotating shadow-

band irradiator. To evaluate the solar energy potential of Peshawar region in Pakistan, ground-based global horizontal irradiance (GHI) and direct normal irradiance (DNI) were compared with satellite-based model SUNY. Ground measurements were done at (University of Engineering and Technology) UET Peshawar with the help of pyranometer and shadowband irradiator.

This study concluded that there was significant difference between satellite and ground-based GHI and DNI. In the months of February, March, and April, ground-based GHI and DNI were overestimated compared to satellite-based GHI and DNI. In rest of the months, satellite-based GHI and DNI were greater than ground-based GHI and DNI. Maximum and minimum difference of 42.90% and -3.83% between satellite and ground-based GHI was found in the month of December and March respectively. For DNI, maximum and minimum difference of 55.86% and -3.34% between satellite and ground-based data was found in the month of November and March respectively. The percentage combined uncertainties between satellite and ground-based GHI and DNI were 11.6% and 17.9%. The maximum percent differences were more compared to the combined uncertainties of ground equipment and satellite model. Therefore, the difference was considerable and it is concluded that this difference needs to be taken into account when solar energy resource is assessed in Peshawar. Moreover, correlation of ground and satellite-based GHI and DNI showed squared correlation coefficient R^2 of 0.8852 and 0.4139 respectively.

Moreover, this study recommends that there should be more ground measurement stations across the country to properly assess the solar resource of the country. The difference between ground measurements and satellite values was considerable and hence real-time measurements are necessary to properly estimate solar energy resource in the country. For establishment of any solar energy program in Pakistan and especially in Peshawar, it is not recommended to rely entirely on satellite modeled data, but rather realistic ground measurements are needed. Satellite modeled data can only provide estimation of solar energy resource but not the exact amount of irradiance received at particular location. This study also recommends the researchers and university students to further research in assessment of solar energy resource in various locations of the country.

Furthermore, the data available for ground-based measurements were only for one year (2017) which is a limitation of this study. The study would be far better if the time series was longer enough. Therefore, the authors suggest it as a future recommendation that such studies should be conducted in different locations of the country with a longer time series of data.

Author Contributions: Conceptualization, A.A. and F.A.; software, A.A., Z.R. and F.A.; validation, M.A.A.I. and A.A.; formal analysis, A.A. and F.A.; investigation, A.A., Z.R. and F.A.; resources, A.A., M.A.A.I., Z.R., F.A., K.R. and J.D.; data curation, A.A. and F.A.; writing—original draft preparation, A.A., Z.R. and F.A.; writing—review and editing, A.A., M.A.A.I., Z.R., K.R., J.D. and F.A.; visualization, A.A. and F.A.; supervision, Z.R. and F.A.; project administration, F.A., M.A.A.I. and Z.R.; funding acquisition, Z.R., K.R. and J.D. All authors have read and agreed to the published version of the manuscript.

Funding: This research received no external funding.

Institutional Review Board Statement: Not applicable.

Informed Consent Statement: Not applicable.

Data Availability Statement: Not applicable.

Acknowledgments: The authors acknowledge the support of University of Engineering and Technology (UET) Peshawar to allow us to utilize the weather station installed at UET Peshawar.

Conflicts of Interest: The authors declare no conflict of interest.

Nomenclature

PV	Photovoltaic
UET	University of Engineering and Technology
GHI	Global Horizontal Irradiance
DNI	Direct Normal Irradiance
SUNY	State University of New York
NSRDB	National Solar Radiation Database
RSI	Rotating Shadowband Irradiometer







References

- Bhattacharya, T.; Chakraborty, A.K.; Pal, K. Effects of Ambient Temperature and Wind Speed on Performance of Monocrystalline Solar Photovoltaic Module in Tripura, India. *J. Sol. Energy* **2014**, *2014*, 817078. [CrossRef]
- Ayaz, A.; Ahmad, F.; Saher, S.; Noman, M. Solar Thermal Opportunities and Challenges in Pakistan. In *IOP Conference Series: Materials Science and Engineering*; IOP Publishing: Bristol, UK, 2020; Volume 899, p. 012008.
- Cuce, E.; Cuce, P.M.; Bali, T. An experimental analysis of illumination intensity and temperature dependency of photovoltaic cell parameters. *Appl. Energy* **2013**, *111*, 374–382. [CrossRef]
- Ayaz, A.; Ahmad, H.; Ahmad, F.; Khan, A.; hasnain Tarmazi, S.M.; Gul, R.M. Self-cleaning of glass surface to maximize the PV cell efficiency. In *IOP Conference Series: Materials Science and Engineering*; IOP Publishing: Bristol, UK, 2020; Volume 899, p. 012006.
- Gueymard, C.A.; Wilcox, S.M. Assessment of spatial and temporal variability in the US solar resource from radiometric measurements and predictions from models using ground-based or satellite data. *Sol. Energy* **2011**, *85*, 1068–1084. [CrossRef]
- Zell, E.; Gasim, S.; Wilcox, S.; Katamoura, S.; Stoffel, T.; Shibli, H.; Engel-Cox, J.; Al Subie, M. Assessment of solar radiation resources in Saudi Arabia. *Sol. Energy* **2015**, *119*, 422–438. [CrossRef]
- AlYahya, S.; Irfan, M.A. Analysis from the new solar radiation Atlas for Saudi Arabia. *Sol. Energy* **2016**, *130*, 116–127. [CrossRef]
- Alnaser, W.; Eliagoubi, B.; Al-Kalak, A.; Trabelsi, H.; Al-Maalej, M.; El-Sayed, H.; Alloush, M. First solar radiation atlas for the Arab world. *Renew. Energy* **2004**, *29*, 1085–1107. [CrossRef]
- Bachour, D.; Perez-Astudillo, D. Ground measurements of Global Horizontal Irradiation in Doha, Qatar. *Renew. Energy* **2014**, *71*, 32–36. [CrossRef]
- Janjai, S.; Laksanaboonsong, J.; Nunez, M.; Thongsathitya, A. Development of a method for generating operational solar radiation maps from satellite data for a tropical environment. *Solar Energy* **2005**, *78*, 739–751. [CrossRef]
- Gueymard, C.A.; George, R. Gridded aerosol data for improved direct normal irradiance modeling: The case of India. In *Proceedings of the American Solar Energy Society Annual Conference, Raleigh, NC, USA, 17–20 May 2011*.
- Ineichen, P. Comparison of eight clear sky broadband models against 16 independent data banks. *Sol. Energy* **2006**, *80*, 468–478. [CrossRef]
- Mueller, R.; Dagestad, K.; Ineichen, P.; Schroedter-Homscheidt, M.; Cros, S.; Dumortier, D.; Kuhlemann, R.; Olseth, J.; Piernavieja, G.; Reise, C.; et al. Rethinking satellite-based solar irradiance modelling The SOLIS clear-sky module. *Remote Sens. Environ.* **2004**, *91*, 160–174. [CrossRef]
- Kostylev, V.; Pavlovski, A. Solar power forecasting performance—towards industry standards. In *1st International Workshop on the Integration of Solar Power into Power Systems, Aarhus, Denmark*; Energynautics GmbH Muhlstraße: Langen, Germany, 2011.
- Vignola, F.; Harlan, P.; Perez, R.; Kmiecik, M. Analysis of satellite derived beam and global solar radiation data. *Sol. Energy* **2007**, *81*, 768–772. [CrossRef]
- Blanksby, C.; Bennett, D.; Langford, S. Improvement to an existing satellite data set in support of an Australia solar atlas. *Sol. Energy* **2012**, *98*, 111–124. [CrossRef]
- Pereira, E.B.; Abreu, S.L.; Stuhlmann, R.; Rieland, M.; Colle, S. Survey of the incident solar radiation in Brazil by use of meteosat satellite data. *Sol. Energy* **1996**, *57*, 125–132. [CrossRef]
- Janjai, S. A method for estimating direct normal solar irradiation from satellite data for a tropical environment. *Sol. Energy* **2010**, *84*, 1685–1695. [CrossRef]
- Nonnenmacher, L.; Kaur, A.; Coimbra, C.F. Verification of the SUNY direct normal irradiance model with ground measurements. *Sol. Energy* **2014**, *99*, 246–258. [CrossRef]
- Perez, R.; Seals, R.; Zelenka, A. Comparing satellite remote sensing and ground network measurements for the production of site/time specific irradiance data. *Sol. Energy* **1997**, *60*, 89–96. [CrossRef]
- Janjai, S.; Pankaew, P.; Laksanaboonsong, J. A model for calculating hourly global solar radiation from satellite data in the tropics. *Appl. Energy* **2009**, *86*, 1450–1457. [CrossRef]
- Tarpley, J.D. Estimating Incident Solar Radiation at the Surface from Geostationary Satellite Data. *J. Appl. Meteorol.* **1979**, *18*, 1172–1181. [CrossRef]
- Gautier, C.; Diak, G.; Masse, S. A Simple Physical Model to Estimate Incident Solar Radiation at the Surface from GOES Satellite Data. *J. Appl. Meteorol.* **1980**, *19*, 1005–1012. [CrossRef]
- Mabasa, B.; Lysko, M.D.; Moloi, S.J. Validating Hourly Satellite Based and Reanalysis Based Global Horizontal Irradiance Datasets over South Africa. *Geomatics* **2021**, *1*, 429–449. [CrossRef]

25. Kheddioui, A.; El Ouiqary, E.M.; Smiej, M. Estimation of the global horizontal solar irradiation GHI for the Moroccan national territory from meteorological satellite images of the Second Generation Meteosat series MSG. *Eur. J. Mol. Clin. Med.* **2021**, *8*, 2814–2826.
26. Jain, S.; Singh, C.; Tripathi, A.K. A Flexible and Effective Method to Integrate the Satellite-Based AOD Data into WRF-Solar Model for GHI Simulation. *J. Indian Soc. Remote Sens.* **2021**, *49*, 2797–2813. [CrossRef]
27. Xing, W.; Zhang, G.; Poslad, S. Estimation of global horizontal irradiance in China using a deep learning method. *Int. J. Remote Sens.* **2021**, *42*, 3899–3917. [CrossRef]
28. Rodríguez-Benítez, F.J.; López-Cuesta, M.; Arbizu-Barrena, C.; Fernández-León, M.M.; Pamos-Ureña, M.Á.; Tovar-Pescador, J.; Santos-Alamillos, F.J.; Pozo-Vázquez, D. Assessment of new solar radiation nowcasting methods based on sky-camera and satellite imagery. *Appl. Energy* **2021**, *292*, 116838. [CrossRef]
29. Alani, O.E.; Ghennioui, H.; Abraim, M.; Ghennioui, A.; Blanc, P.; Saint-Drenan, Y.M.; Naimi, Z. Solar Energy Resource Assessment Using GHI and DNI Satellite Data for Moroccan Climate. In *International Conference on Advanced Technologies for Humanity*; Springer: Cham, Switzerland, 2021; pp. 275–285.
30. Zelenka, A.; Perez, R.; Seals, R.; Renné, D. Effective Accuracy of Satellite-Derived Hourly Irradiances. *Arch. Meteorol. Geophys. Bioclimatol. Ser. B* **1999**, *62*, 199–207. [CrossRef]
31. Lohmann, S.; Schillings, C.; Mayer, B.; Meyer, R. Long-term variability of solar direct and global radiation derived from ISCCP data and comparison with reanalysis data. *Sol. Energy* **2006**, *80*, 1390–1401. [CrossRef]
32. Cebecauer, T.; Suri, M. Accuracy improvements of satellite-derived solar resource based on GEMS re-analysis aerosols. In Proceedings of the Conference SolarPACES, Perpignan, France, 21–24 September 2010.
33. Suri, M.; Cebecauer, T. Satellite-based solar resource data: Model validation statistics versus user’s un-certainty. In Proceedings of the ASES SOLAR 2014 Conference, San Francisco, CA, USA, 7 July 2014; pp. 7–9.
34. Maxwell, E.; Wilcox, S.; Rymes, M. *User’s Manual for SERI QC Software, Assessing the Quality of Solar Radiation Data*; Solar Energy Research Institute: Golden, CO, USA, 1993.
35. Younes, S.; Claywell, R.; Muneer, T. Quality control of solar radiation data: Present status and proposed new approaches. *Energy* **2005**, *30*, 1533–1549. [CrossRef]

Article

Dynamic Evaluation of Desiccant Dehumidification Evaporative Cooling Options for Greenhouse Air-Conditioning Application in Multan (Pakistan)

Hadeed Ashraf ^{1,†}, Muhammad Sultan ^{1,*,†}, Redmond R. Shamshiri ^{2,*,†}, Farrukh Abbas ^{1,†}, Muhammad Farooq ³, Uzair Sajjad ⁴, Hafiz Md-Tahir ⁵, Muhammad H. Mahmood ¹, Fiaz Ahmad ¹, Yousaf R. Taseer ⁶, Aamir Shahzad ⁷ and Badar M. K. Niazi ⁸

- ¹ Department of Agricultural Engineering, Bahauddin Zakariya University, Bosan Road, Multan 60800, Pakistan; hadeedashraf15@gmail.com (H.A.); farukh_56@hotmail.com (F.A.); hamidmahmood@bzu.edu.pk (M.H.M.); fiazahmad@bzu.edu.pk (F.A.)
 - ² Department of Engineering for Crop Production, Leibniz Institute for Agricultural Engineering and Bioeconomy, 14469 Potsdam-Bornim, Germany
 - ³ Department of Mechanical Engineering, University of Engineering and Technology, Lahore 39161, Pakistan; engr.farooq@uet.edu.pk
 - ⁴ Mechanical Engineering Department, National Chiao Tung University, Hsinchu 30010, Taiwan; energysengineer01@gmail.com
 - ⁵ College of Engineering, Huazhong Agricultural University, Wuhan 430070, China; m.tahir@webmail.hzau.edu.cn
 - ⁶ Department of Building and Architectural Engineering, Bahauddin Zakariya University, Bosan Road, Multan 60800, Pakistan; engr.yousafraza@bzu.edu.pk
 - ⁷ Office of the Deputy Director Agriculture (Water Management), Punjab Agriculture Department, Officers Colony, Muzaffargarh Road, Jauharabad, Khushab 41000, Pakistan; ofwm_khb@yahoo.com
 - ⁸ Agricultural Engineering Institute, National Agricultural Research Centre, Park Road, Islamabad 44000, Pakistan; badar.khan.niazi@gmail.com
- * Correspondence: muhammadsultan@bzu.edu.pk (M.S.); rshamshiri@atb-potsdam.de (R.R.S.); Tel.: +92-333-6108888 (M.S.)
- † These authors contributed equally to this work.

Citation: Ashraf, H.; Sultan, M.; Shamshiri, R.R.; Abbas, F.; Farooq, M.; Sajjad, U.; Md-Tahir, H.; Mahmood, M.H.; Ahmad, F.; Taseer, Y.R.; et al. Dynamic Evaluation of Desiccant Dehumidification Evaporative Cooling Options for Greenhouse Air-Conditioning Application in Multan (Pakistan). *Energies* **2021**, *14*, 1097. <https://doi.org/10.3390/en14041097>

Academic Editors: Jan Danielewicz and Krzysztof Rajski
Received: 27 December 2020
Accepted: 14 February 2021
Published: 19 February 2021

Publisher's Note: MDPI stays neutral with regard to jurisdictional claims in published maps and institutional affiliations.



Copyright: © 2021 by the authors. Licensee MDPI, Basel, Switzerland. This article is an open access article distributed under the terms and conditions of the Creative Commons Attribution (CC BY) license (<https://creativecommons.org/licenses/by/4.0/>).

Abstract: This study provides insights into the feasibility of a desiccant dehumidification-based Maisotsenko cycle evaporative cooling (M-DAC) system for greenhouse air-conditioning application. Conventional cooling techniques include direct evaporative cooling, refrigeration systems, and passive/active ventilation, which are commonly used in Pakistan; however, they are either not feasible due to their energy cost, or they cannot efficiently provide an optimum microclimate depending on the regions, the growing seasons, and the crop being cultivated. The M-DAC system was therefore proposed and evaluated as an alternative solution for air conditioning to achieve optimum levels of vapor pressure deficit (VPD) for greenhouse crop production. The objective of this study was to investigate the thermodynamic performance of the proposed system from the viewpoints of the temperature gradient, relative humidity level, VPD, and dehumidification gradient. Results showed that the standalone desiccant air-conditioning (DAC) system created maximum dehumidification gradient (i.e., 16.8 g/kg) and maximum temperature gradient (i.e., 8.4 °C) at 24.3 g/kg and 38.6 °C ambient air conditions, respectively. The DAC coupled with a heat exchanger (DAC+HX) created a temperature gradient nearly equal to ambient air conditions, which is not in the optimal range for greenhouse growing conditions. Analysis of the M-DAC system showed that a maximum air temperature gradient, i.e., 21.9 °C at 39.2 °C ambient air condition, can be achieved, and is considered optimal for most greenhouse crops. Results were validated with two microclimate models (OptDeg and Cft) by taking into account the optimality of VPD at different growth stages of tomato plants. This study suggests that the M-DAC system is a feasible method to be considered as an efficient solution for greenhouse air-conditioning under the climate conditions of Multan (Pakistan).

Keywords: desiccant dehumidification; evaporative cooling; Maisotsenko cycle; greenhouse air-conditioning; Pakistan

1. Introduction

Closed-field production of crops and vegetables by means of greenhouses with different covering materials depends on the efficiency of the climate control system to provide optimum growth conditions with a reasonable energy cost. The extensive solar radiation during the daytime causes a greenhouse effect, resulting in high air temperature and relative humidity that can significantly exceed the optimum conditions. This can lead to a significant loss of yield and fruit quality in the absence of a proper ventilation and dehumidification system. Additionally, the plants and vegetables are more prone to pest/fungus/disease attack in higher relative humidity conditions than normal, which may also affect the production level of the greenhouse. To reduce the impact of suboptimal microclimate conditions on production, passive and active ventilation, in addition to direct evaporative cooling systems by means of pad-and-fans or swamp coolers, are conventionally used by greenhouse growers in Pakistan. The problem with these solutions is that they do not allow control over the relative humidity level of the greenhouse environment, hence leaving the plants and vegetables exposed to pests, fungus, and disease attacks. Therefore, a more appropriate air-conditioning (AC) solution that is cost-efficient and can be implemented in large scale commercial production is required. In this regard, desiccant dehumidification-based indirect evaporative cooling air-conditioning systems are gaining research attention that needs to be evaluated for AC application in different closed-field plant production environments.

The focus of this study is the city of Multan, Pakistan, which lies in a warm desert climate where direct evaporative cooling methods are used in combination with passive and active ventilation methods inside agricultural greenhouses. For the purpose of this research, a desiccant dehumidification-based Maisotsenko cycle evaporative cooling (M-DAC) system is proposed and evaluated as an alternative solution for controlling humidity levels to achieve the optimum vapor pressure deficit (VPD). The objective was to provide a systematic thermodynamic analysis of the proposed M-DAC system from the viewpoints of temperature gradient, relative humidity levels, optimum VPD, and dehumidification gradient. A review of the relevant published literature is summarized in Section 2 to identify the most recent achievements and the gaps. Modeling of the M-DAC and dynamic evaluation by means of the optimality degree and comfort ratio models are described in Section 3. The proposed solution is validated and discussed in Section 4 based on the thermodynamic analysis and the microclimate models. Section 5 concludes the study and highlights the potential aspects for further research and development.

2. Background and Literature Review

Evaporative cooling (EC) systems can potentially be classified into direct evaporative (DEC), indirect evaporative (IEC), and Maisotsenko cycle evaporative (MEC) systems. The MEC system is widely studied by the research community for heating, ventilation, and air-conditioning (HVAC) system applications. Pandelidis and Anisimov [1] numerically studied and compared eight different configurations of a standalone Maisotsenko-cycle evaporative heat and mass exchanger. Caliskan et al. [2] studied energy and exergy analyses of the standalone MEC system for building air-conditioning. Zhan et al. [3] studied counter flow standalone MEC system for building air-conditioning application. Caliskan et al. [4] compared traditional vapor compression air-conditioning systems with the MEC system based on energy and exergy analyses. Chua et al. [5] reviewed environment-friendly air-conditioning options for building applications. Pandelidis et al. [6] numerically simulated the MEC heat exchanger for different air-conditioning applications. Rogdakis et al. [7] numerically simulated and experimentally validated the MEC system for building air-conditioning application for the climatic conditions of Greece. Cui et al. [8] studied the MEC system for precooling of ambient air as an energy-saving technique for hot and humid climatic conditions. Riangvilaikul and Kumar [9] numerically investigated the MEC

system for different inlet conditions. Sultan [10] studied the MEC system for greenhouse air-conditioning and ventilation applications. Anisimov et al. [11] theoretically and experimentally analyzed the standalone MEC system for air-conditioning and found the MEC system to be an efficient way of indirect evaporative cooling. In addition, results from the study concluded that inlet air velocity impacted the performance of the system. Zhao et al. [12] numerically investigated the performance of the MEC system for climatic conditions of the United Kingdom, which resulted in wet-bulb effectiveness of 1.3. Zube and Gillan [13] experimentally studied a commercial type MEC air-conditioning system and evaluated heat mass transfer parameters inside a heat exchanger for the first time. Weerts [14] reported the power-saving potential of commercially available standalone MEC system compared to the vapor compression air-conditioning (VCAC) system. Maisotsenko and Treyger [15] also reported the energy-saving potential of the standalone MEC system compared to standalone VCAC system. Similarly, [16–18] also studied the standalone MEC system in-depth and concluded that the MEC system can potentially be an environmentally friendly air-conditioning option compared to the VCAC system.

The standalone desiccant air-conditioning (DAC) system has been extensively studied in the literature for various applications. Generally, the DAC system better suits regions with higher relative humidity in the ambient air. The DAC system was studied for the possible application of vehicular air-conditioning [19]. Additionally, the authors used a continuous input and output modulator (i.e., proportional-derivative (PD) controller) to increase the efficiency of the system and concluded that the DAC system coupled with the PD controller was energy conservative compared to conventional AC systems in vehicles [19]. Moreover, the DAC system was successfully installed in a wet market in Hong Kong. The authors numerically simulated the energy loads of a hypothetical wet-market using EnergyPlus for the climatic conditions of Hong Kong and compared results with the actual wet market [20]. The authors concluded that the DAC could potentially be used as a replacement for conventional air-conditioning systems in the wet markets. A solar-assisted open cycle DAC system was experimentally tested for grain storage in Melbourne, Australia [21]. The authors concluded that a 5.85 m³ solar collector area was sufficient for cooling of up to 200 tonnes of grain. The coefficient of performance (COP) was a function of surrounding conditions and air mass flow rate. A maximum COP of 86.2 was observed under humid conditions for an air mass flow rate of 0.019 kg/s [21]. The standalone DAC system was studied for a greenhouse air temperature and humidity control system [22]. Moreover, the authors studied the greenhouse air-conditioning from a vapor pressure deficit (VPD) point of view. The standalone DAC system with dual desiccant wheels was studied for residual waste heat recovery in marine ships [23]. The authors concluded that the DAC system was 33.4% more power-efficient compared to traditional air-conditioning systems for marine ships. An EC-coupled DAC system was studied in two modes (i.e., ventilation and recirculation modes) [24]. The authors concluded that conventional ventilation mode is more efficient when humidity ratio is below ~10.9 g/kg, whereas the recirculation mode of the air-conditioning system is more efficient for areas where humidity ratio is above ~10.9 g/kg, consuming a higher amount of input energy. Enteria et al. [25] studied the analyses of the first and second law of thermodynamics for a solar thermal electric desiccant air-conditioning system [25]. A simulated solar-operated evaporative cooling-assisted solid desiccant air-conditioning system was developed in a tropical region of Malaysia [26]. The authors used the TRNSYS simulation environment to simulate the desiccant air-conditioning system for climatic conditions of Malaysia. The authors concluded that two-stage ventilation mode desiccant air-conditioning system is better for tropical conditions such as Malaysia, with a temperature gradient of 17.6 °C at 30 °C ambient temperature [26]. Another study investigated a dual-wheel cooling system [27]. Results from the study indicate that higher regeneration temperature (RT) produces higher total COP at both air mass flow rates (i.e., 100 and 200 m³/h) [27]. Moreover, the performance and energy-saving potential of a two-stage solar-driven rotary wheel DAC system was compared with a conventional vapor compression air-conditioning (VCAC) system

for building air-conditioning [28]. Building energy performance simulation (BEPS) was conducted for Berlin and Shanghai. The DAC system was found to be energy-saving and more efficient for both of the cities compared to VCAC system. However, in the case of Shanghai, the RT of the DAC system was 30 °C higher than that of Berlin [28]. Figure 1 shows the schematic diagram and working principle of a conventional vapor compression air-conditioning system, and solar thermal liquid desiccant dehumidification-based air-conditioning system. Moreover, the authors studied desiccant dehumidification systems and evaporative cooling systems in detail for various applications, including greenhouse air-conditioning [29–32], building air-conditioning [33], livestock air-conditioning [34], and agricultural product storage [35–44].

Song and Sobhani [45] studied solar-assisted desiccant air-conditioning system coupled with a Maisotsenko evaporative cooling system and phase change material for building air-conditioning application. The authors concluded that the maximum total COP of 0.404 was achieved using a solar-operated desiccant air-conditioning system coupled with a Maisotsenko evaporative cooler using a phase change material for air-conditioning of an official building in Iran. In another study, a Maisotsenko cycle-assisted desiccant air-conditioning system was studied for the climatic conditions of Japan [46]. Pandelidis et al. [47] numerically studied the Maisotsenko cycle-assisted desiccant air-conditioning system with two modifications, i.e., bypass and bypass with rotary sensible heat exchanger. The authors concluded that all the configurations successfully managed the sensible load of the environment while being highly dependent on the humidity ratio of ambient air. The addition of a rotary sensible heat exchanger in system configuration 3 increased the cooling capacity up to ~2.35 kW at 40 °C ambient temperature generating ~17.25 °C supply air temperature at the same ambient conditions [47]. Table 1 shows the summary of different desiccant-based Maisotsenko cycle evaporative cooling systems for air-conditioning applications. From Table 1 and the reviewed literature, it is evident that there is a gap in the literature regarding OptDeg and Cft plant thermal comfort indices for the proposed M-DAC system. Moreover, this study aims to use a low and easily achievable regeneration temperature (i.e., 50 °C) coupled with different comfort levels of plant growth stages, which is lacking in previous studies.

Table 1. Summary of different desiccant-based Maisotsenko cycle evaporative cooling systems for air-conditioning applications.

System	Findings	Regeneration Temperature	Ref.
Desiccant based indirect evaporative cooling	For 70 °C T_{regen} , supply flow ratio 0.67, indirect EC flow ratio 0.3 results in maximum performance i.e., COP higher than 20	70 °C	[48]
Maisotsenko cycle desiccant evaporative cooling	For outside conditions of 25 °C, lowest temperature gradient was 14.9 °C	70 °C	[1]
Standalone MEC	For Greek climate conditions, MEC system achieved maximum temperature gradient of 20.4 °C in Athens	–	[7]
Maisotsenko cycle desiccant evaporative cooling	Different desiccant materials studied for greenhouse air-conditioning, only limitation was integration of OptDeg and Cft models for different growth stages of crops	Different regeneration temperatures	[10]
Standalone DAC system	Polymer-based sorbents PS-I and PS-II are studied at regeneration temperatures 50 and 80 °C for greenhouse air-conditioning	Different regeneration temperatures	[30]
Standalone DAC system	Activated carbon powder (ACP) and activated carbon fiber (ACF) were studied for greenhouse air-conditioning at regeneration temperatures 41 to 75 °C, only limitation was the detailed analysis of crop growth and plant comfort indices	Different regeneration temperatures	[49]

The study area (i.e., Multan) lies in a warm desert climate of the Köppen–Geiger climatic classification (Figure 2). Therefore, this justifies the need for an air-conditioning system for greenhouses. Usually, pad-type direct evaporative cooling or natural/forced

ventilation systems are used for greenhouse air-conditioning. These systems are not feasible throughout the year and fail to achieve the required optimum temperature and relative humidity conditions inside a greenhouse. Moreover, the DEC system fails to handle humidity inside the greenhouse environment, which is crucial to the vapor pressure deficit. The desiccant-based hybrid evaporative cooling systems have not been explored for greenhouse air-conditioning applications in Pakistan.

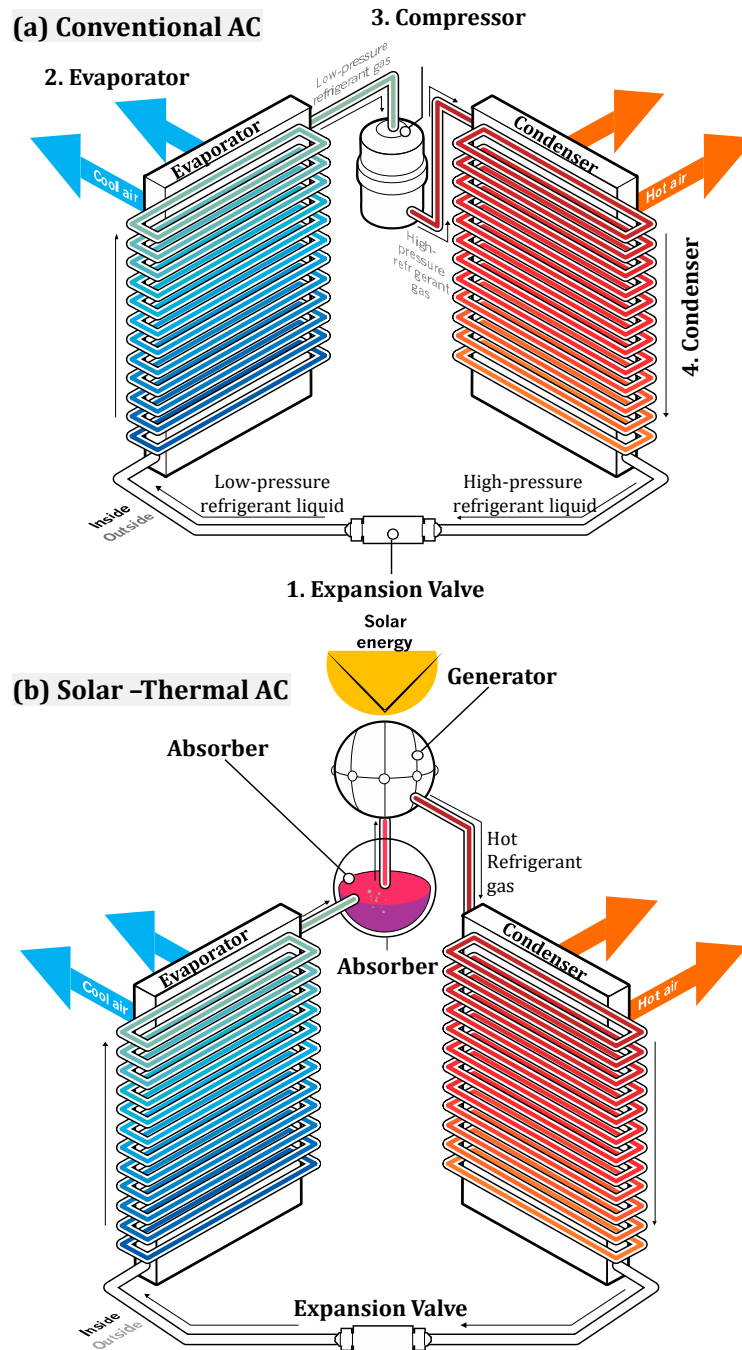


Figure 1. Schematic diagram and working principle of (a) conventional vapor compression air-conditioning system, and (b) solar thermal liquid desiccant dehumidification-based air-conditioning system, reproduced from [50].

Figure 3 shows the ambient climatic conditions of Multan (Pakistan) and the greenhouse optimum temperature and relative humidity zone. Figure 3 was made using Lady-

bug Rhino v6 for the climatic conditions of Multan (Pakistan). A typical meteorological EnergyPlus weather file was used in Ladybug Rhino to represent the hourly weather conditions. In Figure 3, the light fill area shows the average hourly variation, whereas the lines show the average daily variation in climatic parameters. From the viewpoint of the literature reviewed above, pad-type direct evaporative cooling systems are only suitable for controlling the temperature, and fail to achieve the optimum humidity level inside the greenhouse. To overcome this issue, an indirect evaporative cooling system could be used, which provides a sensibly cooled product air with no latent transfer from the wet to dry channels of the IEC system. However, due to the low wet bulb effectiveness of the system, it cannot be considered a suitable option for achieving the required temperature level inside the greenhouse. Additionally, higher levels of humidity inside the greenhouse can potentially result in pest, fungus, and disease attacks on the plants and vegetables. Therefore, in this study, a desiccant dehumidification-based Maisotsenko cycle evaporative cooling air-conditioning (M-DAC) system was thermodynamically analyzed for the climatic conditions of Multan (Pakistan). The performance of the system was analyzed for optimum greenhouse air-conditioning conditions from the viewpoints of temperature gradient, relative humidity level, and wet bulb effectiveness of the systems.

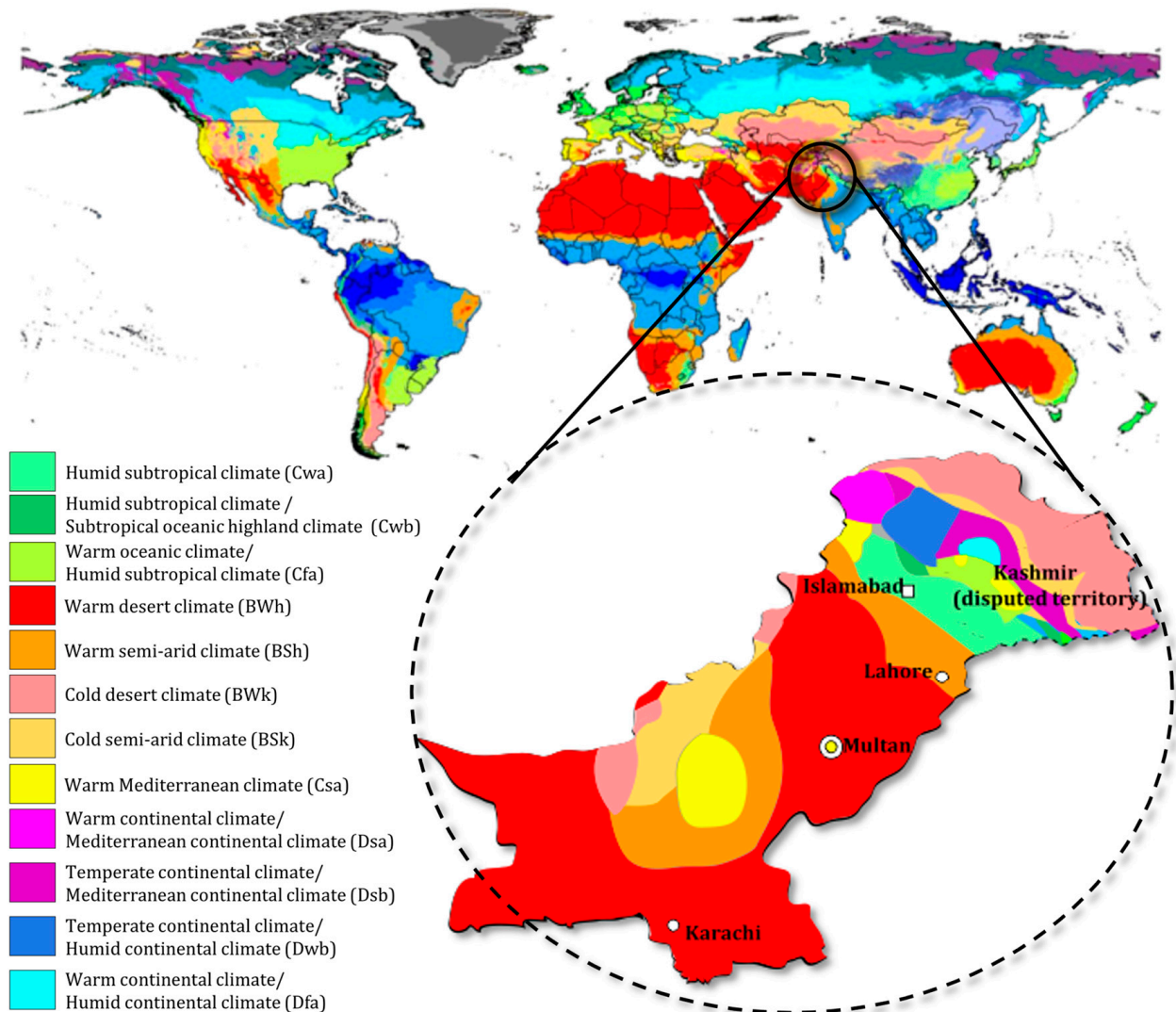


Figure 2. Köppen–Geiger climate classification of Pakistan, reproduced from [51].

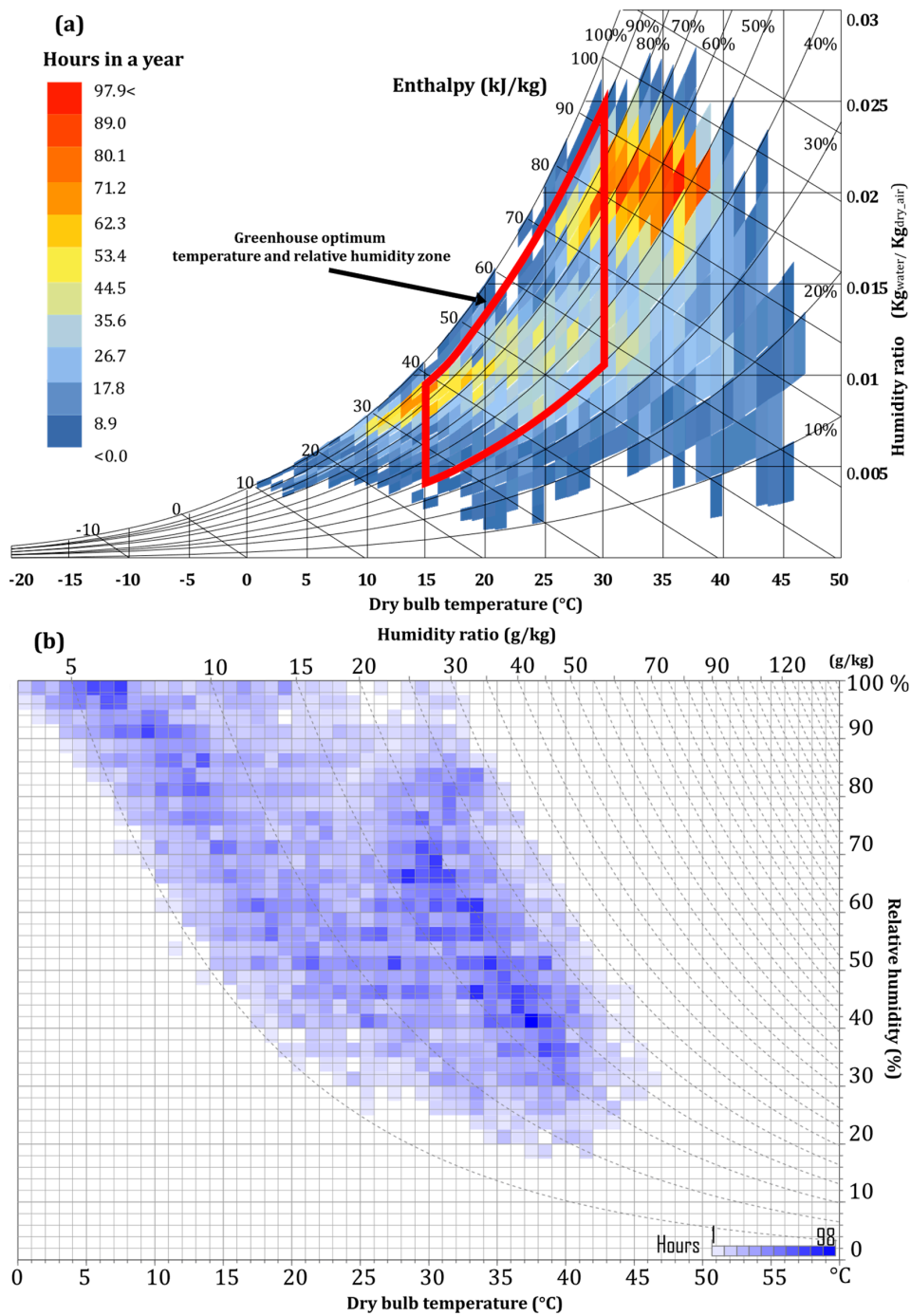


Figure 3. Ambient climatic conditions of Multan (Pakistan) on (a) psychrometric chart, and (b) relative humidity chart.

3. Materials and Methods

3.1. Modelling M-DAC System

A general working principle of the M-DAC system is first shown in Figure 4, followed by a schematic representation in Figure 5 that demonstrates the application of the proposed system for greenhouse air-conditioning for a possible higher yield. Taking into account the climatic conditions of Multan (Pakistan), the performance of a silica gel-based desiccant

wheel for M-DAC system was investigated using Equations (1)–(4), as described in the literature [52,53].

$$F_{1,ip} = \frac{A_1}{(T_{ip} + 273.15)^{1.49}} + B_1 \left(\frac{w_{ip}}{1000} \right)^{C_1} \tag{1}$$

$$F_{2,ip} = \frac{(T_{ip} + 273.15)^{1.49}}{A_2} - B_2 \left(\frac{w_{ip}}{1000} \right)^{C_2} \tag{2}$$

$$\eta F_1 = \frac{F_{1,2} - F_{1,1}}{F_{1,8} - F_{1,1}} \tag{3}$$

$$\eta F_2 = \frac{F_{2,2} - F_{2,1}}{F_{2,8} - F_{2,1}} \tag{4}$$

where $F_{1,ip}$ and $F_{2,ip}$ represent the combined potential as a function of the humidity ratio in kg/kg and temperature in °C of the solid desiccant-based air-conditioning system. ηF_1 and ηF_2 represent the efficiencies of the system correlating to the combined potentials. ηF_1 and ηF_2 have typical values of 0.05 and 0.95 for a high-efficiency silica gel-based solid desiccant wheel air-conditioning system. The coefficients A, B, and C are presented in Table 2.

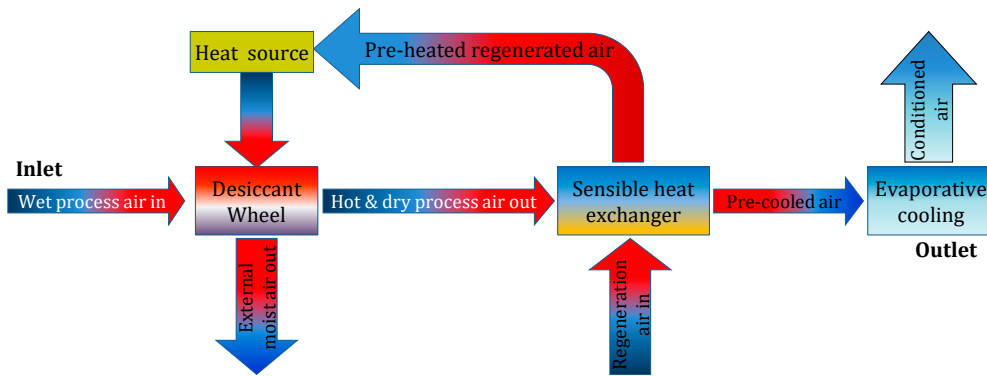


Figure 4. Working principle of a desiccant dehumidification-based evaporative cooling air-conditioning system.

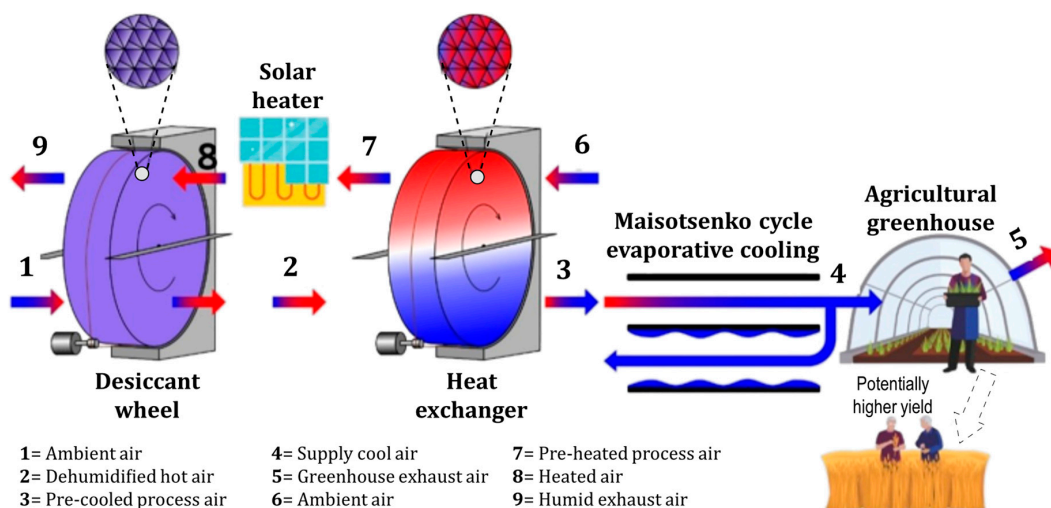


Figure 5. Schematic diagram and working principle of the proposed desiccant dehumidification Maisotsenko cycle evaporative cooling system.

In comparison with the conventional vapor compression air-conditioning systems, the desiccant dehumidification-assisted evaporative cooling air-conditioning system consumes less energy due to the absence of compressor work and is able to operate at lower regenera-

tion temperatures (i.e., 50–90 °C), which are easily attainable using solar thermal, biogas, and waste heat sources. The Maisotsenko cycle evaporative cooling system was modeled using the model of [32]. Equation (5) shows the performance model of the Maisotsenko cycle evaporative cooling system.

Table 2. Coefficients used in the Jurinak model (Equations (1)–(4)).

Coefficient	Value
A ₁	−2865
B ₁	4.344
C ₁	0.8624
A ₂	6360
B ₂	1.127
C ₂	0.07969

$$T_{out} = 6.70 + 0.2630(T_{in}) + 0.5298(w_{in}) \quad (5)$$

where T_{in} represents the inlet temperature of the process air in °C and w_{in} represents the inlet humidity ratio of the process air in kg/kg. Equation (5) models the temperature of product air produced from the Maisotsenko cycle evaporative cooling system. The model was developed by [32] using experimental data of a developed Maisotsenko cycle based evaporative cooling system [11].

The sensible heat exchanger (HX) used in this study was modeled using the heat exchanger standard equation (Equation (6)) provided in the literature by The American Society of Heating, Refrigerating and Air-Conditioning Engineers (ASHRAE) [54].

$$T_3 = T_2 - \varepsilon_{HX}(T_2 - T_1) \quad (6)$$

where T_3 represents the outlet temperature of the sensibly cooled process air resulting from the heat exchanger, T_2 represents the outlet temperature of heated and dehumidified air resulted from the desiccant air-conditioning system, ε_{HX} represents the sensible heat exchange efficiency of the heat exchanger (assumed as 0.9), and T_1 represents the dry bulb temperature of the ambient air inlet into the desiccant air-conditioning system. Figure 5 shows the working principle and schematic of the sensible heat exchanger. Regeneration of the desiccant is done usually through regeneration air at higher than ambient temperature. To heat the regeneration air, the air passes through the heat exchanger which sensibly heats the air to a certain limit. For further heating of the regeneration air before entering the desiccant, a heating unit/source is used. This heating source could be a heating electric coil, solar heater, or biogas-operated thermal heat source. Waste heat from a condenser or any other source in industrial uses can also be used to regenerate the desiccant material and absorb its moisture. For this study, a regeneration temperature of 50 °C was used. This relatively lower temperature is achievable through a solar thermal system, biogas-operated thermal heat source, or waste heat. A flat plate solar collector and heat exchanger were used for this study to provide the required regeneration temperature (i.e., 50 °C). Figure 5 shows the working principle and schematic of a solar thermal heating source.

3.2. Optimality Degree and Comfort Ratio Model

Dynamic assessment of the proposed M-DAC system for greenhouse crop production application was carried out by means of two microclimate models, namely, OptDeg [55] and Cft-ratio [56] that take into account VPD measurements as inputs. The output of the first model, optimality degree of VPD, denoted by $Opt(VPD)_{GS, (Light)} = \alpha : VPD \rightarrow [0, 1]$ is a quantitative value between 0 and 1 that represents how close a VPD reading inside the greenhouse is to the optimum value ($0 \leq \alpha \leq 1$) at a specific growth stage (GS) and light condition. Graphical representation of the membership functions for defining $Opt(VPD)$ under different conditions is provided in Figure 6. In this model, a VPD measurement

in the greenhouse is first calculated from Equation (7) at the time $t_{m,n}$ (where m and n refer to a specific minute and date of the growing stage), and is then mapped to a value between 0 and 1 that quantifies the optimality degree of the microclimate for greenhouse production. In other words, an optimality-degree equal to 1 refers to a high potential yield with marketable value and high-quality fruit.

$$\begin{aligned}
 VPD_{t_{m,n}} &= f(T_{t_{m,n}}, RH_{t_{m,n}}, \tau_{t_{m,n}}) \\
 &= \frac{C_g 10^{(7.5\tau_{t_{m,n}})/(237.3+\tau_{t_{m,n}})}}{1000} \\
 &= \frac{C_g 10^{(7.5T_{t_{m,n}})/(237.3+T_{t_{m,n}})} RH_{t_{m,n}}}{1000 \cdot 100}
 \end{aligned} \quad (7)$$

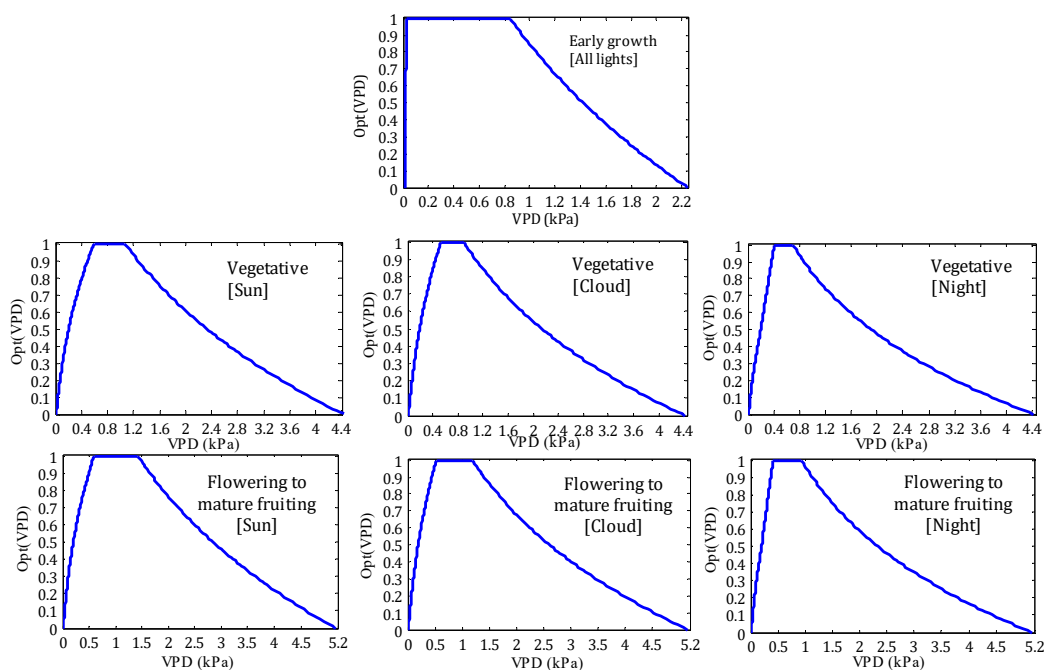


Figure 6. Membership functions for defining optimality degrees of vapor pressure deficit at different light condition and growth stages, reproduced from [40].

It should be noted that there are various functions for calculating VPD that take into accounts different assumptions and constants; however, that presented in Equation (7) is widely accepted and used by meteorologists and commercial greenhouse growers [34]. The first part of Equation (7) represents the vapor pressure of the saturated environment (i.e., the leaf of the plant) in kPa, C_g denotes a coefficient that is equal to 610.7, and τ represents the surface temperature of the leaf, which is usually measured by means of an infrared gun for such experiments. For the sake of simplicity, this parameter was assumed to be equal to the temperature of the air inside the greenhouse at both ambient and evaporative assisted desiccant air-conditioning system supply air temperature. In fact, assuming leaf temperature equal to the surrounding air temperature is normal practice of greenhouse growers. The second part of Equation (7) represents the vapor pressure of the air inside the greenhouse in kPa, T represents the temperature of the air inside the greenhouse in $^{\circ}\text{C}$, and RH represents the relative humidity of the air inside the greenhouse in (%). Because VPD is the function of temperature of the leaf surface, air temperature, and relative humidity, any slight variation in one of the parameters from the optimal values results in restricted growth of the plants, and can have significant consequences on reducing the overall yield and quality.

The OptDeg model determines the variation of a single VPD measurement from the optimal references in an instant time. Although this model can provide an overview of the performance of the M-DAC system in sample time, a different model called comfort ratio, denoted by Cft-ratio, that incorporates a sample time frame, such as 24 h was used. The comfort ratio of VPD, denoted by $Cft(VPD, t, \alpha_s)_{GS} = \beta$, represents the percent of vapor pressure deficit at a specific time t and growth stage, which lies between the reference conditions of vapor pressure deficit related to α_s . Ideal microclimate conditions inside a greenhouse could potentially be defined as $Cft(VPD, t, 1) = 1$. Self-adjusted optimality degree is denoted by α_s to define the reference conditions required for performance evaluation of the proposed M-DAC system or control for microclimate evaluation. The set of Simulink blocks that were implemented to determine the Cft-ratio of the VPD values for different α_s generated from the M-DAC system are shown in Figure 7. For this research, we selected three levels of α_s as 0, 0.5, and 1, representing failure, marginal, and ideal production. It is worth mentioning that OptDeg and Cft-ratio models were derived with a prime focus on improved fruit quality and yield. The derivations at the back of the models (which can be found in published literature) for greenhouse tomato production were condensed for the sake of simplicity in this study.

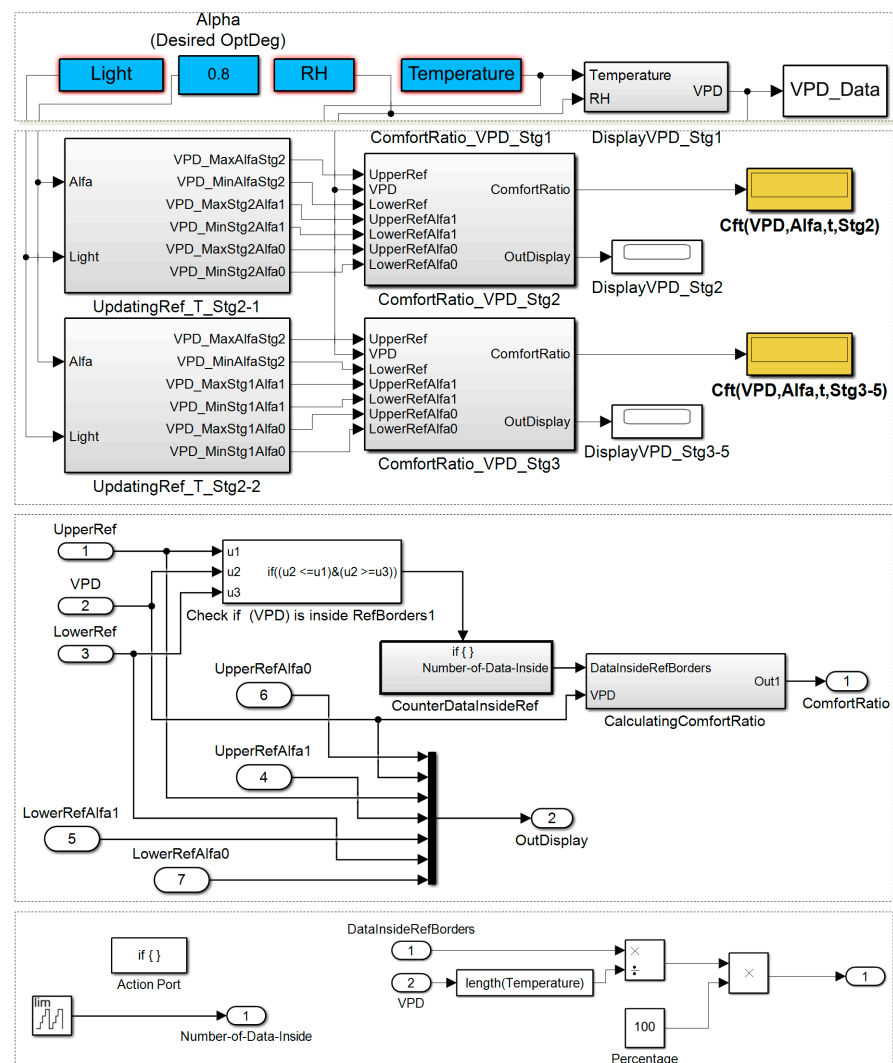


Figure 7. Implementation of the Cft-ratio model using Simulink blocks for validating the performance of the desiccant dehumidification Maisotsenko cycle evaporative cooling (M-DAC) system based on comfort ratios of vapor pressure deficit (VPD) for greenhouse production, reproduced from [56].

4. Results and Discussion

4.1. Validation Based on Thermodynamic Analysis

Figure 8 shows the annual profile of the climatic ambient air conditions of Multan (Pakistan). The daily, hourly, and monthly variation of dry-bulb temperature shows that cooling inside the greenhouse environment is mostly required in summer months (i.e., May to August). However, the applicability of standalone pad-type direct evaporative cooling systems is limited during the monsoon (heavy rainfall season, i.e., July to August, shown in Figure 8, humidity ratio (HR)) which results in excess relative humidity in the air. Consequently, a desiccant dehumidification-based Maisotsenko cycle evaporative cooling system was thermodynamically analyzed for the climatic conditions of Multan. Accordingly, results from the study are presented in Figures 8–13, which show the annual representation of the performance of the proposed system and the profile of the vapor pressure deficit inside the greenhouse.

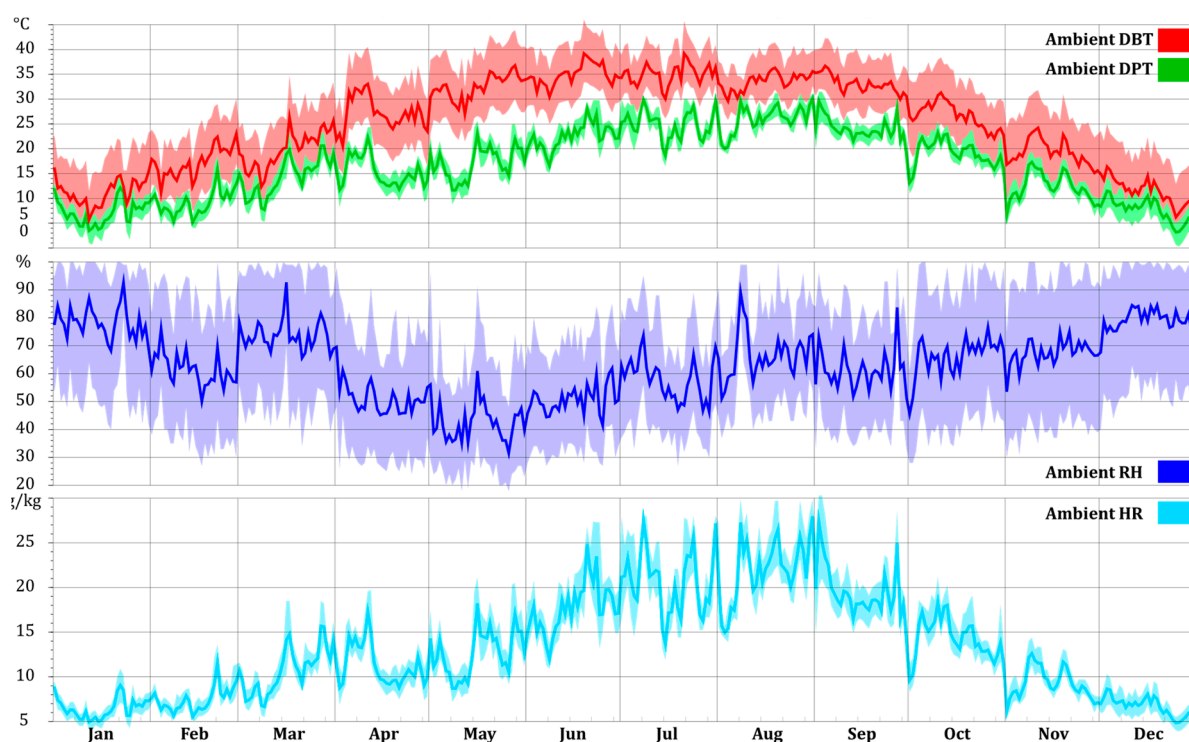


Figure 8. Profile of annual climatic ambient air conditions of Multan (Pakistan).

The standalone DAC system created a maximum temperature gradient, i.e., 8.4 °C more at ambient conditions of 38.6 °C with a humidity ratio of 21.6 g/kg at ambient conditions of 25 g/kg, which lies well outside the required greenhouse optimum temperature and humidity conditions (Figure 9a). It is worth mentioning that the temperature gradient is defined as the difference between the dry bulb temperature of the ambient air and the dry bulb temperature of the product air at the system outlet node. The studied standalone DAC system created unsuitable thermal and humidity conditions inside the greenhouse throughout the year due to a relatively higher temperature and very dehumidified air (Figure 9a). According to Figure 9b, the standalone DAC system coupled with a sensible heat exchanger (DAC+HX) (working efficiency assumed to be 0.9) created a maximum temperature gradient, i.e., 0.77 °C more at ambient conditions of 39.2 °C with a humidity ratio of 16.8 g/kg at ambient conditions of 24.3 g/kg, which lies slightly outside the required greenhouse optimum temperature and humidity conditions (Figure 9b), and is very close to ambient air conditions. The studied DAC+HX system created very close thermal and humidity conditions to ambient conditions inside the greenhouse throughout the year.

Figure 9c shows the psychrometric profile of temperature and relative humidity of the desiccant dehumidification-based Maisotsenko cycle evaporative cooling (M-DAC) system for the climatic conditions of Multan (Pakistan). According to Figure 9c, most of the hourly points of the M-DAC system lie inside the required thermal and humidity conditions of the greenhouse environment. The M-DAC system created a maximum temperature gradient i.e., 21.98 °C. According to Figure 9c, the M-DAC system coupled with a sensible heat exchanger (working efficiency assumed to be 0.9) created a maximum temperature gradient i.e., 21.9 °C more at ambient conditions of 39.2 °C with a humidity ratio of 16.8 g/kg at ambient conditions of 19.6 g/kg, which lies well inside the required thermal and humidity conditions inside the greenhouse environment (Figure 9c).

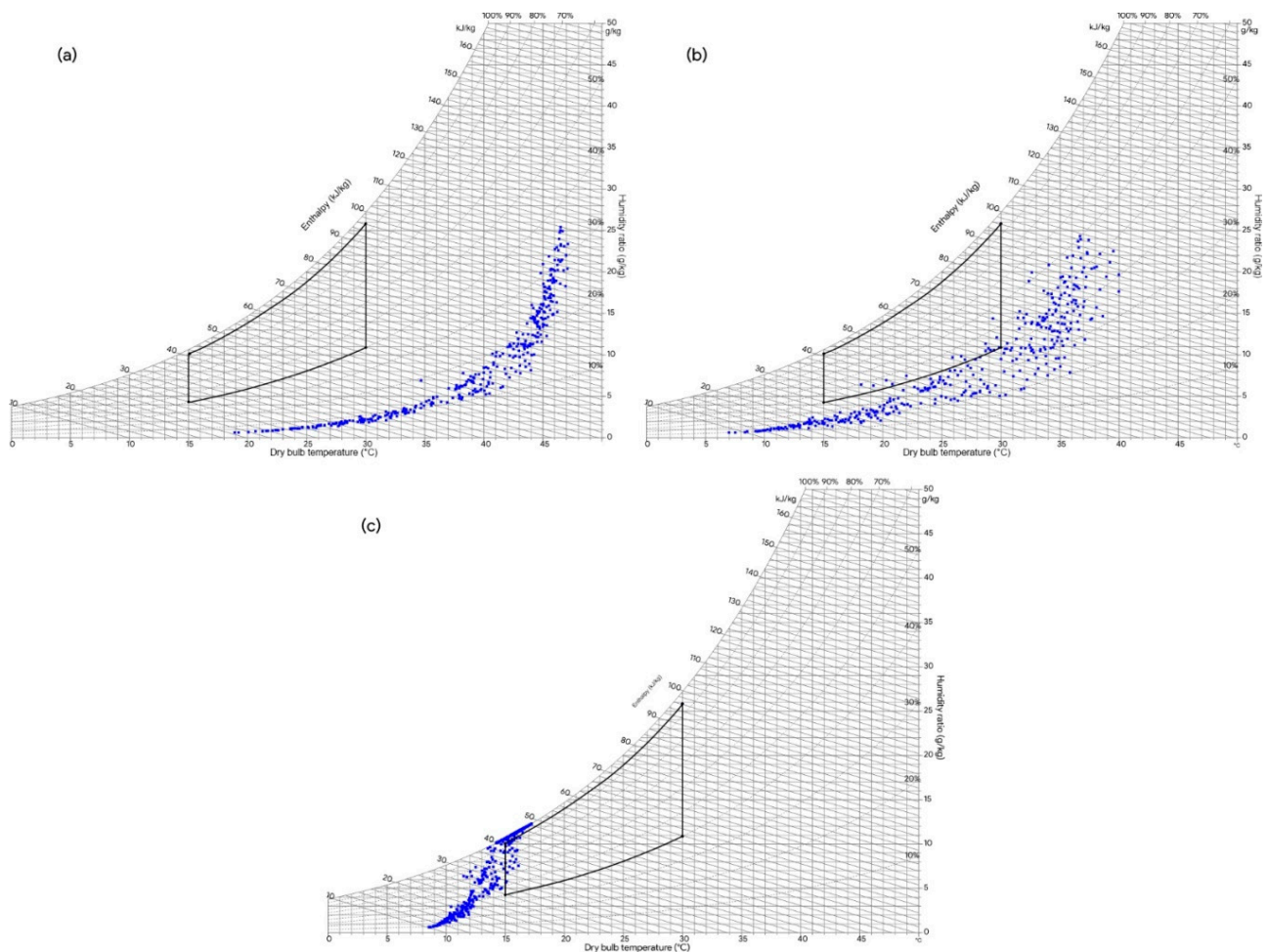


Figure 9. Profile of annual temperature and relative humidity of (a) standalone desiccant air-conditioning (DAC) system, (b) desiccant air-conditioning coupled with sensible heat exchanger (DAC+HX) system, and (c) desiccant dehumidification Maisotsenko cycle evaporative cooling (M-DAC) system, for greenhouse air-conditioning.

Figure 10 shows the vapor pressure deficit (VPD) profile and growth stages of plants inside a greenhouse (for the temperature of the leaf equal to the temperature of the air inside the greenhouse environment). According to Figure 10, the VPD of $<0.4>1.6$ kPa is considered an extremely dangerous zone for over/under transpiration. The VPD of 0.4–0.8 kPa is considered a slightly low transpiration zone (propagation/early vegetative growth of the plants). The VPD of 0.8–1.2 kPa is considered a healthy transpiration zone (late vegetation/early flowering stage of the plants). The VPD of 1.2–1.6 kPa is considered a high transpiration zone (mid/late flowering stage of the plants).

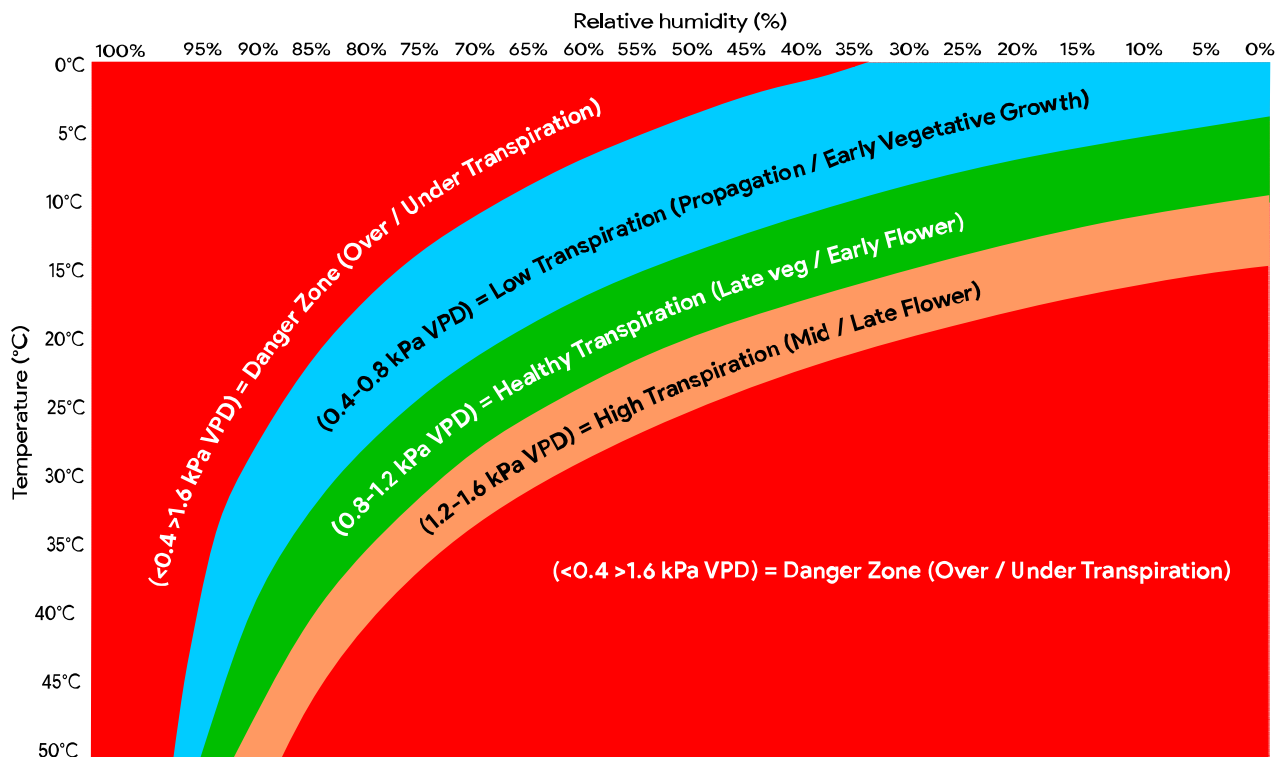


Figure 10. Vapor pressure deficit (VPD) profile and growth stages of plants inside a greenhouse.

Figure 11 shows the temperature profile of the studied systems against the ambient air conditions of Multan (Pakistan) for greenhouse air-conditioning application. The ambient air conditions lie outside the required temperature conditions (marked by the dotted red line, Figure 11) from April to September (i.e., typical summer months) of Multan. Air-conditioning is required inside the greenhouse environment during the summer months. Only M-DAC system created a uniform temperature gradient which lies well inside the required temperature conditions (marked in dotted red line, Figure 11) of the greenhouse environment. Figure 12 shows the temperature gradient of the DAC, DAC+HX, and M-DAC system in the summer months (i.e., May to August) for the greenhouse air-conditioning for the climatic conditions of Multan (Pakistan). The DAC system created higher than ambient temperature conditions throughout the summer months, which is unsuitable for greenhouse air-conditioning requirements (Figure 12). The DAC + HX system created slightly higher/very close to ambient temperature conditions throughout the summer months, which is also not suitable for greenhouse air-conditioning requirements (Figure 12). The M-DAC system created a temperature gradient which is highly suitable for the required temperature conditions throughout the summer months for greenhouse air-conditioning application (Figure 12).

Figure 13 shows the dehumidification profile of the desiccant dehumidification unit of the proposed system for the summer months (i.e., May to August) for the climatic conditions of Multan (Pakistan). The desiccant dehumidification unit created a maximum dehumidification gradient of the ambient air, i.e., 6.61 g/kg at ambient conditions of 14.14 g/kg. It is worth mentioning that the dehumidification gradient is defined as the difference between the ambient air humidity ratio and the humidity ratio of the product air exiting the outlet of the proposed system. Compared to current proposed passive cooling techniques for greenhouse air-conditioning (i.e., pad-and-fan type systems for greenhouse air-conditioning systems), the proposed M-DAC system has the ability to manipulate the moisture inside the greenhouse environment, which is a key factor in defining the vapor pressure deficit inside the greenhouse. In turn, this defines the growth rate and ultimately results in better yield and fruit quality. Moreover, the M-DAC system can easily achieve

the required temperature conditions inside a greenhouse compared to passive cooling techniques, i.e., pad-and-fan type AC systems.

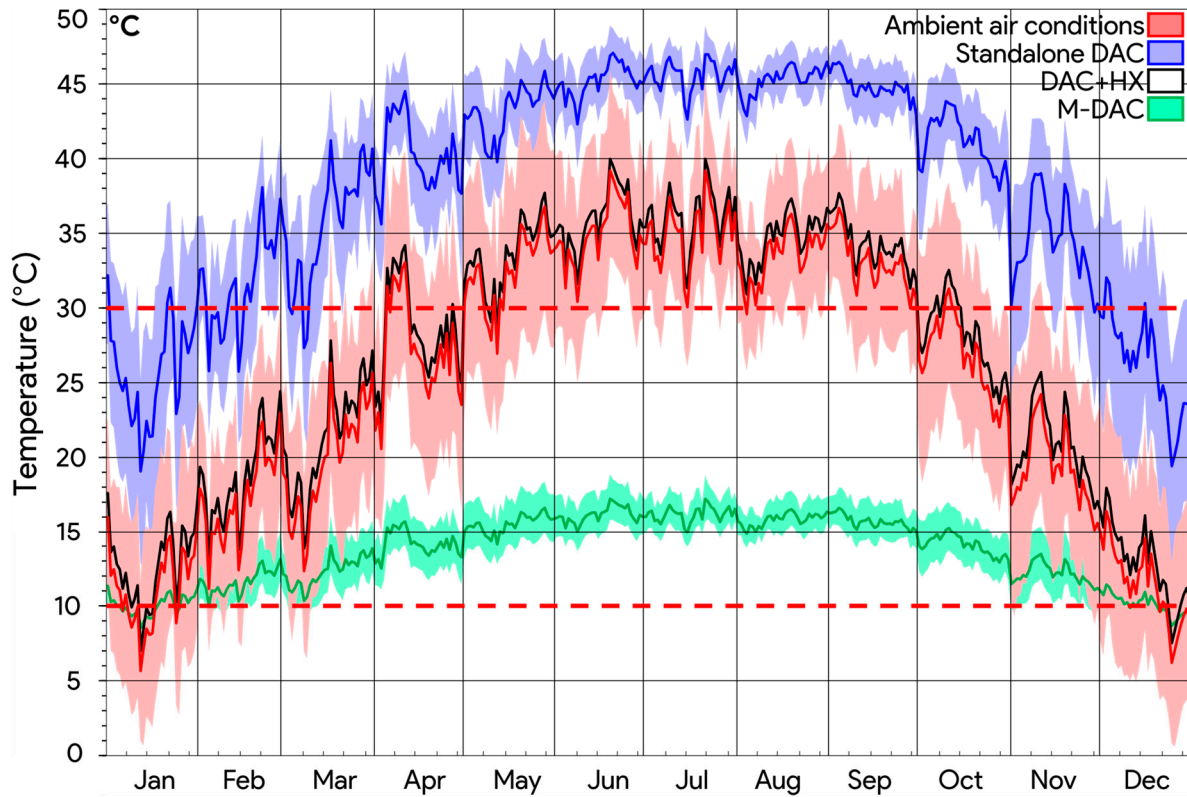


Figure 11. Annual profile of thermodynamic performance of the proposed M-DAC system for greenhouse air-conditioning for the climatic conditions of Multan (Pakistan).

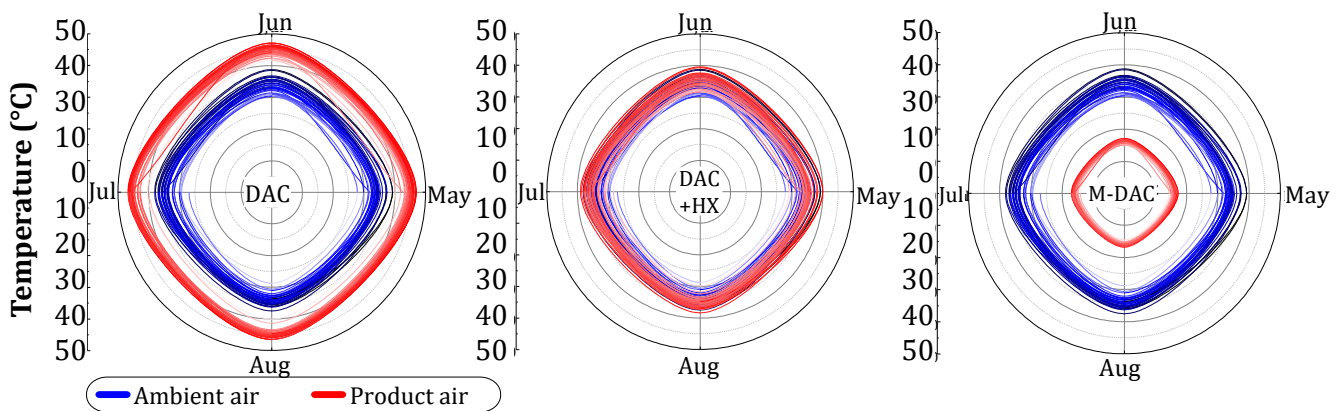


Figure 12. Performance profile of the proposed M-DAC system's temperature gradient in summer months of Multan (Pakistan) for greenhouse air-conditioning application.

4.2. Validation Based on Optimality Degree and Comfort Ratio

Validation of the performance of the proposed M-DC system with respect to the required optimal influential parameters of the greenhouse microclimate (i.e., temperature of the air, inside RH, and vapor pressure deficit) is shown in the plots of Figure 14 for 24 h. Results clearly show that the output of the M-DAC system was very close to the requirement microclimate data generated by the OptDeg model for the vegetative to mature fruiting growth stages. Moreover, the VPD plot implies that during the mid-day hours

(i.e., 13:00–17:00) when the air temperature was at the highest peak and relative humidity had the lowest values, the VPD increased to 2 kPa, which is consistent with the output of the M-DAC system. Results of the VPD data generated from the OptDeg model for actual greenhouse tomato cultivation in 130 days versus the simulated VPD data generated from the M-DAC system are plotted in Figure 15. The first derivative of the VPD data sets, plotted in Figure 15a, shows that the optimum VPD values from the OptDeg model and the VPD values from the M-DAC system are not significantly different. This finding was also verified using the one-way analysis of variance (ANOVA) test for each of the five growth stages. Figure 15b shows the deviation of the VPD data of the M-DAC system from 100% optimal condition ($\alpha = 1$), and compares that with actual VPD data of a commercial greenhouse that operated with ventilation and a pad-and-fan evaporative cooling system.

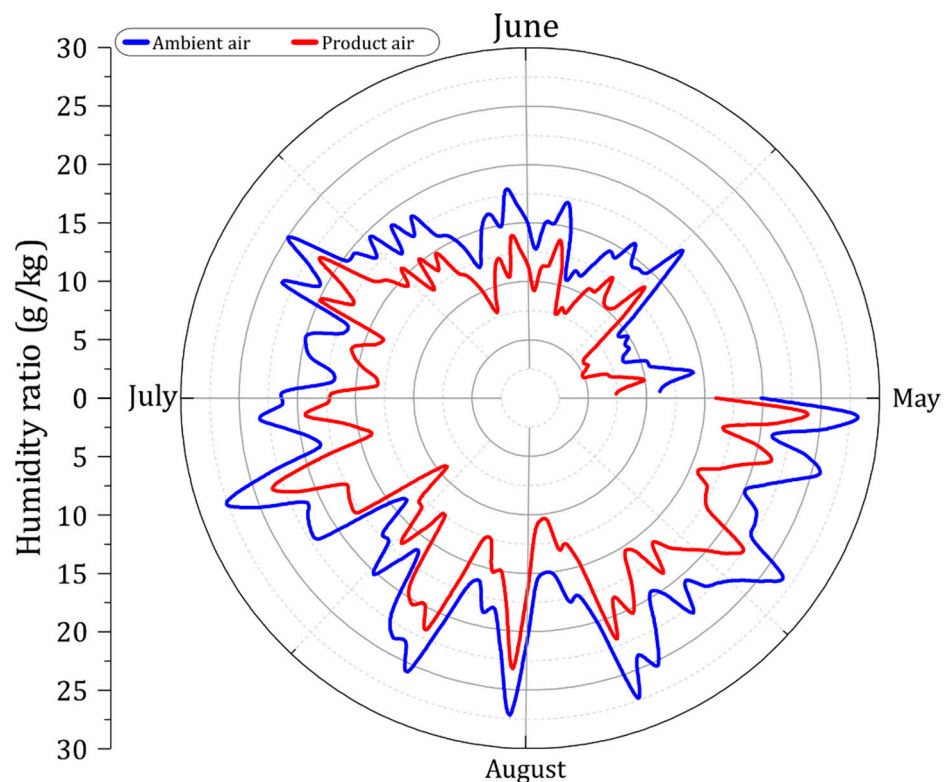


Figure 13. Performance profile of the proposed M-DAC system's humidity ratio in summer months of Multan (Pakistan) for greenhouse air-conditioning application.

A more in-depth result for comparing the performance of the M-DAC system and evaporative pad-and-fan system in a random day of cultivation under fruit formation growth stage is provided by means of the Cft-ratio model in the plots of Figure 16. In Figure 16, the reference conditions related to the optimal, marginal, and failure vapor pressure deficit (i.e., $\alpha_s = 1, 0.5$, and 0, respectively) are presented with a green solid line, blue solid line, and red solid line, respectively. The Cft-ratio Simulink model then determined the percentage of VPD data of each case, shown in Figure 16 that were inside each reference border. From the graphical presentation, it is evident that the VPD data from the M-DAC system resulted in a higher comfort ratio than those from the evaporative pad-and-fan system. In detail, VPD values resulting from the M-DAC system never crossed the marginal reference border, whereas for the conventional pad-and-fan case, during the hours of 13:30–14:30, VPD exceeded this border and increased to 3 kPa, which is considered a failure value for greenhouse production. Sample results of the comfort ratio model for comparing the performance of the evaporative system and M-DAC system in providing optimum vapor pressure deficit for greenhouse production are given in Table 3 for two different growth stages of the tomato plant.

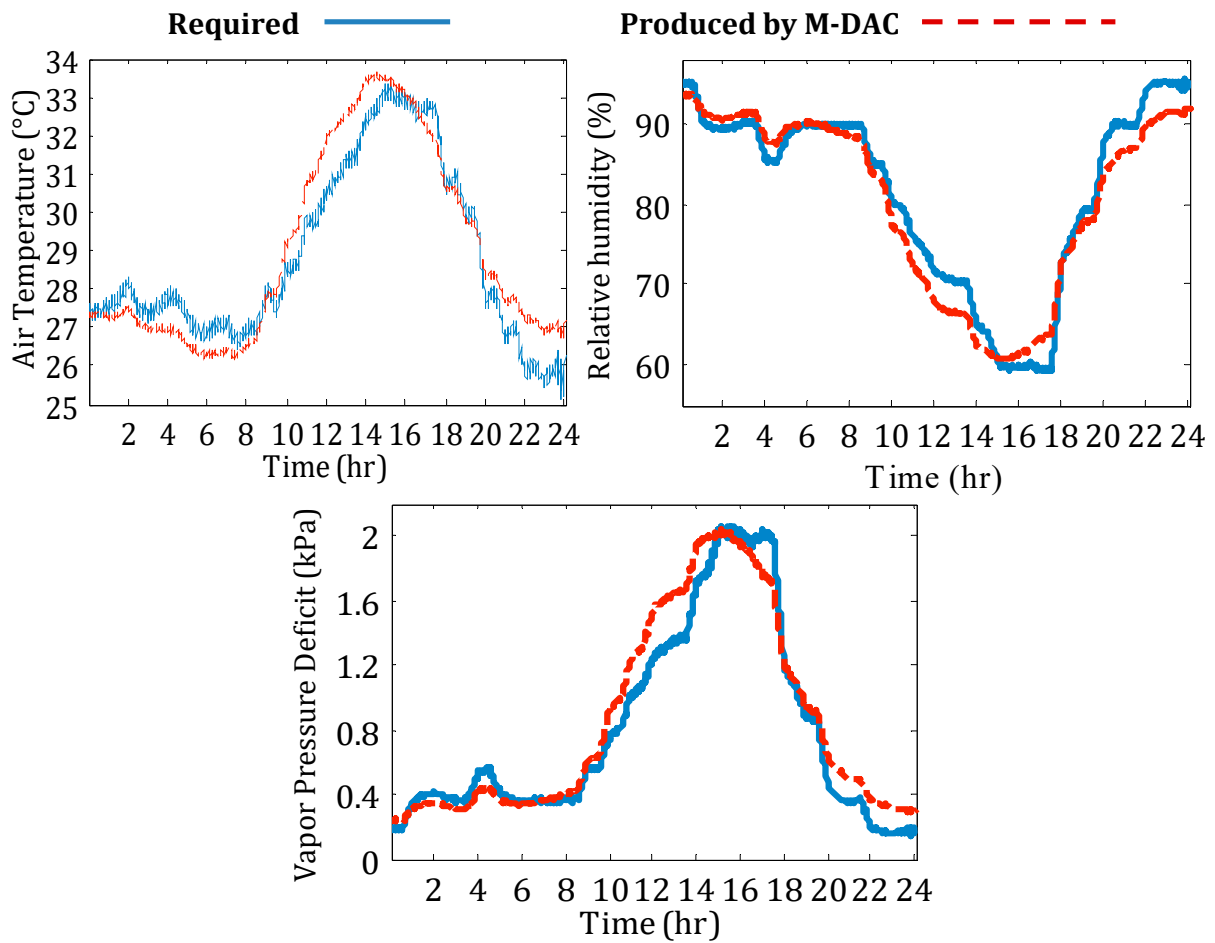


Figure 14. Validation of the performance of the proposed M-DAC with the OptDeg model for 24 h in greenhouse cultivation of tomato under vegetative to mature fruiting growth stages.

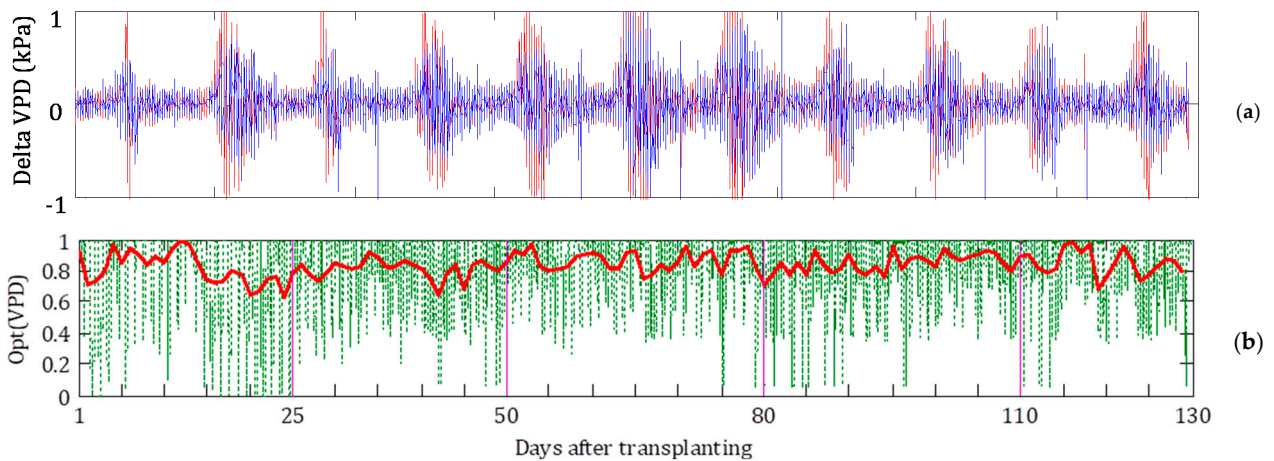


Figure 15. Variation in the VPD data (a), and optimality degree of VPD (b) resulting from the air temperature and relative humidity data of the proposed M-DAC system simulated for greenhouse cultivation of tomato in 130 days.

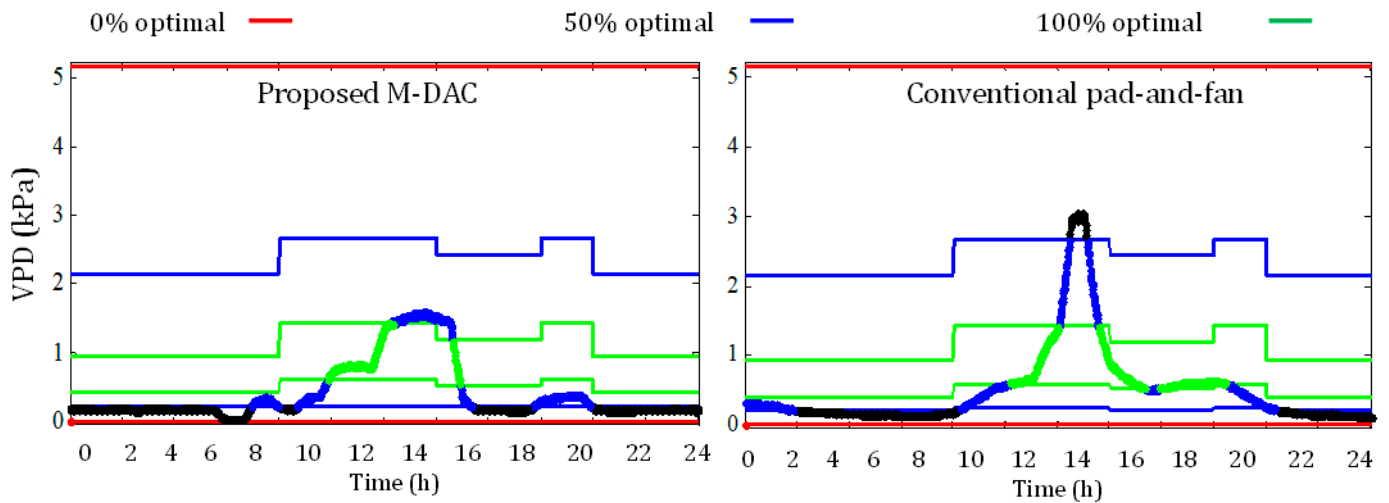


Figure 16. Comparison between comfort ratios of VPD for 24 h resulting from the proposed M-DAC system and VPD data from a conventional evaporative (pad-and-fan) cooled greenhouse.

Table 3. Performance validation of the proposed M-DAC system with the comfort ratio model at $\alpha_s = 1$ in comparison with experimental data from a tomato greenhouse with evaporative pad-and-fan system [57] for 11 days under different growth stages.

Days	Vegetative Growth Stage		Flowering to Mature Fruiting	
	Pad-and-fan Ref. [57]	M-DAC (This Study)	Pad-and-Fan Ref. [57]	M-DAC (this Study)
1	8.6	21.2	11.1	24.7
2	4.9	17.2	19.6	26.7
3	27	11.9	31.9	18.2
4	13.5	20.4	32.1	24.9
5	21.9	16.4	40.9	31.0
6	25.2	36.0	27.5	43.4
7	4.6	17.5	25.8	39.0
8	32.3	51.4	36.3	65.2
9	5	6.4	8.8	25.5
10	4.3	46.8	8.3	51.0
11	18.8	20.5	32.2	29.4
Mean	15.1	24.1	24.9	34.5
SD	10.4	14.3	11.4	14.0
Min	4.3	6.4	8.3	18.2
Max	32.3	51.4	40.9	65.2

5. Conclusions

The present study aimed to investigate the applicability of desiccant dehumidification-based Maisotsenko cycle evaporative cooling (M-DAC) system for greenhouse air-conditioning application for the climatic conditions of Multan (Pakistan). The study area (i.e., Multan) lies in a warm desert climate of the Köppen–Geiger climatic classification. In this regard, air-conditioning is required in greenhouses to optimize the temperature and humidity conditions, which could potentially increase the production level. Therefore, the present study proposed a desiccant dehumidification-based Maisotsenko cycle evaporative cooling system (M-DAC) for greenhouse air-conditioning application. The standalone DAC system created a (maximum) dehumidification gradient (i.e., 16.8 g/kg) at 24.3 g/kg ambient air conditions, and a (maximum) temperature gradient (i.e., 8.4 °C) at 38.6 °C ambient air conditions. The DAC+HX system created a temperature gradient roughly equal to the ambient air conditions, which are unsuitable for greenhouse air-conditioning. The M-DAC system created a (maximum) temperature gradient (i.e., 21.9 °C) at 39.2 °C ambient

air conditions, which lies well within the required optimum temperature conditions of the greenhouse air-conditioning. Additionally, the M-DAC created a dehumidification gradient (i.e., 16.8 g/kg) at 24 g/kg ambient conditions, which also lies inside the range of optimum humidity conditions inside the greenhouse. Moreover, the vapor pressure deficit (VPD) profile of the greenhouse environment related to the growth of plants indicated that a VPD of 0.8–1.2 kPa (for leaf temperature equal to surrounding air temperature) is most suitable for healthy transpiration from the plant leaves at late vegetation and early flowering stages. These results were validated with OptDeg and Cft-ratio microclimate models, which showed that the M-DAC system maintained the VPD of the product air inside the healthy transpiration zone throughout most of the summer months (i.e., May to August). Moreover, the comfort ratio model results of the proposed M-DAC system were compared with experimental results from a tomato greenhouse, indicating that the M-DAC system could potentially achieve the required comfort level compared to a pad-and-fan type air-conditioning system. Thus, the study indicates the M-DAC system is a feasible option for greenhouse air-conditioning for the climatic conditions of Multan (Pakistan).

Author Contributions: Conceptualization, H.A., M.S. and F.A. (Farrukh Abbas); Data curation, H.A. and F.A. (Farrukh Abbas); Formal analysis, H.A., M.S., R.R.S. and F.A. (Farrukh Abbas); Funding acquisition, M.S. and R.R.S.; Investigation, M.S., R.R.S., U.S. and F.A. (Fiaz Ahmad); Methodology, H.A., R.R.S., M.F. and H.M.-T.; Project administration, M.S.; Resources, M.S.; Software, M.H.M.; Supervision, M.S.; Validation, M.S. and R.R.S.; Visualization, U.S., H.M.-T., Y.R.T., A.S. and B.M.K.N.; Writing—original draft, H.A., M.S., R.R.S. and F.A. (Farrukh Abbas); Writing—review & editing, M.F., M.H.M., F.A. (Fiaz Ahmad), Y.R.T., A.S. and B.M.K.N. All authors have read and agreed to the published version of the manuscript.

Funding: This research received no external funding.

Data Availability Statement: Data is contained within the article.

Acknowledgments: This research work has been carried out in the Department of Agricultural Engineering, Bahauddin Zakariya University, Multan-Pakistan. Some of this work is part of the M.Sc. (Hons.) research of Farrukh Abbas. This research was funded by Bahauddin Zakariya University, Multan-Pakistan under the Director Research/ORIC grant entitled “Development and performance evaluation of prototypes of direct and indirect evaporative cooling-based air conditioning systems” awarded to Principal Investigator Muhammad Sultan. The authors acknowledge the financial support by the Open Access Publication Fund of the Leibniz Association, Germany, and the partial research funding and editorial supports from Adaptive AgroTech Consultancy International.

Conflicts of Interest: The authors declare no conflict of interest.

References

1. Pandelidis, D.; Anisimov, S. Numerical analysis of the heat and mass transfer processes in selected M-Cycle heat exchangers for the dew point evaporative cooling. *Energy Convers. Manag.* **2015**, *90*, 62–83. [CrossRef]
2. Caliskan, H.; Dincer, I.; Hepbasli, A. A comparative study on energetic, exergetic and environmental performance assessments of novel M-Cycle based air coolers for buildings. *Energy Convers. Manag.* **2012**, *56*, 69–79. [CrossRef]
3. Zhan, C.; Duan, Z.; Zhao, X.; Smith, S.; Jin, H.; Riffat, S. Comparative study of the performance of the M-cycle counter-flow and cross-flow heat exchangers for indirect evaporative cooling—Paving the path toward sustainable cooling of buildings. *Energy* **2011**, *36*, 6790–6805. [CrossRef]
4. Caliskan, H.; Dincer, I.; Hepbasli, A. Exergetic and sustainability performance comparison of novel and conventional air cooling systems for building applications. *Energy Build.* **2011**, *43*, 1461–1472. [CrossRef]
5. Chua, K.J.; Chou, S.K.; Yang, W.M.; Yan, J. Achieving better energy-efficient air conditioning—A review of technologies and strategies. *Appl. Energy* **2013**, *104*, 87–104. [CrossRef]
6. Pandelidis, D.; Anisimov, S.; Worek, W.M. Performance study of the Maisotsenko Cycle heat exchangers in different air-conditioning applications. *Int. J. Heat Mass Transf.* **2015**, *81*, 207–221. [CrossRef]
7. Rogdakis, E.D.; Koronaki, I.P.; Tertipis, D.N. Experimental and computational evaluation of a Maisotsenko evaporative cooler at Greek climate. *Energy Build.* **2014**, *70*, 497–506. [CrossRef]
8. Cui, X.; Chua, K.J.; Yang, W.M. Use of indirect evaporative cooling as pre-cooling unit in humid tropical climate: An energy saving technique. *Energy Procedia* **2014**, *61*, 176–179. [CrossRef]

9. Rianguvilaikul, B.; Kumar, S. Numerical study of a novel dew point evaporative cooling system. *Energy Build.* **2010**, *42*, 2241–2250. [CrossRef]
10. Sultan, M. Study on Sorption Characteristics of Water Adsorbents for Agricultural Air-Conditioning Systems. Ph.D. Thesis, Kyushu University, Kyushu, Japan, 2015.
11. Anisimov, S.; Pandelidis, D.; Jedlikowski, A.; Polushkin, V. Performance investigation of a M (Maisotsenko)-cycle cross-flow heat exchanger used for indirect evaporative cooling. *Energy* **2014**, *76*, 593–606. [CrossRef]
12. Zhao, X.; Li, J.M.; Riffat, S.B. Numerical study of a novel counter-flow heat and mass exchanger for dew point evaporative cooling. *Appl. Therm. Eng.* **2008**, *28*, 1942–1951. [CrossRef]
13. Zube, D.; Gillan, L. Evaluating Coolerado Corporation's Heat and mass exchanger performance through experimental analysis. *Int. J. Energy Clean Environ.* **2011**, *12*, 101–116. [CrossRef]
14. Weerts, B. Coolerado and modeling an application of the Maisotsenko Cycle. *Int. J. Energy Clean Environ.* **2011**, *12*, 287–307. [CrossRef]
15. Maisotsenko, V.; Treyger, I. Way to energy abundance can be found through the Maisotsenko cycle. *Int. J. Energy Clean Environ.* **2011**, *12*, 319–326. [CrossRef]
16. Khalatov, A.; Karp, I.; Isakov, B. Prospects of the Maisotsenko thermodynamic cycle application in Ukraine. *Int. J. Energy Clean Environ.* **2011**, *12*, 141–157. [CrossRef]
17. Anisimov, S.; Pandelidis, D. Heat and mass-transfer processes in indirect evaporative air conditioners through the Maisotsenko cycle. *Int. J. Energy Clean Environ.* **2011**, *12*, 273–286. [CrossRef]
18. Rogdakis, E.D.; Tertipis, D.N. Maisotsenko cycle: Technology overview and energy-saving potential in cooling systems. *Energy Emiss. Control Technol.* **2015**, *3*, 15.
19. Nagaya, K.; Senbongi, T.; Li, Y.; Zheng, J.; Murakami, I. High energy efficiency desiccant assisted automobile air-conditioner and its temperature and humidity control system. *Appl. Therm. Eng.* **2006**, *26*, 1545–1551. [CrossRef]
20. Lee, S.H.; Lee, W.L. Site verification and modeling of desiccant-based system as an alternative to conventional air-conditioning systems for wet markets. *Energy* **2013**, *55*, 1076–1083. [CrossRef]
21. Ismail, M.Z.; Angus, D.E.; Thorpe, G.R. The performance of a solar-regenerated open-cycle desiccant bed grain cooling system. *Sol. Energy* **1991**, *46*, 63–70. [CrossRef]
22. Sultan, M.; Miyazaki, T.; Koyama, S.; Saha, B.B. Utilization of Desiccant Air-Conditioning System for Improvement in Greenhouse Productivity: A Neglected Area of Research in Pakistan. *Int. J. Environ.* **2014**, *4*, 1–10.
23. Zheng, G.; Zheng, C.; Yang, G.; Chen, W. Development of a new marine rotary desiccant airconditioning system and its energy consumption analysis. *Energy Procedia* **2011**, *16*, 1095–1101. [CrossRef]
24. Bourdoukan, P.; Wurtz, E.; Joubert, P. Comparison between the conventional and recirculation modes in desiccant cooling cycles and deriving critical efficiencies of components. *Energy* **2010**, *35*, 1057–1067. [CrossRef]
25. Enteria, N.; Yoshino, H.; Takaki, R.; Yonekura, H.; Satake, A.; Mochida, A. First and second law analyses of the developed solar-desiccant air-conditioning system (SDACS) operation during the summer day. *Energy Build.* **2013**, *60*, 239–251. [CrossRef]
26. Dezfouli, M.M.S.; Mat, S.; Pirasteh, G.; Sahari, K.S.M.; Sopian, K.; Ruslan, M.H. Simulation Analysis of the Four Configurations of Solar Desiccant Cooling System Using Evaporative Cooling in Tropical Weather in Malaysia. *Int. J. Photoenergy* **2014**, *2014*, 843617. [CrossRef]
27. Enteria, N.; Yoshino, H.; Satake, A.; Mochida, A.; Takaki, R.; Yoshie, R.; Mitamura, T.; Baba, S. Experimental heat and mass transfer of the separated and coupled rotating desiccant wheel and heat wheel. *Exp. Therm. Fluid Sci.* **2010**, *34*, 603–615. [CrossRef]
28. Ge, T.S.; Ziegler, F.; Wang, R.Z.; Wang, H. Performance comparison between a solar driven rotary desiccant cooling system and conventional vapor compression system (performance study of desiccant cooling). *Appl. Therm. Eng.* **2010**, *30*, 724–731. [CrossRef]
29. Sultan, M.; El-Sharkawy, I.I.; Miyazaki, T.; Saha, B.B.; Koyama, S.; Maruyama, T.; Maeda, S.; Nakamura, T. Water vapor sorption kinetics of polymer based sorbents: Theory and experiments. *Appl. Therm. Eng.* **2016**, *106*, 192–202. [CrossRef]
30. Sultan, M.; Miyazaki, T.; Koyama, S.; Khan, Z.M. Performance evaluation of hydrophilic organic polymer sorbents for desiccant air-conditioning applications. *Adsorpt. Sci. Technol.* **2018**, *36*, 311–326. [CrossRef]
31. Sultan, M.; El-Sharkawy, I.I.; Miyazaki, T.; Saha, B.B.; Koyama, S.; Maruyama, T.; Maeda, S.; Nakamura, T. Insights of water vapor sorption onto polymer based sorbents. *Adsorption* **2015**, *21*, 205–215. [CrossRef]
32. Sultan, M.; Miyazaki, T.; Mahmood, M.H.; Khan, Z.M. Solar assisted evaporative cooling based passive air-conditioning system for agricultural and livestock applications. *J. Eng. Sci. Technol.* **2018**, *13*, 693–703.
33. Noor, S.; Ashraf, H.; Sultan, M.; Khan, Z.M. Evaporative Cooling Options for Building Air-Conditioning: A Comprehensive Study for Climatic Conditions of Multan (Pakistan). *Energies* **2020**, *13*, 3061. [CrossRef]
34. Sultan, M.; Miyazaki, T. Energy-Efficient Air-Conditioning Systems for Nonhuman Applications. In *Refrigeration*; Ekren, O., Ed.; InTech: London, UK, 2017; pp. 97–117.
35. Sultan, M.; El-Sharkawy, I.I.; Miyazaki, T.; Saha, B.B.; Koyama, S. An overview of solid desiccant dehumidification and air conditioning systems. *Renew. Sustain. Energy Rev.* **2015**, *46*, 16–29. [CrossRef]
36. Mahmood, M.H.; Sultan, M.; Miyazaki, T.; Koyama, S.; Maisotsenko, V.S. Overview of the Maisotsenko cycle—A way towards dew point evaporative cooling. *Renew. Sustain. Energy Rev.* **2016**, *66*, 537–555. [CrossRef]

37. Raza, H.M.U.; Ashraf, H.; Shahzad, K.; Sultan, M.; Miyazaki, T.; Usman, M.; Shamshiri, R.R.; Zhou, Y.; Ahmad, R. Investigating Applicability of Evaporative Cooling Systems for Thermal Comfort of Poultry Birds in Pakistan. *Appl. Sci.* **2020**, *10*, 4445. [CrossRef]
38. Kanwal, R.; Ashraf, H.; Sultan, M.; Babu, I.; Yasmin, Z.; Nadeem, M.; Asghar, M.; Shamshiri, R.R.; Ibrahim, S.M.; Ahmad, N.; et al. Effect of 1-Methyl Cyclopropane and Modified Atmosphere Packaging on the Storage of Okra (*Abelmoschus esculentus* L.): Theory and Experiments. *Sustainability* **2020**, *12*, 7547. [CrossRef]
39. Shamshiri, R.R.; Kalantari, F.; Ting, K.C.; Thorp, K.R.; Hameed, I.A.; Weltzien, C.; Ahmad, D.; Shad, Z.M. Advances in greenhouse automation and controlled environment agriculture: A transition to plant factories and urban agriculture. *Int. J. Agric. Biol. Eng.* **2018**, *11*, 1–22. [CrossRef]
40. Shamshiri, R.R.; Jones, J.W.; Thorp, K.R.; Ahmad, D.; Man, H.C.; Taheri, S. Review of optimum temperature, humidity, and vapour pressure deficit for microclimate evaluation and control in greenhouse cultivation of tomato: A review. *Int. Agrophysics* **2018**, *32*, 287–302. [CrossRef]
41. Shamshiri, R.; Ismail, W.I.W. A review of greenhouse climate control and automation systems in tropical regions. *J. Agric. Sci. Appl.* **2013**, *2*, 176–183. [CrossRef]
42. Shamshiri, R.; Ismail, W.I.W.; bin Ahmad, D. Experimental evaluation of air temperature, relative humidity and vapor pressure deficit in tropical lowland plant production environments. *Adv. Environ. Biol.* **2014**, *8*, 5–14.
43. Sultan, M.; Miyazaki, T.; Koyama, S. Optimization of adsorption isotherm types for desiccant air-conditioning applications. *Renew. Energy* **2018**, *121*, 441–450. [CrossRef]
44. Sultan, M.; Miyazaki, T.; Saha, B.B.; Koyama, S. Steady-state investigation of water vapor adsorption for thermally driven adsorption based greenhouse air-conditioning system. *Renew. Energy* **2016**, *86*, 785–795. [CrossRef]
45. Song, J.; Sobhani, B. Energy and exergy performance of an integrated desiccant cooling system with photovoltaic/thermal using phase change material and maisotsenko cooler. *J. Energy Storage* **2020**, *32*, 101698. [CrossRef]
46. Miyazaki, T.; Nikai, I.; Akisawa, A. Simulation analysis of an open-cycle adsorption air conditioning system—numeral modeling of a fixed bed dehumidification unit and the maisotsenko cycle cooling unit. *Int. J. Energy Clean Environ.* **2011**, *12*, 341–354. [CrossRef]
47. Pandelidis, D.; Anisimov, S.; Worek, W.M.; Drag, P. Analysis of different applications of Maisotsenko cycle heat exchanger in the desiccant air conditioning systems. *Energy Build.* **2017**, *140*, 154–170. [CrossRef]
48. Goldsworthy, M.; White, S. Optimisation of a desiccant cooling system design with indirect evaporative cooler. *Int. J. Refrig.* **2011**, *34*, 148–158. [CrossRef]
49. Sultan, M.; El-Sharkaw, I.I.; Miyazaki, T.; Saha, B.B.; Koyama, S. Experimental Study on Carbon Based Adsorbents for Greenhouse Dehumidification. *Evergreen* **2014**, *1*, 5–11. [CrossRef]
50. Lim, X. How heat from the sun can keep us all cool. *Nature* **2017**, *542*, 23–24. [CrossRef]
51. Beck, H.E.; Zimmermann, N.E.; McVicar, T.R.; Vergopolan, N.; Berg, A.; Wood, E.F. Present and future Köppen-Geiger climate classification maps at 1-km resolution. *Sci. Data* **2018**, *5*, 180214. [CrossRef]
52. Panaras, G.; Mathioulakis, E.; Belessiotis, V.; Kyriakis, N. Theoretical and experimental investigation of the performance of a desiccant air-conditioning system. *Renew. Energy* **2010**, *35*, 1368–1375. [CrossRef]
53. Panaras, G.; Mathioulakis, E.; Belessiotis, V. Solid desiccant air-conditioning systems—Design parameters. *Energy* **2011**, *36*, 2399–2406. [CrossRef]
54. ASHRAE. *ASHRAE Handbook—Fundamentals*; American Society of Heating, Refrigerating, and Air-Conditioning Engineers: Atlanta, GA, USA, 2017.
55. Shamshiri, R. Measuring optimality degrees of microclimate parameters in protected cultivation of tomato under tropical climate condition. *Measurement* **2017**, *106*, 236–244. [CrossRef]
56. Shamshiri, R.R.; Bojic, I.; van Henten, E.; Balasundram, S.K.; Dworak, V.; Sultan, M.; Weltzien, C. Model-based evaluation of greenhouse microclimate using IoT-Sensor data fusion for energy efficient crop production. *J. Clean. Prod.* **2020**, *263*, 121303. [CrossRef]
57. Rezvani, S.M.; Abyaneh, H.Z.; Shamshiri, R.R.; Balasundram, S.K.; Dworak, V.; Goodarzi, M.; Sultan, M.; Mahns, B. IoT-Based Sensor Data Fusion for Determining Optimality Degrees of Microclimate Parameters in Commercial Greenhouse Production of Tomato. *Sensors* **2020**, *20*, 6474. [CrossRef] [PubMed]

Review

A Review on Geothermal Renewable Energy Systems for Eco-Friendly Air-Conditioning

Adriana Greco ¹, Edison Gundabattini ² , Darius Gnanaraj Solomon ³ , Raja Singh Rassiah ⁴ 
and Claudia Masselli ^{1,*} 

¹ Department of Industrial Engineering, University of Naples Federico II, Piazzale Tecchio 80, 80125 Naples, Italy; adriana.greco@unina.it

² Department of Thermal and Energy Engineering, School of Mechanical Engineering, Vellore Institute of Technology (VIT), Vellore 632 014, Tamil Nadu, India; edison.g@vit.ac.in

³ Department of Design and Automation, School of Mechanical Engineering, Vellore Institute of Technology (VIT), Vellore 632 014, Tamil Nadu, India; dariusgnanaraj.s@vit.ac.in

⁴ Advanced Drives Laboratory, Department of Energy and Power Electronics, Vellore Institute of Technology (VIT), Vellore 632 014, Tamil Nadu, India; rrajasingh@vit.ac.in

* Correspondence: claudia.masselli@unina.it

Abstract: Nowadays, air conditioning consumes, on average, around one-fifth of the total power used in buildings globally. The present paper aims to provide the present status on the employment of Earth-to-Air Heat exchangers (EAHX) to contain the consumption of energy and to reduce the effect on the environment in response to the Montreal and Kyoto protocols in a way to achieve cleaner energy production with a low Global Warming Potential (GWP) and a low ozone depletion potential (ODP). Different peculiarities and applications (direct or hybrid) are critically analyzed and reviewed. Specifically, in this paper, the different hybrid applications presented in the literature, where the Earth-to-Air Heat exchangers are coupled to advanced systems, are reviewed. Finally, an IoT-based EAHX control system plan is reported and discussed to optimize energy efficiency and thermal comfort to suit operating conditions under different time zones.

Keywords: renewable energy; geothermal; Earth-to-Air Heat exchangers; ground source heat pumps

Citation: Greco, A.; Gundabattini, E.; Solomon, D.G.; Singh Rassiah, R.; Masselli, C. A Review on Geothermal Renewable Energy Systems for Eco-Friendly Air-Conditioning. *Energies* **2022**, *15*, 5519. <https://doi.org/10.3390/en15155519>

Academic Editors: Jan Danielewicz and Krzysztof Rajski

Received: 31 May 2022

Accepted: 28 July 2022

Published: 29 July 2022

Publisher's Note: MDPI stays neutral with regard to jurisdictional claims in published maps and institutional affiliations.



Copyright: © 2022 by the authors. Licensee MDPI, Basel, Switzerland. This article is an open access article distributed under the terms and conditions of the Creative Commons Attribution (CC BY) license (<https://creativecommons.org/licenses/by/4.0/>).

1. Introduction

Air conditioning is a crucial point to be considered in the building sector (both residential and commercial), both from energy savings and comfort-ensuring points of view. The conventional and most widely spread are HVAC systems (Heating, Ventilation, and Air Conditioning) based on vapor compression [1,2]. Even if they easily ensure the desired thermal comfort in the building environments, they negatively contribute to energy consumptions since HVACs are energy-intensive systems [3,4]. Furthermore, even if the Montreal Protocol [5] and subsequent amendments [6] have been prescribed to progressively phase out ozone depleting refrigerants, the currently employed fluids (HFC) are due to high global warming potential [7–9]. New alternative fluids for vapor compression systems are found on natural fluids or HydroFluoroOlefins (HFO) [10–13], which have problems with flammability and costs.

Approximately 20% of the electricity used in buildings globally today is used to cool spaces using air conditioning units and ceiling fans. In addition to increasing emissions, the growing demand for cooling systems has created a tremendous burden on the energy infrastructure of many nations. There is little question as to whether the requirement for space conditioning on a worldwide scale and the energy necessary to supply it will increase for several upcoming years in the absence of strong legislative initiatives. However, there is a high likelihood of swiftly altering the surge in conditioning energy consumption by implementing measures to increase system performance [14–16]. In developed countries,

the building sector impacts 30% of global energy consumption [17], and internally to the building sector, the energy consumption deriving from the HVAC operation is 50% of the overall power consumption of the whole expense.

Moreover, from a more global perspective, considering all fields and possible applications, refrigeration, and air conditioning are accountable, based on projections from the International Institute of Refrigeration, for over 20% of the world's power usage, on average, in 2020. This amount changes significantly among the worldwide countries, based both on the level of change and local climatic circumstances: 14% of the overall electricity demand of the USA is to be attributed to air conditioning, whereas in Mumbai (India), it accounts for 40%. The High-Level Board on Climate Change guesses that, considering the expected climate changes, the residential sector expects to see its energy demand for HVAC systems operating more than 13 times from 2000 to 2050 and more than 30 times up to 2100 [18]. If, on the one hand, climate change causes an increase in energy demand for air conditioning, on the other hand, since most systems are based on vapor compression, this increase contributes to the environmental (global warming) and energy crisis in a vicious circle that is dangerous for our future.

Hence, there is an international concern about containing energy consumption, enhancing the productivity performance of buildings, and minimizing the effect on the environment and human health.

The breaking points of the aforementioned vicious circle are: (i) the development of high-impact strategies for energy savings; (ii) an increase in the energy efficiency of air conditioning and refrigeration systems; and (iii) wide employment of renewable energy sources. In fact, improvements in the performance of HVAC systems have become a top priority for green policies. This is demonstrated, for instance, by the manufacturing industry's increasingly stringent efficiency standards for these systems, the creation of building classification and energy conformity assessments, and the consistency of proactive maintenance procedures for those kinds of systems. In particular, as stated explicitly in the European Directive on Renewable Sources and created by the so-called "green building" criteria, the regulations addressing the use of energy in the building industry aim to promote the use of renewable sources.

The growing interest in discovering substitutes for vapor compression-based HVAC systems has pushed researchers to make efforts to develop solutions based on renewable energies. Renewable energy is energy produced from sources that are available in nature and that may be utilized right away or stored through accumulation technologies. The most prevalent renewable energy sources include geothermal heat-based energy, photovoltaic, wind, biomass, precipitation, tidal energy, and waves [19–22]. Perhaps one of them, solar heating/cooling systems, uses solar energy substantially to heat and cool water for home and industrial purposes [23]. Solar power is used to generate electricity using photovoltaic (pv) systems [24].

As a matter of fact, in the panorama of renewable energy sources, next to solar, geothermal, and wind are also sources due to the big potential for electricity generation. Geothermal energy definitely dominated the renewable energy market in terms of installed electricity power about 30 years ago.

In recent times, the potential of employing geothermal sources for electricity generation has been surpassed and dominated by solar and wind. The data reveal [25] that the surpass on geothermal energy by wind and solar has occurred both in terms of growth rate and installed capacity. This is due to the high cost in charge of geothermal systems as an initial investment that couples with a long payback time. Moreover, the construction time is long, and it is difficult to find available spaces. In some cases, another factor is social acceptance in geothermal power generation that could occur differently from country to country. To deepen these aspects, we suggest referring to the comprehensive and critical analysis provided by Li et al. [25] where the differences among worldwide countries in the use of geothermal have also been treated.

However, in addition to these considerations, geothermal is a largely available renewable energy source that is very suitable for air conditioning applications devoted to buildings [26]. The latter case is referenced to a direct use of geothermal energy: one of the most virtuous worldwide countries is Iceland, where until 2011, 66% of primary energy usage exploited geothermal; currently in Iceland, about 96% of the energy consumption coming from heating and cooling derives from this renewable energy source. Heat pumps are the systems that are best suited for the direct use of geothermal energy; however, on a global balance, the rest of Europe is not so virtuous since the International Energy Agency stated that only 3% of the energy consumption coming from building air conditioning is satisfied by geothermal systems.

A push toward developing efficient geothermal energy-based HVAC systems is more necessary than ever. Two main applications currently exist devoted to this purpose:

- Ground Source Heat Pumps (GSHP);
- Earth-to-Air Heat eXchangers (EAHX).

The present paper aims to provide a state-of-the-art study on the employment of these two applications for air conditioning of buildings. In the next sections, the main aspects related to them are discussed, analyzed, and reviewed.

2. Geothermal-Based Applications

2.1. Generalities

The exploitation of geothermal systems can enhance the energy efficiency of HVAC systems without disturbing indoor comfort settings. Geothermal systems have the potential to realize noteworthy outcomes of eco-sustainability and carbon footprint reduction [27]. A hybrid solar-geothermal conditioning unit is investigated to reduce the Global Warming Potential (GWP) according to the Paris Climate Change Agreement and Kigali Amendment, aiming to contain energy consumption and refrigerant use. The objective was to reduce the cooling energy requirements by 25–40% and reduce the refrigerant requirement by 25–30% [28]. Yang et al. [29] analyzed the cooling and heating energy consumption of a model of a plant factory in China using the simulation tool TRNSYS. The annual energy consumption of the plant factory (both for cooling and heating) was estimated, and the analysis revealed that geothermal-based systems, such as the GSHP designed and modeled in their investigation, are sufficient to supply the energy consumption of the farm and even to guarantee the optimal comfort conditions for cultivating vegetables inside them.

Fernández [30] potentially analyzed the reduction in terms of energy demand, environmental impact, and economic expense if geothermal energy were employed in supermarkets. With respect to the different weather conditions, three case studies were considered: a supermarket placed in Germany, Portugal, and Turkey. They concluded that the employment of renewable energy sources, such as geothermal, led to a reduction in consumptions of 45% in Germany, 30% in Portugal, and 36% in Turkey, respectively.

Cadelano et al. [27] deliberated the energy retrofit of a museum arranged in a historical building through the software TRNSYS. Specifically, the energy consumption and environmental impact were evaluated by investigating the energy performances before and after the introduction of GSHP as an HVAC system. They noticed that the energy consumption in the second case was reduced by 24%.

2.2. Earth to Air-Heat eXchangers (EAHX): Requirements, Design, and Recent Breakthrough Investigations

EAHX is an innovative and efficient passive technology that typically uses low-enthalpy geothermal systems, used in many countries to encourage and strengthen the usage of renewable energy sources and, at the same time, to contribute to the achievement of thermal comfort in buildings. The working fluid in EAHX is air. The EAHX system consists of one or more pipes buried at a depth of at least 1.5–2 m below the surface, i.e., where the soil temperature does not change during the year, known as the Earth Undisturbed Temperature (EUT) [31].

A well-designed EAHX system is utilized independently or in conjunction with a conventional HVAC system to suit the building's heating and cooling needs. The cheapest EAHX could be a pipe of the right size that is buried at the right depth and by which ambient air is blown. The pipe has an outlet that lets air into the inhabited space, and one end that serves as an air input [32]. In summer, hot air is cooled by the soil, which is at a lower temperature; subsequently, it is supplied to the environment to be air-conditioned. Dually, in winter, cold air is heated in the basement and supplied inside to guarantee satisfaction with the thermal comfort standard.

A plant with an EAHX system consists of three main components:

- Suction unit: The air essential for the process of the scheme comes from the suction of outdoor air. The suction unit must be sized according to the connected EAHX tube and the pressure loss that is achieved. Regarding the location of outdoor air intake, it is necessary to comply with the requirements of VDI 6022 [33]. The latter requires that the air intake be of excellent quality. When choosing the location of the air suction, the following points must be considered: the vicinity to the road (road traffic) and other buildings; the proximity to leaf-losing trees/shrubs; proximity to vent openings of any kind; and the main wind direction and location of any systems that can generate annoying odors. The suction towers for EAHX must be made of waterproof material and not pose any risk to health, while the height of the suction entrance must be at a sufficient distance from the earth's surface and from any pollutant emitters. The standard also requires that the suction tower be made of stainless steel.
- Filters: The use of filters in the suction unit can serve several functions. You can use a coarse mesh filter to protect EAHX from pollutant external agents. This is also possible with a medium or fine mesh filter. The use of the coarse mesh filter is suitable for normal operation and is sufficient to ensure compliance with standards and directives. The use of a fine mesh filter is preferable if special health protection measures are to be taken, e.g., in the case of allergies. It should be taken in mind that to increase the useful life of a fine mesh filter, a coarse mesh one is always inserted into it. For the complete system comprising an EAHX and a traditional HVAC system, the directives [33] provide for two levels of filtering, one in the intake unit and the other in the traditional ventilation system. Finally, it should be noted that with the use of a fine mesh filter, the pressure drop for the suction unit increases.
- Pipes: The pipes installed in the EAHX constitute the heart of the system, and it is through them that the transmission of heat amid air and soil takes place. For the material of these pipes, directive VDI 6022 provides for specific requirements: it must be closed cell, watertight, and resistant to corrosion; not harmful to health; the material from which it is made should not store moisture and is due to a system to drain the condensate that forms in the summer.

Hence, the key advantages and disadvantages in the employment of EAHX schemes are listed below.

Advantages:

- The employed fluid used is air (unlimited availability and free);
- Power consumption is lower when compared with the prevailing traditional systems;
- Higher coefficient of performance (COP) when coupled with traditional systems;
- The scheme is simple, so it entails less upkeep and functional costs;
- The eco-friendly EAHX exploits geothermal energy, a renewable energy source, and it does not require the use of refrigerants and compressors.

Disadvantages:

- The installation cost is high;
- The requirement of large available free areas to bury the pipes;
- Condensation may occur in the ducts, which must be removed with the help of small submersible pumps;

- The convective mechanism that is triggered in the tube does not allow it to reach uniform temperatures at the outlet of the exchanger;
- Because air is employed as a refrigerant, the presence of microorganisms could become the main cause of the need to couple the EAHX with a filtered ventilation system, with greater energy consumption and a decrease in air quality.

EAHX's could be used in a huge number of schemes, which vary from one another according to the scheme, the geometry of the exchanger, the quantity of pipes mounting the exchanger and how they are arranged, the material the pipes are made of, etc. The optimal and suitable scheme must consequently consider several vital parameters: technical considerations, such as the availability of material or free land surface; energy considerations, such as the size of the cooling/heating load of the building to be air-conditioned; and economic considerations.

EAHXs can be categorized using a wide range of factors. A suggested categorization of EAHXs is shown schematically in Figure 1 [33]. EAHX systems can be classified into open-loop and closed-loop EAHXs based on their architecture and design. While closed-loop EAHXs circulate air from a building until the appropriate temperature is reached, open-loop EAHXs pull air straight from the surroundings. EAHXs might replace traditional conditioners as a practical option while also providing a straightforward design, easing ecological consequences, and lowering expenses. When contrasted to a closed-loop system, which cycles the same air through the pipes, an open-loop system delivers clean, fresh air that rotates through pipes and fulfils building cooling and heating requirements [34].

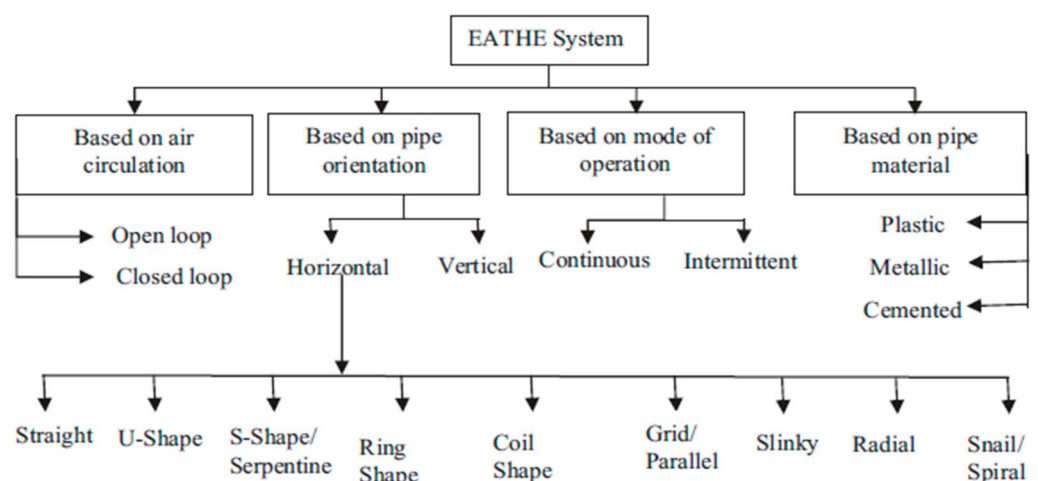


Figure 1. Classification of EAHX systems.

Because of their substantial influence on the lowering of heating/cooling energy loads and the enhancement of interior thermal comfort settings, EAHXs have proven to be appealing technological research. The cooling effectiveness of EAHXs has been researched under diverse geological and environmental circumstances, including relative humidity, air temperature, soil temperature, and air velocity. The EAHX was investigated to see if it might be used to improve energy performance within buildings while also lowering the electrical energy consumption of typical air-conditioning systems. Various upcoming and novel technologies will be useful in augmenting the performance of EAHX with suitable hybrid modes. Hybrid structures comprising hybrid nanofluids and microspray models and by incorporating wavy strips in the structures. These would enhance heat transfer efficiency and provide better thermal comfort as a final outcome [35–39].

2.3. Geometrical Parameters

Rodrigues et al. [40] carried out wide experimental procedures to evaluate the thermal and fluid-dynamic properties of a Y-shaped EAHX. The Energy Performance Indicator (EPI) was used to assess the EAHX's performance. The optimum configuration of the

Y-shaped EAHX boosted the value of EPI while also delivering monthly power savings, according to research [40]. The viability of a novel helical-shaped EAHX over conventional U-shaped EAHX is investigated for evaluating the thermal performances in a restricted ground space. outlet air temperature and effectiveness. The results indicated that the novel design offered an additional 80% of thermally comfortable indoor air conditions, even during peak summer. Similarly, the results also indicated that the novel design is efficient in heating operations to keep interior comfort in the winter spell [41].

Recent studies were also conducted on the impact of functional parameters, together with pipe length and pipe section (circular, rectangular, and elliptical), on the energy performances of EAHX, through sensitivity analysis. The outcomes indicated that the rectangular and elliptical buried pipes with larger surface area are more effective with >88% and >93% in contrast with the conventional (circular) one. The results also indicated that the efficacy of the length of the pipe is better over the pipe cross section [42].

2.4. Physics-Based Parameters

A pure buoyancy-driven EAHX system was recently explored for its practicality and cooling effectiveness by Long et al. [43] in 2022. This system combines solar chimney and thermal mass effects. The testing results revealed that the EAHX system could provide 24 h of varying natural ventilation and passive cooling, as well as significantly improve the indoor thermal environment under hot summer circumstances [43].

Recent studies have indicated that backfilling could augment the thermal potential of an EAHX beyond 400 m in depth to assist emergency ventilation. The backfilling system with low thermal conductivity proved to augment energy efficiency, thermal comfort, and thermal performance up to 100%, in contrast to the original system [44].

2.5. Integrated-Hybrid Systems

In 2022, an integrated passive system comprising a solar chimney with an EAHX (SCEAHX) was investigated by Long et al. [45] for its clean air and cooling capacity.

The SCEAHX system indicated 24 h of natural ventilation in conserving satisfactory indoor thermal comfort and temperature. A SCEAHX system based on Phase-Change Materials (PCM) was also studied to improve the interior thermal environment. The combined PCM-SCEAHX system, according to numerical analysis, not only increased usable cooling capacity but also produced more consistent interior thermal comfort conditions. As a result, the PCM-based SCEAHX system enhanced thermal inertia, regulated airflow rate during the day, and prolonged solar chimney's usage at night [45–47]. A recently developed water-aided EAHX was investigated for its energy efficiency with fins on the internal pipe of the double pipe heat exchanger. The results indicated that the overall heat transfer coefficients were enhanced, changing from 36–68% [48]. Researchers identified that hybrid building integrated photovoltaic/thermal (BIPV/T) and EAHX systems give greater yearly total electrical and thermal energies in contrast to the BIPV/T and EAHX systems. The hybrid system gives around 3% less yearly total thermal and electrical exergy and enviro-economic parameters in contrast with the BIPV/T. The exergo-economic factor of the thermal (BIPV/T) and EAHX systems was >50% of that for the BIPV/T system [49]. Recently, a novel hybrid system was designed comprising a coupled EAHX with a concentric 2-pipes heat exchanger as a clean energy source. The air is cooled when exchanging heat in the concentric 2-pipes heat exchanger, having an internal pipe with longitudinal fins filled with water and ice/mixture of ethylene glycol as a PCM. The outcomes indicated that the convective heat transfer coefficient is noteworthy in the hybrid system with an attractive cooling solution, even during peak periods [50]. Another hybrid semi-transparent photovoltaic thermal (SPVT) greenhouse system, together with an EAHX, has been developed to grow plants in a warm season. The impact of air variations, packing factor on photovoltaic (PV) cells, and mass flow rate of air flowing through EAHX, greenhouse gas, and plant temperatures is examined. Outcomes show that the hybrid SPVT-EAHX unit produces >125 kWh of daily inclusive sustainable exergy [51].

2.6. Climatic Conditions

For use in a desert climate, a numerical analysis of the thermal efficacy of an EAHX was built and presented by Maytorena and Hinojosa [52]. The results were confirmed by contrasting them with numerical and experimental data from previous works collected under comparable environmental circumstances. Investigations focused on determining the EAHX's suitable air velocity inlet, causing the optimal chillness in the room with the proper air inlet and output arrangement [52].

Over the years, EAHX technology has proven to be promising for space heating/cooling. In most regions, however, EAHX alone is insufficient to offer interior thermal comfort in all areas worldwide. However, a hybrid system combining an EAHX with an Air-Source Heat Pump (ASHP) has recently been explored to give interior thermal comfort while also conserving energy. The hybrid system reduced average energy consumption and enhanced the value of COP during the summer and winter months when compared to a standalone ASHP for certain ambient air temperatures and humidity ranges [53]. An inventive vertical solar chimney with fins and an EAHX has been examined as a summertime supplementary ventilation and air-conditioning device in a hot, arid environment. The height, diameter, number of fins, depth, length, and diameter of the pipes that make up the EAHX, among other geometric characteristics of the solar chimney, were explored. The research revealed that this system met the ventilation objectives of labs and residential buildings, and that it was able to save 85% usage at its highest potential [54].

2.7. Coupled System of EAHX Upstream of the AHU

D'Agostino et al. [55] estimated the energy efficacy of a peculiar geothermal energy system in which an EAHX is situated upstream of the Air-Handling Unit (AHU) of an office air conditioning unit in Naples (South Italy). Research outcomes indicated that, using the EAHX, the saving of the thermal energy of the coils in the AHU is >40%. Additionally, the efficiency of the EAHX value reached up to 90% with modifications in the tube length and diameter; this value may settle at around 40–50% for the entire year. Li et al. [56] analyzed an Air-to-Air Heat Recovery (AAHR) device and an EAHX (arranged in series) and evaluated the viability of the novel system in severe cold regions. Performance tests indicated that the novel system brings a significant ecological and economic benefit in contrast to the traditional solution. The EAHX significantly reduced greenhouse gas emissions by 17%, which is an indication of energy savings with payback periods of 2.1 and 2.4 years (return rate of 8%).

Kalbasi et al. [57] verified how, by combining an AAHR, EAHX, with an AHU, the cooling energy reduces to an average 33% and 11% reduction in the overall essential power. Research indicated that the coupled system of AHU and EAHX could bring down the total energy falls by an average of 38% with a 100 m long tube, and this value of reductions could even be reduced by 38–49% with the increased length of the tube. Ascione et al. [58] assessed the consequences of using an EAHX in an air-conditioning system on energy efficacy and ecological impact. The results showed that the pre-treating unit connected with the EAHX (pre-cooling in the summer and pre-heating in the winter) resulted in a 30% energy reduction in winter and an average saving rate of 41% in the summer, for a worldwide saving rate of 31% annually.

D'Agostino et al. [59] analyzed a coupled system of EAHX + AHU for the entire year at various locations identified according to the Koppen classification [60]. The results indicated a best outcome for Milan (Italy), with a cooling and heating capacity saving of 55% for a 100 m tube length, indicative of a huge energy savings. The lowest outcome was in Lampedusa (Italy) and Rio de Janeiro (Brazil), where the heating + cooling capacity reduction was possible up to 39% and 24%, respectively. Nevertheless, the best results could be attained for a 100-m tube length in Ottawa (Canada), where the heating + cooling capacity was reduced by 65% when using the EAHX. D'Agostino et al. [61] also investigated an HVAC system composed of EAHX + AHU. They demonstrated the overall energy saving in the city of Naples (Italy) in winter rises from 17% to 47% for the range of tube lengths,

20 m to 140 m. In addition, the power savings in Ottawa (Canada) reached an all-out of 52% for 140 m tube length.

2.8. Ground Source Heat Pump (GSHP) and EAHX

Shimada et al. [62] analyzed the high energy-saving potential GSHP to promote energy and GHG reductions. GSHP designed based experimental work on a pilot facility was conducted. The simulation results indicated an energy savings of 40% for a 3-year GSHP procedure for a small government building in Bangkok. Fernández [30] analysis indicates that the GSHP system of the Portuguese group could exhibit a 30% drop of energy spending and 30% lessening of carbon dioxide emissions in contrast to the conventional space conditioning system. Similarly, GSHP with vertical- and horizontal-type EAHX reduced electricity consumption by 30% and 18%, respectively, in contrast to an ASHP [63,64].

A Gas Injection EAHX (GI-EAHX) with an air conditioning system was analyzed for peak loads by Richter et al. [65]. Experimental results indicated that there was a reduction in the exit temperature of up to 2 °C and cooling power is increased by 26% compared with an equivalent conventional setup. They indicated that the usage of several GI-EAHX within a larger geothermal field could offer reliable peak load handling with a reduced size of a geothermal system with a good thermal capacity [66]. Several researchers optimized the diameter of the EAHX to augment the heat exchange rate up to 3.45%, and a rise of 18.7% was achieved by using ripped inner pipe walls instead of conventional smooth inner walls [67]. Specific details on these aspects were exhaustively summarized by Florides and Kalogirou [68].

Table 1 summarizes the main investigations in which significant energy savings were detected through the employment of geothermal systems. Different geothermal systems have been analyzed, from the simple EAHX configurations toward the GSHP and hybrid solutions.

Table 1. Energy savings through geothermal systems.

Author	Location	Method	Energy Reduction/Savings	CO ₂ /GHG Reduction
Cadelano et al. [27]	Technical Museum Nikola Tesla in Zagreb	GSHP	48–66%	24%
Fernández [30]	German super markets Portuguese	GSHP	45%/30%	28%/30%
D’Agostino et al. [55]	Office building in Naples (South Italy).	EAHX + AHU	40–50%	–
Li et al. [56]	Cold regions	EAHX + AAHR	8%	17%
Kalbasi et al. [57]		EAHX + AAHR + AHU	38–49%	–
Ascione et al. [58]	Mediterranean climate	EAHX + air conditioning	29–46%	–
	Milan		55%	
	Lampedusa		39%	
D’Agostino et al. [59]	Rio de Janeiro	EAHX + AHU	24%	–
	Ottawa		65%	
	Naples		17.5–46%	
D’Agostino et al. [61]	Ottawa	EAHX + AHU	52%	–
Shimada et al. [62]	Bangkok, Thailand	GSHP	40%	–
Richter et al. [65]	Hamburg University of Technology	GI-BHXs + air conditioning	26%	–

3. Materials Used in Earth-Air Heat Exchangers

The energy converted by the EAHXs depends on design parameters such as the pipe’s material, diameter, and depth [69]. The performance of ground-coupled heat exchanger systems is based on air/liquid flow rate, length, material, depth, diameter of pipe, temperature difference, soil temperature, capacity of blower fan, and different layout of pipes [70]. Sakhri et al. [71] reviewed how many researchers have conducted studies on the performance of EAHXs during summer and winter and found the effects of external and internal

parameters. The materials employed for building an EAHX are also crucial aspects to consider. In their reviews, Darius et al. [72] and Peretti et al. [73] also considered the influence of the thermal properties of the design materials on the energy performance provided by these geothermal systems. Specifically, pipes made of steel, aluminum, plastics, and copper tubes were reviewed by Peretti et al. [73]. The requirements for pipe materials are resistance coefficients, wall roughness, anti-corrosive, and structurally stable. The functions of the tubes are to transport air and exchange heat with the soil.

In their investigation, Bansal et al. [74] reported that pipe materials do not affect performance much due to their thickness; therefore, cheaper materials can be used in pipes. Lekhal et al. [75] analyzed the performance of EAHX using zinc and PVC. The comparative study was conducted under a warm-temperature climate in northern Algeria. The results show that pipe material affects EAHX performance when EAHX passes from heating to cooling mode. The air outlet temperature provided by zinc pipes is 7.5 °C higher than the outlet temperature provided by PVC. Sakhri et al. [76] used two types of pipe materials: PVC and steel. It was found that PVC is better than steel since PVC is cheap, light in weight, easy to assemble, and modification of shape is possible. Figure 2 shows the variety of materials used in the pipes of the EAHX systems.

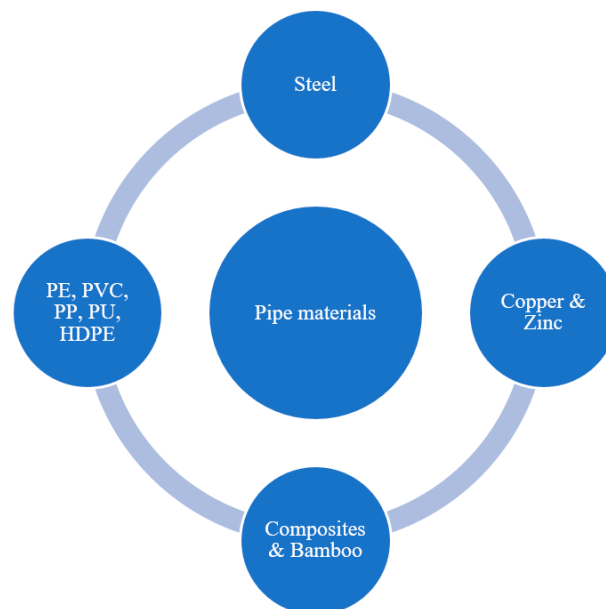


Figure 2. Variety of materials used in Pipes.

Bansal et al. [77] investigated the effects of pipe material and air velocity on the performance of EAHX systems. The investigations on steel and PVC pipes concluded that the velocity of air was found to greatly affect performance. The material having a high coefficient of friction affects the performance of the EAHX system. They concluded that convective heat transfer is dominant compared to conductive heat transfer. The effect of pipe materials on EAHX's performance was investigated. Zinc and PVC materials were used in the study. It was found that zinc EAHX exhibits higher efficiency in a climate with a COP of 9.5 compared to a steppe or arid climate having a COP of 8.2 or 8.1. PVC EAHXs are more suitable in the arid climate with a COP of 9.4 compared to the steppe climate with COPs belonging to the 7.6–8.4 range. The thermal performance of EAHX depends on the geo-climatic conditions and the pipe material [78].

Javadi et al. [79] reported that the most common material used in pipes of EAHXs is polyethylene (PE). Steel is most commonly used after PE. Copper and polyvinyl chloride (PVC) are also common. Polypropylene (PP), polyurethane (PU), composite, high-density polyethylene (HDPE), and polybutylene (PB) are rarely used. 60% of the GHEs use PE, 14% of the GHEs use steel, and 8% of the GHEs use PVC. Composite pipes exhibit better

performance compared with the one provided by EAHXs made of HDPE pipes. The addition of aluminum wires to HDPE pipes increases the thermal conductivity. Steel pipes have greater heat transfer coefficients of pipe length than PE ducts.

Svec et al. [80] investigated the heat flow around an EAHX using plastic piping. It was found that the performance of the EAHX was affected when plastic piping was used.

An experimental investigation was performed in the north-eastern region of India [81]. Tunnel pipes were made of bamboo, and a cement–soil plaster mixture was employed to enhance the conductivity of bamboo pipes. Experiments were performed continuously for 7 days, and the delivered air temperature ranged from 25–26 °C with respect to the air temperature at the inlet, which ranged from 35 °C to 42 °C. The underground fresh air system is an easy and economically feasible technique. It reduces the consumption of energy, meets the power demand, and minimizes changes in climatic conditions in buildings.

4. IOT & Control Systems Used in EAHX

4.1. Control Systems Used in EAHX

The concept of EAHX provided by a control system is shown in Figure 3. As discussed in previous sections, EAHX is a green retrofit for cooling and heating buildings [82–84]. The concept of EAHX enables the insufflation of outdoor air directly into the building, providing more favorable conditions in reaching the required thermal comfort (less energy consumption to reach the indoor setting temperature) when coupled to an AHU or another existing air conditioning system [85,86]. Heat exchanges between earth and air increase with decreasing air velocity, altering the air flow rate in the duct and allowing for modification of its output temperature. Such a control would require measuring tools and a centralized control system on an actual structure. As shown in Figure 3, the main parts of the EAHX system IOT controlled are:

- Heat exchanger tubes;
- Sensors and actuators;
- Monitoring systems;
- Data acquisition system;
- Database server and control units;
- Filters, pump, and pump drives;
- Controllers.

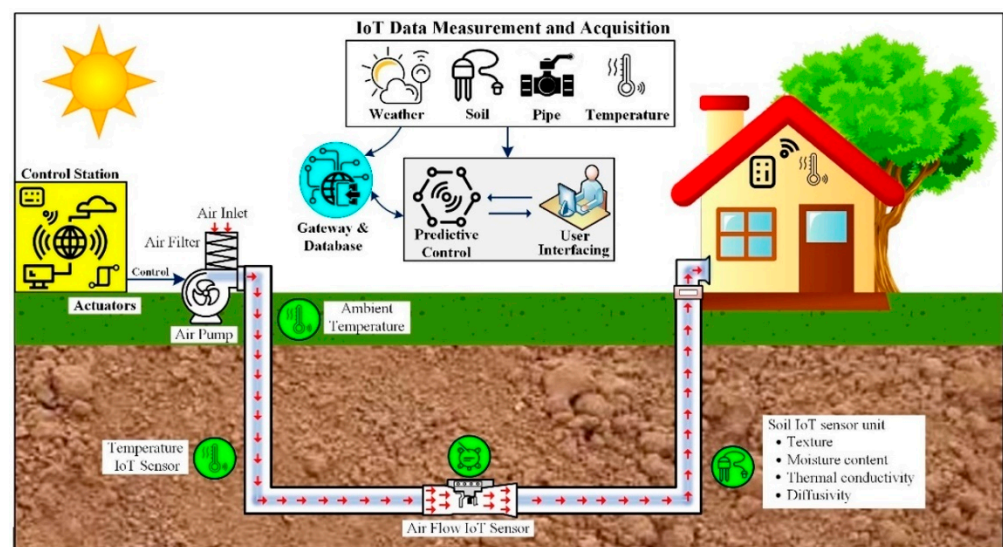


Figure 3. IoT-based control of the EAHX system.

The air pump has on/off control using a temperature sensor for ambient air and extracted room air, which can be set by the user. The aim of this on/off control strategy is

to activate the EAHX air-handling unit. The recommended control set temperature for the EAHX air pump is based on user input and predictive control [87].

EAHX systems are designed to ensure hygrothermal effects in interior building environments, and their automated control can significantly improve end-users' comfort. Implementing novel control architectures and enabling the energy enhancement of EAHX systems without compromising building occupants' thermal comfort is of utmost importance. Combining two key modules—an intelligent control process and a smart physical infrastructure—can accomplish this. Energy enhancement and thermal comfort optimization must be the focus of the first module, while the sensing, communication, data storage, and actuation of the EAHX system in response to end-user demands are handled by the second.

The system continues to operate to keep the temperature within the building practically constant until the ideal temperature is reached. As a result, it discovers an air mass flow rate that uses less energy. Several methods have been developed throughout the decades for EAHX systems that may be taken into consideration in the control algorithm module. The majority are intuitive on/off controllers that are unable to account for significant thermal inertia EAHX processes. In addition, PID controllers with complex tuning for thermal inertia EAHX processes, whose performance may degrade during system dynamics. After reaching a steady-state temperature, the PID controller lowers the system's energy usage [88]. A PID controller may be used to decrease the variation in air fan power, which is a cubic function directly connected to the velocity of the air mass flow rate pumped into the building heat exchanger. Appropriate PID gain settings can further reduce this variation, as demonstrated in this study. This is so that the PID controller does not always have to operate at full capacity. When using a PID controller, the system uses less energy after the air inside the building reaches the desired temperature. This is because there is less energy being removed by the heat exchanger at this point because there is less of a difference between the desired temperature and the ground temperature. Furthermore, since fewer energy resources are required for cooling or heating a structure, PID control can improve both the EAHX 's efficiency as well as the sustainability of the globe.

The advantages of two cutting-edge heat exchanger control techniques, H control and μ -synthesis, are described in [89]. The necessity for a design process that explicitly tackles issues with modeling mistakes led to the development of H_∞ optimal control, frequency-domain optimization, and design theory. The H_∞ control is developed further in the " μ -synthesis theory," where the uncertainty framework is considered while designing. A more effective predictive control strategy has gained traction over the past 20 years. This control method enables the efficient integration of energy efficacy methods into controller construction, together with problems such as disturbance rejection, constraint fulfillment, and slow-operating dynamic control [90]. Furthermore, the implementation of optimum regulating methods for the improvement of energy efficacy and thermal ease is becoming more abrupt and accessible as a result of the falling prices of smart devices. Advances in information and communication technology (ICT) enable the wide availability of dispersed sensors and data analytics tools. Therefore, it becomes clear that model predictive control is meaningless without being connected to a suitable smart infrastructure that enables the collection and transmission of actual data from the field [91]. By enabling the connecting of sensors, actuators, and other items to the internet and enabling both the awareness of the environment and interaction with it, the Internet of Things (IoT) extends a suitable solution.

4.2. IoT-Based Control of EAHX Systems

Due to the confluence of many technologies, things have changed. Digital intelligence is given to otherwise dumb gadgets by linking all these different things and giving them sensors, enabling them to communicate real-time data without a human being's input. The Internet of Things, which connects the real and digital worlds, is making the environment around us smarter and more responsive. Devices that can sense, analyze, and wirelessly transmit data to an unnamed storage place are used. such as the cloud, which stores,

analyses, and presents data in a useful format, the IoT is expected to revolutionize our world by assisting us in monitoring and controlling basic development in our environment [91]. IoT frameworks facilitate communication among “things,” with the majority of these frameworks appearing to focus on real-time data solutions. Big data and the Internet of Things are two developing technologies that may be used to generate information and enable applications for energy-efficient buildings [92]. Effective forecasting of heating and cooling demand is crucial to building energy management. One of the key uses of the IoT paradigm is the effective control of heating, ventilation, and air conditioning systems in smart buildings. The inside atmosphere of smart buildings may be improved for energy efficiency and thermal comfort using an IoT-based EAHX control system design [93]. The components are as follows:

It consists of the following elements:

- A gateway connects the nets of sensors and actuators to the Internet;
- An external application programming interface provides weather forecasts;
- An external database server gathers and forwards data from/to the field and from/to the control unit;
- A network of sensors senses environmental conditions and transmits measurements to a gateway;
- A network of actuators controls the pump and connects with the gateway;
- An IP device that serves as the end-user interface and is connected to the database server and host;
- A control unit that connects with the database server and houses the MPC algorithm;
- A dashboard for keeping track of the environment’s condition and adjusting the control system mode.

The proposed architecture’s mode of operation and information flow are as follows: The network of sensors is used to detect energy usage as well as the internal environmental conditions (temperature, CO₂ level, number of occupants, etc.). The measurements are then transferred in periodic bursts to the control unit, where the Predictive Control algorithm is implemented, and finally to the gateway, which connects to the database server. The control actions provided by this algorithm to the EAHX systems provide the optimal trade-off between energy consumption and comfort for the specified comfort limitations in the foreseeable future. The devices that actuate the EAHX modules get these control commands from the gateway. These control instructions are sent from the gateway to the devices that operate the EAHX modules. The EAHX modules adjust the room’s temperature in accordance with the algorithm’s predictions. The database server also keeps track of temperature and energy use readings. Through the dashboard on an IP device linked to the database server, these measures are shown to the end user. Users may interact with the control unit through the dashboard and choose the preferred temperature and control mode (i.e., either manual or automatic).

5. Conclusions

The surge in worldwide power consumption and CO₂ emissions is due to air conditioning and refrigeration, which has resulted in a massive increase in global warming and ozone depletion potential. The need for energy increased to achieve the required thermal comfort inside houses and business organizations. Renewable energy has to be utilized instead of conventional energy to reduce pollution in the environment. Alternative methods are being developed to achieve thermal comfort inside buildings. Many passive techniques replace conventional methods to reduce energy consumption. Natural resources supply energy when passive techniques are used.

EAHXs are discussed and critically analyzed as possible solutions for cleaner energy generation and low environmental impact. Specifically, the different hybrid applications presented in the literature, where the EAHXs are coupled to advanced systems, are reviewed.

When it comes to the design of an EAHX, the pipe diameter, length of pipe, and number of pipes are the leading parameters to be decided. As the length of the pipe increases, the pressure reduces, resulting in an increase in thermal performance. A long pipe of a small diameter buried at a large depth with less airflow velocity enhances the performance of EAHX. The temperature at certain depths is the same since the soil's thermal inertial property remains the same throughout the year. EAHX is effectively used to heat the air during the winter and cool the air in summer. The temperature of the Earth remains constant at a depth of 2 m throughout the year. This is called Earth's Undisturbed Temperature (EUT). The EUT is higher than air temperature during winter and lower than air temperature during summer.

EAHX utilizes geothermal energy, which is considered renewable energy and sustainable. Since EAHX does not use a refrigerant, there is no greenhouse gas emission. Soil density, soil properties, conductivity, diffusivity, water, and rock beds are the governing factors for selecting the site for EAHX.

In addition, various integrated hybrid systems are discussed to suit the climate conditions of arid, semi-arid, and congested areas. Hybrid systems indicated higher heat transfer coefficients, higher energy performance, and higher enviro-economic values compared to standalone EAHX systems. Phase change materials is a consolidated and viable resourced for this purpose. It is already employed in vapor compression [94] When compared to a standalone EAHX, a hybrid EAHX based on Phase-Change Materials and an Air-Source Heat Pump lowered average energy consumption and enhanced COP value roundly by 10–15%. At its maximum capacity, EAHX with a finned vertical solar chimney could increase energy savings by up to 60–80%. When EAHX is placed upstream of an air conditioning system's AHU, it may achieve improvements in terms of energy performance of up to 85%. In addition, greenhouse gas emissions were reduced by 17%, and worldwide electricity consumption was lowered by 33–43%. Furthermore, when compared to high-density PE pipes, composite pipes perform better. The heat exchange of HDPE pipes was improved using aluminum wire. Steel pipes, however, have a higher heat exchange/meter of pipe length than PE pipes. Finally, an IoT-based and predictive control algorithm-enabled EAHX system is proposed to optimize energy efficiency and regulate room temperature with thermal comfort. From our point of view, these systems are destined to gain more and more space as a renewable energy-based solution for the next future.

Author Contributions: Conceptualization, E.G., D.G.S., R.S.R. and C.M.; methodology, E.G.; resources, A.G.; data curation, E.G., D.G.S. and R.S.R.; writing—original draft preparation, E.G., D.G.S., R.S.R. and C.M.; writing—review and editing, E.G. and A.G.; visualization, A.G.; supervision, E.G. and A.G.; project administration, E.G. and A.G.; funding acquisition, A.G. All authors have read and agreed to the published version of the manuscript.

Funding: This research received no external funding.

Institutional Review Board Statement: Not applicable.

Informed Consent Statement: Not applicable.

Data Availability Statement: Not applicable.

Conflicts of Interest: The authors have no competing interest.

Abbreviations

AAHR	Air-to-Air Heat Recovery
AHU	Air-Handling Unit
ASHP	Air-Source Heat Pump
BHX	Borehole Heat eXchangers
COP	Coefficient Of Performance
EAHX	Earth-to-Air Heat eXchangers
EPI	Energy Performance Indicator

EUT	Earth Undisturbed Temperature
GHG	Green House Gas
GI-BHX	Gas injection borehole heat exchanger
GSHP	Ground Source Heat Pumps
GWP	Global Warming Potential
HDPE	High-Density Polyethylene
HVAC	Heating, Ventilation and Air Conditioning
IoT	Internet of Things
PB	Polybutylene
PCM	Phase-Change Materials
PE	Polyethylene
PP	Polypropylene
PU	Polyurethane
PVC	polyvinyl chloride
SC	Solar chimney

References

- World Bank Open Data—Electric Power Consumption (kWh per Capita). Available online: <https://data.worldbank.org/indicator/EG.USE.ELEC.KH.PC> (accessed on 17 March 2020).
- Armeanu, D.S.; Gherghina, S.C.; Pasmangiu, G. Exploring the causal nexus between energy consumption, environmental pollution and economic growth: Empirical evidence from central and Eastern Europe. *Energies* **2019**, *12*, 3704. [CrossRef]
- IEA. *World Energy Outlook*; International Energy Agency: Paris, France, 2009.
- Apra, C.; de Rossi, F.; Greco, A.; Renno, C. Refrigeration plant exergetic analysis varying the compressor capacity. *Int. J. Energy Res.* **2003**, *27*, 653–669. [CrossRef]
- Velders, G.J.; Andersen, S.O.; Daniel, J.S.; Fahey, D.W.; McFarland, M. The importance of the Montreal Protocol in protecting climate. *Proc. Natl. Acad. Sci. USA* **2007**, *104*, 4814–4819. [CrossRef]
- Birmpili, T. Montreal Protocol at 30: The governance structure, the evolution, and the Kigali Amendment. *Comptes Rendus Geosci.* **2018**, *350*, 425–431. [CrossRef]
- Apra, C.; Greco, A.; Rosato, A. Comparison of R407C and R417A heat transfer coefficients and pressure drops during flow boiling in a horizontal smooth tube. *Energy Convers. Manag.* **2008**, *49*, 1629–1636. [CrossRef]
- Greco, A.; Vanoli, G.P. Evaporation of refrigerants in a smooth horizontal tube: Prediction of R22 and R507 heat transfer coefficients and pressure drop. *Appl. Therm. Eng.* **2004**, *24*, 2189–2206. [CrossRef]
- Apra, C.; Greco, A. An exergetic analysis of R22 substitution. *Appl. Therm. Eng.* **2002**, *22*, 1455–1469. [CrossRef]
- Cabello, R.; Sánchez, D.; Llopis, R.; Catalán, J.; Nebot-Andrés, L.; Torrella, E. Energy evaluation of R152a as drop in replacement for R134a in cascade refrigeration plants. *Appl. Therm. Eng.* **2017**, *110*, 972–984. [CrossRef]
- Sieres, J.; Santos, J.M. Experimental analysis of R1234yf as a drop-in replacement for R134a in a small power refrigerating system. *Int. J. Refrig.* **2018**, *91*, 230–238. [CrossRef]
- Apra, C.; Greco, A.; Maiorino, A.; Masselli, C.; Metallo, A. HFO1234yf as a drop-in replacement for R134a in domestic refrigerators: A life cycle climate performance analysis. *Int. J. Heat Technol.* **2016**, *34*, S212–S218. [CrossRef]
- Apra, C.; Greco, A.; Maiorino, A.; Masselli, C.; Metallo, A. HFO1234ze as drop-in replacement for R134a in domestic refrigerators: An environmental impact analysis. *Energy Procedia* **2016**, *101*, 964–971. [CrossRef]
- Zou, C.; Xiong, B.; Xue, H.; Zheng, D.; Ge, Z.; Wang, Y.; Wu, S. The role of new energy in carbon neutral. *Pet. Explor. Dev.* **2021**, *48*, 480–491. [CrossRef]
- Franzén, I.; Nedar, L.; Andersson, M. Environmental comparison of energy solutions for heating and cooling. *Sustainability* **2019**, *11*, 7051. [CrossRef]
- Cabeza, L.F.; Rincón, L.; Vilariño, V.; Pérez, G.; Castell, A. Life cycle assessment (LCA) and life cycle energy analysis (LCEA) of buildings and the building sector: A review. *Renew. Sustain. Energy Rev.* **2014**, *29*, 394–416. [CrossRef]
- Perez-Lombard, L.; Ortiz, J.; Maestre, I.R. The map of energy flow in HVAC systems. *Appl. Energy* **2011**, *88*, 5020–5031. [CrossRef]
- Coulomb, D. Air conditioning environmental challenges. *REHVA J.* **2015**, *4*, 30–34.
- Alahmer, A.; Ajib, S. Solar cooling technologies: State of art and perspectives. *Energy Convers. Manag.* **2020**, *214*, 112896. [CrossRef]
- Greco, A.; Gundabattini, E.; Gnanaraj, D.S.; Masselli, C. A comparative study on the performances of flat plate and evacuated tube collectors deployable in domestic solar water heating systems in different climate areas. *Climate* **2020**, *8*, 78. [CrossRef]
- Zhang, Y.; Lin, Y.; Lin, F.; Yang, K. Thermodynamic analysis of a novel combined cooling, heating, and power system consisting of wind energy and transcritical compressed CO₂ energy storage. *Energy Convers. Manag.* **2022**, *260*, 115609. [CrossRef]
- Alsagri, A.S.; Chiasson, A.; Shahzad, M.W. Geothermal energy technologies for cooling and refrigeration systems: An overview. *Arab. J. Sci. Eng.* **2021**, 1–31. [CrossRef]
- Anand, S.; Gupta, A.; Tyagi, S.K. Solar cooling systems for climate change mitigation: A review. *Renew. Sustain. Energy Rev.* **2015**, *41*, 143–161. [CrossRef]

24. Fouad, M.M.; Shihata, L.A.; Morgan, E.I. An integrated review of factors influencing the performance of photovoltaic panels. *Renew. Sustain. Energy Rev.* **2017**, *80*, 1499–1511. [CrossRef]
25. Li, K.; Bian, H.; Liu, C.; Zhang, D.; Yang, Y. Comparison of geothermal with solar and wind power generation systems. *Renew. Sustain. Energy Rev.* **2015**, *42*, 1464–1474. [CrossRef]
26. Giambastiani, B.M.S.; Tinti, F.; Mendrinós, D.; Mastroicco, M. Energy performance strategies for the large scale introduction of geothermal energy in residential and industrial buildings: The GEO. POWER project. *Energy Policy* **2014**, *65*, 315–322. [CrossRef]
27. Cadelano, G.; Cicolin, F.; Emmi, G.; Mezzasalma, G.; Poletto, D.; Galgaro, A.; Bernardi, A. Improving the energy efficiency, limiting costs and reducing CO₂ emissions of a museum using geothermal energy and energy management policies. *Energies* **2019**, *12*, 3192. [CrossRef]
28. Aggarwal, V.; Meena, C.S.; Kumar, A.; Alam, T.; Kumar, A.; Ghosh, A.; Ghosh, A. Potential and future prospects of geothermal energy in space conditioning of buildings: India and worldwide review. *Sustainability* **2020**, *12*, 8428. [CrossRef]
29. Yang, G.; Shi, H.; Xu, D.; Shen, Z.; Zhang, Z.; Shen, H.; Wang, Z. Research on simulation of energy consumption of ground water-source heat pump air conditioning system in plant factory. *IOP Conf. Ser. Earth Environ. Sci.* **2021**, *770*, 012044. [CrossRef]
30. Fernández, J.C.R. Integration capacity of geothermal energy in supermarkets through case analysis. *Sustain. Energy Technol. Assess.* **2019**, *34*, 49–50. [CrossRef]
31. Bisoniya, T.S. Design of earth–air heat exchanger system. *Geotherm. Energy* **2015**, *3*, 18. [CrossRef]
32. Khandouzi, O.; Pourfallah, M.; Yoosefirad, E.; Shaker, B.; Gholinia, M.; Mouloudi, S. Evaluating and optimizing the geometry of thermal foundation pipes for the utilization of the geothermal energy: Numerical simulation. *J. Energy Storage* **2021**, *37*, 102464. [CrossRef]
33. Agrawal, K.K.; Misra, R.; Agrawal, G.D.; Bhardwaj, M.; Jamuwa, D.K. Effect of different design aspects of pipe for earth air tunnel heat exchanger system: A state of art. *Int. J. Green Energy* **2019**, *16*, 598–614. [CrossRef]
34. Bisoniya, T.S.; Kumar, A.; Baredar, P. Study on Calculation Models of Earth-Air Heat Exchanger Systems. *J. Energy* **2014**, *2014*, 1–15. [CrossRef]
35. Sani, F.H.; Pourfallah, M.; Gholinia, M. The effect of MoS₂–Ag/ H₂O hybrid nanofluid on improving the performance of a solar collector by placing wavy strips in the absorber tube. *Case Stud. Therm. Eng.* **2022**, *30*, 101760. [CrossRef]
36. Gholinia, M.; Ranjbar, A.A.; Javidan, M.; Hosseinpour, A.A. Employing a new micro-spray model and (MWCNTs–SWCNTs)—H₂O nanofluid on Si-IGBT power module for energy storage: A numerical simulation. *Energy Rep.* **2021**, *7*, 6844–6853. [CrossRef]
37. Shaker, B.; Gholinia, M.; Pourfallah, M.; Ganji, D.D. CFD analysis of Al₂O₃–sylvtherm oil Nanofluid on parabolic trough solar collector with a new flange-shaped turbulator model. *Theor. Appl. Mech. Lett.* **2022**, *12*, 100323. [CrossRef]
38. Ghobadi, A.H.; Armin, M.; Hassankolaei, S.G.; Hassankolaei, M.G. A new thermal conductivity model of CNTs/C₂H₆O₂–H₂O hybrid base nanoliquid between two stretchable rotating discs with Joule heating. *Int. J. Ambient Energy* **2020**, *43*, 3310–3321. [CrossRef]
39. Ghobadi, A.H.; Hassankolaei, M.G. A numerical approach for MHD Al₂O₃–TiO₂/H₂O hybrid nanofluids over a stretching cylinder under the impact of shape factor. *Heat Transf. Res.* **2019**, *48*, 4262–4282. [CrossRef]
40. Rodrigues, M.K.; Vaz, J.; Rocha, L.A.O.; Santos, E.D.d.; Isoldi, L.A. A full approach to Earth-Air Heat Exchanger employing computational modeling, performance analysis and geometric evaluation. *Renew. Energy* **2022**, *191*, 535–556. [CrossRef]
41. Mathur, A.; Kumar, S. Thermal performance and comfort assessment of U-shape and helical shape earth-air heat exchanger in India. *Energy Built Environ.* **2022**, *3*, 171–180. [CrossRef]
42. Benhammou, M.; Sahli, Y.; Mounzar, H. Investigation of the impact of pipe geometric form on earth-to-air heat exchanger performance using Complex Finite Fourier Transform analysis. Part I: Operation in cooling mode. *Int. J. Therm. Sci.* **2022**, *177*, 107484. [CrossRef]
43. Long, T.; Li, Y.; Li, W.; Liu, S.; Lu, J.; Zheng, D.; Ye, K.; Qiao, Z.; Huang, S. Investigation on the cooling performance of a buoyancy driven earth-air heat exchanger system and the impact on indoor thermal environment. *Appl. Therm. Eng.* **2022**, *207*, 118148. [CrossRef]
44. Gao, X.; Xiao, Y.; Gao, P. Thermal potential improvement of an earth-air heat exchanger (EAHX) by employing backfilling for deep underground emergency ventilation. *Energy* **2022**, *250*, 123783. [CrossRef]
45. Long, T.; Li, W.; Lv, Y.; Li, Y.; Liu, S.; Lu, J.; Huang, S.; Zhang, Y. Benefits of integrating phase-change material with solar chimney and earth-to-air heat exchanger system for passive ventilation and cooling in summer. *J. Energy Storage* **2022**, *48*, 104037. [CrossRef]
46. Long, T.; Zhao, N.; Li, W.; Wei, S.; Li, Y.; Lu, J.; Huang, S.; Qiao, Z. Natural ventilation performance of solar chimney with and without earth-air heat exchanger during transition seasons. *Energy* **2022**, *250*, 123818. [CrossRef]
47. Bai, Y.; Long, T.; Li, W.; Li, Y.; Liu, S.; Wang, Z.; Lu, J.; Huang, S. Experimental investigation of natural ventilation characteristics of a solar chimney coupled with earth-air heat exchanger (SCEAHX) system in summer and winter. *Renew. Energy* **2022**, *193*, 1001–1018. [CrossRef]
48. Firfiris, V.K.; Kalamaras, S.D.; Martzopoulou, A.G.; Fragos, V.P.; Kotsopoulos, T.A. Improvement of the Performance of an Earth to Air Heat Exchanger for Greenhouse Cooling by the Incorporation of Water Finned Tubes—A Theoretical Approach. *AgriEngineering* **2022**, *4*, 190–206. [CrossRef]
49. Shahsavar, A.; Talebizadehsardari, P.; Arıcı, M. Comparative energy, exergy, environmental, exergoeconomic, and enviroeconomic analysis of building integrated photovoltaic/thermal, earth-air heat exchanger, and hybrid systems. *J. Clean. Prod.* **2022**, *362*, 132510. [CrossRef]
50. Ouzzane, M.; Bady, M. Investigation of an innovative Canadian well system combined with a frozen water/PCM heat exchanger for air-cooling in hot climate. *Appl. Therm. Eng.* **2022**, *213*, 118737. [CrossRef]

51. Yadav, S.; Panda, S.K.; Tiwari, G.N.; Al-Helal, I.M.; Alsadon, A.A.; Shady, M.R.; Tiwari, A. Semi-Transparent Photovoltaic Thermal Greenhouse System Combined with Earth Air Heat Exchanger for Hot Climatic Condition. *J. Therm. Sci. Eng. Appl.* **2022**, *14*, 081007. [CrossRef]
52. Maytorena, V.; Hinojosa, J. Thermal Analysis of a Generic Earth-to-Air Heat Exchanger Coupled with a Room during the Summer Season in a Desert Climate. *J. Energy Eng.* **2022**, *148*, 4022001. [CrossRef]
53. Guo, X.; Wei, H.; He, X.; Du, J.; Yang, D. Experimental evaluation of an earth-to-air heat exchanger and air source heat pump hybrid indoor air conditioning system. *Energy Build.* **2022**, *256*, 111752. [CrossRef]
54. Kalantar, V.; Khayyamnejad, A. Numerical simulation of a combination of a new solar ventilator and geothermal heat exchanger for natural ventilation and space cooling. *Int. J. Energy Environ. Eng.* **2022**, *13*, 785–804. [CrossRef]
55. D'Agostino, D.; Esposito, F.; Greco, A.; Masselli, C.; Minichiello, F. Parametric analysis on an earth-to-air heat exchanger employed in an air conditioning system. *Energies* **2020**, *13*, 2925. [CrossRef]
56. Li, H.; Ni, L.; Yao, Y.; Sun, C. Annual performance experiments of an earth-air heat exchanger fresh air-handling unit in severe cold regions: Operation, economic and greenhouse gas emission analyses. *Renew. Energy* **2020**, *146*, 25–37. [CrossRef]
57. Kalbasi, R.; Ruhani, B.; Rostami, S. Energetic analysis of an air handling unit combined with enthalpy air-to-air heat exchanger. *J. Therm. Anal. Calorim.* **2020**, *139*, 2881–2890. [CrossRef]
58. Ascione, F.; D'Agostino, D.; Marino, C.; Minichiello, F. Earth-to-air heat exchanger for NZEB in Mediterranean climate. *Renew. Energy* **2016**, *99*, 553–563. [CrossRef]
59. D'Agostino, D.; Greco, A.; Masselli, C.; Minichiello, F. The employment of an earth-to-air heat exchanger as pre-treating unit of an air conditioning system for energy saving: A comparison among different worldwide climatic zones. *Energy Build.* **2020**, *229*, 110517. [CrossRef] [PubMed]
60. Lohmann, U.; Sausen, R.; Bengtsson, L.; Cubasch, U.; Perlwitz, J.; Roeckner, E. The Köppen climate classification as a diagnostic tool for general circulation models. *Clim. Res.* **1993**, *3*, 177–193. [CrossRef]
61. D'Agostino, D.; Esposito, F.; Greco, A.; Masselli, C.; Minichiello, F. The energy performances of a ground-to-air heat exchanger: A comparison among köppen climatic areas. *Energies* **2020**, *13*, 2895. [CrossRef]
62. Shimada, Y.; Uchida, Y.; Takashima, I.; Chotpantarat, S.; Widiatmojo, A.; Chokchai, S.; Charusiri, P.; Kurishima, H.; Tokimatsu, K. A study on the operational condition of a ground source heat pump in Bangkok based on a field experiment and simulation. *Energies* **2020**, *13*, 274. [CrossRef]
63. Chokchai, S.; Chotpantarat, S.; Takashima, I.; Uchida, Y.; Widiatmojo, A.; Yasukawa, K.; Charusiri, P. A Pilot Study on Geothermal Heat Pump (GHP) Use for Cooling Operations, and on GHP Site Selection in Tropical Regions Based on a Case Study in Thailand. *Energies* **2018**, *11*, 2356. [CrossRef]
64. Widiatmojo, A.; Chokchai, S.; Takashima, I.; Uchida, Y.; Yasukawa, K.; Chotpantarat, S.; Charusiri, P. Ground-Source Heat Pumps with Horizontal Heat Exchangers for Space Cooling in the Hot Tropical Climate of Thailand. *Energies* **2019**, *12*, 1274. [CrossRef]
65. Richter, F.; Niemann, P.; Schuck, M.; Grabe, J.; Schmitz, G. Comparison of conventional and variable borehole heat exchangers for use in a desiccant assisted air conditioning system. *Energies* **2021**, *14*, 926. [CrossRef]
66. Luo, J.; Rohn, J.; Bayer, M.; Priess, A.; Wilkmann, L.; Xiang, W. Heating and cooling performance analysis of a ground source heat pump system in Southern Germany. *Geothermics* **2015**, *53*, 57–66. [CrossRef]
67. Kurevija, T.; Kalantar, A.; Macenić, M.; Hranić, J. Investigation of Steady-State Heat Extraction Rates for Different Borehole Heat Exchanger Configurations from the Aspect of Implementation of New TurboCollector™ Pipe System Design. *Energies* **2019**, *12*, 1504. [CrossRef]
68. Florides, G.; Kalogirou, S. Ground heat exchangers—A review of systems, models and applications. *Renew. Energy* **2007**, *32*, 2461–2478. [CrossRef]
69. Bisoniya, T.S.; Kumar, A.; Baredar, P. Experimental and analytical studies of earth-air heat exchanger (EAHX) systems in India: A review. *Renew. Sustain. Energy Rev.* **2013**, *19*, 238–246. [CrossRef]
70. Soni, S.K.; Pandey, M.; Bartaria, V.N. Ground coupled heat exchangers: A review and applications. *Renew. Sustain. Energy Rev.* **2015**, *47*, 83–92. [CrossRef]
71. Sakhri, N.; Menni, Y.; Chamkha, A.; Salmi, M.; Ameer, H. Earth to Air Heat Exchanger and Its Applications in Arid Regions—An Updated Review. *Tec. Ital. J. Eng. Sci.* **2020**, *64*, 83–90. [CrossRef]
72. Darius, D.; Misaran, M.S.; Rahman, M.M.; Ismail, M.A.; Amaludin, A. Working parameters affecting earth-air heat exchanger (EAHX) system performance for passive cooling: A review. In *IOP Conference Series: Materials Science and Engineering*; IOP Publishing: Bristol, UK, 2017; Volume 217, p. 012021.
73. Peretti, C.; Zarrella, A.; De Carli, M.; Zecchin, R. The design and environmental evaluation of earth-to-air heat exchangers (EAHX). A literature review. *Renew. Sustain. Energy Rev.* **2013**, *28*, 107–116. [CrossRef]
74. Bansal, V.; Misra, R.; Agrawal, G.D.; Mathur, J. Performance analysis of earth-pipe-air heat exchanger for winter heating. *Energy Build.* **2009**, *41*, 1151–1154. [CrossRef]

75. Lekhal, M.C.; Mokhtari, A.M.; Belarbi, R. Evaluation of two earth–air heat exchangers efficiency of different pipe materials within a warm temperate climate. In *MATEC Web of Conferences Volume 307 (2020) International Conference on Materials & Energy (ICOME'17 and ICOME'18) Tianjin, China and San Sebastian, Spain, 6–9 July 2017 and 30 April–4 June 2018*; El Ganaoui, M., Liu, B., Bennacer, R., Morsli, S., Darcherif, M., Eds.; EDP Sciences: Les Ulis, France, 2020; p. 01028. [CrossRef]
76. Sakhri, N.; Menni, Y.; Ameer, H. Effect of the pipe material and burying depth on the thermal efficiency of earth-to-air heat exchangers. *Case Stud. Chem. Environ. Eng.* **2020**, *2*, 100013. [CrossRef]
77. Bansal, V.; Misra, R.; Agrawal, G.D.; Mathur, J. Performance analysis of earth–pipe–air heat exchanger for summer cooling. *Energy Build.* **2010**, *42*, 645–648. [CrossRef]
78. Lekhal, M.C.; Benzaama, M.-H.; Kindinis, A.; Mokhtari, A.-M.; Belarbi, R. Effect of geo-climatic conditions and pipe material on the heating performance of earth-air heat exchangers. *Renew. Energy* **2021**, *163*, 22–40. [CrossRef]
79. Javadi, H.; Mousavi Ajarostaghi, S.S.; Rosen, M.A.; Pourfallah, M. Performance of ground heat exchangers: A comprehensive review of recent advances. *Energy* **2019**, *178*, 207–233. [CrossRef]
80. Svec, O.J.; Goodrich, L.E.; Palmer, J.H.L. Heat transfer characteristics of in-ground heat exchangers. *Int. J. Energy Res.* **1983**, *7*, 265–278. [CrossRef]
81. Choudhury, T.; Misra, A.K. Minimizing changing climate impact on buildings using easily and economically feasible earth to air heat exchanger technique. *Mitig. Adapt. Strateg. Glob. Chang.* **2013**, *19*, 947–954. [CrossRef]
82. Bisoniya, T.S.; Kumar, A.; Baredar, P. Energy metrics of earth–air heat exchanger system for hot and dry climatic conditions of India. *Energy Build.* **2015**, *86*, 214–221. [CrossRef]
83. Greco, A.; Masselli, C. The Optimization of the Thermal Performances of an Earth to Air Heat Exchanger for an Air Conditioning System: A Numerical Study. *Energies* **2020**, *13*, 6414. [CrossRef]
84. Maoz, M.; Ali, S.; Muhammad, N.; Amin, A.; Sohaib, M.; Basit, A.; Ahmad, T. Parametric optimization of Earth to Air Heat Exchanger using Response Surface Method. *Sustainability* **2019**, *11*, 3186. [CrossRef]
85. Singh, R.; Sawhney, R.L.; Lazarus, I.J.; Kishore, V.V.N. Recent advancements in earth air tunnel heat exchanger (EATHE) system for indoor thermal comfort application: A review. *Renew. Sustain. Energy Rev.* **2018**, *82*, 2162–2185. [CrossRef]
86. Sobti, J.; Singh, S.K. Earth-air heat exchanger as a green retrofit for Chandigarh—A critical review. *Geothermal Energy* **2015**, *3*, 14. [CrossRef]
87. Boithias, F.; Zhang, J.; El Mankibi, M.; Haghghat, F.; Michel, P. Simple model and control strategy of earth-to-air heat exchangers. In *Proceedings of the 2009 International Conference on Advances in Computational Tools for Engineering Applications ACTEA 2009, Beirut, Lebanon, 15–17 July 2009*; pp. 234–239. [CrossRef]
88. Diaz-Mendez, S.E.; Patiño-Carachure, C.; Herrera-Castillo, J.A. Reducing the energy consumption of an earth-air heat exchanger with a PID control system. *Energy Convers. Manag.* **2014**, *77*, 1–6. [CrossRef]
89. Vasičkaninová, A.; Bakošová, M.; Čirka, L.; Kalúz, M.; Oravec, J. Robust controller design for a laboratory heat exchanger. *Appl. Therm. Eng.* **2018**, *128*, 1297–1309. [CrossRef]
90. Mirakhorli, A.; Dong, B. Market and behavior driven predictive energy management for residential buildings. *Sustain. Cities Soc.* **2018**, *38*, 723–735. [CrossRef]
91. Ruano, A.; Silva, S.; Duarte, H.; Ferreira, P.M. Wireless sensors and IoT platform for intelligent HVAC control. *Appl. Sci.* **2018**, *8*, 370. [CrossRef]
92. Sridharan, M.; Devi, R.; Dharshini, C.S.; Bhavadarani, M. IoT based performance monitoring and control in counter flow double pipe heat exchanger. *Internet Things* **2019**, *5*, 34–40. [CrossRef]
93. Carli, R.; Cavone, G.; Othman, S.B.; Dotoli, M. IoT based architecture for model predictive control of HVAC systems in smart buildings. *Sensors* **2020**, *20*, 781. [CrossRef]
94. Maiorino, A.; Del Duca, M.G.; Mota-Babiloni, A.; Greco, A.; Aprea, C. The thermal performances of a refrigerator incorporating a phase change material. *Int. J. Refrig.* **2019**, *100*, 255–264. [CrossRef]

Article

Impact of Air Density Variation on a Simulated Earth-to-Air Heat Exchanger's Performance

Piotr Michalak 

Department of Power Systems and Environmental Protection Facilities, Faculty of Mechanical Engineering and Robotics, AGH University of Science and Technology, Mickiewicza 30, 30-059 Krakow, Poland; pmichal@agh.edu.pl; Tel.: +48-126-173-579

Abstract: Due to their simple design and reliable operation, earth-to-air heat exchangers (EAHE) are used in modern buildings to reduce ventilation heat losses. EAHE operation in atmospheric conditions results in variation in ambient air temperature and pressure affecting air density. The paper presents the study on the impact of ambient air density variation on the calculated hourly air temperature at the EAHE outlet and the resulting energy use for space heating and cooling of an exemplary residential building. The ground temperature was computed from the model given in EN 16798-5-1. Then, air density was obtained using five various methods. Energy use for space heating and cooling of the building was computed using the 5R1C thermal network model of EN ISO 13790. Depending on the chosen method and concerning the base case without EAHE, a reduction in annual heating and cooling needs was obtained from 7.5% to 8.8% in heating and from 15.3% to 19% in cooling. Annual heating and cooling gain from EAHE were 600.9 kWh and 628.3 kWh for heating and 616.9 kWh and 603.5 kWh for cooling for the Typical Meteorological Years (TMY) and International Weather for Energy Calculation (IWEC) files, respectively. Unit heating and cooling gains per heat exchanger area were from 34.9 kWh/m² to 36.8 kWh/m² and from −35.1 kWh/m² to −36.3 kWh/m². Density variation with temperature from the relevant typical Polish meteorological year at constant pressure, in comparison to the method of EN 16798-5-1, resulted in an hourly difference of that unit gain up to 4.3 W/m² and 2.0 W/m² for heating and cooling, respectively. The same was true in the case of IWEC files that resulted in differences of 5.5 W/m² and 1.1 W/m².

Citation: Michalak, P. Impact of Air Density Variation on a Simulated Earth-to-Air Heat Exchanger's Performance. *Energies* **2022**, *15*, 3215. <https://doi.org/10.3390/en15093215>

Academic Editor: Marco Marengo

Received: 28 March 2022

Accepted: 26 April 2022

Published: 27 April 2022

Publisher's Note: MDPI stays neutral with regard to jurisdictional claims in published maps and institutional affiliations.



Copyright: © 2022 by the author. Licensee MDPI, Basel, Switzerland. This article is an open access article distributed under the terms and conditions of the Creative Commons Attribution (CC BY) license (<https://creativecommons.org/licenses/by/4.0/>).

Keywords: earth-to-air heat exchanger; air density; specific heat of air; barometric formula; EAHE; outlet temperature; ground temperature; EN ISO 13790; 5R1C model; hourly simulation

1. Introduction

Energy consumption in buildings is of special interest at the national level in many countries due to the economic and environmental reasons [1]. In total, energy demand space heating and cooling have the most significant share [2–4]. Its value depends on several components. One of them, regardless of the building's energy standard, is energy for heating and cooling ventilation air [5–7]. Since ventilation works all year round for hygienic reasons, supplying fresh outdoor air while removing polluted indoor air, its operation significantly affects the thermal demand of a building. Consequently, additional energy is needed for heating or cooling of air supplied to the interior of a building zone, in the cold and warm seasons, respectively.

To reduce the amount of that energy, various techniques of heat recovery from ventilation air are used, usually involving crossflow, counter-current or rotary heat exchangers [8,9]. However, together with the growing popularity of alternative and low-energy solutions, earth-to-air ground heat exchangers (EAHE, EAHX) have been gaining interest recently.

The design of EAHE should be performed carefully to avoid changes after it has been built, since correcting the position of a functioning device requires labour-intensive and

costly earthworks. Therefore, numerous studies on the impact of various parameters on the EAHE performance were conducted, including climatic conditions and geographical location, soil type, pipe properties, burial depth and airflow rate [10]. In addition to experiments, theoretical analyses were carried out with the use of numerical simulations. As a result, methods of designing this type of heat exchanger have been developed for use in the heating and cooling of buildings in various climatic zones [11–14].

Since EAHEs are used commonly to reduce losses for heating or cooling the ventilation air, it becomes increasingly important to determine the energy effects of their application. Hence, calculation methods to assess the energy performance of EAHE are of growing significance. For this purpose, various tools have been used in recent studies.

D'Agostino et al. [15] analysed energy savings in an office building equipped with the HVAC system based on fan-coils and primary air, with and without EAHE and an air-to-air heat exchanger (AAHE). The authors used DesignBuilder and EnergyPlus to model the building and an HVAC system. They used the same set of tools in similar studies [16,17] on EAHE connected upstream with an air handling unit (AHU) and fan-coils in an office building. The EAHE model was validated with the two-dimensional finite element method and experimental data provided by other researchers.

Baglivo et al. [18] presented an hourly simulation of an air-cooled heat pump coupled with horizontal EAHE in a residential building. The hourly behaviour of EAHE was simulated in TRNSYS 17. Output results and relevant climatic data were used to compute calculate COP, EER, SCOP and SEER coefficients of the considered heat pump. The same tool was used in [19] to model various options of a ventilation system with EAHE in a residential building. The authors simulated the impact of the pipe numbers, air flow rate and soil thermal conductivity on the building thermal behaviour.

Other tools, as Ansys Fluent [20–22], Ansys CFX [23], Comsol Multiphysics [24], Matlab [25–27] or Scilab [28] were also used. However, although they offer great possibilities, their use requires specialised knowledge and experience. Hence, there is also a need for methods simpler but accurate enough to perform annual simulations with hourly time steps required by current standards and provide reasonable time resolution for thermal phenomena, occupation schedules, weather data and calculation accuracy [29–31], especially in terms of energy certification of buildings.

The EN 16798-5-1 standard [32], among others, gives the calculation method for preheating and precooling with necessary equations for ground temperature, temperature change in EAHE during airflow in the pipe and several auxiliary variables. The method is intended for use with hourly time steps. That standard has been used in several studies recently.

Skotnicka-Siepsiak [33] presented measurements of ground temperature and outlet air temperature of EAHE in a residential building in Olsztyn (northern Poland) in the warm months (May, June, July and August) of 2016, 2017 and 2018. Then, they were compared in the relevant charts with results based on EN 16798-5-1. The model provided comparable results for stable outdoor conditions in July and August. Larger differences were noticed in May and June.

Brata et al. [34] compared outlet temperature and monthly heat and cooling gains measured and calculated from EN 16798-5-1 for EAHE in an existing passive house near Timisoara in Romania. To assess the accuracy of the model authors used a histogram of residuals calculated as the difference between measured and calculated hourly values. They were between -0.9 °C and 2.8 °C. In general, monthly heat gains were slightly underestimated but monthly cooling energy was overestimated.

Michalak [35] coupled the model of EN 16798-5-1 with the thermal network model of a building zone from EN ISO 13790 [36] in an MS Excel spreadsheet to simulate in hourly time step an annual performance of EAHE connected with a ventilation system of a low-energy residential building in south Poland. In this way, hourly, as well as monthly and annual energy use for space heating and cooling and peak power with and without EAHE was estimated simply and efficiently.

It seems that due to its simplicity, this method does not offer as extensive possibilities as professional simulation programs. As mentioned above, they consider many physical properties. The most important of these include soil and pipe material parameters, flow rate and outside air temperature. They determine heat transfer conditions between soil and air flowing through a heat exchanger pipe from its inlet to its outlet. However, the above publications based on the standard model do not consider the influence of air temperature changes on air density [37], which in turn affects outlet air temperature from a heat exchanger. In [34] the air density was assumed constant. In [35,38] no information on the air density was given. Variation of thermal properties of air was considered in Comsol Multiphysics [24] and TRNSYS [38]. However, the review carried out shows that in most cases the authors used a fixed value for the air density and the specific heat of air. It was so in all types of tools, such as TRNSYS [19,39], Matlab [26,27] and Ansys [40,41]. There were also no studies comparing the assessment of these simplifications on outlet air temperature and resulting energy gain.

Therefore, this paper aims to present a detailed simulation study on the influence of changes in the air density and the specific heat depending on atmospheric conditions on a value of the temperature of outlet air from a heat exchanger. The method given in EN 16798-5-1 was used. To better illustrate the scale of the problem, based on the results obtained, the effect in the form of monthly and annual energy demand for heating and cooling of an example residential building was also determined. For this purpose, a well-known thermal resistance-capacitance model of a building zone given in EN ISO 13790 was used. As it is restricted only to sensible heating and cooling, the humidification and dehumidification processes of air were not considered here. Hence, the condensation in the buried pipe was also not analysed.

The following section presents the case building and climatic conditions in the considered location. Then the problem of thermal properties of air, in particular its density and specific heat capacity as a function of air temperature and atmospheric pressure are briefly presented. Moreover, the simulation models to obtain hourly outlet air temperature from EAHE and heating and cooling energy were presented. After them, the results are presented and compared with other studies, and concluding remarks are given.

2. Materials and Methods

2.1. Case Building

For further consideration, a single-story residential building was selected, located in Kraków (south Poland) in the third Polish climatic zone, following the subdivision from zone I to V given in the PN-EN 12831 standard [42] presented in Figure 1.

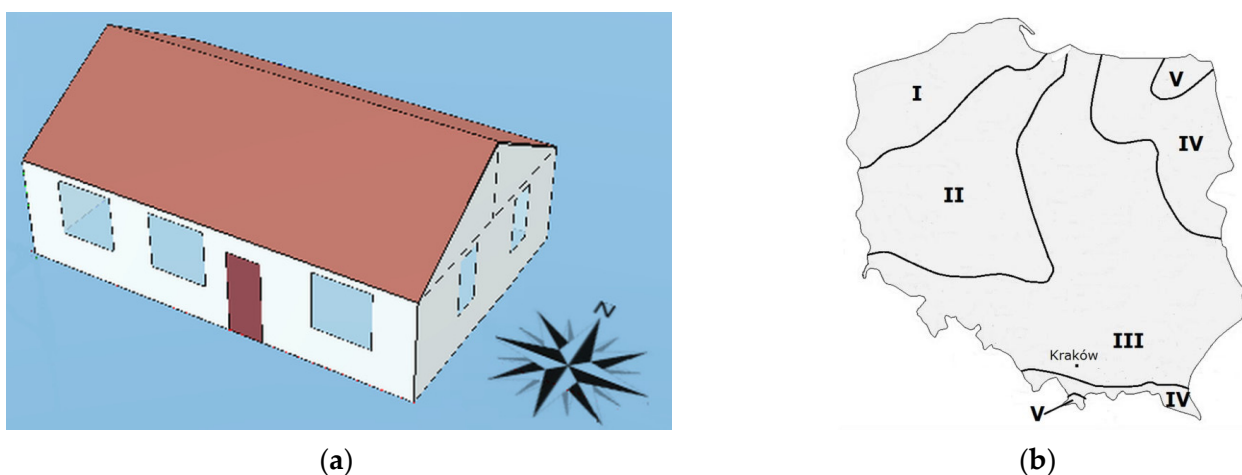


Figure 1. (a) Model of the test building; (b) location of the building.

The building was built with traditional technology. It has external walls made of 25 cm ceramic blocks, insulated with 10 cm of Styrofoam. A 30° gable roof is isolated with a 15 cm layer of mineral wool. The ground floor was insulated with a 10 cm layer of Styrofoam. Following Polish requirements [43,44] ventilation airflow was set at 90 m³/h. The building has a total heated floor area of 65 m², a total volume of 163 m³ and is inhabited by four people.

The mean annual temperature for the period 1971–2000 measured in the meteorological station Kraków-Balice and used to build a typical meteorological year (TMY) amounted to 8.20 °C and varied from 2.6 °C in February to 17.5 °C in July and August [45]. The hourly air temperature was from −20 °C on 16 February at 4:00 to 32.9 °C on 7 June at 12:00. Global horizontal solar irradiance was up to 998 W/m² on 17 May at 11:00 (Figure 2).

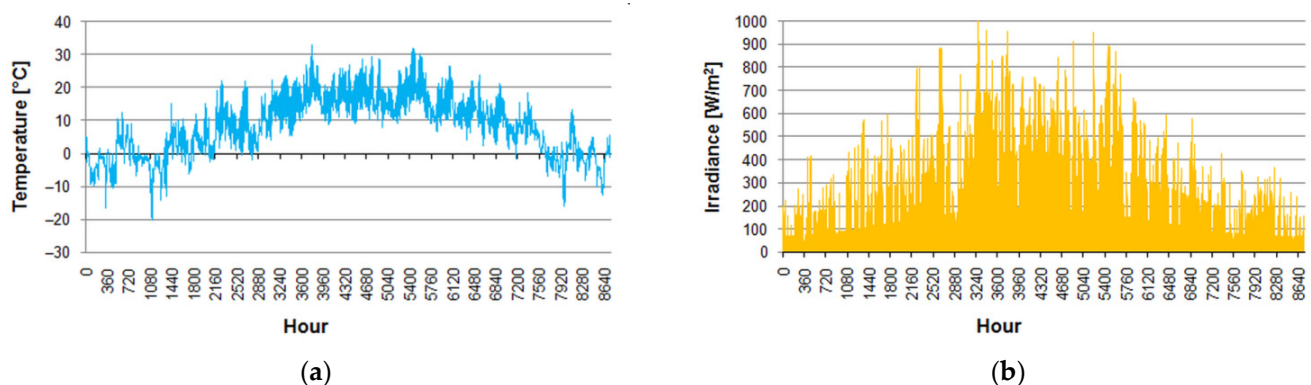


Figure 2. TMY for Kraków: (a) outdoor air temperature; (b) global horizontal irradiance.

2.2. Earth-to-Air Heat Exchanger

As the design issues of EAHEs have been discussed by many researchers recently [23,24,46–49], these results were used to omit time-consuming preliminary considerations.

In the study [24] for Stockholm (Sweden) a 10 m long polyethylene pipe of 20 cm diameter, buried at 2 m was used for a volumetric airflow rate of 60 dm³/s (216 m³/h). For a residential building located in south Italy [50] authors considered 70 m long polypropylene pipes with a 200 mm diameter buried at 1.50 m deep. In another case in a similar location [16] for an office building with a total floor area of 260 m² and ventilation airflow rate of 1300 m³/h authors recommended EAHE from a pipe with 0.2 m diameter, between 80 m and 100 m long and buried between 2 m and 2.5 m. EAHE connected to a ventilation system of a single-family building in Poland presented in [51] consisted of two 25 m long parallel PVC 160/3.6 mm diameter pipes buried with increasing depth from 1.1 m up to 1.6 m at inlet and outlet, respectively. The ventilation airflow rate was 300 m³/h. The next one [33,52] was located in northern Poland. For a residential building with a usable floor area of 115 m² and ventilation airflow rate of 150 m³/h EAHE was built from a 41 m long pipe with 0.2 m diameter buried at an average depth of 2.12 m.

Based on these experiences and the assumed ventilation rate of 90 m³/h, a 30 m-long pipe was chosen, with a diameter of 0.2 m and the burial depth set at 2 m. The main parameters of EAHE are given in Table 1. Assuming pipe wall thickness of 8.8 mm the inner surface area of the duct is $A_s = 17.20$ m². Ground properties were taken from EN 16798-5-1.

Table 1. Parameters of the earth-to-air heat exchanger.

Parameter	Symbol	Value	Unit
Duct length	L	30	m
Air velocity in the duct	v	0.957	m/s
Outer pipe diameter	d _o	0.200	m
Inner pipe diameter	d _i	0.182	m
Average burial depth	z	2.0	m
Thermal conductivity of the duct	λ _{du}	0.27	W/m·K
Density of the ground	ρ _{gnd}	1800	kg/m ³
Specific heat of the ground	c _{gnd}	1300	J/kg·K
Thermal conductivity of the ground	λ _{gnd}	1.50	W/m·K

The base for the EAHE performance simulation is the calculation of the hourly ground temperature at the burial depth. For this purpose, the method given in EN 16798-5-1 was used. Simplification assumptions of that model were given and discussed in [35,53–55]. The most important are as follows:

- The ground is considered as a semi-infinite, homogenous and anisotropic medium,
- The sinusoidal variation of ground surface temperature is assumed,
- The model does not also take into account various environmental factors, as solar irradiance incident on a ground surface and periodic presence of snow cover on the ground.
- The impact of EAHE operation on the ground temperature was omitted.

The hourly ground temperature is given by the expression:

$$T_{\text{gnd}} = T_{e;\text{mn};\text{an}} + (T_{e;\text{max};\text{m}} - T_{e;\text{mn};\text{an}}) \cdot e^{-\xi} \cdot \cos\left(2\pi \frac{t_{\text{an}}}{8760} - \xi - f_t\right). \quad (1)$$

The ξ factor is given by:

$$\xi = z \cdot \sqrt{\frac{\pi \cdot Q_{\text{gnd}} \cdot c_{\text{gnd}}}{\lambda_{\text{gnd}} \cdot 8760 \cdot 3600}}. \quad (2)$$

The time shift factor f_t is expressed by the formula:

$$f_t = \pi \left(\frac{2 \cdot t_{\text{an};\text{min}}}{8760} + 1 \right). \quad (3)$$

Finally, the difference between EAHE inlet and outlet air temperature (change in air temperature) can be computed:

$$\Delta T_{\text{sup}} = (T_{\text{gnd}} - T_e) \cdot \left[1 - e^{-\left(\frac{U_{\text{du}} \cdot A_s}{q_{v;\text{sup}} \cdot \rho_a \cdot c_a}\right)} \right]. \quad (4)$$

Then, ventilation air at temperature:

$$T_{\text{sup}} = T_e + \Delta T_{\text{sup}} \quad (5)$$

is supplied to an interior of a considered building.

The overall heat transfer coefficient of the EAHE is given in the EN 16798-5-1 standard by the relationship:

$$U_{\text{du}} = \left(\frac{1}{2\pi \lambda_{\text{du}}} \cdot \ln \frac{d_o}{d_i} + \frac{1}{h_i} \right)^{-1}. \quad (6)$$

However, it should be pointed out here that this equation is incorrect. According to the heat transfer theory [56] the overall heat transfer coefficient for a cylindrical heat exchanger,

assuming convection only on an internal surface is given per unit inner surface area of a pipe by the expression:

$$U_{du} = \left(\frac{1}{h_i} + \frac{r_i}{\lambda_{du}} \cdot \ln \frac{r_o}{r_i} \right)^{-1} = \left(\frac{1}{h_i} + \frac{d_i}{2\lambda_{du}} \cdot \ln \frac{\frac{r_o}{2}}{\frac{r_i}{2}} \right)^{-1} \quad (7)$$

Finally:

$$U_{du} = \left(\frac{1}{h_i} + \frac{d_i}{2\lambda_{du}} \cdot \ln \frac{d_o}{d_i} \right)^{-1} \quad (8)$$

Then, if all quantities in Equation (4) are expressed as given in “Symbols” section, i.e., U_{du} [W/m^2K], A_s [m^2], $q_{v,sup}$ [m^3/s], ρ_a [kg/m^3] and c_a [$J/(kg \cdot K)$] the fraction in the power of e in Equation (4) is dimensionless. Physically both denominator and numerator are then heat fluxes.

The inside surface heat transfer coefficient is given by:

$$h_i = \left[4.13 + 0.23 \frac{T_{md}}{100} - 0.0077 \left(\frac{T_{md}}{100} \right)^2 \right] v^{0.75} d_i^{0.25} \quad (9)$$

That standard indicates the possibility to set $T_{md} = T_e$ to avoid iterative computations when applying Equation (9).

2.3. The 5R1C Model

The EN ISO 13790 standard introduced the thermal network model of a building zone built from five resistors and one capacitor (Figure 3). It is intended for calculations of sensible energy use for space heating and cooling. Therefore, humidification and dehumidification of air are not considered here. Consequently, condensation processes in the buried pipe of EAHE were not analysed.

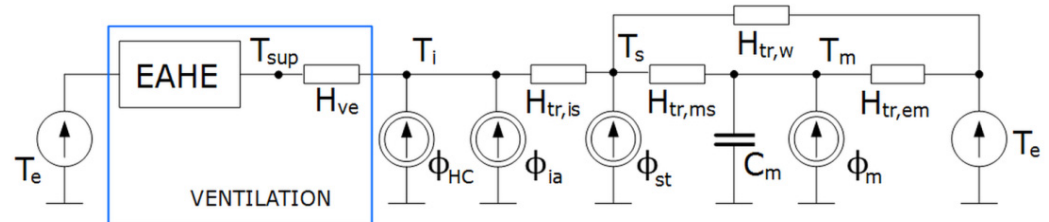


Figure 3. The circuit diagram of the 5R1C thermal network model of a building zone with an earth-to-air heat exchanger to supply ventilation air.

That model was chosen for several important reasons as ease modification for various applications [57–60], low computational requirements [61–63] and its simplicity and possibility to apply in a spreadsheet [64–66] not requiring specialised commercial simulation tools while producing reliable results [67].

External partitions of a building are divided into two categories. The thermally light elements (doors, windows, curtain walls, glazed walls, etc.) are described by the $H_{tr,w}$ thermal transmission coefficient. The thermally heavy elements (walls, ceilings) are included in $H_{tr,em}$ and $H_{tr,ms}$ thermal transmission coefficients, both connected to the thermal capacity, C_m , representing the thermal mass of the building [68]. It is the weak point of this model since this way all the thermal inertia of various elements of a considered zone is considered as a single capacitance.

The ambient environment is represented by the external air temperature (T_e). $H_{tr,is}$ is the coupling conductance between the central node (T_s) and an indoor environment (T_i).

Ventilation air, at temperature T_{sup} , is supplied to a building zone through the heat transfer by ventilation, H_{ve} . To include the operation of EAHE its inlet and outlet were connected to T_e and to T_{sup} , respectively. T_{sup} is calculated from Equation (5).

Heat fluxes from internal sources and solar radiation are split into three parts: φ_{ia} , φ_{st} , and φ_m , connected to the indoor air, the central, and the thermal mass nodes, respectively. Heating or cooling power (φ_{HC}) is supplied to or extracted from the indoor air node. The calculation procedure to obtain heating and cooling power to maintain the required set point temperatures is given in EN ISO 13790 and has been presented in detail recently [69,70].

That procedure requires T_{sup} to be calculated at each time step. In the case when EAHE is not used and external air is directly supplied to a building then:

$$T_{sup} = T_e \quad (10)$$

and ventilation heat flux is given by:

$$\phi_{ve} = H_{ve} \cdot (T_{sup} - T_i) = H_{ve} \cdot (T_e - T_i) \quad (11)$$

with the heat transfer by ventilation:

$$H_{ve} = \rho_a \cdot c_a \cdot q_{v;sup} \quad (12)$$

If EAHE is connected to the ventilation system, as shown in Figure 3, then an additional heat gain (or loss) is added to the heat exchanger during the flow of ambient air in the duct:

$$\phi_{EAHE} = \rho_a \cdot c_a \cdot q_{v;sup} \cdot \Delta T_{sup} \quad (13)$$

The supplying air temperature is calculated from Equation (5) and ventilation flux:

$$\phi_{ve} = \rho_a \cdot c_a \cdot q_{v;sup} \cdot (T_e + \Delta T_{sup} - T_i) \quad (14)$$

As presented in Equations (12)–(14), apart from the temperature difference, the product of $\rho_a \cdot c_a$, called volumetric heat capacity of air, affects the calculated energy effect of ventilation and EAHE operation. Therefore, the dependence of these parameters on external conditions has to be carefully analysed and is presented in the next section.

Depending on the increase or decrease of the temperature of air passing the heat exchanger ($\Delta T_{sup} > 0$ or $\Delta T_{sup} < 0$), it is possible to talk about the heat or cold gain and to determine their monthly values. From this, including Equation (13), the monthly heat gain in EAHE in the m -th month is given by the expression:

$$\text{if } \Delta T_{sup} > 0 : Q_{gH,m} = \sum_{n=1}^h \phi_{EAHE,n} \cdot \Delta \tau_m \quad (15)$$

Consequently, the monthly cooling energy gain in EAHE in the m -th month is given by the expression:

$$\text{if } \Delta T_{sup} < 0 : Q_{gC,m} = \sum_{n=1}^h \phi_{EAHE,n} \cdot \Delta \tau_m \quad (16)$$

Thermal conductance and single capacitance of the RC network model (Figure 3) are given in Table 2. The thermal and physical properties of materials used were taken from manufacturers. Thermal resistances were calculated following ISO 6946 [71]. Thermal bridges were neglected. Thermal capacities were calculated according to the detailed method of ISO 13786 [72] for the calculation period of 24 h. Solar absorptance of the roof and wall surfaces was: $\alpha = 0.8$ and $\alpha = 0.6$, respectively. Constant internal gains of 150 W throughout the year and continuous operation of the ventilation system were also assumed.

Table 2. Thermal network model elements of the building.

Element	Value	Unit
$H_{tr,w}$	10.00	W/K
$H_{tr,is}$	983.32	W/K
$H_{tr,ms}$	1490.13	W/K
$H_{tr,em}$	85.22	W/K
H_{ve}	30.00	W/K
C_m	23.56	MJ/K

EN ISO 13790 assumes constant volumetric heat capacity of air: $\rho_a c_a = 1200 \text{ J}/(\text{m}^3\text{K})$ as in other building simulations [52,68,73]. Hence, applying Equation (12) we get $H_{ve} = 30.0 \text{ W/K}$. This parameter was the same in all simulations to highlight the influence of the variation of air parameters on the operation of the analysed exchanger and not the whole exchanger-building system.

2.4. Thermal Properties of Dry Air in Building Simulations

Since, as stated in the introductory section, humidification and dehumidification of air is omitted in the present study, air shall be considered a dry gas. Within the air temperature and atmospheric pressure variation met in climatic conditions of inhabited areas around the globe it is sufficient to describe the atmosphere by the perfect gas law [74] linking together the absolute temperature (T), absolute pressure (p) and volume (V) for the given mass (M) of gas with a given individual gas constant (R_i):

$$pV = MR_iT. \quad (17)$$

Rearranging the above the unknown density can be calculated:

$$\rho_a = \frac{M}{V} = \frac{p}{R_i T}. \quad (18)$$

According to the International Union of Pure and Applied Chemistry (IUPAC) [75], we assumed the universal gas constant $R = 8.3144598 \text{ J}/(\text{mol}\cdot\text{K})$ and molar mass of dry air $\mu = 28.96546 \text{ g/mol}$. Then, individual gas constant of dry air:

$$R_i = \frac{R}{\mu} = 287.047394 \frac{\text{J}}{\text{kgK}}. \quad (19)$$

From this, at standard conditions defined by air temperature of $T_0 = 273.15 \text{ K}$ (0°C) and barometric pressure of $p_0 = 100 \text{ kPa}$ at the sea level (altitude $h = 0$), we get:

$$\rho_{a,0} = \frac{P_0}{R_i \cdot T_0} = 1.2754 \frac{\text{kg}}{\text{m}^3}. \quad (20)$$

In the same way, dry air density can be computed at a given hourly external (ambient) air temperature and pressure.

If the influence of variable atmospheric conditions on selected physical properties of air is to be considered, the most relevant independent variables and the ranges of their variability encountered in practice must be identified first. Taking into account WMO data [76] it seems reasonable to assume atmospheric pressure variation from 950 hPa to 1050 hPa and air temperature from -50°C to $+50^\circ\text{C}$. The resulting air density variation for presented assumptions, calculated from Equation (18), is presented in Figure 4.

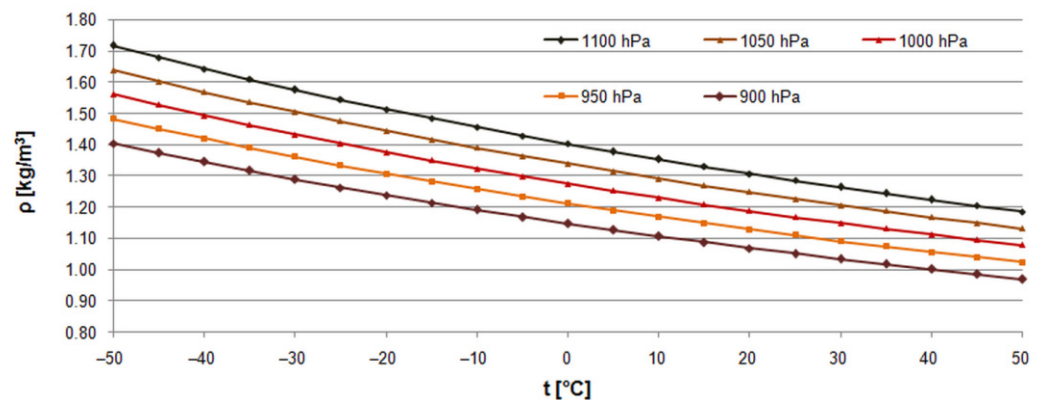


Figure 4. Dry air density variation as a function of its temperature and atmospheric pressure.

Taking a pressure and temperature variation ranges from 950 hPa to 1050 hPa and from $-20\text{ }^{\circ}\text{C}$ to $+20\text{ }^{\circ}\text{C}$, respectively, the air density varies from 1.12896 kg/m^3 (950 hPa and $+20\text{ }^{\circ}\text{C}$) to 1.44497 kg/m^3 at 1050 hPa and $-20\text{ }^{\circ}\text{C}$. In relation to 1.27540 kg/m^3 at $0\text{ }^{\circ}\text{C}$ and 1000 hPa it means the corresponding change of -13.0% and 13.3% .

If atmospheric pressure in a considered location is unknown then it can be calculated to the value at the known altitude from the barometric formula [77,78]. For ideal gas two forms of this equation exist [79]. The first one assumes the isothermal atmosphere, i.e., with a constant temperature independent on a height [80]:

$$T(h) = T_0 \quad (21)$$

and:

$$p(h) = p_0 \cdot \exp\left(-\frac{g \cdot h}{R_i \cdot T_0}\right). \quad (22)$$

Hence, the air density, $\rho_{a,h}$, at a given altitude, h , is given by:

$$\rho_{a,h} = \rho_{a,0} \cdot \exp\left(-\frac{g \cdot h}{R_i \cdot T_0}\right). \quad (23)$$

Standard conditions are used usually as reference. From this, assuming gravity acceleration $g = 9.80665\text{ m/s}^2$, we get from Equation (23):

$$\rho_{a,h} = 1.2754 \cdot \exp\left(\frac{-h}{7995.29}\right). \quad (24)$$

According to this equation the air density decreases from 1.27540 kg/m^3 to 1.19808 kg/m^3 (-6.1%), 1.12545 kg/m^3 (-11.8%), and 0.99133 kg/m^3 (-22.1%) at 500 m, 1000 m and 2000 m above sea level, respectively. However, since inhabited areas cover lands from 79 m below to 5516 m above sea level [81], these differences can be more significant when performing calculations for higher altitudes.

The second form of the barometric formula includes the lapse rate [82], i.e., the rate of decrease of temperature with a height. In the troposphere it amounts $L = -6.51\text{ K/km}$ [83]. Then, in relation to sea level with $h_0 = 0$ we get [84]:

$$T(h) = T_0 + Lh, \quad (25)$$

and:

$$p(h) = p_0 \left(\frac{T(h)}{T_0}\right)^{-\frac{\mu g}{R_i}} = p_0 \left(\frac{T(h)}{T_0}\right)^{5.248}. \quad (26)$$

Density at altitude h is given by:

$$\rho_{a,h} = \rho_{a,0} \left(1 + \frac{L \cdot h}{T_0} \right)^{\frac{Mg}{RT_0} - 1} \quad (27)$$

Inserting the aforementioned constants we get:

$$\rho_{a,h} = 1.2754 \left(1 - \frac{0.00651 \cdot h}{273.15} \right)^{4.248} \quad (28)$$

The EN 16798-5-1 standard recommends use of Equation (27) for $T_{a,ref} = 20 \text{ }^\circ\text{C}$ and air density at sea level $\rho_{a,ref} = 1.204 \text{ kg/m}^3$ at $p = 101,325 \text{ Pa}$. Hence, the above relationship is given in that standard in the following form:

$$\rho_{a,h} = 1.204 \left(1 - \frac{0.00651 \cdot h}{293} \right)^{4.255} \quad (29)$$

Different values of the molar mass of air and universal gas constant were used in that standard which resulted in differences in the power (4.248 and 4.255) of expressions given by Equations (28) and (29).

According to Equation (29), for the given assumptions, air density decreases from 1.204 kg/m^3 to 1.14811 kg/m^3 (−4.6%), 1.09422 kg/m^3 (−9.1%), and 0.99227 kg/m^3 (−17.6%) at 500 m, 1000 m and 2000 m above sea level, respectively. Differences are lower than in the case of Equation (24) but still significant.

Application of Equation (23) at the temperature of $20 \text{ }^\circ\text{C}$ results in changes of density from 1.20413 kg/m^3 to 1.13113 kg/m^3 , 1.06256 kg/m^3 and 0.96734 kg/m^3 in the same order. As the air temperature lapse rate is not included in this relationship, it produces results with the same percentage differences in relation to the sea level as for $0 \text{ }^\circ\text{C}$ for the same altitudes. A comparison of results from Equation (23) at $0 \text{ }^\circ\text{C}$, Equation (23) at $20 \text{ }^\circ\text{C}$ and Equation (29) is given in Figure 5.

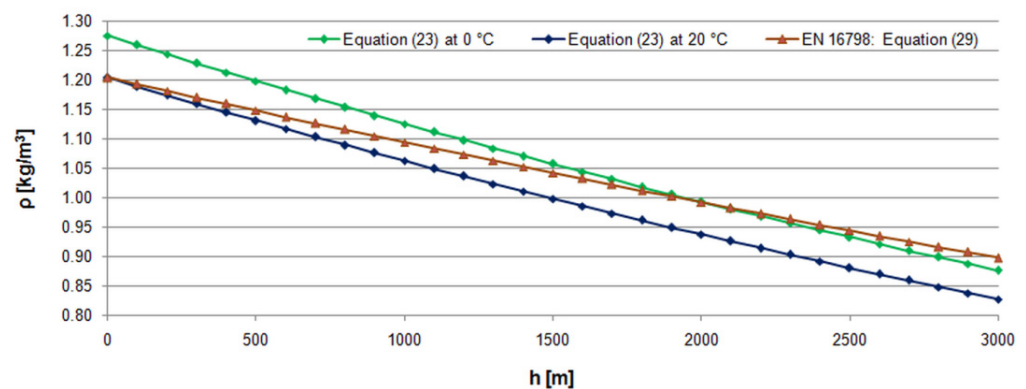


Figure 5. Dry air density variation as a function of altitude.

The impact of air temperature and pressure on the specific heat capacity of air in atmospheric conditions is less significant [85] (Figure 6). Following correlations reported by Lemmon et al. [86] for dry air as an ideal gas, its specific heat at $p = 101,325 \text{ Pa}$ varies from 1006.03 J/(kg K) at 220 K (−53.15 °C) to 1007.41 J/(kg K) at 320 K (46.85 °C) with the minimum of 1005.68 J/(kg K) from 230 K to 280 K (from −43.15 °C to 6.85 °C). According to the next reference [87] at $p = 100 \text{ kPa}$ it varies from 1006.1 J/(kg K) at $-50 \text{ }^\circ\text{C}$ to 1007.7 J/(kg K) at $50 \text{ }^\circ\text{C}$ with the minimum of 1005.7 J/(kg K) at $-20 \text{ }^\circ\text{C}$. Hence, in the considered range, the maximum value of c_a is only 0.3% higher than the minimum in both cases, and for building energy simulation purposes its variation can be omitted using the constant $c_a = 1006.0 \text{ J/(kg K)}$ [37].

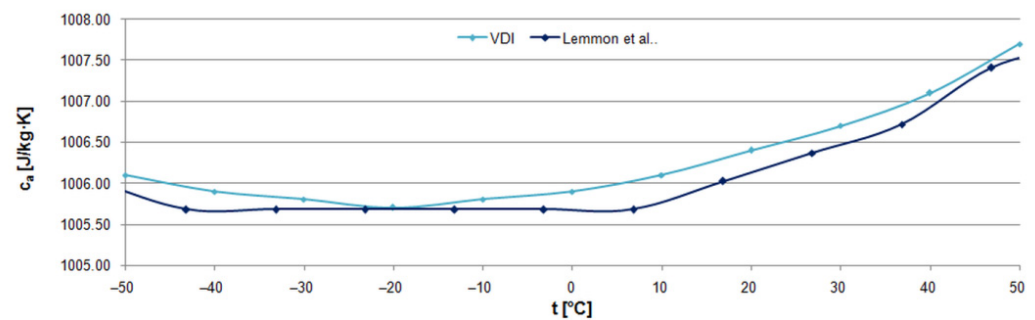


Figure 6. Specific heat of dry air as a function of temperature.

For comparison, it should be noted that the EN 16798-5-1 standard imposes for the specific heat of air use of the constant value $c_a = 0.000279 \text{ kWh}/(\text{kg K}) = 1004.4 \text{ J}/(\text{kg K})$, i.e., approximately 0.12% lower than the minimum values given.

3. Results and Discussion

3.1. Introduction

To present the problem of the air density variation with atmospheric conditions in the chosen location, several simulations were performed. They were based on the hourly data from the hourly typical meteorological year (TMY) for Kraków [45].

As described in [88] Polish TMYs do not include atmospheric pressure. Hence, it is necessary to determine the conditions for the meteorological station altitude using appropriate relationships. For comparison, the second source of meteorological data was also used. It was the International Weather for Energy Calculations (IWECC) weather data file for Kraków provided on the EnergyPlus website [89]. The IWECC weather files for over 200 locations around the world are freely provided by the U.S. Department of Energy [90,91].

It should be noted that air temperature in these two sources varies within a very similar range: from -20 °C to 32.9 °C and from -20.1 °C to 32.0 °C for TMY and IWECC files, respectively. Moreover, monthly values are very close (Figure 7a). However, hourly data differ more significantly (Figure 7b) as they are prepared from different source data.

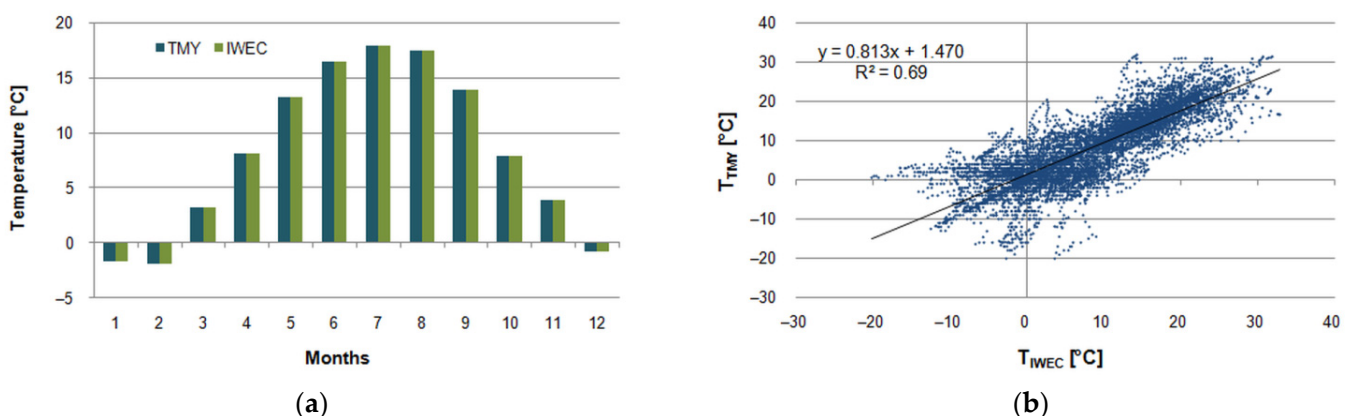


Figure 7. Air temperature in Kraków according to weather data from TMY and IWECC: (a) monthly; (b) hourly.

Then, the hourly operation of EAHE at the same location was simulated assuming five methods:

- (1) Air density and specific heat of air from EN 16798-5-1, TMY;
- (2) Constant volumetric heat capacity of air from EN ISO 13790, TMY;
- (3) Air density from Equations (18) and (29) using the TMY data;
- (4) Air density from Equation (18) using the IWECC data;

(5) Air density and specific heat of air from EN 16798-5-1, IWEC.

As the reference, the first case, i.e., the EN 16798-5-1 standard, was chosen as the recommended one for energy calculations of buildings in Poland. In the second case $\rho_a c_a = 1200 \text{ J}/(\text{m}^3\text{K})$ was used. In the third method, constant barometric pressure was obtained from Equation (29) and then varying air density was computed from Equation (18) using ambient air temperature from TMY. In the next method, as pressure and temperature are given in the IWEC file, air density was obtained from Equation (18). In the last method, air density was calculated following EN 16798-5-1 and the ambient air temperature was taken from the IWEC weather file. Hence, in relation to the previous case, there could be fully assessed the impact of the simplification introduced by that standard.

As the presented resistance-capacitance model of a building zone and the EAHE model are designed for calculations in hourly time steps they both were easily linked and simulated in a spreadsheet using hourly weather data for Kraków. This way no commercial program was necessary and an easily available tool was used.

3.2. Thermal Properties of Dry Air

At first, calculations following EN 16798-5-1 are presented. Meteorological station Kraków-Balice is located at the altitude of $h = 237 \text{ m}$ above sea level. Then from Equation (28) we get:

$$\rho_{a,h} = 1.204 \left(1 - \frac{0.00651 \cdot 237}{293} \right)^{4.255} = 1.177254 \frac{\text{kg}}{\text{m}^3}, \quad (30)$$

and resulting volumetric specific heat of air $\rho_a c_a = 1182.43 \text{ J}/(\text{m}^3\text{K})$. It is lower by about 1.5% from $\rho_a c_a = 1200 \text{ J}/(\text{m}^3\text{K})$ recommended by EN ISO 13790.

In the next step, assuming standard conditions given in Equation (18), from Equation (29) air pressure was calculated: $p(h) = 97,071.05 \text{ Pa}$. Then, from Equation (18), hourly air density at the considered location, following air temperature variations, was obtained (Figure 8).

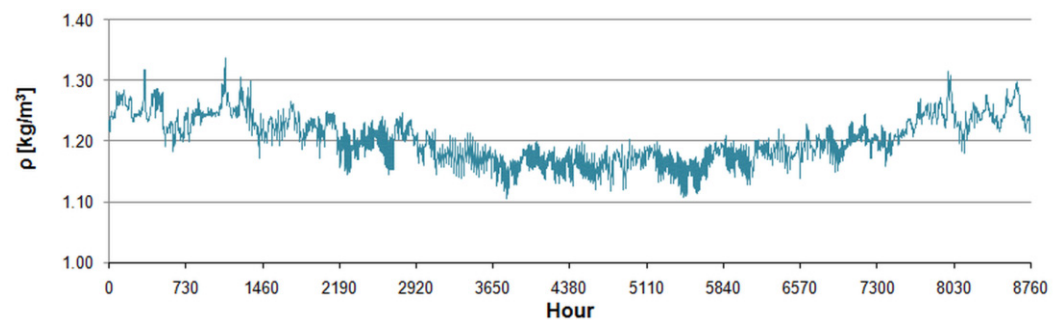


Figure 8. Calculated air density.

It varied from $1.10495 \text{ kg}/\text{m}^3$ on 7 June at 10:00 to $1.33691 \text{ kg}/\text{m}^3$ on 16 February at 4:00, i.e., from -8.1% to 11.1% in relation to the annual average of $1.20286 \text{ kg}/\text{m}^3$, which was only 2.1% higher than $1.177254 \text{ kg}/\text{m}^3$ calculated following EN 16798-5-1. The monthly average density was from $1.1610 \text{ kg}/\text{m}^3$ in June to $1.2504 \text{ kg}/\text{m}^3$ in February.

The air density calculated from the IWEC weather file varied from $1.12822 \text{ kg}/\text{m}^3$ on 8 July from 12:00 to 13:00 to $1.38083 \text{ kg}/\text{m}^3$ on 2 February at 6:00, i.e., from -7.9% to 12.7% in relation to the annual average of $1.22518 \text{ kg}/\text{m}^3$ (Figure 9a). The monthly average density was from $1.1847 \text{ kg}/\text{m}^3$ in August to $1.2704 \text{ kg}/\text{m}^3$ in February. Hourly values differed from those of EN 16798-5-1 (Figure 9b).

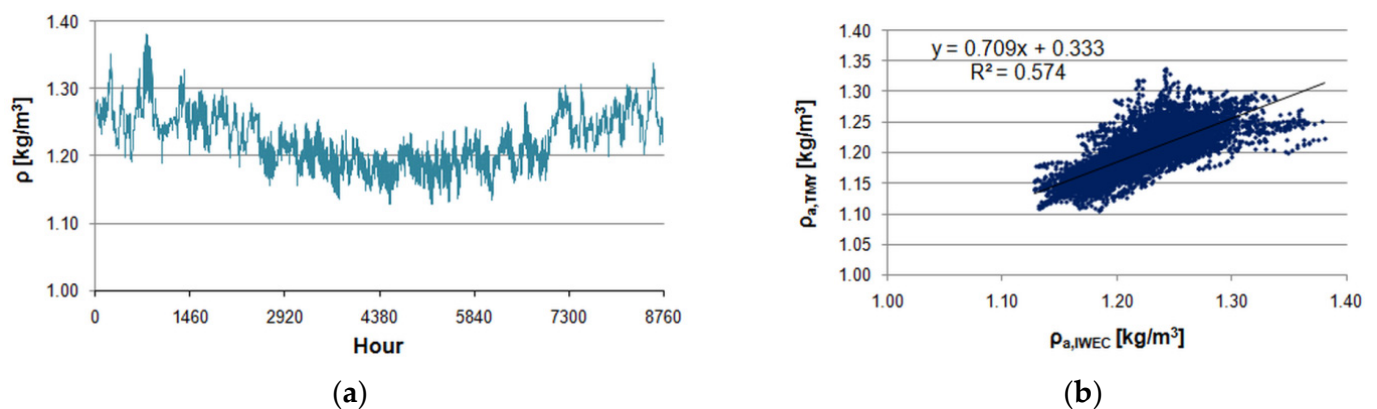


Figure 9. Hourly air density for Kraków calculated from the IWEC data: (a) during the year; (b) correlation of hourly values in relation to the results from EN 16798-5-1.

Volumetric heat capacity for EN 16798 (method 1) amounted to $1182.43 \text{ J}/(\text{m}^3\text{K})$. In the third method, the hourly value (dark green colour in Figure 10) was from $1111.58 \text{ J}/(\text{m}^3\text{K})$ to $1344.93 \text{ J}/(\text{m}^3\text{K})$ in comparison to the annual average of $1210.08 \text{ J}/(\text{m}^3\text{K})$. Monthly averaged values were from $1167.95 \text{ J}/(\text{m}^3\text{K})$ in June to $1257.87 \text{ J}/(\text{m}^3\text{K})$ in February.

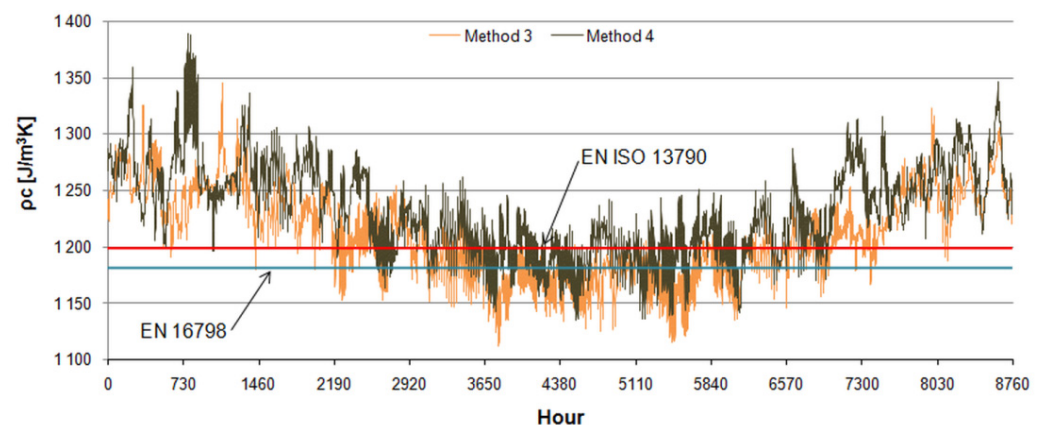


Figure 10. Volumetric specific heat.

The last considered method produced values from $1134.99 \text{ J}/(\text{m}^3\text{K})$ to $1389.12 \text{ J}/(\text{m}^3\text{K})$ with $1232.53 \text{ J}/(\text{m}^3\text{K})$ on average. Monthly averaged values were from $1191.85 \text{ J}/(\text{m}^3\text{K})$ in July to $1277.98 \text{ J}/(\text{m}^3\text{K})$ in February.

3.3. Performance of EAHE

To assess the effect of the considered methods on EAHE performance, we performed hourly simulations of the presented heat exchanger supplying ventilation air to the residential building.

As it could have been predicted from Equations (4) and (5), the influence of the density and specific heat variability on the temperature change in EAHE (ΔT_{sup}) and outlet air temperature from EAHE (T_{sup}) are negligible. These predictions were confirmed by the results of the calculations. In the following paragraphs, they are given in relation to the first method, following Section 3.1, as used in energy calculations in Poland.

Outlet air temperature (Figure 11), calculated according to method (1), in the order presented in Section 3.1, varied from $0.93 \text{ }^\circ\text{C}$ on 16 February at 6:00 to $15.35 \text{ }^\circ\text{C}$ on 16 August at 15:00 (Figure 9). For method (2), it was from $0.90 \text{ }^\circ\text{C}$ on 16 February at 6:00 to $15.37 \text{ }^\circ\text{C}$ on 16 August at 15:00. In the next case, it was from $0.59 \text{ }^\circ\text{C}$ on 16 February at 6:00 to $15.25 \text{ }^\circ\text{C}$ on 16 August at 15:00. According to the fourth method, it varied from $0.65 \text{ }^\circ\text{C}$ on 3 February at 6:00 to $15.05 \text{ }^\circ\text{C}$ on 15 August at 15:00. In the last case, similar values were obtained,

i.e., from 1.09 °C (3 February at 6:00) to 15.12 °C (15 August at 15:00). This shows that the baseline temperature varied within the same limits taking extreme values on the same days.

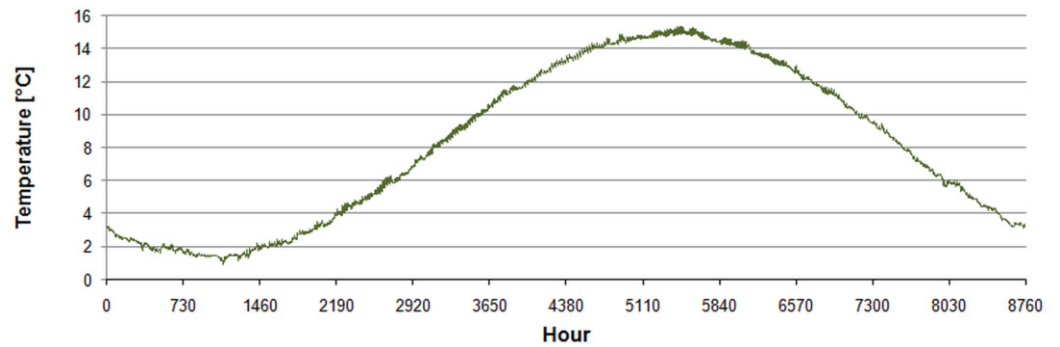


Figure 11. Outlet air temperature (T_{sup}) from EAHE.

Hourly differences between calculated outlet values were also negligible. In relation to method (1), they were from -0.03 °C to 0.03 °C, from -0.02 °C to 0.34 °C, from -0.72 °C to 1.04 °C, and from -0.72 °C to 0.73 °C, respectively. Therefore, strong correlations between them were obtained (Figures 12 and 13).

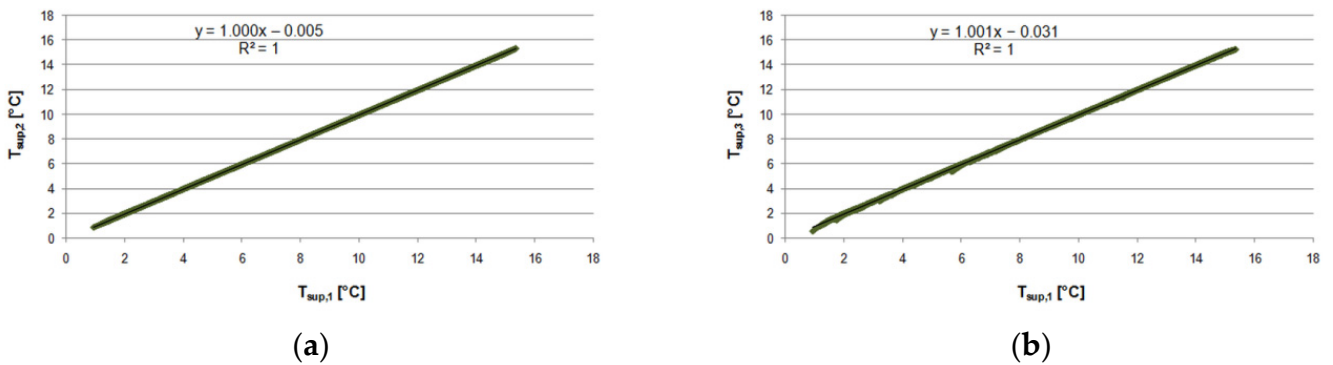


Figure 12. Hourly outlet air temperature from EAHE from method (1) and: (a) method (2); (b) method (3).

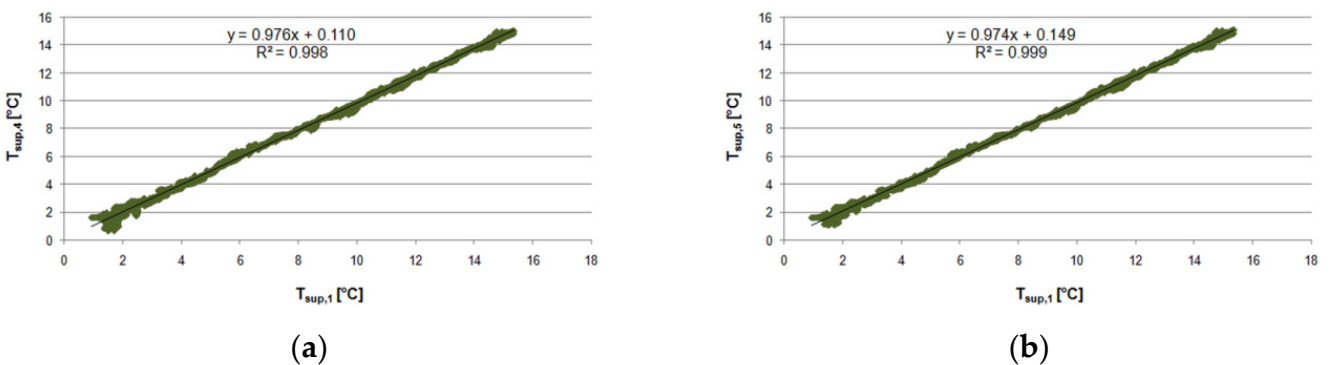


Figure 13. Hourly outlet air temperature from EAHE from method (1) and: (a) method (4); (b) method (5).

For the subsequent methods hourly heat flux gain in EAHE varied following the temperature rise in EAHE (Equation (14)) and was from -631.4 W on 7 June at 12:00 to 638.4 W on 29 November at 6:00, from -639.8 W on 7 June at 12:00 to 646.9 W on 29 November at 6:00, from -597.2 W on 7 June at 12:00 to 704.2 W on 29 November at 6:00,

from -546.4 W on 22 April at 15:00 to 721.2 W on 2 February at 6:00 and from -554.4 W on 22 April at 15:00 to 627.0 W on 2 February at 6:00.

Hourly differences in heating gain in relation to the first method were up to -8.4 W (20 December at 24:00), -74.4 W (16 February at 6:00), from -721.2 W (2 February at 6:00) to 595.6 W (16 February at 4:00) and from -627.0 W (2 February at 6:00) to 596.6 W (16 February at 5:00). In case of cooling these differences were up to 8.3 W, from -34.2 W (7 June at 12:00) to 3.8 W (1 February at 22:00), from -459.7 W (7 June at 12:00) to 483.1 W (4 August at 15:00), and from -461.0 W (7 June at 12:00) to 500.8 W (4 August at 15:00).

As it can be noticed the largest discrepancies were in the last case because of different meteorological datasets. However, from the point of air density variation the most interesting are two comparisons. The first is between methods 1 and 3, i.e., with constant air density and constant specific heat of air from EN 16798-5-1 and air density varying with ambient air temperature from TMY at constant pressure computed from the same standard (Figure 14). The second is a comparison between methods 5 and 4, both based on the IWEC datasets. These two comparisons should be considered the most important for the aim of this study. Thus, the hourly difference in heating and cooling flux between the two last methods was up to -94.2 W (2 February at 6:00), and from 11.4 W (11 March at 12:00) to -18.2 W (8 July at 15:00), respectively (Figure 15).

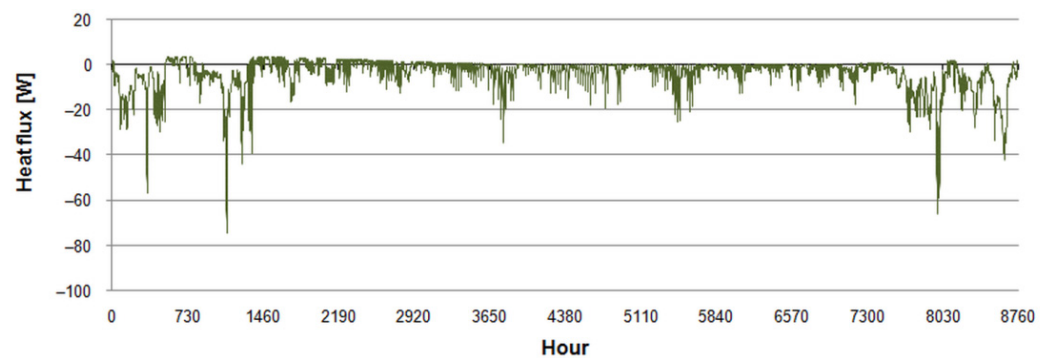


Figure 14. Hourly differences of calculated heat flux from EAHE between methods 1 and 3.

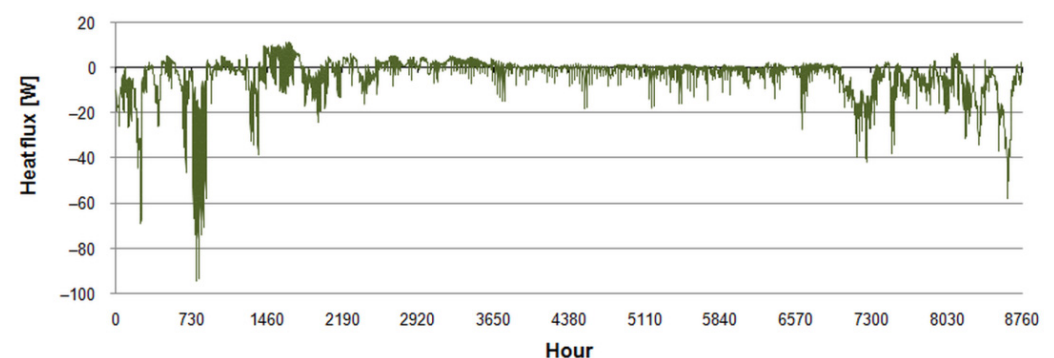


Figure 15. Hourly differences of calculated heat flux from EAHE between methods 5 and 4.

The most significant differences are observed during periods with low outdoor air temperature, between -10 °C and -20 °C, i.e., when ventilation heat loss is significant and heating needs are high. Hence, the design of EAHE in such conditions should include the change in air density with ambient temperature.

Negative differences between simplified and more detailed methods mean that the use of constant air parameters from EN 16798-5-1 results in an underestimation of the resulting heat flux. In the considered cases this effect is especially visible at low outdoor temperatures during the heating period.

In the study [33] for Polish conditions, it was also concluded that the model of EN 16798-5-1 underestimated heat gain and overestimated cooling load. In [34] authors com-

pared the same model and measurements and they stated that annual heating and cooling energy from the model was lower by 20–30% and greater by 8–20% than that from measurements, respectively.

As far as monthly (see Equations (15) and (16)) and annual aggregated values are considered, for the first three methods close monthly gains both for heating and cooling were obtained (Figure 16). However, the application of the last method resulted in more significant discrepancies. Monthly heat gain varied from 1 kWh in June to 128.7 kWh in November, from 1 kWh in June to 130.4 kWh in November, from 1 kWh in June to 136.0 kWh in November, from 3.9 kWh in May to 128.5 kWh in December and from 3.7 kWh in May to 119.1 kWh in December.

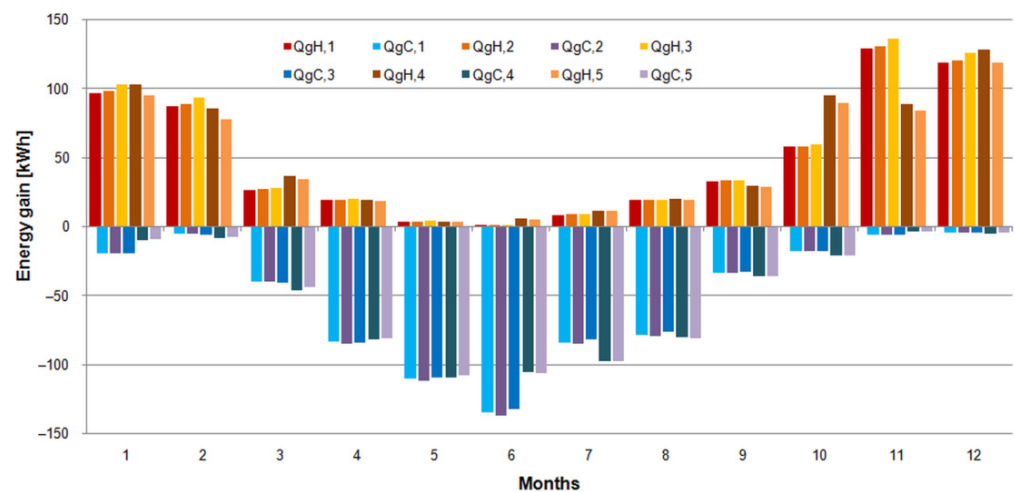


Figure 16. Monthly heating and cooling energy gain in EAHE from methods 1–5.

Nevertheless, annual heat gains were quite similar and amounted to 600.9 kWh, 608.8 kWh, 632.4 kWh, 628.3 kWh and 586.1 kWh. In relation to the internal surface area of EAHE, the annual unit heat was 34.9 kWh/m², 35.4 kWh/m², 36.8 kWh/m², 36.5 kWh/m² and 34.1 kWh/m².

In the case of cooling the situation was quite similar. Monthly cooling energy gain varied from −4.4 kWh in December to −135.0 kWh in June, from −4.5 kWh in December to −136.7 kWh in June, from −4.5 kWh in December to 132.3 kWh in June, from −3.6 kWh in November to −109.5 kWh in May and from −3.5 kWh in November to −108.2 kWh in May. Annual gains amounted to −616.9 kWh, −625.0 kWh, −610.6 kWh, −603.5 kWh and −600.1 kWh. In relation to the internal surface area of EAHE, the annual unit heat was −35.9 kWh/m², −36.3 kWh/m², −35.5 kWh/m², −35.1 kWh/m² and −34.9 kWh/m².

Simulation study for Swedish conditions [24] with a 10 m long polyethylene pipe of 20 cm diameter, buried at 2 m resulted in the estimated annual energy saving at 525 kWh and 300 kWh for heating and cooling season, respectively. It means the average gain per unit surface area of EAHE at 83.6 kWh/m² and 47.8 kWh/m².

Łuczak et al. [92] analysed various configurations of EAHE of EAHE connected with an air conditioning system in Polish conditions using the Rehau company program for the selection of ground heat exchangers. Unit heat gain per internal surface area of EAHE during the heating period (from 1 September to 31 March) was 40.7 kWh/m², 35.2 kWh/m², 34.2 kWh/m², 34.1 kWh/m² for the Tichelmanns' system (200 mm diameter, 1330 m and 182 m long), for the meandering system (315 mm diameter and 120 m long) and for the ring system ((315 mm diameter and 120 m long), respectively.

Simulations of EAHE (5 m long pipe with a diameter of 200 mm and airflow rate of 150 m³/h) located in southern Italy with ANSYS Fluent, presented by Congedo et al. [93], resulted in a total monthly heat gain was from 8.95 kWh in February to 174.70 kWh in November and from −26.26 kWh in August to −167.67 kWh in July.

The experimental study of Skotnicka et al. [94] contains valuable comparative results from a laboratory experiment with EAHE conducted from 1 July to 30 September 2016 in Olsztyn (north Poland). To build EAHE a 41 m long polypropylene pipe with 0.2 m diameter was used. The maximum measured and calculated hourly heating and cooling gain was 0.29 kWh, 0.73 kWh, -0.16 kWh and -0.65 kWh, respectively.

Monthly measured heat gain was 37.24 kWh, 62.42 kWh and 82.41 kWh in July, August and September, respectively. Consequently, it means monthly unit heat gain per internal surface area of EAHE at 1.4 kWh/m², 2.4 kWh/m² and 3.7 kWh/m². Total and unit gain for this period was 182.07 kWh and 7.07 kWh/m², respectively. Calculated monthly heat gains were similar to measured values and amounted for the same months to 44.00 kWh, 58.27 kWh and 95.22 kWh. Hence, unit gains were 1.7 kWh/m², 2.3 kWh/m² and 3.7 kWh/m².

Measured monthly cooling energy in the same months were -6.42 kWh, -4.45 kWh and -1.35 kWh with unit values of 0.25 kWh/m², 0.17 kWh/m² and 0.05 kWh/m². Simulated values were several times greater: -57.58 kWh, -79.92 kWh and -88.32 kWh with unit energy of 2.2 kWh/m², 3.1 kWh/m² and 3.42 kWh/m².

In the next study [34] authors experimentally analysed the hourly performance of EAHE built from the 35 m long pipe with the external and internal diameters of 200 and 185 mm, respectively. Measured annual heating and cooling energy was 1761 kWh and 1152 kWh in 2013 and 1410 kWh and 1063 kWh in 2014, respectively. It leads to energy gains per unit area of 86.6 kWh/m², 56.6 kWh/m², 69.3 kWh/m² and 52.3 kWh/m², respectively. Differences between measured and values calculated according to EN 16798-5-1 of heating, cooling and seasonal energy gain from EAHE were up to 49%, 59% and 79%, respectively.

When analysing the presented outcomes, there should be remembered that humidification and dehumidification processes inside the EAHE were ignored. This simplification is commonly included by other researchers for convenience [23,26,47–49].

However, Niu et al. [95] developed in Matlab the polynomial regression model for predicting the cooling capacity of EAHE including total, sensible and latent cooling capacity as a function of the air temperature, the air relative humidity, the air velocity at the inlet of EAHE, the tube surface temperature and the tube length and diameter.

The presented results showed that the air temperature along EAHE was independent of inlet air humidity. They also showed that in the case of low inlet air relative humidity, below 40%, no condensation along with the length of the tube occurred. Their study was devoted, however, only to cooling demand. In Polish conditions, where heating prevails, the situation can be different.

3.4. Energy Performance of the Building

To estimate the impact of EAHE operation on energy use for space heating and cooling of the considered exemplary residential building the necessary simulations were performed. To estimate the obtained energy effect, the base case was simulated without EAHE at first. Then, the following four cases with EAHE were considered.

In comparison to the base case ($Q_{H,0}$ and $Q_{C,0}$ in Figure 17), the introduction of EAHE resulted in visible energy savings in the considered case regardless of the chosen calculation method. It is especially clear in the months with dominant heating or cooling conditions. However, in varying ambient conditions (March, April, September, and October) and the thermal demand of the building changing during the day from heating to cooling and vice versa, the effect is not so obvious. Then it seems to be more beneficial to introduce a bypass to switch the intake of ventilation air between EAHE and outdoor air [35,50,51,96].

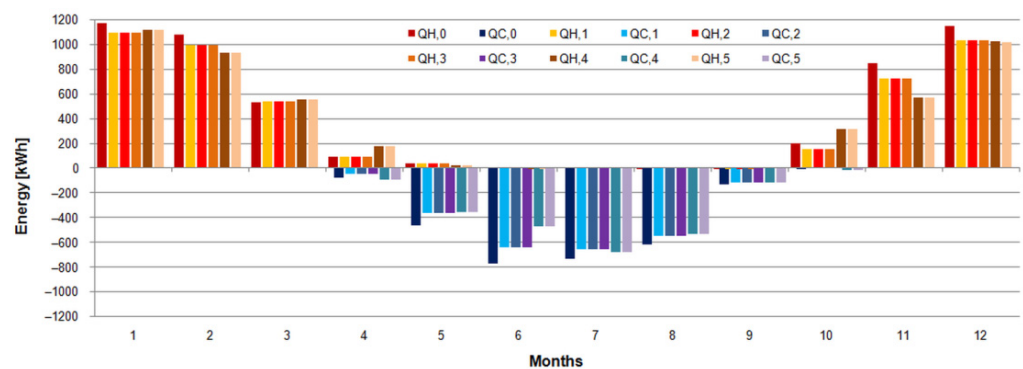


Figure 17. Monthly energy use for space heating and cooling of the building.

Annual heating and cooling energy decreased from 5109 kWh and 2792 kWh in the base case to 4667 kWh and 2364 kWh, 4667 kWh and 2365 kWh, 4670 kWh and 2363, 4724 kWh and 2261 kWh, and 4719 kWh and 2261 kWh according to the successive methods, respectively. Hence, EAHE was responsible for the average annual reduction of 8.8% in heating and 15.3% in cooling energy in the first three methods. For the last one, reductions of 7.5% and 19.0% were obtained.

Figure 17 shows differences in calculated annual energy for space heating and cooling when using different weather datasets. For this reason, the weather files for energy simulations of buildings, especially in the case of energy certification, should be properly prepared. Moreover, atmospheric pressure should be included in Polish typical meteorological years.

Simulations in the Swedish climate [24] resulted in a 5% reduction for heating and a 50% reduction for cooling. In the case of a low-energy building located in Polish climatic conditions [35] EAHE reduced annual simulated heating and cooling needs by 13% and 43%, respectively. Results of long-term measurements of EAHE supplying ventilation air in a residential building located in north Poland presented in [33] showed annual savings of around 20% and 3% for heating and cooling energy, respectively.

The use of EAHE also improved the performance of the thermal energy source. Maximum heating and cooling power decreased significantly (Table 3). Only in the last case, it increase compared to the base case. It was caused by lower outdoor temperatures, especially on 2 February, when it varied from -20.1 °C at 7:00 to -4 °C at 14:00. The peak values of heating power in the remaining cases were noticed on 26 December when the outdoor air temperature was from -9.5 °C at 12:00 to -12.5 °C at 9:00. Moreover, unnecessary ventilation loss was reduced resulting in lower thermal demand for the building.

Table 3. Maximum hourly heating and cooling power.

Parameter	Base Case	1	2	3	4	5	Unit
$\phi_{H,max}$	3104	2471	2471	2480	3672	3658	W
$\phi_{C,max}$	-3657	-3021	-3022	-3017	-3026	-3026	W
$\phi_{ve,max}$	207	0	0	0	0	0	W
$\phi_{ve,min}$	-1206	-644	-644	-644	-619	-620	W
τ_H	3952	3997	3996	3996	3936	3936	h
τ_C	2415	2365	2365	2365	2342	2342	h

The next important aspect of this solution is the annual operation time of heating (τ_H) and cooling (τ_C). It was reduced in the cooling mode in all cases. In heating, it slightly increased, but the share of hourly power above 2000 W dropped rapidly (Figures 18 and 19).

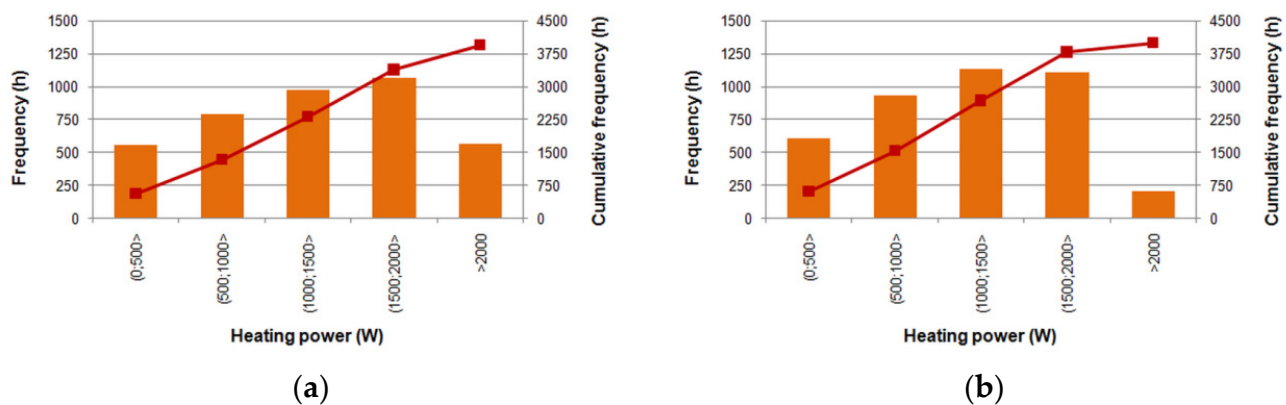


Figure 18. Histograms of heating power: (a) the base case; (b) method 1.

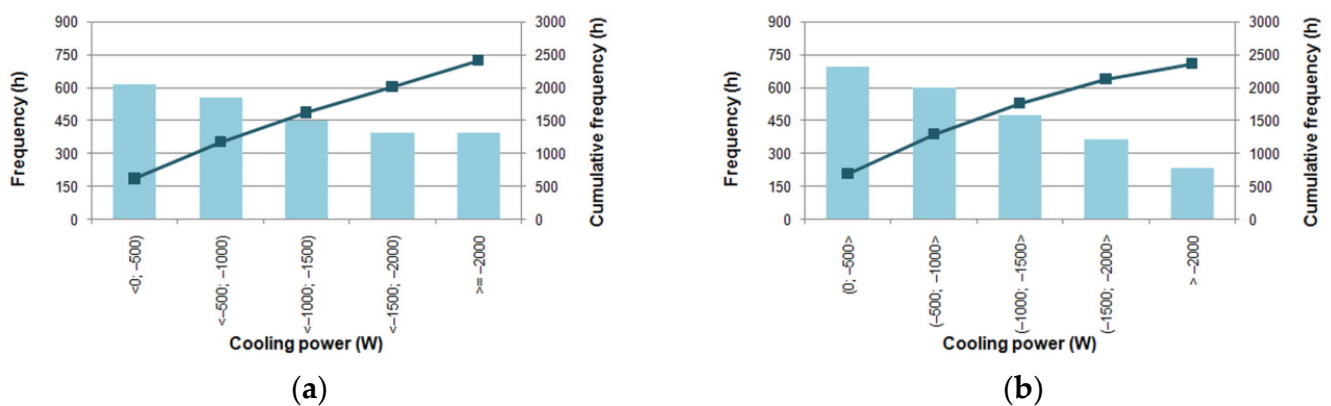


Figure 19. Histograms of cooling power: (a) the base case; (b) method 1.

Presented histograms confirm a more stable operation of the heating and cooling source. In relation to the base case operation with heating and cooling power above 2000 W changed from 567 h to 210 h and from 396 h to 232 h. At the same time, power usage below 500 W increased: from 554 h to 611 h and from 618 h to 695 h.

4. Conclusions

In this study, the impact of air density variation with atmospheric conditions on the operation of the earth-to-air heat exchanger coupled with the ventilation system of the residential building in hourly time steps was studied.

As the Polish hourly typical meteorological years, available for 61 locations and intended for energy simulations of buildings, do not contain atmospheric pressure, the analysis took into account air density variation with ambient air temperature. The barometric pressure was computed as constant in relation to the reference conditions at sea level using the barometric formula at the altitude of the meteorological station. Therefore, air density variation analysis is limited only to one factor influencing its value—air temperature. In such a case, the density variation with temperature from the relevant weather files at constant pressure in comparison to the method of EN 16798-5-1 resulted in hourly differences in outlet air temperature up to 0.34 °C which can be treated as insignificant. Despite this, hourly differences in energy gain per unit area of the heat exchanger were up to 4.3 W/m² and 2.0 W/m² for heating and cooling, respectively.

For comparative purposes also the IWEC file was also used. However, as IWEC files are available only for four locations in Poland they are not used in practice. Instead, Polish TMYs are in common use as prepared for energy calculations of buildings both in monthly and hourly resolution. In this case, where both hourly ambient air temperature and atmospheric pressure were given, hourly differences in relation to the method using

the same weather data but constant air properties from EN 16798-5-1 were up to 5.5 W/m^2 and 1.1 W/m^2 for heating and cooling, respectively.

These values seem not to be large, but analysed EAHE was rather small. So, in the case of larger objects hourly heating and cooling loads can differ more significantly. It was confirmed by comparisons of simplified methods with more detailed. In general, the model from EN 16798-5-1 underestimated heat gain and overestimated cooling load.

The presented considerations also confirmed the impact of the weather dataset used in calculations on monthly and annual energy gain from EAHE. The second one amounted to 600.9 kWh and 628.3 kWh for heating and 616.9 kWh and 603.5 kWh in cooling for the first and fourth methods (TMY and IWEC files), respectively. However, within the same weather data files it occurred that aggregated annual values of energy gain from EAHE were not significantly affected by simplifications regarding thermal properties of air, introduced both by EN 16798-5-1 or EN ISO 13790. As the influence of varying air density on ventilation loss and energy demand for heating and cooling of the building was not considered here, it may be analysed in a separate study.

The application of EAHE significantly decreased the energy demand for the heating and cooling of the building, by 8.2% and 16.8% on average, respectively.

As IWEC files are not used in energy audits or certification of buildings, it seems reasonable to introduce atmospheric pressure in typical Polish meteorological years. It would allow assessing the impact of air density variation on the EAHE performance.

This study shows the need to include atmospheric pressure in typical Polish meteorological years. Similarly, as in the case of heat load calculation following PN EN 12831, the design conditions for EAHE dimensioning in Polish climatic conditions could also be developed. It also indicates the need for future consideration about an assessment of air humidity impact on the simulated EAHE performance.

Funding: This research received no external funding.

Institutional Review Board Statement: Not applicable.

Informed Consent Statement: Not applicable.

Data Availability Statement: Not applicable.

Conflicts of Interest: The author declares no conflict of interest.

Symbols and Abbreviations

A_s	inner surface of the ground heat exchanger, m^2
C_m	thermal capacity of the building, J/K
E_A	unit heating and cooling energy use per unit area of a building, kWh/m^2
$H_{\text{tr,em}}$	external part of the $H_{\text{tr,op}}$ thermal transmission coefficient, W/K
$H_{\text{tr,is}}$	coupling conductance, W/K
$H_{\text{tr,ms}}$	internal part of the $H_{\text{tr,op}}$ thermal transmission coefficient, W/K
$H_{\text{tr,op}}$	thermal transmission coefficient for thermally heavy envelope elements, W/K
$H_{\text{tr,w}}$	thermal transmission coefficient for thermally light envelope elements, W/K
H_{ve}	thermal transmission coefficient by ventilation air, W/K
L	length of the duct, m
Q_C	annual energy use for space cooling, kWh
$Q_{gC,m}$	cooling energy gain in EAHE in m -th month, Wh
$Q_{gH,m}$	heating energy gain in EAHE in m -th month, Wh
Q_H	annual energy use for space heating, kWh
Q_{HC}	annual energy use for space heating and cooling, kWh
ΔQ_{HC}	percentage savings in annual energy use for space heating and cooling, %
T_e	external (outdoor) air temperature, $^\circ\text{C}$
$T_{e,mn,an}$	mean annual temperature of outdoor air, $^\circ\text{C}$
$T_{e,max,m}$	maximum mean monthly temperature of outdoor air, $^\circ\text{C}$
T_{gnd}	hourly ground temperature, $^\circ\text{C}$

T_i	internal (indoor) air temperature, °C
$T_{i,C,set}$	set-point indoor air temperature for cooling, °C
$T_{i,H,set}$	set-point indoor air temperature for heating, °C
T_m	thermal mass node temperature, °C
T_{md}	average air temperature in the duct, °C
T_s	central node temperature, °C
T_{sup}	supply air temperature, °C
c_a	specific heat of air at constant pressure, J/(kg·K)
c_{gnd}	specific heat of the ground, J/(kg·K)
d_i	inner diameter of the duct, m
d_o	outer diameter of the duct, m
f_t	time shift factor,
h_i	inside surface heat transfer coefficient, W/m ² K
h_m	number of hours in m-th month,
$q_{v;sup}$	volumetric airflow rate, m ³ /s
t_{an}	annual hour, with $t_{an} = 0$ h at the beginning of the year; h
$t_{an,min}$	the time of the year when the monthly mean outdoor temperature is minimal, h
v	air velocity in the duct, m/s
z	burial depth of the duct, m
$\Delta\tau_m$	length of the month m, h
λ_{gnd}	thermal conductivity of the ground, W/(m·K)
λ_{du}	thermal conductivity of the duct, W/(m·K)
ξ	damping factor,
ρ_a	air density, kg/m ³
ρ_{gnd}	ground density, kg/m ³
φ_{int}	heat flow rate due to internal heat sources, W
φ_{sol}	heat flow rate due to solar heat sources, W
φ_{ia}	heat flow rate to internal air node, W
φ_{st}	heat flow rate to central node, W
φ_m	heat flow rate to mass node, W
φ_{ve}	heat flow rate by ventilation, W
φ_{EAHE}	heat flow rate from EAHE, W
φ_C	cooling power supplied to or extracted from the indoor air node, W
φ_H	heating power supplied to or extracted from the indoor air node, W
φ_{HC}	heating or cooling power supplied to or extracted from the indoor air node, W

References

- Buildings Performance Institute Europe. Europe's Buildings under the Microscope. 2011. Available online: https://www.bpie.eu/wp-content/uploads/2015/10/HR_EU_B_under_microscope_study.pdf (accessed on 9 March 2022).
- Kesten, D.; Tereci, A.; Strzalka, A.M.; Eicker, U. A method to quantify the energy performance in urban quarters. *HVACR Res.* **2012**, *18*, 100–111. [CrossRef]
- Aksamija, A. Design methods for sustainable, high performance building facades. *Adv. Build. Energy Res.* **2016**, *10*, 240–262. [CrossRef]
- Kneifel, J.; O'Rear, E. Reducing the impacts of weather variability on long-term building energy performance by adopting energy-efficient measures and systems: A case study. *J. Build. Perform. Simul.* **2017**, *10*, 58–71. [CrossRef]
- Witkowska, A.; Krawczyk, D.A.; Rodero, A. Investment Costs of Heating in Poland and Spain—A Case Study. *Proceedings* **2019**, *16*, 40. [CrossRef]
- Chwieduk, D.; Chwieduk, M. Determination of the Energy Performance of a Solar Low Energy House with Regard to Aspects of Energy Efficiency and Smartness of the House. *Energies* **2020**, *13*, 3232. [CrossRef]
- Ballarini, I.; Costantino, A.; Fabrizio, E.; Corrado, V. A Methodology to Investigate the Deviations between Simple and Detailed Dynamic Methods for the Building Energy Performance Assessment. *Energies* **2020**, *13*, 6217. [CrossRef]
- Mardiana-Idayu, A.; Riffat, S.B. Review on heat recovery technologies for building applications. *Renew. Sustain. Energy Rev.* **2012**, *16*, 1241–1255. [CrossRef]
- Xu, Q.; Riffat, S.; Zhang, S. Review of Heat Recovery Technologies for Building Applications. *Energies* **2019**, *12*, 1285. [CrossRef]
- Abbaspour-Fard, M.H.; Gholami, A.; Khojastehpour, M. Evaluation of an earth-to-air heat exchanger for the north-east of Iran with semi-arid climate. *Int. J. Green Energy* **2011**, *8*, 499–510. [CrossRef]
- Tan, L.; Love, J.A. A Literature Review on Heating of Ventilation Air with Large Diameter Earth Tubes in Cold Climates. *Energies* **2013**, *6*, 3734–3743. [CrossRef]


12. Greco, A.; Masselli, C. The Optimization of the Thermal Performances of an Earth to Air Heat Exchanger for an Air Conditioning System: A Numerical Study. *Energies* **2020**, *13*, 6414. [CrossRef]
13. Pakari, A.; Ghani, S. Energy Savings Resulting from Using a Near-Surface Earth-to-Air Heat Exchanger for Precooling in Hot Desert Climates. *Energies* **2021**, *14*, 8044. [CrossRef]
14. Peña, S.A.P.; Ibarra, J.E.J. Potential Applicability of Earth to Air Heat Exchanger for Cooling in a Colombian Tropical Weather. *Buildings* **2021**, *11*, 219. [CrossRef]
15. D'Agostino, D.; Marino, C.; Minichiello, F. Earth-to-Air Versus Air-to-Air Heat Exchangers: A Numerical Study on the Energetic, Economic, and Environmental Performances for Italian Office Buildings. *Heat Transf. Eng.* **2020**, *41*, 1040–1051. [CrossRef]
16. D'Agostino, D.; Esposito, F.; Greco, A.; Masselli, C.; Minichiello, F. Parametric Analysis on an Earth-to-Air Heat Exchanger Employed in an Air Conditioning System. *Energies* **2020**, *13*, 2925. [CrossRef]
17. D'Agostino, D.; Esposito, F.; Greco, A.; Masselli, C.; Minichiello, F. The Energy Performances of a Ground-to-Air Heat Exchanger: A Comparison among Köppen Climatic Areas. *Energies* **2020**, *13*, 2895. [CrossRef]
18. Baglivo, C.; Bonuso, S.; Congedo, P.M. Performance Analysis of Air Cooled Heat Pump Coupled with Horizontal Air Ground Heat Exchanger in the Mediterranean Climate. *Energies* **2018**, *11*, 2704. [CrossRef]
19. Baglivo, C.; D'Agostino, D.; Congedo, P.M. Design of a Ventilation System Coupled with a Horizontal Air-Ground Heat Exchanger (HAGHE) for a Residential Building in a Warm Climate. *Energies* **2018**, *11*, 2122. [CrossRef]
20. Ahmed, S.F.; Khan, M.M.K.; Amanullah, M.T.O.; Rasul, M.G.; Hassan, N.M.S. Performance assessment of earth pipe cooling system for low energy buildings in a subtropical climate. *Energy Convers. Manag.* **2015**, *106*, 815–825. [CrossRef]
21. Ahmed, S.F.; Amanullah, M.T.O.; Khan, M.M.K.; Rasul, M.G.; Hassan, N.M.S. Parametric study on thermal performance of horizontal earth pipe cooling system in summer. *Energy Convers. Manag.* **2016**, *114*, 324–337. [CrossRef]
22. Cao, S.; Li, F.; Li, X.; Yang, B. Feasibility analysis of earth-air heat exchanger (EAHE) in a sports and culture centre in Tianjin, China. *Case Stud. Therm. Eng.* **2021**, *26*, 101654. [CrossRef]
23. Bisoniya, T.S.; Kumar, A.; Baredar, P. Energy metrics of earth-air heat exchanger system for hot and dry climatic conditions of India. *Energy Build.* **2015**, *86*, 214–221. [CrossRef]
24. Havtun, H.; Törnqvist, C. Reducing Ventilation Energy Demand by Using Air-to-Earth Heat Exchangers. Part 1—Parametric Study. In *Sustainability in Energy and Buildings*; Hakansson, A., Höjer, M., Howlett, R., Jain, L., Eds.; Smart Innovation, Systems and Technologies; Springer: Berlin/Heidelberg, Germany, 2013; Volume 22. [CrossRef]
25. Ahmadi, S.; Shahrestani, M.I.; Sayadian, S.; Poshitri, A.H. Performance analysis of an integrated cooling system consisted of earth-to-air heat exchanger (EAHE) and water spray channel. *J. Therm. Anal. Calorim.* **2021**, *143*, 473–483. [CrossRef]
26. Akbarpoor, A.M.; Poshitri, A.H.; Biglari, F. Performance analysis of domed roof integrated with earth-to-air heat exchanger system to meet thermal comfort conditions in buildings. *Renew. Energy* **2021**, *168*, 1265–1293. [CrossRef]
27. Zhang, C.; Xiao, F.; Wang, J. Design optimization of multi-functional building envelope for thermal insulation and exhaust air heat recovery in different climates. *J. Build. Eng.* **2021**, *43*, 103151. [CrossRef]
28. Molcrette, V.F.A.; Autier, V.R.B. New expression to calculate quantity of recovered heat in the earth-pipe-air heat-exchanger operating in winter heating mode. *Arch. Thermodyn.* **2020**, *41*, 103–117. [CrossRef]
29. Hong, T.; Buhl, F.; Haves, P.; Selkowitz, S.; Wetter, M. Comparing computer run time of building simulation programs. *Build. Simul.* **2008**, *1*, 210–213. [CrossRef]
30. Piana, E.A.; Grassi, B.; Socal, L. A Standard-Based Method to Simulate the Behavior of Thermal Solar Systems with a Stratified Storage Tank. *Energies* **2020**, *13*, 266. [CrossRef]
31. Patračević, F.; Dović, D.; Horvat, I.; Filipović, P. A Novel Dynamic Approach to Cost-Optimal Energy Performance Calculations of a Solar Hot Water System in an nZEB Multi-Apartment Building. *Energies* **2022**, *15*, 509. [CrossRef]
32. *EN ISO 16798-5-1*; Energy Performance of Buildings. Ventilation for Buildings Calculation Methods for Energy Requirements of Ventilation and Air Conditioning Systems (Modules M5-6, M5-8, M6-5, M6-8, M7-5, M7-8). Method 1: Distribution and Generation. International Organization for Standardization: Geneva, Switzerland, 2017.
33. Skotnicka-Siepsiak, A. Operation of a Tube GAHE in Northeastern Poland in Spring and Summer—A Comparison of Real-World Data with Mathematically Modeled Data. *Energies* **2020**, *13*, 1778. [CrossRef]
34. Brata, S.; Tănăsă, C.; Dan, D.; Stoian, V.; Doboși, I.S.; Brata, S. Energy potential of a ground-air heat exchanger—measurements and computational models. *Sci. Technol. Built Environ.* **2021**, *28*, 84–93. [CrossRef]
35. Michalak, P. Hourly Simulation of an Earth-to-Air Heat Exchanger in a Low-Energy Residential Building. *Energies* **2022**, *15*, 1898. [CrossRef]
36. *EN ISO 13790*; Energy Performance of Buildings—Calculation of Energy Use for Space Heating and Cooling. International Organization for Standardization: Geneva, Switzerland, 2009.
37. Michalak, P. Ventilation heat loss in a multifamily building under varying air density. *J. Mech. Energy Eng.* **2020**, *4*, 97–102. [CrossRef]
38. Bouhess, H.; Hamdi, H.; Benhamou, B.; Bennouna, A.; Hollmuller, P.; Limam, K. Dynamic simulation of an earth-to-air heat exchanger connected to a villa type house in Marrakech. In Proceedings of the 13th Conference of International Building Performance Simulation Association, Chambéry, France, 25–28 August 2013.

39. Ghaith, F.A.; Razzaq, H.U. Thermal performance of earth-air heat exchanger systems for cooling applications in residential buildings. In Proceedings of the ASME International Mechanical Engineering Congress and Exposition, Pittsburgh, PA, USA, 9–15 November 2018; pp. 1–12. [CrossRef]
40. Badescu, V.; Isvoranu, D. Pneumatic and thermal design procedure and analysis of earth-to-air heat exchangers of registry type. *Appl. Energy* **2011**, *88*, 1266–1280. [CrossRef]
41. Serageldin, A.A.; Abdelrahman, A.K.; Ookawara, S. Parametric study and optimization of a solar chimney passive ventilation system coupled with an earth-to-air heat exchanger. *Sustain. Energy Technol. Assess.* **2018**, *30*, 263–278. [CrossRef]
42. PN-EN 12831-1:2017; Energy Performance of Buildings—Method for Calculation of the Design Heat Load-Part1: Space Heating Load. Polish Committee for Standardization: Warsaw, Poland, 2017.
43. Ferdyn-Grygierek, J.; Baranowski, A.; Blaszcok, M.; Kaczmarczyk, J. Thermal Diagnostics of Natural Ventilation in Buildings: An Integrated Approach. *Energies* **2019**, *12*, 4556. [CrossRef]
44. Sowa, J.; Mijakowski, M. Humidity-Sensitive, Demand-Controlled Ventilation Applied to Multiunit Residential Building—Performance and Energy Consumption in Dfb Continental Climate. *Energies* **2020**, *13*, 6669. [CrossRef]
45. Ministry of Investment and Development. Data for Energy Calculations of Buildings. Typical Meteorological Years and Statistical Climatic Data for Energy Calculations of Buildings. Available online: <https://www.gov.pl/web/archiwum-inwestycje-rozwoj/dane-do-obliczen-energetycznych-budynkow> (accessed on 9 March 2022).
46. Pfafferott, J. Evaluation of earth-to-air heat exchangers with a standardised method to calculate energy efficiency. *Energy Build.* **2003**, *35*, 971–983. [CrossRef]
47. Chlela, F.; Husaunndee, A.; Riederer, P.; Inard, C. Numerical Evaluation of Earth to Air Heat Exchangers and Heat Recovery Ventilation Systems. *Int. J. Vent.* **2007**, *6*, 31–42. [CrossRef]
48. Warwick, D.J.; Cripps, A.J.; Kolokotroni, M. Integrating Active Thermal Mass Strategies with HVAC Systems: Dynamic Thermal Modelling. *Int. J. Vent.* **2009**, *7*, 345–367. [CrossRef]
49. Ralegaonkar, R.; Kamath, M.V.; Dakwale, V.A. Design and Development of Geothermal Cooling System for Composite Climatic Zone in India. *J. Inst. Eng. Ser. A* **2014**, *95*, 179–183. [CrossRef]
50. Stasi, R.; Liuzzi, S.; Paterno, S.; Ruggiero, F.; Stefanizzi, P.; Stragapede, A. Combining bioclimatic strategies with efficient HVAC plants to reach nearly-zero energy building goals in Mediterranean climate. *Sustain. Cities Soc.* **2020**, *63*, 102479. [CrossRef]
51. Trzaški, A.; Zawada, B. The influence of environmental and geometrical factors on air-ground tube heat exchanger energy efficiency. *Build. Environ.* **2011**, *46*, 1436–1444. [CrossRef]
52. Skotnicka-Siepsiak, A. An Evaluation of the Performance of a Ground-to-Air Heat Exchanger in Different Ventilation Scenarios in a Single-Family Home in a Climate Characterized by Cold Winters and Hot Summers. *Energies* **2022**, *15*, 105. [CrossRef]
53. Gwadera, M.; Larwa, B.; Kupiec, K. Undisturbed Ground Temperature—Different Methods of Determination. *Sustainability* **2017**, *9*, 2055. [CrossRef]
54. Larwa, B.; Gwadera, M.; Kicińska, I.; Kupiec, K. Parameters of the Carslaw-Jaeger equation describing the temperature distribution in the ground. *Tech. Trans.* **2018**, *115*, 67–78. [CrossRef]
55. Larwa, B. Heat Transfer Model to Predict Temperature Distribution in the Ground. *Energies* **2019**, *12*, 25. [CrossRef]
56. Bergman, T.L.; Lavine, A.A.; Incropera, F.P.; DeWitt, D.P. *Fundamentals of Heat and Mass Transfer*, 8th ed.; Wiley: Hoboken, NJ, USA, 2018.
57. Panão, M.J.N.O.; Santos, C.A.P.; Mateus, N.M.; da Graça, G.C. Validation of a lumped RC model for thermal simulation of a double skin natural and mechanical ventilated test cell. *Energy Build.* **2016**, *121*, 92–103. [CrossRef]
58. Jayathissa, P.; Luzzatto, M.; Schmidli, J.; Hofer, J.; Nagy, Z.; Schlueter, A. Optimising building net energy demand with dynamic BIPV shading. *Appl. Energy* **2017**, *202*, 726–735. [CrossRef]
59. Shen, P.; Braham, W.; Yi, Y. Development of a lightweight building simulation tool using simplified zone thermal coupling for fast parametric study. *Appl. Energy* **2018**, *223*, 188–214. [CrossRef]
60. Costantino, A.; Fabrizio, E.; Ghiggini, A.; Bariani, M. Climate control in broiler houses: A thermal model for the calculation of the energy use and indoor environmental conditions. *Energy Build.* **2018**, *169*, 110–126. [CrossRef]
61. Lauster, M.; Teichmann, J.; Fuchs, M.; Streblow, R.; Mueller, D. Low order thermal network models for dynamic simulations of buildings on city district scale. *Build. Environ.* **2014**, *73*, 223–231. [CrossRef]
62. Horvat, I.; Dović, D. Dynamic modeling approach for determining buildings technical system energy performance. *Energy Convers. Manag.* **2016**, *125*, 154–165. [CrossRef]
63. Elci, M.; Delgado, B.M.; Henning, H.M.; Henze, G.P.; Herkel, S. Aggregation of residential buildings for thermal building simulations on an urban district scale. *Sustain. Cities Soc.* **2018**, *39*, 537–547. [CrossRef]
64. Tagliabue, L.C.; Buzzetti, M.; Marenzi, G. Energy performance of greenhouse for energy saving in buildings. *Energy Procedia* **2012**, *30*, 1233–1242. [CrossRef]
65. Fabrizio, E.; Ghiggini, A.; Bariani, M. Energy performance and indoor environmental control of animal houses: A modelling tool. *Energy Procedia* **2015**, *82*, 439–444. [CrossRef]
66. Jędrzejuk, H.; Rucińska, J. Verifying a need of artificial cooling—a simplified method dedicated to single-family houses in Poland. *Energy Procedia* **2015**, *78*, 1093–1098. [CrossRef]
67. Fischer, D.; Wolf, T.; Scherer, J.; Wille-Haussmann, B. A stochastic bottom-up model for space heating and domestic hot water load profiles for German households. *Energy Build.* **2016**, *124*, 120–128. [CrossRef]

68. Mora, T.D.; Teso, L.; Carnieletto, L.; Zarrella, A.; Romagnoni, P. Comparative Analysis between Dynamic and Quasi-Steady-State Methods at an Urban Scale on a Social-Housing District in Venice. *Energies* **2021**, *14*, 5164. [CrossRef]
69. Bruno, R.; Pizzuti, G.; Arcuri, N. The Prediction of Thermal Loads in Building by Means of the EN ISO 13790 Dynamic Model: A Comparison with TRNSYS. *Energy Procedia* **2016**, *101*, 192–199. [CrossRef]
70. Costantino, A.; Comba, L.; Sicardi, G.; Bariani, M.; Fabrizio, E. Energy performance and climate control in mechanically ventilated greenhouses: A dynamic modelling-based assessment and investigation. *Appl. Energy* **2021**, *288*, 116583. [CrossRef]
71. ISO 6946:2017; Building Components and Building Elements—Thermal Resistance and Thermal Transmittance—Calculation Methods. International Organization for Standardization: Geneva, Switzerland, 2017.
72. ISO 13786:2017; Thermal Performance of Building Components—Dynamic Thermal Characteristics—Calculation Methods. International Organization for Standardization: Geneva, Switzerland, 2017.
73. Lomas, K.J. Architectural design of an advanced naturally ventilated building form. *Energy Build.* **2007**, *39*, 166–181. [CrossRef]
74. Vestfálová, M.; Šafařík, P. Determination of the applicability limits of the ideal gas model for the calculation of moist air properties. *EPJ Web Conf.* **2018**, *180*, 02115. [CrossRef]
75. Mohr, P.J.; Newell, D.B.; Taylor, B.N. CODATA Recommended Values of the Fundamental Physical Constants: 2014. *J. Phys. Chem. Ref. Data* **2016**, *45*, 043102. [CrossRef]
76. Arizona State University. World Meteorological Organization’s World Weather & Climate Extremes Archive. Available online: <https://wmo.asu.edu/content/world-meteorological-organization-global-weather-climate-extremes-archive> (accessed on 4 March 2022).
77. Berberan-Santos, M.N.; Bodunov, E.N.; Pogliani, L. On the barometric formula. *Am. J. Phys.* **1997**, *65*, 404–412. [CrossRef]
78. Andrews, D.G. *An Introduction to Atmospheric Physics*; Cambridge University Press: Cambridge, UK, 2000.
79. National Ocean and Atmosphere Administration. *U.S. Standard Atmosphere 1976*; Nation Ocean and Atmosphere Administration: Washington, DC, USA, 1976. Available online: <https://www.ngdc.noaa.gov/stp/space-weather/online-publications/miscellaneous/us-standard-atmosphere-1976/> (accessed on 14 March 2022).
80. Dubinova, A.A. Exact explicit barometric formula for a warm isothermal Fermi gas. *Tech. Phys.* **2009**, *54*, 210–213. [CrossRef]
81. Cohen, J.E.; Small, C. Hypsographic demography: The distribution of human population by altitude. *Proc. Natl. Acad. Sci. USA* **1998**, *95*, 14009–14014. [CrossRef]
82. Benenson, W.; Harris, J.W.; Stöcker, H.; Lutz, H. *Handbook of Physics*; Springer: New York, NY, USA, 2002. [CrossRef]
83. Jacobson, M.Z. *Fundamentals of Atmospheric Modeling*, 2nd ed.; Cambridge University Press: Cambridge, UK, 2012. [CrossRef]
84. Corstanje, A.; Bonardi, A.; Buitink, S.; Falcke, H.; Hörandel, J.R.; Mitra, P.; Mulrey, K.; Nelles, A.; Rachen, J.P.; Rossetto, L.; et al. The effect of the atmospheric refractive index on the radio signal of extensive air showers. *Astropart. Phys.* **2017**, *89*, 23–29. [CrossRef]
85. Wagner, W.; Kretschmar, H.J.; Span, R.; Krauss, R. D2 Properties of Selected Important Pure Substances. In *VDI Heat Atlas*; Springer: New York, NY, USA, 2010. [CrossRef]
86. Lemmon, E.W.; Jacobsen, R.T.; Penoncello, S.G.; Friend, D.G. Thermodynamic properties of air and mixtures of nitrogen, argon, and oxygen from 60 to 2000 K at pressures to 2000 MPa. *J. Phys. Chem. Ref. Data* **2000**, *29*, 331–385. [CrossRef]
87. Struchtrup, H. Properties and Property Relations. In *Thermodynamics and Energy Conversion*; Springer: Berlin/Heidelberg, Germany, 2014. [CrossRef]
88. Michalak, P. Modelling of Solar Irradiance Incident on Building Envelopes in Polish Climatic Conditions: The Impact on Energy Performance Indicators of Residential Buildings. *Energies* **2021**, *14*, 4371. [CrossRef]
89. World Meteorological Organization. Weather Data. Available online: <https://energyplus.net/weather> (accessed on 17 March 2022).
90. Bellia, L.; Pedace, A.; Fragliasso, F. The role of weather data files in Climate-based Daylight Modeling. *Sol. Energy* **2015**, *112*, 169–182. [CrossRef]
91. Costanzo, V.; Evola, G.; Infantone, M.; Marletta, L. Updated Typical Weather Years for the Energy Simulation of Buildings in Mediterranean Climate. A Case Study for Sicily. *Energies* **2020**, *13*, 4115. [CrossRef]
92. Łuczak, R.; Ptaszyński, B.; Kuczera, Z.; Życzkowski, P. Energy efficiency of ground-air heat exchanger in the ventilation and air conditioning systems. *E3S Web Conf.* **2018**, *46*, 00015. [CrossRef]
93. Congedo, P.M.; Lorusso, C.; De Giorgi, M.G.; Marti, R.; D’Agostino, D. Horizontal Air-Ground Heat Exchanger Performance and Humidity Simulation by Computational Fluid Dynamic Analysis. *Energies* **2016**, *9*, 930. [CrossRef]
94. Skotnicka-Siepsiak, A.; Wesołowski, M.; Piechocki, J. Experimental and Numerical Study of an Earth-to-Air Heat Exchanger in Northeastern Poland. *Pol. J. Environ. Stud.* **2018**, *27*, 1255–1260. [CrossRef]
95. Niu, F.; Yu, Y.; Yu, D.; Li, H. Heat and mass transfer performance analysis and cooling capacity prediction of earth to air heat exchanger. *Appl. Energy* **2015**, *137*, 211–221. [CrossRef]
96. Romanska-Zapala, A.; Bomberg, M.; Dechnik, M.; Fedorczyk-Cisak, M.; Furtak, M. On Preheating of the Outdoor Ventilation Air. *Energies* **2020**, *13*, 15. [CrossRef]

Article

Peak Power of Heat Source for Domestic Hot Water Preparation (DHW) for Residential Estate in Poland as a Representative Case Study for the Climate of Central Europe

Lukasz Amanowicz 

Institute of Environmental Engineering and Building Installations, Poznan University of Technology,
Pl. M. Skłodowskiej-Curie 5, 60-965 Poznan, Poland; lukasz.amanowicz@put.poznan.pl

Abstract: Due to the energy transformation in buildings, the proportions of energy consumption for heating, ventilation and domestic hot water preparation (DHW) have changed. The latter component can now play a significant role, not only in the context of the annual heat demand, but also in the context of selecting the peak power of the heat source. In this paper, the comparison of chosen methods for its calculation is presented. The results show that for contemporary residential buildings, the peak power for DHW preparation can achieve the same or higher value as the peak power for heating and ventilation. For this reason, nowadays the correct selection of the peak power of a heat source for DHW purposes becomes more important, especially if it uses renewable energy sources, because it affects its size and so the investment cost and economic efficiency. It is also indicated that in modern buildings, mainly accumulative systems with hot water storage tanks should be taken into account because they are less sensitive to design errors (wrongly selected peak value in the context of the uncertainty of hot water consumption) and because they result in acceptable value of peak power for DHW in comparison to heating and ventilation.

Citation: Amanowicz, L. Peak Power of Heat Source for Domestic Hot Water Preparation (DHW) for Residential Estate in Poland as a Representative Case Study for the Climate of Central Europe. *Energies* **2021**, *14*, 8047. <https://doi.org/10.3390/en14238047>

Academic Editors: Jan Danielewicz, Chi-Ming Lai and Krzysztof Rajski

Received: 20 September 2021
Accepted: 25 November 2021
Published: 1 December 2021

Publisher's Note: MDPI stays neutral with regard to jurisdictional claims in published maps and institutional affiliations.



Copyright: © 2021 by the author. Licensee MDPI, Basel, Switzerland. This article is an open access article distributed under the terms and conditions of the Creative Commons Attribution (CC BY) license (<https://creativecommons.org/licenses/by/4.0/>).

Keywords: domestic hot water; peak power; energy performance of buildings; DHW; energy transformation

1. Introduction

The energy consumption in buildings is constantly changing, mainly due to the amendments of legal requirements. Examples of such activities are, for example, energy certification, CO₂ emission limits, local programs supporting the modernization of existing facilities, as well as subsidies for new, energy-efficient buildings and systems. Currently, a lot of emphasis is placed not only on reducing the energy demand itself, but also on increasing the degree of use of renewable energy sources (RES), which favors the reduction of primary energy consumption and reduces the depletion of fossil fuel resources. It can be seen that it is not possible to clearly state how much energy consumption should be reduced, because it depends on many parameters. For example, in the paper [1], the optimum energy usage for residential buildings in developing countries is discussed as vulnerable to the current economic situation in the given country. In the last few decades, much attention has been devoted to the analysis of thermal modernization of buildings and research on the energy efficiency of heating, ventilation and air conditioning systems (HVAC). For example, the article [2] presents the results of long-term research showing energy savings resulting from the use of thermostatic valves, ranging from 7% to 23% for the analyzed cases. The results of the research presented in the article [3] showed that the use of mechanical ventilation systems with heat recovery from the air removed in residential buildings allows for significant savings in the annual amount of energy, and at the same time confirmed that recuperator systems with an integrated wall intake-exhaust devices are safe to use from a hygienic point of view. In the paper [4], the review of the heat recovery methods in ventilation was presented as a way to diminish energy

demand for heating the buildings. Another of the possibilities of reducing primary energy consumption by mechanical ventilation systems is the use of earth-to-air heat exchangers (EAHEs), which has been shown in many works, e.g., in a review article [5] or in more detailed works about supporting ventilation systems by means of ground heat exchangers, e.g., [6–8] or mechanical analysis about improving the efficiency of EAHEs, e.g., [9,10]. Building heating systems that use renewable energy sources, such as heat pumps, achieve the highest efficiency in cooperation with low-temperature heaters. In practice, surface heating systems are mainly used. The most common system is floor heating, but in works [11,12], the innovative ceiling heating and cooling panels have been presented, showing the increase in their efficiency thanks to the use of an appropriately corrugated surface. An important role for the energy efficiency of HVAC systems is also played by controlling their efficiency, which was described in the example of wall heating systems with heat pipes in the article [13]. Renewable energy sources that are most often used to meet the energy needs of buildings are the energy of the sun, wind, ground and the use of the so-called waste heat (heat recovery, i.e., from exhaust air in ventilation). The energy of the sun can be harvested by using solar collectors to prepare domestic hot water, such as in 227 houses in California (USA), the experiences of which are described in the paper [14], or those compared in terms of effectiveness in the article [15]. The collectors may be of the tubular type, such as those mentioned just now, or of the flat type, such as those reviewed in [16]. Another way to obtain energy from the sun is to use photovoltaic panels (PV panels) which are used to generate electricity and were reviewed, for example, in the paper [17]. Wind energy is used much less frequently in buildings, as electricity generation is usually carried out by large wind farms, such as offshore wind farms described in [18] or classic ones, the optimization techniques of which are described in [19]. Soil energy can be used, for example, to heat/cool the ventilation air with the aforementioned earth-to-air heat exchangers or by using ground-type heat pumps, such as those described in [20]. There are many more examples of modern systems that are aimed at decreasing the energy demand in building and increasing the efficiency of its usage. Some of them were mentioned to introduce the Reader to the background of the changes that buildings are currently undergoing in terms of energy efficiency and the structure of HVAC systems.

Due to the changes in building envelope and HVAC systems, described above, the relationship between various components of thermal balance of the buildings is constantly changing. In the article [21] one can find that in the last decades the share of energy demand for ventilation in the energy demand for ventilation and heat transfer from the building increased from about 20% to about 60%. Thanks to the better insulation of the building and using the mechanical ventilation systems with heat recovery from exhausted air and earth-to-air heat exchangers [22,23], the specific heat power for heating the building decreased from about 150 W/m^2 to about 20 W/m^2 . The heat demand for heating the hot water has also changed in the last decades, mainly because of the decreasing water consumption related to individual accounting of consumption and increasing water and energy prices. The decreased hot water usage caused the higher water consumption irregularity which influences the heating peak power of the heat source. In the literature, one can find articles presenting the results of research on the possibility of increasing the efficiency of domestic hot water preparation systems, such as [24], as well as analyzing the possibility of their integration with renewable energy sources [25], usage of phase change materials in solar domestic hot water systems [26,27] or verifying the influence of technical parameters of the hot water preparation system on its effectiveness [28]. The sheer volume of hot water consumption by building residents is also a subject of analysis. In the article [29], based on the example of several single-family houses, it was shown that the values of hot water consumption taken in the calculation of the building's energy performance may differ from the real consumption by up to 39%. The differentiation of user preferences, as well as the duration and time of hot water consumption, make it impossible to accurately determine its instantaneous, maximum flowrate. In practice, only simplified methods are used, based on empirical experience from the operation of existing systems. For this reason, in paper [30],

the authors presented a new approach of quantifying the flexibility potential of residential heat pumps in the context of stochastic character of domestic hot water usage, highlighting the probabilistic meaning of hot water consumption. In the literature on hot water systems, one can find many works that focus on increasing their energy efficiency or comfort of use. Article [31] describes a method to improve control of hot water temperature that can result in significant energy and water savings thanks to using advanced mixing valves. Investigations presented in [32] were focused on research on plate shower heat exchanger to reduce the domestic hot water energy demand. The results of the prototype tests showed the possibility of heat energy savings for a family house up to 300 kWh/year. However, the analysis did not refer to the multitude of calculation methods and the selection of the peak power of devices for DHW preparation. The impact of the use of nanoparticles in the solar fluid on the efficiency of the DHW preparation system was analyzed in [33]. The improvement in the efficiency of the system was not analyzed against the current changes in peak power for heating and ventilation of buildings. In [34], instantaneous heat exchanger with chemical-based disinfection was analyzed, which enables the reduction of hot water temperature in the DHW system, which resulted in a reduction in the circulation heat loss up to 66% for the analyzed multi-family building. The selection of the system power in the context of the amount of hot water demand was not the subject of research. Another way to reduce the energy consumption of a hot water system is to use shower heat exchangers for heat recovery in residential buildings. The possibility of using such a system was presented, for example, in articles [35,36]. Energy savings in DHW systems can also be achieved by appropriate control of their operation, which was demonstrated in the work [37], which focuses on the analysis of the heat storage tank. The improvement of the energy efficiency of the DHW solar system due to the mechanical modification of the heat storage tank structure was the subject of the research presented in [38]. On the other hand, Chandra & Matuska [39] analyzed the quality of temperature stratification in heat storage tanks in the context of the energy efficiency of the DHW system. Heat storage tanks in DHW systems can also take advantage of the phase change phenomenon, if they are filled with PCM materials, as shown, for example, in the papers [40–42]. In turn, the paper [43] presents the importance of the storage tank (cold water inlets and obstacles) structure itself for the energy efficiency of the DHW preparation system, which, if appropriate, may result in up to 15% higher efficiency compared to the non-optimized structure. Optimization of the storage tank structure may also contribute to shortening, by up to 10%, the time of preparing hot water, which improves the comfort of its use and has been analyzed in [44]. In all of these studies on heat storage tanks, the impact of their use on the peak power of the heat source in the context of the available computational methods was not analyzed. The subject of the stochastic nature of the variability of hot water consumption by users was discussed in many articles. In the work [45], neural networks were used to predict the demand for hot water both in single houses and in multi-family buildings. In the analysis presented in the article [46], the DHWcalc and TRNSYS software was used to determine district heating load profiles for domestic hot water preparation. Probabilistic model for predicting occupancy and domestic hot water use was also presented in [47]. In the paper [48], the smart-meter was used to measure the instantaneous consumption of hot water, and the results of the analysis provided in the paper showed that “statistical and machine learning analysis can forecast the seasonal DHW demand”. Nevertheless, the tools used in the above-mentioned works go beyond the workshop of typical engineers, as well as scientists who deal with the subject of improving the energy efficiency of DHW systems by improving control systems or changing the design of system components. For this reason, this paper focuses on the comparison of generally available and popular methods of calculating peak power for DHW preparation purposes. The work [49], as well as [50], deal with the topic of life cycle costs in the context of hot water preparation systems. Important issues of the use of materials from their acquisition through the production and utilization process were emphasized; however, it was not analyzed in the context of various methods of selecting the peak power of heat sources and/or DHW system components. An

interesting idea for increasing energy efficiency is the combination of an air-conditioning system and hot water preparation, which was presented, for example, in the works [51,52]. Thanks to this solution, waste heat from the cooling process of rooms, especially in warm climates, can be used to prepare hot water for household needs.

Due to the changes in the HVAC systems mentioned above, the current view on the selection of heat source peak power in the context of hot water preparation should be revised. In the review paper [53] on sustainable and energy-efficient domestic hot water systems, many publications and studies have been analyzed. Among them, the analyses that concern the determination of the peak power of a heat source for the purposes of preparing domestic hot water in the context of mentioned above changes in the consumption ratio were not found. In this paper, it is considered as a knowledge gap, and at the same time, an important issue to study from a practical point of view. In this article, this problem is discussed in the context of various methods of determining the peak power of a heat source for the purposes of preparing domestic hot water. Contrary to the work presented in the article [29], the focus is given on the power of the heat source, not on the energy consumed in the annual cycle of its operation. The changes that have taken place in buildings in terms of improving the thermal insulation of partitions and improving the efficiency of HVAC systems, in particular the use of heat recovery from the exhaust air in mechanical ventilation systems, have changed the ratio between the peak thermal power needed to prepare domestic hot water and the power for heating and ventilation. This means the need to revise the calculation methods used so far. The above literature review on DHW systems shows that this issue has not been analyzed. DHW systems are usually analyzed in terms of the possibility of using renewable energy sources or in terms of their efficiency, but little attention is paid to the peak power selection which affects the size, cost, heat loss, efficiency and the very possibility of cooperation with RES. Improper assumption of peak power (usually oversizing) will not allow to achieve the required savings and reduce the effectiveness of even the most theoretically effective solution. On the other hand, undersized systems will not provide users with a sufficient level of comfort.

2. Materials and Methods

2.1. Calculating the Heating Power for Preparing Hot Water

The universal formula for calculating the heating power for preparing domestic hot water can be given as:

$$\dot{Q} = \rho_w \cdot \dot{V}_{hw} \cdot c_w \cdot (t_{hw} - t_w) \text{ [kW]} \quad (1)$$

where:

ρ_w —density of water, [kg/m³];

\dot{V}_{hw} —volumetric flowrate of hot water, [m³/s];

c_w —specific heat of water, [kJ/(kg·K)];

t_{hw} —temperature of hot water, usually assumed as 55 °C to avoid diseases connected with bacteria Legionella;

t_w —temperature of cold water, usually assumed as 5 °C for surface water sources and 10 °C for deep ground water sources.

In Equation (1), the assumption of the stream of hot water \dot{V}_{hw} (hot water consumption) is crucial.

2.2. Hot Water Consumption—Standard Method

The instantaneous amount of hot water consumption depends on the behavior of users, which cannot be predicted. Older people and people with small children, people who work at home and people who work shifts, etc., use water in different amounts and at different times. In existing buildings, you can measure the current water consumption with a water meter. This information is not sufficient to predict water consumption in newly built facilities whose users are unknown. Moreover, depending on the users (whether the same people still occupy the buildings) and on time (whether the users age, change

jobs, habits, etc.), the measured value will change. Therefore, it cannot be defined once or unequivocally. For this reason, some simplifications and assumptions as well as various calculation methods are used in practice. Interestingly, they can result in values that differ significantly from each other, as demonstrated later in this work. The literature review shows that the hot water usage is difficult to predict due to unpredictable user behavior. Hot water consumption can be predicted on the basis of many statistical data from already existing buildings, inhabited by people with a similar consumption profile. For this purpose, probabilistic methods or neural networks are used, as indicated by the authors of the studies presented in the works, respectively, [46,47]. Due to the important role of the method of use for temporary water abstraction, the authors of the studies [48] write clearly not about its calculation, but “prediction”, emphasizing the stochastic nature of this consumption, depending on the way the system is used by users. The authors of the review [54] also emphasize a significant impact on energy consumption in buildings, which, although it concerns heating, ventilation and lighting systems, seems to indicate a similar unpredictability of their use, as in the case of DHW systems. The authors of the model for optimizing energy consumption in a building [55], based on user behavior survey, also refer to “prediction” rather than “calculating” the actual values of energy consumption in a building.

Figure 1 shows the example of variability of hot water consumption in the case of a multi-family housing estate for three selected days of the week (Sunday, Thursday, Saturday) at different hours of the day. The chart is taken from a handbook on district heating [56].

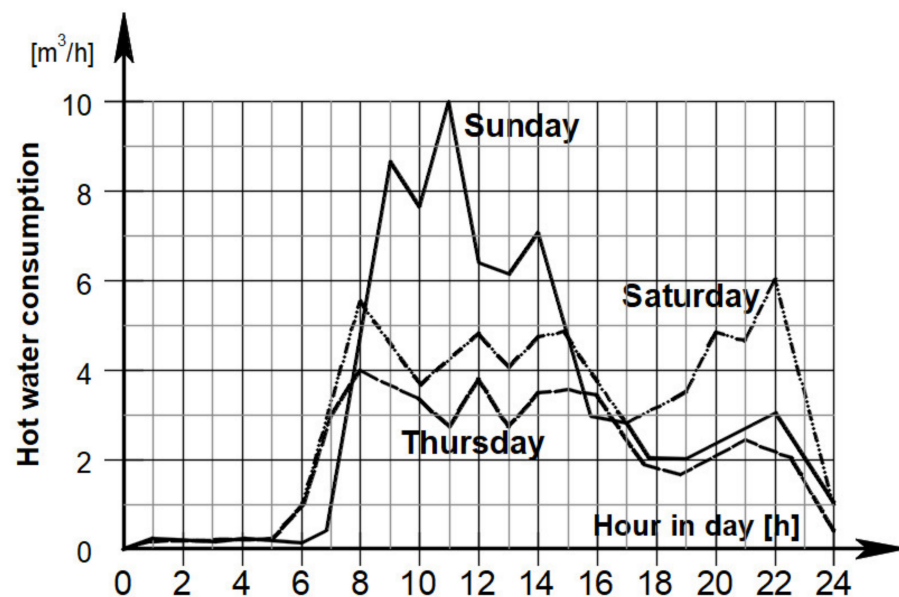


Figure 1. An example of hot water consumption for exemplary residential estate [56].

Due to the high variability of hot water consumption during the day, as well as week, month or year, the method described in the standard PN-B/92-01706 can be used. It allows us to determine the temporary hot water consumption assuming the average daily water consumption per capita and the number of inhabitants. The average daily consumption of hot water is a value that is also subject to fluctuations, not only depending on the users, but also in the long term, e.g., with a change in water and energy prices, a change in the wealth of a given community, or a change in the level of hygiene awareness. Nevertheless, it is a value that is easier to verify, e.g., on the basis of data from water companies. In this method, the daily consumption expressed in $\text{dm}^3/\text{person}/\text{day}$ is then divided by the time of consumption during the day and multiplied by the coefficient of hourly consumption

irregularity k_{h1} , which is an increasing factor aimed at calculating the peak (maximum) value of hourly water consumption:

$$\dot{V}_{hw,max} = \frac{\dot{V}_{hw,av} \cdot M}{\tau} \cdot k_{h1} \quad (2)$$

$$k_{h1} = 9.32 \cdot M^{-0.244} \quad (3)$$

where:

$\dot{V}_{hw,max}$ —peak (maximum) hourly hot water consumption, [dm³/s];

$\dot{V}_{hw,av}$ —average daily hot water consumption per person, [dm³/person/day];

M —the number of residents, [–];

τ —time of hot water consumption during the day, assumed usually as 18–20 h = 64,800–72,000 s, taking into account the time for sleeping;

k_{h1} —coefficient of hourly consumption irregularity, [–].

The coefficient k_{h1} decreases with the increase in the number of inhabitants, which reflects the assumption that the more people live in the housing estate, the greater the uniformity of heat consumption, i.e., the less probable a situation is that many people will take a shower or turn on the faucet in the sink at the same time. This assumption means that in the case of a small group of people, the risk of simultaneous consumption, significantly increased compared to the average value, is greater. This approach seems to be justified also due to the greater accumulation and hence the inertia of large domestic hot water preparation systems designed to serve a larger number of inhabitants.

In the standard PN-B/92-01706 the hot water consumption at the level of 110–130 dm³/person/day was recommended. Due to the water consumption changes (decreased hot water consumption to a level of about 60 dm³/person/day) in 2011, in articles [57,58], it was recommended to assume adjusted value of the lower water stream and the higher irregularity of the consumption:

$$k_{h2} = 8.8 \cdot M^{-0.167} \quad (4)$$

It should be noted that further changes in domestic hot water consumption will affect the value of peak consumption and the irregularity coefficient will increase. A survey presented in the paper [59] showed that “*the perspective of environmental protection is not a sufficient motivator to save energy for heating domestic hot water*” and therefore only the water and energy price model can drive further changes.

2.3. Hot Water Consumption—Experimental Measurements

The second method, taken into account in this study, is calculating the hot water consumption with approximated formulas based on the experimental data published in a book about hot water preparation systems [60] in 2008. Approximated results enable calculation of average and maximum hot water consumption as a function of the number of residents with the assumption of probability that this value would be exceeded (Equations (5)–(8)). For example, the probability of 1% means that the water stream can be exceeded once in one day for 100 days.

$$\dot{V}_{hw,av,1\%} = 0.006386 \cdot M^{0.5} + 0.00102M \text{ [dm}^3/\text{s]} \quad (5)$$

$$\dot{V}_{hw,av,10\%} = 0.003048 \cdot M^{0.5} + 0.00102M \text{ [dm}^3/\text{s]} \quad (6)$$

$$\dot{V}_{hw,max,1\%} = 0.03017 \cdot M^{0.5} + 0.00102M \text{ [dm}^3/\text{s]} \quad (7)$$

$$\dot{V}_{hw,max,10\%} = 0.01429 \cdot M^{0.5} + 0.00102M \text{ [dm}^3/\text{s]} \quad (8)$$

Due to the fact that hot water consumption is random, the use of probability for a mathematical description of this process seems to be the most reliable method. Moreover,

this method allows us to select the comfort level understood as the probability of failure to maintain the continuity of hot water supply within the set parameters (stream and temperature). In this way, in the process of designing the system, it is possible to decide on its size, taking into account the compromise between the comfort (higher consumption values taken for calculations) and the cost of obtaining it (higher cost of purchasing and operating an oversized system), adjusting the solution to the expectations and financial possibilities of users. In this way, one can consciously design a larger system for a five-star hotel and a smaller one for a lower-standard hotel. However, it should be borne in mind that the presented formulas are the result of the approximation of measurement data of housing estates located in a one single city—Szczecin, Poland, Central Europe—for a limited set of buildings and only in the time period covered by the research. This means that the data used for calculations may not be inadequate for other settlements located in other cities or at a different time. It is a specificity related to the estimation of hot water consumption. Consequently, continuous monitoring of hot water consumption should be the subject of research. Recently, there have been published papers that show the changes that have occurred in this area during the COVID-19 pandemic, e.g., [61].

2.4. Hot Water Consumption—Sander’s Method

Another method for calculation of hot water consumption, taken into account in this study, is the Sander’s method described for example in the book [56]. In this method, the water stream for heating source peak power calculation is assumed on the basis of the hot water volume flowing from the water device, temperature of water and time of use:

$$\dot{V}_{\text{hw}} = \frac{\sum N_i \cdot V_i}{\tau \cdot 60} \cdot \varphi \text{ [dm}^3/\text{s]} \quad (9)$$

where:

N_i —number of each type of devices, [–];

V_i —the volume of hot water used during single use, [dm³];

τ —time of single use, [min];

φ —coefficient of non-simultaneous consumption of hot water, [–].

Input values for calculating different water devices are presented in Table 1. The value of the coefficient of non-simultaneous consumption of hot water φ can be read from Figure 2. The coefficient is used to take into account that not all water devices will be used at the same time. This is especially important in the case of housing estates, where the greater value of peak power should be taken for the selection of heat exchangers (e.g., housing heat exchangers), and smaller for the selection of the central heat source (taking into account the non-simultaneous consumption, reading the coefficient for the total number of water devices supplied by the heat source at the whole estate).

Table 1. Typical values of volume flowing from the water device, temperature of water and time of use for calculating the peak power for hot water preparation using Sander’s method.

Device	V [dm ³]	t _{hw} [°C]	τ [min]
Sink	10–15	35–40	2–3
Kitchen sink	30–50	55	5
Bath	150–250	40	15–20
Shower	50	40	6

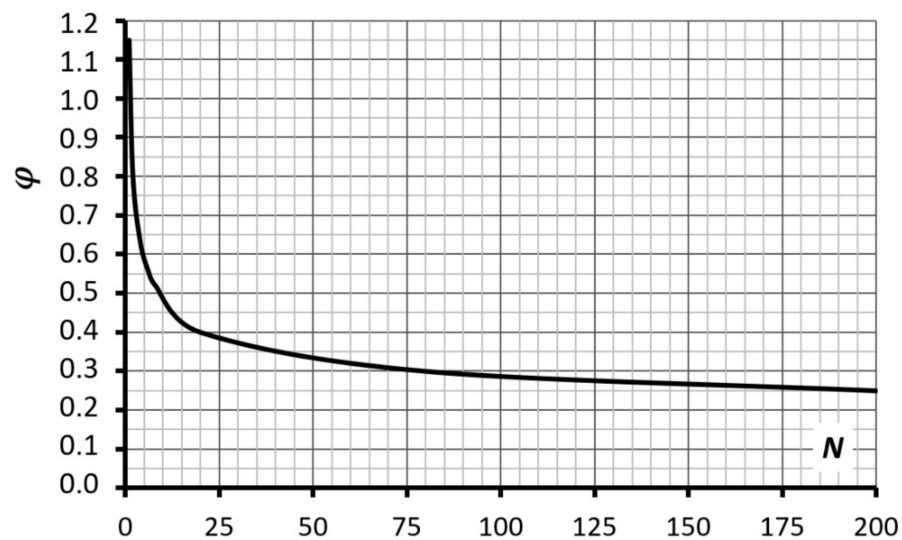


Figure 2. Value of coefficient of non-simultaneous consumption of hot water [56].

In practice for multi-family buildings, it is assumed that only the biggest water device should be taken into account as a representative for each flat. This approach assumes that a temporary and small consumption of hot water from other devices, such as a sink, will not result in a lack of power in the local hot water preparation system, which has a large thermal inertia. Then Equation (9) takes a simplified form, where only the number of baths or showers is taken into account:

$$\dot{V}_{hw} = \frac{N_{bath/shower} \cdot V_{bath/shower}}{\tau \cdot 60} \cdot \varphi \text{ [dm}^3/\text{s]} \quad (10)$$

For the bath, it can be assumed that the $V_{bath} = 150\text{--}200 \text{ dm}^3$ of water at the temperature of $40 \text{ }^\circ\text{C}$ ($100\text{--}133$ of water at the temperature of $55 \text{ }^\circ\text{C}$) is used in a time $\tau = 15$ min. For showers $V = 50 \text{ dm}^3$ at the temperature of $40 \text{ }^\circ\text{C}$ (35 dm^3 at the temperature of $55 \text{ }^\circ\text{C}$) in a time of 6 min. In this method, one can easily take into account the presence of hot water storage tanks by setting a longer water preparation time τ , i.e., 60 min. It is possible to discuss the value of the hot water temperature that should be used in the calculations. The results of studies of two single-family houses in Denmark [62] showed that the temperature of the water used in the shower was $35.5 \text{ }^\circ\text{C}$ to $40.4 \text{ }^\circ\text{C}$, and for hand washing $20.5 \text{ }^\circ\text{C}$ to $26.5 \text{ }^\circ\text{C}$. Taking the bath as a representative device and assuming the hot water temperature of $40 \text{ }^\circ\text{C}$ seems to be justified in the context of the quoted research results.

To calculate the peak power, universal formula (Equation (1)) can be used, but it has to be noted that for different water devices, different values of hot water temperature should be taken into account (see Table 1).

3. Results

3.1. Comparison of Hot Water Consumption

All above-mentioned formulas result in different values of hot water stream. The differences in results are very high, as is shown in Figures 3–5. The assumptions for calculations with Equation (1) are as follows:

- The number of residents per one flat: $M/N = 3.5$;
- PN-B/92, av.: $V_{hw,av} = 120 \text{ dm}^3/\text{person}/\text{day}$;
- PN-B/92, max.: $V_{hw,av} = 120 \text{ dm}^3/\text{person}/\text{day}$, k_h calculated from Equation (2);
- PN modified 2011, av.: $V_{hw,av} = 60 \text{ dm}^3/\text{person}/\text{day}$;
- PN modified 2011, max.: $V_{hw,av} = 60 \text{ dm}^3/\text{person}/\text{day}$, k_h calculated from Equation (3);
- PN-B/92 and PN modified: time of hot water consumption during the day: 18 h;
- Sander, bath, flow-type: $V = 100 \text{ dm}^3$, $\tau = 15$ min;

- Sander, bath, accumulative: $V = 100 \text{ dm}^3, \tau = 60 \text{ min}$;
- Sander, shower, flow-type: $V = 35 \text{ dm}^3, \tau = 15 \text{ min}$;
- Sander, shower, accumulative: $V = 35 \text{ dm}^3, \tau = 60 \text{ min}$.

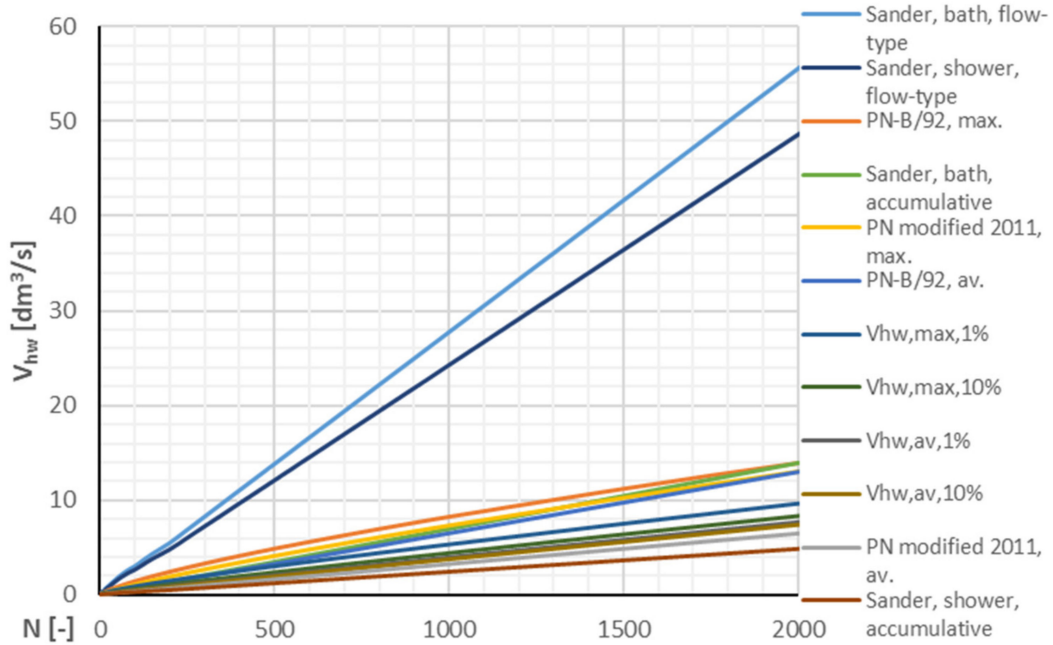


Figure 3. Comparison of hot water consumption calculated with different formulas, the number of flats: $N = 0-2000$.

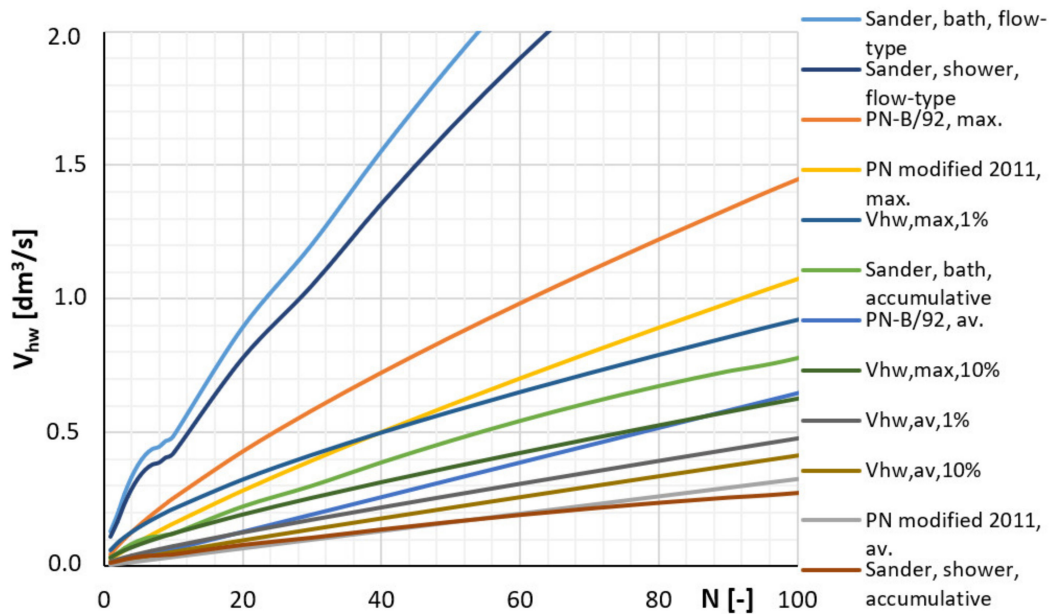


Figure 4. Comparison of hot water consumption calculated with different formulas the number of flats: $N = 1-100$.

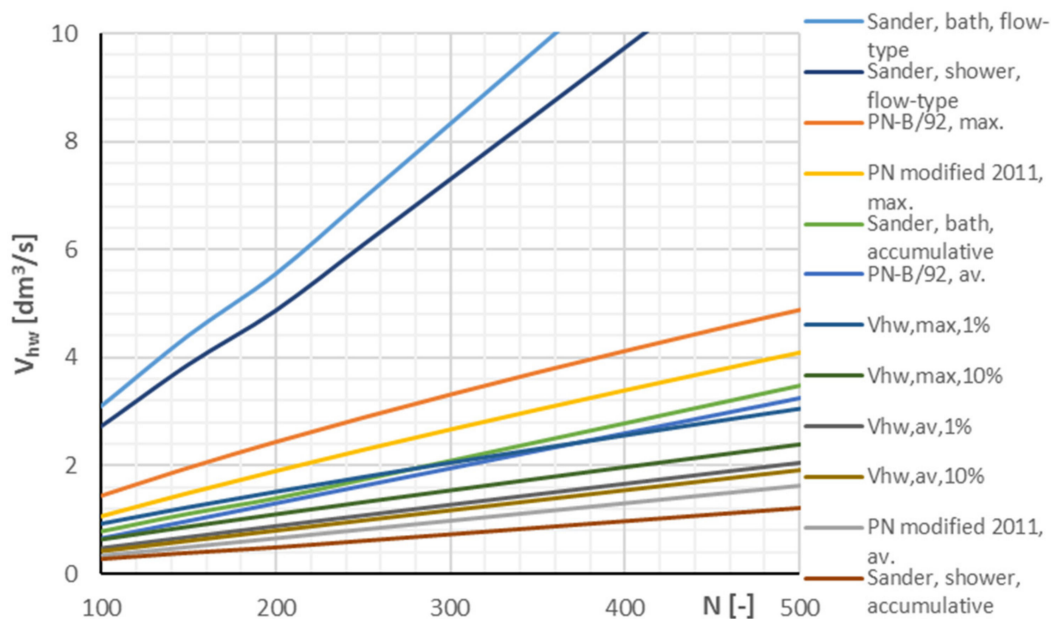


Figure 5. Comparison of hot water consumption calculated with different formulas, the number of flats: $N = 100\text{--}500$.

Results presented in Figures 3–5 show that:

- The highest value of hot water stream is obtained with Sander’s method for flow-type system (without accumulation tanks), assuming baths as representative water devices;
- The lowest value of hot water stream is obtained with Sander’s method for accumulative-type system (with accumulation tanks), assuming showers as representative water devices;
- Similar value as for Sander’s method with accumulation tanks assuming showers was obtained using standard PN-B/92-01706 method and average (not maximum) stream of water (without taking into account coefficient k_h); for the number of residents 0 to 50 the Sander’s method results in higher values and for $N > 50$ lower values (about 33%).

3.2. Peak Power of the Heat Source

For calculation of the heat source power for housing estate the power demand for heating the buildings and for hot water preparation should be taken into account. For buildings with high thermal inertia, the priority of hot water preparation can be assumed to reduce the peak power of the heat source. For traditional buildings with a high demand for thermal power for heating, the peak power could be calculated as a sum of heating needs and average hot water needs, but in the contemporary low energy buildings, this approach fails because of low heating needs. In Figure 4, the comparison of heat demand for heating the buildings in different insulation standards is presented. The results were prepared with assumptions:

- $Q_{hw,av}$ calculated from PN-B/92-01706, $V_{hw} = 60 \text{ dm}^3/\text{person}/\text{day}$;
- $Q_{hw,max}$ calculated from PN-B/92-01706, $V_{hw} = 60 \text{ dm}^3/\text{person}/\text{day}$, k_h calculated from Equation (3);
- Q_{co} calculated with assumption: $q_{co1} = 100 \text{ W}/\text{m}^2$, $q_{co2} = 50 \text{ W}/\text{m}^2$, $q_{co3} = 20 \text{ W}/\text{m}^2$;
- The number of residents per one flat $M/N = 3.5$;
- The average area of a single flat: $A = 55 \text{ m}^2$.

In Figure 6, the heating power for preparing hot water calculated from the Sander’s method (for shower, flow-type and accumulative) and $V_{hw,max,1\%}$ are also presented.

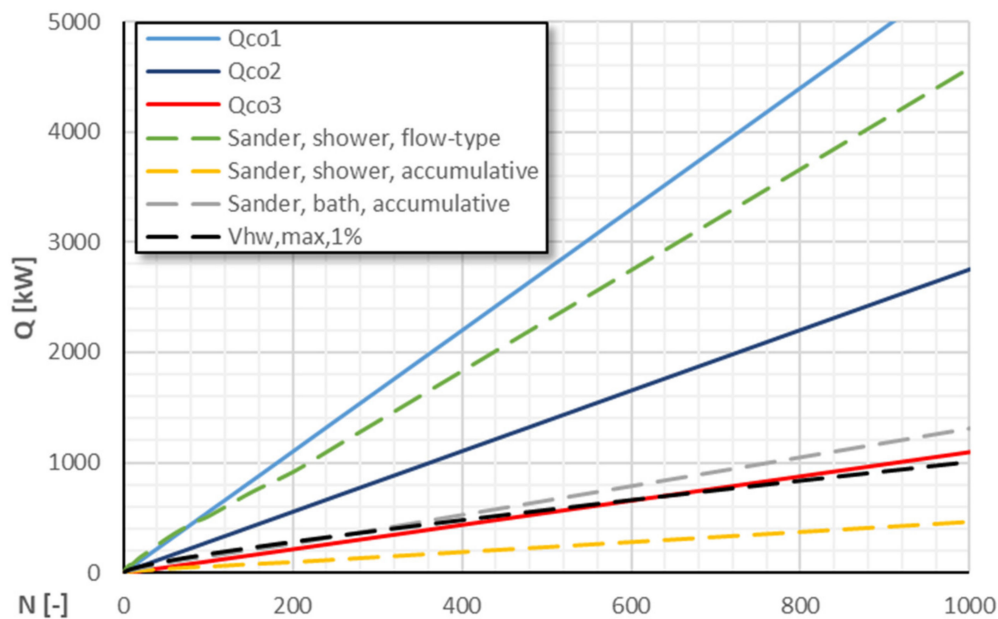


Figure 6. Heat source peak power for heating the buildings in different insulation standards and for preparing the hot water—comparison for N residents.

4. Discussion

The introduction to the work presents information on the energy transformation of buildings towards low-energy buildings. In the future, it will lead to the construction of nearly zero energy buildings (nZEB) or even plus energy buildings—as indicated by the case study showing the methodology of designing such facilities [63]. The results of this analysis showed that with the reduction of the thermal power for heating and ventilation purposes, the proportions between the peak power for these purposes and the power necessary for the preparation of domestic hot water changed significantly, as shown in Figure 6. It can therefore be seen that for low-energy multi-family buildings, the priority of hot water can be not sufficient for heating up hot water, especially when the baths are used instead of showers. For such buildings, the storage tanks are recommended to diminish the heat source peak power. In the context of diminished energy demand for heating and ventilation of the building, the priority of domestic hot water cannot be assumed without checking the peak power for hot water preparation. For the energy efficient buildings, the peak power for heating water can be the same or even higher than the peak power for heating and ventilation purposes. This indicates the need for changes in the approach to designing the peak power of a heat source in countries with a climate such as in Central Europe, where so far in traditional construction, the demand for heating and ventilation purposes was dominant.

In this study, the following methods of calculating the peak power for domestic hot water preparation were analyzed:

- (1) PN-B/92-01706;
- (2) Experimental results;
- (3) Sander's method (flow-type and accumulative).

Each of the methods can be calibrated by changing the input data. In the case of the method based on experimental results, there is a possibility to choose a formula with a different probability of exceeding the peak consumption of hot water.

Method (1) PN-B/92-01706 is outdated and is based on non-updated values of daily hot water demand and uses an unverified coefficient of unevenness of hot water usage. Correcting—making real—the value of daily consumption does not guarantee obtaining reliable results. The method should be updated and validated against experimental data,

taking into account the large number of objects analyzed. An interesting concept would be to make the results dependent on the chosen usage profile, which would be in line with the contemporary occupant-oriented designing trend.

Method (2) is based on the experimental data from the past that was averaged from measurements for a few selected buildings in a single city. For this reason, it is difficult to consider them universal. The advantage of this approach is to obtain the result of the peak hot water stream with information about the probability of the frequency of its exceeding (1% or 10%). Thus, this method enables the user to choose the degree of comfort of receiving hot water, and thus adjust it to the standard of the facility or the wealth of the users' wallet.

Method (3) Sander's method is based on the basic equations from the theory of heat flow. Therefore, it is the easiest to interpret physically, and it is also the easiest to verify the correctness of the entered data, because it is based on data on the amount of water flowing out at a given time from a given equipment. This method makes it possible to assume the hot water temperature depending on the regarded water device and to perform calculations for flow-type or accumulative systems. The only uncertain element of this method is the assumption of the simultaneous consumption factor, which depends on the number of water devices in a given building/estate. It is a data that can be read from a table or graph and cannot be confirmed personally. Nevertheless, according to the author, this method seems to inspire the greatest confidence, and in the case of the use of accumulation systems, results in peak heat power that is acceptable for modern buildings with low heat demand for other purposes (heating and ventilation).

5. Conclusions

Results of the work presented above show that:

- Different methods of calculating hot water consumption result in very divergent results;
- For the number of flats $n = 1$ to 100, the lowest values of hot water consumption are obtained with sander's method (shower, accumulative) and PN-B/92 (average stream, modified in 2011);
- The hot water consumption in the real buildings with the probability of exceed 1% $v_{hw,max,1\%}$ (recommended in book [58]) is almost two times higher than the lowest ones;
- The average value calculated from PN-B/92 for 1–80 flats is lower than $v_{hw,max,10\%}$ and for $n > 80$ is higher;
- For $n = 1$ –80, $v_{hw,max,1\%}$ is the most similar to the maximum water stream calculated from pn-b/92 modified in 2011;
- For $n = 100$ –500, $v_{hw,max,1\%}$ is the most similar to sander's (bath, accumulative);
- The maximum water stream calculated from PN-B/92 modified in 2011 for $n = 100$ –500 is about 16–34% higher than $v_{hw,max,1\%}$;
- The peak power for heating the hot water in the flow-type system can be a few times higher than the peak power needed for heating and ventilation purposes of the contemporary low-energy building.

The present study shows that a thorough analysis of the domestic hot water system is now necessary, as this element may be decisive in the selection of the peak power of the heat source. This is particularly important when using renewable energy sources (RES), when the cost of purchasing oversized units can frustrate investment and discourage RES use. The results of this study show that the reduction of source peak power should then be achieved by using accumulation systems with hot water tanks, which results in an acceptable peak power for DHW preparation in comparison with the power needed for heating and ventilation.

Funding: This research was funded by the Polish Ministry of Science and Higher Education, grant number 504 101/0713/SBAD/0935.

Institutional Review Board Statement: Not applicable.

Informed Consent Statement: Not applicable.

Data Availability Statement: Not applicable.

Conflicts of Interest: The author declares no conflict of interest.

References

1. Basińska, M.; Koczyk, H.; Szczechowiak, E. Sensitivity analysis in determining the optimum energy for residential buildings in Polish conditions. *Energy Build.* **2015**, *17*, 307–318. [CrossRef]
2. Cholewa, T.; Siuta-Olcha, A.; Balaras, C.A. Actual energy savings from the use of thermostatic radiator valves in residential buildings—Long term field evaluation. *Energy Build.* **2017**, *151*, 487–493. [CrossRef]
3. Ratajczak, K.; Amanowicz, Ł.; Szczechowiak, E. Assessment of the air streams mixing in wall-type heat recovery units for ventilation of existing and refurbishing buildings toward low energy buildings. *Energy Build.* **2020**, *227*, 110427. [CrossRef]
4. Zender-Świercz, E. A Review of Heat Recovery in Ventilation. *Energies* **2021**, *14*, 1759. [CrossRef]
5. Agrawal, K.K.; Misra, R.; Agrawal, G.D.; Bhardwaj, M.; Jamuwa, D.K. The state of art on the applications, technology integration, and latest research trends of earth-air-heat exchanger system. *Geothermics* **2019**, *82*, 34–50. [CrossRef]
6. Wei, H.; Yang, D. Performance evaluation of flat rectangular earth-to-air heat exchangers in harmonically fluctuating thermal environments. *Appl. Therm. Eng.* **2019**, *162*, 114–262. [CrossRef]
7. Żukowski, M.; Topolańska, J. Comparison of thermal performance between tube and plate ground-air heat exchangers. *Renew. Energy* **2018**, *115*, 697–710. [CrossRef]
8. Wei, H.; Yang, D.; Du, J.; Guo, X. Field experiments on the effects of an earth-to-air heat exchanger on the indoor thermal environment in summer and winter for a typical hot-summer and cold-winter region. *Renew. Energy* **2021**, *167*, 530–541. [CrossRef]
9. Liu, Z.; Sun, P.; Xie, M.; Zhou, Y.; He, Y.; Zhang, G.; Chen, D.; Li, S.; Yan, Z.; Qin, D. Multivariate optimization and sensitivity analysis of an experimental vertical earth-to-air heat exchanger system integrating phase change material with Taguchi method. *Renew. Energy* **2021**, *173*, 401–414. [CrossRef]
10. Yang, L.H.; Hu, J.W.; Chiang, Y.C.; Chen, S.L. Performance analysis of building-integrated earth-air heat exchanger retrofitted with a supplementary water system for cooling-dominated climate in Taiwan. *Energy Build.* **2021**, *242*, 110949. [CrossRef]
11. Wojtkowiak, J.; Amanowicz, Ł. Effect of surface corrugation on cooling capacity of ceiling panel. *Therm. Sci. Eng. Prog.* **2020**, *19*, 100572. [CrossRef]
12. Wojtkowiak, J.; Amanowicz, Ł.; Mróz, T. A new type of cooling ceiling panel with corrugated surface—Experimental investigation. *Int. J. Energy Res.* **2019**, *43*, 7275–7286. [CrossRef]
13. Amanowicz, Ł. Controlling the Thermal Power of a Wall Heating Panel with Heat Pipes by Changing the Mass Flowrate and Temperature of Supplying Water—Experimental Investigations. *Energies* **2020**, *13*, 6547. [CrossRef]
14. Sanguinetti, A.; Outcault, S.; Alston-Stepnitz, E.; Moezzi, M.; Ingle, A. Residential solar water heating: California adopters and their experiences. *Renew. Energy* **2021**, *170*, 1081–1095. [CrossRef]
15. Zielinko, P.; Krawczyk, D.A. Comparison of the Efficiency of Solar Collectors in Terms of the Working Medium—Review of Selected Technical Solutions. *Environ. Sci. Proc.* **2021**, *9*, 5. [CrossRef]
16. Alam, T.; Balam, N.B.; Kulkarni, K.S.; Siddiqui, M.I.H.; Kapoor, N.R.; Meena, C.S.; Kumar, A.; Cozzolino, R. Performance Augmentation of the Flat Plate Solar Thermal Collector: A Review. *Energies* **2021**, *14*, 6203. [CrossRef]
17. Bhakre, S.S.; Sawarkar, P.D.; Kalamkar, V.R. Performance evaluation of PV panel surfaces exposed to hydraulic cooling—A review. *Sol. Energy* **2021**, *224*, 1193–1209. [CrossRef]
18. Díaz, H.; Soares, C.G. Review of the current status, technology and future trends of offshore wind farms. *Ocean. Eng.* **2020**, *209*, 107381. [CrossRef]
19. Balasubramanian, K.; Thanikanti, S.B.; Subramaniam, U.; Sudhakar, N.; Sichilalu, S. A novel review on optimization techniques used in wind farm modelling. *Renew. Energy Focus* **2020**, *35*, 84–96. [CrossRef]
20. Wang, Z.; Luther, M.B.; Amirkhani, M.; Liu, C.; Horan, P. State of the Art on Heat Pumps for Residential Buildings. *Buildings* **2021**, *11*, 350. [CrossRef]
21. Amanowicz, Ł.; Szczechowiak, E. Zasady projektowania systemów wentylacji budynków energooszczędnych. *Ciepłownictwo Ogrzewnictwo Wentylacja* **2017**, *48*, 72–78. [CrossRef]
22. Amanowicz, Ł.; Wojtkowiak, J. Validation of CFD model for simulation of multi-pipe earth-to-air heat exchangers (EAHEs) flow performance. *Therm. Sci. Eng. Prog.* **2018**, *5*, 44–49. [CrossRef]
23. Amanowicz, Ł. Influence of geometrical parameters on the flow characteristics of multi-pipe earth-to-air heat exchangers—Experimental and CFD investigations. *Appl. Energy* **2018**, *226*, 849–861. [CrossRef]
24. Cholewa, T.; Siuta-Olcha, A.; Anasiewicz, R. On the possibilities to increase energy efficiency of domestic hot water preparation systems in existing buildings—Long term field research. *J. Clean. Prod.* **2019**, *217*, 194–203. [CrossRef]
25. Dudkiewicz, E.; Fidorów-Kaprawy, N. The energy analysis of a hybrid hot tap water preparation system based on renewable and waste sources. *Energy* **2017**, *127*, 198–208. [CrossRef]
26. Douvi, E.; Pagkalos, C.; Dogkas, G.; Koukou, M.G.; Stathopoulos, V.N.; Caouris, Y.; Vrachopoulos, M.G. Phase Change Materials in Solar Domestic Hot Water Systems: A review. *Int. J. Thermofluids* **2021**, *10*, 100075. [CrossRef]

27. Jachura, A.; Sekret, R. Life Cycle Assessment of the Use of Phase Change Material in an Evacuated Solar Tube Collector. *Energies* **2021**, *14*, 4146. [CrossRef]
28. Zukowski, M.; Jezierski, W. New Deterministic Mathematical Model for Estimating the Useful Energy Output of a Medium-Sized Solar Domestic Hot Water System. *Energies* **2021**, *14*, 2753. [CrossRef]
29. Ratajczak, K.; Michalak, K.; Narojczyk, M.; Amanowicz, Ł. Real Domestic Hot Water Consumption in Residential Buildings and Its Impact on Buildings' Energy Performance—Case Study in Poland. *Energies* **2021**, *14*, 5010. [CrossRef]
30. You, Z.; Zade, M.; Kumaran Nalini, B.; Tzscheuschler, P. Flexibility Estimation of Residential Heat Pumps under Heat Demand Uncertainty. *Energies* **2021**, *14*, 5709. [CrossRef]
31. Rahmatmand, A.; Vratonjic, M.; Sullivan, P.E. Energy and thermal comfort performance evaluation of thermostatic and electronic mixing valves used to provide domestic hot water of buildings. *Energy Build.* **2020**, *212*, 109830. [CrossRef]
32. Vavříčka, R.; Boháč, J.; Matuška, T. Experimental development of the plate shower heat exchanger to reduce the domestic hot water energy demand. *Energy Build.* **2022**, *254*, 111536. [CrossRef]
33. Saeed, T.; Ibrahim, M. Improving solar domestic hot water effectiveness using Al₂O₃ and ZnO nanoparticles: Focusing on annual energy-saving. *J. Taiwan Inst. Chem. Eng.* **2021**, *124*, 205–215. [CrossRef]
34. Benakopoulos, T.; Tunzi, M.; Salenbien, R.; Vanhoudt, D.; Svendsen, S. Low return temperature from domestic hot-water system based on instantaneous heat exchanger with chemical-based disinfection solution. *Energy* **2021**, *215*, 119211. [CrossRef]
35. Nagpal, H.; Spriet, J.; Murali, M.K.; McNabola, A. Heat Recovery from Wastewater—A Review of Available Resource. *Water* **2021**, *13*, 1274. [CrossRef]
36. Kordana, S.; Pochwat, K.; Styś, D.; Starzec, M. Opportunities and Threats of Implementing Drain Water Heat Recovery Units in Poland. *Resources* **2019**, *8*, 88. [CrossRef]
37. Huang, T.; Yang, X.; Svendsen, S. Multi-mode control method for the existing domestic hot water storage tanks with district heating supply. *Energy* **2020**, *191*, 116517. [CrossRef]
38. Erdemir, D.; Atesoglu, H.; Altuntop, N. Experimental investigation on enhancement of thermal performance with obstacle placing in the horizontal hot water tank used in solar domestic hot water system. *Renew. Energy* **2019**, *138*, 187–197. [CrossRef]
39. Pal Chandra, Y.P.; Matuska, T. Numerical prediction of the stratification performance in domestic hot water storage tanks. *Renew. Energy* **2020**, *154*, 1165–1179. [CrossRef]
40. Dogkas, G.; Konstantaras, J.; Koukou, M.K.; Vrachopoulos, M.G.r.; Pagkalos, C.h.; Stathopoulos, V.N.; Pandis, P.K.; Lymperis, K.; Coelho, L.; Rebola, A. Development and experimental testing of a compact thermal energy storage tank using paraffin targeting domestic hot water production needs. *Therm. Sci. Eng. Prog.* **2020**, *19*, 100573. [CrossRef]
41. Abdelsalam, M.Y.; Teamah, H.M.; Lightstone, M.F.; Cotton, J.S. Hybrid thermal energy storage with phase change materials for solar domestic hot water applications: Direct versus indirect heat exchange systems. *Renew. Energy* **2020**, *147*, 77–88. [CrossRef]
42. Thonon, M.; Zalewski, L.; Gibout, S.; Franquet, E.; Fraisse, G.; Pailha, M. Experimental Comparison of Three Characterization Methods for Two Phase Change Materials Suitable for Domestic Hot Water Storage. *Appl. Sci.* **2021**, *11*, 10229. [CrossRef]
43. Malec, A.; Cholewa, T.; Siuta-Olcha, A. Influence of Cold Water Inlets and Obstacles on the Energy Efficiency of the Hot Water Production Process in a Hot Water Storage Tank. *Energies* **2021**, *14*, 6509. [CrossRef]
44. Obstawski, P.; Janaszek-Mańkowska, M.; Ratajski, A. Diagnostics of a Domestic Hot Water Storage Tank under Operating Conditions. *Processes* **2021**, *9*, 1771. [CrossRef]
45. Maltais, L.-G.; Gosselin, L. Predictability analysis of domestic hot water consumption with neural networks: From single units to large residential buildings. *Energy* **2021**, *229*, 120658. [CrossRef]
46. Braas, H.; Jordan, U.; Best, I.; Orozaliiev, J.; Vajen, K. District heating load profiles for domestic hot water preparation with realistic simultaneity using DHWcalc and TRNSYS. *Energy* **2020**, *201*, 117552. [CrossRef]
47. Rouleau, j.; Ramallo-González, A.P.; Gosselin, L.; Blanchet, P.; Natarajan, S. A unified probabilistic model for predicting occupancy, domestic hot water use and electricity use in residential buildings. *Energy Build.* **2019**, *202*, 109375. [CrossRef]
48. Lee, J.Y.; Yim, T. Energy and flow demand analysis of domestic hot water in an apartment complex using a smart meter. *Energy* **2021**, *229*, 120678. [CrossRef]
49. Raluy, R.G.; Dias, A.C. Domestic hot water systems: Environmental performance from a life cycle assessment perspective. *Sustain. Prod. Consum.* **2021**, *26*, 1011–1020. [CrossRef]
50. Liu, W.; Chen, C.; Wu, H.; Guo, C.; Chen, Y.; Liu, W.; Cui, Z. Environmental life cycle assessment and techno-economic analysis of domestic hot water systems in China. *Energy Convers. Manag.* **2019**, *199*, 111943. [CrossRef]
51. Congedo, P.M.; Baglivo, C.; Carrieri, L. Application of an unconventional thermal and mechanical energy storage coupled with the air conditioning and domestic hot water systems of a residential building. *Energy Build.* **2020**, *224*, 110234. [CrossRef]
52. Jia, J.; Lee, W.L.; Cheng, Y.; Tian, Q. Can reversible room air-conditioner be used for combined space and domestic hot water heating in subtropical dwellings? Techno-economic evidence from Hong Kong. *Energy* **2021**, *223*, 119911. [CrossRef]
53. Pomianowski, M.Z.; Johra, H.; Marszal-Pomianowska, A.; Zhang, C. Sustainable and energy-efficient domestic hot water systems: A review. *Renew. Sustain. Energy Rev.* **2020**, *128*, 109900. [CrossRef]
54. Chen, S.; Zhang, G.; Xia, X.; Chen, Y.; Setunge, S.; Shi, L. The impacts of occupant behavior on building energy consumption: A review. *Sustain. Energy Technol. Assess.* **2021**, *45*, 101212. [CrossRef]
55. Amasyali, K.; El-Gohary, N.M. Real data-driven occupant-behavior optimization for reduced energy consumption and improved comfort. *Appl. Energy* **2021**, *302*, 117276. [CrossRef]

56. Bagiński, Z.; Amanowicz, Ł. *Ciepłownictwo. Projektowanie Kotłowni i Ciepłowni*; Wydawnictwo Politechniki Poznańskiej: Poznań, Poland, 2018; ISBN 978-83-7775-519-8.
57. Nowakowski, E. Współczynniki godzinowej nierównomierności zużycia ciepłej wody. *Rynek Instalacyjny* **2011**, 7–8, 76–78.
58. Nowakowski, E. Współczynniki chwilowych nierównomierności zużycia ciepłej wody. *Rynek Instalacyjny* **2011**, 9, 60–61.
59. Kordana-Obuch, S.; Starzec, M.; Słyś, D. Assessment of the Feasibility of Implementing Shower Heat Exchangers in Residential Buildings Based on Users' Energy Saving Preferences. *Energies* **2021**, *14*, 5547. [CrossRef]
60. Szaflik, W. *Projektowanie Instalacji Ciepłej Wody w Budynkach Mieszkalnych*; Ośrodek Informacji Technika Instalacyjna w Budownictwie: Warsaw, Poland, 2011; ISBN 978-83-7457-049-7.
61. Kim, D.; Yim, T.; Lee, J.Y. Analytical study on changes in domestic hot water use caused by COVID-19 pandemic. *Energy* **2021**, *231*, 120915. [CrossRef]
62. Marszał-Pomianowska, A.; Jensen, R.L.; Pomianowski, M.; Larsen, O.K.; Jørgensen, J.S.; Knudsen, S.S. Comfort of Domestic Water in Residential Buildings: Flow, Temperature and Energy in Draw-Off Points: Field Study in Two Danish Detached Houses. *Energies* **2021**, *14*, 3314. [CrossRef]
63. Radomski, B.; Mróz, T. The Methodology for Designing Residential Buildings with a Positive Energy Balance—Case Study. *Energies* **2021**, *14*, 5162. [CrossRef]

Article

New Deterministic Mathematical Model for Estimating the Useful Energy Output of a Medium-Sized Solar Domestic Hot Water System

Mirosław Zukowski ^{1,*}  and Walery Jezierski ²

¹ Department of HVAC Engineering, Faculty of Civil Engineering and Environmental Sciences, Białystok University of Technology, Wiejska 45E Street, 15-351 Białystok, Poland

² Department of Energy Efficient Construction and Geodesy, Faculty of Civil Engineering and Environmental Sciences, Białystok University of Technology, Wiejska 45E Street, 15-351 Białystok, Poland; w.jezierski@pb.edu.pl

* Correspondence: m.zukowski@pb.edu.pl

Abstract: According to the authors of this paper, the mathematical point of view allows us to see what sometimes cannot be seen from the designer's point of view. The aim of this study was to estimate the influence of the most important parameters (volume of heat storage tanks, daily consumption of domestic hot water, optical efficiency, heat loss coefficient, and total area of a solar collector) on the thermal power output of solar domestic hot water (SDHW) system in European climatic conditions. Three deterministic mathematical models of these relationships for Madrid, Budapest, and Helsinki were created. The database for the development of these models was carried out using computer simulations made in the TRNSYS software environment. The SDHW system located at the Białystok University of Technology (Poland) was the source of the measurement results used to validate the simulation model. The mathematical optimization procedure showed that the maximum annual useful energy output that can be obtained from 1 m² of gross collector area is 1303 kWh in the case of Madrid, 918.5 kWh for Budapest, and 768 kWh for Helsinki weather conditions.

Keywords: thermal solar collectors; useful energy output; energy simulations; solar domestic hot water system; deterministic mathematical model

Citation: Zukowski, M.; Jezierski, W. New Deterministic Mathematical Model for Estimating the Useful Energy Output of a Medium-Sized Solar Domestic Hot Water System. *Energies* **2021**, *14*, 2753. <https://doi.org/10.3390/en14102753>

Academic Editor: Carlo Renno

Received: 7 April 2021

Accepted: 10 May 2021

Published: 11 May 2021

Publisher's Note: MDPI stays neutral with regard to jurisdictional claims in published maps and institutional affiliations.



Copyright: © 2021 by the authors. Licensee MDPI, Basel, Switzerland. This article is an open access article distributed under the terms and conditions of the Creative Commons Attribution (CC BY) license (<https://creativecommons.org/licenses/by/4.0/>).

1. Introduction

The effects of climate change are becoming more and more visible around the world. It manifests itself mainly in extreme weather events, loss of biodiversity and acidification of waters. The continuous increase in the global mean temperature directly affects the global rise in sea level. The global action plan to combat far-reaching climate change was set out in the Paris Agreement and signed by 195 countries in December 2015 [1]. The next step towards achieving climate neutrality was the decision of the European Commission (EC) taken in December 2020 [2]. EC proposed a 55% reduction in CO₂ emissions in 2030 compared to 1990 levels.

One way to achieve this difficult goal is the widespread use of the conversion of solar radiation into heat and electricity. The most effective devices implementing this process are thermal solar collectors, which support the heating of domestic hot water (DHW). It is difficult to achieve optimal performance of these systems at the design stage and later in the operating conditions. This is due to the large number of components in this system combined with the time-varying effects of weather conditions. Therefore, there are many methods of designing solar domestic hot water (SDHW) systems. Generally, we can divide them into two groups [3]. The first type of methods are based on analytical formulas describing the heat exchange phenomena occurring in these systems. An example might be one of the most frequently used method, i.e., the f-Chart [4,5]. Based on the value of

solar radiation intensity, ambient temperature, and DHW demand, the amount of energy that can be provided by the designed system is calculated. The calculation algorithm of this method is based on the function of two variables whose values are influenced by the design and operational parameters. The error of the f-Chart method largely depends on the accuracy of the data describing a given system and ranges from 5% to 10% [6].

The second way to determine the performance of SDHW systems are computer energy simulations. They allow for very accurate modelling of the equipment characteristics, the system of pipes connecting them, and weather conditions. A large number of parameters describing the entire system requires the use of specialized software. TRNSYS, Design-Builder (based on a computing engine EnergyPlus), GetSolar, T*SOL, RETScreenI, and Polysun are the most popular computer programs often used in scientific analysis.

The authors of this paper focused the most attention on the application of the TRNSYS (Transient System Simulation Program) software package to simulate the operation of the SDHW system during the literature review. This computer program was used in this study.

Essabbani et al. [7] simulated the operation of a SDHW system consisting of 20 m² of flat plate solar collectors (FPC), a 300-L storage tank, and an electric heater. The testing facility was located in Oujda (Morocco) and the period of analysis was from the December 2011 to March 2012. The influence of total solar radiation, ambient temperature, and daily DHW consumption on the system performance was analyzed experimentally. Additionally, a numerical simulation of this installation was applied using the TRNSYS software. As a result of this research, it was found that the average share of solar energy in the total energy demand was 45% in the winter season. In March, the solar fraction was higher than in other months. However, the maximum required auxiliary energy was 740 MJ in December.

Ayompe et al. [8] developed and validated a model of a solar water heating system with forced circulation used in typical European residential homes. The tested rig consisted of two flat plate collectors (a total area of 4 m²), an evacuated tube collector (ETC) with 30 heat pipe tubes, two 300 L hot water storage tanks, a control unit, and a pump station. A quasi-steady state simulation of this SDHW system were made using the TRNSYS software. This model was validated based on the results of measurements performed on a bench located in Dublin (Ireland). As it turned out, the mean absolute error in calculations of the heat collected by the collectors was 14.1% in the case of FPC circuit and 16.8% in the case of ETC loop.

The optimization of SDHW systems intended for single-family housing was performed by Hobbi and Siddiqui [9]. In this analysis, a forced indirect circulation system with a heat exchanger separating the solar circuit from the DHW circuit was considered. A south-facing flat collector with a slope equal to Montreal's latitude (45.5 degrees) was assumed. The share of energy obtained from solar collectors in the total energy demand for water heating was used as the optimization parameter. Computer simulations using TRNSYS software were used in this study. It was found that the designed system can satisfy 83% to 97% (in summer) and 30% to 62% (in winter) of the demand for DHW. It should be noted that the authors of this article did not use any special optimization methods.

The model of the SDHW system consisting of two FPC (5 m² of the absorber area), a heat storage tank (volume of 0.4 m³), and a coil heat exchanger was developed by Mongibello et al. [10]. The operation of this system was simulated using the code written in MatLab environment and using TRNSYS software. The input data was the results of the measurements made at the ENEA Portici Research Center. The results of the calculations from both solvers were compared and it turned out that they are characterized by the good accordance.

Lima et al. [11] simulated a thermosiphon water heating system equipped with FPC, a storage tank, and an auxiliary heater in the climate conditions of Sao Paulo (Brazil). The hourly meteorological data collected by the Institute of Astronomy and Geosciences of the University of de Sao Paulo were used in the calculations. The main conclusion of this analysis was the following: the optimal configuration of this kind of thermosiphon system depends on the investor's concerns and local electricity prices.

The model of the SDHW system equipped with a heat pipe ETC and cooperating with an additional gas heater was made by Mehmood et al. [12] in the TRNSYS software environment. An experimental setup installed at National University of Sciences and Technology, Islamabad (Pakistan) was developed to validate the simulation model. A comparison of the results of calculations and experimental tests showed that the discrepancy between them ranges from 5 to 9%. Based on the computational analysis, it was found that the modelled system can replace conventional gas water heaters, providing 23% to 56% fossil fuel savings annually.

The performance of the ETC and FPC collectors were compared by Mohasseb and Kasaeian [13] in two different climatic conditions: cold weather-Tabriz (Iran) and hot-Bandar-Abbas (Iran). The operation of two SDHW systems with different collectors was simulated using the TRNSYS software. Based on the results of the calculations, it was found that the climatic conditions and inlet temperature had a greater influence on the operation of FPC than ETC. Besides, the annual useful energy from ETC is 30% higher than from FPC in cold climate, and 15% in hot weather conditions.

Mathematical equations that give relationships between the characteristic parameters of the SDHW system were not developed in the analyses described above. Additionally, optimization algorithms were not used to solve the issues related to the selection of the optimal variant.

The main disadvantages of computer simulations is the relatively long time needed for creating a model of the system and the large number of input data. They are dedicated to scientific analysis rather than being a tool used by designers. Therefore, it was decided to apply a deterministic mathematical modelling in order to simplify the method of the energy yield estimation from thermal solar collectors. The article presents a new approach for determining the annual useful energy output based on a multivariable function of volume of heat storage tanks, daily consumption of DHW, and the basic parameters of a solar collector. Climatic conditions are not included as one of the variables because they consist of many factors and cannot be described by one coherent indicator. In optimization analysis, this type of parameter is called uncontrollable and heterogeneous. That is why the numerical experiment was performed separately for three European weather zones. This is a drawback of the method presented here, but on the other hand, the development of a model for a specific climate zone allows to achieve high accuracy of the modelling results.

2. Materials and Methods

2.1. Model of SDHW System Developed in the TRNSYS Software Environment

The development of a simplified method of determining the energy yield from thermal collectors consisted of three main stages. First, the SDHW model of the system was created using the TRNSYS software. The second step was to validate this model based on a measurement database. Deterministic mathematical modelling was the third stage of this study. The selected TRNSYS simulation results created a database for this modelling. The selection of appropriate variants was based on the symmetrical three-level plan.

The modelled system consisted of a circuit with a battery of solar collectors (glycol solution as a heat transfer medium (HTM)) and a DHW circuit (water as a HTM). Both loops were separated by a plate compact heat exchanger. The other elements were heat storage tanks, separate pumps for each loop, a control and regulation system, and an auxiliary water heater. The schematic diagram of the model is shown in Figure 1. The list of the main modules creating this model is presented in Table 1. The model was built on the basis of an example solution presented in [14].

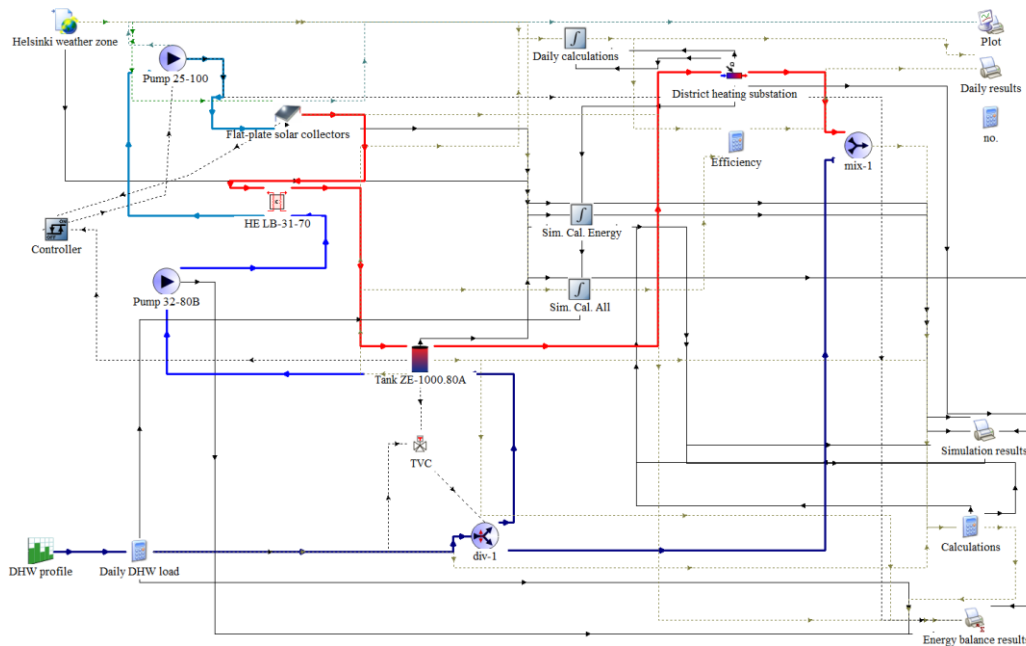


Figure 1. Scheme of the model of SDHW system developed in the TRNSYS software environment.

Table 1. List of the main modules of the SDHW system model.

Type Number	Module Name
1	Solar Collector; Quadratic Efficiency, 2nd Order Incidence Angle Modifiers
11	Controlled flow diverter
14	Time Dependent Forcing Function
15	Weather Data Processor; Combines data reading, radiation processing and sky temperature calculations
24	Quantity Integrator
91	Heat Exchanger with Constant Effectiveness
114	Single Speed Pump
115	Controller for Tempering Valves-Heating Mode
138	Auxiliary Fluid Heater
158	Cylindrical Storage Tank
165	ON/OFF Differential Controller

An important parameter that must be considered when creating this type of model is the consumption profile of DHW for occupants in the housing sector. An example of hourly prediction of DHW consumption was presented in [15]. This research work was based on data from the historical time series of DHW heat use in hotels in Norway. In the review of existing studies on hot water demand [16], we can find structured information on the DHW consumption patterns specified in technical standards for different types of buildings. The authors also noted the important impact of the mains water temperature on the energy consumption for DHW heating. A Time Dependent Forcing Function (TDF) that allowed to employ the DHW consumption profile was used in this simulation. The repeated pattern of this function is established by a set of time-dependent data points shown for this case in Table 2. In order to reduce the time step during the calculations, linear interpolation is used.

Table 2. DHW profile assumed in the model.

Hour	0–7	8	9	10	11	12	13–17	18	19	20	21	22	23–24
Fraction	0	0.2	0.2	0	0.1	0.1	0	0	0.1	0.1	0.1	0.1	0

Three different locations are considered in the current analysis. These are Madrid (Spain), Budapest (Hungary), and Helsinki (Finland) for which different mean annual values of the main water temperatures were assumed: 17 °C, 15 °C, and 12 °C, respectively. On the other hand, the temperature of the hot water collected in the storage tank was constant for each variant and amounted to 55 °C.

Presented above the model of SDHW system, due to its characteristics, is the most dedicated to typical multi-family apartment buildings. That is why the title of the article uses the term “medium size”.

2.2. Validation of the SDHW System Model

As is well known, even a precisely developed numerical model may be inaccurate. Therefore, it was decided to compare the results of computer simulations with the measurement results. The source of the measurement database was the SDHW system located at the Bialystok University of Technology (Poland). The screenshot of the automatic operating parameters recording system is shown in Figure 2. A more detailed description of this measuring stand can be found in [17].

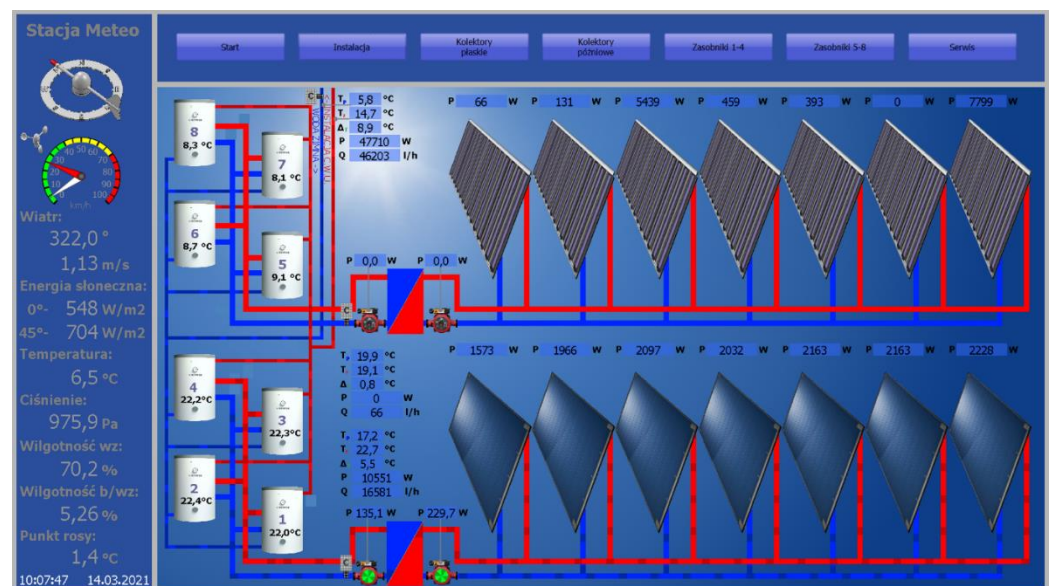


Figure 2. The screenshot of the scheme of the SDHW system and working online data acquisition system.

This active solar heating system consists of:

- Seven rows of flat plate collectors, five connected in series in each row, with a total gross area of 71.9 m²;
- Seven rows of evacuated tube collectors, three connected in series in each row, with an active total area of 74.45 m²;
- Eight heat storage tanks with a volume of 1 m³ each (four for each type of collectors).

The set of FPC was selected for comparative analysis. These solar panels have the following characteristics:

- Coefficient of collector efficiency—0.784 (-);
- Heat loss coefficient—3.64 W/(m²K);
- Temperature dependence heat loss coefficient—0.00185 W/(m²K²);
- Maximum flow rate—0.000033 m³/s;
- Gross area of single panel—2.054324 m².

In order to estimate the accuracy of the model, the measurement results of an annual useful energy output Q_{SC} (in kWh/m²) from 5 years (2016–2020), were selected. The

measurement of this value was made using a heat meter placed on the solar loop next to the heat exchanger. Figure 3 shows the amount of energy supplied by the solar collectors during the year as a function of the intensity of solar radiation Q_{SR} (in kWh/m²) incident perpendicular to the plane of the collectors (blue rhombus).

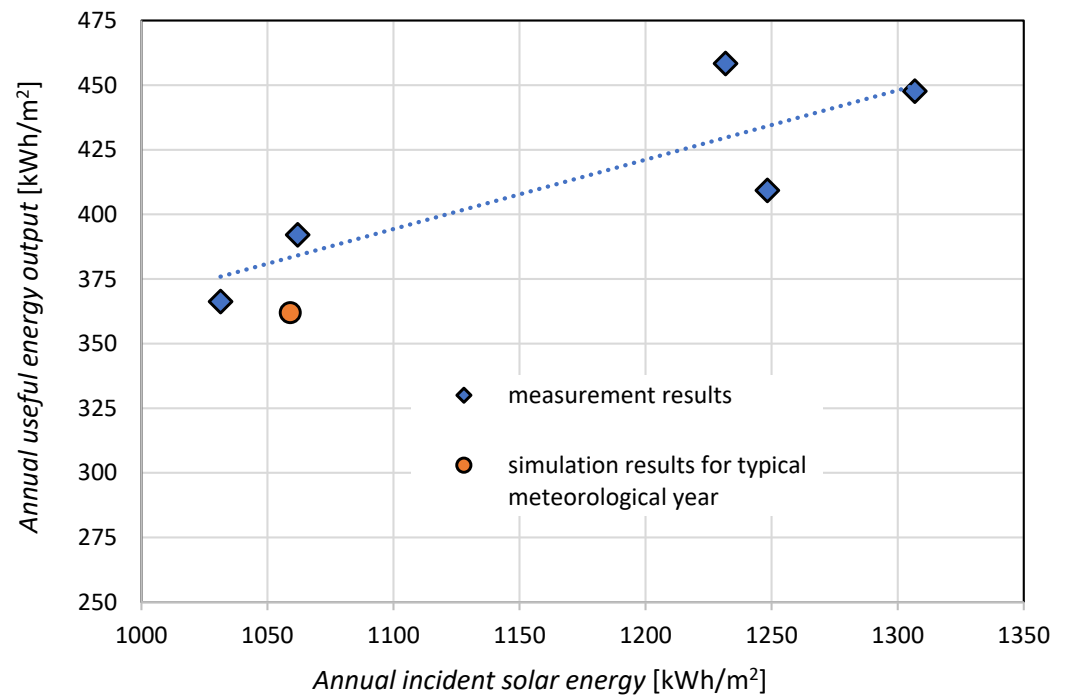


Figure 3. Dependence of annual useful energy output on the intensity of solar radiation for the FPC collector system.

The results of these measurements can be approximated (dashed line in Figure 3) by the following equation: $Q_{SC} = 0.2685 \cdot Q_{SC} + 98.946$.

The error resulting from comparing the result of the computer simulation (circle in Figure 3) for a typical meteorological year (TMY) with the value calculated from the above equation for TMY conditions is 5.87%. Therefore, it should be considered that the developed model of SDHW system reflects the trend of the real complex physical process with relatively good accuracy.

2.3. Mathematical Model for Determining the Solar Collector Useful Energy Output

Mathematical modelling was used as the research method. It allows to describe the operation of the tested object, determine the necessary output data, and determine the optimal values of the input parameters using mathematical relationships. The use of mathematical modelling allows you to resign from physical modelling, reduce the number of samples, and the labor intensity compared to the physical experiment [18]. The main component in such procedure is the mathematical model. Utilitarianism, efficiency, and practical usefulness of this type of model can be ensured by developing short algorithms. In order to obtain the desired information, the most important factors/parameters describing the object under study or phenomenon should be used.

The main goal of this research was to determine the influence of the most important parameters on thermal performance of SDHW systems in European climatic conditions. Thus, it was assumed that the annual useful energy output Q_{SC} of the solar collectors is an objective function Y , and the value of Y depends on the following parameters:

- Volume of heat storage tanks V_{ST} [m³] (variable X_1),
- Solar collector total area F_{SC} [m²] (variable X_2),
- Intercept (maximum) efficiency of solar collector η_o [-] (variable X_3),

- Heat loss coefficient a_1 [W/(m²K)] (variable X_4),
- Daily consumption of DHW m [kg/day] (variable X_5).

The useful energy output makes a clear physical sense and is strongly explicit. The selected factors (X_1 – X_5) are measurable, controllable, independent, and consistent, i.e., they meet the basic requirements of mathematical modelling [19]. It should be noted that climatic conditions cannot be considered as a parameter in such mathematical models. This factor is presented by a set of various meteorological indicators, which are difficult to combine with one coherent parameter. In optimization, this is the so-called heterogeneous and uncontrollable parameter. As mentioned before, it was decided to choose three different locations: (group I) Madrid (Spain)—($Q_{I,SC} = Y_{I,i}$), (group II) Budapest (Hungary)—($Q_{II,SC} = Y_{II,i}$), and (group III) Helsinki (Finland)—($Q_{III,SC} = Y_{III,i}$), the characteristics of which are shown in Table 3. The parameters listed in this table were calculated using the TRNSYS software using the data for a typical meteorological year. Additionally, three charts that show the variability of the basic meteorological parameters during the year for three selected locations are created. Figure 4 shows the average daily air temperature, Figure 5 shows wind velocity, and the distribution of total horizontal solar radiation is presented in Figure 6.

Table 3. List of the main modules of the SDHW system model.

Group Number	Town	Average Annual Outside Temperature [°C]	Average Annual Wind Velocity [m/s]	Solar Beam Radiation on Horizontal Surface [kWh/m ²]	Solar Diffuse Radiation on Horizontal Surface [kWh/m ²]
I	Madrid	13.9	2.6	1006	654
II	Budapest	10.4	3.0	529	668
III	Helsinki	4.5	3.6	463	483

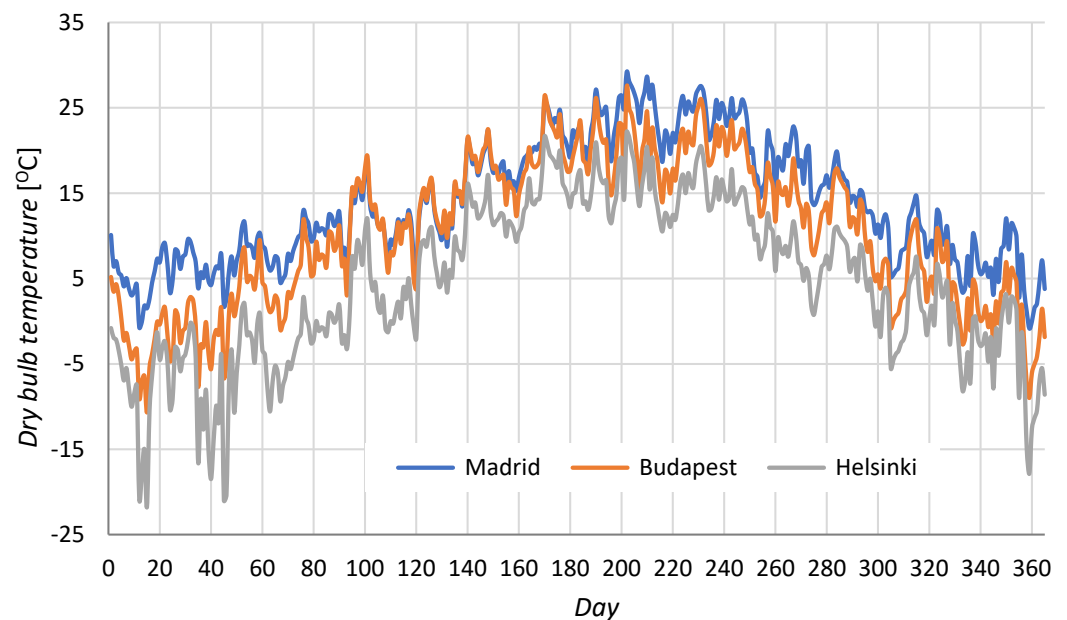


Figure 4. Average daily dry bulb temperature.

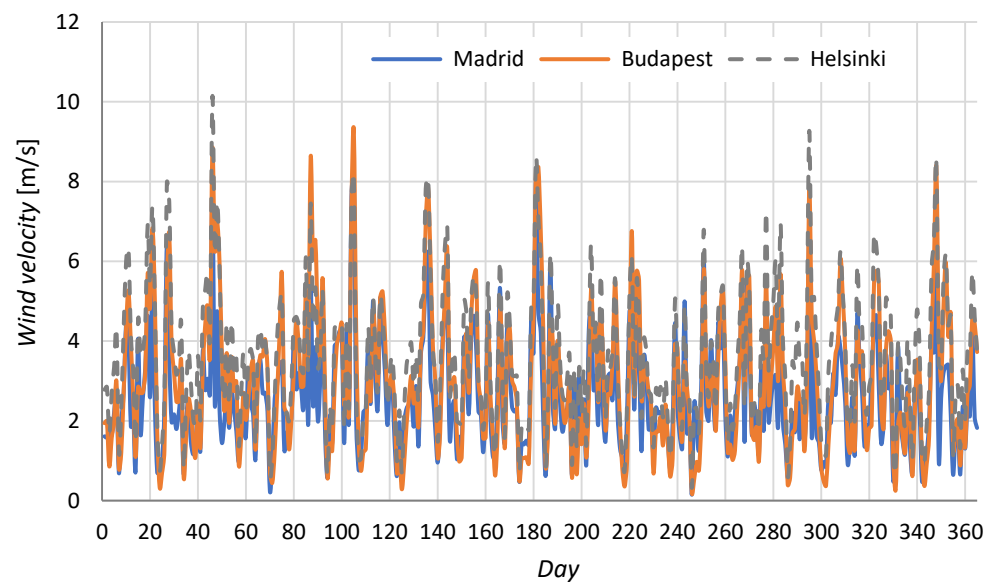


Figure 5. Average daily wind velocity.

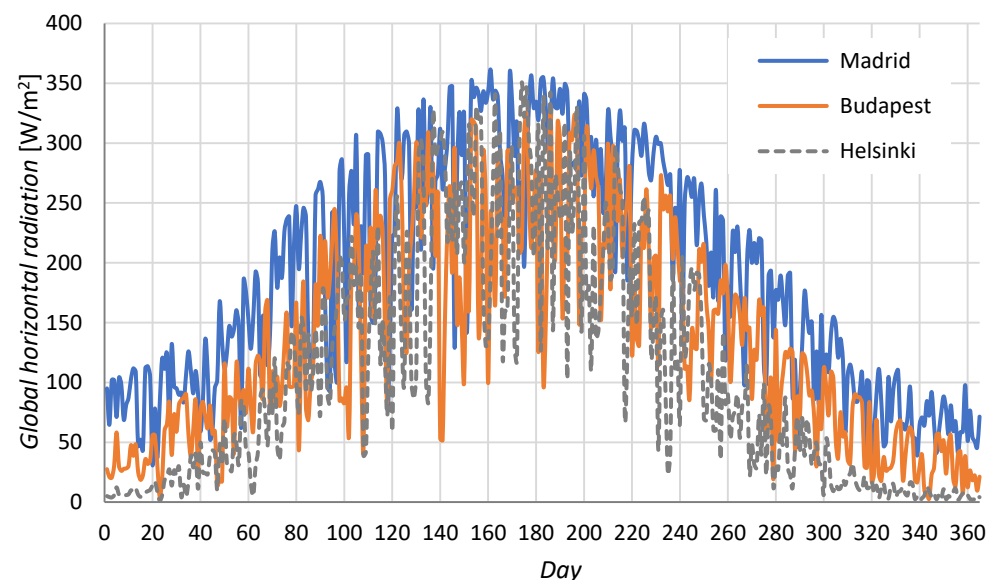


Figure 6. Average daily global solar radiation incident on a horizontal plane.

As can be seen from the characteristics presented in Table 3, the best conditions for converting solar energy into the heat exist in Madrid. This location is characterized by a high average annual temperature of the outside air, relatively low windiness, and a high value of solar radiation with a higher share of beam fraction (61%). Budapest is a city with moderate weather conditions. In this case, the total intensity of solar radiation is relatively high, but a predominance of the diffusion fraction (56%) is observed. The worst conditions in terms of installation of solar collectors are in Helsinki. There is a low outside air temperature, the lowest insolation value, and a relatively high average wind velocity.

Each of these locations differs in latitude and the share of direct and diffused solar radiation. Therefore, the optimal solar panel inclination angle β has been determined for each city separately. The results of the multivariate calculations are presented in the form of three graphs in Figure 7 for Madrid, Figure 8 for Budapest, and Figure 9 for Helsinki. The maximum annual useful energy output allowed to determine the optimal value of β , which is 36 degrees for Madrid, 39.5 degrees for Budapest, and 47.5 degrees for Helsinki. In the case of Madrid, we can observe an interesting phenomenon. It consists in the fact that the

optimal inclination of the collector is in a wide range from 35 to 44 degrees with only small deviations. The opposite is Budapest, where we have a very clearly marked maximum.

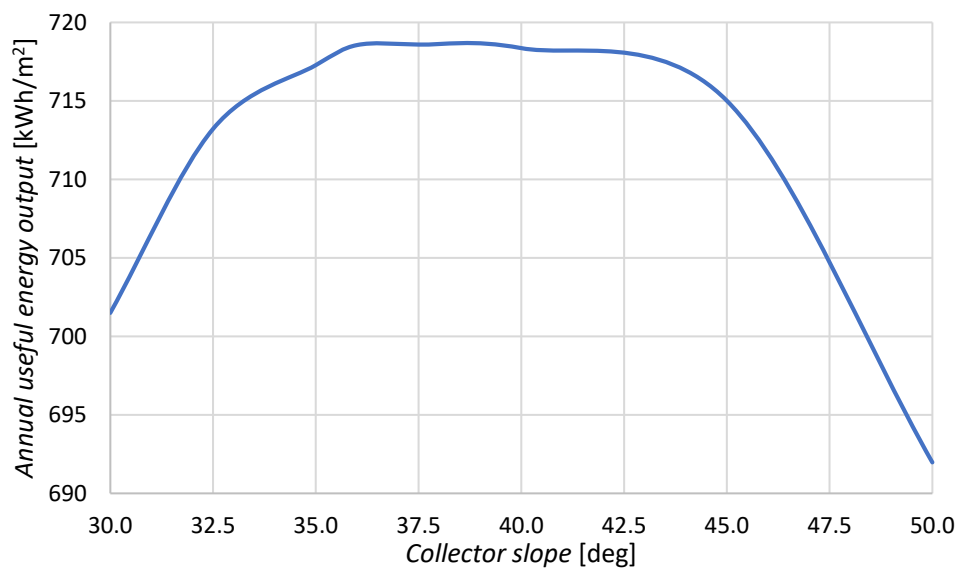


Figure 7. Dependence of the inclination angle of the solar collector on annual useful energy output for Madrid.

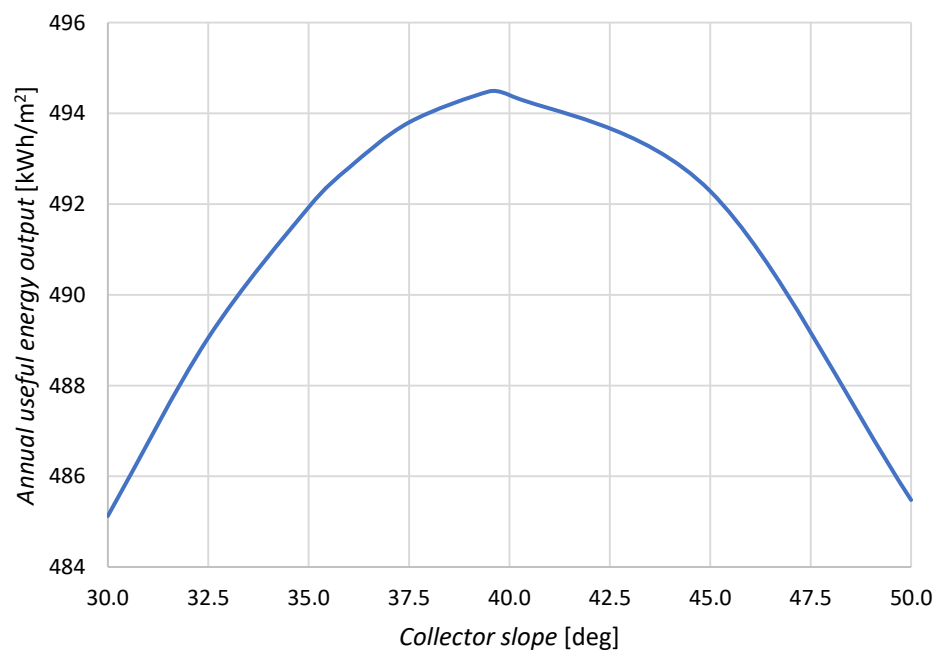


Figure 8. Dependence of the inclination angle of the solar collector on an annual useful energy output for Budapest.

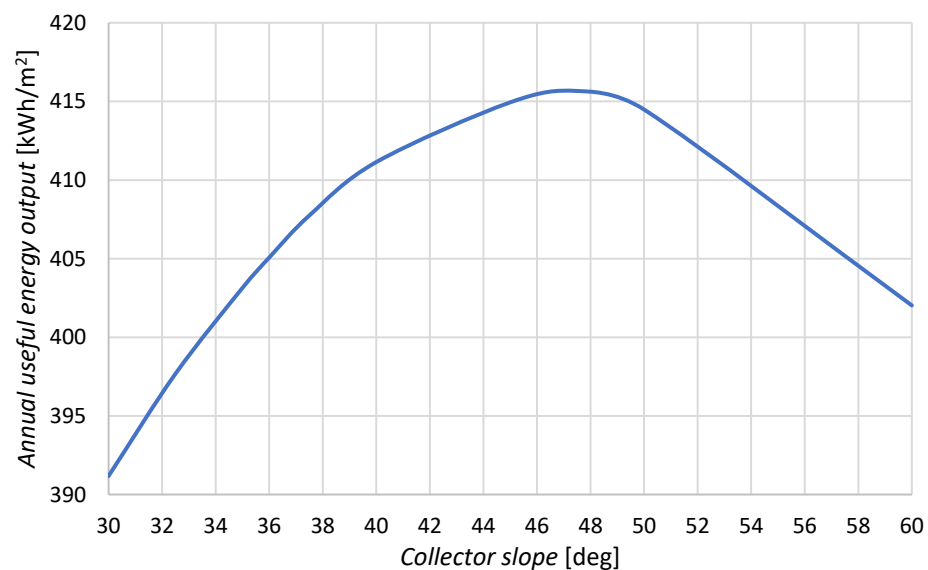


Figure 9. Dependence of the inclination angle of the solar collector on an annual useful energy output for Helsinki.

Thus, due to the heterogeneous nature of the weather factors, three new mathematical models for each of the groups of climatic conditions were developed. It was assumed that the relationship $Y = f(X_1, X_2, X_3, X_4, X_5)$ can be described as a second-degree polynomial equation in the following form:

$$Y = a_0 + a_1X_1 + a_2X_2 + a_3X_3 + a_4X_4 + a_5X_5 + a_{12}X_1X_2 + a_{13}X_1X_3 + a_{14}X_1X_4 + a_{15}X_1X_5 + a_{23}X_2X_3 + a_{24}X_2X_4 + a_{25}X_2X_5 + a_{34}X_3X_4 + a_{35}X_3X_5 + a_{45}X_4X_5 + a_{11}X_1X_1 + a_{22}X_2X_2 + a_{33}X_3X_3 + a_{44}X_4X_4 + a_{55}X_5X_5 \quad (1)$$

The ranges of variability for each of the factors were assumed at three levels:

- Low-marked as (−1),
- Medium-marked as (0),
- High-marked as (1).

Table 4 presents the natural values of the factors $\dot{X}_1 \div \dot{X}_5$ and the corresponding normalized values $(X_1) \div (X_5)$, which are defined by the following formula [19]:

$$X_i = \frac{\dot{X}_i - 0.5 \cdot (\dot{X}_{i,max} + \dot{X}_{i,min})}{0.5 \cdot (\dot{X}_{i,max} - \dot{X}_{i,min})} \quad (2)$$

where: \dot{X}_i , $\dot{X}_{i,max}$, $\dot{X}_{i,min}$ —current, maximum and minimum natural values of the i -th factor, respectively.

Table 4. Natural and standardized values of the factors.

Factor Level \dot{X}_i	V_{ST} [m ³] (X_1)	F_{SC} [m ²] (X_2)	η_o [-] (X_3)	a_1 [W/(m ² K)] (X_4)	m [kg/d] (X_5)
Low (−1)	2.0	30.0	0.58	2.0	1200
Medium (0)	7.0	100.0	0.78	6.0	4800
High (+1)	12.0	170.0	0.98	10.0	8400
Range of variability ΔX_i	5.0	70.0	0.20	4.0	3600

The range of collector surfaces, volumes of accumulation tanks, and consumption of DHW have been selected to represent the SDHW medium-sized system.

In order to create a database for the description of Y relationship (Equation (1)), a series of computer simulations were performed in TRNSYS environment software. Based on a symmetrical three-level plan [18], only 26 series of calculations were made. The $Q_{SC,i}$ (Y_i) estimation results for three different locations are shown in Table 5.

Table 5. Planning matrix and calculation results of annual useful energy output [kWh/m²].

No	V_{ST}	F_{SC}	η_o	a_1	m	$Q_{I,SC}$	$Q_{II,SC}$	$Q_{III,SC}$
	X_1	X_2	X_3	X_4	X_5	$Y_{I,i}$	$Y_{II,i}$	$Y_{III,i}$
1	2 −1	30 −1	0.58 −1	2 −1	8400 +1	721	504	425
2	12 +1	30 −1	0.58 −1	2 −1	1200 −1	570	407	339
3	2 −1	170 +1	0.58 −1	2 −1	1200 −1	118	108	98
4	12 +1	170 +1	0.58 −1	2 −1	8400 +1	500	349	293
5	2 −1	30 −1	0.98 +1	2 −1	1200 −1	641	545	474
6	12 +1	30 −1	0.98 +1	2 −1	8400 +1	1289	901	758
7	2 −1	170 +1	0.98 +1	2 −1	8400 +1	505	438	373
8	12 +1	170 +1	0.98 +1	2 −1	1200 −1	145	141	133
9	2 −1	30 −1	0.58 −1	10 +1	1200 −1	286	192	161
10	12 +1	30 −1	0.58 −1	10 +1	8400 +1	570	391	331
11	2 −1	170 +1	0.58 −1	10 +1	8400 +1	133	99	85
12	12 +1	170 +1	0.58 −1	10 +1	1200 −1	75	52	45
13	2 −1	30 −1	0.98 +1	10 +1	8400 +1	799	575	490
14	12 +1	30 −1	0.98 +1	10 +1	1200 −1	508	355	300
15	2 −1	170 +1	0.98 +1	10 +1	1200 −1	97	75	64
16	12 +1	170 +1	0.98 +1	10 +1	8400 +1	294	203	171
17	2 −1	100 0	0.78 0	6 0	4800 0	376	272	229
18	12 +1	100 0	0.78 0	6 0	4800 0	450	310	260
19	7 0	30 −1	0.78 0	6 0	4800 0	791	544	455
20	7 0	170 +1	0.78 0	6 0	4800 0	296	207	173
21	7 0	100 0	0.58 −1	6 0	4800 0	330	227	191

Table 5. Cont.

No	V_{ST}	F_{SC}	η_o	a_1	m	$Q_{I,SC}$	$Q_{II,SC}$	$Q_{III,SC}$
	X_1	X_2	X_3	X_4	X_5	$Y_{I,i}$	$Y_{II,i}$	$Y_{III,i}$
22	7 0	100 0	0.98 +1	6 0	4800 0	544	384	322
23	7 0	100 0	0.78 0	2 −1	4800 0	661	505	425
24	7 0	100 0	0.78 0	10 +1	4800 0	309	213	178
25	7 0	100 0	0.78 0	6 0	1200 −1	193	159	139
26	7 0	100 0	0.78 0	6 0	8400 +1	509	354	297

The results of these calculations $Q_{I,SC}$, $Q_{II,SC}$, $Q_{III,SC}$ (Table 5) were used to approximate the functions of the examined objects. The least squares method was chosen for this approximation. This procedure was performed using matrix calculus $\mathbf{A} = (\mathbf{X}^T \mathbf{X})^{-1} \mathbf{X}^T \mathbf{Y}$. In this vector notation: \mathbf{A} denotes the column vector of the coefficients a_i , \mathbf{X} -experiment plan matrix, \mathbf{Y} -column vector of the calculation results, and superscript \mathbf{T} means matrix transpose. In this way, the three mathematical models were developed:

Madrid

$$\hat{Y}_I = 444.07 + 40.28X_1 - 222.80X_2 + 84.39X_3 - 115.50X_4 + 149.27X_5 - 20.56X_1X_2 - 16.43X_1X_3 - 24.18X_1X_4 + 21.19X_1X_5 - 54.68X_2X_3 + 24.31X_2X_4 - 23.56X_2X_5 - 2.31X_3X_4 + 38.81X_3X_5 - 44.43X_4X_5 - 31.07X_1X_1 + 99.42X_2X_2 - 7.08X_3X_3 + 40.92X_4X_4 - 93.07X_5X_5, \quad (3)$$

Budapest

$$\hat{Y}_{II} = 313.51 + 16.72X_1 - 152.33X_2 + 71.56X_3 - 96.83X_4 + 98.89X_5 - 13.3X_1X_2 - 20.56X_1X_3 - 8.94X_1X_4 + 12.06X_1X_5 - 39.56X_2X_3 + 14.81X_2X_4 - 9.94X_2X_5 - 11.43X_3X_4 + 26.06X_3X_5 - 24.81X_4X_5 - 22.51X_1X_1 + 61.98X_2X_2 - 8.02X_3X_3 + 45.48X_4X_4 - 51.01X_5X_5, \quad (4)$$

Helsinki

$$\hat{Y}_{III} = 262.68 + 12.83X_1 - 127.66X_2 + 62.02X_3 - 82.94X_4 + 81.67X_5 - 9.75X_1X_2 - 17.37X_1X_3 - 6.63X_1X_4 + 10.10X_1X_5 - 34.12X_2X_3 + 11.38X_2X_4 - 9.25X_2X_5 - 11.25X_3X_4 + 20.63X_3X_5 - 18.62X_4X_5 - 18.18X_1X_1 + 51.31X_2X_2 - 6.19X_3X_3 + 38.81X_4X_4 - 44.68X_5X_5. \quad (5)$$

A characteristic feature of deterministic models is their unambiguous agreement between the external influence and the reaction to that influence. This principle was applied when the adequacy of the model was checked. The relevance of the Equations (3)–(5) were assessed by comparing the variance of the mean value S_y^2 and the residual variance S_r^2 :

$$S_y^2 = \frac{\sum(Y_i - \bar{Y})^2}{N - 1}, \quad (6)$$

$$S_r^2 = \frac{\sum(\hat{Y}_i - \bar{Y})^2}{N - N_b}, \quad (7)$$

where N is the number of calculations ($N = 26$) and N_b is the number of coefficients in the regression equation ($N_b = 21$).

The Fisher criterion [18,20], commonly known as the F -test, was used to exam the above models:

$$F = \frac{S_y^2(N-1)}{S_r^2(N-N_b)} \quad (8)$$

The regression equation approximates the calculation results correctly if the Fisher criterion F is much higher than the tabular value F_t . For Equations (3)–(5), the value of F is 152.47, 30.98, and 32.38 for Madrid, Budapest, and Helsinki, respectively. However, the tabular value of F_t [19] is smaller and equal to 4.52. Therefore, it can be concluded that the developed models are adequate because F_t is many times lower than F . A particularly good fit of the regression predictions to the calculation results is confirmed by the coefficient of determinations R^2 , which are in the range from 0.9935 to 0.9942. Additionally, the significance of the coefficients of the regression equations was also checked using the t -criterion [19], with a positive result. The description of this procedure was omitted due to its complexity. Therefore, it was found that the models (Equations (3)–(5)) should be considered useful for further analysis.

In conclusion, it should be mentioned that the data set for the development of the mathematical model and its subsequent testing was created using the TRNSYS software. The model was validated on the basis of the measurement data collected by the corresponding author of this paper.

3. Results and Discussion

The analysis of the influence of the examined factors $X_1 \div X_5$ on the annual useful energy output Q_{SC} of the collector was performed on mathematical models described by equations Equations (3)–(5). The center of the multivariate-space is formed by the average level of coefficients, i.e., in this case:

- Volume of heat storage tanks $V_{ST} = 7 \text{ m}^3$ ($X_1 = 0$),
- Solar collector total area $F_{SC} = 100 \text{ m}^2$ ($X_2 = 0$),
- Intercept (maximum) efficiency of solar collector $\eta_o = 0.78$ ($X_3 = 0$),
- Heat loss coefficient $a_1 = 6 \text{ W}/(\text{m}^2\text{K})$ ($X_4 = 0$),
- Daily consumption of DHW $m = 4800 \text{ kg/day}$ ($X_5 = 0$).

The annual useful energy output of the collector for selected groups of weather conditions are as follows: for Madrid (group I) $Q_{I.SC} = 444 \text{ kWh}/\text{m}^2$, for Budapest (group II) $Q_{II.SC} = 313 \text{ kWh}/\text{m}^2$, and for Helsinki (III group) $Q_{III.SC} = 263 \text{ kWh}/\text{m}^2$. As can be seen from the above results, the Q_{SC} value for the same solar collector fluctuates significantly, i.e., compared to Madrid it decreases by 29.5% for Budapest and as much as 41.0% for Helsinki. It is caused by changes in various climatic parameters, especially by total tilted surface solar radiation, which decrease by 27.6% for Budapest and 38.1% for Helsinki. However, when comparing the decrease in solar radiation on a horizontal plane, these values are slightly different: 27.9% for Budapest and 43.0% for Helsinki. This proves that the use of simple mathematical equations where Q_{SC} is only a function of the radiation intensity can cause some errors in designing SDHW systems.

The influence of each factor on the Q_{SC} was then estimated from a mathematical point of view. In each of the considered models, the level of parameters impact varies. When changing the selected factors from the lower to the higher level, as could be expected, the energy output increases with the increase of the $V_{ST}(X_1)$, $\eta_o(X_3)$, $m(X_5)$ and decreases with increasing factors $F_{SC}(X_2)$ and $a_1(X_4)$. The effects of changes in $\Delta Q_{i.SC}$ (natural and percentage) for each model are given in Table 5. As can be seen, weather conditions do not change the nature of the influence of the factors under consideration, but strongly change the degree of this influence. The most interesting and useful information for designers is the data on the interaction of factors in the obtained models. When analyzing the signs and values of the coefficients with double interactions certain regularities were noticed. They apply to all locations because the nature of the influence of the factors does not change in them.

Analysis of the results from Table 6 shows that increasing the capacity of the storage tank from 2 m³ to 12 m³ causes a change in Q_{SC} : the highest increase by 21.6% is achieved in hot weather conditions (Madrid) and the smallest by 11.1% in more severe climatic conditions (Helsinki).

Table 6. Effects of changing $X_1 \div X_5$ factors from lower to higher level on annual useful energy output [kWh/m²/%].

Group Number	V_{ST}	F_{SC}	η_o	a_1	m
		X_2	X_3	X_4	X_5
I	+80.56 (21.6%)	−445.60 (−58.2%)	+168.78 (+47.9%)	−231.00 (−38.5%)	+298.54 (+148%)
II	+33.44 (+12.2%)	−304.66 (−57.7%)	+143.12 (+61.2%)	−193.66 (−42.5%)	+197.78 (+120.9%)
III	+25.66 (+11.1%)	−255.32 (−57.8%)	+124.12 (+63.8%)	−165.88 (−43.1%)	+163.34 (+119.8%)

Furthermore, it can be stated that increasing the collector area from 30 to 170 m² strongly reduces the collector's energy output and shows the highest negative effect among the factors under consideration. Despite the fact that the natural values of this decrease strongly fluctuate in various weather conditions, the percentage decrease in all locations is around −58%.

While change the optical efficiency of the collector η_o from 0.58 to 0.98 significantly increases the collector's energy production, which ranges from 48% for Madrid to 64% for Helsinki. The increase in heat loss of the collector, characterized by the a_1 coefficient, significantly reduces the Q_{SC} value. The average percentage change in this value is about 41% and slightly differs for all meteorological conditions.

The daily DHW consumption has the highest (positive) impact on the collector's energy yield. Q_{SC} increases from 148% (Madrid) to 120% (Helsinki) with a change of m from 1200 kg/day to 8400 kg/day.

The interactions between the five parameters tested in this study are discussed below. Regarding the $V_{ST}(X_1)$, it can be observed that the positive effect of this factor decreases with the increase of the factors $F_{SC}(X_2)$, $\eta_o(X_3)$, $a_1(X_4)$, but increases with the increase of $m(X_5)$. For the two factors $V_{ST}(X_1)$ and $m(X_5)$ there is a synergism phenomenon, because when increasing them together, it affects more strongly than it would be when increasing them separately. The large negative effect of $F_{SC}(X_2)$ increases with the increase of the factors $V_{ST}(X_1)$, $\eta_o(X_3)$, $m(X_5)$, but it decreases with the increase of $a_1(X_4)$.

For the factor $\eta_o(X_3)$, its positive effect decreases with the increase of the factors $V_{ST}(X_1)$, $F_{SC}(X_2)$, $a_1(X_4)$, but increases with the increase of $m(X_5)$. For the two factors $\eta_o(X_3)$ and $m(X_5)$ there is also a synergy, as when each of them increase together the influence is stronger than it would be with a separate increase. For the factor $m(X_5)$, the high positive impact will be the stronger, with the greater factors $V_{ST}(X_1)$ and $\eta_o(X_3)$. For these two pairs of factors $V_{ST}(X_1) - m(X_5)$ and $\eta_o(X_3) - m(X_5)$ there is synergism, as each of them influences more strongly when increased together than with their separate increased. The positive influence of factor $m(X_5)$ will be smaller if the factors $F_{SC}(X_2)$ and $a_1(X_4)$ increase.

Next, the procedure of optimizing the value of energy produced by the collectors was carried out. As could be expected, the optimal values of the SDHW system parameters occur on the boundaries of the factor space. The maximum of the examined functions was achieved with the extreme values of the factors $X_2 = -1$, $X_3 = +1$, $X_4 = -1$, $X_5 = +1$. Only factor X_1 changed the optimal value in different locations.

Thus, the maximum annual useful energy output (Y_1) is 1303 kWh/m² for Madrid. $Y_{1, \max}$ is achieved with the following parameters: the storage tank capacity $V_{ST} = 12$ m³, the collector area $F_{SC} = 30$ m², the collector's optical efficiency $\eta_o = 0.98$, the linear heat loss coefficient $a_1 = 2$ W/m²·K, and the daily DHW consumption $m = 8400$ kg/day. In the case

of Budapest weather zone, the function Y_{II} has a maximum of 918.5 kWh/m^2 for storage tank capacity $V_{ST} = 10.5 \text{ m}^3$, and for the function Y_{III} (Helsinki weather conditions) the maximum of 768 kWh/m^2 is obtained for $V_{ST} = 10 \text{ m}^3$.

It should be noted that the above analysis makes perfect sense from the point of view of mathematical relations. However, in design practice, sometimes a slightly different approach to such issues is needed. It often happens that in practical conditions we cannot obtain the maximum or optimal value of an objective function $Y_{i, \max}$ estimated as a result of solving the optimization problem. In the case of SDHW systems, this may be due to the inability to install the appropriate number of collectors due to the insufficient roof area. Sometimes it also happens that it is not possible to design an appropriate volume of hot water storage tanks due to the lack of space in the district heating substations.

Using mathematical models, Equations (3)–(5), we can check whether the designed system is far from the optimal parameters in a given situation. To visualize this issue, three charts have been drawn up. The first one shows the effect of changing the amount of accumulated hot water on the useful energy output of the collectors (Figure 10). The second one shows the change of DHW consumption effects on the same parameter characterizing the collectors (Figure 11). The impact of the collector surface on their performance is presented in Figure 12. The calculations were made for the parameters located in the center of the multivariate-space that is formed by the average level of coefficients, i.e., equal to 0.

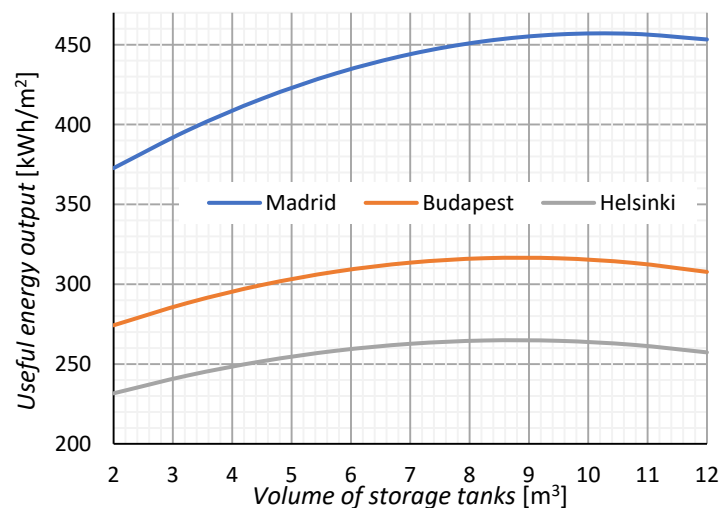


Figure 10. Dependence of the volume of heat storage tanks on an annual useful energy output.

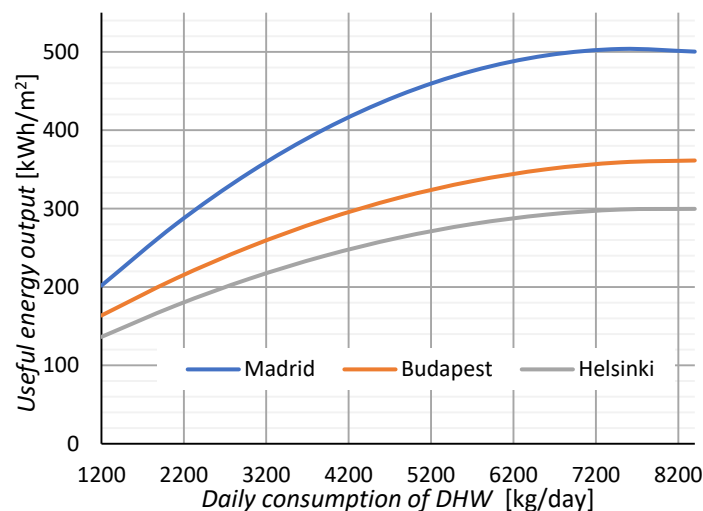


Figure 11. Dependence of the daily consumption of DHW on an annual useful energy output.

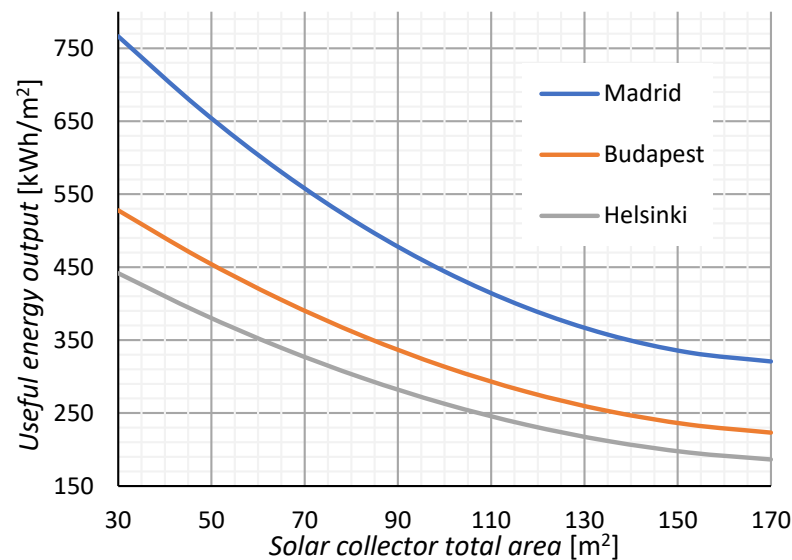


Figure 12. The influence of the collector surface area on an annual useful energy output.

The trend of the influence of the storage tanks capacity on the collector performance (Figure 10) clearly shows that an increase in tank volume above 8 m³ does not make any practical sense in the case of Madrid, although the optimum is 10 m³. For the other two locations (Budapest, Helsinki), the maximum volume is between 8 m³ and 9 m³. However, as in the previous case, reducing the storage tank capacity by 2 m³ causes a decrease in useful energy output only by about 2.5%.

As can be seen in Figure 11, the change in the DHW consumption has a significant impact on the useful energy output of the collectors. An almost linear increase in the Q_{SC} of solar collectors in 70% of the range of DHW consumption change can be observed. In operating conditions, it often happens that the energy efficiency of the SDHW system is lower in summer, when the demand for DHW decreases due to holiday trips.

Sometimes it happens that an excessive number of collectors is designed when, for example, there is a large roof area to be used. As can be seen from the charts presented in Figure 12, the amount of energy converted into the heat by 1 m² of solar panels significantly decreases with increasing their surface area. So, as we can see, the oversizing of the SDHW system significantly reduces its efficiency.

Figure 13 shows the effect of DHW consumption on the outlet temperature T_{OUT} of the solar collectors. The calculations were made for Madrid, 30 m² of collector area and 4 m³ of storage tank capacity in the period from 1 to 15 September. As could be expected, the highest temperature is achieved with the lowest DHW demand of 1200 kg/day. A 3.5-fold increase in daily consumption lowers T_{OUT} value by an average of 21.2%, while its 7-fold increase reduces this temperature by slightly less, i.e., by 25%. Lowering the temperature of the water flowing out of the solar collectors will be associated of course with the need to provide more energy from a supplementary heat source.

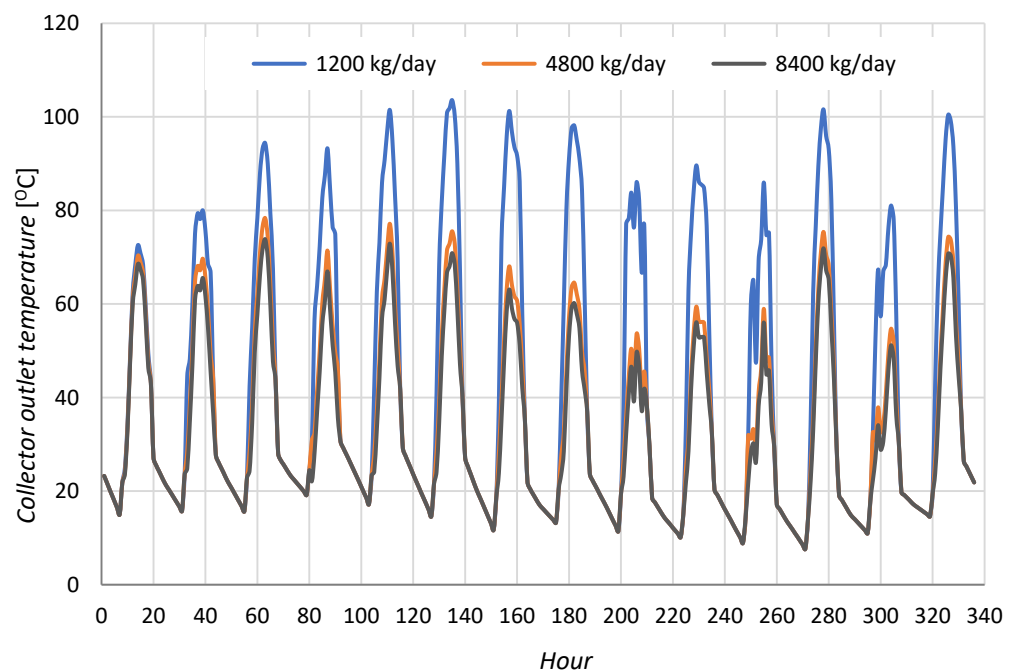


Figure 13. Outlet temperature from the solar collectors depending on the DHW consumption.

4. Conclusions

This article presents a mathematical approach to the issue of the influence of selected parameters on the thermal performance of a solar collector. Based on the results of the computational experiment for hot (Madrid), moderate (Budapest) and cold (Helsinki) climatic zones, three new deterministic mathematical models (Equations (3)–(5)) were developed. These equations can be used to determine the influence of five factors: volume of heat storage tanks, solar collector total area, maximum efficiency, and heat loss coefficient of solar collector, and daily consumption of DHW on the annual useful energy output. Based on these models, the degree and nature of the influence of the examined factors were estimated. It should be noted that the analysis presented in this article is the most appropriate for medium-sized SDHW systems.

The change of the examined factors from the lower to the upper level showed significant fluctuations in their impact both for individual factors and for the weather zones (Table 5). The useful energy output Q_{SC} of thermal solar collectors to a large extent depends on the weather conditions and, above all, the intensity of solar radiation. The Q_{SC} value is 29.5% lower for Budapest and 41% lower for Helsinki compared to the most suitable solar conversion zone in which Madrid is located.

The results of the optimization procedure according to the energy criterion showed that the maximum annual useful energy output, which is possible to supply from solar collectors, is 1303 kWh/m² for Madrid weather conditions, 918.5 kWh/m² for Budapest, and 768 kWh/m² for Helsinki conditions.

The above results can be obtained at the optimum collector inclination β for a particular location, i.e., 36 degrees for Madrid, 39.5 degrees for Budapest, and 47.5 degrees for Helsinki. These values were not calculated based on the latitude that designers usually estimate it at. The novelty is the determination of the β value using the method described in this article.

It is planned to develop similar models for selected main cities in Europe. The obtained dependencies will allow to write a simple application that can be used for a relatively precise determination of the annual useful energy output of thermal collectors. It is also planned to carry out a similar mathematical experiment using Solar Fraction as the objective function.

Author Contributions: Conceptualization, M.Z. and W.J.; methodology, M.Z. and W.J.; energy simulations, M.Z.; mathematical modelling, W.J.; validation, M.Z.; formal analysis, W.J. and M.Z.; investigation, M.Z. and W.J.; writing—original draft preparation, M.Z. and W.J.; writing—review and editing, M.Z. and W.J.; project administration, M.Z.; funding acquisition, M.Z. and W.J. All authors have read and agreed to the published version of the manuscript.

Funding: This work was supported by the Bialystok University of Technology and financed by the Ministry of Science and Higher Education of the Republic of Poland [grant numbers WZ/WB-IIS/9/2019, WZ/WB-IIL/5/2019].

Institutional Review Board Statement: Not applicable.

Informed Consent Statement: Not applicable.

Data Availability Statement: Not applicable.

Conflicts of Interest: The authors declare no conflict of interest.

References

1. Paris Agreement. Available online: <https://unfccc.int/process-and-meetings/the-paris-agreement/the-paris-agreement> (accessed on 15 March 2021).
2. Decision of the European Commission. Available online: https://ec.europa.eu/clima/policies/eu-climate-action/2030_ctp_en (accessed on 15 March 2021).
3. Kulkarni, G.N.; Kedare, S.B.; Bandyopadhyay, S. Determination of design space and optimization of solar water heating systems. *Sol. Energy* **2007**, *81*, 958–968. [CrossRef]
4. Klein, S.A.; Beckman, W.A.; Duffie, J.A. Design Procedure for Solar Heating Systems. *Sol. Energy* **1976**, *18*, 113–126. [CrossRef]
5. Beckman, W.A.; Klein, S.A.; Duffie, J.A. *Solar Heating Design by the F-Chart Method*; Wiley & Sons, Inc.: New York, NY, USA, 1977.
6. Haberl, J.S.; Cho, S. *Literature Review of Uncertainty of Analysis Methods (F-Chart Program)*; Report to the Texas Commission on Environmental Quality; Energy Systems Laboratory, Texas A&M University: College Station, TX, USA, 2004.
7. Essabbani, T.; Moufekkir, F.; Mezrhab, A.; Naji, H. Numerical Computation of Thermal Performance of a Simulation of a Solar Domestic Hot Water System. *Appl. Sol. Energy* **2015**, *51*, 22–33. [CrossRef]
8. Ayompe, L.M.; Duffy, A.; McCormack, S.J.; Conlon, M. Validated TRNSYS model for forced circulation solar water heating systems with flat plate and heat pipe evacuated tube collectors. *Appl. Therm. Eng.* **2011**, *31*, 1536–1542. [CrossRef]
9. Hobbi, A.; Siddiqui, K. Optimal design of a forced circulation solar water heating system for a residential unit in cold climate using TRNSYS. *Sol. Energy* **2009**, *83*, 700–714. [CrossRef]
10. Mongibello, L.; Bianco, N.; Caliano, M.; de Lucad, A.; Graditi, G. Transient analysis of a solar domestic hot water system using two different solvers. *Energy Procedia* **2015**, *81*, 89–99. [CrossRef]
11. Lima, J.B.A.; Prado, R.T.A.; Taborianski, V.M. Optimization of tank and flat-plate collector of solar water heating system for single-family households to assure economic efficiency through the TRNSYS program. *Renew. Energy* **2006**, *31*, 1581–1595. [CrossRef]
12. Mehmood, A.; Waqas, A.; Said, Z.; Rahman, S.M.A.; Akram, M. Performance evaluation of solar water heating system with heat pipe evacuated tubes provided with natural gas backup. *Energy Rep.* **2019**, *5*, 1432–1444. [CrossRef]
13. Mohaseb, S.; Kasaeian, A. Comparing the Performance of Flat Plate Collector and Evacuated Tube Collector for Building and Industrial Usage in Hot and Cold Climate in Iran with TRNSYS Software. In Proceedings of the Ninth International Conference on Engineering Computational Technology, Napoli, Italy, 2–5 September 2014.
14. TRNSYS 18. *TRaNsient SYstem Simulation Program*; Tutorials; Solar Energy Laboratory, University of Wisconsin-Madison: Madison, WI, USA, 2020; Volume 9.
15. Ivanko, D.; Sorensen, A.L.; Nord, N. Selecting the model and influencing variables for DHW heat use prediction in a hotel in Norway. *Energy Build.* **2020**, *228*, 110441. [CrossRef]
16. Fuentes, E.; Arce, L.; Salom, J. A review of domestic hot water consumption profiles for application in systems and buildings energy performance analysis. *Renew. Sustain. Energy Rev.* **2018**, *81*, 1530–1547. [CrossRef]
17. Zukowski, M.; Radzajewska, P. A New Method to Determine the Annual Energy Output of Liquid-Based Solar Collectors. *Energies* **2019**, *12*, 4586. [CrossRef]
18. Durakovic, B. Design of Experiments Application, Concepts, Examples: State of the Art. *Period. Eng. Nat. Sci.* **2017**, *5*, 421–439. [CrossRef]
19. Korzynski, M. Metodyka eksperymentu. In *Planowanie, Realizacja i Statystyczne Opracowanie Wynikow Eksperymentow Technologicznych*; WNT: Warszawa, Poland, 2006.
20. Hartmann, K.; Lezki, E.; Schär, W. *Statistische Versuchsplanung und—Auswertung in der Stoffwirtschaft*; VEB: Leipzig, Germany, 1977.

Article

Designing for the Environment: An Example of Multi-Criteria Analysis Used for Solar Hot Water System Selection

Agnieszka Żelazna  and Justyna Gołębiowska * 

Faculty of Environmental Engineering, Lublin University of Technology, 40B Nadbystrzycka Str., 20-618 Lublin, Poland; a.zelazna@pollub.pl

* Correspondence: j.golebiowska@pollub.pl; Tel.: +48-8153-844-06

Abstract: In the European Union, the building sector accounts for more than 40% of final energy consumption, contributing to the deterioration of the quality of the environment. Among the various solutions that aim to reduce the negative environmental impact caused by the operation of buildings, solar hot water systems (SHW) are popular. The choice of a SHW system is associated with the comfort of use and the access to low-cost energy. The design guidelines include the technical parameters for system operation such as materials, dimensions, sizing and operation temperatures. However, the legitimacy of choosing a particular solution and the available technical parameters are key issues. In the presented study, a multi-criteria analysis was proposed as a basis for the proper selection of system parameters, e.g., collector type, solar tank volume. A model of the SHW system was used to calculate the possible solutions, ensuring the same comfort of usage for several design options. The analyzed model was then used for the calculation of three various indicators: Simple Payback Time (SPBT), Primary Energy consumption (PE) and IMPACT 2002+. The application of a multi-criteria analysis based on a Life Cycle Assessment allowed for beneficial solutions to be found from the point of view of economics, non-renewable resources and environmental protection.

Keywords: solar thermal energy; SHW system; multi-criteria analysis; SPBT; EPBT; primary energy; IMPACT 2002+; LCA; sustainable design

Citation: Żelazna, A.; Gołębiowska, J. Designing for the Environment: An Example of Multi-Criteria Analysis Used for Solar Hot Water System Selection. *Energies* **2022**, *15*, 65. <https://doi.org/10.3390/en15010065>

Academic Editor: Jan Danielewicz

Received: 24 November 2021

Accepted: 20 December 2021

Published: 22 December 2021

Publisher's Note: MDPI stays neutral with regard to jurisdictional claims in published maps and institutional affiliations.



Copyright: © 2021 by the authors. Licensee MDPI, Basel, Switzerland. This article is an open access article distributed under the terms and conditions of the Creative Commons Attribution (CC BY) license (<https://creativecommons.org/licenses/by/4.0/>).

1. Introduction

At present, energy seems to be an essential element for living in a modern society. The change in our lifestyle observed in recent decades resulted in a significant increase in energy consumption, especially in the case of the electricity, but also in other forms such as heat, required to meet the rising housing needs [1–3]. The growing interest in new renewable technologies in recent years is caused by several issues, such as the depletion of fossil resources, necessity to reduce air pollution, response to the problem of global climate change and the social expectations in the field of raising living standards and the comfortable use of buildings [4,5].

Among the renewable energy sources, solar energy is one of the most popular options because of several advantages. The energy supplied from the Sun to our planet exceeds the human demand for energy per year by about 8000 times. In theory, this means that the electromagnetic radiation from the Sun is able to cover the global demand for energy without the additional use of other energy sources. This energy is almost unlimited and does not cause environmental pollution, unlike conventional energy sources. The current level of radiation energy conversion technology does not allow the Sun's energy potential to be utilized in its entirety, which is why there is an aim to improve the devices that convert solar radiation into heat or electricity. An important disadvantage of using solar energy potential is that its absorption requires a large amount of space and favorable conditions [6]. The amount of solar radiation reaching the Earth's surface decreases with many factors, such as increasing cloudiness, as well as air contamination [7,8].

In the scientific literature of the last several years, an increasing interest in the subject of Life Cycle Assessment of solar systems can be observed; this applies to both technological processes and specific devices or materials. Various Life Cycle Impact Assessment (LCIA) methods are used. These include: Global Warming Potential (GWP), Cumulative Energy Demand (CED) and Eco-indicator 99. Some studies deal with the Life Cycle Assessment of solar energy installations and devices, including domestic hot water preparation systems and solar collectors themselves.

Over time, there have been significant advancements achieved by various research groups in the field of solar–thermal systems LCA [9–13]. Some of these include the LCA analysis of flat solar collectors [14] from raw material extraction, through production to obtaining a finished commercial product. The environmental load resulting from the transport of materials to the production plant was also taken into account. This research was based on the energy and ecological characteristics of the input products. The highest value of environmental load was connected with the following impact categories: primary energy consumption and acidification. The energy payback period, understood as the time needed to recover the energy expenditure incurred for the production of the collector, excluding the other elements and energy required for operation, was shorter than 1 year [14].

Another study [15] presented the Life Cycle Impact Assessment carried out for a solar heating installation located in Greece. The production stages of individual elements of the installation and their impact on the environment were considered. The system boundaries include the production of raw materials (steel, glass, copper, and aluminum), operation of the installation and final disposal. The installation consisted of a flat solar collector with a copper absorber (4 m^2) and a domestic hot water tank with a capacity of 200 dm^3 . An electric heater was an additional heat source. Studies showed that the system provided 1702 kWh per year, with solar energy accounting for 58.8% of this value. An LCIA analysis was carried out using the Eco-indicator 99 method, which showed that the largest environmental impact came from the solar hot water tank. Moreover, the greatest environmental burden was connected with the following impact categories: soil acidification, smog production and impact on global warming.

An environmental analysis was also used for the assessment of the selective surface for flat-plate solar collectors, which was carried out using the following methods: CED, GHG (Greenhouse Gas Protocol method based on the set of characterization factors by Intergovernmental Panel for Climate Change IPCC GWP 100a) and Eco-indicator 99. The authors compared the conventional method of selective surface production with the latest production method—roll to roll (R2R).

Research showed that the annual energy demand for the production of $200,000 \text{ m}^2$ of selective surface is equal 7.91 TJ. Additional research based on CED allowed the energy payback time for R2R production to be determined, which was only 3–4 days. Among the analyzed factors, copper has the greatest impact on the environment, as it also requires the highest amount of energy in the production of selective surfaces. The results of the analysis clearly showed that the production of the selective surface for flat-plate solar collectors with the conventional method was much more harmful to the environment than the production by means of the roll-to-roll method [16].

A study in Munich (temperate climate conditions) presented an analysis of the life cycle of two hot water preparation systems with glazed solar collectors and unglazed polypropylene collectors. The Eco-indicator 99 method was used to assess the entire life cycle. The main components of both systems were solar panels and a 300 dm^3 buffer tank. The glazed panel consisted of an outer aluminum frame, two layers of mineral wool, a copper absorber and a copper alloy absorber piping system. The whole construction was hermetically closed with 4 mm thick transparent glass. In contrast, the plastic collector considered in this study was a polypropylene strip 7 mm thick, 313 mm wide and of variable length, which allowed the panel to be modular. The duration of the operation of both installations was 10 years. For glazed solar collectors, the calculated index was 49.7 points, while for plastic collectors it was 18.7 points. The largest share here was the

use of fossil fuels: 52% and 68%, respectively. On the other hand, the GWP calculated over a period of 100 years was 1670.92 kg CO_{2eq} for a glazed solar collector and 105.06 kg CO_{2eq} for a plastic collector. The economic payback time, in comparison to the natural gas boiler, is in the range 9–11 years/8–13 years for the system with unglazed/glazed panels, respectively [17].

To conclude, it should be emphasized that the analyses carried out so far concern the production of materials, the entire life cycle of the installation or case studies [18–21]; however, attention is rarely paid to proper design parameters. In the literature, few research works address the topic of the life cycle of installations that operate under the temperate climatic conditions, such as the Polish climate, and relate to a long-term perspective. The present study significantly supplements the current state of knowledge due to the implementation of the selected design criteria into the analyzed model of life cycle.

2. Materials and Methods

In the current study, an attempt to conduct a holistic, multi-criteria analysis of a solar thermal system was presented in order to set the designer's guidelines and frames for correct system selection. A typical installation of solar hot water system (SHW), supported by an electric heater in the winter period was chosen as the subject of the analysis. The scheme of the typical solar installation is presented in Figure 1. The analysis included 6 variants of installations located in Central Europe (Poland, Łódź: 51.759247° N, 19.455982° E), with orientation towards the south (azimuth 0°) and inclination of 40°. The daily domestic hot water demand was assumed at constant level of 180 L. The characteristics of the technical parameters for different variants of installations are shown in Table 1. The aim of the modeling was to estimate the influence of selected design parameters (type of collector, piping and water tank capacity) on the economical, energetic and environmental aspects of SHW operation.

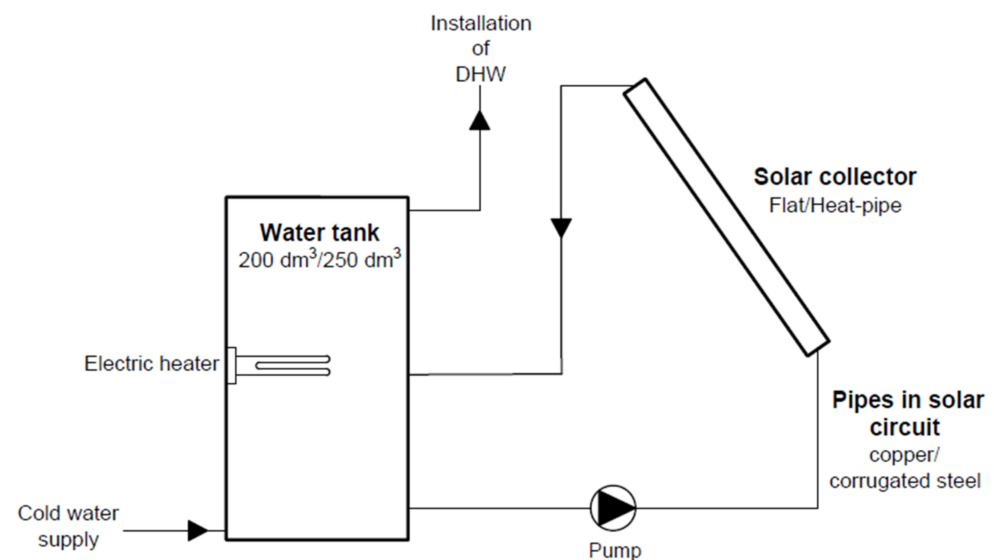


Figure 1. Scheme of the simulated installation.

Table 1. Technical parameters of the analyzed system variants.

Variant of Installation	Solar Collector	Absorber Area	Pipes	Water Tank	Solar Energy	Annual Efficiency
-	-	m ²	-	dm ³	kWh/yr	%
Variant I	Flat-plate, CU absorber	4.66	Copper	200	1602	30
Variant II	Flat-plate, CU absorber	4.66	Copper	250	1627	30.5
Variant III	Flat-plate, CU absorber	4.66	Steel (corrugated)	200	1576	29.5
Variant IV	Flat-plate, CU absorber	4.66	Steel (corrugated)	250	1600	30
Variant V	Heat pipe	4.29	Copper	200	1842	37.5
Variant VI	Heat pipe	4.29	Copper	250	1865	37.9
Variant VII	Heat pipe	4.29	Steel (corrugated)	200	1810	36.8
Variant VIII	Heat pipe	4.29	Steel (corrugated)	250	1834	37.3

The base scenario for comparison with the design options included an electric heater, while the annual electricity consumption equaled 2727 kWh. Modeling of solar energy gains was performed by using GetSolar software (Hottgenroth Software GmbH & Co. KG, Germany), a popular tool using f-chart-based estimation of energy gains from SHW systems in a chosen location (Łódź, Poland), characterized by the total annual solar radiation of 3710.8 MJ/m² and the average annual total insolation of 1560.4 h.

The main inputs to the analysis include: solar irradiance on collector plane and ambient temperature data (from WetSyn weather data synthesis program integrated with GetSolar software), type of solar system (single, combined, etc.), collector parameters (including optical efficiency and collector area), heat losses, water tank volume, inclination and azimuth, mass flow of solar fluid, pipes length and pipes diameter. The more detailed description of the f-chart model can be found in [22].

A detailed inventory, based on cost of materials and energy consumption estimated for every variant of system, was then used for the detailed Life Cycle Assessment. Modeling of the life cycle was based on the use of SimaPro v. 8.0.5.13 software (PRE Consultants, Amersfoort, The Netherlands) and Ecoinvent v. 3 database (Ecoinvent Association, Zurich, Switzerland), which was used for the description of unit processes. Life Cycle Impact Assessment was performed by means of the the IMPACT 2002+ and CED v. 3 methods.

The IMPACT 2002+ method allows for the assessment of environmental stress connected with the life cycle of the solar system. The indicator (expressed in points: Pt) links all types of inventory results throughout the fourteen midpoint categories into four main damage categories: Human Health, Ecosystem Quality, Climate Change and Resources. The higher the indicator calculated by using this method, the greater the environmental impact of the system [23]. The functional unit was 1 kWh of energy generated by the system.

Cumulative Energy Demand (CED) method was used to estimate the total primary energy consumption (expressed in MJ) of the solar system throughout its entire lifetime, including the direct and indirect energy streams associated with the particular phases of life cycle [24].

For the validation of final results in CED, Monte Carlo statistical simulations (lognormal distribution) were implemented in order to compare the possible error between the achieved results.

In the multi-criteria analysis, the economic and environmental issues were discussed according to the following scheme. Firstly, Simple Payback Time (SPBT) was calculated for every variant of installation according to the definition, expressing the total cost of investment and operation divided by yearly savings [11].

In the next step, Energy Payback Time (EPBT) was calculated as a basis for technological foundations of the functioning of the system. EPBT was based on the CED results: in this case, statistical processing of data was a basis for the determination of the confidence interval. In the third part of evaluation, IMPACT 2002+ was calculated as an environmental criterion. The results obtained during the mentioned stages were then evaluated to indicate the most advantageous option with the use of the Weighted Sum Method.

3. Results

In the following subsection, the results of the economic, energetic and environmental evaluation of the analyzed SHW systems are presented with special attention paid to the financial and energetic payback times, as well as to the environmental damage categories affected by the production and operation of the systems. All of the detailed calculations are finally used to evaluate the selected installation options based on the ratings awarded in the multi-criteria analysis.

3.1. Solar Hot Water Systems: Economic Evaluation

The economic evaluation of the SHW system in variants I–VIII was based on the on-line price catalogues and average market cost of installation, with the use of direct contact with the owners and investors. The data on the operation of the installation and service costs were obtained from the users of the installation in the form of an interview confirmed by billing documentation.

The pump operation cost was based on the measured energy consumption in a 3-year operation period of heat-pipe collector installation [11] and the price of energy in Poland in 2018 (0.5055 PLN/kWh recalculated to 0.1113 Euro/kWh) according to the Energy Regulatory Office [25].

According to the data presented in Table 2, the Simple Payback Time in the basic option (investment cost covered by the owner only) exceeds 11 years in all of the variants, assuming a constant price of electricity. However, while considering the popular support programs such as Prosument 2, the payback time may be shorter. In this case, financing the investment by taking up credit is a clear approach, which may worsen the presented results. In the case of the support programs financed by the local authorities, where the discount may reach 70%, SPBT decreases by almost threefold to 4.1 years in the most effective options of installation.

Table 2. Results of economic evaluation for the analyzed system variants.

Variant of Installation	Investment Cost	Pump Operation Cost	Servicing/Utilization Cost	Savings	SPBT *	SPBT **	SPBT ***
-	Euro	Euro/yr	Euro	Euro/yr	Years	Years	Years
Variant I	1795.43	13.56	220.26	164.8	12.2	9.8	4.6
Variant II	1998.07	13.77	220.26	167.4	13.3	10.5	4.9
Variant III	1759.91	13.34	220.26	162.1	12.2	9.8	4.6
Variant IV	1962.56	13.54	220.26	164.6	13.3	10.6	4.9
Variant V	1871.53	15.59	220.26	189.5	11.0	8.8	4.1
Variant VI	2074.17	15.78	220.26	191.9	12.0	9.5	4.4
Variant VII	1836.01	15.32	220.26	186.2	11.0	8.8	4.1
Variant VIII	2038.66	15.52	220.26	188.7	12.0	9.5	4.4

*—own investment, **—Prosument 2 program, 30% discount, 10 years credit, ***—local programs with 70% discount.

3.2. Solar Hot Water Systems: Energy Balance

Energy balance of the SHW system was considered with the use of the CED method, as well as the calculation of the energy generated by the solar system. It is worth underlining that the predicted energy consumption in the 20-year operation period was included in the calculation, according to Figure 2.

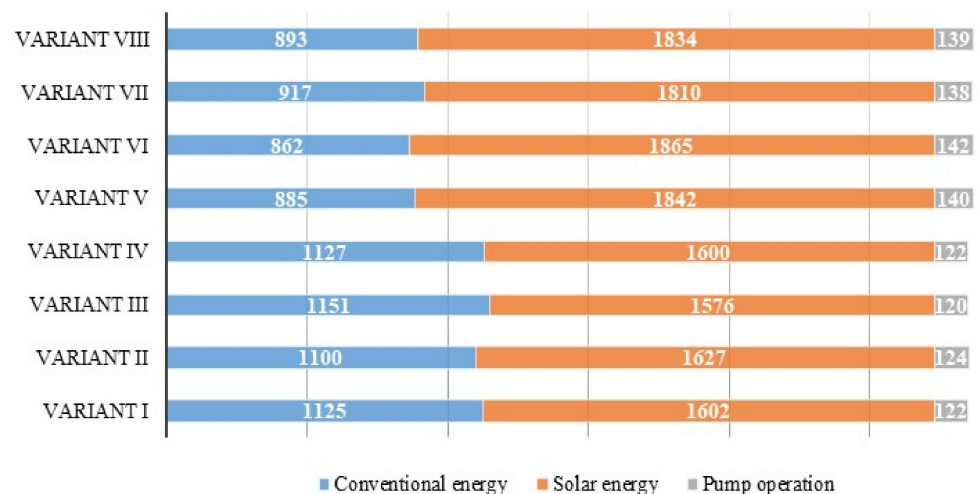


Figure 2. Energy balance of one-year operation of system according to the applied model.

The obtained EPBT results (Table 3) are higher than in some literature studies [17]. This may be caused by both the differences in solar irradiation, as well as the type of system and source of energy used for pumping. In all the considered cases, the EPBT indicator was significantly shorter than the predicted lifespan, assumed as 20 years.

Table 3. Results of energetic and economic evaluation.

Variant of Installation	CED	Energy Generated	EPBT
	MJ	MJ/yr	Years
Variant I	50,513.62	5767.20	8.76
Variant II	51,545.74	5857.20	8.80
Variant III	50,849.69	5673.60	8.96
Variant IV	51,364.05	5760.00	9.00
Variant V	53,830.63	6631.20	8.12
Variant VI	54,819.90	6714.00	8.17
Variant VII	54,038.12	6516.00	8.29
Variant VIII	55,048.82	6602.40	8.34

The results of LCIA conducted using CED indicator were subjected to a sensitivity analysis by means of the Monte Carlo statistical method (Figure 3). All system inputs and outputs were successively changed in the frames of standard deviation in 1000 trials, which allowed the scale of possible error to be shown in the calculations. The confidence level was assumed as 95%. In all the variants, the scale of possible error was similar, and the statistical distribution was positively skewed with a higher mean than the median in all analyzed cases.

3.3. Solar Hot Water Systems: Environmental Impact Indicators

The impact on the environment, considered as ecosystems, resources, human health and climate change, was assessed with the IMPACT2002+ method. The results of the impact assessment stage, recalculated to the functional unit (1 kWh of energy generated by the system) are presented in Figure 4. The share analysis on the level of processes shows that the electricity used for pumping is the most influential process in the SHW system life cycle. Other important elements include solar collectors and water tanks due to the high consumption of materials.

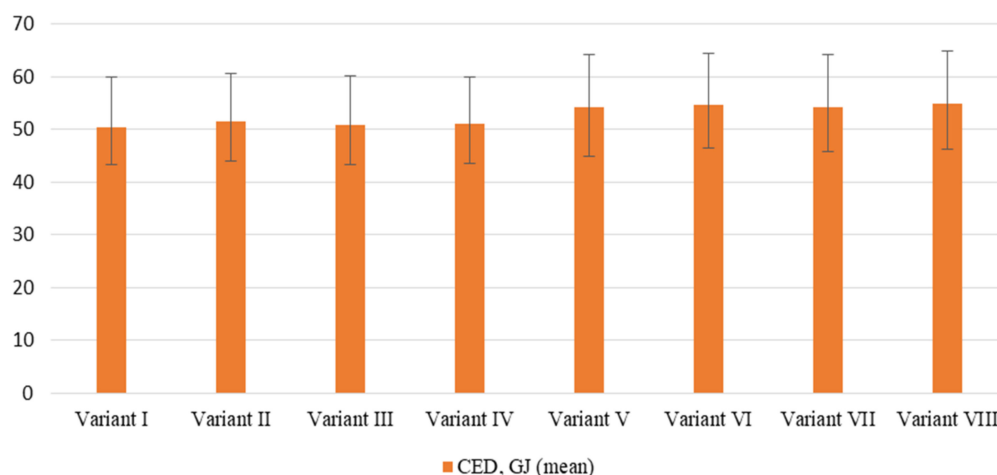


Figure 3. Results of CED calculation with the statistical error based on the Monte Carlo analysis.

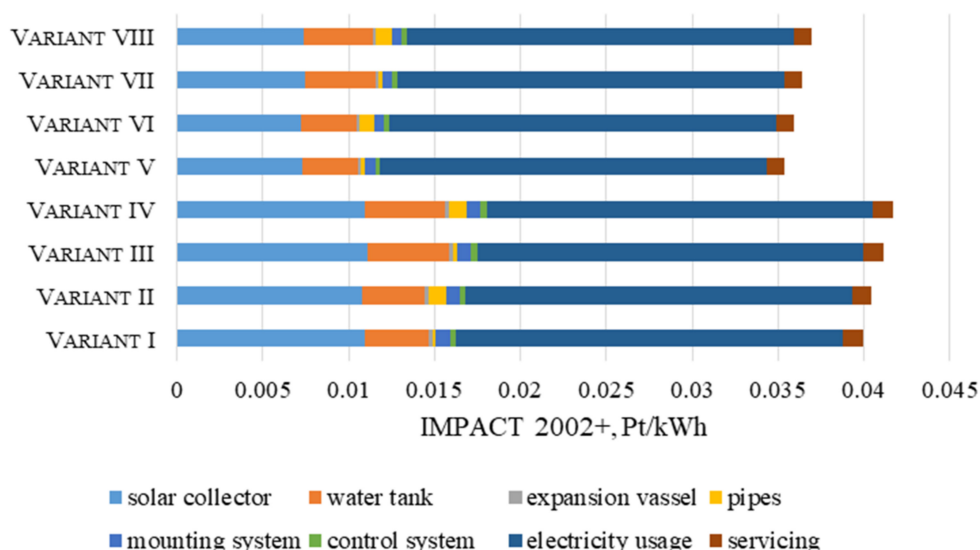


Figure 4. Results of IMPACT 2002+ calculation per functional unit, Pt/kWh.

According to the share analysis on the damage categories level, the results obtained for the analyzed systems are similar for Variants I-VIII, with the highest contribution from the Human health, Climate change and Resources categories. This is caused mostly by the similarities in construction and the supporting conventional energy used (Figure 5).

3.4. Solar Hot Water Systems: Multi-Criteria Analysis

The analysis performed in this study aimed to compare several alternatives of solar hot water system construction on the basis of SPBT, EPBT and IMPACT 2002+ indicators. Assuming equal weights for all the analyzed criteria, the MCA results were presented by means of the Weighted Sum Method indicator as a percentage of the difference between the actual and minimal parameter related to the difference between the maximal and minimal parameter (Table 4).

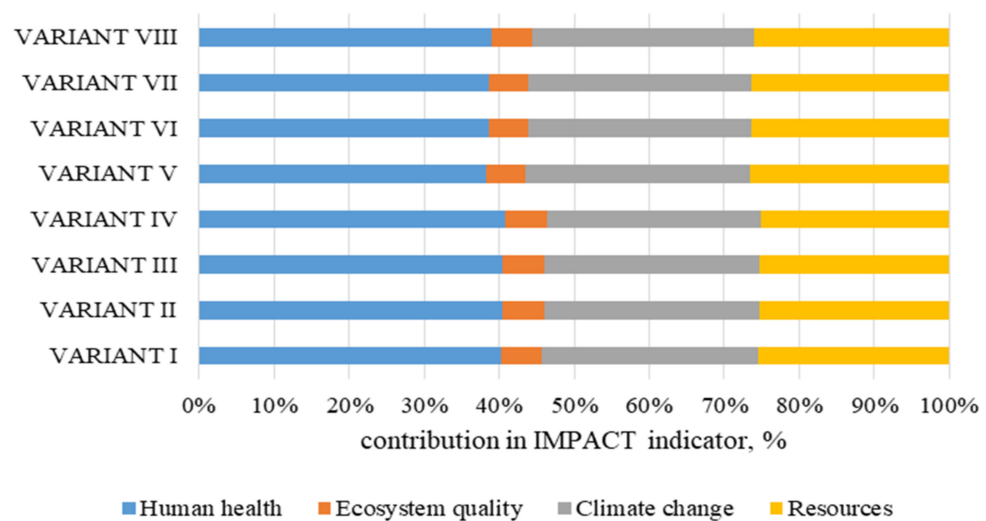


Figure 5. Share analysis of IMPACT2002+ indicator on damage category level.

Table 4. Results of multi-criteria evaluation.

Variant of Installation	SPBT	EPBT	IMPACT 2002+	WSM Result
-	Years	Years	Pt/kWh	%
Variant I	4.6	8.8	0.040	68%
Variant II	4.9	8.8	0.040	85%
Variant III	4.6	9.0	0.041	83%
Variant IV	4.9	9.0	0.042	100%
Variant V	4.1	8.1	0.035	0%
Variant VI	4.4	8.2	0.036	16%
Variant VII	4.1	8.3	0.036	13%
Variant VIII	4.4	8.3	0.037	29%

According to the data in Table 4, the best option is Variant V of installation, where all of the analyzed parameters were minimal due to the high efficiency of the system. Conversely, Variant IV can be assessed as the worst due to the longest payback periods and the highest environmental impact indicator. Following the specification of the analyzed systems, one can state that the most meaningful parameter is the type of solar collector. This contributed to approximately a 60% difference between systems (Variant I–IV vs. Variant V–VIII). The other analyzed parameters, such as water tank capacity (16–17% difference), and pipe material (13–15%) were also important. In turn, compared to the literature values, the analyzed solutions are characterized by higher payback times. This is connected with the method of analysis, e.g., covering the additional conventional energy spent on system operation, as well as various climate conditions.

4. Conclusions

According to the presented results, the most favorable solution included a heat-pipe-evacuated tube collector, copper pipes and 200 dm³ water tank. Although the selection of a higher-capacity tank led to the optimization of solar energy conversion efficiency, the increase in this parameter was not crucial for the conducted research. However, it should be underlined that the values of the calculated indicators are comparable for all cases. For example, the payback times for both energy and financial inputs differed by no more than 11 months. Therefore, the analyzed systems can be assessed as green solutions, significantly minimizing the environmental impact connected with conventional energy usage.

The multi-criteria analysis, covering several aspects of systems' life cycle, can be used as a tool for the optimization of their selection in the green designing process. More-

over, the additional criteria used for sustainable designing can significantly improve the environmental balance of the analyzed technologies.

Author Contributions: Conceptualization, A.Ż.; methodology, A.Ż.; software, A.Ż. and J.G.; validation, A.Ż.; formal analysis, A.Ż. and J.G.; investigation, A.Ż.; resources, A.Ż.; data curation, A.Ż.; writing—original draft preparation, A.Ż.; writing—review and editing, A.Ż. and J.G.; supervision, A.Ż. and J.G.; project administration, A.Ż. and J.G. All authors have read and agreed to the published version of the manuscript.

Funding: The publication is supported from funds FD-20/IS-6/012 and FD-20/IS-6/042 granted by Faculty of Environmental Engineering, Lublin University of Technology.

Data Availability Statement: Not applicable.

Conflicts of Interest: The authors declare no conflict of interest.

References

1. Van Ruijven, B.J.; De Cian, E.; Wing, I.S. Amplification of future energy demand growth due to climate change. *Nat. Commun.* **2019**, *10*, 1–12. [CrossRef] [PubMed]
2. Jackson, R.B.; Le Quéré, C.; Andrew, R.M.; Canadell, J.G.; Korsbakken, J.I.; Liu, Z.; Peters, G.P.; Zheng, B. Global energy growth is outpacing decarbonization. *Environ. Res. Lett.* **2018**, *13*, 120401. [CrossRef]
3. Żelazna, A.; Gołębiowska, J.; Zdyb, A.; Pawłowski, A. A Hybrid vs. On-Grid Photovoltaic System: Multicriteria Analysis of Environmental, Economic, and Technical Aspects in Life Cycle Perspective. *Energies* **2020**, *13*, 3978. [CrossRef]
4. Asdrubali, F.; Baldinelli, G.; D’Alessandro, F.; Scrucca, F. Life cycle assessment of electricity production from renewable energies: Review and results harmonization. *Renew. Sustain. Energy Rev.* **2015**, *42*, 1113–1122. [CrossRef]
5. Żelazna, A.; Zdyb, A.; Pawłowski, A. The influence of selected factors on PV systems environmental indicators. *Annu. Set Environ. Prot.* **2016**, *18*, 722–732.
6. Olczak, P.; Matuszewska, D.; Zabagło, J. The Comparison of Solar Energy Gaining Effectiveness between Flat Plate Collectors and Evacuated Tube Collectors with Heat Pipe: Case Study. *Energies* **2020**, *13*, 1829. [CrossRef]
7. Mularczyk, A.; Husa, B. Rozwój i perspektywy energii solarnej w Polsce i Województwie Śląskim. *Zesz. Naukowe. Organ. Zarządzanie Politech. Śląska* **2015**, *86*, 361–377. (In Polish)
8. Olczak, P. The comparison of solar installation heat gains and SHW simulation results—case study. *Polityka Energetyczna* **2020**, *23*, 41–54. (In Polish) [CrossRef]
9. Hang, Y.; Qu, M.; Zhao, F. Economic and environmental life cycle analysis of solar hot water systems in the United States. *Energy Build.* **2012**, *45*, 181–188. [CrossRef]
10. Souliotis, M.; Arnaoutakis, N.; Panaras, G.; Kavga, A.; Papaefthimiou, S. Experimental study and Life Cycle Assessment (LCA) of Hybrid Photovoltaic/Thermal (PV/T) solar systems for domestic applications. *Renew. Energy* **2018**, *126*, 708–723. [CrossRef]
11. Saint, R.M.; Pomponi, F.; Currie, J.I. A method for a cradle-to-cradle life cycle assessment of integrated collector-storage solar water heaters. *IOP Conf. Ser. Mater. Sci. Eng.* **2019**, *556*, 012061. [CrossRef]
12. Kalogirou, S. Thermal performance, economic and environmental life cycle analysis of thermosiphon solar water heaters. *Sol. Energy* **2009**, *83*, 39–48. [CrossRef]
13. Żelazna, A. The influence of collector type on emission indicators in solar systems life cycle assessment. *Annu. Set Environ. Prot.* **2013**, *15*, 258–271.
14. Głuszek, A.; Magiera, J.; Neupauer, K. Analiza cyklu życia (LCA) cieczowego kolektora słonecznego. *Inżynieria Apar. Chem.* **2010**, *49*, 35–36. (In Polish)
15. Koroneos, C.J.; Nanaki, E.A. Life cycle environmental impact assessment of solar water heater. *J. Clean. Prod.* **2012**, *37*, 154–161. [CrossRef]
16. Altun-Ciftcioglu, G.A.; Gokulu, O.; Kardigan, F.; Kardigan, M.A.N. Life cycle (LCA) of solar selective surface produced by continuous process and solar flat collectors. *Sol. Energy* **2016**, *135*, 284–290. [CrossRef]
17. Comodi, G.; Bevilacqua, M.; Caresana, F.; Paciarotti, C.; Pelagalli, L.; Venella, P. Life cycle assessment and energy-CO₂-economic payback analyses of renewable domestic hot water systems with unglazed and glazed solar thermal panels. *Appl. Energy* **2016**, *164*, 944–955. [CrossRef]
18. Milousi, M.; Souliotis, M.; Arampatzis, G.; Papaefthimiou, S. Evaluating the Environmental Performance of Solar Energy Systems Through a Combined Life Cycle Assessment and Cost Analysis. *Sustainability* **2019**, *11*, 2539. [CrossRef]
19. Mahmud, M.A.P.; Huda, N.; Farjana, S.H.; Lang, C. Environmental Impacts of Solar-Photovoltaic and Solar-Thermal Systems with Life-Cycle Assessment. *Energies* **2018**, *11*, 2346. [CrossRef]
20. De Laborderie, A.; Puech, C.; Adra, N.; Blanc, I.; Beloin-Saint-Pierre, D.; Padey, P.; Payet, J.; Sie, M.; Jacquin, P. Environmental Impacts of Solar Thermal Systems with Life Cycle Assessment. In *The World Renewable Energy Congress*; Linköping University Electronic Press: Linköping, Sweden, 2011; pp. 8–13. Available online: <https://hal-mines-paristech.archives-ouvertes.fr/hal-00668172/document> (accessed on 10 May 2021).

21. Barbir, F. Fuel Cell Applications. In *PEM Fuel Cells, Theory and Practice*, 2nd ed.; Barbir, F., Ed.; Academic Press: Cambridge, MA, USA, 2013; pp. 373–434.
22. Astudillo-Flores, M.; Zalamea-Leon, E.; Pelaez-Samaniego, A.B.E.M.; Calle-Siguencia, J. Modelling of solar thermal energy for household use in equatorial latitude by using the F-Chart model. *Renew. Energy Power Qual. J.* **2021**, *19*, 269–275. [CrossRef]
23. Jolliet, O.; Margni, M.; Charles, R.; Humbert, S.; Payet, J.; Rebitzer, G.; Rosenbaum, R. IMPACT 2002+: A New Life Cycle Impact Assessment Methodology. *Int. J. LCA* **2003**, *8*, 324–330. [CrossRef]
24. Frischknecht, R.; Wyss, F.; Knöpfel, S.B.; Lützkendorf, T.; Balouktsi, M. Cumulative energy demand in LCA: The energy harvested approach. *Int. J. Life Cycle Assess.* **2015**, *20*, 957–969. [CrossRef]
25. Energy Regulatory Office. Available online: <https://www.ure.gov.pl/en> (accessed on 4 May 2021).

MDPI
St. Alban-Anlage 66
4052 Basel
Switzerland
Tel. +41 61 683 77 34
Fax +41 61 302 89 18
www.mdpi.com

Energies Editorial Office
E-mail: energies@mdpi.com
www.mdpi.com/journal/energies



MDPI
St. Alban-Anlage 66
4052 Basel
Switzerland
Tel: +41 61 683 77 34
www.mdpi.com



ISBN 978-3-0365-7368-7